Shallow Magmatic Plumbing Systems and Edifices of Monogenetic Volcanic Fields

Charlotte Elizabeth McLean
BSc (Hons)

Submitted in fulfilment of the requirements for the Degree of Doctor of Philosophy

School of Geographical and Earth Sciences

College of Science and Engineering

University of Glasgow

April 2017

Abstract

Magmatic plumbing systems of monogenetic volcanic fields comprise an interconnected network of sills, dykes and inclined sheets; however, the morphology, distribution and emplacement mechanisms of these shallow plumbing systems are often overlooked due to the lack of observable field data. Using seismic data provides an opportunity to understand these systems and integrate seismic-scale features with macro-scale observations from the field.

Using a seismic dataset from the Faroe-Shetland Basin, NW Scotland, the Ben Nevis Monogenetic Volcanic Field (BNVF), this research provides an insight into how monogenetic volcanic fields are fed, and how the distribution of edifices can be primarily influenced by the structure of the substrate. By comparing the seismic data with field observations from three separate field studies, this research focuses in on the shallow, ductile zone (<1 km) between the feeding intrusion(s) and the volcanic edifice, in order to determine the processes that occur during emplacement at a sub-seismic scale. This study provides a comprehensive assessment of the features of very shallow plumbing systems (<200 m) within a variety of water-saturated settings, including: passive and dynamic peperite (blocky and fluidal); R-T structures; clastogenic dykes; gas cavities; slurry cavities; protopillows and subsurface pillows; aligned intrusive pods; volcaniclastic injectites; and magma lobes and fingers.

The range of features displayed within the four case studies demonstrates that a variety of processes affect the emplacement of magma in the ductile zone. These processes include: (1) exploiting preferential horizons by host-rock fluidisation; (2) exploiting boundaries in the host-rock by the rotation of principal stresses; (3) explosive magmatic degassing; (4) cooling–contraction fragmentation; (5) explosions caused by rapid vapourisation of porewater; (6) a variety of molten fuel-coolant interactions (non-explosive to highly explosive); and (7) density contrasts.

Monogenetic volcanic fields and their plumbing systems have been identified in reflective seismic data in exploratory offshore sedimentary basins (e.g. Southern Australia Margin and the NE Atlantic Margin). This research presents unprecedented quantitative analysis of the thermal influence of diatremes using a range of techniques (vitrinite reflectance analysis, Raman spectroscopy and fluid inclusion techniques) to produce local isothermal models of the host-rock surrounding diatremes.

This aims to provide a better understanding of the overall thermal effect of monogenetic plumbing systems on reservoir porosity and permeability, and source maturity.

Table of Contents

List of Figures

List of Tables

Acknowledgements

This research was funded by a University of Glasgow, College of Science and Engineering Scholarship. Several grants were obtained to supplement this scholarship including: the Sir Alwyn Williams Postgraduate Scholarship for 6 months of seismic interpretation at the University of Aberdeen; a Mineralogical Society Postgraduate Student Bursary for fieldwork in Iceland; and the Timothy Jefferson Field Research Fund from the Geological Society of London for fieldwork and fluid inclusion analysis at the University of Aberdeen.

Whilst undertaking my PhD, I was knocked down by a motorbike in Malaysia, fell off a cliff in Fife and underwent cardiothoracic surgery so I would like to say thank you to some people for all their support in the last three and a half years. I would first like to thank my supervisors, Davie and Nick. Davie, thank you for showing me the importance of field geology; showing me that field studies should not be deemed "old-fashioned" and resigned to the dusty corners of geological science; teaching me that fieldwork is still incredibly important, applicable and scientifically valid. I really appreciate all the advice, support, comradery, and knowledge you have imparted. Nick, thank you for all the insight into the world of academia and the O&G industry.

Many thanks also go to Brian Bell, Rod Brown and the other staff members on the Ardnamurchan field course (Rhian Meara, Iain Allison, John MacDonald, Daniel Koehn) for their esteemed wisdom and experience, usually divulged on the slopes of Ben Hiant or at the front of a minibus. I have learned an incredible amount from observing how you teach and interact with students. I would also like to thank Dave Muirhead at the University of Aberdeen, for his assistance and perseverance with the fluid inclusion and Raman analysis. A special mention to the technicians, John Gilleece, Robert MacDonald and Kenny Roberts, at the University of Glasgow, and Nic Odling at the University of Edinburgh for providing thin sections, lab assistance, crushing rocks, providing field equipment and XRF training. Statoil are thanked for providing the Brendans Dome 3D volume. PGS are thanked for donation of the CRRG 2D GeoStreamer® data used in Figure 3.3. I would also like to thank the VMRC, for allowing me the opportunity to attend several field courses and workshops.

I would like to thank the members of Vo@G (Jonny, Sapphire, Pamela, Katie and Iain) and the members of the VMRC (Sam, Kirstie, Pete, Bansri) for all the useful discussions and informal chats in the pub. In particular, thanks to Jonny for all the banter on fieldwork. Thanks also to Ann at Grannies Harbour B&B in St. Monans, providing a warm, cosy home away from home after rainy days in the field and a special mention to the paramedics that salvaged my field notebooks from impending doom.

To the other PhD students (Jill, Eric, Rebecca, Caroline, Callum, Sarah, Heidi, Kirsty, Crystal), the chat in the PG office and pub was always a welcome distraction and having your experience on hand was extremely valuable. Cat, Jen, Jenna, Pooja and Laura, you dragged me out of PhD-world and reminded me there's a life on the other side. Thank you for the field assisting and support which has been incredible over the last three years. A few special thanks are given to:

Doug. Thank you for all our discussions that encouraged me to expand my thinking and broaden my mind. With your constant, fiercely uncompromising faith in me, you made me believe I could take on the world.

Heather. One of the greatest assets I have gained from this PhD, is my friendship with you. From Mountain Home adventures, to trekking the Sumatran jungle and scuba diving in paradise, you have always been there to offer support, advice, welcome distractions and buckets of coffee and cake. I said it on our first fieldtrip together in 2013 and I'll say again now: You are and will always be my yoda.

Paul. Our adventures gave me breathing space during the hard slog of writing and gave me something to work toward which I am so grateful for. You pulled me out of the darkness on my lowest ebbs and offered reassurance at the end of every single day. Your patience, kindness and generosity are a testament to the wonderful man you are.

The most important thank you goes to my family, especially my mum and sister. There's no words to describe how your support and inspiring strength has bolstered me through this PhD. Your tough love prompted me to just get on with things even when it all seemed impossible. Thank you for

inspiring me and supporting me to embrace the adventure of life, to break away from the ordinary and to follow my dreams, whichever path that takes. I hope I've made you proud.

I wish to dedicate this to my wonderful gran who passed away in the last few weeks of writing this thesis. I was so excited to show her the finished article but unfortunately this wasn't to be. She meant so much to me and was everything I aspire to be as a woman. I wouldn't be the person I am today without her. She was an incredibly special person and I am so proud to be her granddaughter.

Author's Declaration

I declare that this thesis, except where acknowledged to others, represents my own work carried out in the School of Geographical and Earth Sciences, University of Glasgow. The research presented here has not been submitted for any other degree at the University of Glasgow, nor at any other institution. Any published or unpublished work by authors has been given full acknowledgement in the text.

Charlotte E. McLean

Chapter 1 Introduction

An increasing amount of evidence compiled in recent decades supports the assertion that the shallow magma plumbing systems beneath monogenetic volcanic fields are far more complex than the dyke-dominated systems first suggested (Németh et al. 2003; Németh and Martin 2007; Johnson et al. 2008; Németh 2010; Brown and Valentine 2013; Re et al. 2015; Albert et al. 2016; Muirhead, J.D. et al. 2016a). The research discussed here employs several techniques to study the morphologies of intrusions and intrusion networks in the shallow subsurface and within monogenetic edifices, explores the influence of water in shallow magma emplacement beneath monogenetic volcanic fields, provides evidence for the role of host-rock structure in edifice distribution, and investigates the effects of diatreme formation on host-rock.

This research focuses on three extinct monogenetic volcanic fields: the Upper Palaeocene Ben Nevis Monogenetic Volcanic Field in the Faroe-Shetland Basin, offshore Scotland; two Upper Pleistocene monogenetic edifices along the south coast of Iceland (Dyrhólaey and Reynisdrangar); and several Upper Carboniferous-Lower Permian diatremes in a monogenetic field in East Fife, Scotland. The findings of this research have implications for our global understanding of the plumbing systems beneath monogenetic volcanic fields. It can also provide significant information on the volcanic risk to urbanized areas within active monogenetic fields (e.g. Mexico City, Mexico and Auckland, New Zealand); for example, uplift and overburden deformation owing to the lateral emplacement of intrusions pre-eruption. In addition, this study, aims to add to the growing understanding of how magmatic systems can affect hydrocarbon basins (Schutter 2003). The study of monogenetic volcanism and the processes that occur in their formation and distribution are, therefore, significantly important to understand both for scientific reasons and societal ones.

1.1. Research Rationale

Geochemical analysis of monogenetic magmatic systems often assumes a vertical magmatic system, where the magma reservoir is located directly below the volcanic edifice, and does not always consider the structure and spatial distribution of monogenetic plumbing systems in the shallow subsurface (Figure 1.1) (Németh et al. 2003; Johnson et al. 2008; Smith et al. 2008; Kereszturi &

Németh 2012; Albert et al. 2016; Magee et al. 2016). Recent field studies of eroded plumbing systems (Ferrar-Karoo, South Africa and Antarctica; Pauite Ridge, Nevada, USA; Hopi Buttes, Arizona, USA; Western Hungary) demonstrate that sills and inclined sheets play a significant role in magma storage and transport in the shallow subsurface beneath monogenetic volcanic fields (Valentine and Krogh 2006; Németh and Martin 2007; Polteau et al. 2008; Muirhead, J.D. et al. 2012; Re et al. 2015; Magee et al. 2016; Muirhead, J.D. et al. 2016a). Often these field studies, however, do not fully demonstrate the complexity of the plumbing system due to incomplete exposure. Reliance on geochemical analysis and inadequate field exposures can, therefore, prevent a comprehensive assessment of the intrusion characteristics, lateral migration of magma, magma interaction with crustal structures and, spatial and temporal development of shallow plumbing networks beneath monogenetic volcanic fields from being developed (Magee et al. 2016; Muirhead, J.D. et al. 2016a).

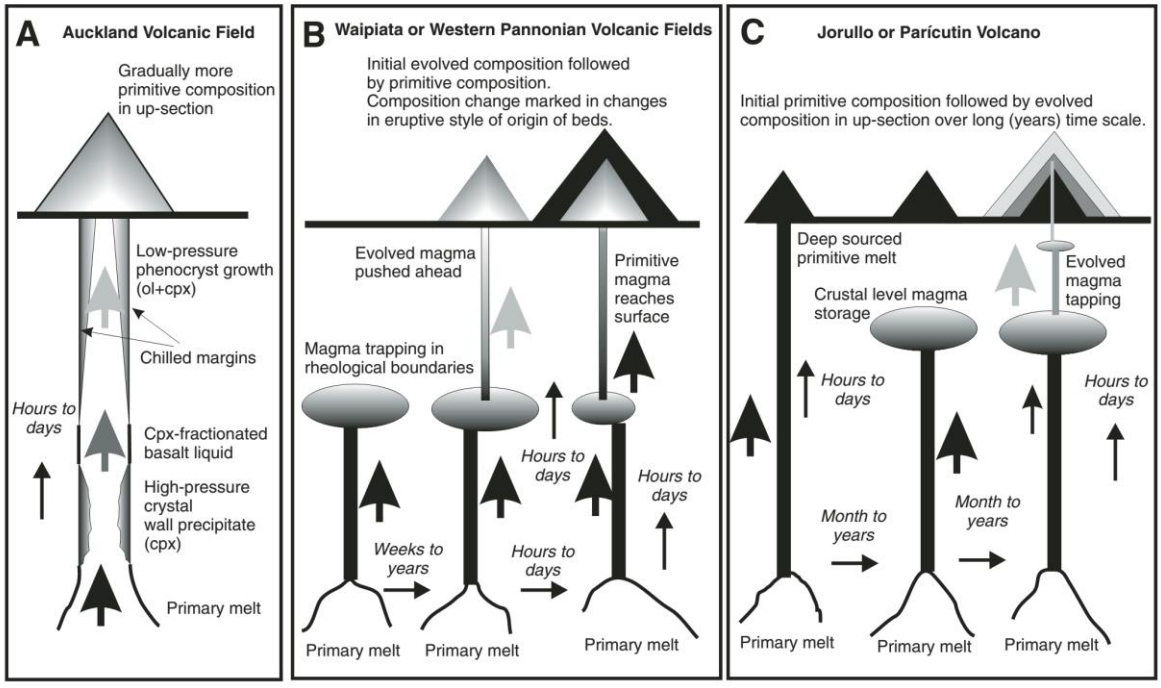

Figure 1.1: Typical theoretical models of the plumbing system of monogenetic volcanoes based on geochemical data. Geochemical models tend to assume a vertical plumbing system and disregard any potential lateral migration of magma. From Németh (2010). Evolved compositions are represented by light grey shading and primitive compositions are represented by black shading. (A) Model based on Crater Hill in the Auckland Volcanic Field, New Zealand (Smith et al. 2008) where magmas evolve from an evolved magma to a primitive composition during a single uninterrupted eruption. (B) Model based on the western Pannonian Basin, Hungary (Németh et al. 2003) where magmas evolve from an evolved magma to a primitive composition during a dual-phase eruption. (C) Model based on Parícutin and Jorullo, Mexico (Johnson et al. 2008) where magmas evolve from a primitive magma to a more evolved composition over a relatively long timescale (for a monogenetic edifice).

Understanding the plumbing system structure beneath monogenetic volcanic fields is important as it can provide significant insight into the following aspects: (1) the dominant control on the distribution of monogenetic volcanic edifices (e.g. tectonic stress orientation versus local crustal structure) and, therefore, assessment of the location of the next eruption centre in an active field (Buck et al. 2006; Le Corvec et al. 2013); (2) the estimated total magma volume in a system (Richardson et al. 2015; Muirhead, J.D. et al. 2016a); (3) the geochemical evolution of magmas and potential magma stalling or assimilation sites (Németh et al. 2003; Johnson et al. 2008; Smith et al. 2008; Albert et al. 2016); (4) the distance of lateral migration of magma from 'source' to surface (Muirhead, J.D. et al. 2012, 2016b; Airoldi et al. 2016; Magee et al. 2016); (5) controls on the emplacement mechanics and geometry of intrusions (Thomson and Schofield 2008; Lefebvre et al. 2012; Schofield et al. 2012; Kavanagh et al. 2015; Re et al. 2016); and (6) magma-water interaction which is particularly prevalent in the shallow subsurface (Kokelaar 1982; Wohletz 1986). It is, therefore, vital that a comprehensive approach to understanding shallow monogenetic plumbing systems is undertaken, and that this approach considers the plumbing system at a range of scales.

By comparing seismic data with field observations, this research is able to understand complex plumbing systems at a basin scale as well as zooming-in on the characteristic features of plumbing systems at macroscopic and microscopic scales. The research focuses on the shallow sub-surface zone (<1 km), to better understand ductile emplacement intrusion characteristics, to determine the processes that occur between the magma reservoir and the edifice, to better understand the the structure of monogenetic edifices, and to determine the effects of diatreme emplacement on the host-rock.

1.1.1. **Ductile intrusions**

The reconstruction of plumbing systems under volcanic edifices, using kinematics, fluid mechanics petrology and rheology studies (e.g. Galland et al. 2006, Kavanagh et al. 2006, Menand 2008, Goulty et al. 2008, Daniels et al. 2012), is important in understanding the complexity and morphologies of sub-surface intrusive networks. As magma enters the so-called "soft-rock" environment (weak host-rock and/or sediment) ponding becomes more frequent as density contrasts and significant lithological differences between host-rock strata control emplacement mechanism (Lorenz and

Haneke 2004). At shallow depths (<1 km), the sediment/rock is typically more water saturated and may be unconsolidated or partially unconsolidated. These conditions support ductile magma emplacement and sub-surface magma-water interaction (non-explosive to phreatomagmatic explosions; Kokelaar 1986), which can promote the formation of peperite, host injectites and irregular intrusion characteristics. The transition from hard-rock to soft-rock, therefore, has an important influence on how magma is emplaced into this shallow zone, and how it fragments as it approaches volcanic edifices (Schofield et al. 2010).

Due to poor preservation of this zone and limited studies of such shallow intrusions, the detail of these feeder systems has not been investigated fully. The mechanisms of magma emplacement are well documented within literature, including the differences between ductile and brittle emplacement mechanisms and the formation of magma fingers and lobes (e.g. Schofield et al. 2012), yet the descriptors of intrusions emplaced by ductile mechanisms is usually limited to "highly irregular" dykes or some such. This research (Chapters 4-6) has catalogued the features of intrusion emplacement by ductile mechanisms and highlights the processes and products that are evident within the very shallow subsurface.

1.1.2. **Edifice construction**

Monogenetic edifices take on a series of forms depending on the availability of water. Depending on conditions such as water-saturation, consolidation and depth of substrate, magma extrusion at the surface can create tuff cones, tuff rings, tindars, tuyas, maar-diatremes and scoria cones (White et al. 2000; Jerram and Stollhofen 2002; Ross et al. 2005; McClintock and White 2006). We often look upon monogenetic deposits to determine the mechanisms of magma-water interaction and fragmentation however, recently White and Valentine (2016) have suggested relying on a range of tephra characteristics can be somewhat inaccurate. This research (Chapters 4-6) describes three original examples of monogenetic edifices in water-saturated environments to better understand the construction of these edifices and the processes of magma emplacement in edifices during monogenetic eruptions. Investigating intrusion features can help to deduce the type of magma-water interaction that occurs and the environmental conditions during magma emplacement (e.g. confining pressure, water-saturation, amount of fuel-coolant mixing and magma-water ratios).

1.1.3. **Hydrocarbon systems.**

Globally, monogenetic volcanism is the most common and widespread type of volcanism, forming in all tectonic environments, yet it is only within the last decade or so that monogenetic volcanic fields have been readily identified in reflective seismic data in exploratory and producing offshore sedimentary basins (due to improvements in seismic resolution), including the Southern Australian Margin and the NE Atlantic Margin (Figure 1.2) (Hansen 2006; Jackson 2012; Magee et al. 2013; Schofield et al. 2015; Reynolds et al. 2016; McLean et al. 2017). It is, therefore, imperative to consider the impact of such volcanic systems on the thermal and hydrothermal history of sedimentary basins.

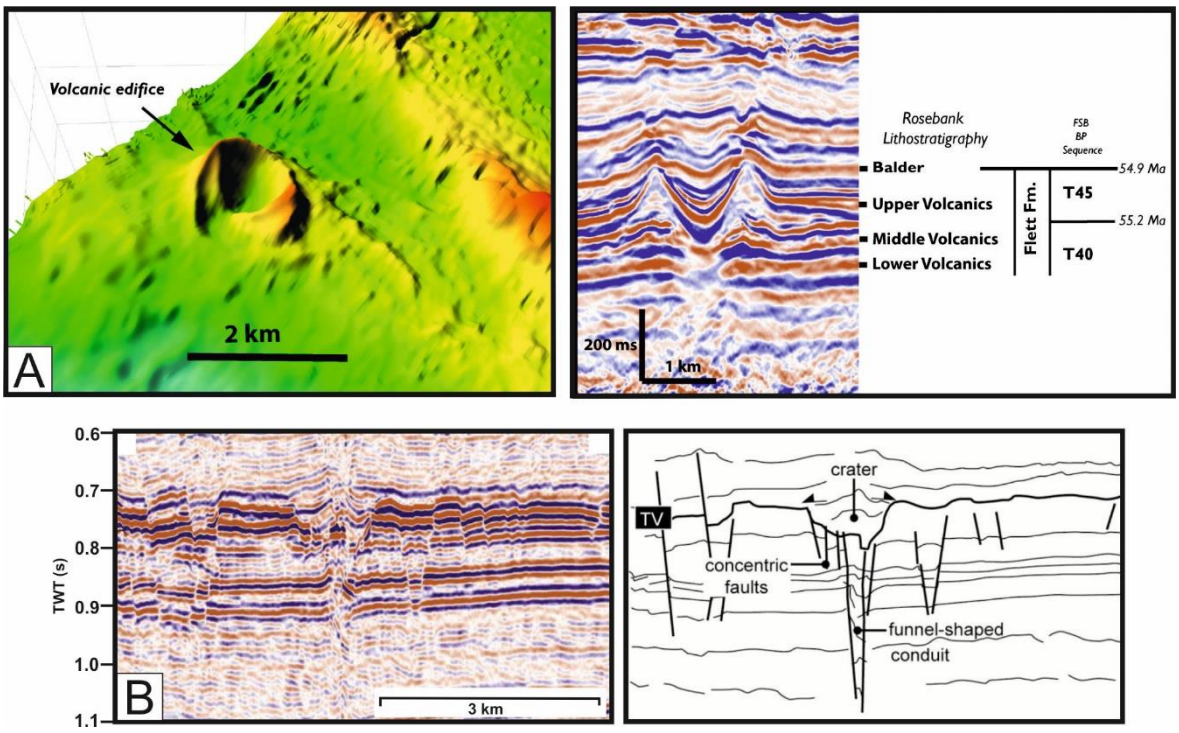

Figure 1.2: Examples of monogenetic edifices within areas of active petroleum exploration. (A) Seismic line through a 2 km scoria cone edifice from the Rosebank Field, Faroe-Shetland Basin, NE Atlantic Margin. Image on the left shows the central crater. From Schofield et al. (2015). (B) Seismic data through a maar crater showing the underlying diatreme from the Bass Basin, Southern Australian Margin. From Reynolds et al. (2016).

There are many studies that have assessed and quantified the thermal effects of magmatic intrusions and how these heating effects can modify the characteristics of the host-rock, for example the organic matter maturation, porosity and permeability (Raymond and Murchison 1991; Barker et al. 1998; Ahmed 2002; Suchy et al. 2004; Cooper et al. 2007; Fjeldskaar et al. 2008; Santos et al. 2009; Muirhead, J.D. et al. 2012; Senger et al. 2014; Schofield et al. 2015). However, in establishing the

overall thermal effect of the plumbing systems on sedimentary basins, one aspect of the plumbing system has been significantly overlooked: diatremes.

Maar-diatremes are the second-most common type of volcanic landform after scoria cones yet little is known about the thermal, hydrothermal and physical effects of diatreme formation on the surrounding host-rock (e.g. Wood 1980; Cas and Wright 1987; Wohletz and Heiken 1992; Ross et al. 2013). Diatremes form when magma explosively interacts with groundwater in the sub-surface (White and Ross 2011). This explosive interaction forms conical-shaped structures in excess of 1500 m deep in the subsurface, filled with brecciated host-rock, dyke fragments and juvenile material (Lorenz 1986). During formation continuous emplacement of dykes into the structure feeds further explosive eruptions in the subsurface and at, or near, the surface (Valentine and White 2012). Diatreme formation causes extensive physical and thermal disruption to the host-rock, which can potentially alter fluid migration pathways and the porosity and permeability of the substrate. This disruption is significant if it affects either reservoir quality sands or seals, or the early maturation of source rocks. Until now, there has been no significant or thorough investigation into the thermal effects of diatreme formation on host-rock. This research (Chapter 7) documents the mechanisms of physical disruption surrounding several diatremes and uses various techniques (vitrinite reflectance, Raman spectroscopy and fluid inclusions analysis) to assess the heating effects of diatreme formation.

1.2. Research Aims and Objectives

In order to gain a comprehensive understanding of the emplacement of magma in the shallow subsurface the following research objectives have been set:

a) To better understand how magma migrates in the shallow sub-surface and feeds monogenetic volcanic edifices through detailed analysis of 3D seismic data. In particular, analysing the varying effects of host-rock lithology and structure on magma emplacement and gaining a better understanding of how these factors affect the distribution of monogenetic volcanic edifices.

b) To recognise the connectivity of shallow monogenetic plumbing systems using both seismic data and field data. This has implications for the geochemical and the petrological signature of magma erupted from monogenetic volcanoes.

c) To document and characterise the geometries, scales and morphologies of shallow-level intrusions that have been emplaced by ductile mechanisms. Assess how magma-water interaction plays a role in the shallow subsurface and document how this affects intrusion morphology and fragmentation.

d) Comprehensively map, log and record the monogenetic edifices which the intrusions are emplaced into (three field case-studies), to better understand the eruption histories of the edifice prior to and during magma emplacement. This will also help to understand the characteristics of the host-rock during magma emplacement and allow an assessment of environmental conditions (e.g. confining pressure, magma-water ratios and magma-host mixing) suitable for certain intrusion features.

e) Use the field studies to determine the sub-seismic characteristics of shallow plumbing systems in order to aid recognition of the impact of monogenetic volcanism in hydrocarbon-bearing volcanic basins.

f) To better understand the effects of monogenetic plumbing systems on sedimentary basins, particularly the effects of diatreme formation which has never been examined quantitatively before.

1.3. Methods

1.3.1. **Reflective seismic (adapted from McLean et al. 2017)**

Work on the Ben Nevis data (Chapter 3) was undertaken using Kingdom seismic software and required accurate seismic picking of multiple horizons, correlating well data with seismic, interpretation of sill and vent geometries, and acquisition of high-quality images. Significant horizons were picked to constrain the basin structure, including top volcanic and base volcanic, top of the Cretaceous (Ben Nevis Structure), sills and the Balder Formation, a formation containing multiple tuff horizons.

The high acoustic impedance (the product of seismic velocity and density of a rock) between igneous material (intrusions, lavas, tuffs) and surrounding sedimentary host-rock allows for good imaging of igneous features (Neidell 1979; Bell & Butcher 2002; Smallwood & Maresh 2002; Schofield et al. 2015). Intrusions, in particular, are easily identified owing to their lateral discontinuity with host-rock, high-amplitude seismic reflectors and lateral limitation (Thomson & Schofield 2008). The 3D data presented in Chapter 3 is time-migrated, zero-phase with European polarity, seismic reflection data. The inlines and crosslines are oriented NW–SE and NE–SW respectively, with spacings of 25 m between inlines and crosslines. It is important to note that below the depth of >2000 m, low seismic resolution and overlying basalt cover restricts imaging of single intrusions less than c. 40 m thick (Schofield et al. 2015). Schofield et al. (2015) suggested that because of the depth of many sills within the contemporaneous basin fill of the Faroe–Shetland Basin, seismic data can omit up to c. 88% of the sills within a basin and therefore capturing the full complexity of the sill complex can be difficult, although major magma conduits can be assessed.

Using 3D volume visualization techniques, such as opacity rendering, the morphology of the key volcanic features is constrained. Opacity rendering allows the transparency of particular amplitudes to be separately controlled, which is highly effective when considering mafic igneous bodies, as they tend to demonstrate much higher acoustic impedance than the surrounding rock (Bell & Butcher 2002; Schofield et al. 2015). Spectral decomposition is also used. This imaging technique uses frequency domains to image time–thickness variability of seismic reflection data (McArdle & Ackers 2012). Application of this technique, which produces enhanced images of the subsurface, has recently been useful in analysing volcanic vents and lava distribution patterns in the Faroe– Shetland Basin (Schofield & Jolley 2013; Wright 2013).

1.3.2. **Fieldwork**

The three field sites discussed in Chapters 4, 5 and 6 were chosen for the following reasons:

- High-levels of exposure to fully record subsurface intrusions.
- A range of monogenetic edifices formed by varying levels of magma-water interaction, to be able to compare and contrast with seismic data.

- Pervasive intrusions with a variety of intrusion morphologies and features.

The fieldwork involved producing small-scale (tape and compass mapping) and 1:5000 maps (where appropriate), stratigraphical logs of the host-rock stratigraphy and eruption deposits, clast counts of eruption deposits (using a 100 cm x 100 cm square grid, taking 100 readings per count), and recording detailed descriptions of the different lithofacies at each locality. Rock samples were collected for petrographical analysis and include intrusions, eruption deposits, host-rock deformation and peperite.

1.3.3. **Samples and Petrography**

Thin sections were prepared from samples taken from the three field localities (Chapter 4, 5 and 6) at the University of Glasgow for petrographical analysis. All 30 μm thick, unpolished thin sections were analysed using a polarising microscope and photomicrographs were collected using an Olympus DP25 camera.

1.3.4. **XRF**

Basalt samples were collected from the East Fife field locality and analysed using XRF in Chapter 6. Samples were analysed for major and trace elements (although only major elements are used within this thesis) at the School of GeoSciences at the University of Edinburgh. Major element concentrations are measured on fused glass discs prepared by a method similar to that of Norrish and Hutton (1969) and outlined here.

Samples were crushed and ground to a very fine powder. The powder was dried at 110 °C overnight. A representative of each sample (0.9 g and 1.0 g) was placed inside individually weighed crucibles. A lid was placed on each crucible and the crucible was ignited at 1100 °C for 20 minutes. The crucibles were then swirled and transferred to a cooling block in a desiccator for 10 minutes and subsequently reweighed. The flux addition was calculated as five times the weight of the original sample weight plus 0.03 g (to anticipate loss of volatiles from the flux). The flux used was Spectroflux 105 which consists of a mixture of 47% lithium tetraborate, 37% lithium oxide and 16% of La_2O_3 as a x-ray heavy absorber. The calculated flux was added to each crucible and mixed with the samples with a small spatula. A lid was placed on each crucible and ignited at 1100 °C for 20 minutes until the sample and flux are completely dissolved. Again, the crucibles are removed from the furnace,

swirled and transferred to a cooling block in a desiccator for 10 minutes. The crucibles are then reweighed and flux is added to the exact target weight calculated. The weight must be recorded to within ±0.0003 g. A lid is placed on each crucible and re-fused on a meker burner for approximately 3 minutes, whilst continuously swirling the sample. The samples are then cast onto graphite discs on a hot plate set to 220 °C using an Al plunger and steel guide ring. The glass discs anneal under the glass cover and are moved to a cooler hot plate (110 °C) after 10 minutes, where they remain until cooled after approximately 10 minutes. The excess glass from the disc rim is trimmed and the samples labelled. The discs were analysed using a Philips PW2404 wavelength dispersive sequential X-ray spectrometer with a Rh anode end window X-ray tube.

1.3.5. **Vitrinite Reflectance**

Vitrinite reflectance (%R) was used to analyse the thermal maturity of shale samples from the East Fife field locality in Chapter 7. Vitrinite reflectance is a measurement of the percentage of light reflected off a vitrinite maceral, an organic component of coal or shale. The reflectivity of vitrinite macerals increases in response to thermal alteration and is used to define maturity levels and predict the thermal history of organic-rich rocks (Marshall et al. 1994). Aromatization of carbon occurs during heating which causes the increase in reflective properties. Vitrinite reflectance of shale samples in Chapter 7 was undertaken by GHGeochem. The procedure followed the methodology of Barker (1983).

1.3.6. **Raman Spectroscopy**

Raman spectroscopy was used to analyse shale samples from the East Fife field locality in Chapter 7. As carbonaceous rocks are thermally altered, the carbon undergoes a series of reactions which reorders the chemical structure towards a stacked arrangement, known as graphite (Tuinstra & Koenig 1970; Landis 1971; Nemanich & Solin 1979; Knight & White 1989; Ferrari & Robertson 2001; Beyssac et al. 2002; Muirhead, D.K. et al. 2016). Quantification of this structural reordering, and hence the amount of thermal alteration, is based on several parameters of two broad first order Raman bands (spectral peaks): (1) the G peak (graphite peak, also known as the O peak) at c. 1585 cm^{-1}, and (2) the D peak (disordered peak) at c. 1350 cm^{-1} (Figure 1.3) (Muirhead, D.K. et al. 2016). The G peak is composed of several amalgamated spectral peaks at 1615 cm^{-1}, 1598 cm^{-1}, and 1545

cm^{-1}. Peak deconvolution is implemented on the G peak as it is not possible to separate these bands in disorganised carbon (Beyssac et al. 2002).

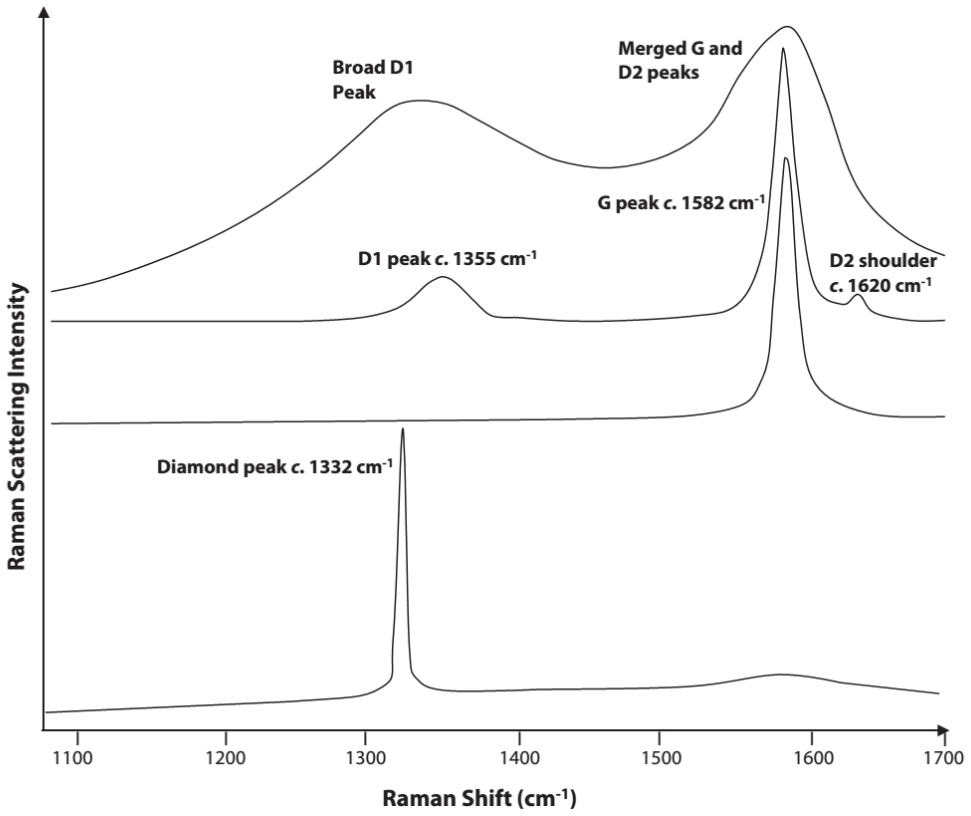

Figure 1.3: Graphical summary of Raman spectral features. Top plot: very disordered carbon with a broad D peak and a merged G peak, indicating a relatively thermally unaltered rock. Middle-top plot: Increasingly more ordered carbon with a small D peak and shoulder peak beyond the G peak. Middle-bottom plot: Ordered graphite with a single G peak at 1582 cm^{-1}. Bottom graph shows the diamond peak. From Muirhead, D.K. et al. 2016.

Ten representative shale samples were collected from the host-rock the East Fife case study at varying distances from the diatreme margin. A control sample was taken at a locality that was remote from any igneous intrusions or diatremes which may have enhanced the thermal alteration of the rocks in their immediate vicinity. Raman measurements were performed on whole rock samples on a Renishaw inVia reflex Raman spectrometer at the University of Glasgow. Whole-rock samples were used to prevent inaccurate data due to polishing (Mostefaoui et al. 2000). A Leica DMLM reflected light microscope was used to centre the Ar+ green laser (wavelength 514.5 nm). The laser power was between c. 0.15 and 0.3 mW. A charge-coupled device detector recorded the dispersed scattered light. Data was centred on 1400 cm^{-1} and collected between 1000 and 2000 cm^{-1} with a spectral resolution <3 cm^{-1}. The duration of the accumulations was typically up to 2 s for three accumulations per reading. Ten readings were obtained from each sample (where possible).

To ensure the sample did not experience any laser-induced heating or alteration, the laser power was gradually increased per sample. The sample was also carefully analysed using the microscope before and after heating to check for signs of heating (e.g. holes) that may disrupt the accuracy of the reading. The procedure for spectral deconvolution followed the methodology of Muirhead, D.K. et al. (2016). The Renishaw WiRE 2.0 curve-fitting software was used for spectral deconvolution. Smoothing and baseline extractions were completed on each sample, including a cubic spline interpolation with peak-fitting using a combination of Gaussian and Lorentzian algorithms (Bonal et al. 2006). To remove any background signal and to ensure reproducibility, each sample was deconvoluted at least three times. The peak position of the G peak and the peak full-width at half-maximum (FWHM-G) were measured in wavelength (cm^{-1}).

1.3.7. **Fluid Inclusion Analysis**

Fluid inclusion analysis was used in Chapter 7 to analyse the thermal history of sandstone samples from the East Fife field locality. Fluid inclusion microthermometric analysis is used for estimating the timing, pore fluid origin and temperature of several diagenetic minerals in reservoir rocks (Walderhaug 1990; Barker and Goldstein 1990; Tobin and Claxton 2000). Fluid inclusions record the minimum temperature of precipitating fluids during quartz cementation (amongst other uses) and can constrain the possible sources of quartz or calcite cement. Fluid inclusions are typically concentrated at the boundaries between quartz grains and quartz overgrowths (Walderhaug 1990, 1994). By measuring the homogenisation temperature of fluid inclusions (T_h), the temperature at which the fluid inclusion formed can be recorded (Barker and Goldstein 1990).

To measure the T_h, sandstone samples were collected from varying distances from the St. Monans diatreme (Chapter 7). Fluid inclusion wafers (<0.5 mm thick) were produced from the samples and examined on a temperature controlled microscope stage, the THMSG600 heating and freezing stage. Fluid inclusions were microscopically identified and the T_h was analysed by heating the stage. During heating, the fluid inclusion would begin to oscillate and decrease in size. The temperature at which the fluid inclusion was no longer present was recorded. This process was repeated on up to 20 fluid inclusions to get an accurate representative of T_h. The maximum temperature of the heating stage is 330 °C, therefore homogenisation temperatures above this are not recorded accurately.

1.4. Thesis Outline

Chapters 2-8 are briefly summarised below. The individual case-studies (Chapters 3-7) contain an introduction, a geological history of each area, descriptions, interpretations and a separate discussion, highlighting the main outcomes of the chapter. The case-studies presented are all wet monogenetic edifices and examine magma-water interaction in the shallow subsurface and the effects of water on intrusion morphology.

Chapter 2: an introduction to the main themes of this research and relevant literature including: (1) magma emplacement and intrusion characteristics; (2) magma-water interaction; (3) monogenetic volcanic edifices and monogenetic volcanic fields; and (4) host-rock deformation during magma emplacement.

Chapter 3: a 3D seismic study of the Ben Nevis Monogenetic Volcanic Field in the Faroe-Shetland Basin, NW Scotland. This study highlights the complex and interconnected network of intrusions that form the plumbing system beneath the monogenetic volcanic field. This chapter highlights the importance of underlying basin structures in influencing the sites and development of sub-aerial monogenetic fields and provides an example of a monogenetic plumbing system in the shallow subsurface (200 m to 2 km). The following chapters (Chapter 4, 5 and 6) offer field studies of the plumbing systems at the sub-seismic scale.

Chapter 4: a field study of an eroded Upper Pleistocene tuff cone and tuff platform situated at Dyrhólaey on the south coast of Iceland. This case-study investigates the development of the Dyrhólaey tuff cone platform, how magma is emplaced into tuff platforms and feeds subsequent eruptions. This chapter focuses on the controls of magma emplacement in emergent volcanic islands, where host-rock tends to be water-saturated. A basic continuum of the explosivity of magma-water interaction is presented.

Chapter 5: a field study of an Upper Pleistocene tindar situated at Reynisdrangar on the south coast of Iceland. The cliff section at Reynisdrangar presents a cross-section through a monogenetic tindar and its associated shallow plumbing system. This case-study investigates how magma is emplaced into a subglacial tindar to feed a continuous monogenetic eruption and how glacial meltwater influences eruption behaviour.

Chapter 6: an extensive field study of five Upper Carboniferous - Lower Permian diatremes along the East Fife coast in Scotland. The coastal exposure at these diatremes allows for the detailed examination of a horizontal cross-section through each diatreme, permitting the analysis and interpretation of the lithofacies and intrusion morphologies within the diatreme structure. This chapter focuses on explosive magma-water interaction and the type and form of intrusions in diatremes.

Chapter 7: This chapter explores the physical and thermal deformation that occurs in the host-rock surrounding diatremes and uses the diatremes in East Fife to illustrate the types and scale of deformation that occurs due to diatreme formation. Using various geothermometers, including vitrinite reflectance, Raman spectroscopy and fluid inclusion analysis, quantification of the heating effect can be obtained.

Chapter 8: a discussion chapter comprising a synthesis of the findings from all of the field studies and discussing the various characteristic features of shallow intrusions. The field and seismic data is incorporated to allow for a more accurate model of shallow plumbing systems, particularly at sub-seismic scale. Having elucidated the features and morphologies of shallow plumbing systems in the seismic data, the relevance and importance of this research, in terms of the volcanological community and the hydrocarbon industry is assessed.

Appendix: Included within the appendix are: (1) a paper published as a case-study into soft sediment deformation in the Bulletin of Volcanology: "Extensive soft sediment deformation and peperite formation at the base of a rhyolite lava: Owyhee Mountains, SW Idaho, USA" (McLean et al. 2016); (2) published seismic data, descriptions and interpretations used in Chapter 3. Published in the Journal of the Geological Society of London: "3D seismic imaging of the shallow plumbing system beneath the Ben Nevis Monogenetic Volcanic Field: Faroe-Shetland Basin" (McLean et al. 2017); (3) Fold out A3 map of the East Fife diatremes in Chapter 6; (4) XRF data used in Chapter 6; (5) vitrinite reflectance data used in Chapter 7; and (6) the Raman spectra used in Chapter 7.

Chapter 2 Geological Background

This chapter introduces the terminology and basic concepts that form the foundations for this research. It is important to note that this chapter is not exhaustive, and serves as a summary to the many processes and products of magma emplacement in the shallow subsurface. Intrusion emplacement has been extensively studied using a variety of modelling techniques, including numerical, experimental and field. This review introduces the mechanisms of magma emplacement highlighting how changes in host-rock affect intrusion morphology and the differences between brittle and ductile emplacement processes. It also highlights the processes that occur during magma-water interaction and magma fragmentation in the shallow subsurface and explains the difficulties in identifying the products of each process. The different types of monogenetic edifices are also discussed to understand the differences in formation processes in different environmental settings. Finally, this chapter focusses on the variety of host-rock deformation processes and products that occur during magma emplacement, which is an important factor in determining how shallow intrusion emplacement affects hydrocarbon systems. Discussions of the regional geology are contained in the appropriate chapters.

This study will use the classification of Muirhead, J.D. et al (2012) to define intrusions depending on their inclination angle: dykes are inclined to an angle >70°, sills at an angle <10°, and inclined sheets somewhere between the two end members. Primary volcaniclastic terminology of White and Houghton (2006) is used to describe the deposits of monogenetic eruptions.

2.1. Magma emplacement

2.1.1. **Dykes**

Dyke propagation

The rate of emplacement and final geometry of any dyke is determined by a number of factors including: (1) driving and resistive forces; (2) elastic deformation of host-rock; (3) resistance and strength of host-rock; (4) buoyancy of magma; (5) viscosity of magma; and (6) viscosity resistance to flow (Kavanagh et al. 2006, Daniels et al. 2012). As a dyke propagates by brittle failure, a crack must be able to propagate ahead of the magma front (Figure 2.1). To do this, the strength of the

host rock must be less than the stresses around the crack tip, which are controlled by the crack length, l, and the overpressure, P_o, (magma pressure that exceeds ambient stress). For example, the longer a crack is, the easier it is to propagate (McLeod and Tait 1999; Kavanagh et al. 2006; Daniels et al. 2012). For magma to intrude into the crack, magma pressure must exceed elastic pressure, P_e. Therefore, a high magma pressure is needed to deform a host-rock with a high Young's shear modulus (i.e. a host-rock that is rigid) (Kavanagh et al 2006).

Ductile emplacement will occur in host-rock with a low mechanical strength (low Young's shear modulus) e.g. unconsolidated or unlithified rocks in the shallow subsurface (<1.5 km). The progression of intrusions by ductile mechanisms is inhibited by the inability of mechanically weak host-rock to form fractures (Lorenz and Haneke 2004; Schofield et al 2012). Unlithified host-rocks have little or no internal cohesion and so magma can thoroughly disrupt and exploit these units. Disruption is caused by fluidisation at the leading edge of the magma (Figure 2.1). Due to the failure of lithospheric strength, the magma can propagate further through the host-rock by displacing the fluidised sediment from around the leading front (Figure 2.1). This can create a bulbous or blunt front to the intrusions and result in irregular dyke geometries (Figure 2.1) (Brown et al. 2007;

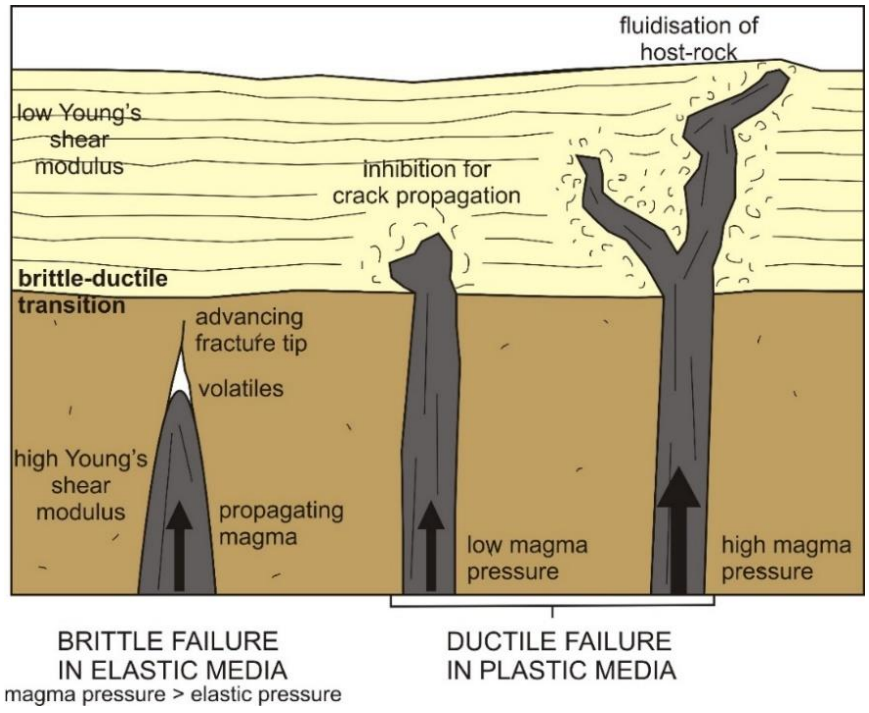

Figure 2.1: Dyke emplacement into an elastic media with a high Young's shear modulus (below) and a plastic media with a low Young's shear modulus (top). In elastic media, a crack propagates ahead of the advancing magma front. Volatiles that have exsolved from the magma may fill a cavity that forms between the propagating crack tip and the magma front (Kavanagh et al. 2006). In the shallow subsurface, in a plastic media, crack propagation is prohibited and dykes advance by fluidising the surrounding host-rock.

Martin and Németh 2007; Schofield et al 2010; Kavanagh and Sparks 2011; Daniels et al. 2012; Schofield et al 2012).

Dyke thickness

Dyke thickness is attained by inflation during emplacement (Lorenz and Haneke 2004). Daniels et al. (2012) suggest that if a dyke passes through a host-rock interface, this trigger can cause a significant vertical change in dyke thickness. This can cause bulging or thinning of the dyke depending on the change of lithostatic strength of the host-rock or -sediment. When dykes pass through a heterogeneous media, the principle stress orientations rotate and the dykes can segment and bifurcate (Daniels et al. 2012).

Dyke buds are widened zones along a dyke and form in two ways: (1) two offset *en echelon* dyke segments re-join increasing the dyke thickness, and (2) a segment of the dyke is thicker than the rest of the dyke (Figure 2.2). Dyke buds are comprised of solidified magma or monolithic breccias, and are surrounded by a carapace of peperite (Delaney and Pollard 1981; Hooten and Ort 2002 White and Ross 2011). Host-rock fragments can be incorporated into the "bud" forming heterobreccias (White and Ross 2011). "Buds" are inferred to represent the root zones of kimberlites and diatremes (Clement 1982; Lorenz and Kurszlaukis 2007).

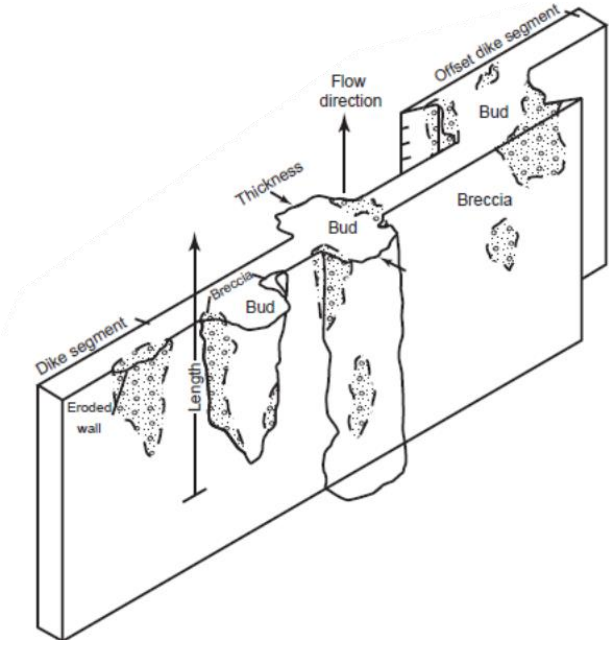

Figure 2.2: Schematic diagram of typical dyke bud morphology, where dyke segments are offset causing localised thickening of dykes. Buds can occur where offsets are rejoined or in the centre of the segment. Buds are comprised of coherent solidified magma, monobreccias and peperite (shaded). From White and Ross (2011), after Delaney and Pollard (1981).

Dyke termination

Dykes terminate by: (1) a weakening of host-rock strength (no brittle fracture); and (2) a weakening of magma pressure. The mechanical properties of unconsolidated or poorly consolidated sediments results in the regional stress field being significantly diminished in the shallow subsurface. This inhibits crack propagation due to the change from brittle to ductile deformation of host-rock (Figure 2.1). Host-rock interfaces can aid or impede brittle failure (Burchardt 2008). High cohesion between layers can prevent fractures from opening when magma intrudes, depending on the shear strength of the magma. Shear stress applied by the intruding magma determines whether the magma can overcome the cohesion and friction between host-rock layers and cause a failure in the host-rock.

In contrast, when magma pressure becomes too small to overcome tectonic stress, the dyke can no longer propagate. The pressure at this point is called the "stopping pressure" and is proportional to dyke thickness (Daniels et al. 2012). A dyke propagating away from a magma source experiences a negative regional stress gradient and a loss of magma pressure. Large dykes can propagate with a smaller overpressure than smaller, thinner dykes (Jaupart and Allégre 1991).

2.1.2. **Sills**

Sills were typically defined by their concordant relationship with both the overlying and underlying host rock however, field, seismic and experimental data have shown that sills can have complex morphologies, for example, they may have transgressive segments, depending on the tectonic environment and lithology they are intruded into (Planke et al. 2005; Magee et al. 2016). Sill emplacement is dependent on: (1) the direction of principal stresses of host-rock (Anderson 1951; Pollard 1973; Kavanagh et al 2006; Valentine and Krogh 2006; Menand 2008; Mathieu et al. 2008; Galland et al. 2009; Menand 2011); (2) the mechanical contrasts in material toughness and Young's modulus at host-rock interfaces (elastic mismatch) (Gudmundsson 2011; Barnett and Gudmunsson 2014); and (3) the exploitation of compliant or ductile horizons (Pollard et al. 1975; Liss 2004; Planke et al. 2005; Thomson 2007; Schofield et al. 2010; 2012; 2014; Muirhead, J.D. et al. 2016a).

Principal stress rotation

For sills to form, sigma 1 or the principal stress, must be horizontal (Anderson 1951; Kavanagh et al 2006; Valentine and Krogh 2006; Gudmundsson 2011; Barnett and Gudmundsson 2014). In

extensional tectonic settings (e.g. rift zones) sigma 1 is vertical and sigma 3 is horizontal. However, a host-rock interface with contrasting mechanical properties can cause the rotation of sigma 1 from vertical to horizontal and promote the propagation of sills (Burchardt 2008). Mechanically, the rotation of principal stresses is achieved by the combined stress of sigma 2 and 3 overcoming the lithostatic load or vertical stress of sigma 1. This occurs because magma pressure is added to sigma 3. When sigma 2, sigma 3 and the horizontal stress of the ascending magma, exceeds the lithostatic load (sigma 1) the stress field flips and the intrusion can propagate horizontally. This local stress field can be preserved beneath the newly-developed sill, which can impart a thermal, rigidity or strength anisotropy on to subsequent injections and further promote horizontal propagation of future intrusive events (Menand 2008, Burchardt 2008). These successive injections can stack up and form laccoliths (Menand 2008).

Elastic mismatch across host-rock interfaces

One significant emplacement mechanism is elastic mismatch (Gudmundsson 2011; Barnett and Gudmundsson 2014). When a subvertical dyke reaches a subhorizontal interface between two layers with contrasting mechanical toughness and Young's modulus, its direction is determined by the material strength of the overlying layer, the stress intensity factor for mode I and mode II fractures and the Dundurs elastic mismatch parameter, which is a function of contrasting Young's shear modulus' across the interface (Magee et al. 2016). If a mechanically weak, ductile host-rock lies stratigraphically below a brittle, rigid strata, the feeder dykes would propagate horizontally and sills would transgress along the brittle-ductile interface. However, the rigidity difference must be enough to prohibit failure and promote horizontal propagation (Kavanagh et al. 2006; Menand 2008; Gudmundsson 2011; Barnett and Gudmundsson 2014).

Experimental data by Kavanagh et al. (2006) demonstrate that in a layered heterogeneous system with a low rigidity ratio (<1; less rigid and less dense upper layer), the experimental dyke narrows before reaching the interface and propagates through the boundary without deflection (Figure 2.3). On the contrary, experiments with a high rigidity difference (>10) results in sill propagation along the interface (Figure 2.3). When driving pressure of the magma just exceeds the overpressure

required to form fractures, a dyke-sill hybrid is formed. Dyke-sill hybrids form when the rigidity contrast between layers is only just greater than 1 (Figure 2.3).

Dyke-sill hybrids may be more common than previously thought as rigidity contrasts between layers are generally greater than 1 but less than 10. Similarly, magma pressure is normally only marginally greater than host-rock strength so pressure difference tends to be low, again assisting the formation of the dyke-sill hybrid (Figure 2.3) (Menand 2008). The dykes that extend from the interface in a dyke-sill hybrid tend to only propagate a relatively short distance as driving pressure decreases below fracture pressure, P_f. The magma flow in the sill will accelerate and the length of the sill will quickly overtake the length of the protrusion dyke which has a constant velocity. As fracture pressure is determined by crack length, the magma flow direction will favour the sill and the dyke protrusions will terminate (Kavanagh et al. 2006).

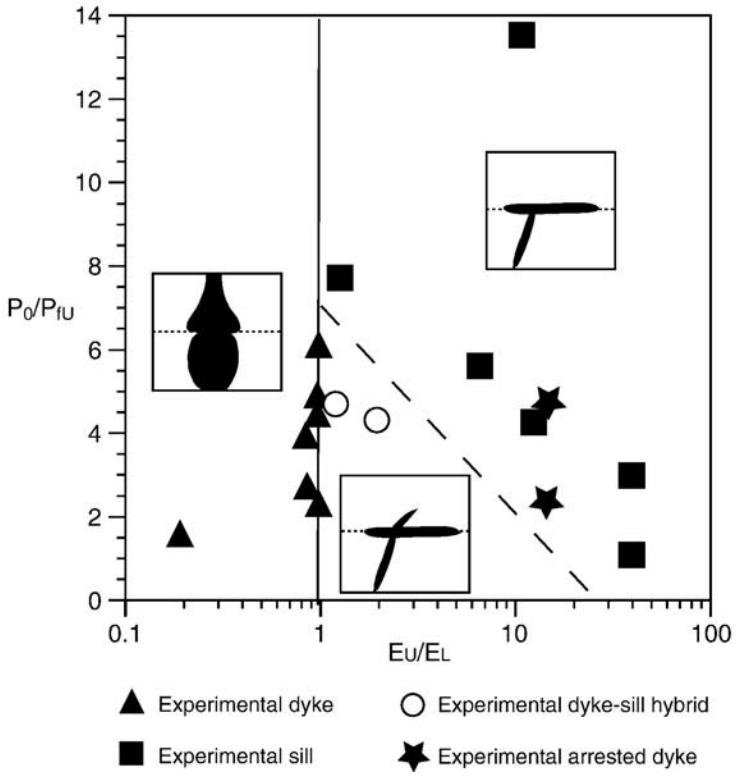

Figure 2.3: A graph showing the ratio of driving and resistive pressure scales, P_0/P_{fU}, against the ratio of upper and lower rigidities, E_U/E_L. The solid line is the boundary between the formation of dykes and sills and the dashed line represents the formation of sills and dyke-sill hybrids. From Kavanagh et al. (2006) and Menand (2008).

Ductile emplacement

In the ductile regime, it is often the nature of the host-rock which is the primary control on magma emplacement (Schofield et al. 2012; Magee et al. 2016). Mechanically weak rocks can be fluidised to

behave as a viscous fluid during intrusion emplacement, impeding the propagation of brittle fractures and supporting the formation of magma fingers and lobes (Schofield et al. 2012; 2014). Host-rock fluidisation occurs at depths up to 1.6 km to 2.2 km below the surface (Figure 2.4) (Kennedy and Holser 1966; Kokelaar 1982). Below this depth, the hydrostatic pressure is too high to allow adequate pore vapour expansion for fluidisation (Kokelaar 1982). Furthermore, at such depths a greater degree of host-rock strength must be overcome. Fluidisation may be initiated by magmatic heating and/or expansion and volatilisation of pore fluids (Einsele et al. 1980; Schofield et al. 2010, 2012; Jackson et al. 2013). Plastic deformation and porosity reduction in the host-rock allows the host-rock to accommodate the volume of the intrusion (Jackson et al. 2013; Magee et al 2016).

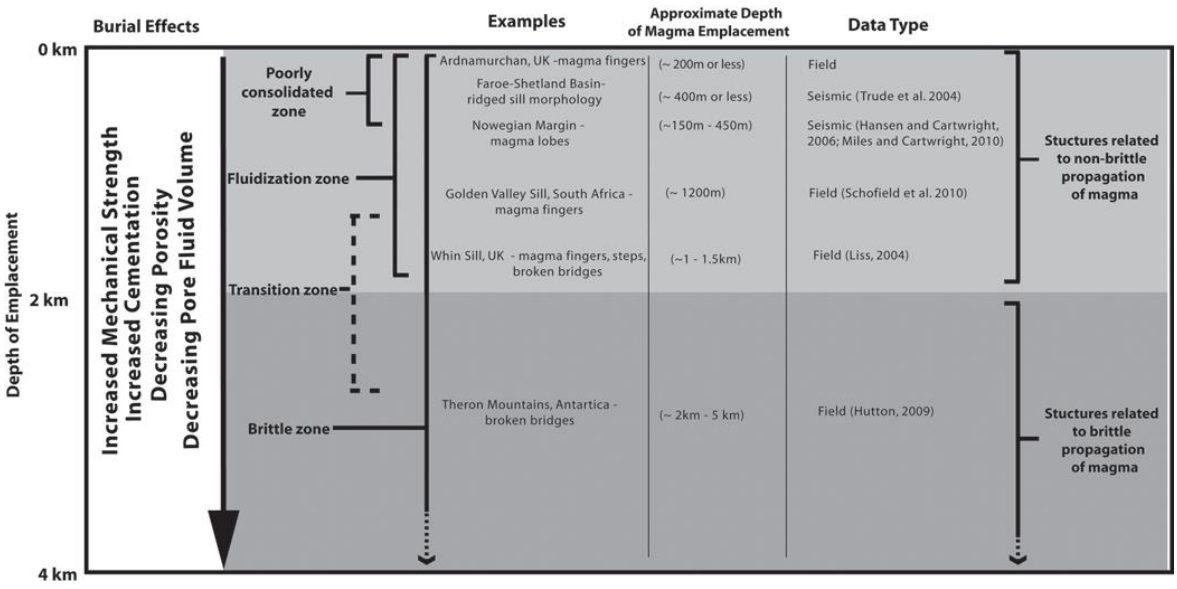

Figure 2.4: The relationship between depth, emplacement mechanisms and intrusion morphologies. An increase in depth, typically implies there is an increase in mechanical strength, an increase in cementation, a decrease in porosity and pore fluid volume in the host-rock. Brittle mechanisms can occur at any depth depending on the host-rock strength. The frequency of ductile features decreases with depth up until a maximum depth of 1.6 – 2.2 km. From Schofield et al. 2012.

Individual host-rock lithologies are affected differently by intrusion emplacement and fluidisation:

Coal: When coal is heated it becomes fluid-like or becomes a metaplast. Coal is thermally unstable and its plastic behaviour is dependent on the speed it is heated (Schofield et al. 2012). As it is heated, it softens and becomes fluid-like and can then interact with fluid magma (Skilling et al. 2002, Schofield et al. 2012).

Shale: Shale horizons are easily exploitable by intrusions as they tend to behave in a ductile manner when exposed to heat and strain (Thomson and Schofield 2008). As a result, sills can propagate

horizontally along shale horizons. Shales fluidize when there is an instantaneous drop in pore pressure. As sills intrude shale, the pore fluid between grains becomes volatile, which leads to an increase in pore fluid pressure and a sequential drop in effective stress, which allows magma to propagate (Thomson and Schofield 2008). A decrease in pore fluid pressure may also result in fluidisation if the shale horizon is located at a relatively shallow depth (Thomson and Schofield 2008). As well as fluidisation, dehydration of clay minerals and the generation of liquid hydrocarbons can also raise pore fluid pressure. If the volatile pore fluids are driven off, the volume percentage of shale host-rock will decrease (Thomson and Schofield 2008).

Unconsolidated or partially consolidated sediment: Sediments become more lithified and mechanically stronger with depth and therefore, will react to stress in a brittle manner (Lorenz and Haneke 2004). However, at shallow depths, sediments are usually unconsolidated or partially unconsolidated, and tend to be water-saturated. These rocks are termed the "soft-rock" environment and are susceptible to fluidisation when magma is emplaced within them. In unconsolidated or partially consolidated sediments/rocks, there are greater heterogeneities in permeability and pore space between units or sub-units.

Carbonate: When brought into contact with the heat from an intruding magma, carbonate horizons release carbon dioxide which lowers the effective stress of the host-rock and aids horizontal propagation of sill intrusions (Thomson 2007).

Salts: Non-brittle and brittle intrusion emplacement can occur in salts, depending on their chemical structure. Intrusions will preferentially exploit horizons of hydrous salts that lose their structural water at temperatures <200 °C, for example, carnallite, gypsum and bischofite (Schofield et al. 2014). Heating from intrusion emplacement causes the hydrous salt sequences to behave as a viscous fluid (Urai et al. 2008). Fluid-fluid interaction between ductile salt and intruding magma causes irregular and bulbous intrusion morphologies (Schofield et al. 2012; 2014). The addition of igneous material is accommodated by either fluid release from the chemical structure (e.g. carnallite converts to sylvite) or out-section flow of salt (Schofield et al. 2014). Anhydrous salts which have a higher decomposition/melting temperature, for example, halite, typically react in a brittle manner during intrusion emplacement (Rubin 1995; Schofield et al. 2014).

Sill morphologies and features

There have been various attempts to categorise different sill morphologies. Planke et al. (2005) categorises the geometry of sills into: (1) layer parallel; (2) saucer-shaped; (3) planar transgressive; and (4) fault block. Although the nomenclature used by Planke et al. (2005) is not always used, these four categorises summarise the general morphologies of sills. "Layer parallel" describes sills which are concordant with the surrounding host-rock stratigraphy and define the bedding structure. Saucer-shaped intrusions are characterised by an inner, strata-concordant dish with inclined sheets extending upwards and away from the inner dish (Thomson and Hutton 2004). The inclined sheets transfer magma into shallower stratigraphical levels and facilitate magma ascent in sedimentary basins (Thomson and Hutton 2004; Cartwright and Hansen 2006; Holford et al. 2012; Magee et al. 2013; 2014; 2016). Climbing saucer intrusions or half-saucer shaped intrusions are formed from an inclined sill limb transgressing up from the inner dish on one side. Planar transgressive sills have an inclined sheet morphology and transgress the host-rock stratigraphy. Magma pathways can also exploit fault planes and stratigraphic weaknesses to form irregular sill morphologies.

Depending on the mode of emplacement, certain characteristic features can develop in sills. The development of magma finger and lobe formation is associated with ductile emplacement mechanisms, whereas intrusive steps and bridges tend to require brittle emplacement mechanisms (although can be formed by ductile emplacement mechanisms, see below) (Hansen and Cartwright 2006; Hutton 2009; Schofield et al. 2012). Field- and seismic-based studies of intrusion mechanisms (brittle versus ductile) show similar depths of <2 km for brittle features (steps and bridges) and >2 km for ductile features (magma fingers and lobes) (Figure 2.4) (Schofield et al. 2012; Magee et al. 2014).

Steps: Step structures in sills result from offset segments of intrusions and are parallel to the flow direction (Rickwood 1990). Steps are formed in two ways: (1) fracturing at the leading edge of the intrusion and further propagation of magma into the fracture, which records the initial geometry of the fracture (Baer 1991); (2) exploitation of bedding planes or host-rock beds with lower tensile strength (Schofield et al 2012). Steps can either form in one direction (Figure 2.5A) or along multiple horizons (Figure 2.5B) depending on formation mechanism (Schofield et al. 2012). Steps are typically

found on the outer rims of saucer-shaped intrusions where there is a drop in magmatic pressure and therefore tensile strength (Thomson and Hutton 2004; Goulty and Schofield 2008). Consequently, magma flows along easier pathways such as bedding planes and preferential, non-brittle horizons (Schofield et al. 2012) (Figure 2.5).

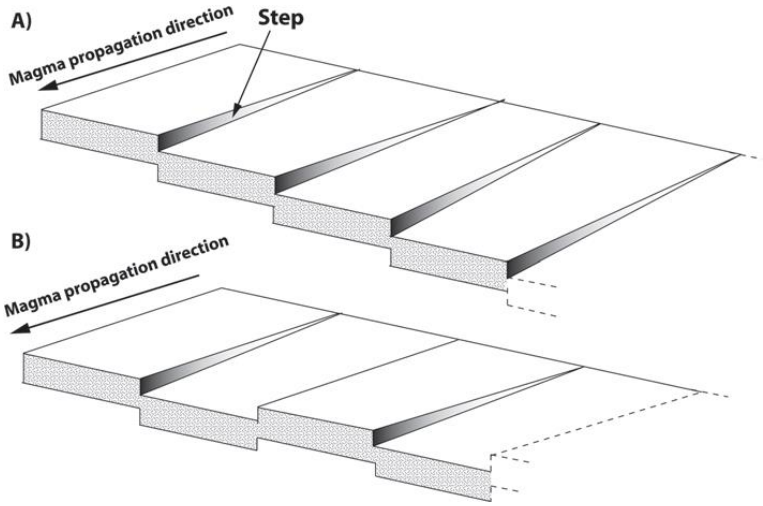

Figure 2.5: Schematic illustration of a sill with en echelon steps (after Rickwood 1990, from Schofield et al. 2012). (A) A staircase sill, steps form in one direction (B) Sill stepping onto different horizons.

Broken Bridges: Broken bridges are formed when two magmatic intrusive bodies on different stratigraphical levels overlap, trapping pockets of host-rock (Figure 2.6) (Hutton 2009). As the intrusions inflate, they apply pressure and stress to the surrounding host-rock, and cause a series of perpendicular tensile fractures to open in zones of maximum flexure (Figure 2.6). The bridge can then undergo brittle failure and become separated from the host-rock horizons. The remnants of the bridge can become host-rock rafts within the intrusion (Figure 2.6) (Schofield et al. 2012).

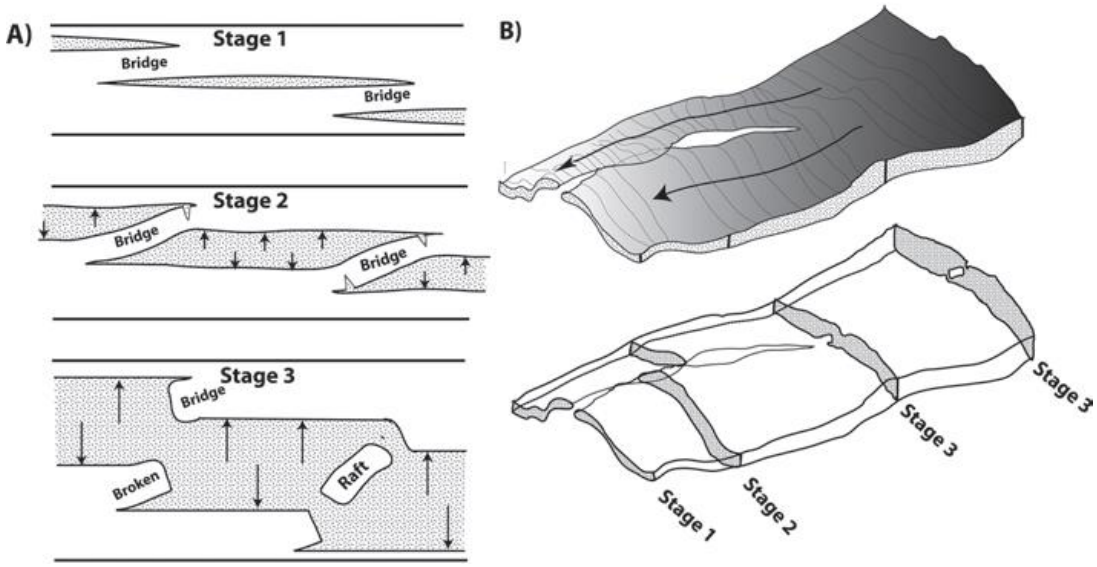

Figure 2.6: Schematic illustration showing how offset sills can form broken bridges (from Schofield et al. 2012). (A) Stage 1, bodies of a sill intrusion propagates on different schematic horizons whilst overlapping. Stage 2, bodies inflate and host-rock bridge becomes trapped between two sill bodies where it starts to bend and deform. Stage 3, As inflation continues, flexure becomes too much and the brittle fractures segment the sandwiched bridge of host-rock. If it happens at both sides of the bridge, the host-rock segment becomes rafted in the sill intrusion. (B) A 3D illustration of broken bridge development.

Magma fingers: Magma fingers are separate elliptical protrusions that may coalesce (Figure 2.7) (Pollard et al. 1975; Schofield et al. 2010; 2012). Pollard et al. (1975) questioned how fingers are initiated and using experimental models, determined that if a portion or portions of magma extends beyond the main body due to some homogenisation in the magma, the extended fingers will encounter less resistance and accelerate ahead. If several fingers extend ahead of the magma body, they can coalesce periodically, closing from the base (nearest the magma body) to the tip (Figure 2.7) (Pollard et al. 1975; Schofield et al. 2010). The emplacement of magma fingers is associated with ductile emplacement mechanisms, where one viscous fluid (magma) intrudes into another viscous fluid (fluidised host-rock) (Pollard et al. 1975).

Magma fingers tend to form on the limbs of saucer shaped sills which are formed by a two stage process suggested by Goulty and Schofield (2008). Magma intrudes along a plane of weakness and inflates causing doming of the overburden. Fractures open at the tip of the sill which causes a sudden drop in hydrostatic pressure and fluidises the host-rock (can only occur in the shallow subsurface where host-rocks can be fluidised; Kokelaar 1982). The resultant fluid-fluid interaction between fluidised host-rock and magma instigates the formation of magma fingers (Schofield et al. 2010). Since the fractures open in the roof of the sill, the sill transgresses upwards (Schofield et al. 2010).

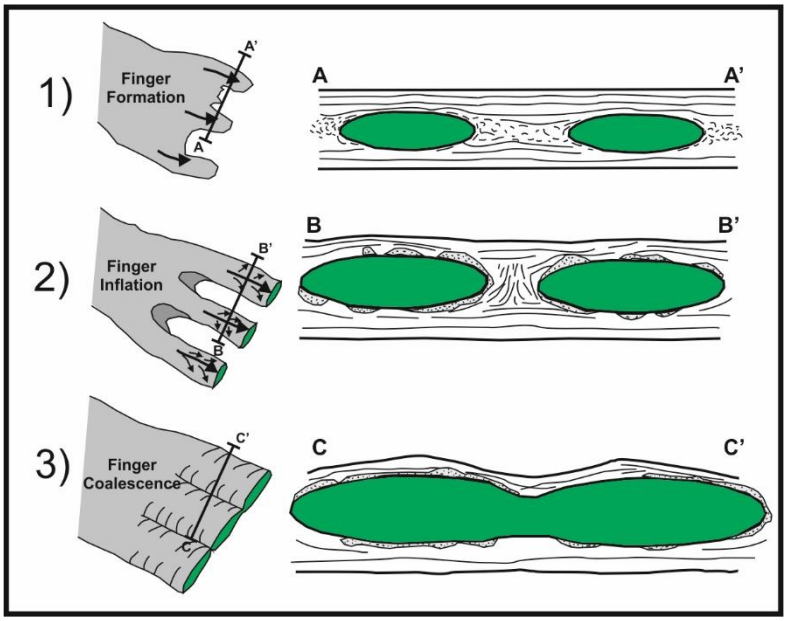

Figure 2.7: Schematic diagram showing the formation of magma fingers with time in cross-section and plan view. (1) Magma fluidises surrounding host-rock causing ductile emplacement of fingers. (2) Fingers will propagate and inflate both vertically and laterally if magma supply continues. (3) Fingers coalesce to form a continuous sheet. The propagating magma may stop at any stage. Magma fingers will only reach the final stage if magma run-through rate is high enough throughout the formation of the fingers to prevent solidification. Adapted from Schofield et al. 2012, based on Pollard et al. 1975.

Magma lobes: Magma lobes are lobate protrusions that grow and expand away from their source (Thomson and Hutton 2004; Schofield et al. 2012). Magma lobes are identified in 3D seismic data and range in size from hundreds of metres to kilometres (Thomson and Hutton 2004; Hansen and Cartwright 2006; Schofield et al. 2012). Magma lobes tend to be constructed from coalesced magma fingers (Schofield et al. 2010).

2.1.3. **Inclined sheets**

Inclined sheets form independently within or at the margins of saucer-shaped or half-saucer shaped sills. There are several proposed mechanisms for inclined sheet formation and development: (1) during inflation of sub-horizontal sills, σ_1 is inclined inwards (Gudmundsson 2002; 2006; Malthe-Sørenssen et al. 2004; Barnett and Gudmundsson 2014); (2) mixed mode I and II fracturing (Airoldi et al. 2011; Magee et al. 2012; Mathieu et al. 2015); (3) overburden doming causing strain and fractures at the lateral tips of the sills (Jackson and Pollard 1990; Goulty and Schofield 2008; Thomson and Schofield 2008; Schofield et al. 2010; Muirhead, J.D. et al. 2012; Magee et al. 2013; 2016); (4) the emplacement of magma along reverse faults (Thomson and Schofield 2008; Magee et al. 2016); (5) intrusion along pre-existing faults (Magee et al. 2013); and (6) the intrusion of magma along inclined unconformity surfaces (McLean et al. 2017).

2.1.4. **Exploitation of faults**

Pre-existing faults in sedimentary basins can be exploited by magma to provide suitable ascent pathways to shallower stratigraphical levels (Price et al. 1997; Planke et al. 1999; Gaffney et al. 2007; Magee et al. 2013; 2016). Using an example from the Flett Basin in the North Atlantic, Thomson and Schofield (2008) used seismic data to identify deep saucer-shaped sills, which have flowed along faults and have traversed across deeply dipping sedimentary beds to reach higher stratigraphical levels (~200 m) to form laccoliths. Field studies of the Saar-Nahe Basin, Germany, demonstrate sills and their corresponding feeder dykes exploiting bedding planes and faults, creating a complex geometry to the intrusion system (Lorenz and Haneke 2004). Pre-existing faults may also restrict or deflect magma propagation, particularly if footwall basement rocks are adjacent to hanging wall sedimentary lithologies (Magee et al. 2016).

Dykes can also intrude into pre-existing fractures providing they have an appropriate stress orientation (Gaffney et al. 2007). A shear component can occur during dyke intrusion into pre-existing fractures if the fracture is obliquely orientated to the principle stress direction (e.g. σ_1). This results in overlapping dyke segments and fingers and the subsequent bridging of dykes (Daniels et al. 2012).

2.2. Magma-water interaction

Assessing the mechanisms and products of magma-water interaction has proven to be difficult and is one of the grand challenges that the volcanology community faces, partially because eruptions are usually not, or only partly, visible and deposits are generally inaccessible or incomplete (Cas and Giordano 2014; White and Valentine 2016). It is important to understand the processes of magma-water interaction to help to identity the eruption history of the edifices in Chapters 4, 5 and 6.

The experimental studies of magma-water interaction tend to focus on assessing the effect of hydrostatic pressure on the amount of magma-water interaction and do not assess other constraints to the same degree, including: bulk modulus of water (compressibility and deformability); thermal conductivity and heat capacity of water; specific volume of water under pressure by magmatic temperatures (water-magma ratio) (Wohletz and McQueen 1984; Cas and Giordano 2014). In Figure 2.8, Wohletz and McQueen (1984) show how the eruption energy is dependent on the ratio of magma to water, and in turn how this affects the type of deposits produced.

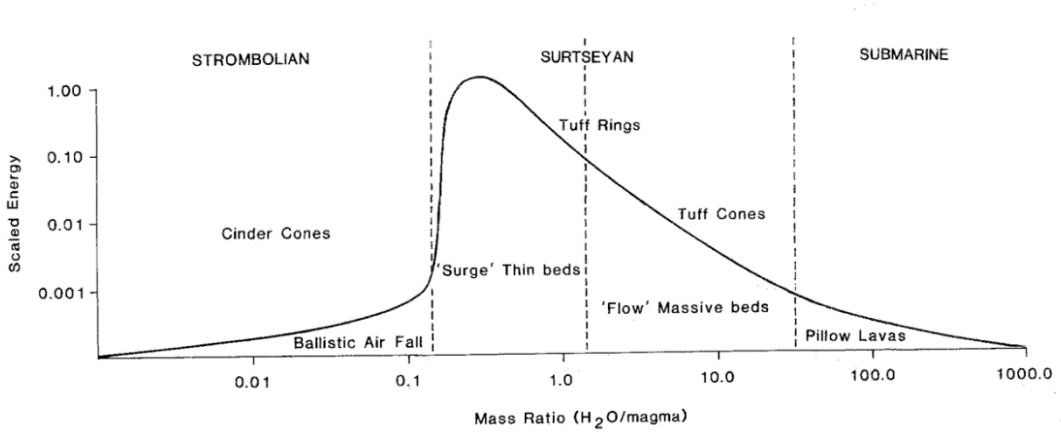

Figure 2.8: Relationship of magma-water ratio and energy, and the resulting eruption styles, edifice type and the typical deposits (from Wohletz and McQueen 1984). Note that tuff rings (maar-diatremes) are produced by the "optimum" water-magma ratio (0.3 – 0.4) and high energy explosions indicating molten fuel-coolant interactions. Contrastingly, scoria cones (cinder cones) have very low water-magma ratios and low energy explosions indicating magmatic processes (explosions by volatisation).

2.2.1. Mechanisms

There are three processes which involve the break-down of coherent magma bodies into volcanogenic particles by magma-water interaction, as outlined by Kokelaar (1986). These occur in submarine, subglacial and subsurface settings and are: (1) non-explosive cooling-contraction granulation; (2) energetic steam explosions; and (3) high energy thermohydraulic explosions induced

by molten fuel-coolant interactions (Wohletz 1983; Kokelaar 1986). Furthermore, vesiculation of magma can also cause simultaneous fragmentation of magma depending on the overlying pressure.

Cooling-contraction granulation

Cooling-contraction granulation is the primary fragmentation mechanism in submarine, subglacial and phreatomagmatic eruptions and occurs at any depth or pressure (Kokelaar 1986). The outside of a magma droplet cools more rapidly than the core due to contact with water. This forms a rigid rind on the droplet. As the core cools, it contracts more than the rigid rind can allow, cracking the rind and causing fragmentation and disintegration of the magma droplet (Kokelaar 1986). Evidence for cooling-contraction granulation is evident at the margins of extrusive and intrusive bodies, where glassy rims and tachylite formation are present, and volcaniclastic particles, comprising equant to sub-equant fragments of tachylite or glass, are common.

Evidence for cooling-contraction processes also presents as columnar jointing in magmatic bodies, or radial jointing in submarine pillows, which form perpendicular to surfaces of equal tensile stress (typically the cooling surface) (Spry 1962; Long and Wood 1986; Doyle 2000). The high cooling rates cause a network of contractional cooling fractures to propagate inwards from the surface of the magma (Cas and Giordano 2014). Planar fractures on the magmatic surface may also reflect cooling by cooling-contraction granulation mechanisms (Doyle 2000).

Experimental studies of cooling-contraction granulation produced grains of all sizes depending on the amount of strain (Zimanowski et al. 2003). Cooling-contraction of a vesicular magma can cause the vesicles to become interconnected, allowing water to be drawn further into the magma body and cause further fragmentation of the magma (Whitham and Sparks 1986). The presence of vesicles (bubbles) increases the stress in the surrounding groundmass during cooling-contraction granulation and therefore controls the geometry of the fracturing magma (Liu et al. 2015). This process often produces finely granulated, glassy particles between larger, often angular, lapilli and blocks (Cas and Giordano 2014). Similarly, recent field studies have suggested that fragments in the fine-medium ash fraction were most likely to be produced by quench-related fragmentation processes (Fitch et al. 2017).

Steam explosions

When ascending magma in shallow plumbing systems comes into contact with high porosity surface rocks or wet, unconsolidated sediment, the water trapped and confined in pore spaces within the surrounding substrate or trapped in the magma, converts to steam (Kokelaar 1986). Expansion of steam inside the magma exerts pressure internally and the magma fragments into particles around this rapidly expanding steam. The magma is also shattered by associated pressure waves (Kokelaar 1986; Büttner et al. 2002).

Steam explosions are an increasingly significant mechanism at shallow depths where steam explosivity is not inhibited by pressure controls (Kokelaar 1986). The intensity of explosive fragmentation (by expanding steam) is dependent on the rate of heat exchange between magma and pore-water, the rate of pressure build-up due to containment of the steam, and the mingling energy between the two fluids (Kokelaar 1986; Zimanowski and Büttner 2002). Furthermore, as fluid vapourises from the sediment, there is an increase in water pressure (if confined) and/or a 50-fold increase in water volume as it flashes to steam (Delaney 1982).

Steam explosions are particularly significant in emerging submarine or Surtseyan explosions (Schipper and White 2016). If water was to be completely engulfed by magma (such as in the volcanic slurry at the top of a Surtseyan vent) it would be continuously heated, flash boil to steam and the steam would expand (Kokelaar 1983). Magma can more readily mingle with particle-bearing slurry than with pure water (White 1996). Steam explosions can occur below the maximum 130 m water depth for explosive interaction, if the water or steam was trapped and contained within porous sediments (Kokelaar 1983; Kokelaar 1986).

The products of steam explosions tend to be characterised by rounded particles with smooth margins as they are formed in the ductile regime (Büttner et al. 2002). These particles can be elongated if they have been incorporated into subsequent explosions as part of the slurry and expelled at high velocities out of the vent (Büttner et al. 2002).

High energy thermohydraulic explosions

MFCI (molten fuel-coolant interaction) involves a hot fluid, the "*fuel",* coming into contact with a cold, volatile fluid, the "*coolant"* (Buchanan 1974; Sheridan and Wohletz 1983; Wohletz 1986;

Kokelaar 1986; Zimanowski et al. 1991; 1997; Hooten and Ort 2002). There are two main stages of MFCI (Wohletz 1986; Zimanowski et al. 1997; Hooten and Ort 2002):

(1) The initial stage occurs when the preliminary contact between fuel and coolant is made. During this initial contact, a vapour film between the magma and host is established which acts as an insulator (Wohletz 1986). Density contrasts between the two fluids can produce instabilities and results in increased magma-water mingling (Wohletz 1986; Hooten and Ort 2002; Büttner et al. 2002).

(2) In later stages, if the vapour film becomes unstable, oscillates and collapses, the magma surface deforms into wave-like geometries which causes the magma to fracture and fragment (Wohletz 1986; Kokelaar 1986; Zimanowski et al. 1997). The vapour film can also collapse by a low-energy shock wave (e.g. triggered by collapse of wall-rock) (Zimanowski et al. 1995). The insulating properties become ineffective and rapid heat transfer between the interfaces allows for explosive interaction, thus, resulting in the fragmentation of magma. With this increase in heat transfer, there is an associated increase in mingling between the two interfaces. When the vapour film collapses, the rapid change in pressure and volume conditions creates a very strong shock wave which propagates through the magma-water mixture and causes the magma to fragment into fine particles (Wohletz 1986; Zimanowski et al. 1997).

The term "MFCI" is a general term to describe a wide range of processes determined by which stage the process terminates at (Wohletz 1986; Zimanowski et al. 1997). Experimental studies on explosive interactions between magma and fluid (groundwater, pore fluid and surface water) have been carried out in the last 30 years to better understand the magmatic processes and their interaction with host-rock (Sheridan and Wohletz 1983; Wohletz 1983, 1986; Zimanowski et al. 1991; 1997; Lorenz et al. 2002; Martin and Németh 2007). The MFCIs can range from non-explosive to violently explosive and are dependent on several factors such as: (1) rate of heat transfer; (2) amount of fuel-coolant mixing, (3) fuel viscosity, (4) amount of vapourisation; (5) impure coolants, and (6) water-magma mass ratios (Sheridan and Wohletz 1983; Wohletz and McQueen 1984; Zimanowski et al. 1997; Hooten and Ort 2002). For explosive interactions to occur the most

favourable water/magma mass ratio is approximately 0.35 (Sheridan and Wohletz 1983; Kokelaar 1986; Taddeucci et al. 2010). For non-explosive interactions, such as the formation of pillow lavas, the vapour film insulates the magma, whilst the surrounding water is slowly heated (Kokelaar 1986).

The explosivity of MFCIs is also determined by the confining pressure (hydrostatic pressure), mechanical strength of the host-rock, and the mechanical forcefulness of the emplacement of lava into water, sediment or rock. Explosive interaction does not occur at hydrostatic pressure above 50 MPa (Kokelaar 1986; Wohletz 1986). However, explosive interaction can occur at depths of up to 5 km, if phreatomagmatic explosions have excavated the overlying host-rock reducing the hydrostatic and lithostatic pressure, or if it was triggered by a strong earthquake (Wohletz 1986; White and Ross 2011).

Rapid heat transfer after the vapour film has collapsed produces high energy explosions and causes very fine fragmentation of magma (Wohletz 1986). Phreatomagmatic deposits typically have a higher proportion of lithic constituents than dry deposits, because of thermohydraulic fracturing of the host-rock and incorporation of these fragments into the eruption (Funiciello et al. 1976; Delaney 1982; Wohletz 1986).

Vesiculation and magmatic explosivity

Volatiles within ascending magma may exsolve, expand and fragment magma if the hydrostatic pressure is low enough (McBirney and Murase 1971; Sparks 1978; Kokelaar 1986; Houghton and Wilson 1989). For example, in subaqueous settings, the hydrostatic pressure of the water depth adds an additional confining pressure constraint on exsolution and therefore, the vesiculation depth is much shallower for a magma erupting at a seafloor than for a magma erupting at the subaerial surface (Cas and Giordano 2014). The vesiculating pressure for basaltic magmas tends to correspond to a maximum of 500 m (of water) but tends to be shallower (~100-200 m), depending on the water content and volatile content of the magma (McBirney 1963; Moore and Schilling 1973; Cas et al. 1989; Downey and Lentz 2006; Cas and Giordano 2014).

As a submarine volcanic pile grows, the magma-water interface becomes shallower. At shallower levels, not only does a lower hydrostatic pressure increase hydromagmatic explosivity, but it allows for more rapid vesiculation of magma due to the expansion of magmatic volatiles and superheated

seawater (Cas et al. 1989). Contrastingly, subterranean emplacement and fragmentation of magma causes excavation of the overlying host-rock, decreasing the hydrostatic pressure and prompting volatisation of magma even at depths greater than the volatile fragmentation depth (Fisher and Schminke 1984; Ross and White 2012). Thus, typically there is a non-vesicular to vesicular trend in clasts within diatremes (Ross and White 2012). Hydrovolcanic processes can prematurely stop or prevent bubble development, limiting the size and amount of vesicularity in ejected material (Houghton and Wilson 1989; Sorrentino 2011).

Eruptions that involve magma-water interaction, therefore, tend to produce particles with a large range of vesicularities, ranging from completely non-vesicular to scoriaceous (>70%) (Houghton and Wilson 1989; Cole et al. 2001; White and Valentine 2016). However, this concept is somewhat disputed as recent studies of purely magmatic eruptions also contain clasts with a wide range of vesciularities (Stovall et al. 2012; Gurioli et al. 2014; White and Valentine 2016).

2.2.2. **Identification of magma-water processes within deposits**

Typically, fragmentation mechanisms of pyroclasts are inferred by a range of textural criteria including particle morphology; particle size; abundance and shape of vesicles; degree of quenching (glass/tachylite/sideromelane); abundance of host-rock fragments; bulk proportions; degree of particle aggregation and proportion of fines (Houghton and Wilson 1989; Graettinger et al. 2013) (Table 2.1). White and Valentine (2016) have, however, established that while these criteria can give some indication of magmatic fragmentation mechanisms, they are not entirely diagnostic and many of the features commonly associated with magma-water interaction are also found in many purely magmatic or dry eruptive products.

A common problem with small scale monogenetic eruptions is that particles can be recycled in multiple eruptions and, therefore, do not record the mechanisms of the eruption that deposited the particle but instead record an eruption that preceded it (White and Valentine 2016). Consequently, it is important to use a wide range of criteria to interpret volcanic deposits.

	Parameter	Magmatic	Phreatomagmatic	Diagnostic tool use
vesicles	Vesicularity (%)	>75%	<40%	**Low.** Indicates whether a magma experiences degassing. Only records a portion of the degassing history (Schipper et al. 2010).
	Vesicle number density	10^3 - 10^8	10^2 - 10^5	**Very Low.** Used to assess conditions and rate of magma ascent but no connection between VND and magma-water interaction (White and Valentine 2016).
	Vesicle morphology	spherical to tube	spherical (but may preserve vesicle texture pre-fragmentation)	**Moderate.** Reflects the relative timing of degassing and cooling. May indicate post-fragmentation degassing (Graettinger et al. 2013).
	Vesicle texture at clast margin	deformed vesicles at margin	fractured with no trend in vesicles	**High.** Indicates the timing of degassing relative to fragmentation.
particle morphology	Ash clast morphology	fractures at margins controlled by vesicles	blocky	**Low.** Used in unison with other parameters (Graettinger et al. 2013). Only 30 wt% of grains <130μm show characteristics of direct magma-water interaction (Büttner et al. 2002; Liu et al. 2015).
	Lapilli clast morphology	fluidal; ragged; blocky	blocky; globular; accretionary lapilli	**Low.** Cooling-contraction granulation produces blocky lapilli, which can occur during magmatic and phreatomagmatic processes (Graettinger et al. 2013).
	Bomb morphology	diverse shapes incl. breadcrust, ribbon, cow pie	cored bomb; blocky; some fluidal; cauliflower	**Low to Moderate.** Used in unison with other parameters. Surface fracturing of bombs can be found in dry and wet eruptions (White and Valentine 2016)
content	Lithic abundance	low	typically high	**Moderate/High.** The presence of lithic clasts does not preclude magmatic activity. Diatreme-forming phreatomagmatic eruptions are typically associated with lithic fragments (White and Ross 2011). However, lithic fragments can be found in high abundances in basaltic eruptions (Houghton and Nairn 1991; White and Valentine 2016)
	Sideromelane vs. tachylite	tachylite-dominated	sideromelane-dominated	**Moderate**. Dependent on grain size and preservation. Sideromelane can be produced in dry basaltic eruptions but this is rare (Stovall et al. 2012)

Parameter	Magmatic	Phreatomagmatic	Diagnostic tool use
Crystal content	0-50%	3-20%	**Low.** Higher crystallinity is associated with slower cooling time. Free crystals may be indicative of efficient fragmentation processes (De Rosa 1999).
Abundance of fine ash	low to moderate	moderate to high	**Moderate/High.** The presence of finer grains indicates highly efficient fragmentation, likely magma-water explosions (Sheridan and Wohletz 1981; Wohletz and McQueen 1984; Wohletz 1986; Zimanowki et al. 1997). However, environmental factors such as water flushing or deposition of aggregate particles selectively influence grain size (White and Valentine 2016)
Deformation regime	ductile	brittle	**Low to Moderate.** Indicates rate of strain relative to viscosity of magmatic fluid. Dependent on rate of eruption, vent geometries and fluid viscosity (Graettinger et al. 2013).
Welding	low to high	low (emergent, littoral; submarine)	**High.** Only when present. The absence of welding does not exclude magmatic processes (Graettinger et al. 2013). Agglutination of pyroclasts can take place in phreatomagmatic and magmatic explosions (Valentine and Cortés 2013; Lefebvre et al. 2013; Schipper and White 2016; White and Valentine 2016)

Table 2.1: Typical parameters used as criteria to determine magma fragmentation processes (adapted from Graettinger et al. 2013). It must be noted that natural eruptions show highly variable eruptive styles and deposits so the parameters listed here cannot be used independently and a range of corroborating parameters must be used instead.

2.3. Monogenetic Volcanism

Shallow magma emplacement and magma-water interaction can lead to monogenetic eruptions forming a range of edifices. This sub-chapter defines the monogenetic terminology (as used in Chapters 4,5 and 6) and highlights the processes that occur at each monogenetic edifice type.

Monogenetic volcanoes are typically defined as small-volume (<0.1 km^3 dense rock equivalent total eruptive products), short-lived volcanoes that generally occur in large numbers in linear or clustered arrangements (Németh 2010). Monogenetic volcanoes are typically formed in basic or ultrabasic volcanic fields, although intermediate monogenetic volcanoes are known (Lorenz and Kurslaukis 2007; Valentine and White 2012). Rarely do monogenetic edifices occur autonomously; edifices tend to be arranged in assemblages as monogenetic fields. Depending on the availability of water for magma-water interaction, magma can extrude at the surface and form scoria cones, tuff cones, tindars and maar-diatremes (White et al. 2000; Jerram and Stollhofen 2002; Ross et al. 2005; McClintock and White 2006). If environmental conditions change during an eruption (e.g. the accessibility of water) the style of eruption can change and the edifice can evolve into other forms of monogenetic volcano (Zanon et al. 2009). Figure 2.9 illustrates this concept, where changing environmental conditions can produce complex edifice morphologies (Kereszturi and Németh 2012).

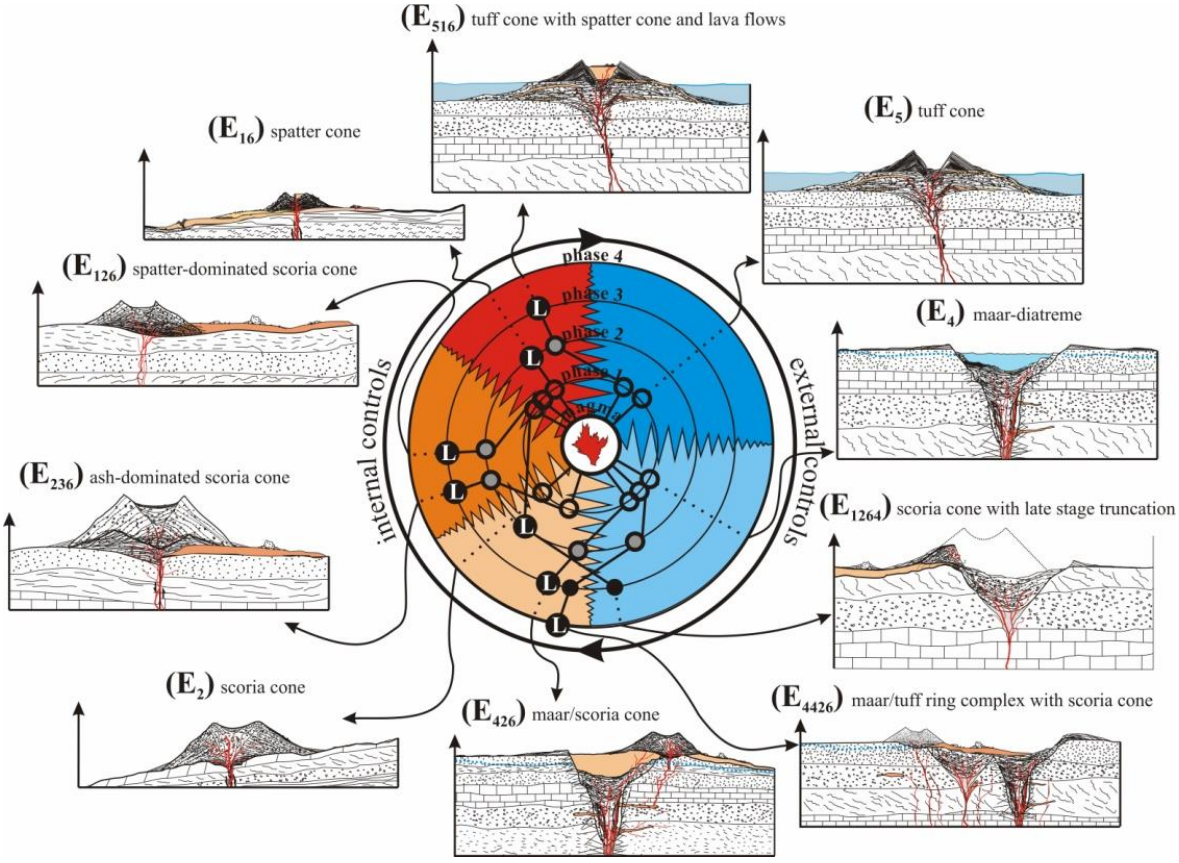

Figure 2.9: Genetic evolution of monogenetic edifices due to environmental changes (water availability, arrival of a new magma batch, movement of extrusion point). From Kereszturi and Németh (2012). Colours in circle correspond to type of eruption: red = Hawaiian; dark orange = violent Strombolian; light orange = Strombolian; light blue = phreatomagmatic; dark blue = Surtseyan. Phase 1, the beginning of the eruption, begins in the middle of the circle and later phases are indicated by the concentric circles extending outwards. The product of each combination of phases are indicated by the illustrations of edifices and are each given an eruption history code (E).

2.3.1. **Scoria Cones**

Scoria cones are not the primary focus of this thesis and will only be discussed briefly. Scoria cones are formed in relatively short durations (<1 day to 15 years) and so their magmas tend to undertake a limited geochemical evolution (Johnson et al. 2008). Scoria cones are the dry end-member of monogenetic volcanism, constructed of deposits produced by Strombolian processes, namely volatile–driven explosions (Wood 1980; Valentine et al. 2005). The deposits are made up of ash, coarse lapilli, spatter and bombs (fluidal and angular).

A well accepted theory of scoria cone development is the combination of ballistic emplacement and grain avalanching (McGetchin et al. 1974). If the crater becomes blocked by mass flows, subsequent explosions may re-eject previously erupted material (Valentine et al. 2005). Substantial fallout deposits (several metres thick in proximal zones near the cone) are also recorded at many scoria cones (Self 1976; Heiken 1978; Valentine et al. 2005). The fallout deposits gradually thin over several

kilometres from the cone (Valentine et al. 2005). The presence of fallout deposits suggests sustained eruption columns are also common during scoria cone development. Sustained eruptions can be produced if there is an increase in magma viscosity due to the presence of microlites, which prevent large bubbles from forming and results in small bubbles fragmenting the magma into fine grained particles (Valentine et al. 2005).

Scoria cones are fed by dykes which are typically a few metres wide, have a strike length of several kilometres and form as a series of *en echelon* dykes (Keating et al. 2008; Németh 2010). Magma becomes progressively more directed into one of the dykes, into a central vent area, and rapidly constructs the scoria cone (Keating et al. 2008). Recent studies of eroded scoria cone fields in Paiute Ridge (southern Nevada, USA) and San Rafael (Utah, USA) suggests that plumbing systems of monogenetic scoria cones can be more complex than first thought and a network of sills and dykes can feed scoria cones (Valentine and Krogh 2006; Richardson et al. 2015). Historical eruptions of scoria cones, (e.g. Paricutín, Mexico in 1943; Jorullo, Mexico in 1759; Chinyero, Tenerife in 1909; Teneguia, La Palma in 1971) were all preceded by seismic unrest and suggests subvolcanic reservoirs and more complex plumbing systems (Albert 2016). The eruption of Paricutín in 1943 is particularly significant as it lasted 9 years and evolved from an olivine-bearing basaltic andesite to a hypersthene andesite, suggesting some crustal assimilation during stoping and storage in the crust (McBirney et al. 1987).

2.3.2. **Tuff Cones**

Tuff cone formation

Tuff cones are steep sided edifices (>25°) which form in shallow to fairly deep marine shelf or lacustrine settings (Wohletz and Sheridan 1983; Fisher and Schmincke 1984; White 1996; Sohn and Park 2005). Tuff cones are built on submarine volcanic piles comprising tephra, hyaloclastite, reworked material and pillow lavas (Kokelaar 1983). When magma encounters water (seawater or lake), explosive and non-explosive interactions can occur. Non-explosive interaction tends to occur at the onset of submarine volcanism when hydrostatic pressure inhibits explosive interaction (Kokelaar 1986). Explosive magma-water interaction occurs when water enters the top of the vent, producing violent explosions and sending tephra jets upwards (Kokelaar 1983). When seawater is

restricted and no longer gains access to the vent opening, due to a cone-shaped ring of tephra enclosing the vent, the explosive activity is prohibited and magmatic processes arise. Any explosive activity that occurs after water has been cut off is due to the release of volatiles from the magma. Erosion can often cause the tuff cone surrounding the vent to fail resulting in a water influx into the vent and a reactivation of Surtseyan processes (Kokelaar 1983) (Figure 2.10). It is widely thought that all four magma fragmentation processes (as outlined in Section 2.2.1) occur during emergent volcanism and there is feedback between all processes (Schipper and White 2016).

Surtseyan explosions are characterized by jets of tephra that are ejected from the vent (Kokelaar 1983). Tephra jets frequently occur at approximately one jet per second and can occur in any orientation (Kokelaar 1983). The jets can be ejected up to 1 km into the atmosphere and are removed from the proximal vent zone by convection and atmospheric currents. The remaining tephra falls or is ejected into the proximal vent zone where it can build the vent, tephra cone or platform which the vent is located on (Kokelaar 1983).

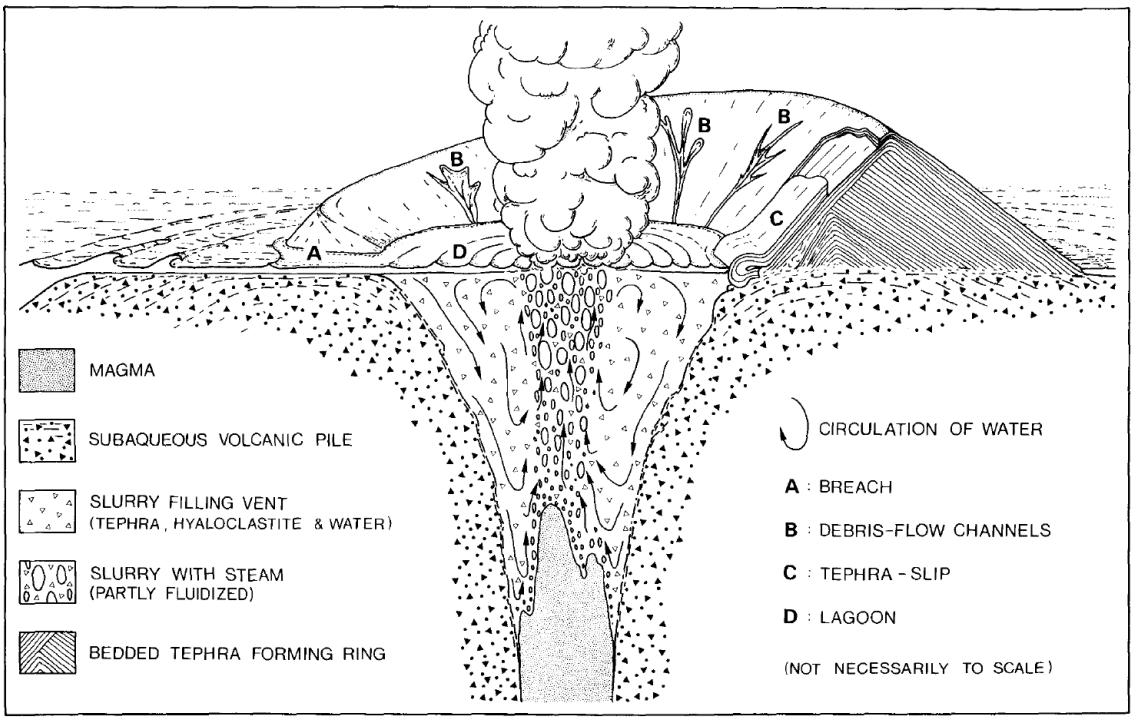

Figure 2.10: Cartoon model of Surtseyan-type eruption where steam forming around magma rises to the surface and forms a slurry of water, steam and hyaloclastite. When magma is emplaced into the slurry, bulk steam explosions occur and produce tephra jets. A breach in the tuff cone, allows seawater to flood the vent (from Kokelaar 1983).

Tephra jets form when steam, forming around the magma, rises to the surface (Figure 2.10). The steam mixes with the slurry of material found in the base of the vent cone, including tephra, hyaloclastite and water (Figure 2.10). When a magma batch ascends it mixes with the steam and slurry mix causing bulk steam explosivity and creating Rayleigh-Taylor instabilities (Kokelaar 1986). The steam rapidly expands as it is emitted out of the vent due to heating and a decrease in pressure upon entering the atmosphere. These steam ejections produce tephra jets. If the frequency of tephra jets is high, and steam is emitted almost continuously; this phenomena is known as continuous uprush (Kokelaar 1983; 1986). Continuous uprush occurs with a lower water-magma ratio than tephra jets and results in an increase in pyroclastic density currents (Solgevik et al. 2007).

Syn-depositional arcuate faults form around the crater rim with the crater on the downthrown side (Kokelaar 1986). This promotes continual collapse of inwardly dipping cone slopes, adding material to the vent slurry in the crater (Kokelaar 1986; Lorenz 1986; Sohn and Park 2005). Eruption-induced shock waves can cause liquidisation of wet vent wall deposits, causing them to become unstable and the volcanic pile becomes victim to slope failure, slumping and sliding (Kokelaar 1986).

Tuff Cone stratigraphy

The stratigraphy of tuff cones is deposited under a variety of processes. Ballistic ejection of coarse material, clearing of the funnel of slurry in the top of the vent, deposition from tephra jets, fall out deposition from continuous uprush plumes, pyroclastic density currents (PDCs), gravitational slope failure of steep cone sides (debris flows and slides), turbidites, and reworking by sedimentary processes, have all been recorded in sedimentary and stratigraphical studies of tuff cones (Sohn and Chough 1992; Houghton and Smith 1993; Sohn and Park 2005). The stratigraphy and sedimentary structures vary with distance from the vent and may be divided into three zones: proximal (0 – 350 m), medial (350 – 500 m) and distal (>500 m). Stratigraphical and textural studies of tuff cones have recorded the changes in the lithofacies within these zones (e.g. North Otago, New Zealand (Maicher 2003; Murphy et al. 2008); Chatham Island, New Zealand (Sorrentino et al. 2011); Jeju Island, South Korea (Brenna et al. 2011; 2012; Sohn et al. 2011); Cheju Island, South Korea (Sohn and Chough 1989, 1992; Sohn et al. 1993); Surtsey, Iceland (Kokelaar and Durant 1983); NW

Colorado, USA (Leat and Thompson 1988); SW Japan (Kano 1990); Capelinhos, Azores (Cole et al. 2001); Sao Miguel, Azores (Solgevik et al. 2007; Mattsson 2010).

Alternating stratifications of fine ash and coarse lapilli reflects a regular alternating change in eruption explosivity occurring during one tuff cone eruption. Fine-graded beds indicate a more optimal water-magma ratio and increased fragmentation during explosion, whereas coarser stratification indicates less fragmentation and explosivity at the vent (Sorrentino et al. 2011; Sheridan and Wohletz 1983). Couplets of ash and lapilli suggest different mechanisms of deposition with finer ash being deposited as a plume fallout deposit and coarse lapilli as a product of a PDC. Alternating layers of both PDC and fallout deposit suggest a combination of both processes occurring contemporaneously during one sustained eruption (Zanon et al. 2009). The presence of ballistic bombs with impact sag structures reflects subaerial impacts. If the block were to be emplaced into water, the bomb would not form sag structures due to drag velocity of the seawater (Sorrentino et al. 2011).

Laterally extensive, low-angle, finely laminated beds are the products of high-concentration grain flows (Sohn and Chough 1993; Solgevik et al. 2007; Corcoran and Moore 2008). Occurrences of reverse-graded stratifications are formed due to gravitational settling or dispersive pressure during grain flows (Corcoran and Moore 2008). Normal-graded beds are formed during suspension fall-out (Sohn and Chough 1992). Minor syn-depositional faulting may occur due to seismic shaking due to eruptions and/or the emplacement of magma into the shallow substrate, causing partial fluidisation of beds. High-angle trough cross-beds indicate reworking of tuff cone tephra by wave-processes or current-processes (Sohn and Chough 1993; Corcoran and Moore 2008).

2.3.3. **Tindars**

Tindars are hyaloclastite ridges comprised of pillow lavas and consolidated, palagonitised tephra and are formed from subglacial eruptions (Jones 1969). Subglacial eruptions are driven by explosive magma-water interaction and are described as "Surtseyan-like" eruptions by Thordarson and Höskuldsson (2008). Similar to typical Surtseyan eruptions, subglacial eruptions produce both continuous uprush explosions and tephra jets (Gudmundsson 2003). The main difference between submarine and subglacial eruptions is that products of subglacial eruptions are not widely distributed

but are confined by ice-cover, forming isolated tindars (hyaloclastite ridges) and tuyas (subrectangular or circular mountains) (Matthews 1947; Jones 1969; Moor and Calk 1991; Smellie 2000; Björnsson 2003; Gudmundsson et al. 2004; Jakobsson and Gudmundsson 2008; Stevenson 2014). If the eruption breaks through the ice cover, the eruption style changes and spatter, lavas and widespread tuff deposits form (Bjornsson, 2003). Like other monogenetic eruptions, subglacial eruptions are typically small (< ~1 km^3) (Thordarson and Höskuldsson 2008).

Tindar stratigraphy

Tindars are typically formed of several units defined by the amount of overlying pressure: (1) a bottom unit formed under high confining pressures producing pillow lavas and pillow breccias; (2) as the ice melts, the overlying pressure decreases allowing explosive magma-water interaction to occur and producing a unit composed of fragmented tephra; (3) if the eruption continues and melts the ice above the edifice completely, subaerial Hawaiian and Strombolian processes can occur and form spatter units and lava flows; and (4) hyaloclastite delta foresets can form surrounding the ridge, if effusive lavas advances into a surrounding lake (Jones 1969; Schopka et al. 2006). If the glacier above the edifice does not melt completely, stages (3) and (4) do not occur and the subaerial facies do not form. Similarly, if the glacier is relatively thin and the overlying pressure is low enough, stage (1) does not occur and the magma is able to interact explosively with the water beneath the glacier at a very early stage, resulting in a lack of pillow breccias at the base of the tindar (Schopka et al. 2006). Explosive interaction can occur beneath relatively thick glaciers because the overlying ice can be supported by the sides of the glacier, lowering the effective overlying pressure (Schopka et al. 2006).

2.3.4. **Maar diatremes**

Maar-diatreme volcanoes form when magma rises through a feeder intrusion and interacts explosively with groundwater, inducing explosive phreatomagmatic eruptions. These eruptions form a conical diatreme beneath a crater, called a maar. Typically a tuff ring or cone forms around the maar from the tephra deposited by PDCs and direct fallout. Maar volcanoes are distinguished from other small, constructive volcanoes by having the base of the crater below the pre-eruptive surface (Lorenz 1986; White and Ross 2011).

Diatreme Formation

Maar-diatreme volcanoes are produced by explosive thermohydraulic eruptions at depth due to explosive magma-water interaction. A hydrostatic pressure of approximately 3 MPa or more will inhibit thermohydraulic phreatomagmatic explosions (Valentine and White 2012). This pressure is known as the hydrostatic pressure barrier and is equivalent to 200 to 300 m in the subsurface, however diatremes can reach depths of up to 2 km beneath the pre-eruptive surface (Lorenz and Kurszlaukis 2007; Valentine and White 2012). There are two current models that explain the development of a diatreme and the ability for phreatomagmatic explosions to occur at such depths. The theory of a lowering of groundwater hydrostatic pressure around the explosion site was established by Lorenz (1986) and revised by Valentine and White (2012).

Lorenz (1986) suggests that phreatomagmatic explosions lower hydrostatic pressure locally around the explosion site. This forms a cone of depression and will result in the deepening of the barrier depth and allow for subsequent explosions at lower depths (Lorenz 1986, Lorenz and Kurszlaukis 2007). The root zone excavates downward (Figure 2.11A). These explosions tend to take place directly above the top of the feeder dyke. To allow for the excavation of a diatreme, a few hundred to a few thousand individual phreatomagmatic explosions must occur (Lorenz and Kurszlaukis 2007).

Valentine and White (2012), however, argue that magma can ascend into the diatreme fill and cause phreatomagmatic explosions at any level as long as the water pressure is below the hydrostatic pressure barrier. The site of these phreatomagmatic explosions are known as intra-diatreme fragmentation zones (White and Ross 2011). The diatreme has the typical conical shape because

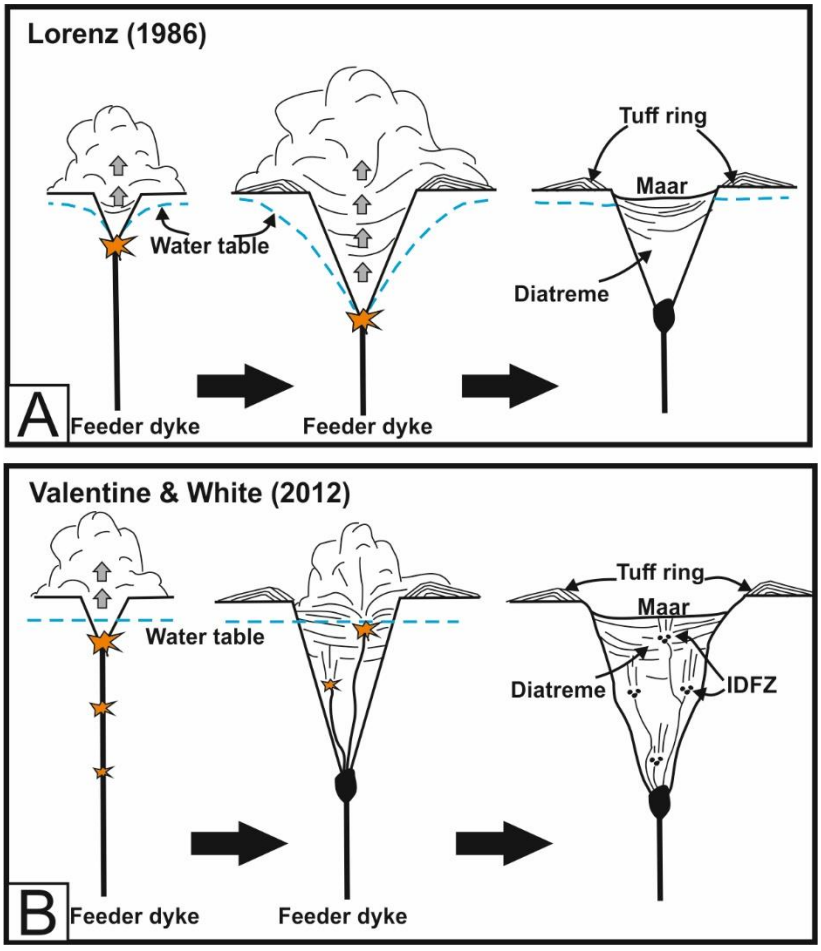

Figure 2.11: Comparison of the two diatreme formation models. (A) Adapted from Lorenz (1986) and Valentine and White (2012). The deepening of the water table due to excavation of host-rock forms a cone of depression around the diatreme which allows for phreatomagmatic explosions to occur at greater depths than the hydrostatic pressure barrier. (B) Adapted from Valentine and White (2012) Alternative model of Valentine and White (2012) where intrusions can feed phreatomagmatic explosions anywhere in the diatreme structure. Explosions are more efficient at the top of the diatreme which causes the diatreme to widen more effectively at the top.

the diatreme widens at its top faster than at its bottom (Valentine and White 2012). This occurs because: (1) in the top of the diatreme, the hydrostatic pressure is lower and the phreatomagmatic explosions are more effective; (2) the strength of the host-rock will be weaker at the top of the diatreme than the bottom so that phreatomagmatic explosions in the top of the diatreme will brecciate a larger volume of the surrounding host-rock, widening it more efficiently at the top; and (3) the walls of the diatreme can collapse more easily in the upper portion of the diatreme (Figure 2.11B) (Valentine and White 2012).

The initial depth of explosions and morphology of the root zone is often dependent on the type of host-rock. For example, in a soft-rock environment there is a greater volume of pore water which can generate a greater amount of steam-driven disruption. In a soft-rock environment, a lower lithostatic pressure also allows for fluidisation and liquefaction of host-rock/sediment. Alternatively,

in a hard-rock environment, phreatomagmatic explosions occur locally where there are faults and or fractures within the host-rock allowing magma to access groundwater in the fractures. In this respect, root zones can form at very shallow depths due to poor or very poor permeability and access to groundwater (Lorenz and Kurszlaukis 2007).

Explosion chambers are formed during phreatomagmatic explosions due to the brecciation and collapse of the host-rock and the upward ejection of fine ash and dyke fragments away from the explosion site (Lorenz and Kurszlaukis 2007). Gravity-driven collapses of host-rock fill the explosion chamber. Further fragmentation can occur by steam-driven eruption columns (Lorenz and Kurszlaukis 2007). The subsidence associated with the filling of the explosion chamber, allows for the upwards propagation of curvilinear faults. The low density and heavily fractured and jointed nature of the halo around diatremes aids the propagation of these curvilinear faults into the host-rock as well as the overlying diatreme fill. Subsidence along these faults into the main diatreme structure allows for diatreme growth (Lorenz and Kurszlaukis 2007; Barnett 2006).

There are two ways of vertically mixing the diatreme fill (including the host-rock clasts): (1) debris jets expelling the solid phase of explosion columns into higher levels of the diatreme structure (Lorenz and Kurszlaukis 2007; Valentine and White 2012); and (2) wall rock collapse, later becoming entrained into subsequent debris jets columns and transported elsewhere in the diatreme. The consequence is a homogenisation of the diatreme fill (Valentine and White 2012).

Intrusions form dykes, sills and plugs in the very shallow subsurface below the maar crater (Lorenz and Kurszlaukis 2007). Cooled or partially cooled intrusions can be fragmented and brecciated by entrainment in eruption columns (Lorenz and Kurszlaukis 2007, Valentine and White 2012). If the intrusions breach the crater surface, scoria cones and lava lakes can form. If the intrusions extrude into a maar lake, a hyaloclastite body would form (Lorenz and Kurszlaukis 2007). Phreatomagmatic explosions will cease when either; (1) the input of magma stops or (2) there is no access to groundwater.

Diatreme Structure

The general structure of a maar-diatreme comprises: (1) feeder intrusions; (2) a root zone; (3) lower, unbedded diatreme facies; (4) upper, bedded diatreme zone; and (5) tuff ring or tuff cone (Figure 2.12) (White and Ross 2011; Valentine and White 2012). These terms do not necessarily determine the structural level of diatreme fill. Within the diatreme structure, intra-diatreme fragmentation zones feed debris jets which extend upwards into the upper levels of the diatreme.

Feeding Intrusions

Diatremes are fed by dykes and sills; however thorough studies of sill feeders are presently lacking in the literature (Gevers 1928, Francis 1959; Clement 1982, Németh and Martin 2007). Intrusions disintegrate in one of three ways: (1) phreatomagmatic explosions, when magma comes into contact with pore-water or groundwater, (2) fragmentation due to an increase in the pore pressure in low-permeability host-rock, and (3) hydraulic fracturing caused by extensive thermally-driven fluids, can fragment the intrusions (Brown et al. 2007; White and Ross 2011).

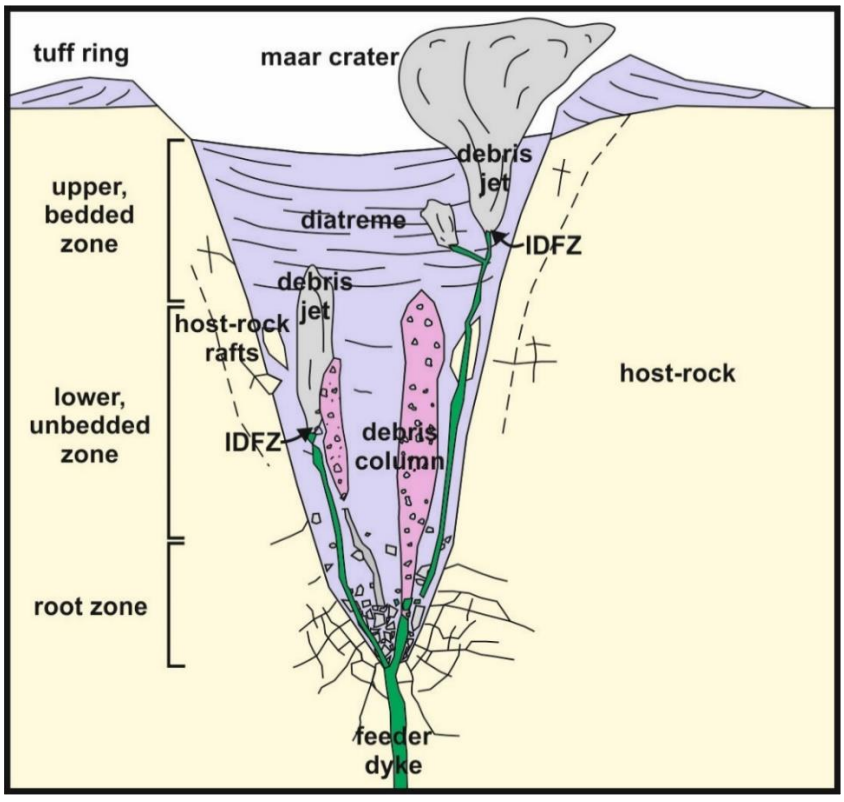

Figure 2.12: Structure of a maar-diatreme volcano. Magma interacts with groundwater causing subsurface phreatomagmatic explosions. The diatreme is divided into four distinct zones: (1) Root zone where dykes are emplaced and fragmented; (2) Lower diatreme zone comprising massive, unbedded fill; (3) Upper diatreme zone has centroclinal dipping beds of tuffs, lapilli-tuffs and breccias; and (4) tuff ring comprising erupted deposits (PDCs and fallout deposits). Debris columns cross-cut diatreme stratigraphy and represent debris jets. Debris jets form when phreatomagmatic explosions eject fragmented material to the surface. The site of phreatomagmatic explosions that do not occur in the root zone are defined as intra-diatreme fragmentation zones (IDFZs). Adapted from Lorenz (2003).

Root zone

The transition from feeding intrusion to diatreme fill is termed the root zone (Figure 2.12) (Clement 1982). Root zones are less well understood than the overlying diatreme as they are rarely exhumed at the modern day surface. Examples of exposed root zones include Hopi Buttes, Arizona (White 1991; 2000) and the Gross Brukkaros Volcanic Field, Namibia (Lorenz and Kurszlaukis 1997). Root zones can also be examined by drill cores, although this rarely gives an indication of the 3D structure of these zones and their relationship with the overlying diatreme (Lorenz and Kurszlaukis 2007; White and Ross 2011).

Root zones can form as wide as 50 m and can extend vertically as much as 500 m (Lorenz and Kurszlaukis 2007). Rootzone breccias contain host-rock clasts, coherent igneous bodies from brecciated feeding dykes, and diatreme-fill input from the above diatreme deposits, resulting in a heterogeneous and unstructured mix (White and Ross 2011). The primary features of root zones are: (1) highly irregular geometries; (2) chaotic and irregular host-rock margins; (3) bulges and overhangs that extend into the host-rock; (4) elongation at depth, and (5) contact breccias (Lorenz and Kurszlaukis 2007).

Contact breccias (Lorenz and Kurszlaukis 2007) or monobreccias (Delaney and Pollard 1981) are homogenous breccias that form in-situ and comprise only host-rock sourced from the surrounding substrate. Jig-saw fit textures are common. Clasts can be differentially rotated, forming cavities within the breccia (Lorenz and Kurszlaukis 2007). The high stress rate required to brecciate unweathered and normally jointed host-rock is achieved by explosion shock waves, as discussed above (Grady and Kipp 1987). Only 20% of the kinetic energy, released from the phreatomagmatic explosions, fragments the magma into very fine ash with the remaining 80% of the kinetic energy is converted to shock waves which are released as a consequence of magma fragmentation (Lorenz and Kurszlaukis 2007). These shock waves can fracture, fragment and fluidises the surrounding host-rock.

Lower Diatreme Zone

The unbedded diatreme zone has experienced the most subsidence and reflects the "oldest" diatreme fill (Figure 2.12). The lower diatreme is comprised of relatively unstructured homogeneous lapilli-tuffs and breccias. Host-rock clasts and inclusions within the diatreme fill can be sourced from

adjacent host-rock anywhere along the diatreme margin. Floating reefs or host-rock rafts are brecciated and subsided host-rock up to 200 m wide within the diatreme fill (Figure 2.12) (Clement 1982; Lorenz and Kurszlaukis 2007).

As this zone is closest to the explosion sites in the root zones, the tephra in the lower diatreme fill is disrupted by: (1) explosion shock waves; (2) the migration of debris jets, causing inflation and subsequent deflation (by fluidisation) of the tephra (Figure 2.12); (3) collapse of the feeder conduit walls after the eruption cloud has passed; and (4) collapse of diatreme fill into the root zone (Lorenz and Kurszlaukis 2007).

Upper Diatreme Zone

The upper diatreme zone is comprised of bedded lapilli-tuffs and tuffs which dip in a centroclinal pattern (Figure 2.12). The collapse of root zone breccias into the vacant explosion chamber causes instability of the overlying diatreme fill and results in the differential subsidence of the upper diatreme beds. This explains the saucer-shaped structure of the upper diatreme zone (Lorenz 1986; Lorenz and Kurszlaukis 2007).

Intra-diatreme fragmentation zone

With similar attributes to the root zone of diatremes, the intra-diatreme fragmentation zone (IDFZ) can also be mistaken for the base of diatremes. Technically, IDFZs are the root zones of small diatremes within the larger diatreme structure (White and Ross 2011). Intra-diatreme fragmentation zones are found at any level in the diatreme as long as the hydrostatic groundwater pressure is below the hydrostatic pressure barrier (Figure 2.12) (Valentine and White 2012).

Like root zones, IDFZs are the result of feeding intrusions fragmenting by phreatomagmatic explosions. The significant difference between root zones and IDFZs, is the lack of country-rock, either brecciated or fluidised, incorporated in to the IDFZs (White and Ross 2011). Intra-diatreme dykes that feed the IDFZs can exhibit bulbous shapes and bifurcations because of ductile emplacement (Valentine and White 2012). Only late-stage IDFZs are preserved as these have not been subject to the churning and mixing of the diatreme fill.

The height of IDFZs and their associated feeding dykes is dependent on the magma flux, which can change over the duration of maar-diatreme forming events, and the porewater saturation of the

diatreme fill host-rock. Some intra-diatreme feeder dykes stall at higher levels in the diatreme and peperite is formed (Valentine and White 2012).

Examples of intra-diatreme fragmentation zones are highlighted in previous studies of Hopi Buttes, Arizona and the Coombs Hills (Ross 2005; White and McClintock 2006; Ross and White 2006; McClintock et al. 2008; Ross et al. 2008; White and Ross 2011). The Coombs Hills IDFZ displays both gradational and sharp contacts with surrounding non-bedded lapilli-tuff. Sharp contacts have been attributed to the IDFZ being much later than the initial diatreme formation (less heat in diatreme deposits). Within the IDFZ are pods of coherent igneous material which are randomly orientated and irregular in structure. Locally, peperite forms at the pod margins suggesting non-explosive interaction with wet diatreme fill (Ross 2005; White and Ross 2011). Non-explosive interaction would not form debris jets. White and Ross (2011) note that the spectrum of processes within IDFZs, ranging from non-explosive peperite forming interaction to abruptly expansive and explosive interaction, are poorly understood. The source of explosive interaction is difficult to locate as products of this type of interaction are typically dispersed.

Debris jets and columns

Debris jets form towards the end of individual phreatomagmatic explosions when groundwater is super-critically vaporized. Juvenile ash grains are entrained in the debris jet and as it ascends through the diatreme pipe, it can further entrain host-rock inclusions and juvenile clasts from earlier deposits. The passing debris jet homogenises breccias and lapilli-tuffs from early deposits and disrupts bedded diatreme fill in the upper diatreme zone. The result of passing debris jets is an unstructured, homogenous column, called a debris column (Figure 2.12). Debris columns range from 30 m to 70 m wide and typically consist of massive, unsorted rock (Lorenz and Kurszlaukis 2007). Once the debris jet passes through, parts of the column wall can collapse and subside.

If the maar-diatreme volcano is still in the early stages of formation and excavation, these debris jets have the potential to eject a portion of the diatreme fill (juvenile clasts, host-rock inclusions and clasts of earlier tephra fill). At greater depths, this process is impossible due to the weight of the diatreme fill and the column fails (Lorenz and Kurszlaukis 2007). Failure of the debris jet is more likely at the end of the phreatomagmatic phase as the explosions do not have the energy to erupt

from depth to the surface. At this point diatreme development slows and ends (Figure 2.12) (Lorenz and Kurszlaukis 2007).

Tuff Rings and Cones

Tuff rings form on the top surface around the maar-crater and are formed by the ejected debris jets (Figure 2.12). The collapse of the eruption columns at the surface produces pyroclastic density currents and causes fallout deposits to form. Depositional processes control the edifice morphology (i.e. tuff ring or tuff cone). If the magma supply reaches high levels within the diatreme, ejecta rings tend to be broader and there is greater lateral transport of ejecta away from the vent (White and Ross 2011).

Maar-ejecta ring deposits develop good stratification. The thickness of each individual tephra bed is a result of the ratio between the reflux of groundwater into the root zone and the volume of magma intruding into the base of the root zone (Lorenz and Kurszlaukis 2007). Reworked tephra formed as a result of mass flows (lahars, rock falls, rock slides, screes) due to the subsidence of the crater flow and subsequent collapse of the tephra ring walls (Lorenz and Kurszlaukis 2007) are also present. Cumulative tephra thicknesses on the maar crater floor can reach up to 1 km (Lorenz and Kurszlaukis 2007).

2.3.5. **Monogenetic Volcanic Fields**

Monogenetic volcanic fields are found in all tectonic environments: intraplate (e.g. Auckland, New Zealand); back-arc (e.g. Abu, Japan); continental rifting (e.g. Eifel, Germany); and basin and range (e.g. Springerville, USA), and were once thought to have been fed by predominantly dyke dominated plumbing systems (Kereszturi and Németh 2012; Le Corvec et al. 2013). It is now widely accepted that lateral magma migration can be significant in monogenetic volcanic fields (Cartwright and Hansen 2006; Svensen et al 2012; Magee et al. 2014; 2016; McLean et al. 2017). Interconnected sill and sheet networks can facilitate magma transport from source to surface by up to 4100 km laterally and therefore affect the geochemical and petrological characteristics of monogenetic products (Magee et al. 2016).

The number of edifices within a monogenetic volcanic field ranges from tens to several hundreds (Le Corvec et al. 2013). Monogenetic volcanic edifices are typically arranged in clusters (e.g.

Auckland Volcanic Field. New Zealand; Magill et al. 2005) or alignments (Yucca Mountains, Nevada, USA; Connor et al. 2000). The spatial distribution of edifices is influenced by the source of the magma, the morphology of the plumbing system, the magma flux and the regional stress field (Connor and Conway 2000; Valentine and Perry 2007; Le Corvec et al. 2013). Strong alignments of edifices tend to form where there is strong fissure behaviour, where lava is erupted along the length of the fissure before being focused at one or two points, producing edifices, for example the Vestmannaeyjar islands, Iceland (Figure 2.13Figure 2.13: The Vestmannaeyjar Islands, along the south coast of Iceland, are comprised of a series of tuff cones and monogenetic edifices that are aligned along a propagating rift system. Photo taken in July 2015 by CM.) (Németh 2010). Alignments may also be controlled by the regional stress direction and by faults or pre-existing crustal structures, which change the stress regime of the area and affect the emplacement of magma, for example the West Eifel Volcanic Field in Germany (Lorenz 1984; Valentine and Krogh 2006; Gaffney et al. 2007; Németh 2010; Kereszturi and Németh 2012; Le Corvec et al. 2013; Magee et al. 2015; McLean et al. 2017). In monogenetic fields with a high magma flux, frequent dyke injection can produce a random or clustered arrangement (Németh 2010).

Figure 2.13: The Vestmannaeyjar Islands, along the south coast of Iceland, are comprised of a series of tuff cones and monogenetic edifices that are aligned along a propagating rift system. Photo taken in July 2015 by CM.

2.4. Host rock deformation

As magmatic intrusive bodies come into contact with sediment or rock, the sediment/rock may interact in a variety of ways, including: (1) uplift of the overburden inducing forced folding; (2) fluidisation and textural homogenisation; (3) fracturing and brecciation; (4) fluid-fluid shearing and formation of density structures; (5) peperite formation; and (6) alteration, cementation and contact metamorphism (Duffield et al., 1986; Skilling et al. 2002, Maltman and Bolton, 2002; Magee et al. 2016). It is important to understand the various processes of host-rock deformation due to magma emplacement to enable recognition of the type and scale of host-rock interaction in Chapter 7. A soft sediment deformation case-study was undertaken using a field example from Owyhee, Idaho and is presented as Appendix 10.1.

2.4.1. **Forced folding**

The emplacement of intrusions can lead to the formation of forced folds directly above the intrusions (Bell and Butcher 2002). Forced folds form in one of two ways: (1) due to the emplacement and inflation of intrusions causing updoming in the overlying strata (Figure 2.14) (Pollard and Johnson 1973; Smallwood and Maresh 2002; Hansen and Cartwright 2006; Jackson et al. 2013; Magee et al. 2014), and (2) differential compaction of host-rock surrounding intrusions (Figure 2.14B) (Hansen and Cartwright 2006; Magee et al. 2014). Type 2 forced folds form gradually over time due to greater compaction rates in sediments surrounding the intrusion (Figure 2.14B) (Hansen & Cartwright 2006).

Folding due to uplift of the overburden occurs when there is a viscosity contrast between two layers of a sediment pile (Figure 2.14A) (Duffield et al 1986). The emplacement of the intrusion can be expressed at the surface as wide, flat topped periclinal antiforms or mounds (Bell and Butcher 2002). These mounds can be onlapped by subsequent stratigraphy (Bell and Butcher 2002; Hansen and Cartwright 2006; Magee et al. 2014).

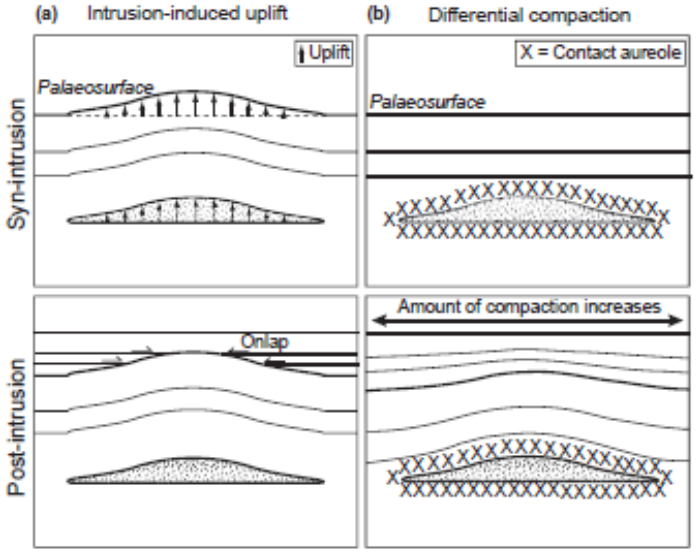

Figure 2.14: Schematic diagrams of the two intrusion-related fold mechanisms and the consequent reflection configurations (from Hansen & Cartwright 2006 and Magee et al. 2014).

2.4.2. **Liquidisation, Fluidisation and Mobilisation**

Liquidisation is defined by Allen (1984) as sediments that have previously had a yield strength becoming liquidised with the same mechanical properties as a Newtonian fluid. There are several driving mechanisms of mobilisation: (1) sensitive sediments; (2) liquefaction; (3) fluidisation; (4) shear stress; and (5) reverse-density gradients (Mills 1983; Jones and Omoto 2000; Maltman and Bolton 2003). Liquidisation and remobilisation is initiated by triggers, including (but not limited to) rapid loading (e.g. intrusion emplacement), seismic activity, slope failure, heat, and the oscillation of groundwater currents and water waves (Owen et al. 2011; McLean et al. 2016).

Subsurface mobilisation is dependent on pore-fluid pressure, which typically increases with depth (Figure 2.15; Maltman and Bolton 2003; Owen et al. 2011). The increase in pore fluid pressure can occur by both internal and external means, either by the application of a load with which pore fluid drainage is unable to keep pace and remain at constant hydrostatic pressure, or by pore fluid vaporisation and expansion (Mills 1983; McLean et al. 2016). External loading is defined as an external source acting as a mechanical load, whereby the pore fluid supports the extra weight (Maltman and Bolton 2003). The external source is typically later sedimentation, either by slow and steady sedimentation, fast emplacement of sediment or magma (e.g. tectonic or volcanic mechanisms), or cyclic loading (e.g. ocean waves and the accumulation of overpressure in a series of pulses over time) (Owen et al. 2011). Internal loading is applied to pore fluid from an internal

source (e.g. increasing the volume of pore fluids within the same porosity by mineral dehydration, hydrocarbon generation, the release of gas hydrates at depth, or the cementation of pore spaces) (Maltman and Bolton 2003).

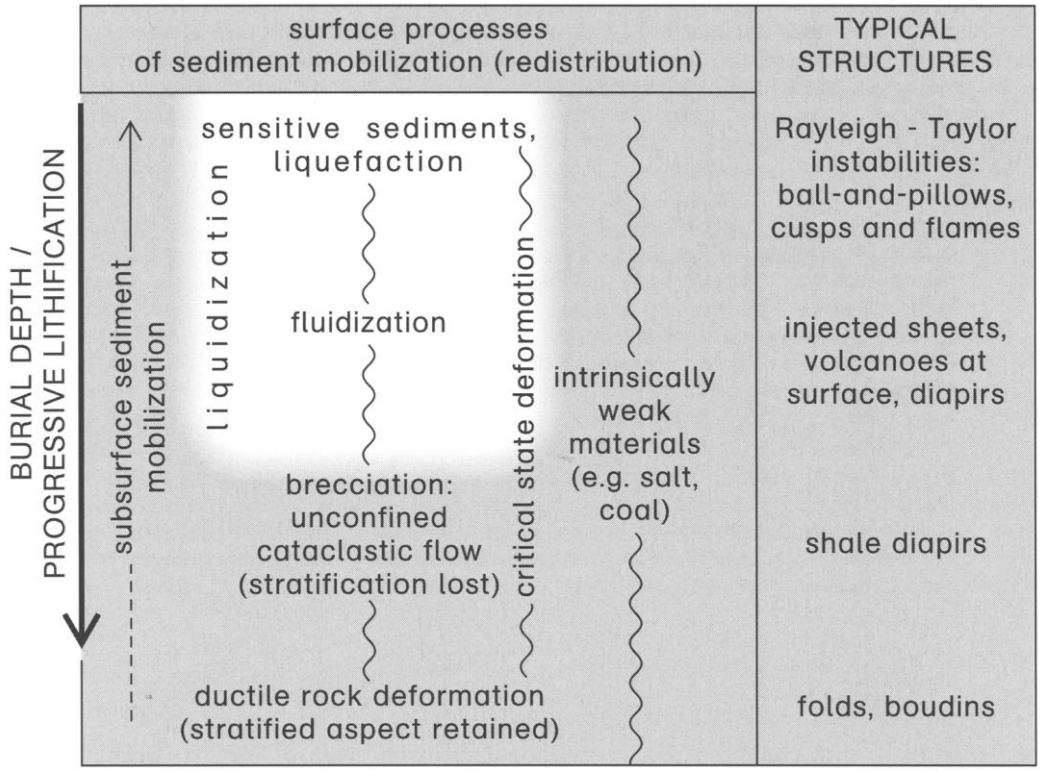

Figure 2.15: Conceptual view of burial depth related to type of mobilisation and the resulting structures. White shading highlights the processes that occur in the shallow subsurface discussed in this research (from Maltman and Bolton 2003).

The depth window where sediments can be mobilised is dependent on the efficiency of pore-fluid drainage and the overlying lithostatic load (Figure 2.15). The efficiency of pore fluid drainage, and consequently pore-fluid pressure, is dependent on permeability. If rock/sediment has a high permeability, mobilisation occurs by externally-pressured fluids filtering into pore spaces, causing an overpressure between grains. Conversely, low permeability allows inefficient draining of pore-fluids and hence overpressures can be trapped in existing pore fluids, which causes weaknesses in the sediment.

Liquefaction. Liquefaction is where the loading of sediment is supported solely by pore-fluid. During liquefaction there is little or no cohesion between grains and thus, no strength. This results in the sediment deforming as a fluid (Allen 1982; Mills 1983; Owen 1996; 2003; Owen et al. 2011). If drainage of pore fluids is insufficient, the pore fluid pressure reduces frictional strength between

grains and the sediment can become liquidised (Maltman and Bolton 2003). Deformation by liquefaction occurs homogeneously throughout the sediment unit or units (McLean et al. 2016).

Fluidisation: Fluidisation is the transmitting of fluids through sediment causing the particles to become supported and entrained within a fluid or vapour (Allen 1982; Owen 1996; Skilling et al. 2002; Owen et al. 2011). The shear stress of the upward directed fluid matches the weight of the grains (Owen et al. 2011). Fluidisation typically occurs locally within a unit, with fluid movement controlled by vertical conduits (e.g. fluid escape structures and clastic dykes) (Owen et al. 2011).

When mobilised, the sediment will move in the direction of lower pressure. Sediment movement only occurs when the pressure gradient is sustained. The general direction of transportation is upwards although vectors can show sideways and even downward movement (Maltman and Bolton 2003). Coarser sediments are more susceptible to fluidization and liquefaction due to their high poro-perm at shallow depths; however, as they are heavier than fines, they require a larger flow velocity to allow entrainment and transportation. Sands become increasingly less susceptible to liquefaction and fluidisation at depth due to the exponential decrease in porosity. Comparatively, silt and clay are more likely to become mobilised at deeper depths, where loading is greater and can increase pore-fluid pressure enough to overcome mechanical intergranular strength.

2.4.3. **Density Structures**

Soft-sediment deformation structures occur in completely or partially unconsolidated, fluid-saturated sediments and form when sediments are remobilised (Anketell et al. 1970; Mills 1983; Jones and Omoto 2000; Owen 2003). Density contrasts can deform the interface between two contrasting layers, where negative buoyancy controls the downward movement of the upper, denser layer into the lower, less dense layer (McLean et al. 2016). This process can produce a spectrum of deformation structures, for example, simple load casts, pendulous load casts and detached pseudonodules (Figure 2.16; Owen 2003). Similarly, if both layers are liquefied the interface is controlled by the less dense layer and swirly, highly convolute Rayleigh-Taylor structures (R-T structures) form (Mills 1983; Hindmarsh and Rijsdijk 2000; McLean et al. 2016). Load structures form at the interface between sub-horizontal intrusive bodies and sediment substrate. If the magma cools or the sediment solidifies, the R-T structures can no longer form and

only true load structures (load casts, pseudonodules etc.) can develop (Owen 2003; McLean et al. 2016).

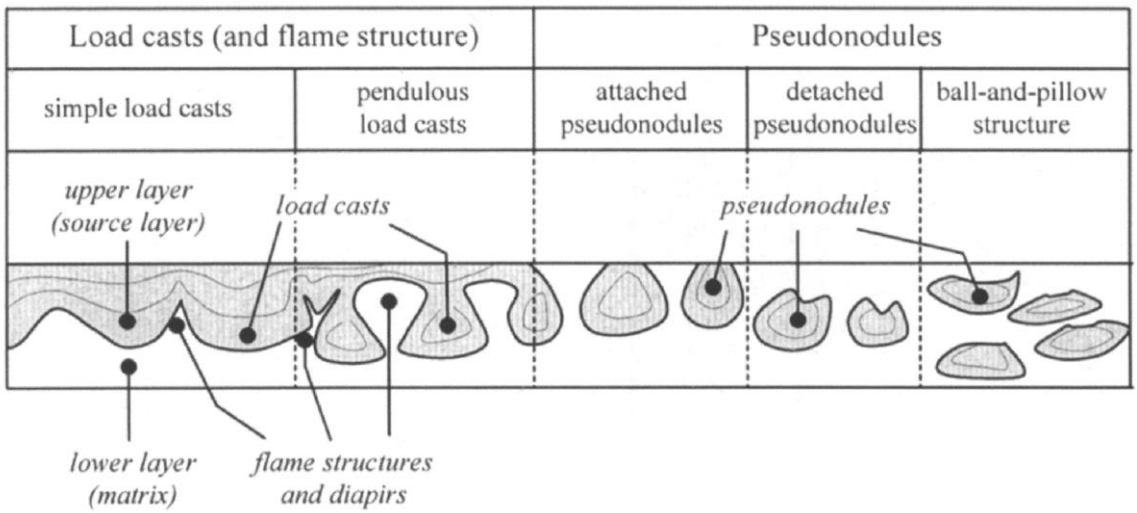

Figure 2.16: Spectrum of loading structures created by a density contrast between an upper layer (denser) and a lower layer (less dense) (from Owen 2003). Simple load casts are defined as a continuous upper layer and wavy interface. Pendulous load casts are a perpetuation of deformation process, attached to the upper layer by a narrow neck. Detached pseudonodules develop from pendulous load casts if the rising of the lower layer is more vigorous than the sinking of load casts (Owen 2003).

2.4.4. **Peperite Formation**

Peperite is formed in situ by the disintegration of magma intruding and mingling with un-consolidated or poorly consolidated, typically wet sediments (Busby-Spera and White 1987; White et al. 2000; Hooten and Ort 2002; Lorenz et al 2002; Skilling et al. 2002; Squire and McPhie 2002). The formation of peperite is a multi-stage process whereby many factors influence its formation, including: (1) magma rheology; (2) volatile content of magma; (3) porosity and permeability of host-sediment; (4) structure of sediment; (5) host-sediment rheology; (6) magma/water mixing ratio; (7) volume of magma versus volume of sediment mingled; (8) rate of magma-sediment mingling; (9) magma injection velocity; (10) confining pressure; (11) the nature of stress fields; and (12) total volume of pore water heated (Kokelaar 1982; Busby-Spera and White 1987; Hanson and Wilson 1993; Doyle 2000; Squire and McPhie 2002; Skilling et al. 2002).

2.4.4.1. Fragmentation

Magma can fragment due to: (1) density contrasts between magma and sediment; (2) explosive vesiculation; (3) quenching of magma against cold sediment; (4) mechanical stress; (5) hydromagmatic explosions; (6) shearing of magma against moving pore-water and sediment flows;

and (7) surface tension effects (Skilling et al. 2002). Busby-Spera and White (1987) recognised two primary types of peperite: fluidal and blocky (Figure 2.17). Fluidal peperite consists of lobate and globular shaped clasts with fluidal margins that are formed by ductile mechanisms where intact vapour films between the magma and sediment act as an insulator and protect the magma from thermal shocking. This type of fragmentation prevents direct contact of pore fluid and magma, so fragmentation occurs by density contrasts, fluid shearing, fuel-coolant interactions, and associated film instabilities.

Conversely, blocky peperite consists of equant to sub-equant clasts with planar surfaces and is formed by brittle fragmentation (i.e. thermal contraction or granulation; Fisher and Schminke 1984; Skilling et al. 2002), mechanical stress (cooled, rigid outer carapace of juvenile clasts is broken by continued magma movement; Kokelaar 1982) and steam explosions. Poorly sorted, coarse sediment with high permeability favours blocky peperite formation (Busby-Spera and White 1987). Similarly, sediments with a high strain rate will also influence the formation of blocky peperite (Squire and McPhie 2002).

Due to the initial high temperature gradient, the emplacement of intrusions into unconsolidated sediment supports development of fluidal peperite morphologies as the vapour film will insulate the magma. As emplacement progresses, the magma is liberated from the confines of the film and can surround pockets of sediment and pore fluid (Squire and McPhie 2002). Greater surface area allows super-fast cooling and quenching, and the fragmentation of the magma to produce blocky clasts interspersed into the host sediment. This temporal evolution of peperite highlights how magma temperature and hence magma viscosity has a direct influence on peperite formation.

Skilling et al. (2002) describe other clast shapes as ragged, platy and tapered, which are both variations of elongated clasts fractured parallel to magmatic flow (Figure 2.17). Ragged juvenile clasts are formed by a non-explosive mafic magma with little or no volatile content and are formed under the ductile regime.

2.4.4.2. Mingling and Sediment Movement

Host sediment is often found within cracks, fractures and vesicles of juvenile peperite clasts (Busby-Spera and White 1987). As magma quenches, angular fractures open and relieve pressure in the

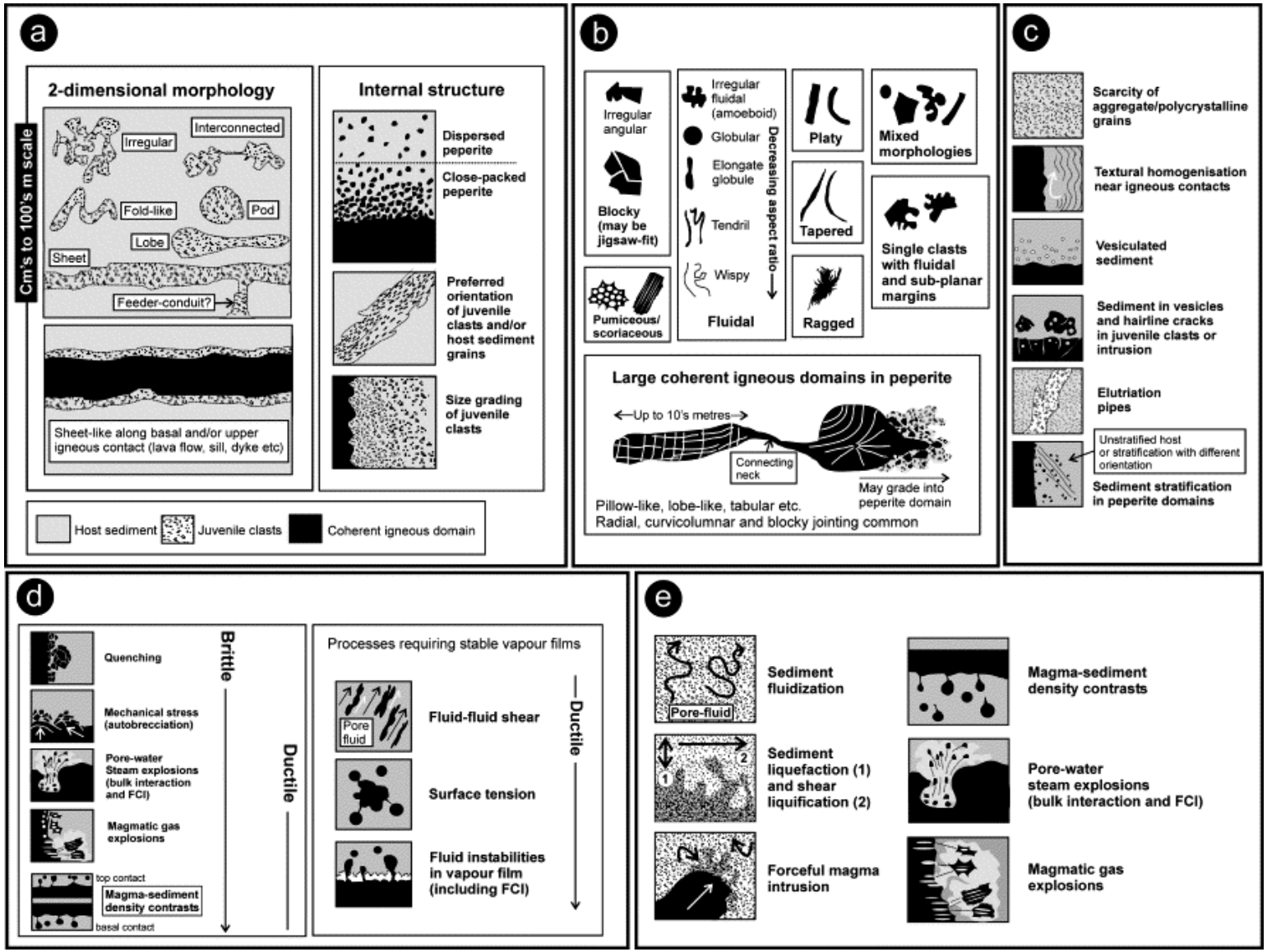

Figure 2.17: Summary of the interaction between igneous material and host- sediment. (a) morphology of peperite; (b) morphology of juvenile clasts; (c) nature of host-sediment interface; (d) brittle-ductile transition and juvenile clast generation; (e) interaction between juvenile clasts and host sediment. From Skilling et al. 2002

surrounding host-rock, vaporising pore fluids and forming a pressure gradient (Kokelaar 1982; Hanson and Wilson 1993; Doyle 2000; Skilling et al. 2002). Mobilised host-rock can become entrained within pore-fluids and injected into the newly opened fractures (Skilling et al. 2002). Sediment entrained within the vaporised pore fluid or within the vapour film that develops around juvenile clasts can be transported along the sediment-magma interface (Kokelaar 1982; Busby-Spera and White 1987). Fluidisation of the host, due to peperite formation, can cause complete destruction of original sedimentary structures.

Localised zones of peperite (passive peperite; Rawcliffe 2016) are caused by either small-scale fluidisation or by hydromagmatic explosions. Both processes typically occur at the beginning of magma injection and account for wide dispersal and mingling of juvenile clasts (Maltman and Bolton 2003). Large-scale mingling (dynamic peperite; Rawcliffe 2016) can be produced by sustained fluidisation of the host, which is achieved by continued injection of large volumes of magma. Dynamic peperite is defined as 'the complete disruption and mingling of the host-rock domain by and with the magma (Rawcliffe 2016). Mingling can also occur due to density contrasts between magma and host-sediment, whereby buoyant material (e.g. rhyolite) can rise upwards from the upper magma-sediment contact through the sediment and form fluidal juvenile clasts, or dense magma (e.g. basalt) can sink through more buoyant sediment from the basal contact (Skilling et al 2002).

2.4.5. **Contact Metamorphism**

Peperite formation can also be associated with contact metamorphism, although extensive metamorphism will restrict or prevent peperite formation (Skilling et al., 2002) as thermal hardening increases the lithostatic strength. According to Lorenz and Haneke (2004), the thickness of the aureole around an intrusion depends on three parameters: 1) thickness of the intrusion; 2) thermal conductivity of surrounding water-bearing sediments; and 3) how easily heat is transferred from intrusion to host-rock.

Chapter 3 Ben Nevis Monogenetic Volcanic Field; Faroe-Shetland Basin, UK

3.1. Introduction

This chapter is adapted from the published paper; "3D seismic imaging of the shallow plumbing system beneath the Ben Nevis Monogenetic Volcanic Field: Faroe-Shetland Basin" (McLean et al. 2017). The co-authors of this paper contributed by offering supervision (Nick Schofield and David Brown), by donating the data (Alexander Reid at Statoil) and offering advice and comments on the regional stratigraphy (David Jolley). The published paper is given as Appendix 10.2.

A 3D reflective seismic survey from the North of the Faroe-Shetland Basin, UK, reveals a series of monogenetic volcanic edifices and the underlying plumbing system. 3D seismic data is a powerful tool in understanding how monogenetic volcanoes are fed and how pre-existing crustal structures act as the primary influence on their spatial and temporal distribution. This seismic study, the Ben Nevis Prospect, examines the structure and lithology of host-rock as an influence on edifice alignment and allows for an assessment of the complex multi-level plumbing network, the morphology of the intrusions, and the connectivity of the monogenetic plumbing systems beneath these volcanoes.

Improved imaging in reflective seismic data of magmatic plumbing systems, particularly in the last 15 years, has significantly enhanced our understanding of shallow (<2 km) sill complexes, their relationship to overlying magmatic vent structures, and the development of monogenetic volcanic fields (Bell and Butcher 2002; Schofield et al. 2012; Jackson 2012; Magee et al. 2013; Schofield et al. 2015; Magee et al. 2016). The dataset encompasses the Ben Nevis Structure (BNS), a complex anticlinal structure covering an area of 300 km^2. It should be noted that the structure is so called due to its morphological similarity, rather than any geological reason, to the topographic dome of the Ben Nevis Mountain, located on the NW Scottish mainland. This chapter also provides an explanation for the presence and timing of the uplift of the Ben Nevis Structure and its interdependent association with local and regional magmatic activity along the North Atlantic Margin.

The anticlinal Ben Nevis Structure (BNS), located in the northerly extent of the Faroe-Shetland Basin, NE Atlantic Margin, was uplifted during the Late Cretaceous and Early Palaeocene by the emplacement of a laccolith and overlying "Christmas-tree" arrangement of sills. The data reveals multiple intrusions migrated up the flanks of the BNS after its formation, approximately 58.4 Ma (Kettla-equivalent), and fed a series of scoria cones, Surtseyan edifices and diatreme-like structures. The monogenetic edifices are aligned along the crest of the BNS and are fed from a complex network of sills and transgressive sheets, where lateral migration of tens of kilometres occurs before extrusion at the surface. This chapter highlights the importance of underlying basin structures in influencing the sites and development of sub-aerial monogenetic fields and provides an example of a monogenetic plumbing system in the shallow subsurface (200 m to 2 km). The following chapters (Chapter 4, 5 and 6) offer field studies of the plumbing systems in the sub-seismic scale.

3.2. Geological Background

3.2.1. **Geological History of the FSB**

The Faroe-Shetland Basin (FSB) is a hydrocarbon producing basin between NW Scotland and the Faroe Islands (Figure 3.1), NE Atlantic. The FSB is a collective name given to a series of NE-SW trending sub-basins, formed during rifting events post-Caledonian Orogeny (ca. 390 Ma) (Ebdon et al. 1995). The regional orientation of maximum horizontal compressional stress is largely NW-SE (Holford et al. 2016). The FSB is characterised by intra-basinal highs (Rona, Flett, Westray and Corona ridges; Figure 3.1A) separating half-grabens that contain accumulations of Jurassic and Cretaceous sedimentary rocks (up to 6 km) blanketed by Palaeocene to Recent sediments (Naylor et al. 1999; Moy and Imber 2009). The initiation of rifting of the North Atlantic in the Early Palaeocene, and the speculated impingement of a deep mantle plume, instigated magmatic activity, producing extensive lava fields, widespread ash horizons and large intrusive complexes, comprising a network of sills, connected by sub-vertical dykes and inclined sheets (White 1989; Smallwood et al. 1999; Smallwood and White 2002; Ellis and Stoker 2014). Large volcanic centres, that predate the rifting-associated volcanism, are identified in the northern FSB and in the Rockall Basin, West of Scotland by large isostatic gravity and positive, circular free-air anomalies (Passey and Hitchen 2011) (Figure 3.1C). The initial volcanic activity occurred at ca. 62 Ma (mid-Thanetian) and extended into the Early Eocene (Doré et al. 1997; Naylor et al. 1999; Smallwood and White 2002; Schofield et al. 2015). The volcanic activity produced a thick flood basalt sequence covering an area of 120,000 km^2 (Passey and Jolley 2008). The lava series is up to 5,000 m thick on the Faroe Islands and thins to the southeast (Waagstein 1988; Passey and Jolley 2008). The Faroe-Shetland Escarpment (Figure 3.1A and B) marks the palaeo-shoreline-shelf transition where subaerial lavas entered water, producing prograding foresets of hyaloclastite-pillow breccias and migrating the palaeo-shoreline seaward (Wright et al. 2012).

NW-SE trending lineaments are recognised in the FSB, cross-cutting the continental shelf (Figure 3.1A) (Rumph et al. 1993; Lamers and Carmichael 1999; Moy and Imber 2009; Ritchie et al. 2011; Schofield et al. 2015). The origins of these lineaments are unclear, however, hypotheses include reactivated Pre-Cambrian shears (Knott et al. 1993) and oblique extension features formed as a

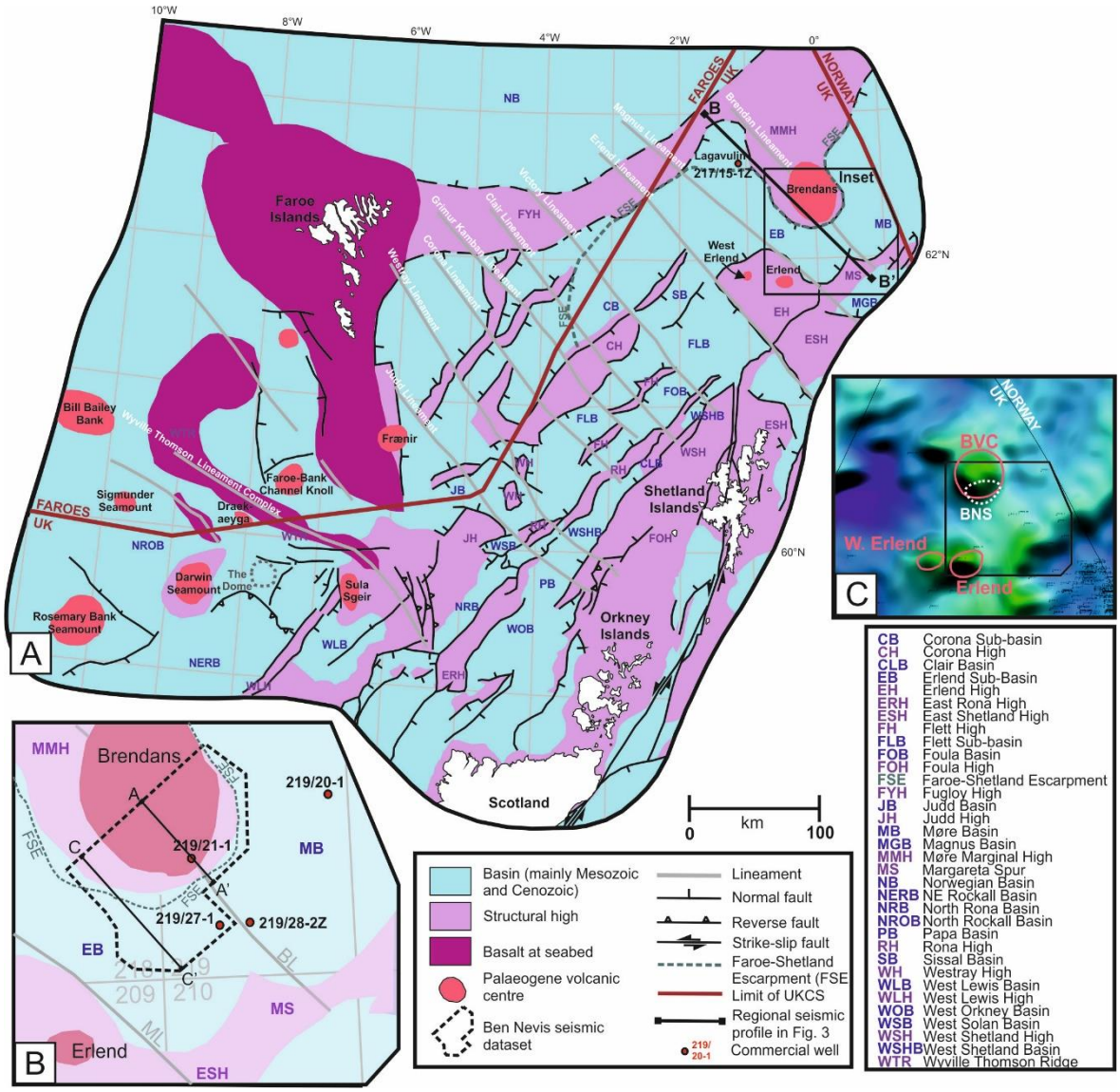

Figure 3.1: (A) Structural map of the Faroe-Shetland Basin and NE Rockall, highlighting the NE-SW trending sub-basins and NW-SE trending lineaments. Faroe-Shetland Escarpment marked by dashed line (from Ritchie *et al.* 2011 and Archer *et al.* 2005). Location of the Rockall Dome (Dome 164/7-1) marked by dotted line. Cross-section B-B' shown in Figure 3. Inset shown in (B). (B) Location of 3D seismic dataset (dashed line) and distribution of wells are marked. Cross-sections A-A' in Figure 2 and C-C' in Figure 5 (solid black line). (C) Gravity data over the Brendan's Volcanic Centre (BVC). Green shading shows high (positive) gravity response; blue shows low (negative) gravity response. Locations of gravity anomalies highlighted by red solid lines. Bouguer anomaly across the BVC is +80mGal. White dotted lines highlight the proposed structural highs including the BNS. Black solid line shows location of (B).

response to Mesozoic rifting (Rumph et al. 1993). The lineaments are an important feature in controlling basin segmentation, the location of transfer zones, the source input direction and distribution of Palaeocene and Eocene sediments, and possibly controlling the input and distribution of magma in the FSB in respect to intra-basinal highs (Schofield et al. 2015), including the various volcanic centres (Rumph et al. 1993; Archer et al. 2005; Moy and Imber 2009; Muirhead et al. 2015). Post-rifting subsidence and later Oligocene-Miocene localised compression resulted in minor folding

of Palaeocene lavas in the FSB and deposition of marine sediments (Doré and Lundin 1996; Ritchie et al. 2003).

3.2.2. **The Ben Nevis Structure: Hydrocarbon Exploration History**

The Ben Nevis Structure (BNS), which forms a broad anticlinal 4-way dip-closed structure, is unconformably overlain by a sequence of extrusive Palaeogene basaltic rocks and the Late Palaeocene monogenetic field, and was drilled by Shell (and partners) in 2003. Figure 3.2 displays a representative seismic line through the structure and location of the well. The pre-drill prognosis was a series of alternating Cretaceous shales and sands, however, upon drilling the pre-well prognosis was found to be incorrect. The BNS was found to be dominated by Cretaceous (Maastrictian and Campanian) mudstone sequences intruded by a series of Palaeogene dolerite intrusions (Figure 3.2). The intrusions gave rise to a series of high amplitude reflections that had been wrongly interpreted in the pre-drill prognosis as potential sandstone-reservoir/mudstone-seal pairs, in an almost identical scenario to a well drilled in 1997 in the Rockall Trough ("Dome Prospect") (Archer et al. 2005).

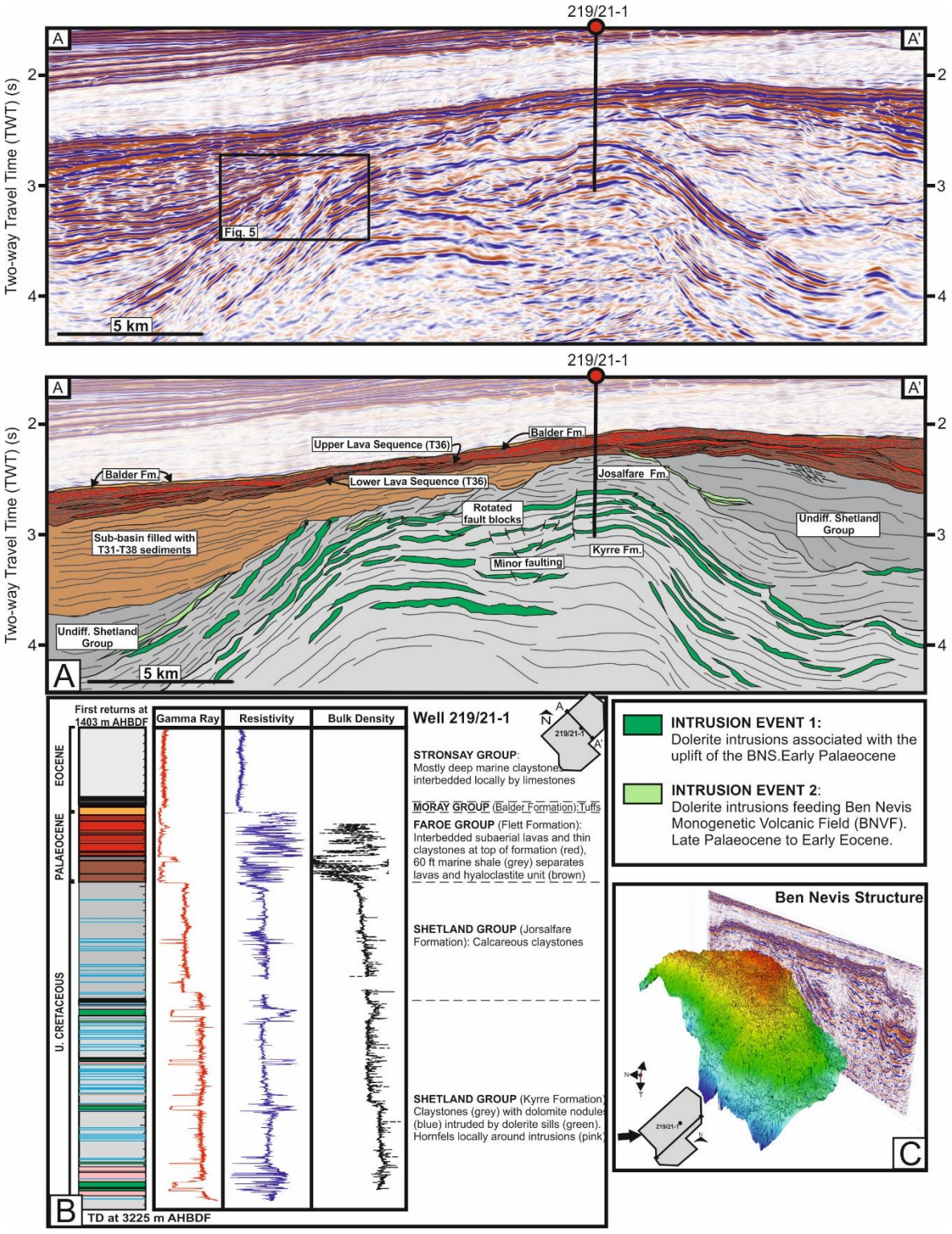

Figure 3.2: (A) Representative seismic line and interpreted line of the Ben Nevis Structure (BNS) (A-A') displaying location of well 219/21-1. Note the variation in thickness of the Upper Cretaceous on either side of the BNS and the truncation of bright reflectors on the flank of the NW BNS. Location of cross-section shown in Figure 3.1B. (B) Chronostratigraphic log of well 219/21-1. Sills in Kyrre Formation dated by Rohrman (2007). (C) 3D structural map of the BNS showing 4-way dip structure.

3.3. Seismic observations

To better understand the distribution of the monogenetic volcanic field above the BNS, we first need to understand the temporal evolution of the subsurface structure and its influence on the dispersal of volcanic edifices.

3.3.1. **Brendan's Volcanic Centre (BVC) and regional stratigraphy**

A regional gravity anomaly map shows the centre of a large (c. 50 km diameter), positive Bouguer gravity anomaly (+80mGal) in the northeastern FSB, identified as the Brendan's Volcanic Centre (BVC) (Passey and Hitchen, 2011) (Figure 3.1C). The anomaly is interpreted as a result of a large magmatic body intruded at depth. Equally it could be a collection of smaller igneous intrusions which would give rise to a singular gravity anomaly due to their proximity to each other and the low resolution of the geophysical data. The BVC is situated along one of the NW-SE trending lineaments, the Brendan's Lineament, which likely controls the site of the igneous centre (Figure 3.1A) (Archer et al. 2005).

The lithostratigraphy in the Ben Nevis (219/21-1) and Lagavulin (217/15-1z) wells have been extrapolated across a newly acquired regional line in Figure 3.3, constraining the stratigraphy across the northern margin of the FSB (Figure 3.4). Onlapping onto the BNS from the west is a sequence of T38 – T31 sedimentary rocks (Sullom-Lamba Formation), locally intruded by sills (Figure 3.3 and Figure 3.4). This T38 - T31 sequence is onlapped from a westerly direction by a sequence of T40 volcanic rocks (Flett Formation) (Figure 3.4). The T40 volcanic package thickens towards the Lagavulin prospect and is comprised of tabular lavas, volcaniclastics and hyaloclastites (Millett et al. 2015) (Figure 3.3). The T36 lava field (Lamba Formation), which is situated around the BNS, is also discretely onlapped by the T40 flows. The T36 lava field is a Kettla Member-correlative (a regional ash horizon marker) and is age equivalent to a number of small-scale rift flank volcanoes and associated lava fields in the Northern Foula Sub-basin (208/21-1) and in the Judd Sub-basin (204/28-1) (Schofield et al. 2015) (Figure 3.1). The T36 lava field (and age-equivalent volcanic rocks in the FSB) marks the onset of widespread volcanism in the basin ca. 58.4 Ma (Schofield et al. 2015).

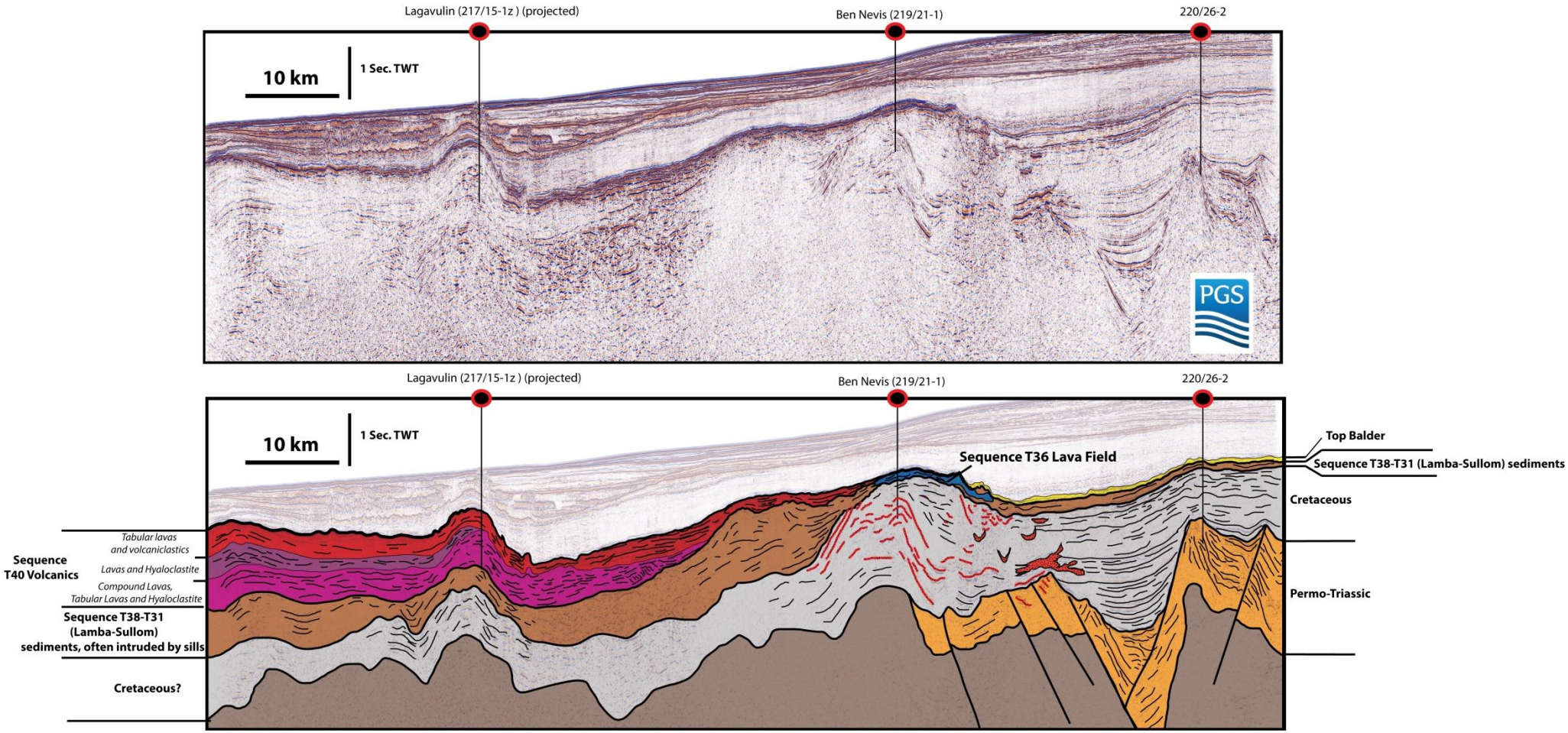

Figure 3.3: Interpreted regional seismic line across between the Ben Nevis Structure (BNS) and Lagavulin prospects (Data courtesy of PGS CRRG 2D GeoStreamer®). The location of the cross-section shown in Figure 3.1A (B-B'). "B" is on the left and "B"' is on the right of the seismic line. Well sites labelled. Interpreted stratigraphy shows the western margin of the BNS is onlapped by T38-T31 sediments and T40 volcanic rocks extrapolated from the Lagavulin well shown in Figure 3.1A. The lava sequence in the Ben Nevis seismic dataset (Figure 3.2) is an earlier and localised T36 lava field (blue). Red lines and stippled red shading are interpretated as magmatic intrusions. T-sequence stratigraphy in Figure 3.4.

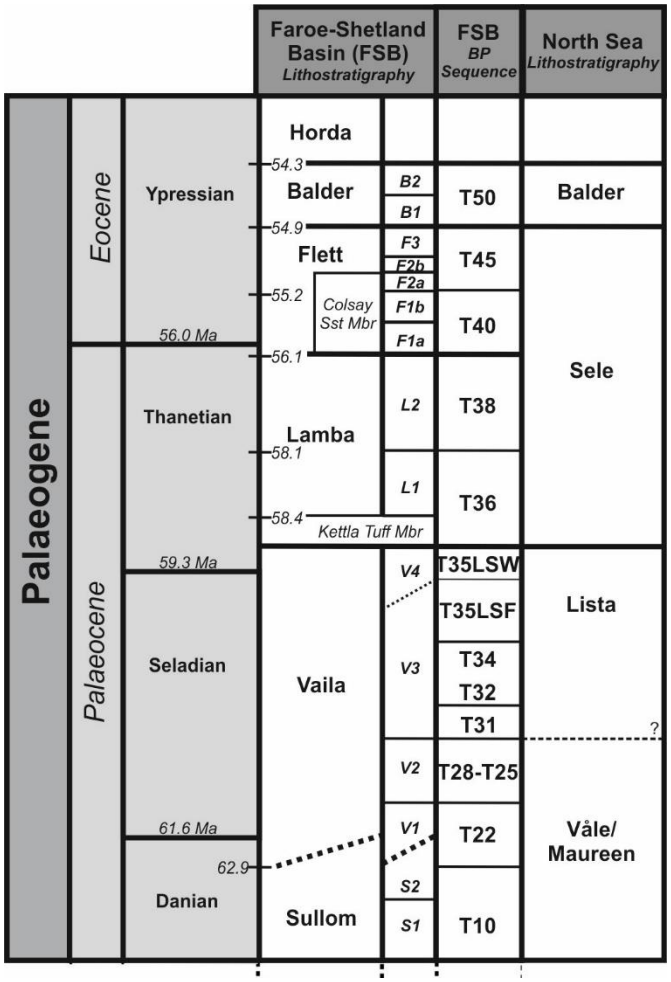

Figure 3.4: Palaeogene stratigraphy of the Faroe-Shetland Basin (FSB) (adapted from Schofield and Jolley 2013), with BGS lithostratigraphy (Ritchie *et al.* 2011); BP T-sequence stratigraphy (after Ebdon *et al.* 1995), and the North Sea equivalent Hordaland Group lithostratigraphy (found in wells east of the BNS).

3.3.2. **The Ben Nevis Structure (BNS) and Thanetian volcanic rocks**

The BNS is situated 15 km southeast of the centre of the Bouguer anomaly of the Brendans Volcanic Centre (Figure 3.1C). The BNS is defined by several high amplitude reflectors, that record a series of sills intruded into the Cretaceous stratigraphy, and which delineate the morphology of the anticlinal 4-way dip-closed structure (Figure 3.2). The sills are generally laterally extensive for tens of kilometres within the structure and are likely concordant to the bedding of the Cretaceous stratigraphy (Figure 3.2). The intrusions appear to exploit the Kyrre Formation in particular, allowing the boundary between the Kyrre Formation and the later Jorsalfare Formation to be more readily identified (Figure 3.2). The sills along the NW flank and crest of the BNS terminate at the Upper Cretaceous-Palaeocene unconformity and are subsequently onlapped by T38 - T31 sediments and volcanic rocks (Figure 3.5). The truncation of sills demonstrates that the sills were in place prior to the uplift, erosion and creation of the Upper Cretaceous angular unconformity.

Surrounding wells to the east of the BNS (219/20-1, 219/27-1 and 219/28-2Z; Figure 3.1) record between 262 m and 317 m of Selandian-aged stratigraphy (Lista Formation, Figure 3.4). However, across the crest of the BNS, the Lista Formation, or equivalent Vaila Formation (Figure 3.4), are absent and the T36 lava field (ca. 58 Ma) directly overlies the Upper Cretaceous unconformity. At the top margin of the anticline, sills are offset by normal faults, defining rotated ~1 km-across fault blocks in the Jorsalfare Formation (Figure 3.2). Normal faulting is also evident within the Kyrre Formation (Figure 3.2).

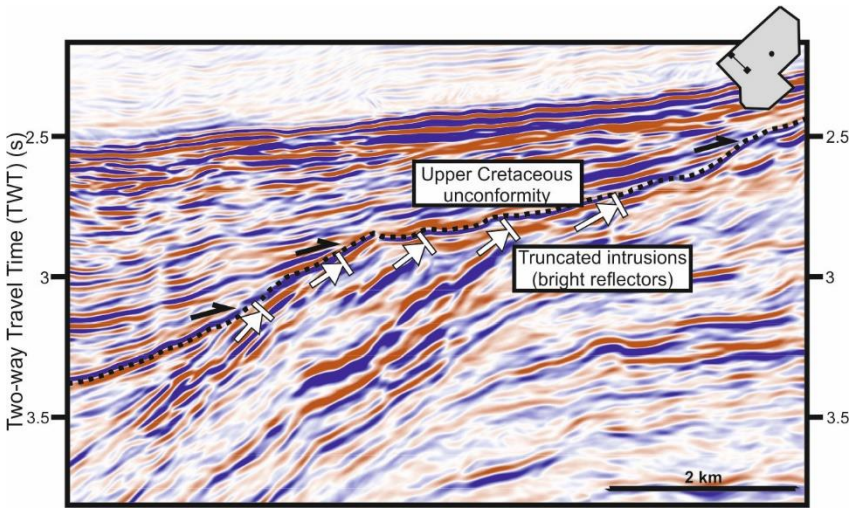

Figure 3.5: Truncation of sills along the Upper Cretaceous unconformity and subsequent onlapping of Upper Palaeocene stratigraphy. Location of Figure 3.5 shown in Figure 3.2.

Above the unconformity, the T36 lava field (c. 270 m thick) is represented on the seismic data by a series of bright, hard-kick reflectors that are relatively smooth and laterally continuous (Figure 3.6). The T36 volcanic sequence generally thickens towards the northwest from a few tens of metres in the southeast to hundreds of metres in the northwest. From well data, the lava sequence is divided by a thin, seismically unresolved shale unit (18.6 m thick) into an upper and lower lava sequence (Figure 3.2). The lower lava sequence is organised in a series of low-angle dipping reflectors separated by disorganised reflector packages (Figure 3.6). In contrast, the upper lava sequence is characterised by laterally continuous, flat reflectors. The Faroe-Shetland Escarpment (FSE) (~200 – 300 m high) marks the NW margin of the Erlend Sub-basin (Figure 3.1 and Figure 3.6). The FSE is reflected by a change in seismic responses over the scarp from continuous reflectors to a series of prograding foresets characterised by highly disorganised, bright reflector packages over the scarp (Figure 3.6A). The reflector package thickens over the FSE but thins out into the basin (Figure 3.6A).

The thickness of the Shetland Group on either side of the BNS is also markedly different (Figure 3.2). The thickness of the Shetland Group is exclusively related to the thickness of the overlying volcanic succession (e.g. a reduced Upper Cretaceous strata underlies a thick volcanic succession).

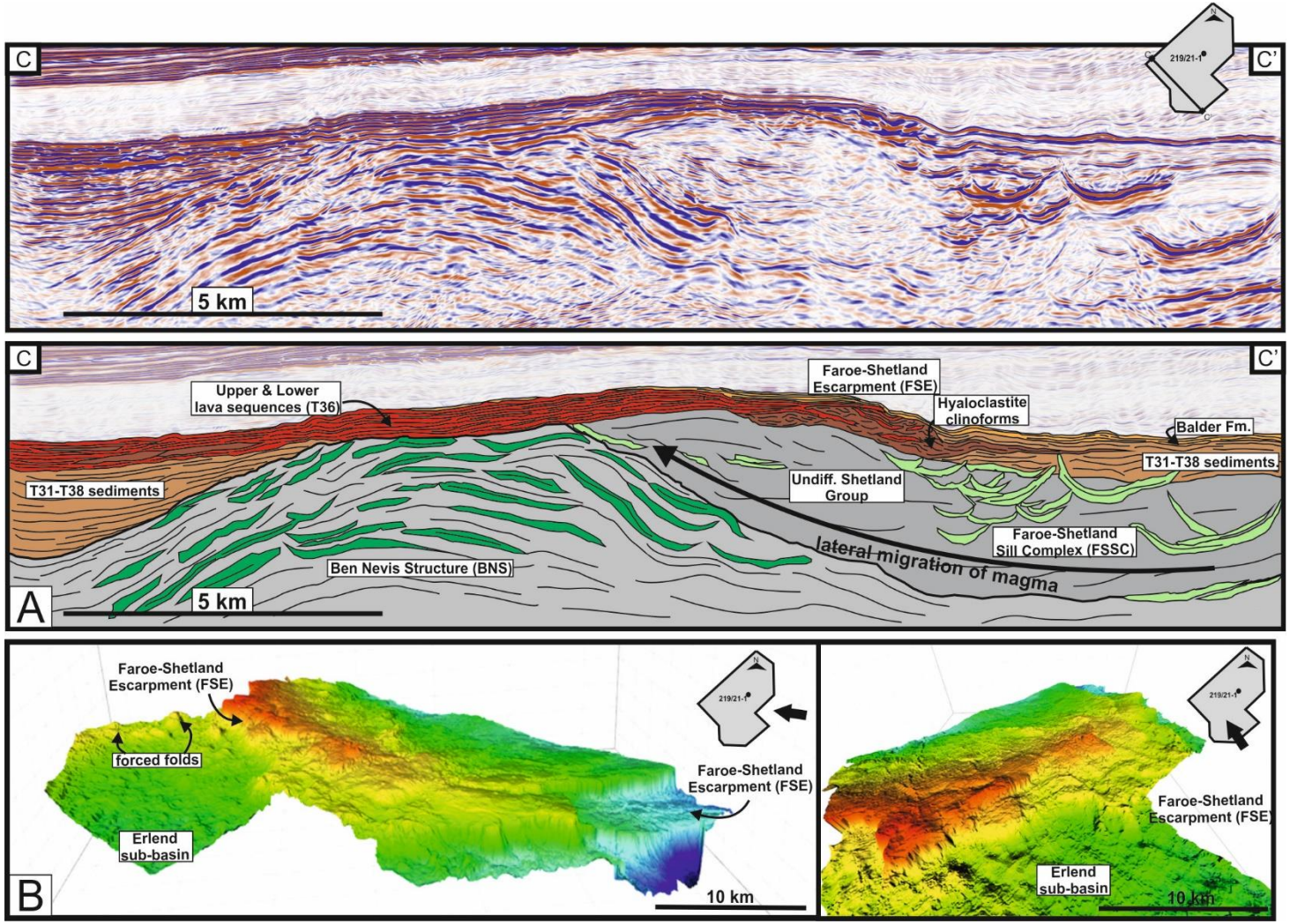

Figure 3.6: (A) Seismic line and interpreted line (C-C' in Figure 3.1B) showing the relationship between the BNS and the underlying sill complex. Magma migrates from the Faroe-Shetland Sill Complex (FSSC) towards the palaeo-high (BNS), where it encounters the inclined flank of the BNS, allowing magma to migrate towards the surface. Lateral magma migration is up to 10 km. The Faroe-Shetland Escarpment (FSE) is clearly distinguished, marked by a change in seismic responses from high amplitude, continuous reflectors to a chaotic package of discontinuous bright reflectors over the scarp, representative of lavas feeding hyaloclastite foresets. (B) Top volcanic surface with the FSE indicated. Mounds in the Erlend Sub-basin highlighted as a series of forced folds, caused by the emplacement of shallow intrusions.

3.3.3. **The Ben Nevis Monogenetic Volcanic Field (BNVF) and plumbing system**

The seismic data reveals a series of well-preserved monogenetic volcanic edifices (up to 10 possible edifices), primarily located on the top surface (~1900 ms to 2300 ms) of the T36 lava field (Figure 3.7), hereafter referred to as the Ben Nevis Monogenetic Volcanic Field (BNVF). The edifices are estimated to be between ~145 m to 380 m in height, <2 km in diameter, and have an estimated external slope of between 11˚ and 35˚. The internal structure of each cone is represented by ordered, discrete seismic packages and when observed on time-slices (horizontal slices through data), the edifices are circular or elliptical, signifying a highly organised internal

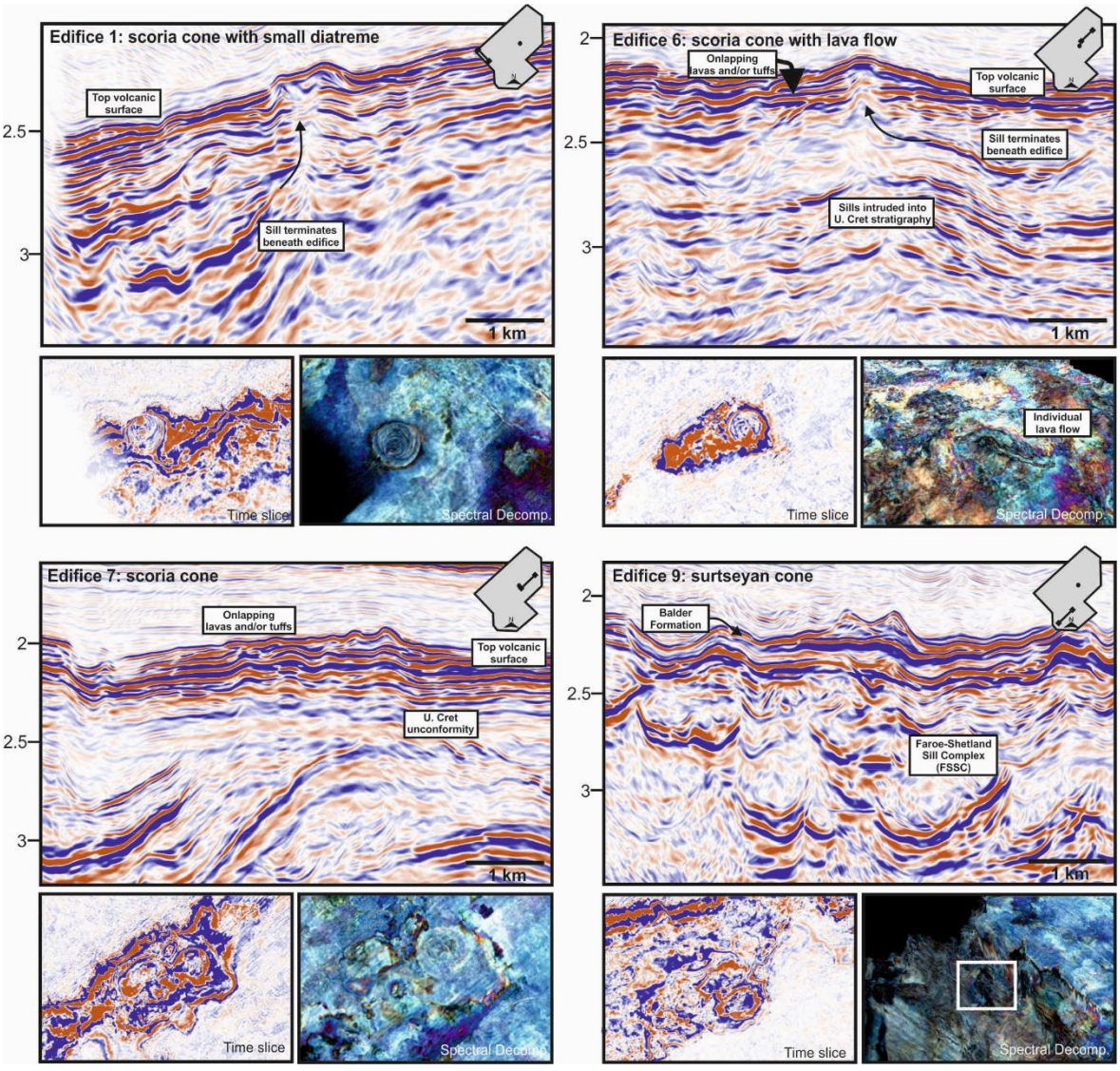

Figure 3.7: Seismic cross-sections with interpretations through some of the monogenetic edifices showing an affinity between the volcanic cone on the top volcanic surface and an underlying sill. Time slices of each edifice show an organised internal structure. Edifice 9, the submarine volcanic cone, appears to have a more disorganised structure. Spectral decomposition of the top volcanic surface highlights the lava flows emanating from edifice 6 and 7. Map insets show location of each edifice. Seismic lines are in TWT (s).

structure (Figure 3.7; Edifices 1,6 and 7). On several of the edifices, bright seismic reflectors cap the top of the cone and extend for several kilometres (Figure 3.7; Edifice 6). Edifices 8 and 9 are present in the Erlend Sub-basin along the Faroe-Shetland Escarpment (Figure 3.7; Edifice 9). These edifices (8 and 9) are represented by an internal chaotic zone beneath bright reflectors and are typically steep sided with a large central crater (Figure 3.7; Edifice 9).

Locally, sub-circular excavations are present within the BNVF which are underlain by a ~1 km wide funnel-shaped feature that excavates several hundred metres into the Palaeogene volcanics (Figure 3.8A). The steep-sided funnel is filled with lower amplitude reflections (than the surrounding Palaeogene volcanic sequence) and the reflections are arranged in a centroclinal pattern. The crater is expressed as a bowl-shaped reflection within the top volcanic surface and is surrounded by a raised ring. This is particularly visible using spectral decomposition of the top volcanic surface (Figure 3.8B).

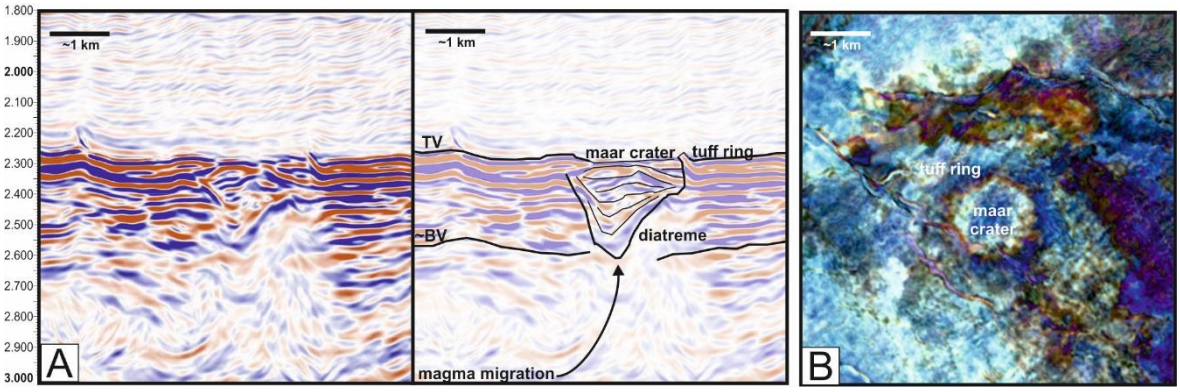

Figure 3.8: (A) Seismic cross-sections with interpretations through a maar-diatreme structure. The excavation crater in the top volcanic surface (TV) is surrounded by a raised ring representing a maar crater and tuff ring. Underlying the crater, a steep-sided funnel-shaped features excavates into the Palaeogene volcanics beneath. (B) Spectral decomposition of the top volcanic surface which highlights the morphology of the maar crater and tuff ring.

The edifices are underlain by vertical zones of reflector discontinuity (<2 km) that appear to connect with the lateral tips of very high amplitude reflectors, identified as sills (Figure 3.7; Edifices 1,6 and 7). The sills appear to feed upwards into these conical zones of disruption and terminate. The clear spatial connection between edifice and underlying sill indicates that the two features are intimately related (Figure 3.7 and Figure 3.9). The high amplitude reflectors display a complex, vertically stacked and laterally extensive series of interconnected sheets and sills (Figure 3.6). The sills are intruded between 4200 ms and 2500 ms which equates to <500 m to 3 km beneath the monogenetic

edifices at the time of intrusion (based on time-depth data of well) (Figure 3.9A-C). The intrusions are expressed as tuned reflection packages and so thickness can only be estimated, with an estimated maximum thickness of ~100 m. The intrusions are relatively small in diameter (<1–3 km). Several intrusion morphologies have been identified and are shown in Figure 3.9A-C, including: (A) saucer-shaped intrusions composed of a concordant inner sill that transgresses upwards at the margins forming a radial or bilateral geometry (Magee et al. 2014) (Figure 3.9A); (B) climbing saucer-shaped intrusions composed of a saucer-shape intrusion that is typically less transgressive on one rim than another (Planke et al. 2005) (Figure 3.9B); and (C) inclined sheets comprised of reflections that are inclined and discordant to surrounding strata (Planke et al. 2005) (Figure 3.9C). The majority of the saucer-shaped and half-saucer shaped intrusions are located beneath the Erlend Sub-basin (Figure 3.9D). The high amplitude reflectors interpreted as inclined sheets are located along the inclined Upper Cretaceous unconformity (Figure 3.6), and delineate the structure of the BNS (Figure 3.9D).

Opacity rendered views of the seismic data enables the intrusion morphologies in the subsurface to be evaluated. The intrusions are shown to consist of a series of lobes, or coalesced fingers, which allow interpretation of the direction of magma migration (Hansen and Cartwright 2006; Schofield et al. 2010; Schofield et al. 2012) (Figure 3.9E, F). Magma lobes are also evident on the inclined sheets and are seen climbing upwards to the base of the volcanic edifice (Figure 3.9E, F).

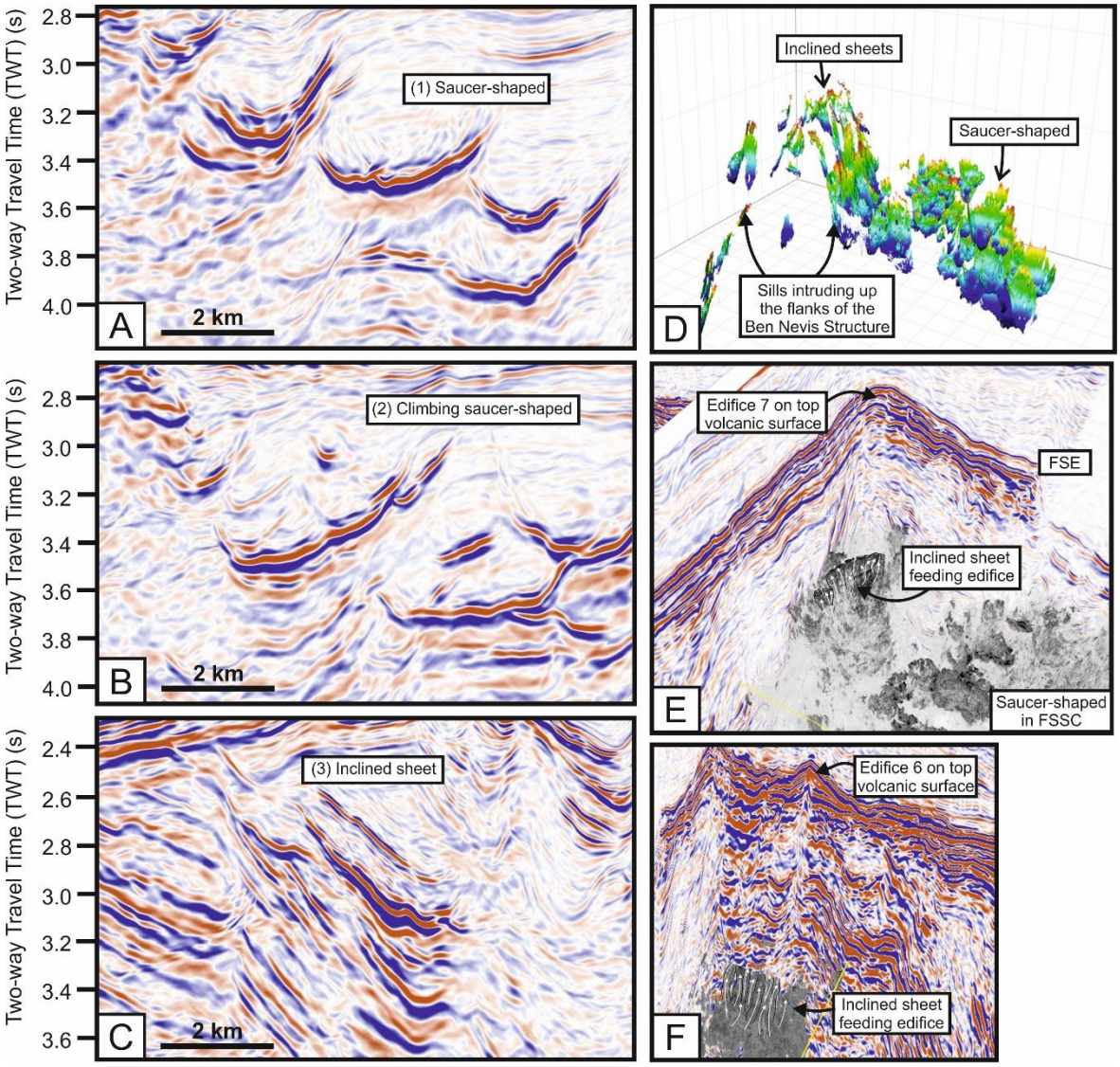

Figure 3.9: Comparison of sill morphologies. Bright reflectors indicate intrusions. (A) saucer-shaped; (B) climbing saucer-shaped; and (C) planar transgressive sheet (Planke *et al.* 2005). (D) Distribution of sill morphologies, where transgressive sheets are located along the flanks of the BNS, whereas saucer and climbing-saucer shaped sills are exclusively within the Erlend Sub-basin. (E)(F) Opacity rendered images of transgressive sheets feeding edifices on the top volcanic surface. Coalesced magma lobes are evident and are used as a magma flow indicator. Map insets show direction of view.

Cone-like structures are also identified near the base of the T36 volcanic succession and are onlapped and subsequently buried by 1.5 km of volcanic rocks (lavas and hyaloclastite) (Figure 3.10A). High amplitude reflectors outline the cone edifice and an organised internal structure can be identified. On the timeslice views (plan view), these cones are near-circular, up to 380 m in height and <2 km in diameter. Bright reflectors are identified emanating away from the buried cones and are laterally extensive for up to c. 2 km (not consistently surrounding the cone), suggestive of localised lava flows.

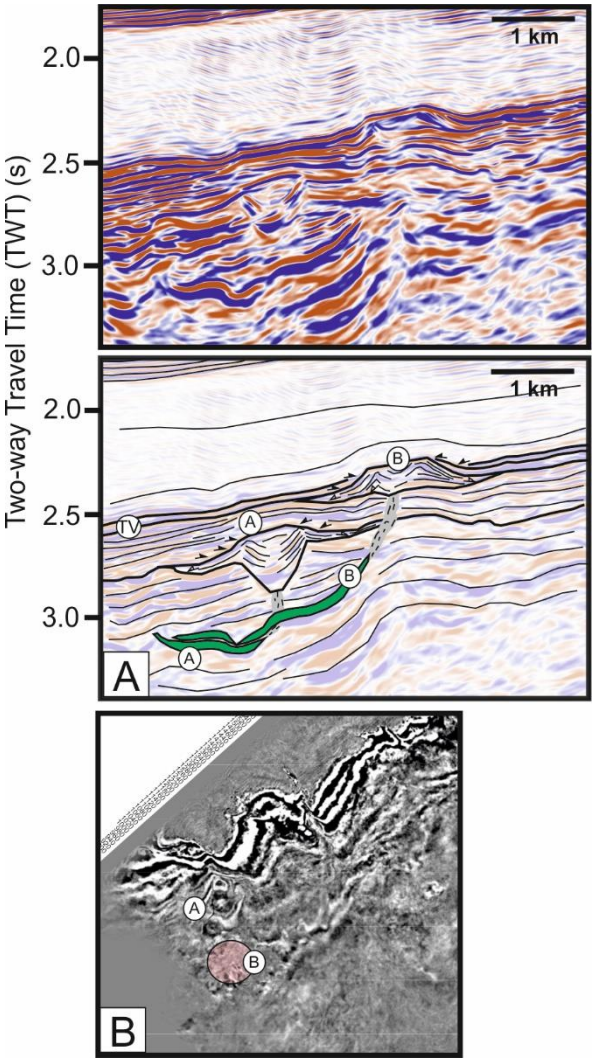

Figure 3.10: (A) Seismic line and interpreted line through a buried cone (A) beneath a later edifice (B). Edifice A is onlapped by lavas and inter-lava sediments. A singular intrusion appears to feed both edifice-forming events, however the high amplitude reflector likely represents multiple, stacked intrusions. Sill A fed Edifice A and sill B fed Edifice B. (B) Structural map of the top volcanic surface showing the location of the Edifice B. Location of the buried cone, Edifice A, is highlighted by circle. The structural map shows the lateral proximity of the cones to each other.

3.3.4. **Edifice Distribution**

The edifices are arranged around the crest of the underlying BNS (Figure 3.11A). There is an apparent ENE-WSW alignment of five edifices that lies sub-parallel to the axis of the BNS (Figure 3.11). A statistical alignment analysis of the monogenetic edifices was conducted to assess the spatial relationship between the edifices in the alignment using the method of Paulsen and Wilson (2010). Best-fit ellipsoids of each of the edifices were used to determine the centroid of the edifice and a best-fit line was established. The total length of the proposed alignment is 28.42 km. The alignment can be classified into four reliability grades (A > B > C > D) by considering four factors: (1) number of edifices in alignment; (2) the orthogonal distance from the centroid of an edifice to the best-fit line; (3) spacing distances between edifices; and (4) angle of deviation from the best fit line to the

long axis of elliptical edifices (Figure 3.11B) (Paulsen and Wilson 2010; Bonini and Mazzarini 2010; Magee et al. 2015).

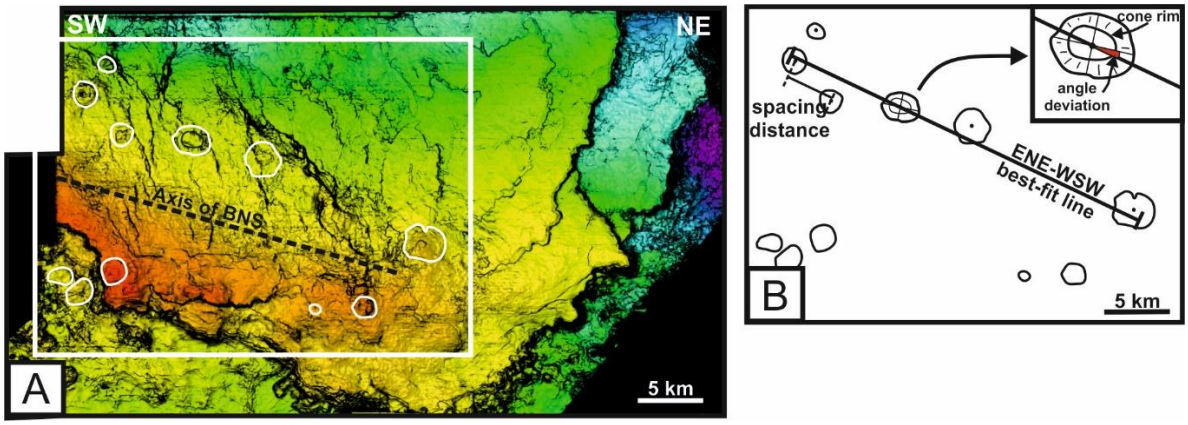

Figure 3.11: Structural map of the top volcanic surface. Edifices are highlighted by solid white lines and appear to be distributed around the axis of the BNS pericline (black dashed line). On the NW side of the BNS axis, an ENE-WSW and NE-SW alignment is apparent. (B) Outlines of the edifices were used to create a best-fit line and each spacing distance was measured. Inset, the angle between the longest axis and the best-fit line was also measured. Using the Paulsen and Wilson (2010) method for statistical alignment analysis, this alignment was deemed statistically invalid, however an alignment is clearly evident.

The alignment has been assigned a reliability grade of 'D' primarily due to the large spacing distances between edifices (3.36 km to 14 km) and the lack of elongate edifices. Elongate edifices (axial ratios >1.2) are useful for defining reliable regional vent alignments (Figure 3.11B) (Paulsen and Wilson 2010; Magee et al. 2015), however only two edifices in the BNVF have a long-short axis ratio of >1.2. The 'D' reliability grading suggests the alignment is statistically invalid on the basis of the parameters of the analysis (spacing distances, elongation axis), however, there is a clear visual alignment (Figure 3.11A).

3.4. Seismic interpretations

3.4.1. **Establishing the timing and mechanism of uplift of the BNS**

The sills at the top of the BNS structure (not feeding the BNVF) were dated using Ar/Ar to an age of 55.6 ± 0.8 Ma (sequence T40; Flett Fm.) (Figure 3.2 and Figure 3.4; Rohrman 2007) however, reliance on argon dating techniques in mafic systems is highly questionable due to the lack of potassium in basic igneous bodies, high levels of alteration, and particularly small radiogenic ^{40}Ar yields (Fitch et al. 1988, Archer et al. 2005). Conversely, it is clear from the seismic data that, due to the truncation of these intrusions (Figure 3.5), they were emplaced much earlier than the Ar/Ar age suggests. The sills are truncated by the Upper Cretaceous unconformity which is onlapped by the T38 – T31 stratigraphy (ca. 60 Ma).

From the absent Selantian-aged Vaila/Lista Formations (Figure 3.4) above the BNS, it is assumed that uplift and updoming of stratigraphy forming the BNS occurred between the end of the Cretaceous and the Early Palaeocene (Danian and Selantian), c. 65 - 59 Ma. The angular unconformity and truncation of the top of the Jorsalfare Formation and sills suggests the uplift of the dome structure formed a local topographic high during the Early Palaeocene, which caused significant subaerial erosion of the Cretaceous sequences (Figure 3.12).

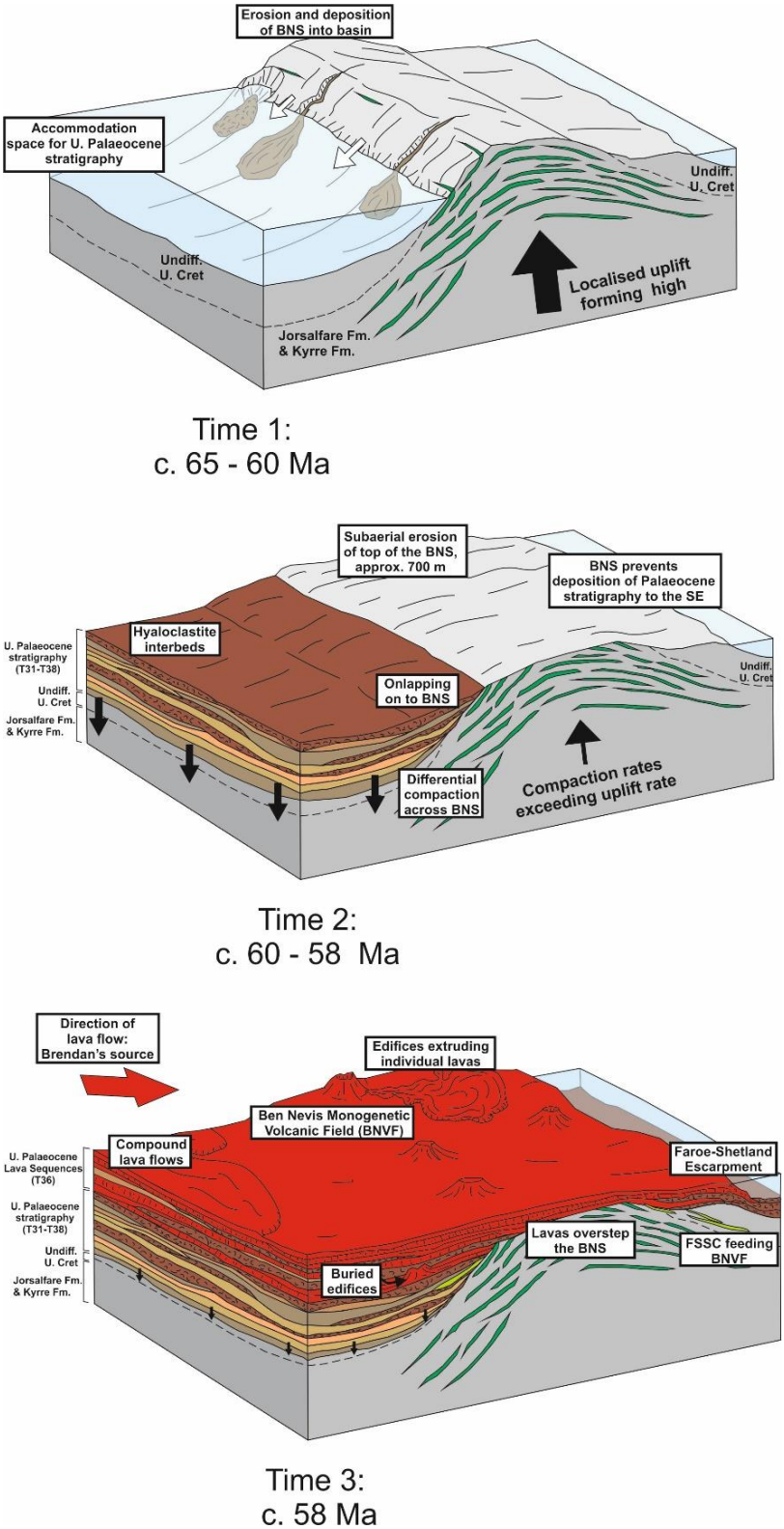

Figure 3.12: Illustrated reconstruction of the evolution of the BNS structure and subsequent volcanic activity. Not to scale. Time 1: Emplacement of laccolith and associated intrusions created uplift and updoming of the U. Cretaceous stratigraphy, creating a local palaeohigh which was subsequently exposed to subaerial erosion. Time 2: Continued erosion of the palaeohigh causing truncation of intrusions and creation of the U Cretaceous unconformity. Upper Palaeocene stratigraphy deposited into sub-basin to the NE of the palaeohigh, likely sourced from the erosion of the structure and from products and reworked products of the Brendans Volcanic Centre (to the NE). Compaction of the U. Cretaceous stratigraphy occurs only on the NE of the palaeohigh due to localised deposition of Palaeocene strata. Time 3: Onset of main volcanic activity initiated by deposition of hyaloclastite packages, and lava flows. The former palaeohigh (now fully eroded) is overstepped by subsequent lava flows feeding hyaloclastite packages when they reach the FSE on the SE of the BNS. Monogenetic volcanism occurs throughout main volcanic activity, producing isolated lavas.

Vitrinite reflectance analysis from Well 219/21-1 shows 3.0% to 5.0%, in the sub-volcanic BNS stratigraphy (2000 – 3000 m depth), corresponding to 220 °C to 270 °C (Rohrman 2007). Furthermore, a reconstructed temperature history (Rohrman 2007) shows a heat spike at 65–60 Ma of 90 mW/m^2 which cannot be explained by just heat conduction from the sills (Rohrman 2007). This elevated heat signature implies that there was a deep-seated heat source directly below the BNS before the onset of Late Palaeocene volcanism (Rohrman 2007). It is therefore likely that the intrusions were emplaced synchronously with an underlying laccolith that created the mechanism for uplift (Figure 3.13). The laccolith uplifts the overburden causing forced folding that induces bedding plane slip in the overlying stratigraphy (Figure 3.13; Archer et al. 2005). The sills exploit the weakness in the bedding planes during early inflation of the pluton creating stacked sills that emanate from the larger body (Figure 3.13; Archer et al. 2005). Continuous doming caused by inflation of the laccolith is assisted by the inflation of the sills, producing a significant amount of updoming of the overburden. Both magmatic events (laccolith and associated intrusions) caused significant heating of the Upper Cretaceous stratigraphy (Figure 3.13).

In the Rockall Basin, 530 km to the SW (Figure 3.1), a similar structure to the BNS is recorded in the Cretaceous stratigraphy (Archer et al. 2005). The intrusions forming the Rockall Dome Structure were dated to 63.3 Ma to 64.2 Ma using Ar/Ar in biotite, a much more reliable dating source (Archer et al. 2005). The occurrence of very similar structures in the Danian approximately 530 km apart suggests a potential regional magmatic event in the Late Cretaceous/Early Palaeocene across the NE Atlantic Margin. Furthermore, this magmatic episode (around c. 63-64 Ma) appears to be focussed along NW-SE trending lineament structures (Brendan's Lineament and Wyville Thomson Lineament Complex; Figure 3.1) and/or transfer zones, and may appear elsewhere along the North Atlantic Margin.

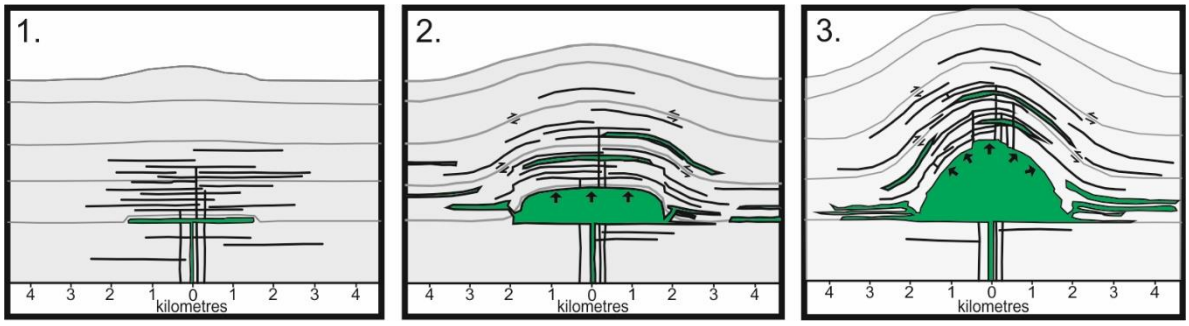

Figure 3.13: (B) Jackson and Pollard (1988) three-stage model on the progression of laccolith emplacement and uplift at the Henry Mountains, Colorado Plateau, USA.

3.4.2. **Effect of the BNS palaeo-high on T36 volcanic rocks**

During the Late Palaeocene, the uplifted BNS was exposed subaerially forming a broadbacked palaeo-high (Figure 3.12). By assessing the original height of the BNS, it is estimated that up to 700 m of eroded material was removed from the top of the BNS. Differential compaction of the Cretaceous stratigraphy occurred on either side of this palaeo-high due to the variable thickness of the overburden (volcanic succession) (Smythe et al. 1983; Passey and Hitchen 2011). Sediment accumulation in the west increased compaction and subsidence of the Cretaceous strata, forming accommodation space on the west side of the BNS, which filled with T38–T31 sediments, hyaloclastite packages and lavas, represented on the seismic as bright reflectors onlapping the top Cretaceous unconformity (Figure 3.3 and Figure 3.12). It is likely the lack of T38-T31 sediments on the east side of the BNS is partially depositional, however, sagging onlap reflectors on the west margin of the BNS (Figure 3.5) provide evidence that subsidence occurred synchronously with deposition, which is not evident on the east margin.

Eruption of the T36 lava field (ca. 58.4 Ma) was likely sourced from localised, rift-flank volcanoes similar to other T36 lava fields, for example in the Northern Foula Sub-basin and the Judd Basin (Schofield et al. 2015). By assessing the thickness of the volcanic succession (thickens towards the NW), the source of the lavas are expected to be NW of the dataset. The BNS palaeo-high prevented the earliest lava flows in the T36 lava field from advancing towards the east. Subsequent lava flows were able to breach the palaeo-high and flowed towards the east and the FSE (Figure 3.12). A change in seismic responses over the FSE (Figure 3.6) are attributed to shallow hyaloclastite deltas fed by the lavas and are indicative of where subaerial lavas entered the Erlend Sub-basin

(Naylor et al. 1999; Passey and Hitchen, 2011). Small-volume lavas produced by the BNVF edifices add to the complexity of the lava field.

3.4.3. **Ben Nevis Monogenetic Volcanic Field (BNVF) and underlying plumbing system**

3.4.3.1. The plumbing system and linking to edifices

In the Late Palaeocene/Early Eocene, the Cretaceous stratigraphy in the NE Erlend Sub-basin was heavily intruded by an extension of the Faroe-Shetland Sill Complex (FSSC) (Bell and Butcher 2002; Passey and Hitchen 2011; Schofield et al. 2015), comprising >130 resolvable saucer-shaped and half-saucer-shaped intrusions (Figure 3.9). The FSSC is part of a wider complex of sills across the North Atlantic Margin (Schofield et al. 2015). The intrusion of these sills is thought to have occurred relatively synchronously across this margin around 55 Ma; however, earlier magmatic phases are reported throughout the FSB, beginning from the Late Cretaceous through to Flett Formation times (55.2 Ma) (Schofield et al. 2015).

During the emplacement of the sill complex, as magma encountered the BNS, the magma appears to have exploited the Upper Cretaceous unconformity and the boundary between the Jorsalfare and Kyrre Formations (Figure 3.9). Mechanical contrasts across these boundaries creates conditions that promote intrusion parallel to bedding (Kavanagh et al. 2006). This channelled magma to the surface, resulting in inclined sheets intruding up the flanks of the dome structure feeding edifices around the crest of the underlying BNS on the contemporaneous surface (Figure 3.11A). Alignment analyses suggest the alignment corresponding to the northern flank of the BNS crest is statistically invalid (Figure 3.11B). More statistically reliable (hydrothermal and magmatic) vent alignments tend to form in response to magma (or hydrothermal fluids) exploiting faults, if magma exploits along the entire fault length (Paulsen and Wilson 2010; Bonini and Mazzarini 2010; Magee et al. 2015). Magee et al. (2015) suggest the convex-upwards, upper tip-line geometry of faults can direct fluids to the fault centre, locally limiting hydraulic failure of the overburden and localizing vent distribution along the fault trace. This effective channelling of magma does not occur as efficiently beneath the BNVF as the magma exploits bedding planes, not faults, which results in a less definitive alignment due to the irregular structure of the underlying anticline (BNS).

Conical zones of disruption are identified in seismic data between the feeder sills and some of the edifices in the BNVF (Edifice 1 in Figure 3.7). This feature is commonly found beneath all vent/mound types (e.g. hydrothermal, sediment and magmatic) (Bell and Butcher, 2002; Svensen et al. 2006; Grove 2013; Magee et al. 2014; Galland et al. 2014; Jackson 2012; Manton 2015) and may represent: (i) vertically mobilised sediment induced by hydrothermal fluids around sills (Grove 2013); (ii) the migration of phreatic fluids (hydrothermal complexes) (Svensen et al. 2006); (iii) phreatomagmatic diatreme structures formed by several hundred phreatomagmatic explosions in the subsurface (White and Ross 2011); and (iv) dense, magmatic feeder dykes. In the case of the BNVF, disrupted zones beneath edifices most likely represent abundant feeder dykes due to the magmatic nature of the edifices.

3.4.3.2. Monogenetic volcanic edifices

The formation of the BNVF was contemporaneous with the T36 lava field suggesting that the intrusions feeding the BNVF were associated with an early phase of FSSC emplacement at ca. 58 Ma, near the onset of widespread volcanism in the basin (Figure 3.12). The majority of the monogenetic volcanic field is comprised of scoria cones, represented as constructional edifices with typically steep external slope angles and internal craters, and capped by bright reflectors reflecting individual low-volume lava flows (< 0.1 km^3; Németh 2010) (Figure 3.7; Edifices 1,6 and 7). Using spectral decomposition, imaging of these lava flows has been obtained and individual lava flows can be mapped (Figure 3.7). The edifices differ from hydrothermal vents, commonly represented as craters, mounds or eye-shaped seismic structures (Planke et al. 2005; Svensen et al. 2006; Hansen et al. 2008). Although hydrothermal vents are typically located above the tips of sills, like the BNVF edifices, they tend to have a disorganised internal structure and an underlying sag-like structure, representative of a subsidence-formed crater, which are not apparent beneath the BNVF edifices (Figure 3.7) (Jamtveit et al. 2004; Svensen et al. 2006; Hansen et al. 2008). Furthermore, the internal structure of the BNVF edifices is clearly defined by high amplitude reflectors indicating a well-organised structure comprised of lavas and volcanic material (Figure 3.7). Locally, however, craters with underlying funnel-shaped features have comparable dimensions and characteristics to maar-diatreme volcanoes, formed by phreatomagmatic explosions at depth creating an explosion crater at the palaeosurface (Figure 3.8) (White and Ross 2011).

The edifices present on the margin of the Faroe-Shetland Escarpment (Figure 3.7; Edifice 9) are inferred as submarine magmatic vents due to their location next to the FSE (which marks the palaeoshoreline during the Late Palaeocene/Early Eocene), and their internal chaotic seismic character (Figure 3.7; Edifice 9). The type of submarine edifice (pillow-lava dominated or hyaloclastite dominated) is determined by the water depth at point of magma extrusion (Kokelaar 1986). Where water depths are greater than 130 m, vesiculation of magma is suppressed and pillow lavas will be extruded typically forming low angle mounds (Kokelaar 1986). At shallow water depths (<130 m), submarine fountaining of magma can occur, causing intensive quenching and fragmentation of magma and the production of edifices comprised of hyaloclastite, tephra, pillow lavas and reworked material (Kokelaar 1983). The submarine edifices (Figure 3.7; Edifice 9) are steep sided with a large central crater, suggesting that high rates of submarine magma fountaining (and therefore instantaneous quenching and fragmentation of magma) built hyaloclastite dominated submarine volcanic cones (Kokelaar 1983; Bell and Butcher 2002).

3.5. Discussion

3.5.1. **Significance of sills and transgressive sheets in monogenetic plumbing systems**

The Ben Nevis seismic data indicates that lateral migration of magma can occur for up to 10 km before the eruption of magma at the surface (Figure 3.6). Vertically extensive, stacked sill complexes (<10 km) feeding monogenetic edifices, similar to the BNVF, are also recorded in the Møre and Vøring basins in offshore Norway and the Ceduna Sub-basin offshore Australia (Cartwright and Hansen 2006; Jackson 2012; Magee et al. 2013; Manton 2015). Seismic imaging and field based studies of such intrusion networks clearly shows sills and inclined sheets can provide the dominant magma storage and transport pathway beneath monogenetic volcanic fields in primarily extensional tectonic settings (and back arc extensional regimes) (Cartwright and Hansen 2006; Valentine and Krogh 2006; Németh and Martin 2007; Jackson 2012; Kiyosugi et al. 2012; Muirhead, J.D. et al. 2012; Magee et al. 2013; Magee et al. 2014; Re et al. 2015; Richardson et al. 2015; Magee et al. 2016; Muirhead, J.D. et al. 2016b).

Interrelated sills and inclined sheets at Hopi Buttes, Arizona, featuring ramped step and stair, saucer-shaped and half-saucer-shaped intrusion morphologies, form at least 30% of the total magma volume

of the monogenetic plumbing system (Muirhead, J.D. et al. 2016a). At San Rafael Monogenetic Volcanic Field, this percentage increases to 93% (Richardson et al. 2015). An absence of dykes in the Crown Butte complex at Hopi Buttes, and the ratio between magma storage in sills versus dykes at San Rafael demonstrates the significance of sills and inclined sheets in transporting magma to the surface beneath monogenetic fields (Muirhead, J.D. et al. 2016a). However, the total volume of magma storage in sills and transgressive sheets cannot be fully elucidated by just field data due to the current level of exposure of some fields, where the complex, stacked nature of the sill complexes are not fully exposed.

Seismic unrest studies have suggested stalling of magma in the upper crust can occur up to two years before a monogenetic eruption, indicating multiple potential intrusion events pre-eruption. For example, the 2011 eruption offshore of El Hierro in the Canary Islands was preceded by 4-5 years of seismic unrest activity, suggestive of the development of a complex plumbing system (Albert et al. 2016). The evidence for shallow (<2 km) plumbing systems is further corroborated by geochemical studies which allude to the presence of sub-horizontal, shallow (<2 km) plumbing systems where crustal assimilation, crystallization and melt storage is recorded (Németh et al. 2003), especially beneath relatively long-lived scoria cones such as Jorullo and Paricutin (15 yr and 9 yr respectively) in the Michoacán–Guanajuato Volcanic Field of the Trans-Mexican Volcanic Belt (McBirney et al. 1987; Johnson et al. 2008).

The BNVF demonstrates that although each individual monogenetic edifice stems from a discrete magma reservoir or intrusion, the overall plumbing system of a volcanic field can be interconnected and genetically related. Consequently, two distinct magma batches feeding separate edifices can share a common plumbing system and still produce different compositional trends due to the isolation of the individual feeding intrusions. In other words, assimilation trends for each individual edifice may not be identical across a monogenetic volcanic field but would record the trends of a separate branch of a shared plumbing system.

3.5.2. **Emplacement of monogenetic plumbing systems and influence of the local crustal structure**

It is important to consider why sill-dominated plumbing systems form as opposed to dyke-dominated systems. For sub-horizontal intrusions (including saucer-shaped sills and inclined sheets) to form, two main constraints must be overcome to convert magma from a vertical pathway to a horizontal one: (1) magma driving pressure must exceed host-rock strength or, in this case, the tensile strength of a pre-existing plane of weakness (Valentine and Krogh 2006); (2) the rotation of the principal stress (sigma 1) from vertical to sub-horizontal (and compressive stress, sigma 3, to a sub-vertical orientation) (Kavanagh et al. 2006; Valentine and Krogh 2006; Menand 2008). Unconformities or host-rock interfaces with sufficiently contrasting mechanical and rheological properties (rigidity, strength, pore fluid pressure) can cause the rotation of the principal stress (sigma 1) from vertical to horizontal, and can subsequently promote the propagation of a sub-horizontal intrusion (Kavanagh et al. 2006; Menand 2008; Thomson and Schofield 2008; Gudmundsson 2011; Magee et al. 2013; Kavanagh et al. 2015; Tibaldi 2015; Magee et al. 2016). In some cases sill intrusion into a pre-existing weakness or bedding plane does not require a rotation

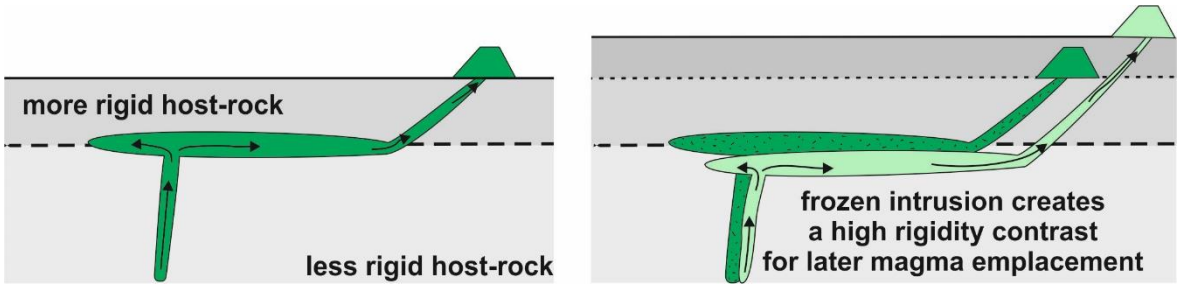

Figure 3.14: Schematic diagram illustrating the development of stacked intrusions (adapted from Kavanagh et al. 2006). Sub-horizontal propagation occurs at a host-rock interface where there is a high rigidity contrast. Arrows show direction of magma migration. When the sill freezes, it creates a rigidity contrast with the surrounding host-rock, generating a favourable environment for later magma emplacement.

of sigma 3 to horizontal. This occurs when the sill intrudes obliquely to the least compressive stress (sigma 3) (Jolly and Sanderson 1997). Horizontal or sub-horizontal propagation is, therefore, a function of magma pressure, tectonic stress and the strength of the weakness.

Compliant lithologies are exploited by magma through ductile deformation of the host-rock, for example: coal (e.g. Raton Basin, Colorado, USA; Schofield et al. 2012); salt (e.g. Werra-Fulda Basin, Germany; Schofield et al. 2014); and shale (e.g. Golden Valley Sill, South Africa; Schofield et al.

2010). The mechanically weak layers can inhibit vertical crack propagation, limiting vertical migration of magma and promoting horizontal migration along the compliant layer (Thomson 2007; Schofield et al. 2012). Therefore, in thick sedimentary sequences, it is likely that sill complexes will develop either by exploiting host-rock interfaces in the strata, and/or by exploiting compliant horizons (Figure 3.14) (Eide et al. 2016).The abundance of saucer-shaped and half-saucer shaped intrusions in the BNVF plumbing systems is likely a result of strong host-rock control and exploitation of compliant horizons in the Upper Cretaceous stratigraphy (e.g. shales). In the case of the inclined sheets, the magma exploited the mechanical difference along the inclined Cretaceous-Palaeocene unconformity (claystones and extrusive volcanic rocks) and between the Jorsalfare Formation (Figure 3.15A). Due to the orientation and nature of the BNS structure, these planes of weakness were inclined and supported the injection and propagation of magma upwards towards the surface (whilst also contributing to lateral magma migration), forming inclined sheets and dictating the location of the edifice (Figure 3.15A).

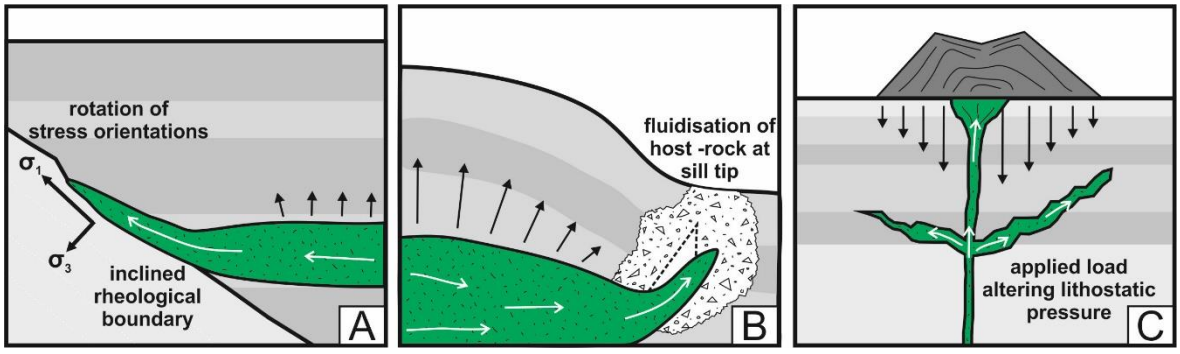

Figure 3.15: Mechanisms of transgressive sheet propagation. (A) Inclined rheological boundary with a sufficient rigidity contrast to rotate σ 1, allows propagation of magma along an inclined pathway. (B) The inflation of an intrusion causes forced fold formation in the overburden. Extensional fractures develop at the tip of the sill, instigating host-rock fluidisation around the sill tip. Magma exploits fluidised host-rock. Adapted from Schofield et al. (2010). (C) Application of load to the top surface (in this case, the development of a scoria cone), reorients the compressive stresses of the host-rock, promoting the migration of magma in an inclined sheet. Adapted from Re et al. (2015).

Inclined sills are formed by various other mechanisms. The formation of the inclined limbs of a saucer-shaped sill may be instigated by forced folding of the overburden above a sill, where extensional fractures form near the termination of the sill (Thomson 2007) (Figure 3.15B). The rapid decrease in hydrostatic pressure due to the opening of these fractures, instigates localised host-rock fluidisation (also caused by heating of host-rock pore-fluids) (Schofield et al. 2010). Magma exploits these failures, propagating upwards into the fluidised host-rock as a series of localised flow

pathways (magma fingers) which coalesce into a singular sheet (Figure 3.15B) (Thomson 2007; Schofield et al. 2010). The saucer morphology is formed by radially upward-propagating magma fingers surrounding an inner sill (Schofield et al. 2012). Field evidence for this type of structure is found at the Golden Valley Sill in the Karoo Basin, South Africa, where undulations in the transgressive rim, provide evidence for coalesced discrete magma pathways, or fingers, and host-rock fluidisation structures are observed surrounding magma fingers (Schofield et al. 2012). Alternatively, transgressive sheets may also develop as a result of changes to the lithostatic pressure of the host-rock environment. Re et al. (2015) suggest that the application or destruction of a load at the surface (e.g. by the development of a volcanic edifice or the development of a diatreme) will alter the compressive stress regime (sigma 1 and 3) in the host-rock strata, preventing vertical dyke propagation and resulting in an inclined magma pathway (Figure 3.15C).

Extensional monogenetic volcanic fields tend to show one or more edifice alignment orientations, typically a regional stress-controlled orientation and/or alignments controlled by pre-existing (dipping) crustal fractures and normal faults (Le Corvec et al. 2013; Magee et al. 2013; Muirhead et al. 2015; Schofield et al. 2015; Mazzarini et al. 2016; Muirhead, J.D. et al. 2016b). Pre-existing faults are known to influence the distribution of monogenetic edifices depending on the fault dip angle, the orientation of the fault plane, the mechanical properties of the adjacent host-rock, and the localised stress regime around the fault (Gaffney et al. 2007; Magee et al. 2013; Le Corvec et al. 2013). Basin-scale flexures in the hanging wall of half-graben basins in rift settings can trigger extensional faulting and fracturing, and may also control the alignment of edifices (Muirhead, J.D. et al. 2016b). The BNVF consistently demonstrates just one vague alignment orientation (corresponding to the crest of the BNS structure; Figure 3.11). This ENE-WSW alignment of edifices contradicts the regional stress orientation (NW-SE) (Holford et al. 2016) and no fault pathways have been identified on the seismic data (although potential faults could be obscured by the poor sub-basalt imaging). As a result, we suggest that the primary influence on edifice distribution in the BNVF is the inclined rheological boundaries in the subsurface strata. Magma interaction with local crustal structures (e.g. folds, inclined rheological boundaries), has been overlooked as a dominant influence over the distribution of monogenetic edifices but should be considered when assessing future eruption sites of active monogenetic fields.

3.5.3. **Reactivation of magma migration pathways during the lifetime of a monogenetic volcanic field**

The observation of buried volcanic edifices beneath the BNVF (Figure 3.10) gives a unique perspective of the distribution of monogenetic edifices and how they are distributed spatially and temporally. The offset between the buried cones and the later monogenetic edifices is less than 1 km (Figure 3.10). The lateral proximity between the buried cones and later edifices suggests a similar magma pathway for both edifice-forming events. One example, beneath Edifice 1 (Figure 3.10A), shows a high amplitude reflector inclining vertically into the base of an earlier cone and then transgressing further into the base of a later edifice (Figure 3.10A). The timescale between the emplacement of magma beneath the earlier cone (onset of lava, ca. 59 Ma) and the emplacement of magma beneath the later cone (final stages of lava field development, ca. 58 Ma) is too long for the magma pathway to stay molten in a <80 m thick intrusion at such a shallow depth (<1.5 km beneath the palaeosurface) due to high cooling and crystallisation rates (Figure 3.10A). It is therefore suggested that the high amplitude reflector signifies multiple stacked intrusions (Figure 3.10B). The majority of sills observed in seismic are expressed as tuned packages of reflectors, thus making it difficult to discern whether a thick bright reflector is the product of one sizable intrusion or a series of incrementally emplaced or stacked intrusions (Magee et al. 2016). A newly-developed intrusion can impart a thermal, rigidity or strength anisotropy on to subsequent injections and further promote horizontal propagation of future intrusive events (Figure 3.14) (Gudmundsson and Brenner 2004; Kavanagh et al. 2006; Menand 2008; Burchardt 2008). We interpret that after feeding the earlier (buried) cone, the sill provided a strong mechanical discontinuity between the sill and the surrounding host-rock (Annen et al. 2015; Magee et al. 2016) (Figure 3.14). The new magma pulse, feeding the monogenetic edifices on the top volcanic surface, exploited this contact, stacking the intrusions and increasing the apparent thickness of the sill in seismic (Magee et al. 2016) (Figure 3.14). This stacking of intrusions spatially and temporally can have significance for the thermal and chemical evolution of the later magma batch (e.g. slower cooling intrusions) (Annen et al. 2015; Magee et al. 2016).

Chapter 4 Submarine setting; Dyrhólaey, Iceland

4.1. Introduction

A locality along the south coast of Iceland, Dyrhólaey, has been studied to show the intrusion geometries and emplacement mechanisms of shallow plumbing systems (<1 km) beneath emergent volcanic islands. Dyrhólaey represents the eroded remains of a tuff cone and its underlying platform that were formed by a series of hydromagmatic explosions. The former island is now connected to the mainland by a series of sand bars comprised of sandur deposits (formed by glacier outwash from subglacial activity beneath Katla during the Holocene; Watton et al. 2013). The tuff cone was intruded by a series of sills and dykes which likely fed subaerial volcanic edifices. Erosion of parts of the tuff cone, enables the examination of this late-stage plumbing system.

The tuff cone at Dyrhólaey [63.4029; -19.1174] formed in the Upper Pleistocene (IGC excursion guide 2008). Continuous submarine extrusion of magma allowed the tuff platform to emerge out of the sea and form an edifice. This was subsequently followed by a subaerial phase, where a series of subaerial pahoehoe lavas were extruded and onlapped the tuff cone. The intrusions which fed both the late stage tuff cone and the lavas are preserved and exposed. The intrusions are emplaced with a variety of geometries, including concordant stepped sills and highly irregular and disseminating dykes. Subsurface pillows were formed at the tips of some of the intrusions.

This case-study investigates the development of the Dyrhólaey tuff cone platform, how magma is emplaced into tuff platforms and feeds subsequent eruptions. Sedimentological investigations, including detailed logs of the tuff cone deposits were undertaken, to understand the geometry of the eroded tuff cone platform and a textural analyses of the later plumbing system was undertaken to fully understand the controls of magma emplacement in subsequent subaerial eruptions on emergent volcanic islands.

4.2. Geological Overview

4.2.1. **Icelandic Overview**

The oceanic island of Iceland began forming at ~24 Ma at the intersection between a adiabatic divergent plate boundary, the Mid-Atlantic Ridge, and a deep-seated mantle plume (Sæmundsson 1979; Jóhannesson 1980; Kristjánsson 1982; Vink 1984, Óskarsson et al. 1985; White et al. 1995; Bjarnason et al. 1996; Hardarson et al. 1997; Wolfe et al. 1997; Allen et al. 1999; Thordarson and Larsen 2007; Einarsson 2008; Jakobsson and Johnson 2012). The active spreading occurs along two main rift zones, the West Volcanic Zone (WVZ) and the North Volcanic Zone (NVZ), extending from Reykjanes in the southwest to Öxarfjörður in the northeast (Thordarson and Höskuldsson 2014) (Figure 4.1). These zones are the subaerial equivalent of the Mid-Atlantic Ridge, the only place globally where a divergent spreading centre can be seen terrestrially (Flóvenz and Sæmundsson 1993; Thordarson and Höskuldsson 2014). The main rift zones (WVZ and NVZ) are connected by seismically active transform zones, volcanic rift belts or oblique rifts (e.g. Reykjanes Volcanic Belt (RVB), Mid-Iceland Belt (MIB), Tjörnes Fracture Zone (TFZ), Öræfi Volcanic Belt (OVB) and Snæfellsnes Volcanic Belt (SVB)) (Einarsson 2008) (Figure 4.1). The rift zones are comprised of thousands of normal faults, fissure swarms and active central volcanoes (Flóvenz and Sæmundsson 1993), which delineate the youngest rocks. At present, the East Volcanic Zone is spreading along the western side of the Vestmannaeyjar Islands to the south (Hardarson et al. 1997) and has been the most active zone in postglacial times (e.g. Skjaldbreiður, Trölladyngja, Surtsey, Eyjafyallajökull and Katla eruptions) (Thordarson and Höskuldsson 2014). Ultimately, redirection of the main rift zone will transfer from the WVZ to EVZ (Hardarson et al. 1997).

The stratigraphy of Iceland can be subdivided into three main groups, defined by the amount of glaciation and volcanism: (1) Miocene and Lower Pliocene (16 – 3.3 Ma); (2) Upper Pliocene to Lower Pleistocene (3.3 – 0.7 Ma); and (3) Upper Pleistocene to Recent (<0.7 Ma) (Figure 4.1 and Figure 4.2). The Miocene and Lower Pliocene (16 to 3.3 Ma) is characterised by warmer global temperatures and a complete lack of glaciation in Iceland. Similar volcanic and tectonic processes as today were occurring, where central volcanoes and fissure systems produced ~85% of the geology (Thordarson and Höskuldsson 2014). Significantly, the Miocene and L. Pliocene Formations

are defined by interbasaltic red-beds, lignite horizons and leaf impressions, indicating a build-up of soil and vegetation during volcanic hiatuses and a warm, temperate climate (Walker 1964; Einarsson and Albertsson 1988; Hardarson et al. 1997; Kristjansson et al. 2003).

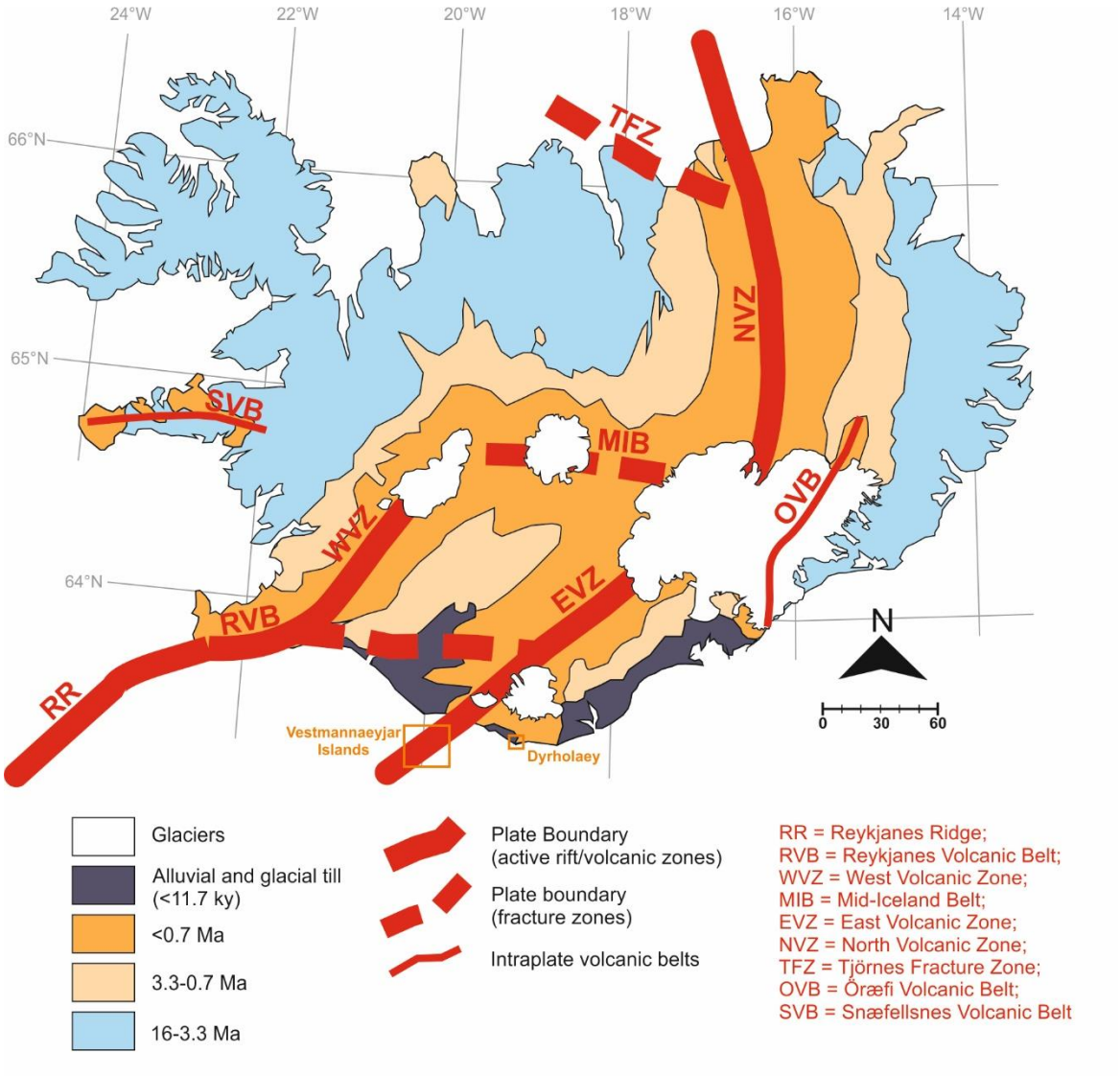

Figure 4.1: Active rifting zones and connective fractures zones and volcanic belts in Iceland. Location of both case-studies labelled EVZ is a future rift centre. From Thordarson and Höskuldsson (2014).

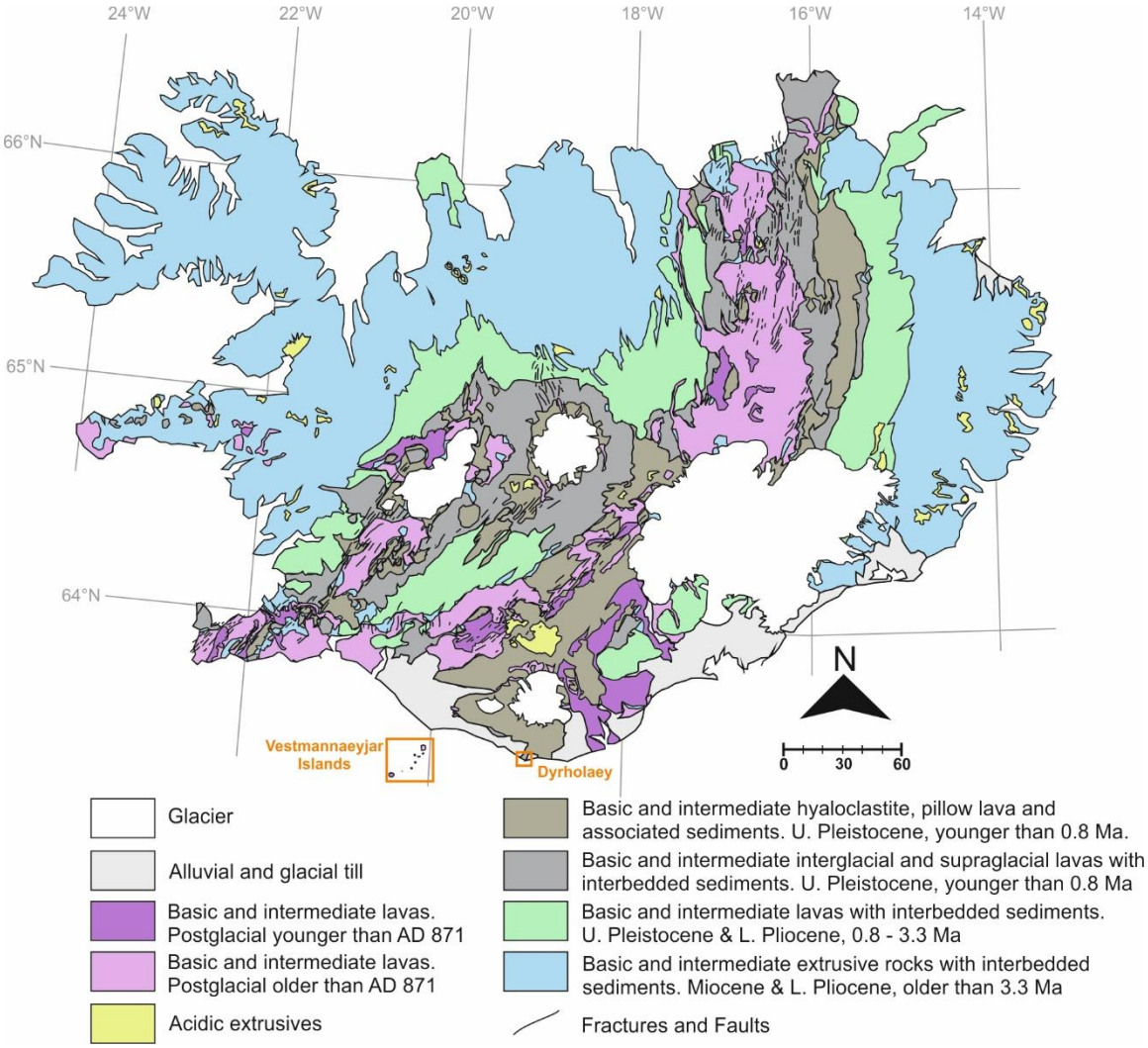

Figure 4.2: Simplified geological map of Iceland showing locations of Dyrhólaey and the Vestmannaejar archipelago. From Jóhannesson (2014).

The U. Pliocene and L. Pleistocene are demarcated by multiple interglacial and glacial cycles. Glacially derived marine deposits and products of subglacial volcanism (pillow lavas, hyaloclastites and tuffs) are identified from c. 5 Ma, however the presence and distribution of such deposits around the Pliocene-Pleistocene boundary shows a distinctive trend towards ice-sheet growth during the Upper Pliocene (Geirsdóttir 2004). The Ice-Age glacial cycles, that covered large swaths of the Northern Hemisphere, began at c. 2.2 Ma to 1.6 Ma (Thordarson and Höskuldsson 2014) and are marked by extensive glacial deposits that cover the entirety of Iceland (Geirsdóttir 2004). During the glacial cycles throughout this epoch (3.3 Ma to 0.7 Ma), subglacial volcanic features were formed, including móberg sheets, tindars and tuyas (Jakobsson and Johnson 2012). These subglacial volcanic deposits are distributed along the current rift system as isolated, palagonitized mountains, although many have been subsequently eroded by later glaciation cycles, or submerged by later subaerial lava flows (Einarsson and Albertsson 1988; Jakobsson and Gudmundsson 2008) (Figure 4.1 and Figure

4.2). Glacial-derived sediments and breccias, fluvial, marine and lacustrine deposits are interbedded between subaerial lavas and tuff horizons deposited during interglacials (e.g. the Hreppar Formation in southern Iceland) (Einarsson and Albertsson 1988).

Frequent cyclical changes between interglacial and glacial periods (120,000 – 140,000 years duration) continued throughout the Upper Pleistocene and into the Holocene (Gudmundsson 1997; Thordarson and Höskuldsson 2014) (Figure 4.2). The Weichselian glaciation from 120 Ka to 10 Ka covered the whole of Iceland and extended across Northern Europe (Einarsson and Albertsson 1988). When the global climate began to warm towards the end of the Weichselian stage, fluvial systems emerging from the melting ice caps deposited vast quantities of glacially-derived sediments into large sandur plains along the south coast (Figure 4.2), which have subsequently been added to by the large glacial outwash from Vatnajökull and Myrdalsjökull (Krigström 1962; Maizels 1993). Holocene and historical, post-glacial, subaerial lava flows cover much of the active rift zones (Gudmundsson 1986).

4.2.2. **Surtseyan Volcanism in Iceland**

In historic time, there has been ~20 Surtseyan eruptions in Iceland (Thordarson and Höskuldsson, 2008). Surtseyan edifices are concentrated in the offshore sections of the Reykjanes Peninsula (RVB), the NVZ and the Vestmannaejar volcanic system, along the EVZ (Mattsson and Höskuldsson 2003; Thordarson and Höskuldsson 2008) (Figure 4.1 and Figure 4.2). Surtseyan volcanism is eponymously named after the island of Surtsey, which famously erupted from 1963-1967 in the Vestmannaejar archipelago (Figure 4.2). The Vestmannaejar archipelago is comprised of a series of 17 emergent islands and over 60 submarine mounds which are collectively described as a monogenetic volcanic field associated with the tip of the propagating EVZ rift (Figure 4.2) (Oskarsson et al. 1982). The islands are comprised of tuff cones, tuff rings and scoria cones erupted from discrete volcanic eruptions and multi-phase eruptions (erupted continuously from submarine to subaerial). The most recent of these eruptions formed the scoria cone, Eldfell, on the island of Heimaey in 1973.

Dyrhólaey is one of three Pleistocene emergent islands distributed along the southern coast of Iceland (Figure 4.3). The former islands stand as isolated hills surrounded by glacial moraine and

fluvial deposits. The structures represent the remnants of a Pleistocene-aged archipelago of emergent submarine volcanic islands, comparable to the present-day Vestmannaejar Islands (IGC excursion guide 2008).

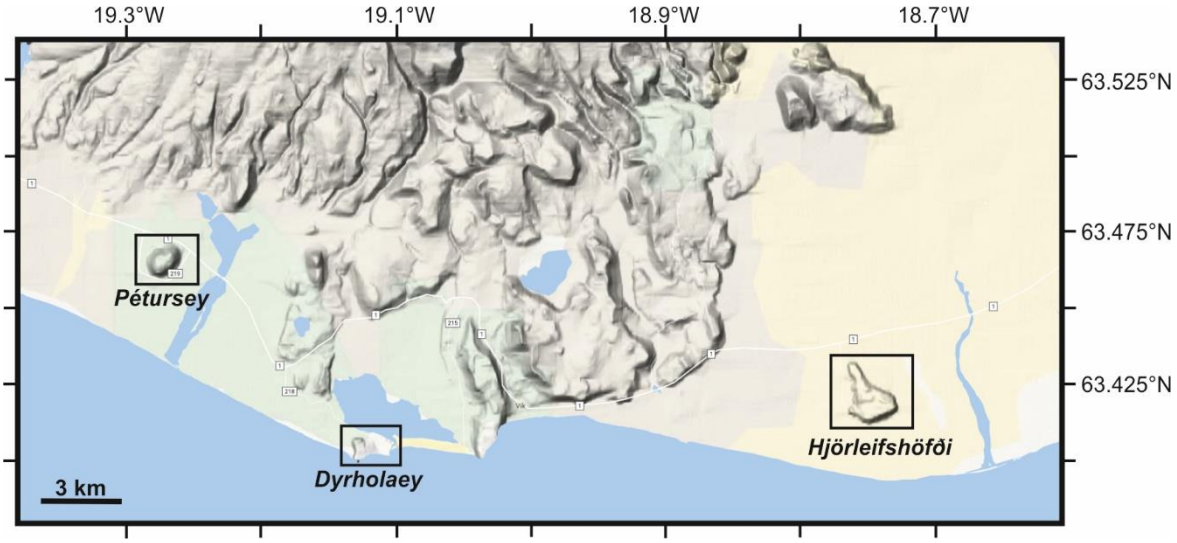

Figure 4.3: Digital elevation model of the south of Iceland showing the locations of Dyrhólaey, Pétursey and Hjörleifshöfði; Pleistocene Surtseyan islands that are now surrounded by glacial moraine and fluvial deposits. This series of former islands are attributed to a Pleistocene version of the Vestmannaejar Islands.

4.3. Location and Geomorphology

The island of Dyrhólaey, the most southerly point of Iceland (Figure 4.4A), is comprised of an upland area to the west (elevation approx. 120 m) and a lowland area to the east (elevation approx. 10-20 m) (Figure 4.4B). There are accessible cliff exposures along portions of the southern coast and in the south-eastern corner of the island. The locality numbers are labelled in Figure 4.4C.

The upland area is dominated by well-bedded, stratified and massive, tuff, lapilli-tuff and breccia units formed during emergent submarine volcanism. The sea cliffs surrounding the upland area have a distinctive orange colour due to subsequent alteration of volcanic glasses (sideromelane) to palagonite (Figure 4.4). Photographic examination of several sea stacks to the south of the island (approx. 500 m from shore) indicate the tuff cone deposits extend to the south of the island and have since been eroded. Consequently, it can be conjectured that the original tuff cone and tuff cone platform was up to 2.5 km wide. The erosion of parts of the tuff cone enables the examination of the late-stage plumbing system.

The slope between highland and lowland marks the geological transition from tuff cone building processes to subaerial volcanic processes (Figure 4.4B and C). The lowland is dominated by thin pahoehoe lava flows and spatter that onlap the tuff cone deposits (Figure 4.4C). Basaltic intrusions, in the south-eastern corner of Dyrhólaey (Figure 4.4C and Figure 4.6) are thought to have fed subsequent subaerial extrusions of magma. In the SE corner, a series of sill lobes have intruded into stratified tuffs and lapilli-tuffs of the eroded tuff cone platform and the thin pahoehoe lavas. Firstly, it is important to examine the nature of the host-rock.

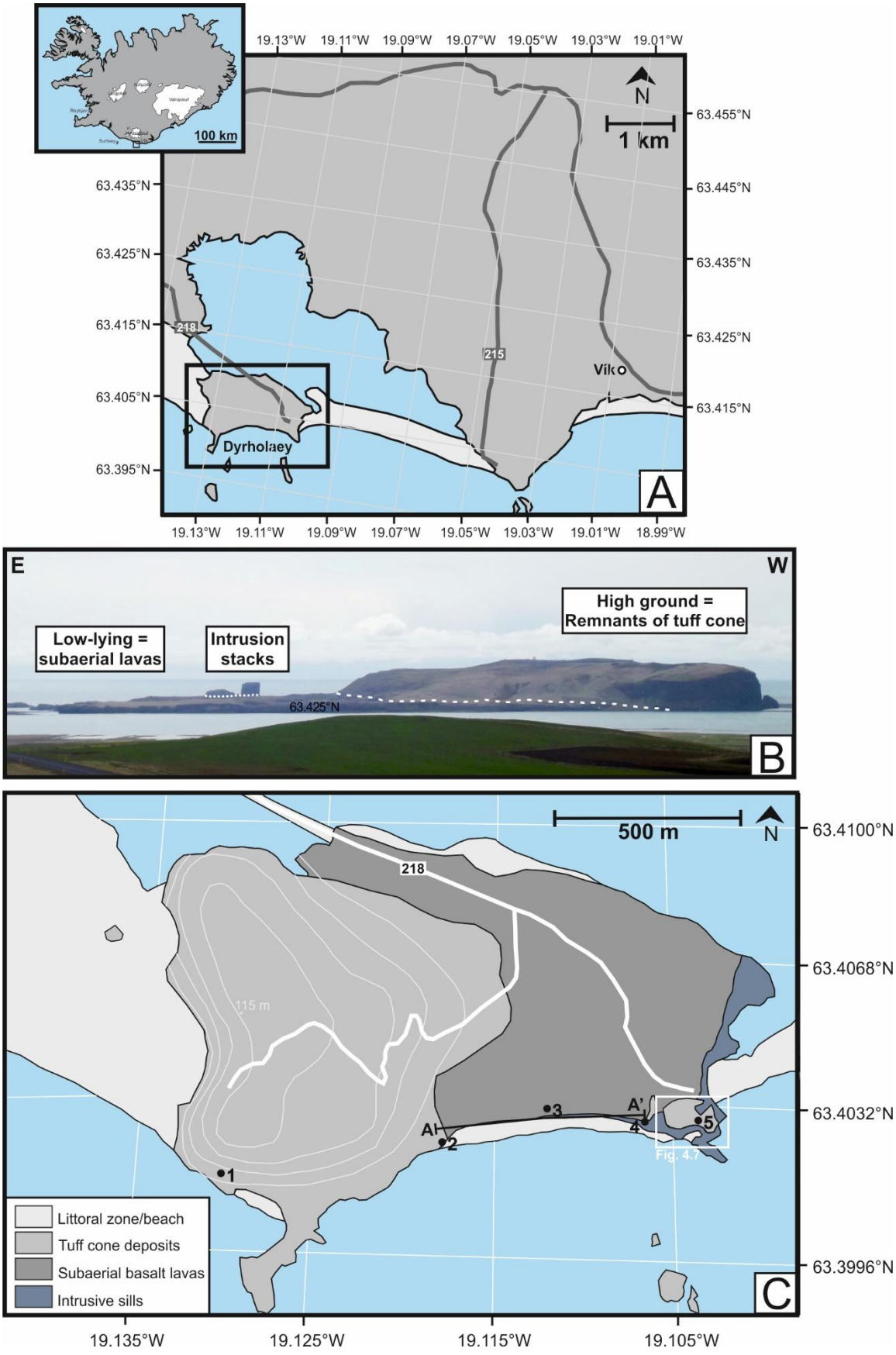

Figure 4.4: A) Location of Dyrhólaey on the south coast of Iceland. B) Photograph of Dyrhólaey taken from the north, highlighting the change in geomorphology across the island. C) Simplified geological map of Dyrhólaey Dip directions are shown. Cross section (A-A') in Figure 4.6 is indicated along the south coast. Inset shown in Figure 4.7. Locations mentioned in text are shown.

4.4. Petrographical and tephra characteristics.

Depositional and structural features are used to divide the tuff cone deposits into facies and subfacies. Compositionally, however, the deposits are made of fragmental aphyric and vesicular tachylite clasts, sideromelane, and aphyric basalt clasts. The original texture of the lapilli-tuffs and tuff units would have comprised an openwork texture of clast-supported scoriaceous and glassy material, indicating a fairly high porosity and permeability at the time of deposition. However, low temperature hydration has altered the majority of small basaltic clasts (<0.1 mm) to palagonite, sealing the original pore-space (Figure 4.5A). There are two forms of palagonite present at the Dyrhólaey tuff cone: fibrous palagonite, which has a distinctive orange-yellow colour, is birefringent and can contain protocrystallites (Zanon et al. 2009); and gel palagonite, a dark brown variant (Figure 4.5A). Fibrous palagonite coats fragmental tachylite clasts (Figure 4.5A). Gel palagonite forms in the initial stages of the hydration of sideromelane, and subsequently is replaced by fibrous palagonite. As the end-member of the hydration process, fibrous palagonite is dominant (Zhou and Fyfe 1989). The alteration of sideromelane to palagonite can occur over a very short geological timescale, as evident on the islands of Surtsey and Campelinos, which both exhibit highly palagonitised hydromagmatic products that were erupted less than 60 years ago (Kokelaar and Durant 1983; Cole et al. 2001). The palagontization of the tuff cone deposits increases the durability of the cone morphology (Figure 4.4B) (Zanon et al. 2009).

The tuff cone is comprised of alternating very fine to gravel-grade fragments (Figure 4.5B and C). Tachylite clasts are predominantly angular and sub-angular, occasionally exhibiting jagged, fragmental morphologies (Figure 4.5C). Sideromelane clasts are variably vesicular: clasts range from completely non-vesicular or mildly vesicular (vesicularities between <5% - 20% vol%) (Figure 4.5B and C), to clasts with high vesicularity (>50% vol%) (Figure 4.5A and D). These clasts contain plagioclase microlites that are often aligned within the clast. Ophitic textures are identified within the sideromelane clasts (Figure 4.5C and D). Large aphyric basaltic pyroclasts are sub-rounded. Clasts with high vesicularity exhibit ragged morphologies (Figure 4.5D). These tephra characteristics demonstrate fragmentation by both hydroclastic processes and by the exsolution of magmatic volatiles (Houghton and Wilson 1989; Maicher 2003). The matrix is comprised of both gel and

fibrous palagonite; tachylite shards and rare dispelled plagioclase feldspar crystals are also present (< 0.1 mm) (Figure 4.5B and C).

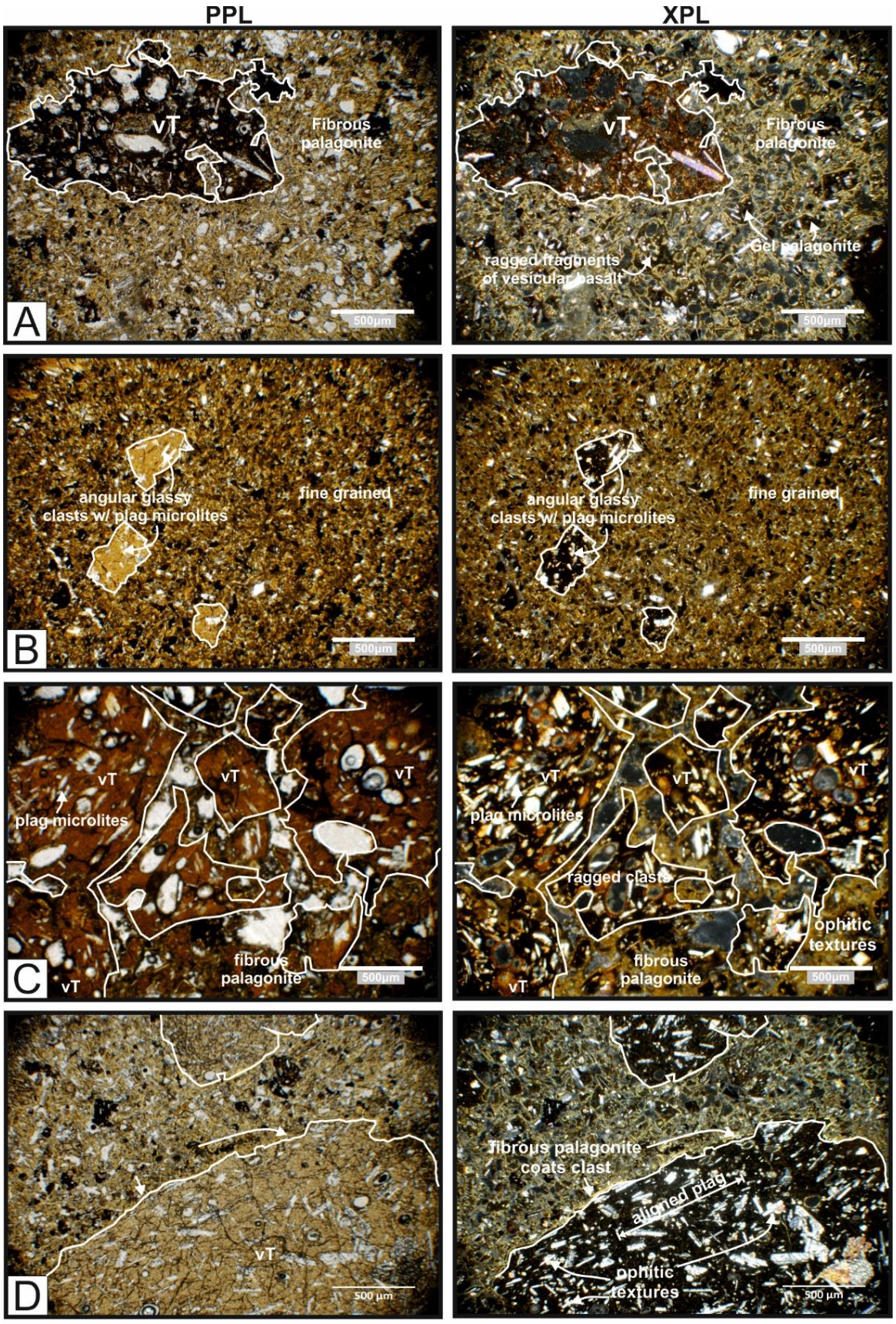

Figure 4.5: Figure caption on next page.

Figure 4.5: PPL and XPL images of petrographical characteristics of Dyrhólaey deposits. (A) Brown gel palagonite and birefringent fibrous palagonite seals porosity and coats fine grained tachylite angular fragments. Fragments contain plagioclase microlites. Large clast (~ 2 mm) has ragged morphology due to vesicularity. Plagioclase laths < 0.5mm. (B) Fine-grained tuff containing angular tachylite fragments. (C) Coarse-grained tuffs with ragged clast morphologies. Sideromelane clasts are highly vesicular and contain plagioclase microlites. Sample taken from between pahoehoe lavas in Locality 3 (discussed later). (D) Large sideromelane clast exhibiting aligned plagioclase laths. Ophitic textures are also evident. Fibrous palagonite coats clasts in (C) and (D). vT = vesicular tachylite.

4.5. Tuff cone host-rock

Tuff cones are recognised by their steep outwardly dipping beds, comprising pyroclastic density currents (PDC), gravitational mass movement, ash fall and tephra ejection deposits, and their less steep inwardly dipping beds. If the tuff cone edifice is not directly identifiable due to erosion and further external deposition, the dip and orientation of beds at outcrops can be used to identify the location of such beds in the tuff cone morphology. At locality 4 (Figure 4.4C and Figure 4.6), the bedding of the lapilli-tuffs and tuffs has been disrupted and a clear bedding direction is not apparent. The variable dip directions can be attributed to the emplacement of intrusions into the substrate, where magma inflation can distort the original bedding orientation and jack up (volcanic) sedimentary sequences.

To understand the development of the monogenetic edifice, the stratigraphy of the tuff cone edifice must first be established. To do so the distribution and characteristics of the tuff cone deposits have been categorised into different lithofacies, lithofacies associations and subfacies and sorted by locality in Figure 4.4C, cross-section A-A' in Figure 4.6 and a surface map in Figure 4.7 . The deposits are explained at each of these main localities and summarised in Table 4.1. .

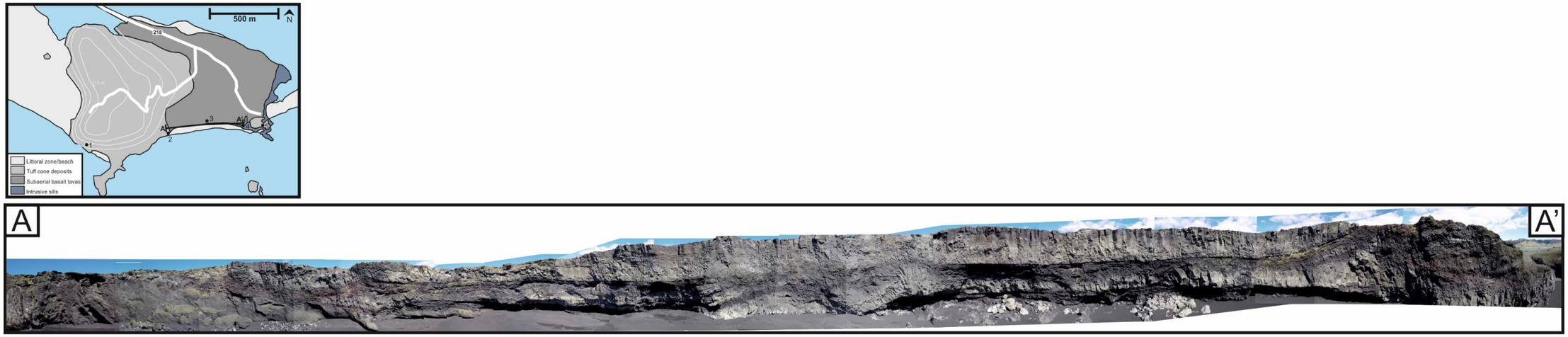

Figure 4.6: Photographic and annotated cross section along southern cliff face. Location of A-A' shown in Figure 4.4C. Green shading represents intrusive bodies. Localities of different lithofacies are labelled as described in text. Logs in Figure 4.8 are labelled. Magma steps and host-rock bridges are labelled. These indicate a brittle and ductile intrusion emplacement mechanism.

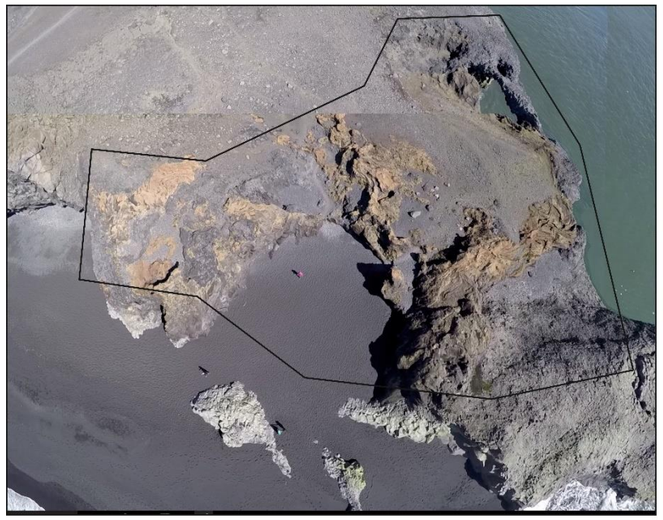

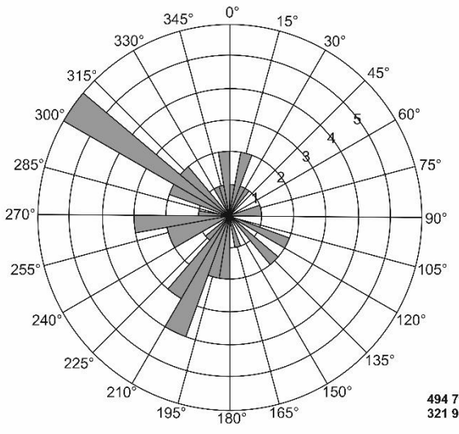

KEY

Lithofacies

- **D** — **Dolerite:** Coherent, columnar jointing (spacing - 15 cm to 80 cm), fine-grained, vesicle pipes (sub-vertical to sub-horizontal).
- **B** — **Basalt:** Heavily fractured, locally glassy and vesicular, irregular margins, locally ropey pahoehoe textures
- **dsLTl** — **LFA E: Diffusely stratified lapilli tuff (rounded lithic-rich):** Silt grade, dark grey matrix (~80%), reworked, randomly orientated rounded basalt clasts
- **//sLT** — **LFA F: Stratified tuffs and lapilli tuffs**: Mostly parallel but locally cross-strat and channel cut. Reworked hyaloclastite. Mostly palagonitized.
- **dsLT** — **Lithofacies G: Very diffusely stratified lapilli tuff:** Parallel stratification.Clast-supported. Locally scoriaceous, glassy fragmental basalt clasts (>90%). Palagonitized.
- **HPBr** — **Lithofacies H: Hyaloclastite Pillow Breccia:** Massive unit deposited into depo-centre, 80% basalt clasts, (pillows, fragmented pillows, rinds, scoriaceous material). Palagonitized.
- **Peperite:** Blocky and irregular, vesiculated sediment
- **Sediment fluidisation:** loss of internal stucture
- **Pillow:** radial fractures, glassy, ropey rind and vesicular centre

Bedding

- dip/strike of bedding
- bedding

Boundaries

- planar boundary
- diffuse boundary

Structure

- F — fault
- mobilised sand conduit

Geography

- alluvium/scree
- sea
- coastline

N

0 metres 10

494 792
321 931

494 845
321 970

494 869
321 965

494 794
321 914

494 821
321 902

494 857
321 889

LOG 6
LOG 10
LOG 7
LOG 5
LOG 8
LOG 8

B
D
dsLTl
HPBr
//sLT
dsLT
NO EXPOSURE

Figure 4.7: Geological map of the SE corner of Dyrhólaey as shown as Locality 5 in Figure 4.4. Distribution of Lithofacies E-H and location of stratigraphical logs are shown. Dispersal of peperite and fluidisation features are also highlighted by a triangle pattern and spotted pattern respectively. Rose diagram shows average dip of beds.

Lithofacies & lithofacies associations	Abbrev	Locality	Description	Interpretation	Distance from vent
LFA A: Pillow breccia, fragmented pillows and cross-stratified lapilli-tuffs	dxsLT	1	Thick beds (<2 m) of breccia, interbedded by lapilli-tuff and pillow-dominated layers. Coarse angular fragments and blocks. Lapilli-tuff interbeds are normally graded, diffusely cross-stratified and form channels.	LFA A was formed at the onset of submarine volcanism due to the presence of intact pillows, and thick beds. The breccias in LFA A were likely deposited by fallout deposits from tephra jets or continuous uprush processes, where pillows were ripped from the tuff cone platform, fragmented, erupted and deposited within a tephra jet.	Proximal
Lithofacies B: Angular basalt breccia	mBr	2	Sub-vertical column cross-cutting stratified deposits. Consists of clast-supported breccia comprising a highly chaotic structure made up of heterogeneous-graded angular and sub-angular basalt clasts and rounded, globular tachylite clasts. The facies fingers into the surrounding sediment and diffusely stratified host-rock rafts are evident within the facies.	Lithofacies B represents the cone of mobile slurry, comprised of hyaloclastite, water, tephra and basaltic clasts that exist beneath Surtseyan vents. The vent walls are irregular and indistinct, and liable to failure, forming rafts that are preserved in the slurry. Expansion of steam inside the magma exerts pressure internally and the magma fractures and fragments producing angular basalt clasts. This type of explosivity is called bulk steam interaction. These steam ejections produce tephra jets. If the frequency of tephra jets is high, and steam is emitted almost continuously, this phenomenon is known as continuous uprush (Kokelaar 1986).	Proximal
LFA C: Crudely-bedded lapilli-tuff	dsLT	2	Massive or diffusely stratified lapilli-tuffs that are defined by coarse, clast-supported breccia beds (maximum clast size 350 mm). The lapilli-tuffs are clast-supported and demonstrate local fining upward sequences. Clasts angular and many of the clasts are significantly vesicular (~20%).	LFA C was deposited by either multiple column collapses from PDCs with a high particle concentration and little to no turbulence, and/or relatively high concentration particle fallout.	Medial
LFA D: Spatter and lava	mBrsc	3,4	Interbedded spatter and thin (<1 m) pahoehoe flow lobes. Agglutinated spatter is highly vesicular (>20% ves), clast-supported and contains rope-like clast morphologies. The basalt lavas exhibit a relatively coherent and aphanitic core with <5% vesicularity, vesiculated margins (20 - 30 vol. %); and vitrified and fractured rinds with rope-like textures.	The subaerial volcanic activity involved Strombolian fire fountaining initially producing a thick unit of highly fragmental and vesicular spatter which agglutinated upon deposition and was followed by thin pahoehoe lava flows. LFA D likely represents several lava lobes of the one lava eruption separated by small Hawaiian fountaining episodes.	Medial
LFA E: Planar stratified tuffs and lapilli-tuffs	//T	5	Fine, stratified and diffusely stratified tuff beds with discrete lenses of dispersed basalt clasts. Indistinct normal grading is evident and locally, beds and laminations have erosive bases. Occasionally large blocks are present in scoured channels.	LFA E is reworked material which was initially deposited into water or eroded from the tuff cone edifice. Gentle to medium current reworking would produce enough energy to form scoured channels.	Distal

Lithofacies & lithofacies associations	Abbrev	Locality	Description	Interpretation	Distance from vent
LFA F: Chaotic and cross-cutting lapilli-tuffs	xsLT	5	LFA F beds are laterally discontinuous, extensively cross-cut one another and have convex bottom boundaries imitating channel-like deposits or erosional surfaces. They are comprised of diffusely laminar lapilli beds (subfacies F1), massive lapilli beds (subfacies F2), finely laminated tuff lenses (subfacies F3), clast-rich breccia lenses or "lapillistones" (subfacies F4), and cross-stratified coarse lapilli (subfacies F5).	Alternating stratifications of fine ash and coarse lapilli reflect a regular change in eruption explosivity and/or material deposited by a PDC. Equally, irregular contacts between internal layers and zones of massive lapilli suggest internally changing conditions, including changes in grain concentration, velocity and shear stress across the substrate, and reflects cyclic changes in turbulence within the PDC. Similarly alternating normally graded and inversely graded sequences suggest waxing and waning of current competence during individual eruptions.	Medial- distal
Lithofacies G: Massive lapilli-tuff	mLT	5	Coarse, clast-supported massive lapilli-tuff. Clasts have ragged, fragmental morphologies and are composed of highly vesiculated material.	Fluidisation of LFA F as a result of intrusion emplacement has severely disrupted the stratification, forming a massive unit. Additionally peperite formation has formed large fragmental clasts within the unit.	Distal (intrusion)
Lithofacies H: Hyaloclastite pillow breccia	HPBr	4,5	Vesicular basalt fragments and fragmented, equant crystals (pyroxenes) (<5%), together with pillows, fragmented pillows, polyhedral blocky clasts, bounded by curviplanar surfaces, and lava lobes. The pillows in Lithofacies H typically have: lobate, bulbous geometries; a glassy, dimpled rind, often with a ropey texture; a vesicular centre with radial, quaquaversal vesicles; hyaloclastite locally found in the centre of the pillows; and radial jointing. Lithofacies H is intimately related to highly fragmented intrusions.	Intrusions non-explosively fragmented forming subsurface pillows and proto-pillows. These magma fragments were incorporated into the surrounding host-rock forming a coarse, densely-packed breccia made up of angular dyke fragments and fragmented pillows which still retain pillow characteristics (e.g. vitrified, ropey rinds).	Distal (intrusion)
Coherent sills	-	2,3,4,5	Sill lobes are connected by magma steps. These sill lobes range in thicknesses from < 2 m to > 20 m and have regular, widely spaced, subvertical columnar jointing. The margins of the sills are irregular and undulating with local cm-scale fingering and deformation of surrounding host-rock. The dolerite is fine to medium grained and contains fine plagioclase phenocrysts (sub-mm). The sills also exhibit convex-lens shaped vesicle trails at their margins	Magma steps and bridges formed as a response to brittle emplacement mechanisms, and magma fingers and irregular, fingering margins, formed as a response to ductile emplacement mechanisms. The sills were initially emplaced by exploiting compliant horizons, where they subsequently fed irregular dyke-like bodies and fingered into the surrounding host-rock by fluidising the host-rock and intruding by ductile processes	n/a
Fragmented dykes	-	4,5	Highly irregular dyke-like bodies disseminate above and away from the sills. Blocky peperite has formed around these dykes, locally with jigsaw fit. The dyke-like bodies are	The emplacement of the dyke-like bodies was likely a complex process involving non-explosive (pillow-forming, cooling-contraction granulation) and explosive processes	n/a

Lithofacies & lithofacies associations	Abbrev	Locality	Description	Interpretation	Distance from vent
			generally 10 cm to 800 cm thick and exhibit vitrified, occasionally ropey, outer margins and polyhedral jointing. Multiple dykelets and finger-like protrusions extend from the edges of the intrusions, locally forming pillow-like structures, or proto-pillows.	(degassing of volatiles causing fragmentation). Shallow (<200 m) intrusion emplacement into water-saturated sediment formed subsurface pillows and proto-pillows. It is likely pillows formed in the subsurface due to: (1) the water-saturated nature of the host-rock; (2) the very shallow depth of emplacement (<100 m) providing the right pressure conditions for pillow production; and (3) low magma flux.	

Table 4.1: Summary of the characteristics of all the facies recorded at Dyrhólaey and a description of how and where these facies were deposited or intruded (in reference to the location of the vent).

4.5.1. **Lithofacies Association A (LFA A): Interbedded pillow breccia and lapilli-tuff (Locality 1)**

Lithofacies association A (LFA A) characterises the tuff cone stratigraphy that make up the 100 m cliffs and geomorphological arch to the West of Dyrhólaey (Figure 4.8A). This is described as Locality 1 (Figure 4.4C). Due to the inaccessible cliff face, Facies A was mostly examined from a distance using photographic evidence. A log was produced where access allowed but this only provides detail of some of the stratigraphy (Figure 4.8E). LFA A is comprised of interbedded breccia, lapilli-tuff and pillow-dominated layers. The pillows appear to have radial morphologies, smooth external surfaces indicating glassy rinds, and have quaquaversal jointing patterns (Figure 4.8B). The pillow-dominated layers are not laterally extensive and form decimetre scale lenses. These lenses are interbedded between lapilli-tuff and angular basalt breccias, as illustrated in the stratigraphical log in Figure 4.8E. The breccia layers are clast-supported sub-units comprised of angular and sub-rounded (pillow-like) clasts. The angular clasts are likely to be fragmented pillows as many exhibit glassy rinds and polyhedral, block jointing (Figure 4.8C). Approximately 25% of these clasts are moderately vesicular, the remaining are non-vesicular. The lapilli-tuff interbeds are diffusely stratified and locally normally graded. Many layers exhibit trough cross-bedding and coarse lapilli-tuff grade channel-like bodies (Figure 4.8D). Large metre-scale hummocky cross-stratification can be identified along the cliff face (Figure 4.8D).

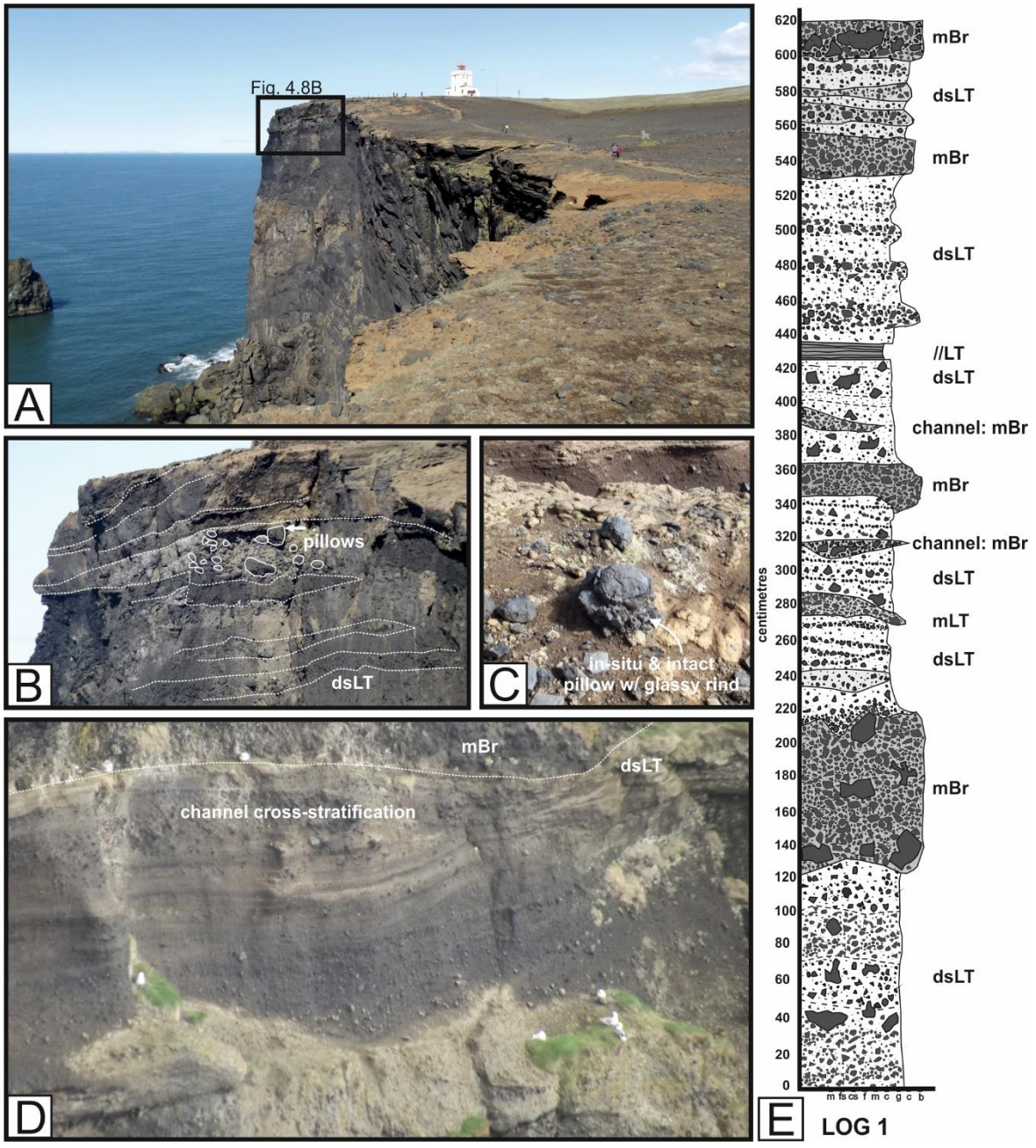

Figure 4.8: Lithofacies association A (LFA A) at Locality 1 comprises alternating layers of //LT, xsLT and breccias. (A) Photographic examination of the cliff face shows interbedded pillow-dominated layers and LT. Inset shows location of (B). Pillows exhibit rounded or lobate shapes. Diffuse stratifications are observed in the cliff face. (C) Intact pillow with glassy rind. Breccias are comprised of fragments of pillows. (D) Interbeds between mBr at the top of the image and diffusely stratified lapilli tuffs. Channel-like bodies and cross-stratification are evident in the cliff face. (E) Schematic log through LFA A showing finer detail in the stratigraphy. dsLT = diffusely stratified lapilli-tuff; mBr = massibe breccia; mLT = massive lapilli-tuff; //LT = parallel-stratified lapilli-tuff.

4.5.2. **Lithofacies B: Angular basalt breccia, mBr (Locality 2)**

Lithofacies B, located at the far western end of the beach in Figure 4.4C (Locality 2), is a sub-vertical column of clast-supported breccia comprising a highly chaotic structure made up of heterogeneous-graded angular and sub-angular basalt clasts and rounded, globular basaltic clasts. The lithofacies has a sub-vertical western boundary with the surrounding units and clearly cross-cuts the local stratigraphy (Figure 4.9A and D). The less steep eastern margin is clearly defined at the base of the cliff and becomes less distinct towards the top of the cliff face where it fingers into the surrounding host-rock in a series of metre-scale lobes and fingers, and disperses (Figure 4.9A, B, C). Facies B is unsorted and clast-supported (>90% clasts); however, where present, the matrix consists of fine, palagonitised basalt clasts (Figure 4.9D). Clasts are up to 420 x 540 mm in diameter. Locally, these larger clasts (> 200 mm) are vesicular, containing cm-scale unfilled vesicles, however the clasts are primarily non-vesicular (<5% vesicles) (Figure 4.9E). The globular clasts are comprised of an outer glassy rim with a crystalline interior (Figure 4.9F).

The breccia grades from this clast-supported, chaotically structured unit on the western margin to a less densely-packed and matrix supported sequence on the eastern margin. In the centre of this unit, diffuse laminations are evident that are dipping steeply to the east (Figure 4.9A). These laminations are defined by matrix-supported layers with few large clasts and are deci-centimetre in scale. The laminations steepen towards the western, chaotically structured breccia and an indistinct margin between massive breccia and laminated lapilli-tuffs can be seen.

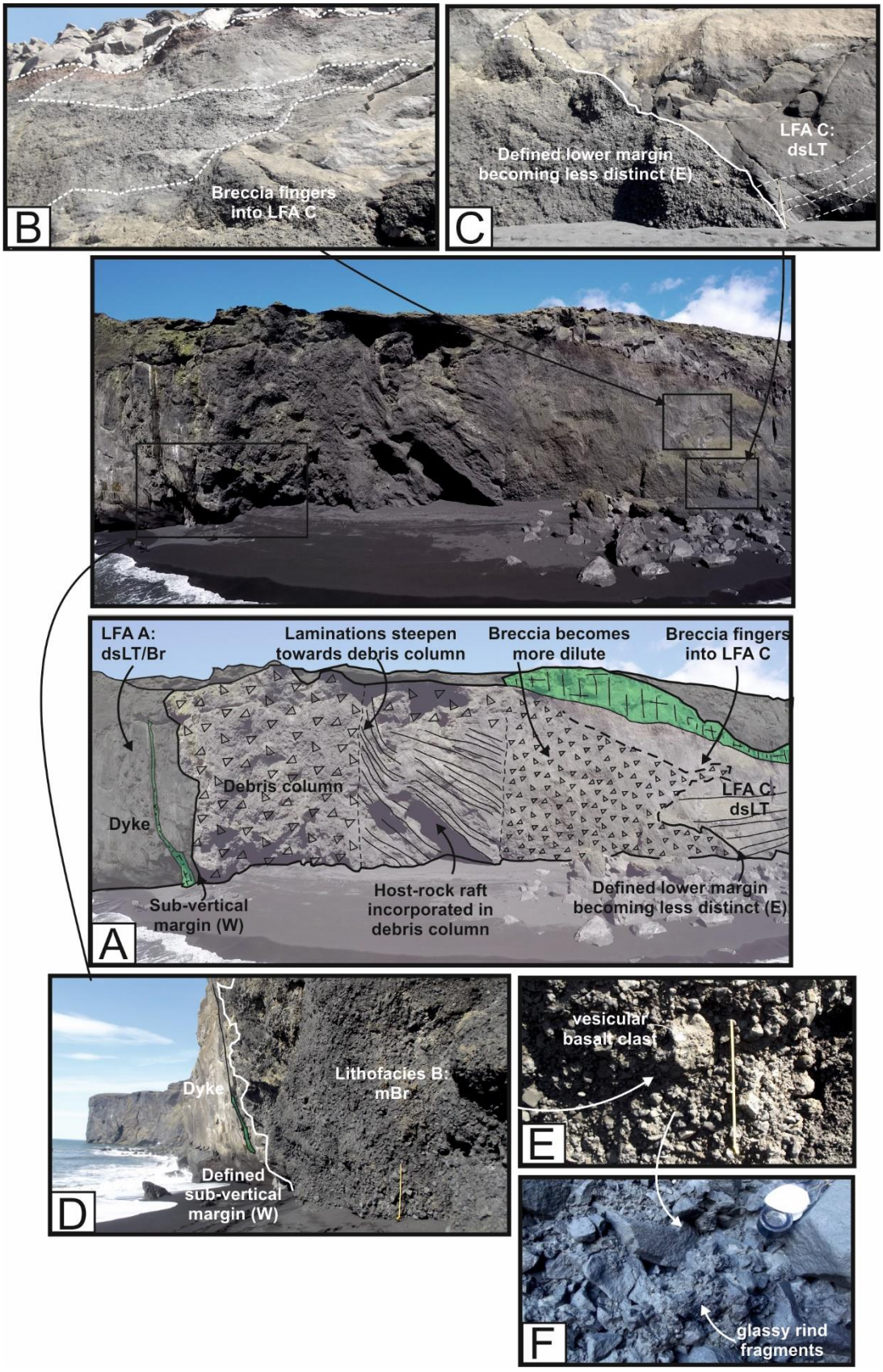

Figure 4.9: Lithofacies B at Locality 2 (A) Annotated structure of Lithofacies B. (B) and (C) Eastern margin of sub-vertical column that grades from a distinctive boundary at the base of the cliff (C) to a diffuse, lobate margin (B). (D) Defined western margin of column. (E) Clast-supported breccia in dense, chaotic portion of Lithofacies B with large vesicular clasts (40 cm). (F) Glassy rinds with a globular texture. No matrix. Tape measure is 1 m long.

4.5.3. **Lithofacies Association C (LFA C): Crudely bedded lapilli-tuff and breccia (Locality 2)**

This lithofacies association typically comprises massive or diffusely stratified lapilli-tuffs that are defined by coarse, clast-supported breccia beds (maximum clast size 350 mm). The lapilli-tuffs are clast-supported, with little or no palagonite matrix (<15 %); however, LFA C becomes significantly more matrix-supported to the east of Locality 2. Local fining upward sequences demonstrates normal grading in some of the lapilli-tuff layers (Figure 4.10). Clasts in the breccia are distinctly angular and many of the clasts (approx. 10-40 % of the clast population) have a vesicularity of greater than 20 vol. %. Within the coarse lapilli stratifications, discontinuous lenses of matrix-supported breccia are present (Figure 4.10). Clast sizes within the lenses are a maximum of 21 cm. Figure 4.10 illustrates three log sections through LFA C.

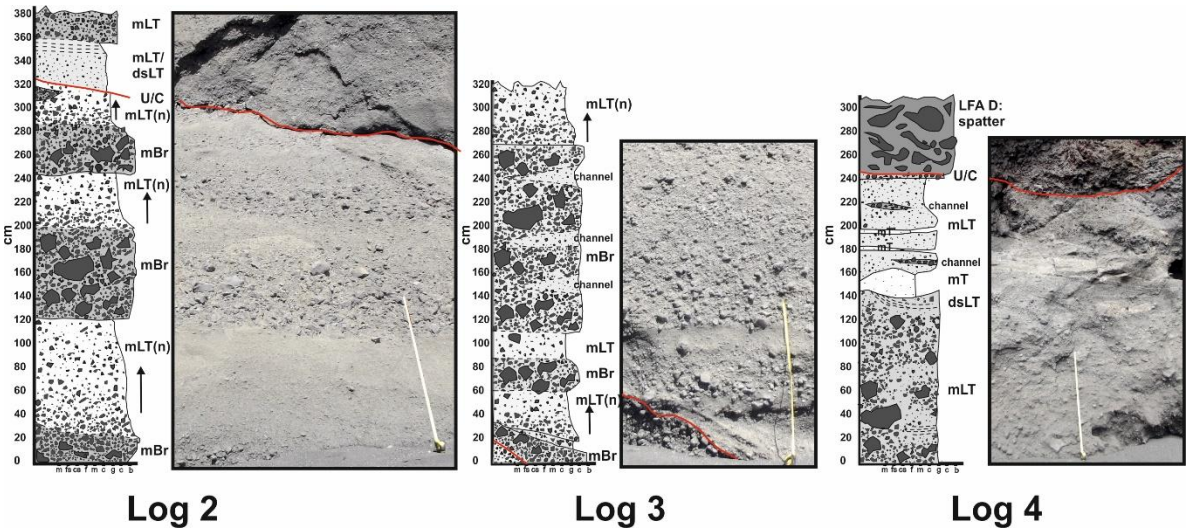

Figure 4.10: Schematic stratigraphic logs at three locations through Lithofacies association C (LFA C), showing normally graded sequences, chaotic breccia layers and laterally discontinuous lenses of fine lapilli-tuff. Localities of logs are labelled on Figure 4.6. Tape measure is 1m long.

4.5.4. **Lithofacies Association D (LFA D): Interbedded spatter and pahoehoe lavas (Locality 3)**

At the cliff exposure at Locality 3 (Figure 4.4 and Figure 4.6), there are a series of incrementally extruded, pahoehoe lavas interbedded with highly fragmental, basaltic breccias and agglutinated spatter deposits (Figure 4.11). The lavas onlap onto the tuff cone deposits (LFA A and C) to the west (Figure 4.6). The extent of the lavas to the east is obscured by the intrusions at Locality 4. At the base of LFA D are highly fragmental and vesicular spatter deposits that have agglutinated during deposition (Figure 4.11C and D). Spatter clasts are up to 650 mm across (longest axis) and have

vesicles up to 50 mm across. The spatter unit is 3-4 m thick, clast supported and contains rope-like clast morphologies (Figure 4.11C and D).

Above the spatter sub-unit are over seventeen identifiable individual pahoehoe lavas with lava thicknesses ranging from <0.5 m to 2 m (Figure 4.11A). Towards the west, the thicknesses of these lavas gradually decreases and pinches out (only the thicker lavas onlap the cone deposits) indicating the extrusion source is to the east (Figure 4.11B). The basalt lavas exhibit a relatively coherent and aphanitic core with <5% vesicularity, vesiculated margins (20 - 30 vol. %); and vitrified and fractured rinds with rope-like textures. Between the lavas are clast-supported breccia interbeds up to 6 m thick. The clast-supported breccia is comprised of: highly vesicular and angular basalt blocks (<10 cm); tachylite clasts with ragged clast morphologies; and highly fragmented, relatively small, pillow-like clasts (< 30 cm) and broken rinds. The spherical vesicles within the basalt blocks are up to 1 cm in diameter, and constitute 30 vol.%. The boundary between lava and breccia is highly irregular and locally the breccia cuts down and erosively overlies the lava beneath.

Semi-concordant intrusions are emplaced into the lavas and are discussed later (shaded green in Figure 4.11A). Above the intrusions the definition of each lava flow is difficult to identify and likely to be a result of disruption by sill intrusion (Figure 4.11A).

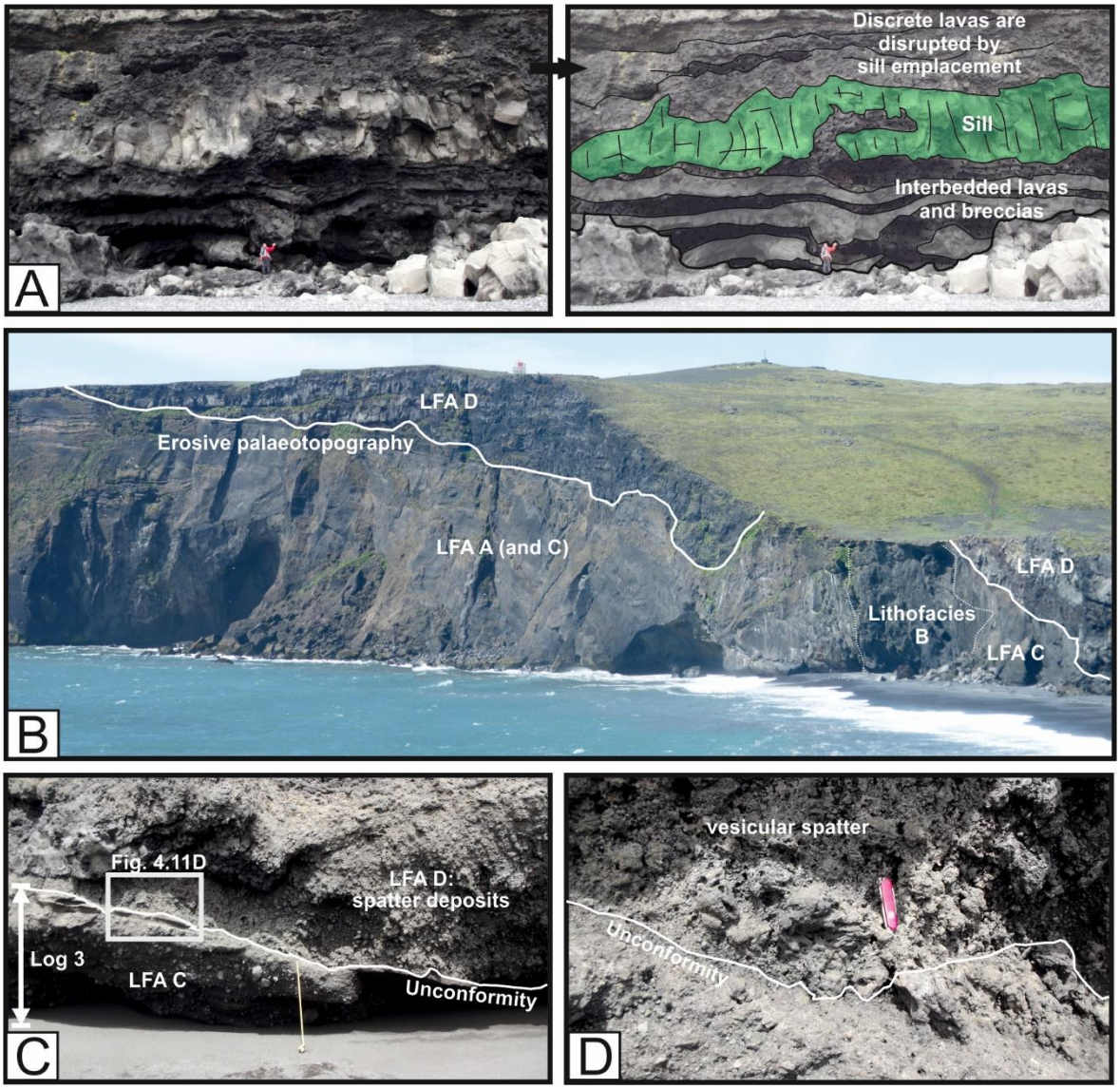

Figure 4.11: Lithofacies association D (LFA D) at Locality 3 (see Figure 4.4). (A) Original and annotated photo of LFA C. Interbedded compound pahoehoe lavas and clast-supported, spatter-dominated breccias. Sill (shaded in green) is intruded into the lavas. Above the sill, the lavas and breccias are highly disrupted and individual lavas cannot be distinguished (B) Western extent of LFA D onlapping on to tuff cone structure. Notice the highly undulating unconformity representing an erosive palaeotopography. (C) At base of LFA D, spatter deposits are evident. Log 3 in Figure 4.10 is shown. Spatter unit is up to 4 m thick, (D) and comprises ropey clast morphologies and highly fragmented basalt.

4.5.5. **Lithofacies Association E (LFA E): Stratified tuffs and interbedded coarse lapilli-tuff (Locality 5)**

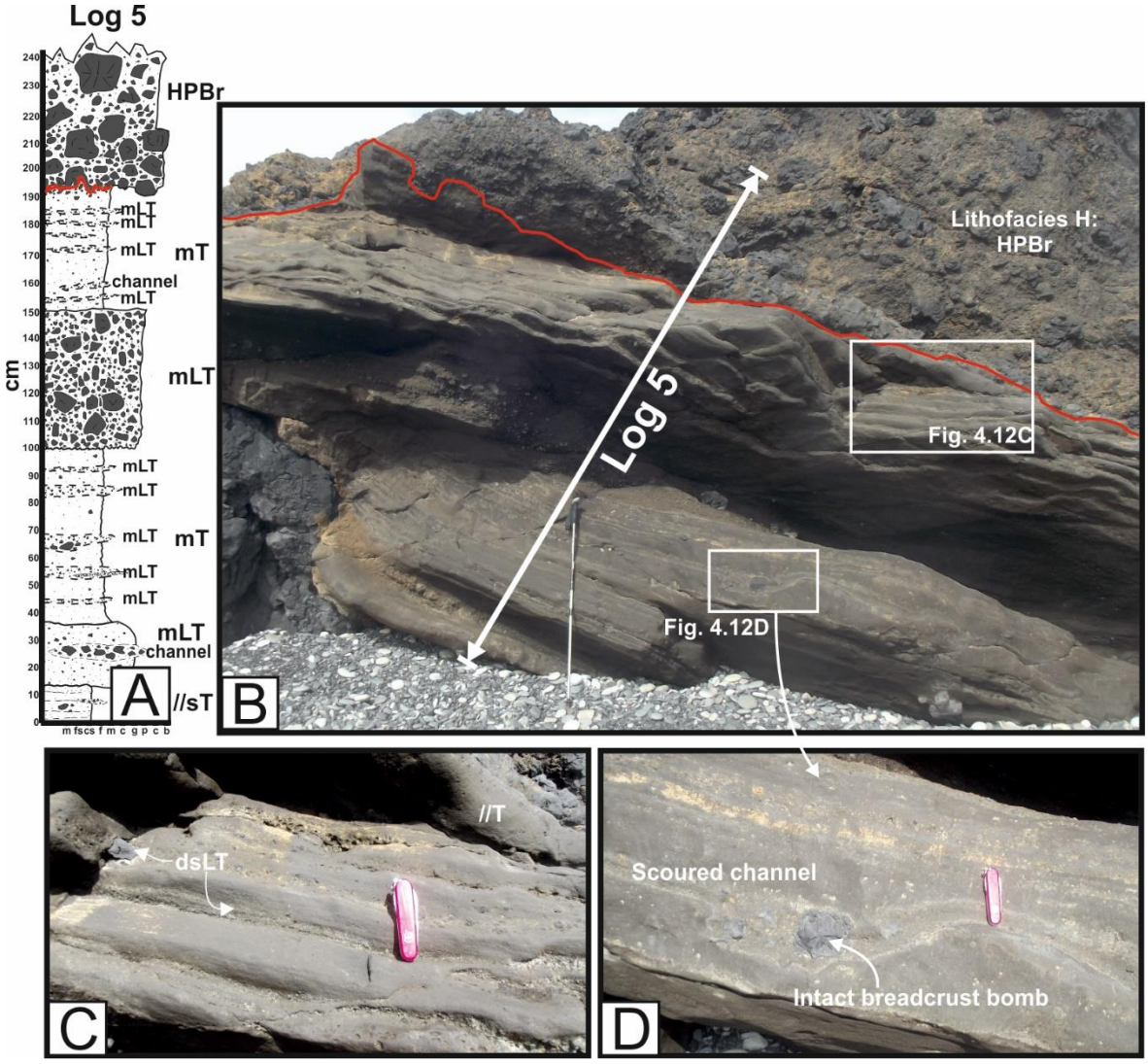

Figure 4.12: Lithofacies Association E at Locality 5 (A) Stratigraphical log through LFA E (Log 4 on Figure 4.10). Planar stratified tuffs interbedded with coarse lapilli-tuff layers and onlapped by Lithofacies H, the hyaloclastite pillow breccia unit. //sT = planar stratified tuff; mLT = massive lapilli-tuff; mT = massive tuff, HPBr = hyaloclastite pillow breccia (C) Stratified tuff with coarse lapilli-tuff lenses. (D) Scoured channel where coarse clasts and a breadcrust bomb fill the channel.

Lithofacies association E (LFA E) comprises a series of fine, stratified and diffusely stratified tuff beds with discrete lenses of dispersed basalt clasts (Figure 4.12). Beds are laterally continuous. Lenses are laterally discontinuous for up to 1.5 m and are comprised of angular and sub-angular basalt clasts. Indistinct normal grading is evident and grains are closely-packed. Locally, beds and laminations have erosive bases and occasionally large blocks are present in scoured channels, which have subsequently filled with coarser tuffs and fine lapilli-tuff graded tephra and blocks, up to 10 cm (Figure 4.12C). Blocks have a quenched and glassy rind that appear to be fractured like a breadcrust bomb. This facies is interbedded with thick, clast-rich lapilli-tuff interbeds (10 to 50 cm thick)

(Figure 4.12A). The relatively large clasts (0.8 cm to 16 cm) however, have glassy, ropey rinds and vesiculated centres, suggesting the material has originated from pillow-like bodies that have since been fragmented. There are no internal structures or grading within the lapilli-tuff subfacies.

4.5.6. **Lithofacies Association F (LFA F): Chaotic and cross-cutting stratified lapilli-tuffs (Locality 5)**

Lithofacies association F (LFA F) is divided into subfacies. LFA F comprises layers of lapilli on a cm-scale (10 cm – 30 cm) defined by alternating coarse lapilli and fine lapilli. LFA F beds are laterally discontinuous, extensively cross-cut one another and have convex bottom boundaries imitating channel-like deposits or erosional surfaces (Figure 4.13 and Figure 4.14). The lower margin is distinctive and planar (no evidence for erosion). Channels are laterally continuous for up to 8 m. These metre-scale channel-like bodies have been infilled by diffusely laminar lapilli beds (subfacies F1), massive lapilli beds (subfacies F2), finely laminated tuff lenses (subfacies F3), clast-rich breccia lenses or "lapillistones" (subfacies F4), and cross-stratified coarse lapilli (subfacies F5).

The diffusively laminar lapilli beds (F1) are mainly inversely graded; however, locally at the base of some of these diffusely laminated beds, are large, angular basaltic blocks (mildly vesicular) and coarse lapilli. Blocks are up to 15 cm in diameter. Throughout the subfacies, channels of coarse lapilli erode into diffuse laminations. Channels are thin (up to 10 cm) and extend laterally for tens of centimetres. The layers of massive fine to coarse lapilli (F2) have no internal structure or grading and contain disparate clast-rich zones and matrix-rich zones, ranging from 10% to 60% clast proportion. Within layers of F2 are discrete, clast-supported blocks in a diffuse lens-like structure, which are diffusely integrated within the subfacies.

Lenses of finely laminated tuff (F3) are also present and are up to 10 cm thick and <1 m laterally continuous. Laminations are on a mm-scale. Rare angular basaltic clasts are also present within F3. Subfacies F4, a matrix-supported breccia, contains (sub-) angular basaltic and glassy blocks within a coarse lapilli matrix, and appears to have a greater amount of alteration due to its darker orange appearance. Blocks comprise up to 80% of the subfacies and are variably vesiculated from aphyric and aphanitic to highly vesiculated (approx. 65% vol%). Locally, blocks are sub-rounded and have a glassy, ropey rind.

Subfacies F5 comprises low angle cross-laminated lapilli and tuffs (3° to 10° to WNW). Laminations are on a sub-mm to cm-scale. Each lamination fines upwards and locally has an erosive base. The laminations are not palagonitized. Thin, diffuse lenses of blocks are distributed throughout the subfacies. Minor faults and slumping disrupt LFA F (Figure 4.14C).

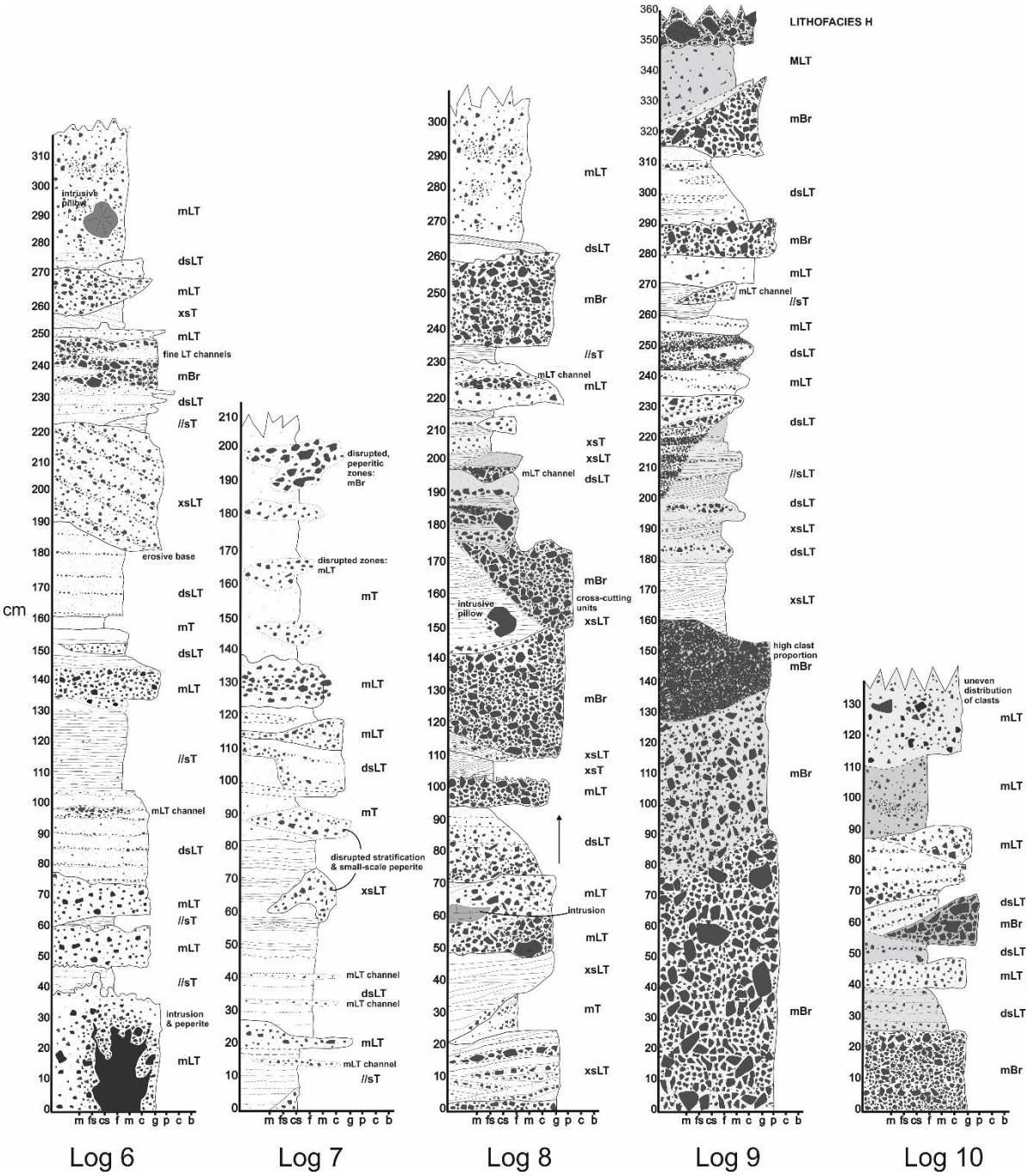

Figure 4.13: Lithofacies association F at Locality 5. A series of stratigraphical logs through LFA F to demonstrate the highly irregular beds, channels and stratifications that are laterallydiscontinuous. Sub-facies are labelled (F1, F2, F3, F4 and F5). Locations of logs displayed in Figure 4.7.

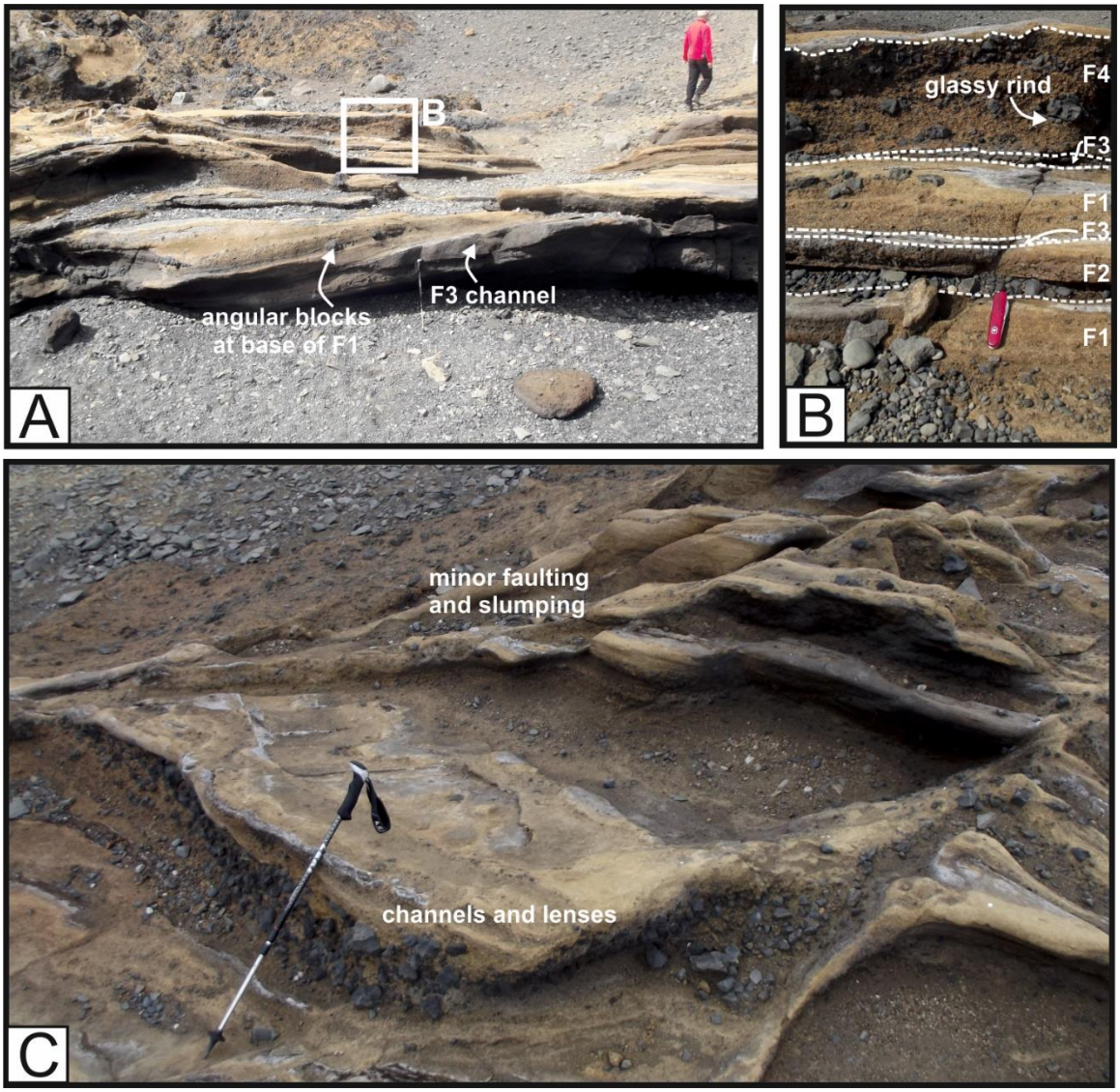

Figure 4.14: LFA F at Locality 1. (A) Multiple cross-cutting channels and lenses comprising all sub-facies (F1-F5). Angular blocks at base of F1. (B) Annotated stratifications between subfacies. (C) Photo highlighting highly irregular structure of cross-cutting channels and laterally discontinuous beds. Minor faulting and slumping is recognised throughout Locality 1.

4.5.7. **Lithofacies G: Massive lapilli-tuff (Locality 5)**

Lithofacies G comprises fragmental basaltic material, in a highly palagonitized coarse lapilli matrix. The facies is clast-supported and the clasts have ragged, fragmental morphologies. Clasts are composed of highly vesiculated material (>50%) and tachylite lapilli, with a maximum diameter up to approx. 25 cm. Locally, very diffuse stratifications are recorded but generally the lithofacies has a massive structure. The boundary between Lithofacies G and the adjacent LFA F is gradational and diffuse.

4.5.8. **Lithofacies H: Hyaloclastite pillow breccia (HPBr) (Locality 5)**

This facies includes a coarse lapilli, strongly altered palagonitized matrix comprised of comminuted glass (tachylite) (35%), variably vesicular basalt fragments and fragmented, equant crystals (pyroxenes) (<5%), together with pillows, fragmented pillows, polyhedral blocky clasts bounded by curviplanar surfaces, and lava lobes (Figure 4.15A). The pillows in Lithofacies H typically have: lobate, bulbous geometries; a glassy, dimpled rind, often with a ropey texture; a vesicular centre with radial, quaquaversal vesicles; hyaloclastite locally found in the centre of the pillows; and radial jointing. The pillows are dispersed randomly and maximum pillow diameter reaches 1.5 m x 0.9 m (Figure 4.15B, C and D).

Pillows have been comminuted into angular fragments, identifiable as pillow fragments by an intact rind and/or a vesiculated centre (Figure 4.15E). Locally, jig-saw fit textures is recorded, indicating in-situ fragmentation. The hyaloclastite matrix has been injected into fractures at the edges of the pillows and fragmented pillows suggesting rapid cooling, quenching and fluidisation of matrix, in-situ (Figure 4.15E). Basalt blocks are also present within the hyaloclastite matrix. These blocks tend to be non- to mildly- vesiculated and have visible plagioclase feldspar phenocrysts (<0.1 mm). Fractures at the edges of the blocks have been exploited by hyaloclastite.

The HPBr units (Lithofacies H) are intimately related to highly fragmented intrusions (Figure 4.15A). The western boundary between the HPBr and LFA F is gradational. At this locality LFA F is riddled with highly irregular, sinuous intrusions (Figure 4.15A). The abundance of intact pillows, especially large pillows (> 50 cm), in the HPBr decreases away from this margin. Near the edge of this boundary, within the HPBr unit, are several lava lobes (approx. 3 m x 0.2 m) that extend into the HPBr unit at a dip of 21°. The lava lobes have similar characteristics to the lava pillows in LFA F: vesiculated centres, radial fractures and a glassy rind. The other HPBr margins are more definitive, where there is a clear transition from the underlying facies to the HPBr. The jacked up and dipping beds of LFA C form a palaeo-topographic depression which has subsequently been filled by the HPBr unit.

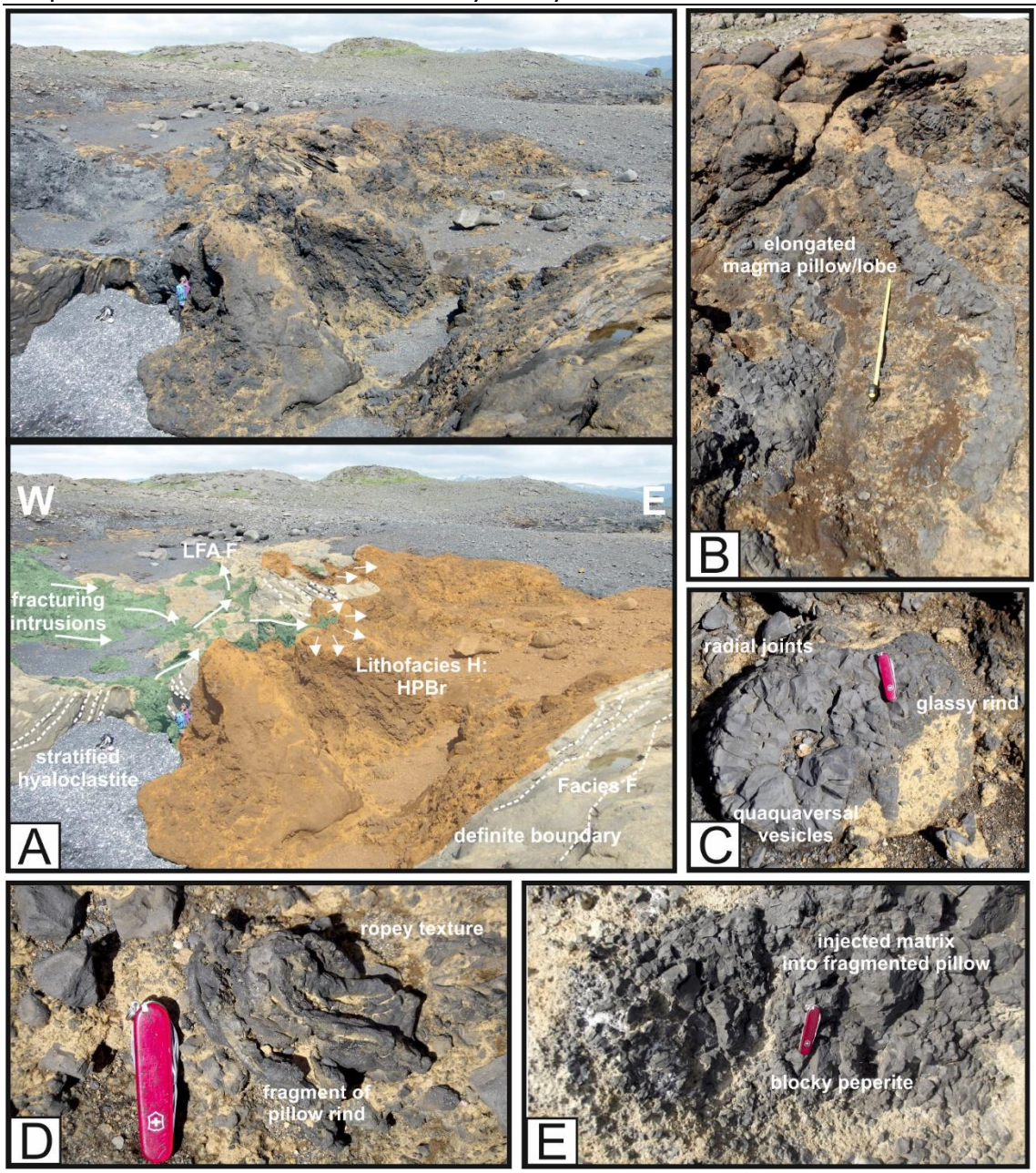

Figure 4.15: Lithofacies H, Hyaloclastite Pillow Breccia (HPBr) at Locality 1: (A) Original and annotated photo of the distribution of Lithofacies H. The boundary between LFA F and the HPBr on the west is irregular and diffuse. Intrusions fragment, disperse and likely feed the HPBr from this margin. (B) Elongated pillow lobe at the western margin of the HPBr. Polyhedral blocky jointing within the pillow. (C) Globular pillow lava with glassy rind, quaquaversal vesicular pattern and radial joints. (D) Pillow fragments exhibit glassy rinds with ropey texture. (E) Highly fragmented pillow lava forming peperite at the margins and a blocky jointing pattern. Palagonite is injected into fractures within the pillow.

4.5.9. **Coherent, stepped sills**

Dolerite sills have intruded into the lowland stratigraphy of Dyrhólaey (Figure 4.4) forming several stepped structures where sill lobes, at different heights, are connected by magma steps (Figure 4.6). The sill lobes range in thicknesses from <2 m to >20 m; however, some of the lobes are partially buried. The sills have regular, widely spaced, subvertical columnar jointing (Figure 4.16). The margins of the sills are irregular and undulating with local cm-scale fingering and deformation of surrounding host-rock. The dolerite is fine to medium grained and contains fine plagioclase phenocrysts (sub-mm). Pyroxene crystals are visible up to 5 mm in length. In the core of the thickest sills (Lobe 3 in Figure 4.16A), there are vertical, convex-lens shaped vesicle trails up to one metre in length and. on average, spaced 30 cm from one another (Figure 4.16B). Sub-horizontal vesicular zones at the base of the cliff exposure disseminate into non-vesiculated dolerite. At the edges of the intrusions, the jointing becomes highly irregular, multidirectional and the thickness of the columnar jointing is reduced (Figure 4.16A). The irregularity of the jointing indicates water infiltrated the magma as it cooled. The sills are not completely horizontal but have curvilinear geometries, localised inflated sections and winged edges, all conducive to a very shallow emplacement in the subsurface (<100 m) (Figure 4.16A).

Several magma steps are exposed along the south cross-section connecting sill lobes on marginally different heights, although some are obscured or buried (Figure 4.16A, Figure 4.17). A sub-vertical magma step connects Lobe 3 (sill in the centre of Figure 4.16A) to a partially buried lobe (Lobe 2). The direction of columnar jointing indicates magma flow direction (Figure 4.17A). Lobe 2 is further linked to a thick sill lobe that crops out in the far SE corner of Locality 5 (Lobe 1) (Figure 4.17A). Although some lobes and steps are not clearly exposed, the field observations show a series of intrusions have been emplaced in incrementally stepped sheets. One well-exposed step connects a thick sill lobe (Lobe 5; >20 m) to a lobe (Lobe 6) emplaced concordantly into the pahoehoe lava sequence, forming a 7 m thick sill, and exploiting the hard-rock substrate (Figure 4.17B). Dykelets propagate upwards from the transition between sills (Figure 4.17B). Gas cavities are evident at the margins of this conduit where the basalt is highly vesicular, glassy and, along the gas cavity walls, magma blisters are present (Figure 4.16C). Vesicle trails are abundant along the lower margins of the bridge, where the arrangement of vesicles demonstrates ascension and sub-horizontal flow

direction of magma (Figure 4.17C). Vesicles within the trails have elongated morphologies and appear to have been sheared by the magma flow. The sill lobe extends to the west for 500 m, gradually decreasing in thickness. In places, the magma has inflated and has caused the sill to dome, jacking up and disrupting the adjacent interbedded breccia and lava substrate (Figure 4.11A).

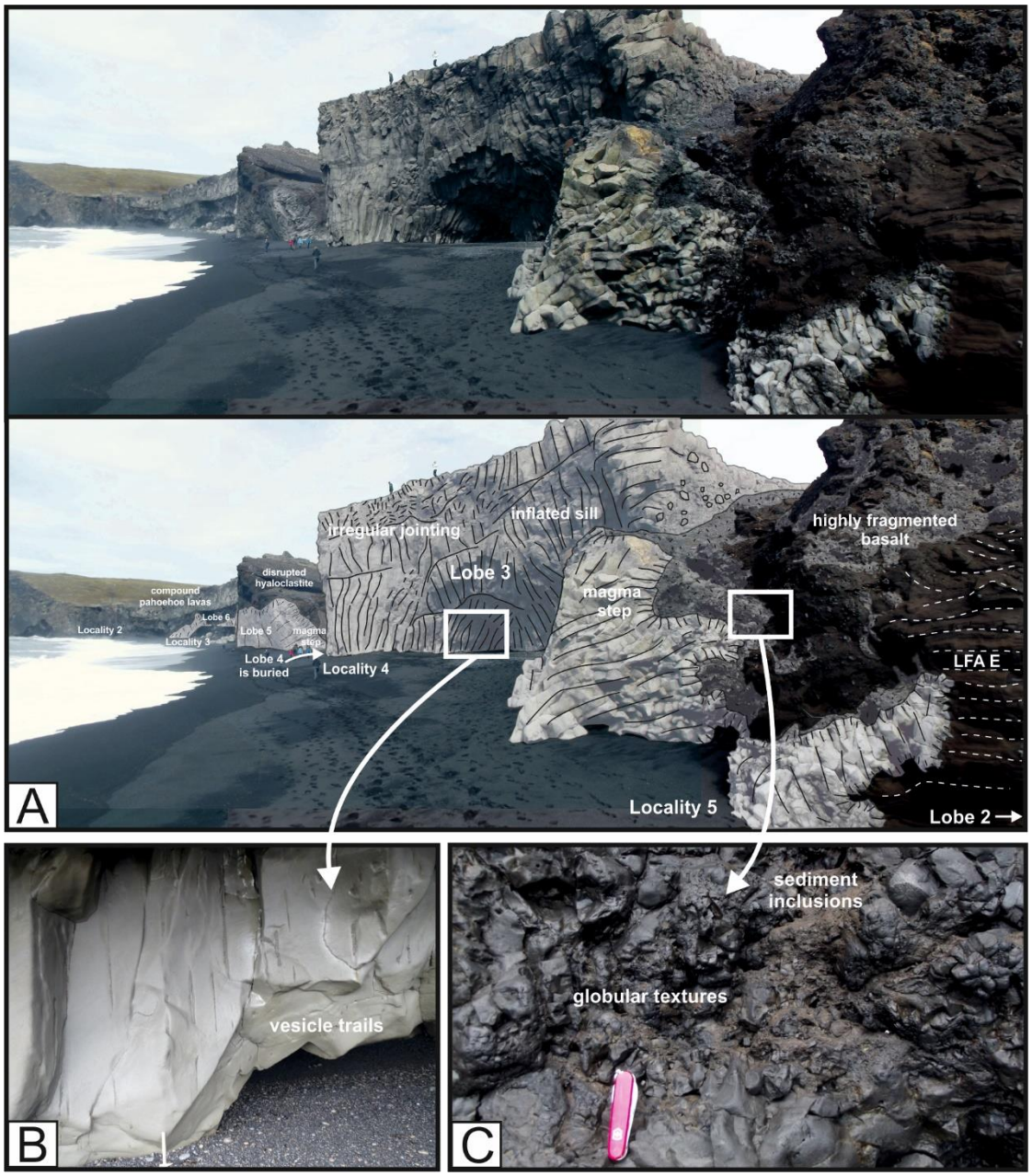

Figure 4.16: (A) Original and annotated photograph along the beach from Locality 5. Thick inflated sill in centre of the photo (Lobe 3) and Lobe 2 (not visible in photo) feed disseminated intrusions and intrude into the host-rock in blocky fragments. Jointing patterns become more irregular and chaotic at the sill margin. A partially buried magma step links Lobe 2 (stratigraphically lower lobe) to Lobe 3. Lobe 4 is buried between Lobe 3 and Lobe 5, only the magma step is exposed linking Lobe 4 to Lobe 5 (B) Sub-vertical vesicle trails up to 1 m long. (C) Sediment inclusions are incorporated at the margin of the intrusions.

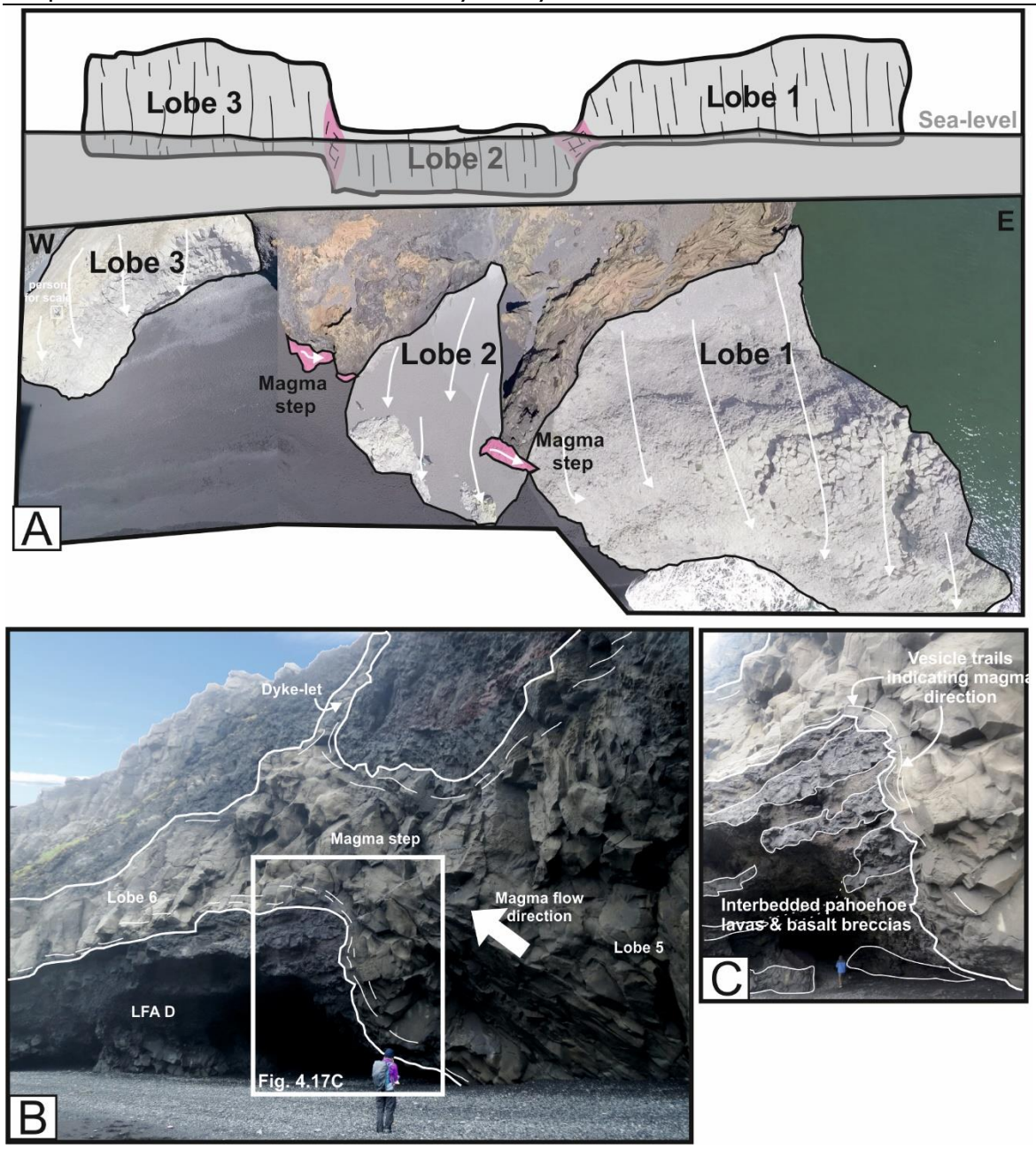

Figure 4.17: (A) Aerial view of multiple sill lobes (shaded in white) arranged on several stratigraphical levels and connected vertically by magma steps (shaded in pink). Direction of magma flow indicated by white arrows. Person for scale on Lobe 3. Magma step between Lobe 2 and 3 in Figure 4.16A. (B) Well-exposed magma step connecting Lobe 5 and Lobe 6 (a thin concordant sill). A dykelet propagates upwards from the junction between the two lobes. Person for scale. (C) Mineral alignment and elongated vesicle trails indicate magma flow direction. Person for scale.

Along the cliff face in Figure 4.6, Lobe 7 and 8 overlap on different stratigraphical levels (approximately 2 – 3 m vertically apart) and are not connected. This overlap has formed a host-rock bridge indicative of non-brittle emplacement and shallow emplacement. There is also evidence for magma fingers, a succession of elliptical finger-like structures formed from lateral inflation toward each other (Schofield et al. 2012). Locally, the fingers coalesce (Figure 4.6).

4.5.10. **Fragmented, irregular dyke-like bodies, proto-pillows and pillows**

Lobe 2, Lobe 3 and Lobe 5 disseminate highly irregular dyke-like bodies into the hydrovolcanic host-rock (LFA E and F) above and adjacent to the sills (Figure 4.7, Figure 4.16A, Figure 4.17). The intrusions emanate from the sills in all directions, forming magma fingers and lobes (Figure 4.16A). As the intrusions have been emplaced, the dyke-like bodies have disintegrated in-situ, forming blocky peperitic margins, locally with jigsaw fit texture (Figure 4.18). Peperite blocks range from sub-mm to 18 cm in size. Interaction at the margins between fine-grained material (e.g. LFA E) and the intrusion is minimal; no peperite or finger-like projections are formed and the margin is vitrified. Where peperite has formed, stratifications have been disrupted and dewatering, elutriation structures are evident in the finer hydrovolcanic deposits (Figure 4.18B).

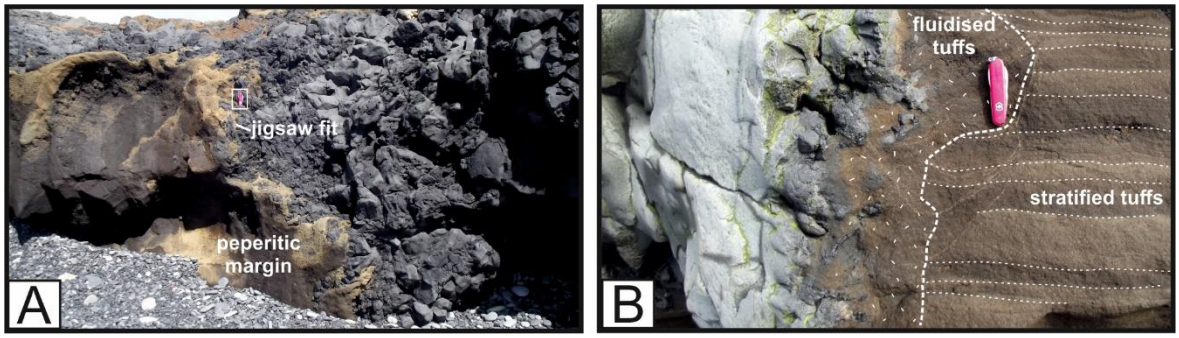

Figure 4.18: Peperitic margins around shallow (<100 m) intrusions. (A) Highly irregular dyke-like body intruded into LFA F. Peperite is formed at the margins as globular, sub-angular clasts. Pen-knife is 10 cm long (boxed). (B) Small scale peperite forming at the margins with LFA E. Zone of fluidised tuffs surround intrusion where stratifications have been disrupted by fluidisation and mobilisation of grains during intrusion event.

The dyke-like bodies are generally 10 cm to 800 cm thick and exhibit vitrified, occasionally ropey, outer margins and polyhedral jointing. The dendritic intrusions extend into the stratigraphy for approximately 40 m, becoming increasingly more fragmented (Figure 4.19A, B). Multiple dykelets and finger-like protrusions extend from the edges of the intrusions, locally forming pillow-like structures, or proto-pillows (Figure 4.19B, C). In places, the pillow structures have become disseminated or spalled from the leading edge of the intrusion, forming isolated magma pillows within the substrate (Figure 4.19C). Pillows are highly fractured where fractures are filled by the tuff host-rock. Pillows are typically ~10 cm to 200 cm in diameter. Generally, the pillow structures remain attached to the main intrusive body, demonstrating the characteristics of a lava pillow (spherical or lobate geometries; glassy, ropey rind; radial jointing; and vesiculated centres) but quite clearly intrusive in nature (Figure 4.19C). Vitrified outlines of proto-pillows are contained within

more coherent intrusions, formed by subsequent advancing intrusions engulfing already spalled pillows. The intrusive bodies appear to have fed the HPBr facies, as the margin between irregular dyke-like bodies with attached proto-pillows and the HPBr (Lithofacies H) is gradational (Figure 4.15A and Figure 4.19D).

The disseminated intrusions are generally mildly vesicular; however, there are concentrated zones of vesicles and gas cavities, mostly confined to the centre of the magma pillows and magma fingers (Figure 4.19C). Large gas cavities are observed in many of the intrusions (Figure 4.20A). The gas cavities are up to ~60 cm in diameter and have a typically irregular oblate shape. Large prolate-shaped and spherical vesicles (< 4cm) surround the larger gas cavities, suggesting the gas cavities are an agglutination of several larger vesicles (Figure 4.20B). Prolate vesicles disseminate sub-perpendicular from the gas cavities (Figure 4.20B). The walls of the gas cavities comprise vitrified basalt, and magma blisters and rope-like textures are evident (Figure 4.20A and C).

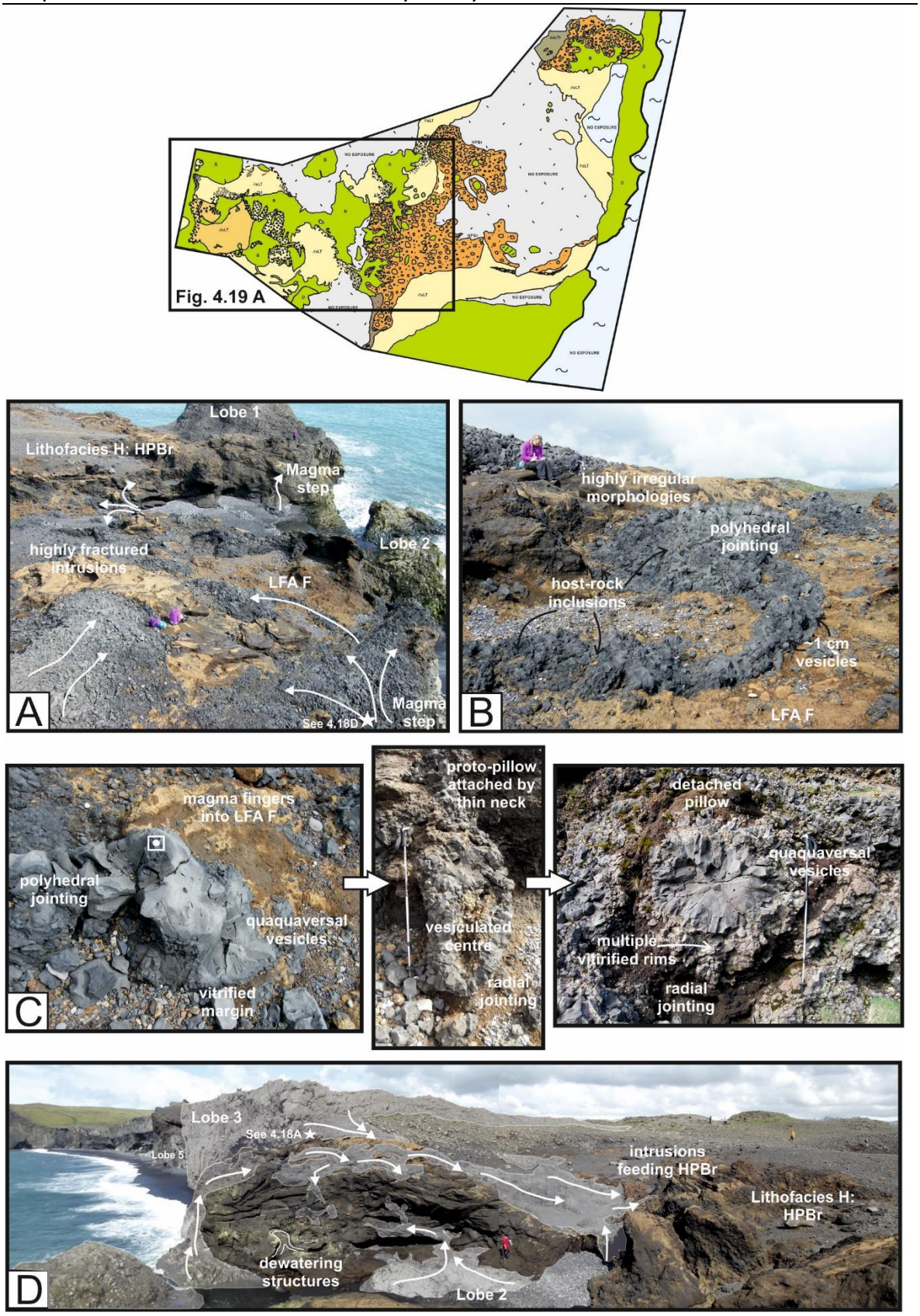

Figure 4.19: Disseminating intrusions fed by sill lobes. Map shows location of intrusions. See Figure 4.8 for key. (A) Bottom right of the image shows intrusions fed from Lobe 3 in Figure 4.17A, and the partly buried Lobe 2. The intrusions become more fractured further from their source input. White star is location of white star in (D). (B) Highly irregular morphologies demonstrating polyhedral jointing and host-rock inclusions. (C) Spectrum of magma fingers, proto-pillows attached by a thin neck to the main intrusion and a completely detached pillow. All proto-pillows and magma fingers demonstrate quaquaversal vesicles, a vesicular centre, radial jointing and a vitrified margin. The image on the far right shows multiple vitrified rims. Coin is 3 cm (boxed). Walking stick is 1 m. (D) Intrusions feed Lithofacies H. Dewatering structures are also evident on a metre scale. Upward and down ward magma propagation.

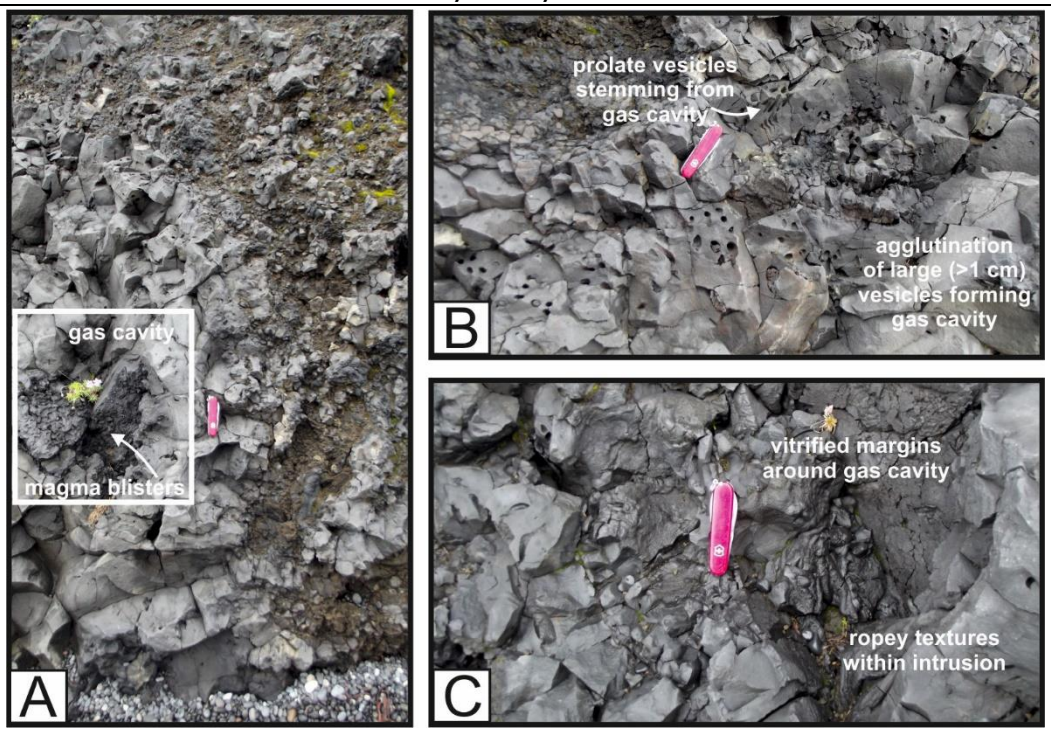

Figure 4.20: Gas cavities within disseminating intrusions. (A) Large gas cavity ~40 cm in length. Walls of gas cavity are comprised of vitrified basalt, where magma blisters are apparent. Pen-knife is 8 cm. (B) Densely packed vesicles form gas cavity approx. 25 cm across. Prolate vesicles extend away from the gas cavity (4 cm). (C) Wall of gas cavity is comprised of vitrified basalt with ropey textures.

4.6. Interpretation

4.6.1. **Surtseyan development of the tuff cone edifice**

The facies and sub-facies that comprise the Dyrhólaey tuff cone, described above, provide an insight into the initial and late-stage development of the edifice. The distribution and characteristics of each of the facies shows a continually moving primary venting zone and a switching from Surtseyan processes to magmatic subaerial processes.

4.6.1.1. Proximal to distal: LFA A, C, E, F

LFA A: The physical features of LFA A, with its abundant pillow lavas, pillow-like bombs, coarse broken pillow fragments and breccias (Figure 4.8A-C), imply that the southwest corner of Dyrhólaey was the location for the initial development of the tuff cone on the tuff cone platform. Pillow lavas form where water pressures are sufficient enough to suppress vesiculation of magma, and therefore tend to form at the onset of submarine volcanism (Kokelaar 1983). Isolated, rounded, pillow-like clasts seen in LFA A (Figure 4.8C) are produced from submarine fire-fountaining. The roundness of these clasts is controlled by the surface tension and hydrodynamic forces across molten bombs when they are ejected into water (Simpson and MacPhie 2001). The outer, vitrified rims of these clasts were generated by instantaneous quenching of magma in contact with seawater (Simpson and MacPhie 2001). There are no corresponding impact structures with the bombs as ejection and deposition into water slows impact.

Breccias comprised of clasts with angular morphologies and partial vitrified margins are likely to be broken pillow fragments that underwent brittle fragmentation during transportation (clast-to-clast collision) and deposition. The coarse decimetre scale clasts suggest the facies was deposited proximal to the vent source, where little to no transportation and fining took place. The relatively thick beds (1-4 m) further support this. These breccias were produced by explosive activity near the vent that deepened and widened the main edifice either in the form of distinct tephra jets or continuous uprush explosions. The breccias in LFA A were therefore likely deposited by fallout deposits from tephra jets or continuous uprush processes, where pillows were ripped from the tuff cone platform, fragmented, erupted and deposited within a tephra jet.

The presence of metre-scale trough cross-bedding in the lapilli-tuff interbeds in LFA A (Figure 4.8D, E) suggests a phased eruption, where waxing and waning of these tephra jets and continuous uprush explosions coincided with pyroclastic density currents which produced cyclical beds of lapilli-tuffs and breccias. The lapilli-tuff beds likely formed at a proximal to medial distance from the vent location as part of a high density, granular-flow dominated pyroclastic density current (Branney and Kokelaar 2002). The precise location of the initial vent is not exposed but likely to be buried by later tephra deposits under the highland part of the island, in the southwestern corner.

LFA C: Similar to LFA A, LFA C is comprised of normally graded beds with relatively coarse clasts (decimetre-scale) at the base that fine upwards to a fine lapilli-tuff (Figure 4.10). Normal-graded beds are formed during suspension fall-out (Sohn and Chough 1992) and/or waning PDCs which suggests that LFA C was located further from the vent source than LFA A and most likely represents a proximal to medial zone (<500 m from the vent). It is therefore proposed that LFA C was deposited by either multiple column collapses from PDCs with a high particle concentration and little to no turbulence and/or relatively high concentration particle fallout. The size of the clasts at the base of each bed further supports a proximal to medial location from the vent as larger clasts are deposited first by direct fallout. The clasts are vesicular which suggests that the magma had time to degas before explosive magma-water interaction occurred. This suggests that LFA C was deposited when the submarine edifice had breached the water surface or was just below and the tuff cone edifice was fully developed. Exsolution of volatiles occurs <500 m below the surface (Kokelaar 1983).

LFA F: LFA F comprises alternating tuffs, lapilli-tuffs and localised breccias. Alternating stratifications of fine ash and coarse lapilli reflect a regular change in eruption explosivity and/or material deposited by a PDC. Equally, irregular contacts between internal layers and zones of massive lapilli suggest internally changing conditions, including changes in grain concentration, velocity and shear stress across the substrate, and reflects cyclic changes in turbulence within the PDC (Sohn and Chough 1993; Dellino et al. 2004; Solgevik et al. 2007). Similarly alternating normally graded and inversely graded sequences suggest waxing and waning of current competence during individual eruptions. The lack of coarse material (although locally present) and relatively thin beds (<1m) (Figure 4.13)

suggest LFA F was deposited at a medial to distal location from the vent (approx. 350 m to 1 km), where mostly only the latter stages of PDCs could reach. This is further substantiated by the lack of impact sags, where decimetre basalt clasts at the base of subfacies F5 have likely rolled or slid along the deposit surface instead of being ejected and impacted (Figure 4.14A). Channel-like bodies and locally erosive bases are observed throughout Facies F (Figure 4.14C) which suggests these PDCs still had enough energy to cause significant erosion of deposits from earlier explosions. The highly irregular structure of LFA F and draping of the sub-facies over each other suggest the erosive bases and channels are also likely to have been caused by minor debris flows and/or slumping which occurred synchronously with the deposition of the PDC deposits. Eruption-induced shock waves can result in liquidisation of wet vent deposits, causing them to become unstable, and can trigger such debris flows and slumping (Kokelaar 1986).

Interbedded lapilli-tuffs (F2) and cross-stratified lapilli-tuffs (F5) are interpreted as being deposited by fully dilute PDCs through either traction-dominated or direct fallout processes (Branney and Kokelaar 2002). This involves particles becoming suspended in a dilute and turbulent fluid phase. F2 (massive lapilli-tuff) is aggraded by settling out of the fluid. F5 (cross-stratified lapilli-tuffs), however, is subjected to high shear stress at the flow boundary which produces stratification and cross-stratification of particles. The subfacies F1, the diffusely-bedded lapilli-tuffs, and F4, the massive lapilli-tuffs/lapillistones, are not laterally extensive and form cross-cutting channels and lenses which suggest that they were not deposited by fallout. The characteristics of F1 and F4 likely indicate they were deposited by pyroclastic currents with high-particle concentrations and little to no turbulence, where kinematic sieving and overpassing of larger particles result in a preferential deposition of fine material, and produces a diffusely stratified deposit (Branney and Kokelaar 2002). The characteristics of sub-facies F3, a stratified tuff, including continuous bedding and a fine, well-sorted grain size are features that are commonly associated with fallout deposits (Houghton et al. 1999).

LFA E: Facies E is a fine, diffusely planar laminated tuff with erosive scoured channels filled with lapilli-tuff (Figure 4.12). LFA E exhibits erosive bases and scoured channels. It is, therefore, suggested LFA E is reworked material which was initially deposited into water or eroded from the tuff cone edifice.

Gentle to medium current reworking would produce enough energy to form scoured channels. Reworking suggests LFA E was deposited distally from the vent source.

From the descriptions of LFA A, C, E and F and from the decrease in bed thickness, there is clearly a continuum from proximal to distal deposits from west to east across Dyrhólaey, further supporting the suggestion that the main vent source is in the south western corner. Figure 4.21 illustrates this gradation, indicating the typical characteristics at each zone (proximal, medial and distal) and likely mechanisms of deposition.

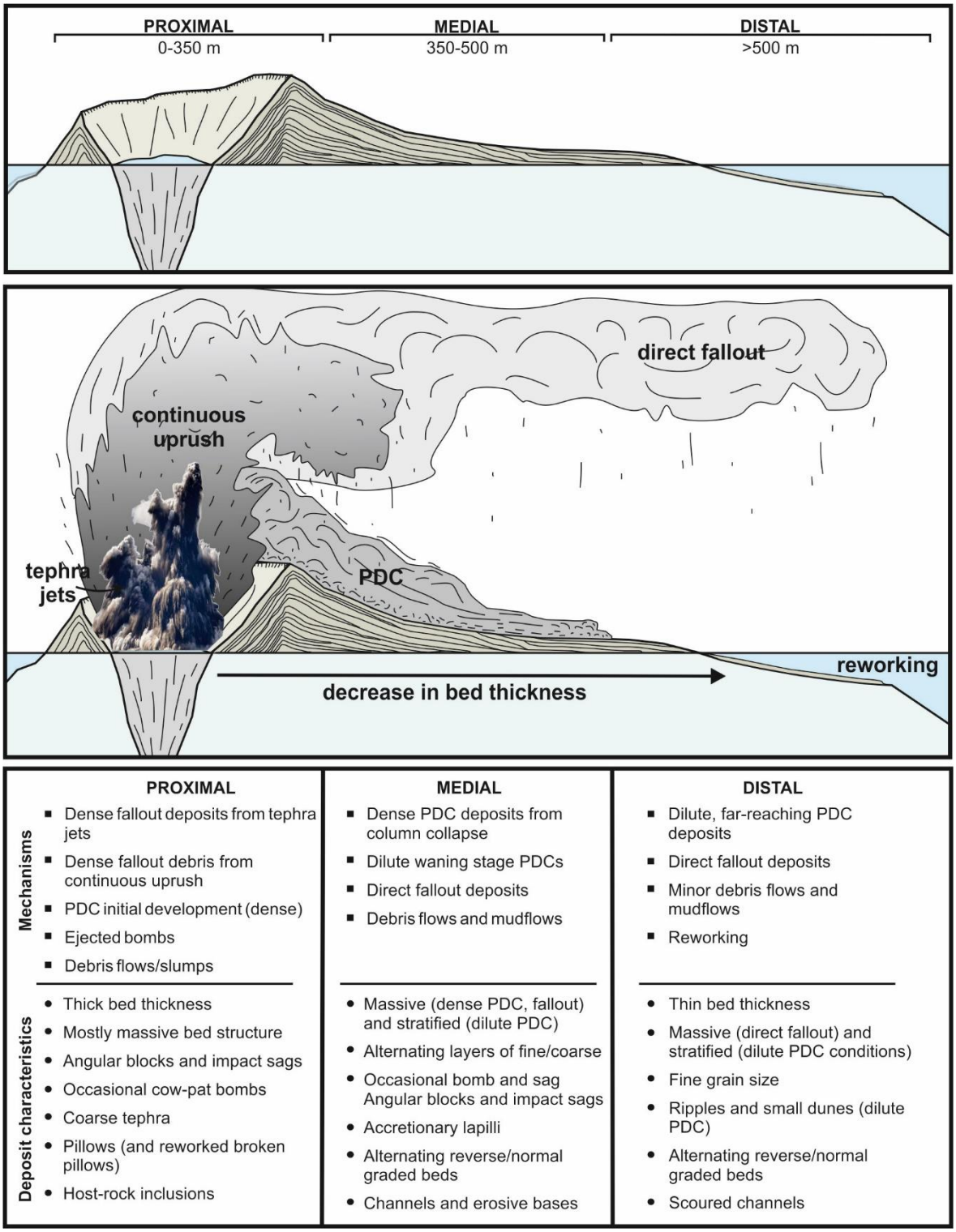

Figure 4.21: Proximal to distal deposition mechanisms and typical deposit characteristics.

4.6.1.2. Vent slurry: Lithofacies B

The model proposed by Kokelaar (1983) suggests that the tuff cone visible above sea level is the top part of a funnel-shaped vent (Figure 4.22). Within this vent, Kokelaar (1983) proposes a mobile slurry of hyaloclastite, water, tephra and basaltic clasts, where the vent walls are irregular and indistinct, and liable to failure. Lithofacies B is interpreted as the frozen record of such a slurry of

material. Several characteristics provide evidence for this interpretation, for example: (1) the discordant, sub-vertical margins of Lithofacies B suggests it has intruded into LFA A and C (Figure 4.9A); (2) intrusion and fingering of the slurry into surrounding host-rock indicates the slurry is a fluid, capable of invading into host-rock as a series of lobes (Figure 4.9B); (3) presence of stratified host-rock rafts indicating slumping and sliding of parts of the tuff cone and/or margins of the surrounding host-rock into the vent and incorporation into the slurry (Figure 4.9A); (4) the laminations in the host-rock raft steepen towards the main debris column zone (Figure 4.9A) suggesting the force of upward-driven slurry current caused shearing at the margins of the raft; (5) highly chaotic, open framework structure made up of heterogenous-graded basalt clasts and hyaloclastite suggests a constantly moving and dynamic system, where the material within the slurry is continuously mixed, erupted and returned to the vent (Figure 4.9E, F); (6) glassy rinds on clasts show rapid cooling and quenching of magma (Figure 4.9F); (7) vesiculated clasts with cm-scale vesicles shows volatiles had exsolved indicating that the slurry is at a shallow depth just below the palaeosurface, and (8) magma blisters and rounded pillow-like clasts which are likely to have formed near the base of the slurry due to higher pressures, and were brought to shallower levels by continuous eruptions and fallback of tephra jets into the crater.

As ascending, vesiculating magma enters the slurry, the water trapped in the slurry and confined pore spaces of the surrounding unconsolidated volcanic pile converts to steam. If water was completely engulfed by magma it would be continuously heated, flash boil to steam and the steam would expand (Kokelaar 1986). Expansion of steam inside the magma exerts pressure internally and the magma fractures and fragments producing angular basalt clasts (Figure 4.9E). The steam expands, fluidising the slurry material. The steam mixes with the slurry of material by Rayleigh-Taylor instabilities and causes fluid-fluid interactions (Schipper and White 2016). Due to the coarse nature of Lithofacies B, evidence of Rayleigh-Taylor instabilities are not observed. The steam rapidly expands as it is emitted out of the vent due to heating (by subsequent magma) and a decrease in pressure upon entering the atmosphere (Kokelaar 1983). These steam ejections produce tephra jets and continuous uprush (Figure 4.22).

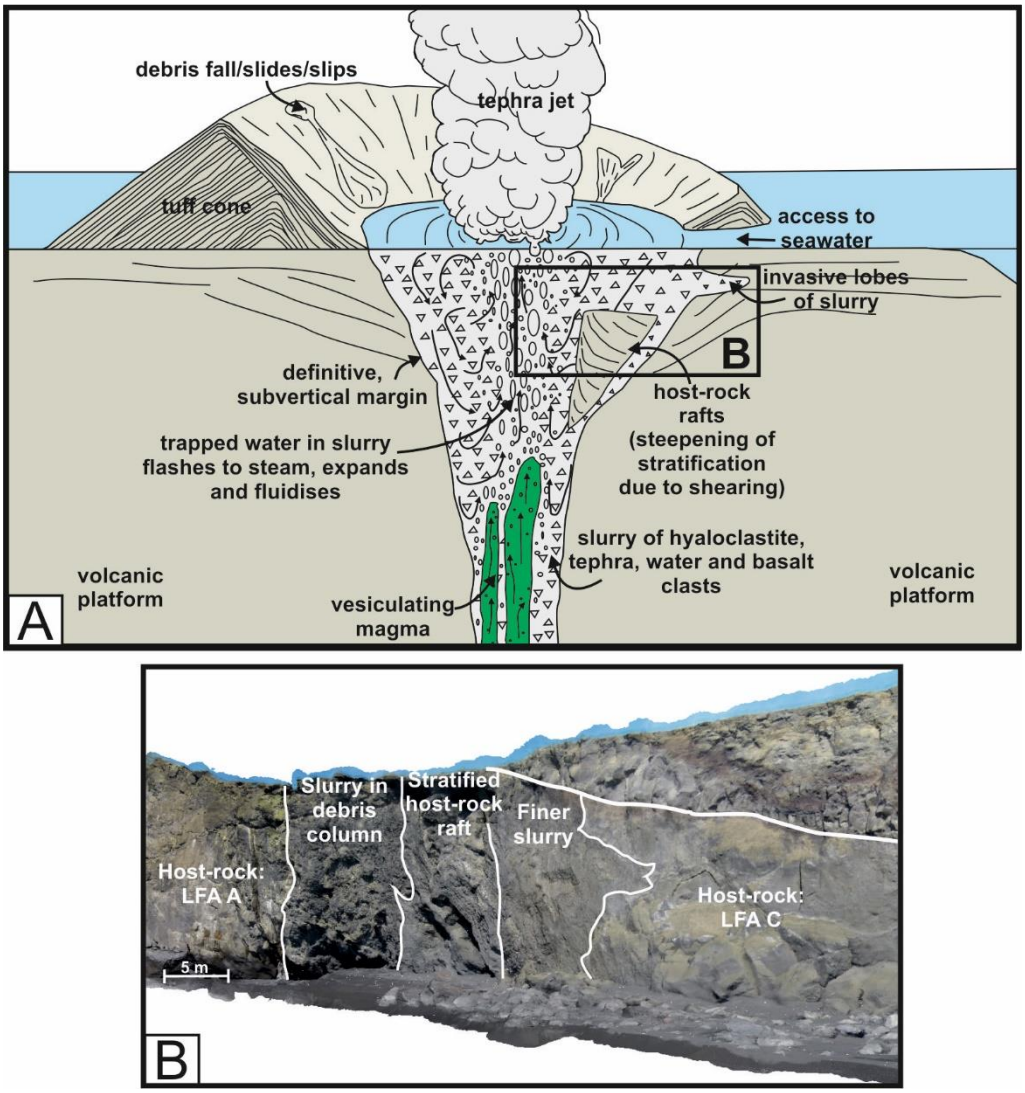

Figure 4.22: (A) Illustration of the funnel-shaped vent beneath the tuff cone edifice (adapted from Kokelaar 1983). The vent is comprised of a fluid slurry of hyaloclastite, basalt clasts, tephra and water. When magma is injected into the slurry (green shading), the water within the slurry heats and converts to steam. The steam expands, fragmenting the magma and creating hydrothermal convection currents within the slurry. The steam and slurry material is emitted out of the vent due to rapid expansion of steam (decrease in pressure when released to atmosphere, and by further heating) forming tephra jets. The highlighted box refers to 4.22B. (B) An interpreted model of Locality 2 and Lithofacies B.

The venting zone/debris column at Locality 2 is relatively small (<25 m wide) and cross-cuts pre-existing tuff cone stratigraphy. It is, therefore, proposed that the venting zone at Locality 2 is a late-stage venting zone of the Dyrhólaey tuff cone, and not the main tuff cone platform-producing vent that produced most of the island we see today (likely to be in the southwestern corner of the island). This suggests that venting zones of Surtseyan eruptions are not stationary but migrate around a singular tuff cone platform.

4.6.2. **Subaerial development of the tuff cone edifice**

4.6.2.1. Erosion of tuff cone

From the onlap surface in Locality 2 and 3 in Figure 4.6 and truncation of LFA C bedding, it is clear that erosion of the tuff cone and tuff cone platform occurred before the onset of subaerial volcanic eruptions. Tuff cones are highly susceptible to erosion, especially immediately after deposition and before palagonitization (Kokelaar and Durant 1983). A modern day example of the rapid rate of submarine erosion of a Surtseyan tuff cone platform is the submarine island of Surtla, situated in the Vestmannaeyjar Islands, 55 km to the west of Dyrhólaey (Figure 4.2, Figure 4.4). In the six weeks post-eruption, wave action caused 23 m of erosion off the top of the Surtla platform (Kokelaar and Durant 1983). The Dyrhólaey tuff cone was either likely to have been eroded rapidly, like Surtla, after the suspension of volcanic activity (pre-subaerial volcanism), or was subjected to isostatic rebound after the melting of the Younger Dryas ice cap (Sigmundsson 1991).

4.6.2.2. Spatter and pahoehoe lavas

The erosion of the tuff platform created a surface for the subsequent eruptions of the subaerial lavas in LFA D. The scoria cone/s that produced these lavas have subsequently been eroded and therefore the location of these vents are not clear. However, as the lava sequence is thickest in the southeastern corner of Dyrhólaey and the direction of onlap is from east to west (Figure 4.11B), it is proposed the scoria cone/s that produced these lava flows were located in the southeastern corner of the island. This further supports the idea of a consistently migrating volcanic centre and venting zone. The subaerial volcanic activity involved Strombolian fire fountaining initially producing a thick unit of highly fragmental and vesicular spatter which agglutinated upon deposition (Figure 4.11D) and was followed by thin pahoehoe lava flows separated by highly vesicular, fragmental spatter and tephra (Figure 4.5C, Figure 4.11A,B). The spatter has highly fragmental clast morphologies (Figure 4.5C) suggesting magma was fragmented by expanding gas as it approached the surface before eruption (Wohletz 1986). There are over seventeen identified lava flows, (Figure 4.10B); however, it is unlikely these represent discrete lava eruptions but are instead likely to characterise several lava lobes of the one lava eruption separated by small Hawaiian fountaining episodes. The lava fills palaeotopography (Figure 4.11B).

4.6.3. **Emplacement of intrusions**

4.6.3.1. Emplacement mechanisms

In the SE corner of Dyrhólaey, shallow (<100 m), stepped sills have later intruded into the tuff cone platform and likely fed a series of edifices at the palaeo-surface due to the volume of magma stored at such a shallow level in the stratigraphy (<100 m below the palaeosurface). The sill lobes have jacked up the overlying host-rock (LFA E and F). The large gas cavities and vesicle trails suggest extensive exsolution of volatiles and degassing indicating shallow emplacement (Figure 4.16B). The sills are arranged in a series of lobes offset at slightly different stratigraphical levels and connected by magma steps (Figure 4.6; Figure 4.16A; Figure 4.22A). Magma steps are formed by two mechanisms: (1) magma seeks out preferential horizons or exploits bedding planes; and (2) the fracture that propagates ahead of the magma has a stepped geometry so when magma invades the stepped fracture, the geometry is preserved (Schofield et al. 2012). Schofield et al. (2012) suggest that if the sills have a stepped nature which steps inconsistently up and down (like Dyrhólaey; Figure 4.23A) then the sills have exploited weak horizons and/or bedding planes. This is evident at Dyrhólaey as Lobe 6 (Figure 4.16A) invades the boundary between two discrete pahoehoe lava flows, likely exploiting a spatter-dominated breccia interbed and intruding under ductile mechanisms (Figure 4.11A). The sills at Dyrhólaey provide evidence for the formation of magma steps in the very shallow subsurface (<100 m below the palaeosurface).

The overlapping emplacement of sill lobes has also formed host-rock bridges (Figure 4.6). Bridges are formed when two magmatic intrusive bodies on different stratigraphical levels overlap, trapping pockets of host-rock (Nicholson and Pollard 1985; Hutton 2009; Schofield et al. 2012) (Figure 4.23B). As the intrusions inflate, they apply pressure and stress to the host-rock, which can cause a series of perpendicular tensile fractures to open in zones of maximum flexure (Schofield et al. 2012) (Figure 4.23B). The bridges remain intact in the sills observed at Dyrhólaey. Bridges differ from magma steps because the initial sill lobes overlap laterally (Schofield et al. 2012). It is thought that magma steps and host-rock bridges form in conjunction with each other due to their similarities and tend to form along the flat outer rim of saucer-shaped intrusions because of a drop in magma pressure (Schofield et al. 2012). The geometry and distribution of the sills in the SE corner of

Dyrhólaey allude to being a part of a larger saucer-shaped structure (Figure 4.23D), where the flat, inner dish corresponds to sills located beneath the carpark and the cross-section of sill lobes along the south coast reflect the inclined magma lobes that extend away from the inner sill (Figure 4.23E).

The cross-section of inflated magma fingers in Figure 4.6 and the small, invasive lobes and fingers that extend from the sills suggests that as well as brittle emplacement of sills, there are also non-brittle or ductile mechanisms which the sills are intruded by. Magma fingers form as a response to fluidisation and local host-rock deformation around sills due to inflation and heating (Figure 4.23C). LFA D surrounding the magma fingers in Figure 4.6 is highly disrupted, where individual lava flows and breccia interbeds are deformed and discrete flows are unidentifiable. Fluidisation is likely to have occurred in the breccia interbeds between lava flows. Due to its hard-rock nature the pahoehoe lavas are not fluidised but have instead been jacked up by the inflating intrusion causing minor brittle failures in the lavas, which fragment the coherent host-rock. The fragments of lava are displaced further by the inflation of the intrusions (Figure 4.11A).

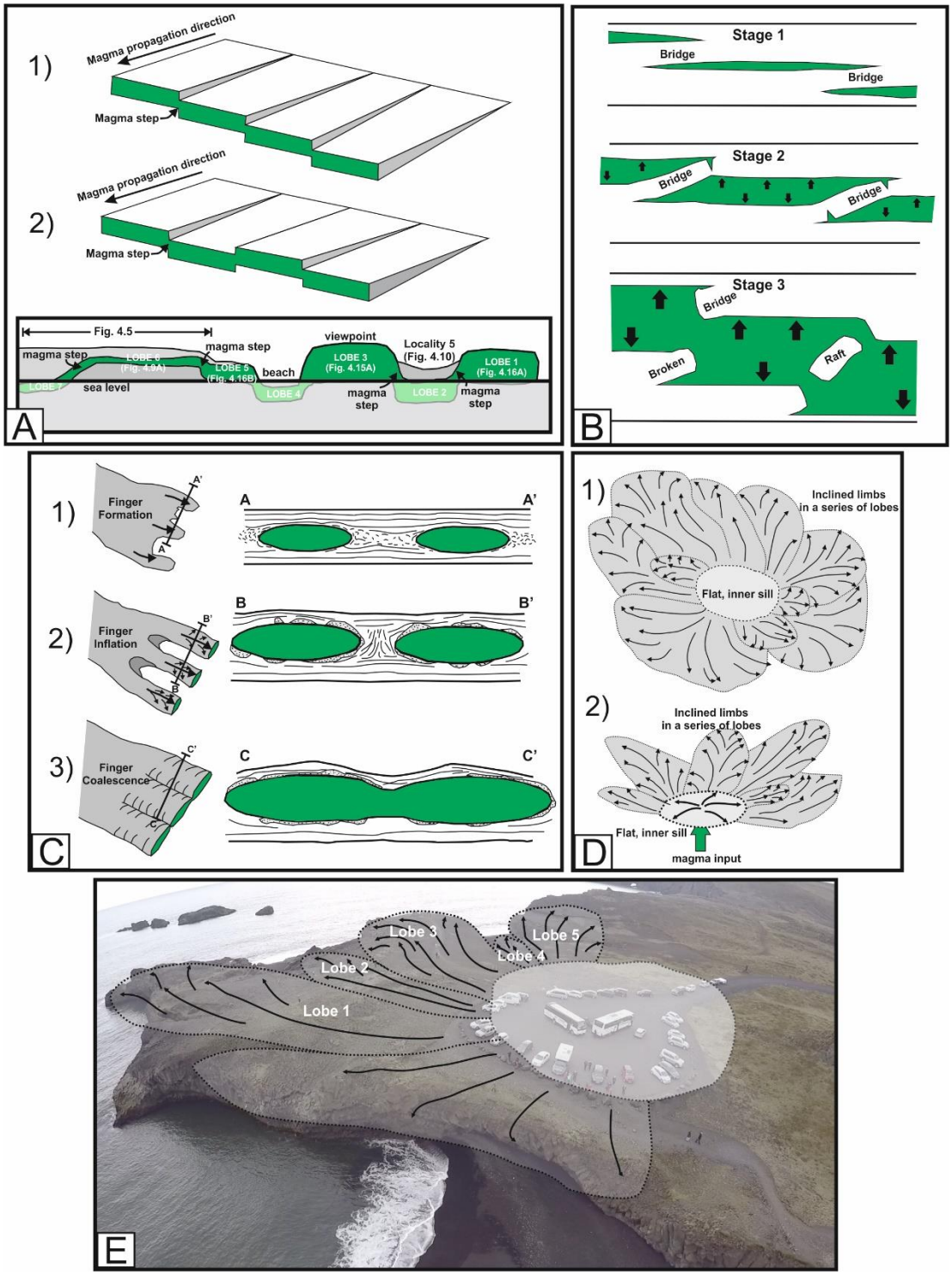

Figure 4.23: Schematic diagrams of the formation of some of the sill features observed at Dyrhólaey. (A) The growth of en echelon steps in a sill. Increasing offset further from magma source. 1) Steps trend in one direction. 2) Stepping in all directions as seen at Dyrhólaey (inset showing the step pattern along the south coast of Dyrhólaey) (adapted from Schofield et al. 2012). (B) Formation of host-rock bridges and broken bridges. Stage 1: magma migrates as a series of straigraphically offset, overlapping sills. Stage 2: Magma inflates, forming a bridge of host-rock between two overlapping sills. The bridge starts to deform and fractures can form. Stage 3: continued inflation, fractures extend and cause the bridge to disconnect form the host-rock (adapted from Schofield et al 2012). (C) Formation of magma fingers in cross-section and plan view. 1) Magma fluidises surrounding host-rock causing ductile emplacement of fingers. 2) Fingers will propagate and inflate both vertically and laterally. 3) Fingers coalesce. The magma fingers at Dyrhólaey stall at Stage 2 (adapted from Schofield et al. 2012). (D) Plan (1) and oblique views (2) of a saucer-shaped sill (redrawn from Thomson and Hutton 2004). (E) Potential distribution of sill lobes and a saucer-shaped sill at Dyrhólaey.

Fragmental dyke-like bodies disseminating away from the tops of the sills are evident at Locality 5 where the sills have been emplaced into the hydrovolcanic host-rock (Figure 4.19). This further suggests the intrusions were emplaced at a very shallow level (<100 m), where lithostatic pressure is low enough to not be an influential factor in the resultant magma pathways. The irregularity and dendritic nature of these bodies indicates the substrate (LFA E and F) was partially unconsolidated to unconsolidated at the time of emplacement allowing for extensive fluidisation and ductile emplacement. Magma may follow irregular pathways through host-rock if the rock/sediment is unstable and fluidised (Kokelaar 1982). Fluidisation of the hydrovolcanic deposits surrounding the intrusions at Dyrhólaey is evident in the form of peperite formation (Figure 4.18A), elutriation structures and loss and/or disruption of laminations.

It can be concluded that due to the presence of both magma steps and bridges, and magma fingers and irregular margins, the intrusions were emplaced under non-brittle mechanisms. The sills were initially emplaced by exploiting compliant horizons, where they subsequently fed irregular dyke-like bodies and fingered into the surrounding host-rock by fluidising the host-rock and intruding by ductile processes (Figure 4.24).

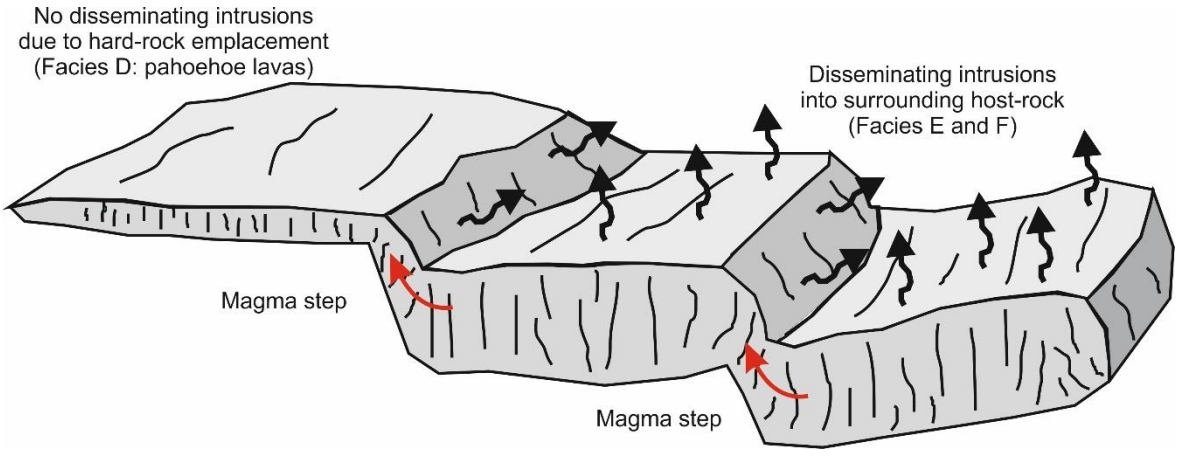

Figure 4.24: Stepped sill connected by magma steps. Dyke-lets disseminate from top of sill into soft, partially consolidated host-rock only, which form proto-pillows and-pillows bud from the intrusion tip.

4.6.3.2. Magma interaction with water and fragmentation processes

The margins of the sills display highly irregular columnar jointing (Figure 4.16A). This is commonly associated with the interaction of magma and water that has percolated into the magma, resulting in a more rapid cooling at the margins than the centre of the sill.

At the inferred depth of emplacement for the Dyrhólaey plumbing system (<100 m) and given the presence of peperite, the host-rock was likely to be water-saturated. The interaction between magma and water can cause a range of subsurface MFCIs (molten fuel-coolant interactions), and can lead to the injection of the substrate material into the surrounding substrate and extensive fragmentation of host-rock and magma (Heiken et al. 1988; Maicher 2003). The degree of explosivity is dependent on several factors (Wohletz and McQueen 1984, Hooten and Ort 2002): (1) confining pressure, (2) amount of fuel-coolant mixing, (3) fuel viscosity, amount of vapourisation, and (4) water-magma ratios.

The relationship and features displayed between the intrusions and host-rock at Locality 5 suggests non-explosive interaction. There is little evidence for intensive mingling between the magma and host-rock and no production of explosive pyroclasts. At the depth of emplacement of the Dyrhólaey intrusions (<100 m), explosive interaction is viable; however, it is suggested that there was a high magma flux and/or not enough water available to produce explosive thermohydraulic interactions.

The intrusions feed proto-pillows and pillow-like bodies that have been spalled from the intrusion tip in the subsurface. This is one of only a few examples of pillows forming beneath the surface (Smellie and Hole 1997; Sorrentino 2011). It is likely pillows formed in the subsurface due to: (1) the water-saturated nature of the host-rock; (2) the very shallow depth of emplacement (<100 m) providing the right pressure conditions for pillow production; and (3) high water flux. The formation of pillows in the subsurface further substantiates the theory that non-explosive interaction occurred during magma emplacement, as pillows only form by non-explosive processes (Kokelaar 1986). During non-explosive interaction, the vapour film remains intact and insulates the magma from the surrounding water (Kokelaar 1986).

Numerical and theoretical models tend to model pillows formed in water, where explosive interaction is inhibited above a hydrostatic pressure of 1.3 MPa (approximately 130 m water depth) (Kokelaar 1986; Wohletz 1986). At Dyrhólaey, the pillows or proto-pillows are formed in the subsurface where the confining pressure (lithostatic pressure and hydrostatic pore pressure) of the overburden is much higher than the hydrostatic pressure of the equivalent depth in water. This increase in ambient pressure stabilizes vapour films preventing instability and collapse of the vapour film, stopping the rapid heat transfer from magma to the surrounding water and supporting non-explosive interaction (Kokelaar 1986). It is concluded that a relatively high ambient pressure and low volumes of magma-water mixing has resulted in non-explosive interaction and pillow development.

The intrusions are heavily fractured and host-rock inclusions are evident within the intrusions (Figure 4.19B and C). At the margins of the intrusions, evidence for small-scale cooling-contraction granulation is apparent (Figure 4.15E). The glassy fragments surrounding the intrusions are dominantly of gravel-size grade or larger and locally show in-situ shattering and jig-saw fit, suggesting that the fragments have been spalled off from the intrusions and disaggregated into the fragments by quench contraction. Cooling-contraction granulation is not dependent on confining pressure and has no bearing on depth (Kokelaar 1986). Similarly, the larger fragments (cm-scale or larger) and the cracks at the margins of the intrusions form as a result of the differential cooling rate between the centre of the intrusion and the outer margin, leading to brittle fracturing at the margins and the incorporation of host-rock inclusions (Figure 4.19B and C).

Vesiculation of magma may have played a key role in fragmentation of magma surrounding Lobes 4 and 5, and a minor role in the intrusions surrounding Lobe 1, 2 and 3. The intrusions surrounding Lobes 4 and 5 contain large vesicles, pipe vesicles and gas cavities, indicating the magma was undergoing extensive exsolution of volatiles at time of emplacement (Figure 4.20B). Magma blisters have formed along the walls of the gas cavities due to the cooling of a thin skin of basalt around trapped gas bubbles (Figure 4.20A and C). Fragmentation occurs when these blisters burst or when trapped volatiles ascend through the magma and burst through the top of the magma, which causes fragmentation of magma at the edges of the intrusion (Figure 4.20A) (Parfitt 2004).

The emplacement of the dyke-like bodies was likely a complex process involving non-explosive (pillow-forming, cooling-contraction granulation) and explosive processes (degassing of volatiles causing fragmentation) as described, that worked in unison to fragment the magma. The fragments were then incorporated into the surrounding host-rock forming a coarse, densely-packed breccia made up of angular dyke fragments and fragmented pillows which still retain pillow characteristics (e.g. vitrified, ropey rinds).

4.7. Discussion and conclusions

4.7.1. **Development of Dyrhólaey and migration of venting zone**

Volcanism at Dyrhólaey was initiated with typical submarine processes including the extrusion of pillow lavas, graded hyaloclastite units and pillow-like bombs produced by fire-fountaining (Figure 4.25). These volcanic deposits built the tuff cone platform, which likely built from a venting zone in the southwestern corner of the island. As the platform grew, Surtseyan volcanic processes commenced due to the shallowing water depths, producing tephra jets and continuous uprush plumes, which subsequently collapsed forming PDCs and dense fallout clouds (Figure 4.25).

It is proposed that the centre switched from the initial venting zone to a vent, now exposed along the south coast of the island in Locality 2 (Lithofacies B), which likely formed or partly formed another (now eroded) tuff cone edifice (Figure 4.25). Surtseyan processes then paused and erosion of the tuff cone edifice and underlying platform ensued. The period of erosion was relatively short as the island remained in the subaerial regime before volcanism restarted. Scoria cones, producing both thin pahoehoe lava flows and Hawaiian and Strombolian fire fountaining deposits, were likely situated on the eastern side of the island, suggesting the locus of the venting zone switched again (Figure 4.25). A series of intrusions were then emplaced into the tuff cone platform and lava flows, which likely fed further subaerial eruptions in the southeastern corner (Figure 4.25). The products of these eruptions are no longer exposed because of erosion. The intrusions feeding the initial lava-producing scoria cones are obscured by these later intrusions, which exploited the former scoria cones pathways to the surface (Figure 4.25). It is suggested that magmatism was continuous throughout the initial lava forming scoria cones and later emplacement of intrusions due to the similarity in the venting location.

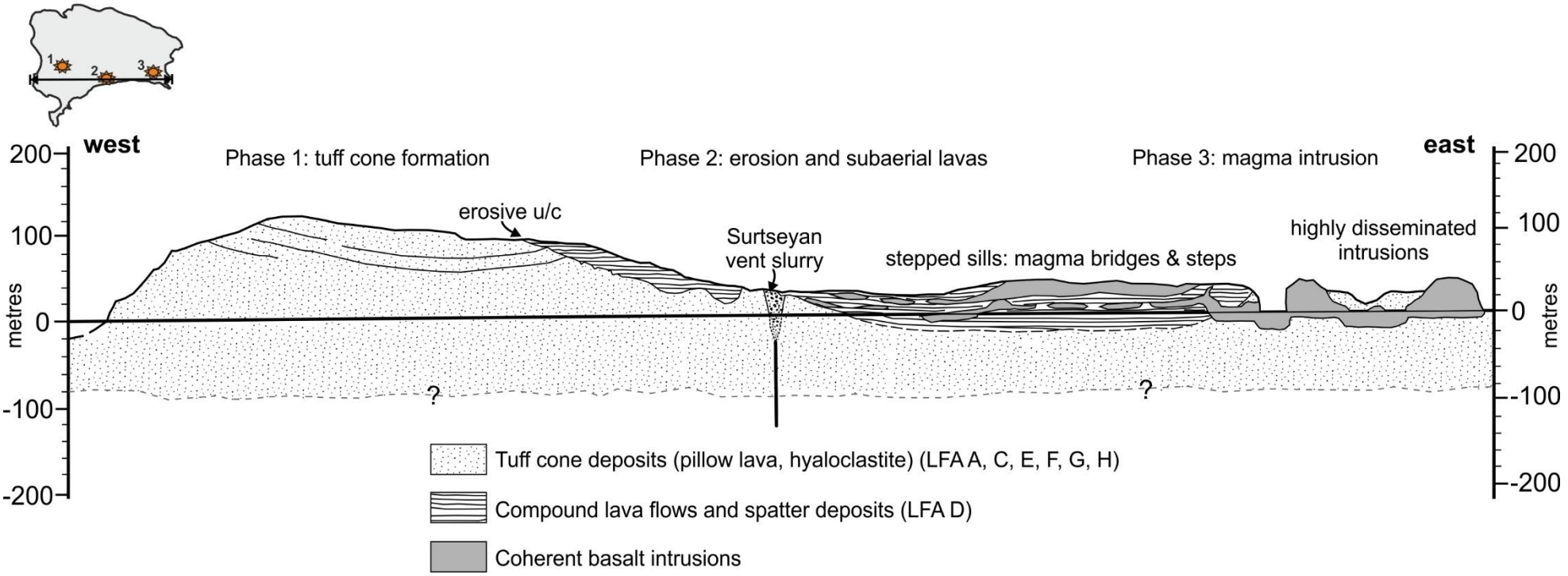

Figure 4.25: Cross-section through the island of Dyrholaey. Inset shows the location of cross-section and locus of the venting zone as discussed in text (represented by an orange star at the proposed site). Phase 1: ubmarine eruption of magma including extrusion of pillow lava, hyaloclastite and shallow fire fountaining. When the platform grows, the decreasing hydrostatic pressure increases explosivity of magma and Surtseyan processes ensue. The product is a large wide-based tuff cone platform. Phase 2: erosion of the tuff cone edifice. Eruption of subaerial lavas and spatter deposits onlapping the tuff cone. Phase 3: Sills intrude into the stratigraphy, potentially feeding more scoria cones (due to the depth of emplacement).

Evidence for the migration of the venting zones spatially around the island of Dyrhólaey suggests multiple monogenetic eruptions built the island, similar to Heimaey and Surtsey in the Vestmannaeyjar Islands, 55 km to the west of Dyrhólaey. Venting zone migration is a common characteristic in the eruption of small basaltic volcanoes (Houghton and Schmincke 1989; Thordarson and Self 1993; Houghton et al. 1999; Cole et al. 2001). For example, Heimaey and Surtsey are comprised of several individual tuff cones, tuff rings and scoria cones, and their associated deposits, that each represent discrete monogenetic eruptions and a complex spatial and temporal island-forming process (Mattsson and Höskuldsson 2003). Vent migration occurs because of: (1) clogging of the initial vent and relocation to a locality with a clear pathway to the surface (Sohn and Park 2005; Befus et al. 2008); (2) the access to water for phreatomagmatic processes has changed or moved (Sohn and Chough 1992); (3) different magma batches, reacting to the host-rock in different ways (Sohn et al. 2011). It is suggested that the distribution of shallow level plumbing systems (formation of sills and inclined sheets) in the subsurface may also provide an explanation for vent migration, where two edifices can form out of the same sill complex plumbing system (see Chapter 3).

The island of Heimaey reflects a presently active version of Dyhorlaey, having formed from the Upper Pleistocene to the present day, most recently the 1973 eruption of Eldfell (Mattsson and Höskuldsson 2003). Stratigraphical and geomorphological features described at Dyrhólaey are comparable to characteristics seen on Heimaey and the other islands in the Vestmannaeyjar archipelago (Figure 4.26).

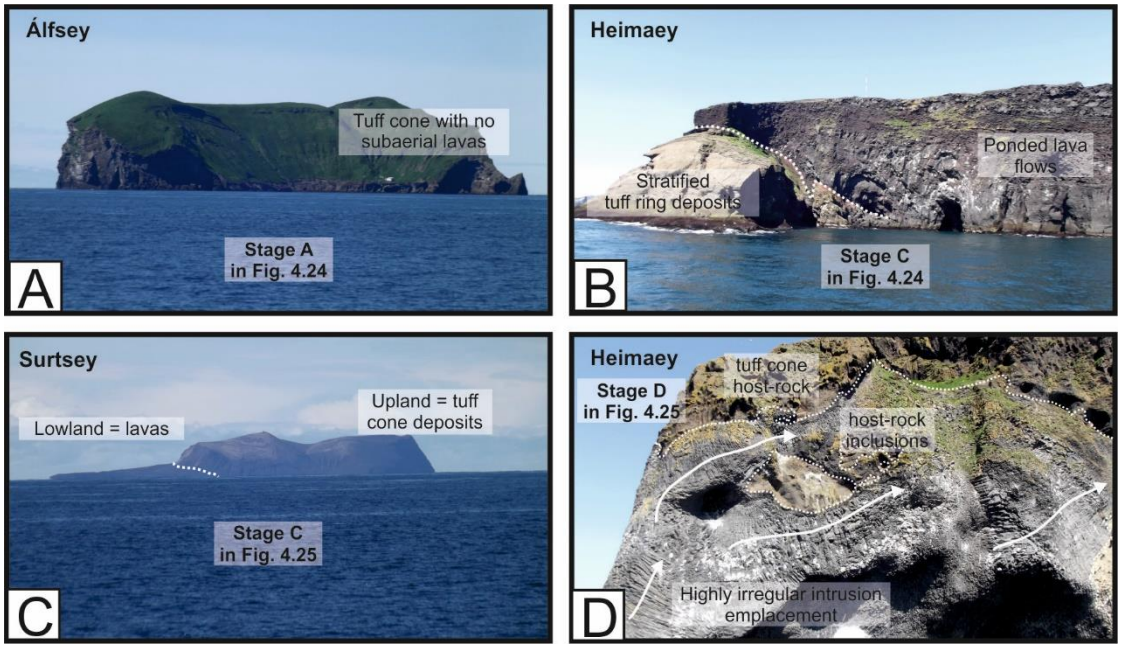

Figure 4.26: Features of other monogenetic Surteyan islands in the Vestmannaeyjar Islands, 55 km west of Dyrhólaey. The Vestmannaeyjar islands were formed mostly in the Holocene but dates from drill cores suggest volcanism extended back to the Upper Pleistocene (Mattson and Höskuldsson, 2003). (A) The island of Álfsey is comprised of a tuff cone edifice. No lava flows suggest volcanism stopped before the switch to subaerial volcanic processes. The resultant island is the equivalent of Stage A in the development of Dyrhólaey (Figure 4.25). (B) Lavas onlap the stratified tuff ring created by phreatomagmatic eruptions on Heimaey, and correspond to Stage C in Figure 4.25. (C) The island of Surtsey erupted in 1963 and produced an island comprised of a tuff-dominated upland and lava-dominated lowland, similar to the geomorphology of Dyrhólaey (Figure 4.4B). The resultant island is the equivalent to Stage C in the development of Dyrhólaey (Figure 4.25). (D) The famous Elephant Rock in the NW of Heimaey, where intrusions have been emplaced into the tuff host-rock. Highly irregular columnar jointing suggests rapid cooling and infiltration of water. White arrows show direction of magma migration. Equivalent to the emplacement of intrusions in Figure 4.25D.

4.7.2. **Surtseyan islands can be fed by shallow sills.**

The sills in the SE corner of Dyrhólaey are likely to have fed monogenetic edifices at the surface due to their very shallow proposed depth of emplacement (< 100 m) and highly vesicular and volatile rich-nature. Ponding of magma in the very shallow subsurface beneath monogenetic volcanoes is therefore likely, where host-rock properties are appropriate for lateral migration of magma. Very shallow sills (<150 m beneath the palaeosurface) have been recorded in other monogenetic systems although these are dry monogenetic volcanic fields (producing scoria cones). These include Pauite Ridge, Nevada, USA (Valentine and Krogh 2006); Hopi Buttes Volcanic Field (Arizona, USA) (Re et al. 2015; Muirhead, J.D. et al. 2016a); San Rafael Monogenetic Volcanic Field (Utah, USA) (Kiyosugi et al. 2012; Richardson et al. 2015); Karoo and Ferrar Igneous Provinces (Muirhead, J.D. et al. 2012), and the Bakony-Balaton Highland Volcanic Field (Hungary) (Németh and Martin 2007). Valentine and Krogh (2006) attribute the formation of sills in the very shallow subsurface as a response to the interaction between sill emplacement and uplift of the Earth's free surface, lifting the overburden

(rather than elastic deformation) and forming forced folds above the sills. Another requirement for sill emplacement in the shallow subsurface is the presence of a mechanical weakness in the host-rock, allowing for stress rotation in the host-rock. At Dyrhólaey, this comes in the form of the boundary between two interbedded lava flows. Ductile emplacement of intrusions also occurs at Dyrhólaey.

4.7.3. **Magma-water interaction**

Unlike the examples of shallow intrusions listed above, the sills at Dyrhólaey have been emplaced in a Surtseyan setting, where the host-rock is extensively water saturated, and therefore the intrusions undergo extensive magma-water interaction.

Due to the low lithostatic pressure in the very shallow subsurface at the time of intrusion emplacement, dykes spreading from the tops of the sills have very irregular morphologies. Water-saturated host-rock causes rapid cooling and quenching of these dykes, forming highly irregular jointing patterns due to uneven filtering of water into the dyke body. Magma-water interaction also causes the dykes to fracture (non-explosively) into fragments, forming peperite and irregular, bulbous dyke morphologies. The formation of pillows at the edges and tips of dykes also suggest the host-rock was highly water-saturated (Smellie and Hole 1997).

Documentation of subsurface pillow formation, or as it has been termed here proto-pillows, is limited (Smellie and Hole 1997; Sorrientino 2011). This is likely due to pillows forming only in water-saturated host-rock and below the pressure/depth limit for explosive interaction between magma and water (<1.3MPa) (Henry and Miyazaki 1978; Wohletz 1986; Kokelaar 1986). The lack of detailed description of subsurface pillows may also be a result of limited or incomplete exposure of dykes in the Surtseyan edifice.

The majority of the plumbing system at Dyrhólaey interacted non-explosively with pore-water (Figure 4.27). However, evidence for extensive exsolution of volatiles and disruption of basalt around highly vesicular zones suggests the shallow emplacement of the intrusions enabled a release in lithostatic pressure, which could have potentially caused some minor explosivity in the subsurface.

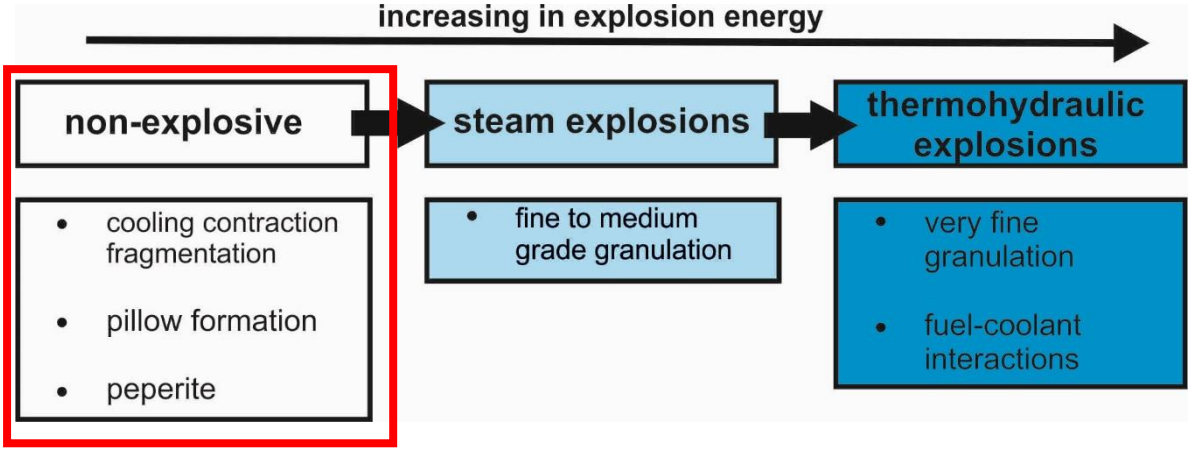

Figure 4.27: Magma-water explosivity index, indicating characteristic features of each type of magma-water interaction. Red box marks the magma-water interaction seen around the intrusions in Dyrhólaey.

Chapter 5 Subglacial setting; Reynisdrangar, Iceland

5.1. Introduction

A locality along the south coast of Iceland, Reynisdrangar, has been studied to show the intrusion geometries and emplacement mechanisms of shallow plumbing systems beneath tindars. The cliff section at Reynisdrangar, near Vík, on the south coast of Iceland presents a cross-section through a monogenetic tindar and its associated shallow plumbing system. The tindar extends northwards behind the cliff section forming an >150 m (in height) elongated topographic high, surrounded by sandur deposits (formed by glacier outwash from subglacial activity beneath Katla during the Holocene; Maizels 1993).

Subglacial eruptions are driven by explosive magma-water interaction and are described as "Surtseyan-like" eruptions by Thordarson and Höskuldsson (2008). Similar to typical Surtseyan eruptions, subglacial eruptions produce both continuous uprush explosions and tephra jets (Gudmundsson 2003) (see Chapter 4). The main difference between submarine and subglacial eruptions is that products of subglacial eruptions are not widely distributed but are confined by the ice-cover, forming isolated tindars and tuyas (Matthews 1947; Jones 1969; Moore and Calk 1991; Smellie 2000; Björnsson 2003; Gudmundsson et al. 2004; Jakobsson and Gudmundsson 2008; Stevenson 2014). If the eruption breaks through the ice cover, the eruption style changes and spatter, lavas and widespread tuff deposits form (Bjornsson 2003).

The tindar at Reynisdrangar [63.4027; -19.0416] formed during the Upper Pleistocene, when Iceland was subjected to multiple glacial cycles, during which an extensive ice cap covered the entirety of Iceland (Geirsdóttir 2004). Continuous extrusion of magma explosively interacted with the ice cap, resulting in extensive explosive magma-water interaction and producing a large elongate hyaloclastite ridge. Intrusions continuously fed the eruption allowing the magma to breach the ice cover and form a series of lavas that now cap the ridge. The intrusions that fed these eruptions are preserved along the cliff section at Reynisdrangar and demonstrate a highly irregular and fragmental nature. Large volumes of magma are stored at very shallow levels beneath the palaeosurface. Large gas cavities (>1 m) are also preserved within the intrusions and magma blisters are observed.

This case-study investigates how magma is emplaced into a tindar to feed a continuous monogenetic eruption and how glacial meltwater influences eruption behaviour. Due to the inaccessibility of the top of the cliff (the cliff is ~150 m high), the development of the hyaloclastite portion of the tindar cannot be examined. However, a full textural analysis on the morphologies displayed in the intrusion and how they interact with the host-rock has been undertaken.

5.2. Geological Setting

5.2.1. **Icelandic Overview**

Please refer to Section 4.2.1 for an overview of the geological setting of Iceland (Figure 5.1).

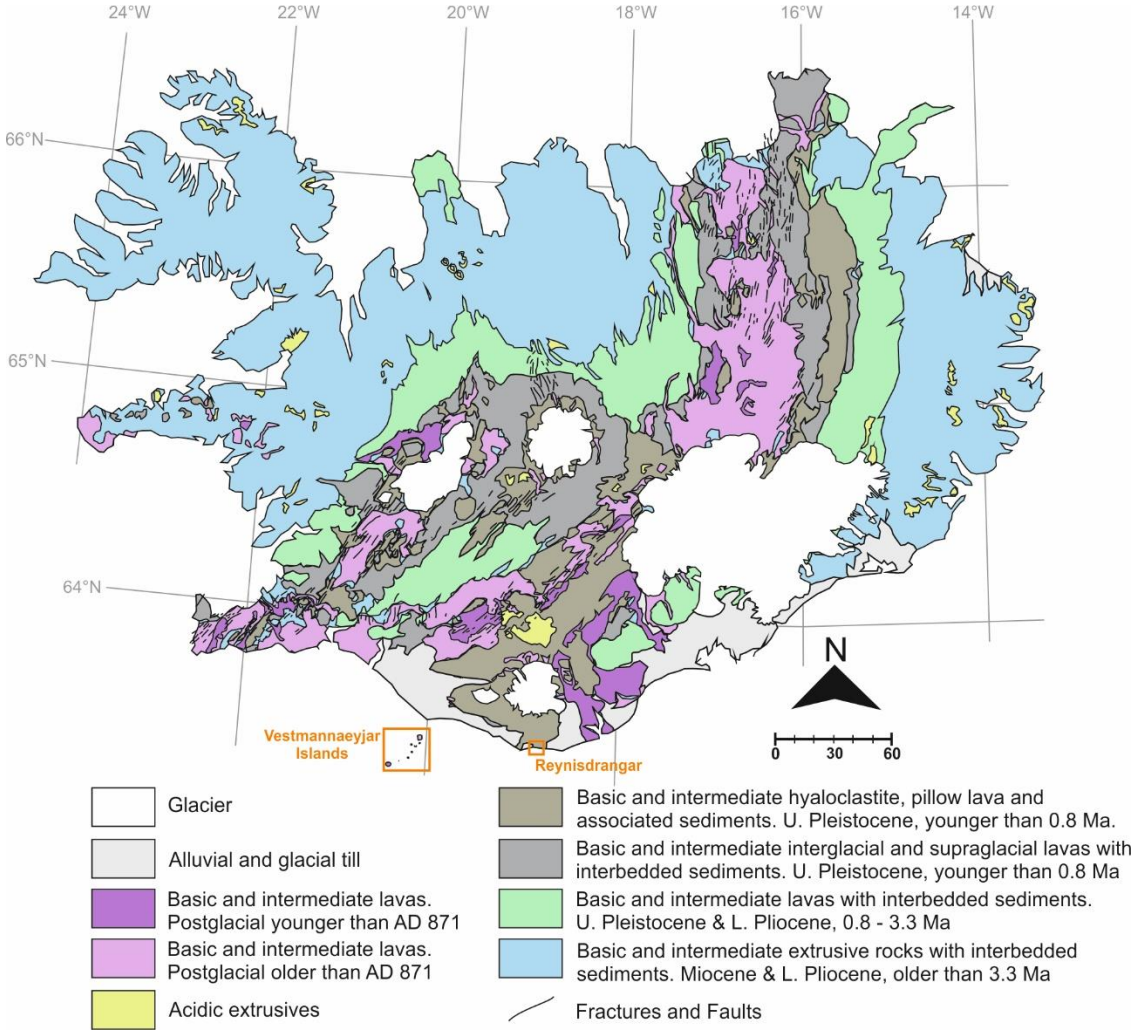

Figure 5.1: Simplified geological map of Iceland showing the location of Reynisdrangar. From Jóhannesson (2014).

5.2.2. **Subglacial volcanism in Iceland**

The products of basaltic subglacial volcanism are common throughout Iceland and are recognised as hyaloclastite ridges composed of consolidated palagonite and pillow lavas known as tindars and

circular table mountains known as tuyas (Gudmundsson 2003; Schopka et al. 2006). Subglacial deposits are common within the Móberg (Palagonite) Formation, a chronostratigraphical unit generally considered (by analysis of magnetic polarity) to be Upper Pleistocene in age (0.01 – 0.78 Ma) (Jones 1969; Jakobsson and Gundmundsson 2008). This corresponds to widespread ice caps across the Northern Hemisphere during the interglacial/glacial cycles in the Upper Pleistocene, which formed hyaloclastite formations and pillow lavas in volcanic areas across Iceland, Canada and the Antarctic (Hickson 2000; Smellie 1999; Gudmundsson 2003). The Móberg Formation is extensively found across the whole of Iceland, demonstrating a widespread, thick ice-cap in the Upper Pleistocene (Jones 1969; Jakobsson, 1979; Bjornsson, 2002; Schopka et al. 2006).

In Iceland, tindars tend to originate from fissure eruptions and produce sheets or ridges of palagonitised tephra (Allen 1980; Jakobsson and Gundmundsson, 2008). Many of these ridges, despite being prone to erosion, form a series of parallel elongated mounds up to 44km in length and are found in Iceland's central graben and along all Iceland's major rift zones (Figure 4.1; Jones 1970; Allen, 1980; Smellie and Skilling 1994; Hoskuldsson et al. 2006; Schopka et al. 2006; Jakobsson and Gudmundsson 2008). The boundary between hyaloclastite and subaerial lavas marks the transition between subglacial to subaerial processes and can demonstrate the thickness of the ice cover. Along the Reykjanes Ridge, for example, tindar heights reach 300 – 400 m above sea level, corresponding to at least 300m of ice cover at the time of eruption (Schopka et al. 2006). In the Kverkfjöll volcanic centre in the NVZ, the ice was much thicker, corresponding to ridges that reach up to 900 m in height (Höskuldsson et al. 2006).

Although many tuyas are relatively large in size (<50 km^3), numerous tindars and tuyas in Iceland display a monogenetic nature. Subglacial eruptions cause extensive melting of the ice cover, which can generate some of the most catastrophic floods in Iceland. These are known as jökullhlaups and their deposits are widespread across Iceland (Bjornsson 2003; Thordarson and Höskuldsson 2008).

Ten percent of Iceland is currently ice-covered, and the ice covers 60% of active volcanic zones (Bjornsson 2003), therefore subglacial eruptions are common in the historical and present records (Gudmundsson et al 1997; Larsen 2002). In fact, in the last century there have been >16 subglacial

volcanic eruptions (Bjornsson 2003, most notably beneath the Vatnajökull glacier (e.g. Grímsvötn) and beneath Myrdalsjökull (e.g. Katla).

5.3. Location and Geomorphology

Reynisdrangar, is situated 3 km to the east of Dyrhólaey and 2 km southwest of the town of Vík (Figure 5.2A). The exposure comprises of a 150 m high cliff exposure which cuts a cross-section through the tindar (Figure 5.2C). The protruding hill extends behind the cliff for 5.2 km (north) and is 1.3 km at its widest (Figure 5.2B). The tindar reaches a height of 340 m above the sandur plains. Several sea stacks, up to 66 m high, comprised of palagontized tephra and fractured basalt columns, extend out to sea, showing that the tindar has been subjected to erosive processes, most notably wave action.

At the southwestern corner of the cliff, impressive basalt columns form a 100 m wide intrusion, which feeds a highly irregular sill that has intruded along the base of the cliff (Figure 5.2C). This sill feeds subvertical dendritic bodies which intrude into the tindar deposits.

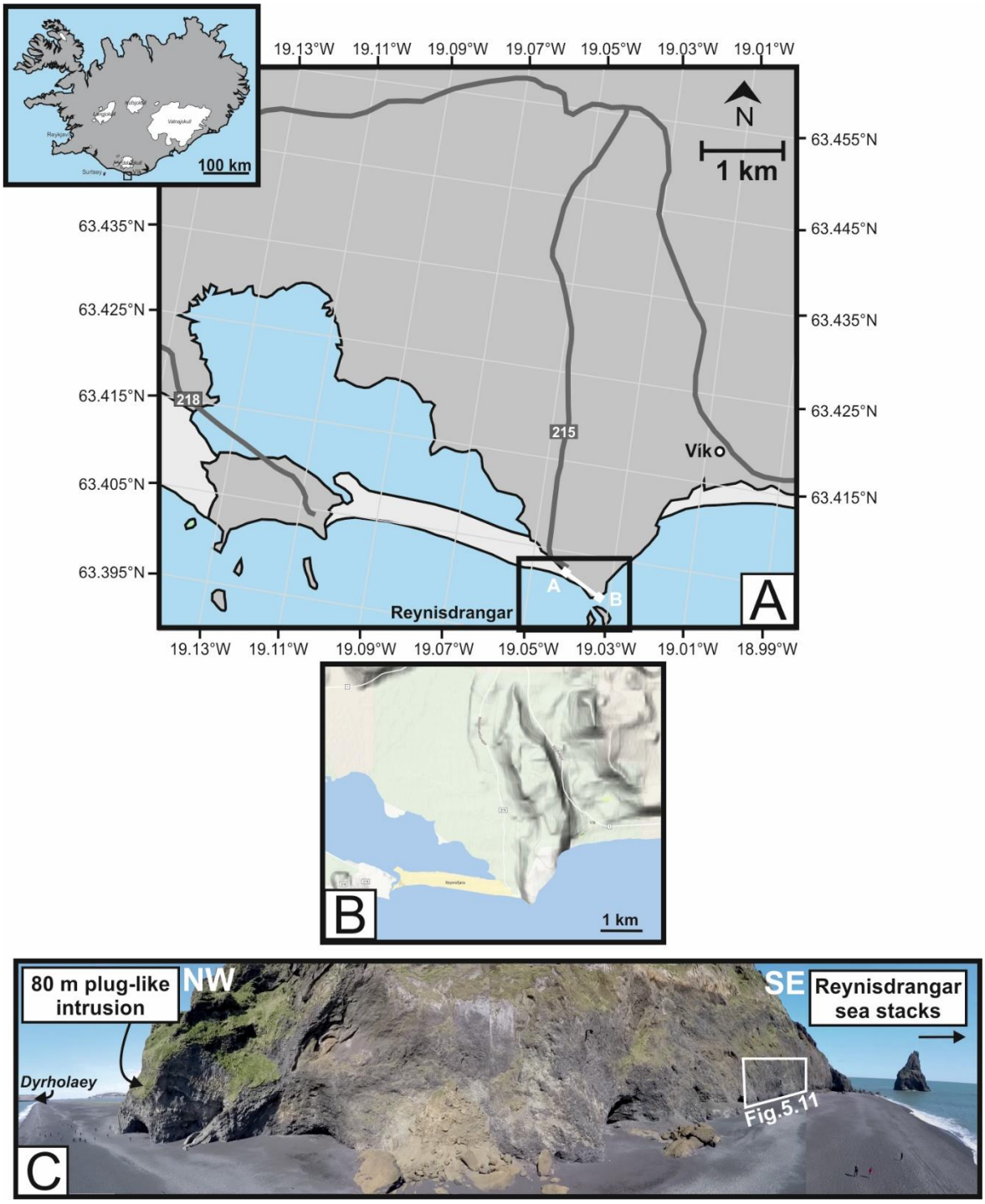

Figure 5.2: (A) Inset: Map of Iceland showing location of (A). Location map of Reynisdrangar. 2 km SW of Vík and 3 km E of Dyrhólaey. Location of the photo transect in (C) is labelled from A-B. (B) Geomorphological expression of the hyaloclastite ridge, extending up to 5.2 km behind the cliff section along the coast. (C) Photo transect along the base of the cliff section. People on beach for scale.

5.4. Field Observations

5.4.1. **Host-rock stratigraphy**

Due to the inaccessibility of the top of the cliff, the host-rock stratigraphy was examined using drone footage and by examining large fallen blocks (>4 m long) that have not been disturbed by erosive processes (e.g. they are still in the same place as when they had fallen from the cliff face). The generalised stratigraphy is shown in Figure 5.3. Lithofacies and lithofacies associations were distinguished in the field using bedding characteristics, structure grain size and clast morphology.

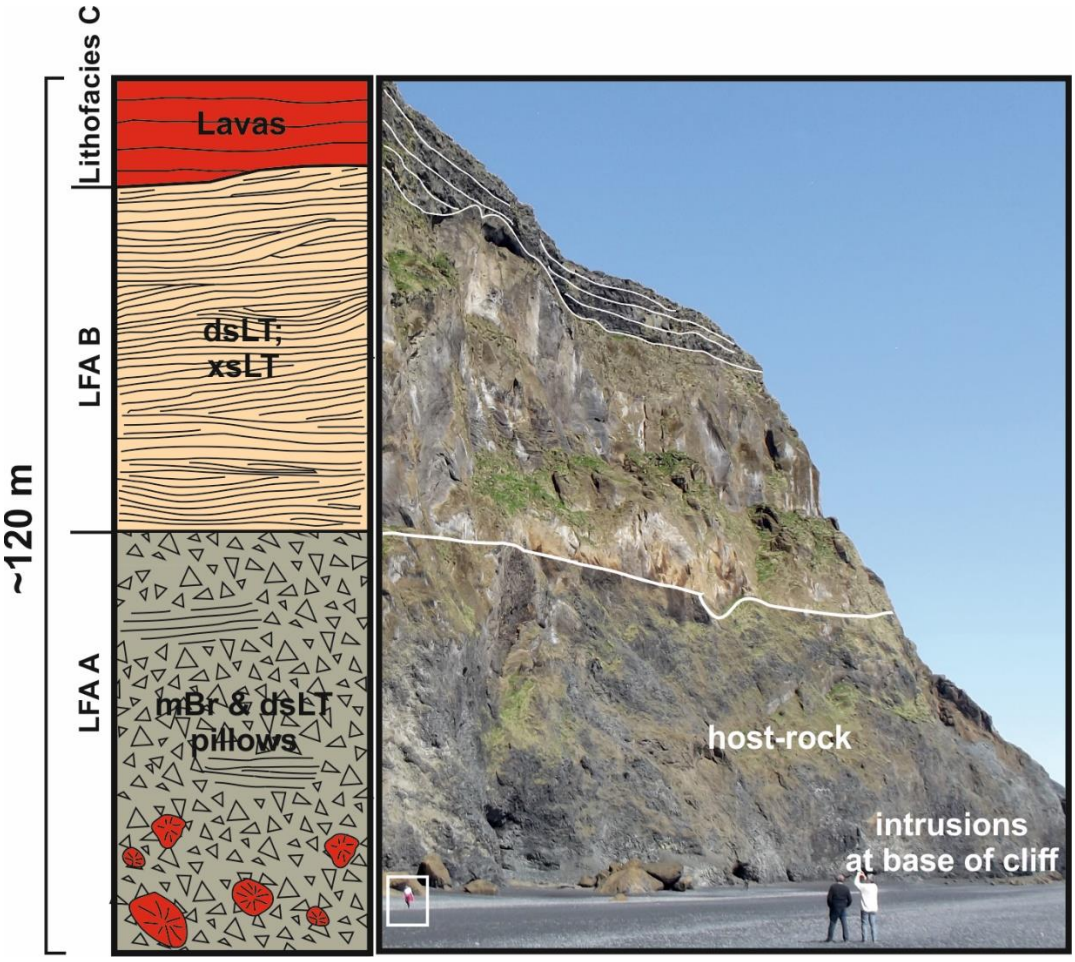

Figure 5.3: Generalised stratigraphical log of the host-rock. Person for scale in box. The base of the cliff is comprised of a highly disrupted unit comprising mBr and dsLT. Locally, pillows are evident. Above Lithofacies association A (LFA A) is a >30 m unit of diffusely-stratified and cross-stratified lapilli-tuffs and tuffs (Lithofacies association B), which is subsequently overlain by a series of thin pahoehoe lavas (Lithofacies C) that infill and onlap palaeotopography.

5.4.1.1. Lithofacies Association A (LFA A): massive breccia and lapilli-tuffs with diffusely laminated sub-units

The base of the cliff (>60 m) is comprised of massive basalt and hyaloclastite breccia, and lapilli-tuff sub-units (LFA A), which are heavily intruded by highly irregularly-shaped intrusions. Pillows bud from the intrusion tips and peperite forms at their edges and tips, making the original texture of

LFA A difficult to readily identify and individual units indistinguishable. The matrix of the breccia makes up to 65% and is comprised of orange palagonite and fine, non-palagonitised, vitrified basalt fragments and shards (<1 mm). Within the matrix are fine clasts of basalt, tachylite and sideromelane (sub-mm to 35mm) (Figure 5.4). The tachylite clasts are mostly aphanitic with a range of vesicularities from 0% to ~15% (Figure 5.4A and B). Clasts with a high vesicularity have fragmental and cuspate geometries (Figure 5.4A). The tachylite clasts contain <0.1 mm plagioclase feldspar crystals and fragmented olivine crystals (0.2 mm) (Figure 5.4B). Petrographical examination of some of the tachylite shows zonation within the clasts, where fluidal and very fine crystallised basalt clasts have been engulfed by tachylite melt matrix (Figure 5.4B). Sideromelane clasts are also present within the matrix and display relatively high vesicularity (10-30%) and have fragmental, cuspate margins (Figure 5.4C). Locally, vesicles are elongated within the clasts, indicating the clast was fragmented near the top of the feeder conduit (Figure 5.4C). LFA A has an open framework of clasts and apparent porosity is high (5-15%) (Figure 5.4).

The breccia-dominated sub-unit is clast—supported, poorly sorted and contains cm-scale angular and sub-angular basalt clasts (up to 27 cm), sub-rounded pillows (10.5 cm to 71 cm in diameter), and angular pillow fragments (Figure 5.5A and B). The pillows display the typical characteristics of magma pillows, including a vitrified outer rind, radial jointing and vesicular centres (Figure 5.5B). The outer rind locally displays ropey, pahoehoe textures and a dimpled outer surface. Some pillows display fractures that extend from the rind into the centre of the pillow and are filled with a hyaloclastite matrix. Pillow fragments are distinguishable from angular basalt clasts by their vitrified rinds on one or more of their outer surfaces. Lenses of matrix-supported and diffusely stratified lapilli-tuff (< 2.5 m long, ~30 cm wide) are locally evident within the breccia sub-unit.

The lapilli-tuffs are typically coarse, and locally planar laminated or diffusely laminated, where laminations are defined by tuff-grade stratifications (Figure 5.5C and D). Stratifications and beds are between 4 cm and 2 m. Assemblages of the breccia unit are found in lenses and irregular, cross-cutting bodies. Where intrusions have been emplaced into the lapilli-tuffs, there is evidence for fluidisation from the presence of dewatering structures and disrupted laminations around the intrusions.

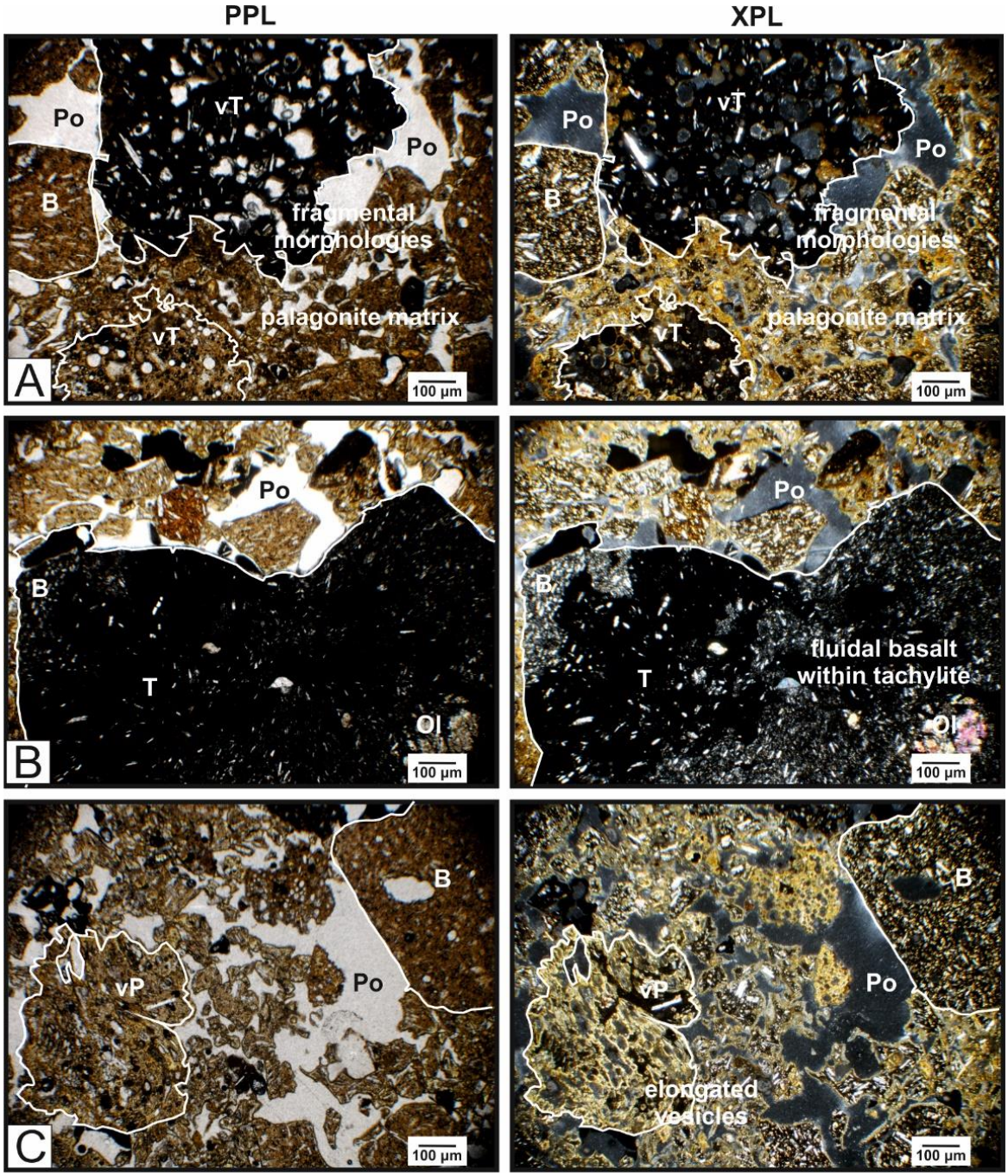

Figure 5.4: Petrography of LFA A. (A) Basalt and tachylite clasts in a palagonite matrix. Vesicular tachylite clasts display fragmental, cuspate morphologies. (B) Large tachylite clast with plag and olivine crystals. Fluidal outlines of basalt are observed within the clast. (C) Palagonitised basalt clast with elongate vesicles. B = basalt; vT = vesicular tachylite; T = tachylite; Po = porespace; Ol = olivine crystal; vP = vesicular sideromelane.

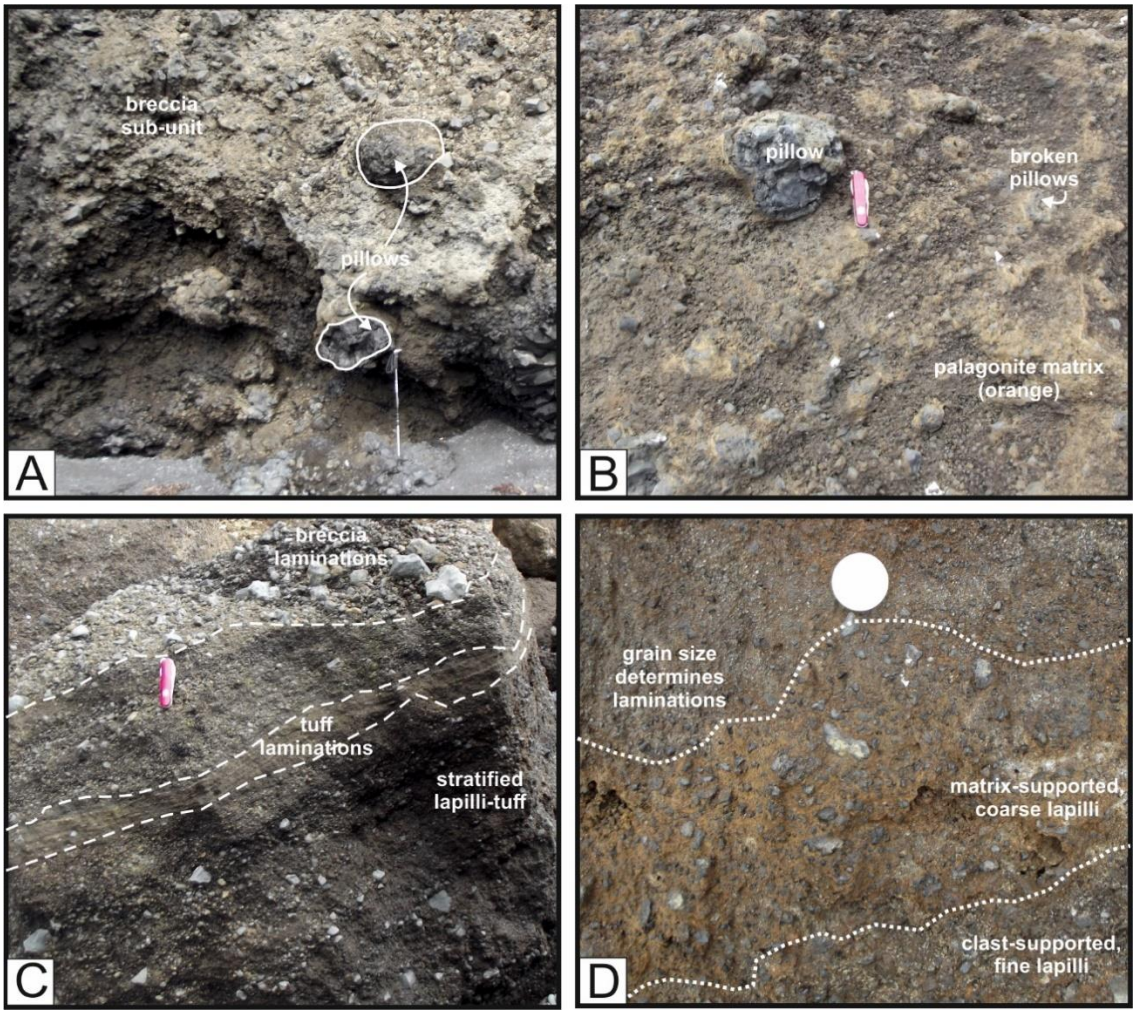

Figure 5.5: Field photographs of LFA A. (A) Poorly-sorted, massive breccia-dominated sub-unit with angular basalt clasts, pillows and fragmented pillows in a palagonite matrix. Walking stick is 1 m. (B) Close-up of a pillow showing a vitrified rind, within a clast-supported matrix. Matrix is made up of cm-scale basalt fragments partially cemented by palagonite. Pen-knife is 10 cm. (C) Diffusely stratified and stratified sub-unit of LFA A, consisting of clast-supported breccia laminations, tuff laminations and matrix-supported lapilli-tuffs. Pen knife is 10 cm. (D) Close-up of diffusely stratified lapilli-tuff. Diffuse laminations defined by alternating matrix-supported coarse lapilli and clast-supported fine lapilli horizons. Coin is 2.2 cm.

5.4.1.2. Lithofacies Association B (LFA B): stratified and diffusely stratified tuffs and lapilli-tuffs

From drone footage, Lithofacies association B is made up of shallow dipping stratified and diffusely stratified tuffs and lapilli-tuffs; and is comprised of palagonite, giving its distinctive orange colour. The boundary between LFA A and B is fairly distinct; however, in places it is diffuse and irregular (Fig, 5.6A and B). A fallen block that preserves the boundary between A and B enables more detailed examination of at the boundary and the characteristics of LFA B (Figure 5.6B). At the base of the unit, there is a 1 m thick bed of diffusely stratified lapilli-tuffs which grades normally into a series of cross-stratified tuffs and fine lapilli-tuffs (Figure 5.6B). Stratification thicknesses range from 2 mm to 5 cm and have a cross-cutting relationship with each other. Coarse lapilli-tuff filled channels and

lenses of coarse material (>0.5 mm to 2 cm thick) are evident throughout the sequence (Figure 5.6C).

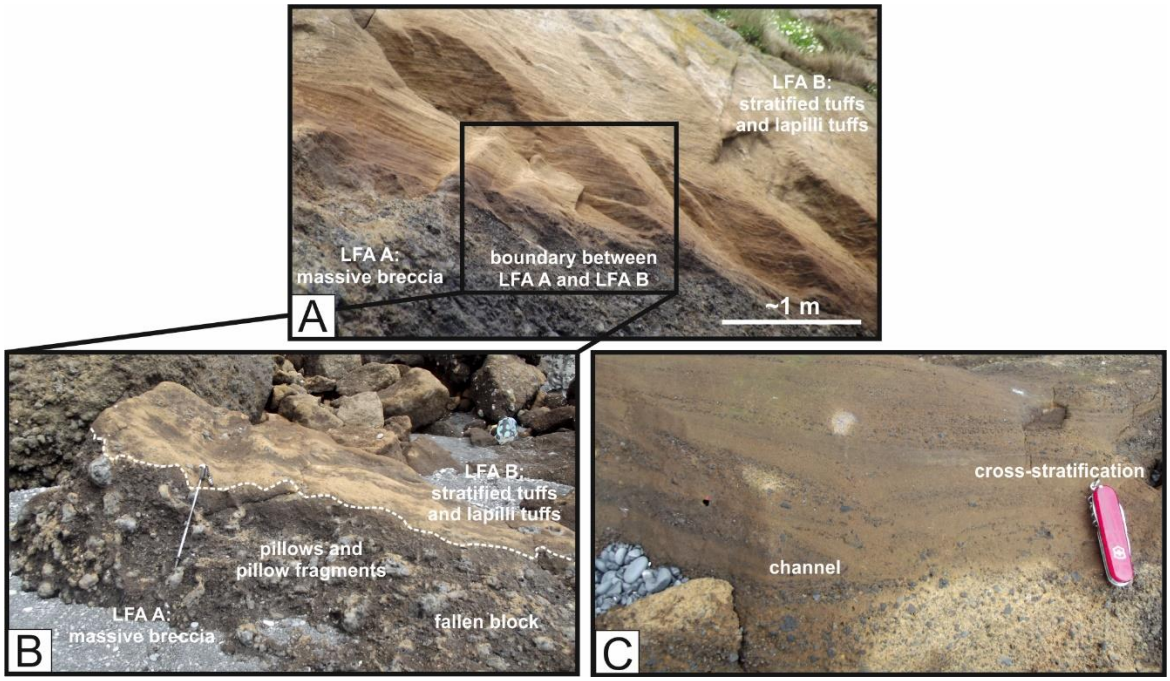

Figure 5.6: Field photographs of LFA B. (A) Boundary between LFA A and LFA B which is relatively well defined but is locally diffuse and irregular. (B) Fallen block showing the boundary between LFA A and LFA B. Walking stick is 1 m. (C) Example of cross-stratification in the tuffs. Channel-filling lapilli-tuffs. Pen knife is 10 cm.

5.4.1.3. Lithofacies C: compound pahoehoe lavas

Lithofacies C comprises several thin pahoehoe lava flows (<5 m thick) (Figure 5.7A). The lavas infill and onlap the palaeotopography created by LFA B (Figure 5.7C). Lithofacies C thickens towards the west, where there are approximately 5 to 6 lavas that can be identified (Figure 5.7B). Towards the east, only 3 separate lava flows are distinguishable (Figure 5.7C). The lava at the base of the unit (Lava 1) is the thickest of the lava flows (~5 m thick) and is localised in the west (Figure 5.7B). It onlaps LFA B in the east. This lava flow displays columnar jointing that locally splays into fan jointing (Figure 5.7B). The overlying flows are <1.5 m thick and do not display any polyhedral or columnar jointing. Exposure of Lithofacies C continues along the elongate side of the tindar exposure (N-S transect), where the thickness of Lithofacies C is ~20 m (Figure 5.8).

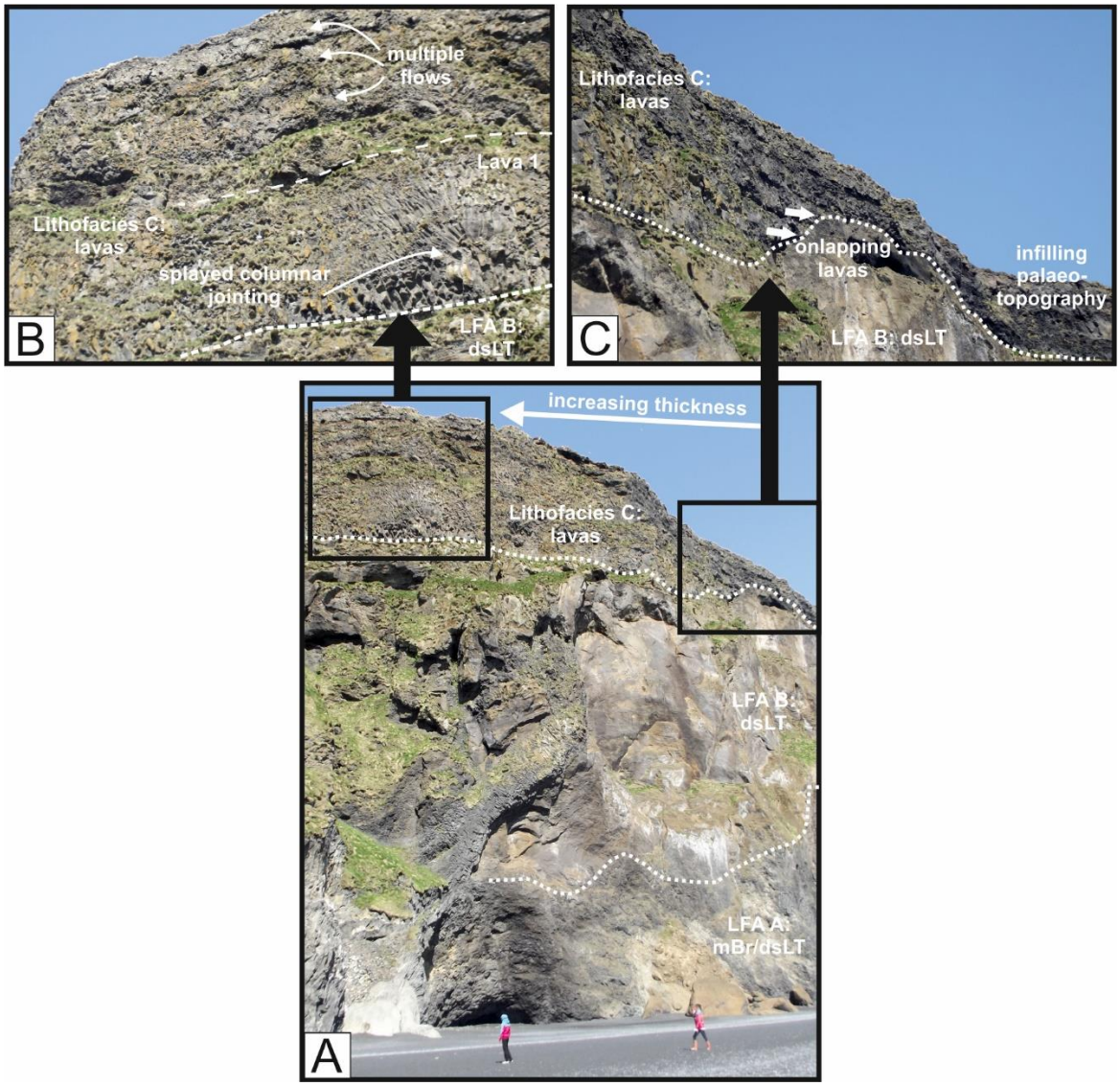

Figure 5.7: Lithofacies C. (A) Lithofacies C thickens towards the west. Boxes show location of (B) and (C). (B) Thickest section of Lithofacies C with approximately 6 flows. The lowest lava (Lava 1) appears to be the thickest (~5-7 m thick) and displays splayed columnar jointing. (C) The lavas thin towards the east and onlap palaeotopography created by LFA B. In the east there are only 3 distinguishable thin lavas.

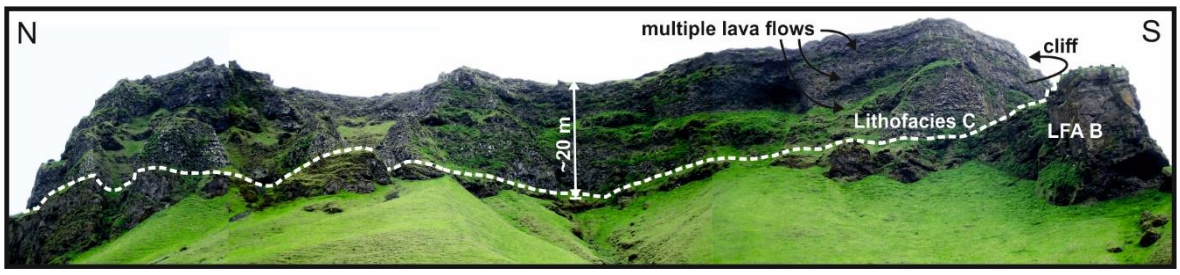

Figure 5.8: Exposure of the lavas continues around from the cliff face. The thickness of lavas is approximately 20 m.

5.4.2. **Intrusive bodies**

5.4.2.1. Plug-like magmatic body

In the southwestern corner of the tindar, several magma pulses into the host-rock have produced intrusions with highly complex morphologies. Firstly, a plug-like dolerite intrusive body has been intruded into the tindar. The magmatic plug is up to 100 m wide and is exposed for 60 m in height (Figure 5.9A). The termination of the intrusion appears to be at a similar height to the boundary between the subglacial tindar deposits (LFA A and LFA B) and the subaerial lava flows (Lithofacies C). It is likely this intrusion or a subset of this intrusion partially fed Lithofacies C, although the relationship between lavas and intrusions has been subsequently eroded or is inaccessible (Figure 5.9B). At the base of the plug, the dolerite has regularly spaced, subvertical columnar jointing up to 80 cm spacing (Figure 5.9A and B). The regular jointing grades into more irregular, closely spaced (<20 cm) and chaotic jointing patterns (Figure 5.9A and B). The dolerite is fine to medium grained (<0.2 mm) and aphyric. Petrographical analysis of the dolerite plug shows that it is comprised of pyroxene and plagioclase, and a minor component of olivine crystals (< 5%) and metal oxides (< 10%) (Figure 5.9C). Locally, there are accumulations of medium-grade crystals forming in glomerocrysts (Figure 5.9D). The plagioclase crystals have a strong fabric alignment indicating direction of magma flow (Figure 5.9C). At either side of the plug, there are zones where the irregular jointing grades into highly cleaved dolerite (Figure 5.9A and B; 5.10C). The planes of dolerite are 1 to 3 cm thick and the dolerite is coarser (crystals <0.3 mm) than the regularly jointed part of the intrusion.

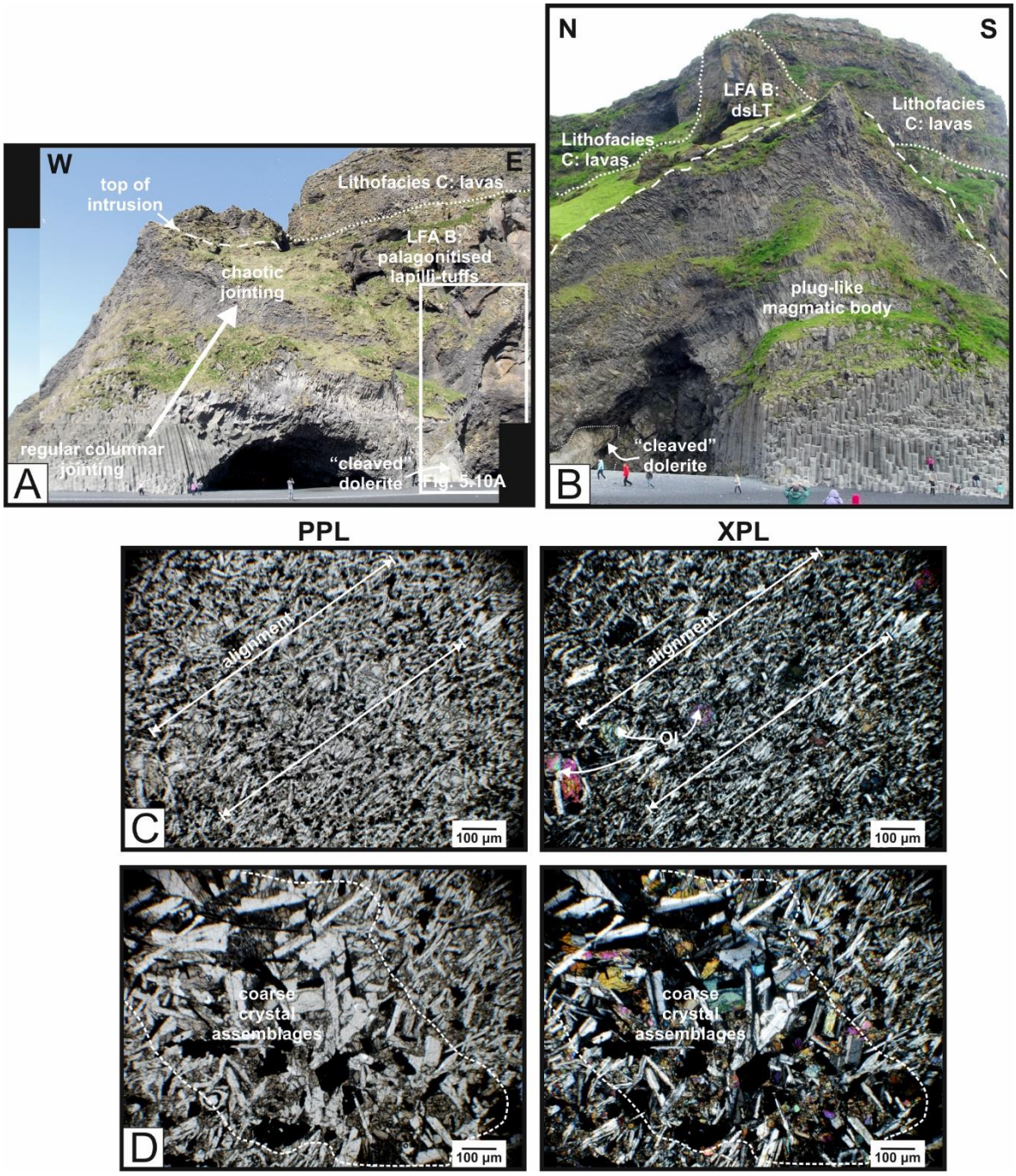

Figure 5.9: Dolerite intrusion at SW corner of the tindar. (A) Large plug-like body that is 100 m wide and exposed for 60 m from the base of the cliff. At the base, large columnar jointing (< 80 cm) grades into more chaotic and irregular jointing. Location of the photo in Figure 5.10A marked. People on beach for scale. (B) Irregularly-shaped intrusion, up to 100 m wide. Zones of "cleaved" dolerite are seen in (A) and (B). People on beach for scale. (C) Petrographical analysis of dolerite showing alignment in the plagioclase feldspar crystals and (D) coarse crystal assemblages.

5.4.2.2. Coherent inclined sheets

The plug feeds several coherent inclined sheets and sills that extend through the host-rock stratigraphy (Figure 5.10). The inclined sheet in Figure 5.10A, extends to the east away from the plug to a height of ~30 m, and a maximum width of 5 m at the base. The sheet terminates 5-10 m below the subglacial-subaerial palaeo-interface. However, the 2D exposure of the intrusion restricts

the interpretation of the relationship between the inclined sheet and the lavas, where it is possible that the sheet has fed the lava flows. At the termination of the inclined sheet, a large zone of brecciated basalt protrudes away from the tip of the intrusion. Fingers of basalt breccia extend subvertically away from the intrusions (Figure 5.10A). At the base of the inclined sheet, the "cleaved" dolerite grades into regularly jointed dolerite and forms a coherent sill along the base of the cliff (Figure 5.10B and C). At the point where the inclined sheet feeds the sill, the direction of jointing rotates by up to 47° (Figure 5.10D). The sill feeds upward-propagating dyke-lets (up to 10 m high) which locally feed subsurface proto-pillows and pillows (Figure 5.10A).

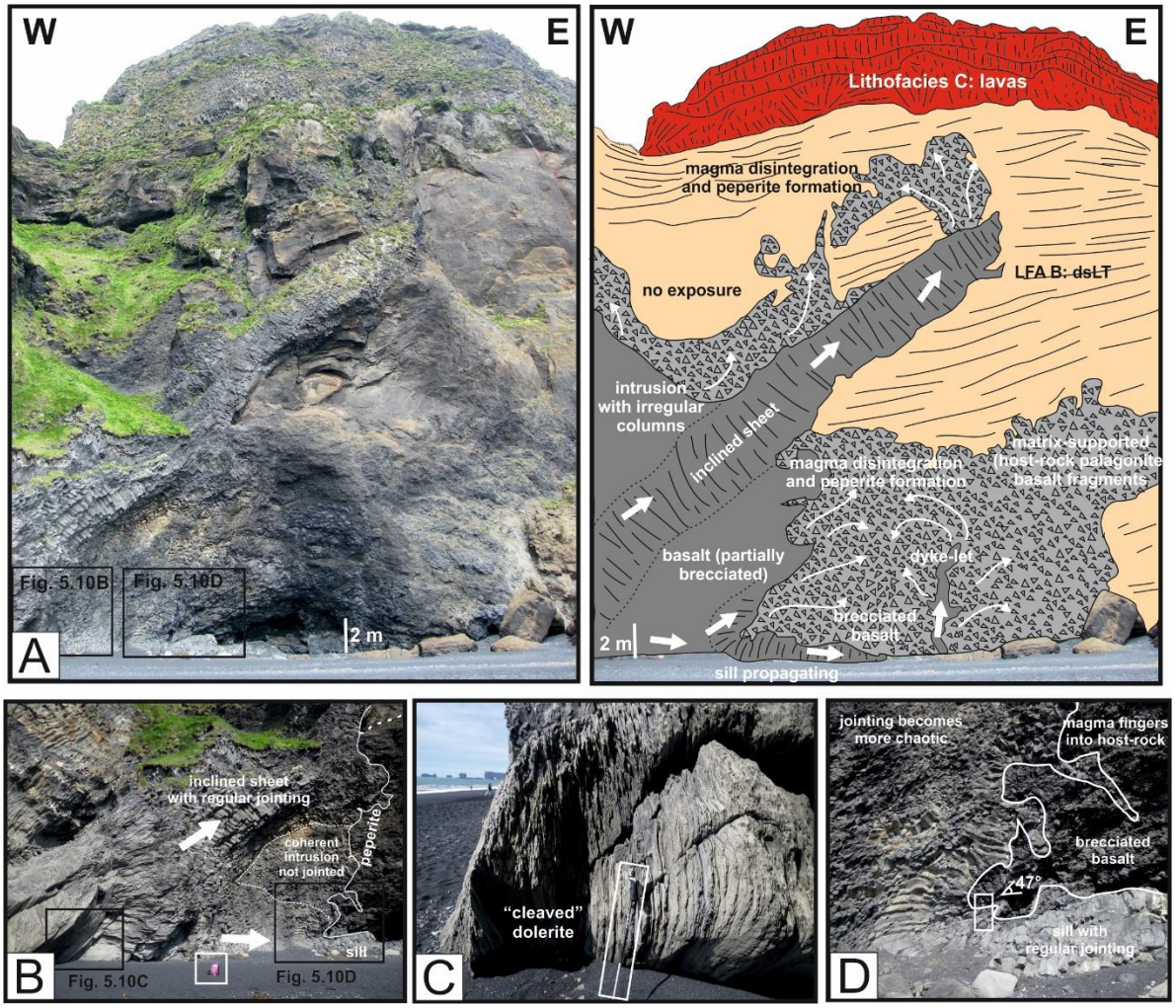

Figure 5.10: Morphology of inclined sheets and sills, fed by the intrusion in Figure 5.9. (A) Photograph and annotated photograph of inclined sheet fed by the plug like intrusion in the far SW corner of the tindar. The inclined sheet terminates before reaching the palaeosurface, where it fragments into brecciated basalt (mBr). The plug-like intrusion also propagates along the base of the cliff forming a coherent sill with regular jointing. Dyke-lets emanate from the sill. Magma flow direction is indicated by the white arrows. Locations of figures 5.10B and D indicated. (B) Gradational change from "cleaved dolerite" to regularly spaced columnar joints at the base of the inclined sheet. Rucksack for scale is ~ 50cm. (C) "Cleaved" dolerite. (D) Rotation of columnar joints by ~47° feeding sub-horizontal sill. Magma extensively fragments at margins of intrusion and forms brecciated basalt clasts in a host-rock (palagonite) matrix. The brecciated basalt is clast-supported.

5.4.2.3. Irregular sills

Along the base of the cliff, a thick, irregular sill is exposed (>20 m in thickness). The sill displays highly variable and splaying columnar joints which are regularly spaced and frequently change orientation (Figure 5.11A and D). The margin along the top of the sill is highly irregular with small intruding fingers (<1 m) and dyke-lets (<25 m) that propagate sub-vertically away from the sill into the host (Figure 5.11C). The sub-vertical dyke-lets are askew, become more brecciated away from the top of the sill, and pond into highly fluidal, bulbous bodies (Figure 5.11B and C). These magmatic bodies have a coherent basalt core but are highly fragmented at the margins and finger into the host-rock, forming "dynamic" peperite that is dispersed into the host (Figure 5.11B). The term "dynamic peperite" is defined here as 'the complete disruption and mingling of the host-rock domain by and with magma (Rawcliffe 2016). The ponded basalts are up to 10 m in diameter and contain abundant host-rock inclusions.

The majority of the interface between the sill and the surrounding host is highly diffuse, where the coherent dolerite becomes increasingly more fragmented towards the margin and starts to mingle with the host, producing the fragmental basalt breccia discussed in Section 5.3.2. The fragmented margins around the sill can be up to 25 m wide (Figure 5.11D). Blocky peperite is also evident along the boundary between the intrusion and host.

The sill is primarily aphyric and non-vesicular, however, locally, vesicle accumulations have formed creating large gas cavities up to 40 cm in diameter (Figure 5.12A). The jointing is distributed radially around the gas cavities showing that the direction of cooling is directed towards the gas cavity (Figure 5.12A). The walls of the gas cavity have a ropey, pahoehoe texture and are vitrified or very fine grained (Figure 5.12B and C). Magma blisters, up to 8 cm across have also formed within the gas cavity (Figure 5.12C). The sill also exhibits elongate cavities that interconnect multiple gas cavities and are filled with fine ash to lapilli-graded basalt particles (Figure 5.12D, E and F).

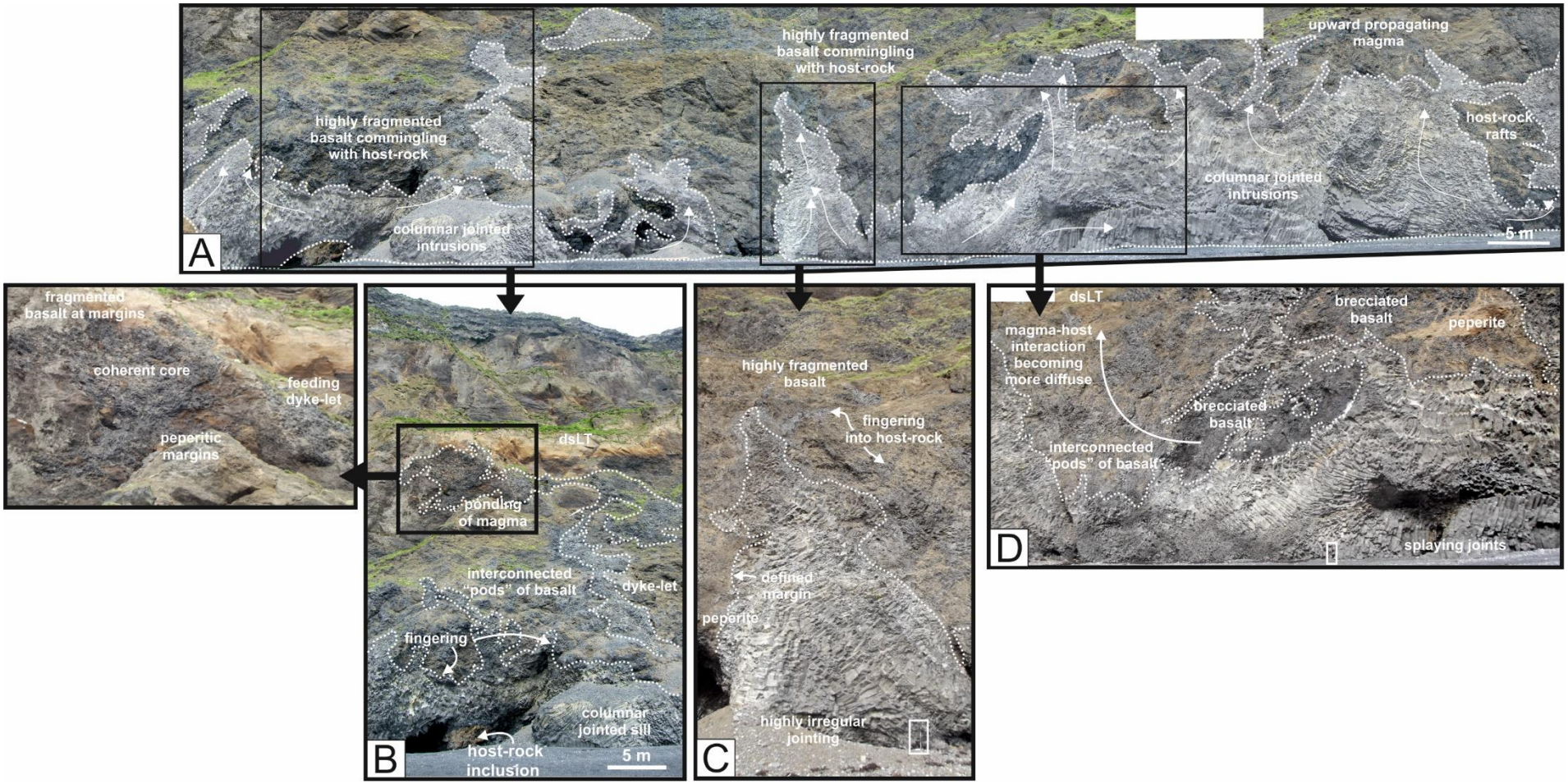

Figure 5.11: (A) Transect showing the irregular sill at the base of the cliff. Location of transect shown in Figure 5.2. The top margin of the sill is highly irregular and fingers into the host-rock. Dyke-lets also extend from the upper margin and propagate subvertically. Surrounding the intrusion is a zone of highly fragmented basalt that has commingled with the host-rock. Host-rock rafts are enclosed within the intrusion. (B) Askew dyke-lets that extend from the top margin of the sill into the overlying host and pond half-way up the cliff. Inset: Close-up image of the bulbous magmatic body with a coherent core and highly fragmented outer margins. Blocky peperitic margins are observed. (C) Dyke-let fingering sub-vertically into host. (D) Close-up of the margin between the coherent sill (with multi-directional columnar jointing) and the host. The margin becomes more diffuse from a highly fractured basalt into a matrix-supported breccia. Pods of basalt are interconnected with each other. Peperite has formed at the margin. Walking stick is 1 m.

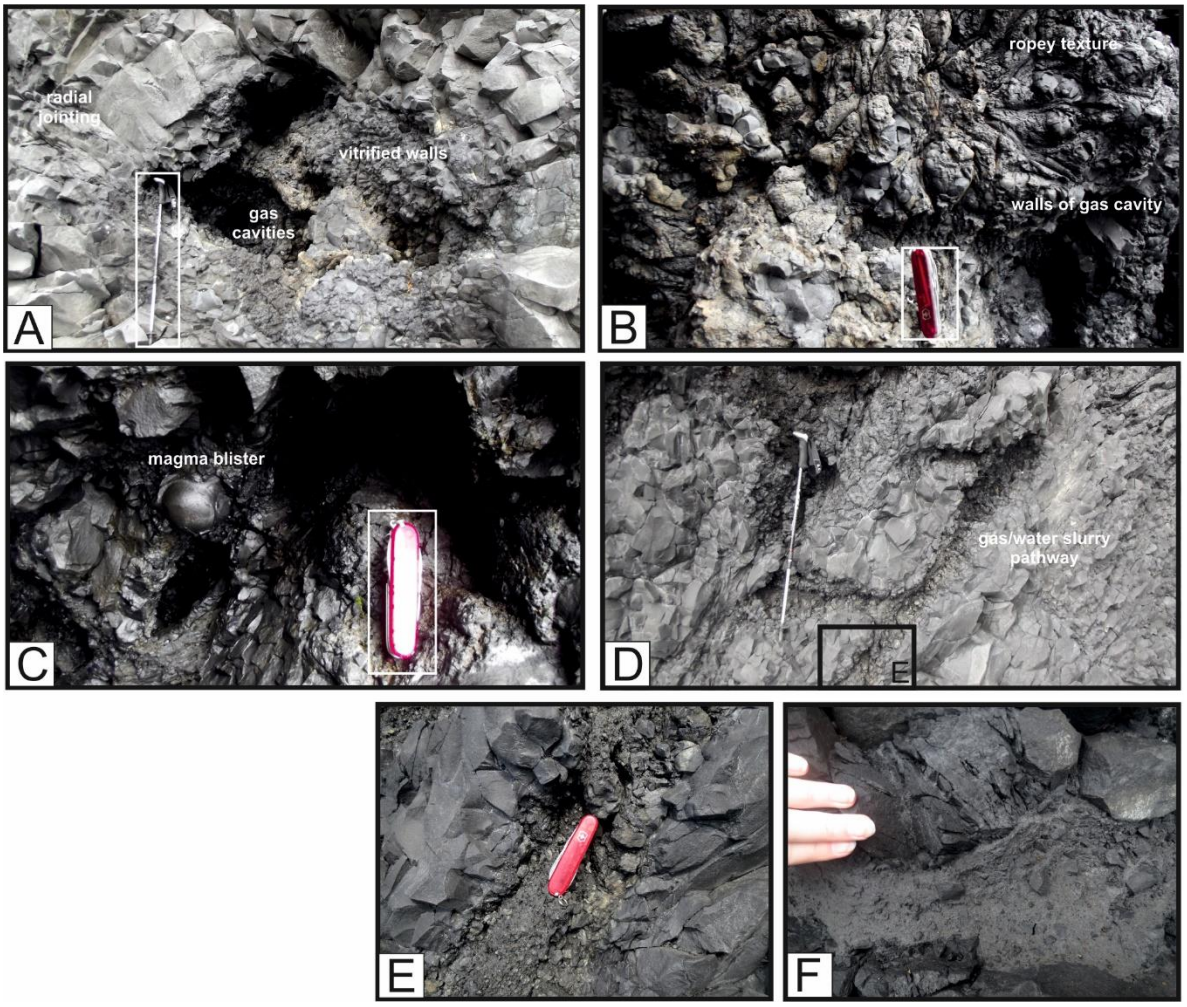

Figure 5.12: Gas cavities in irregular sill. (A) Gas pockets within the sill. Radial jointing around gas cavities. Walking stick is 1 m. (B) The walls of the cavity have a ropey texture. Pen-knife is 10 cm. (C) Magma blisters are present along the walls of the gas cavity. Pen-knife is 10 cm. (D) Elongated cavities filled with fine-grained, quenched basalt, likely to be a pathway for gas/water/slurry mix. Walking stick is 1m. (E) and (F) Close-up photograph of the centre of the elongated cavities. Pen-knife is 10 cm.

5.4.3. **Magma-host-rock interaction**

5.4.3.1. Fragmental basalt breccia with host-rock inclusions

The coherent intrusions grade into a zone of highly fragmented basalt, containing clasts of dolerite and basalt, locally vitrified, in a hyaloclastite host-rock matrix. The margin between the coherent intrusion and the brecciated zone is mostly diffuse and convolute where fingers of coherent basalt (<1.5 m) extend into the basalt breccia (Fig, 5.11D). Locally, however, the dolerite intrusion has a defined and vitrified margin. The fragmental breccia becomes more diffuse at a greater distance from the intrusions: from a proximal subfacies, directly in contact with the intrusions that has little to no matrix, to a distal subfacies where the breccia commingles with the surrounding host (Figure 5.10A, B and 5.11D).

Proximal: Adjacent to the intrusions, the breccia is clast-dominated with clasts on a cm-scale. The breccia in this proximal zone is comprised of basalt clasts that exhibit a globular texture, where magma has collected into spherical globules of basalt (<5 cm) with vitrified and/or dimpled outer rinds (Figure 5.13A and B). Some of these rinds exhibit a ropey texture (Figure 5.13C). The globular texture may be the result of large vesicles coated in molten magma that when cooled preserve the magma bubble. The basalt has varying degrees of vesicularity, and locally elongated pipe vesicles are present. The basalt breccia facies close to the intrusions also contain subsurface proto-pillows, which have budded from the tips of the intrusions (Figure 5.13D). The proto-pillows show typical pillow characteristics, including rounded to sub-rounded geometry, radial fracturing and vesicular centres (Figure 5.13D).

The fragmented basalt breccia also contains host-rock inclusions that are generally comprised of fine to coarse grained, matrix-supported hyaloclastite (Figure 5.13E). The inclusions are massive in structure, likely because fluidisation has destroyed any stratification. The margins of the inclusions grade into the surrounding basalt breccia, where the hyaloclastite commingles with the brecciated basalt fragments (Figure 5.13E). The intensive mixing suggests the host-rock inclusion was fluidised. Peperite also locally forms at the margins of the inclusion (Figure 5.13E).

Distal: The breccia becomes more matrix-supported (<15 % matrix) away from the intrusions (Figure 5.10A). The matrix is comprised of coarse grained angular basalt fragments (sub-mm to 3 mm) and palagonite. Within the matrix are isolated angular pods of coherent basalt (<5 m across) that display polyhedral jointing and have irregular shapes (Figure 5.13F and 5.11B and D). These pods are surrounded by highly fragmented basalt rims (< 1m thick) that grade out into the matrix. Locally these pods are interconnected with one another and finger into the globular basalt or hyaloclastite matrix.

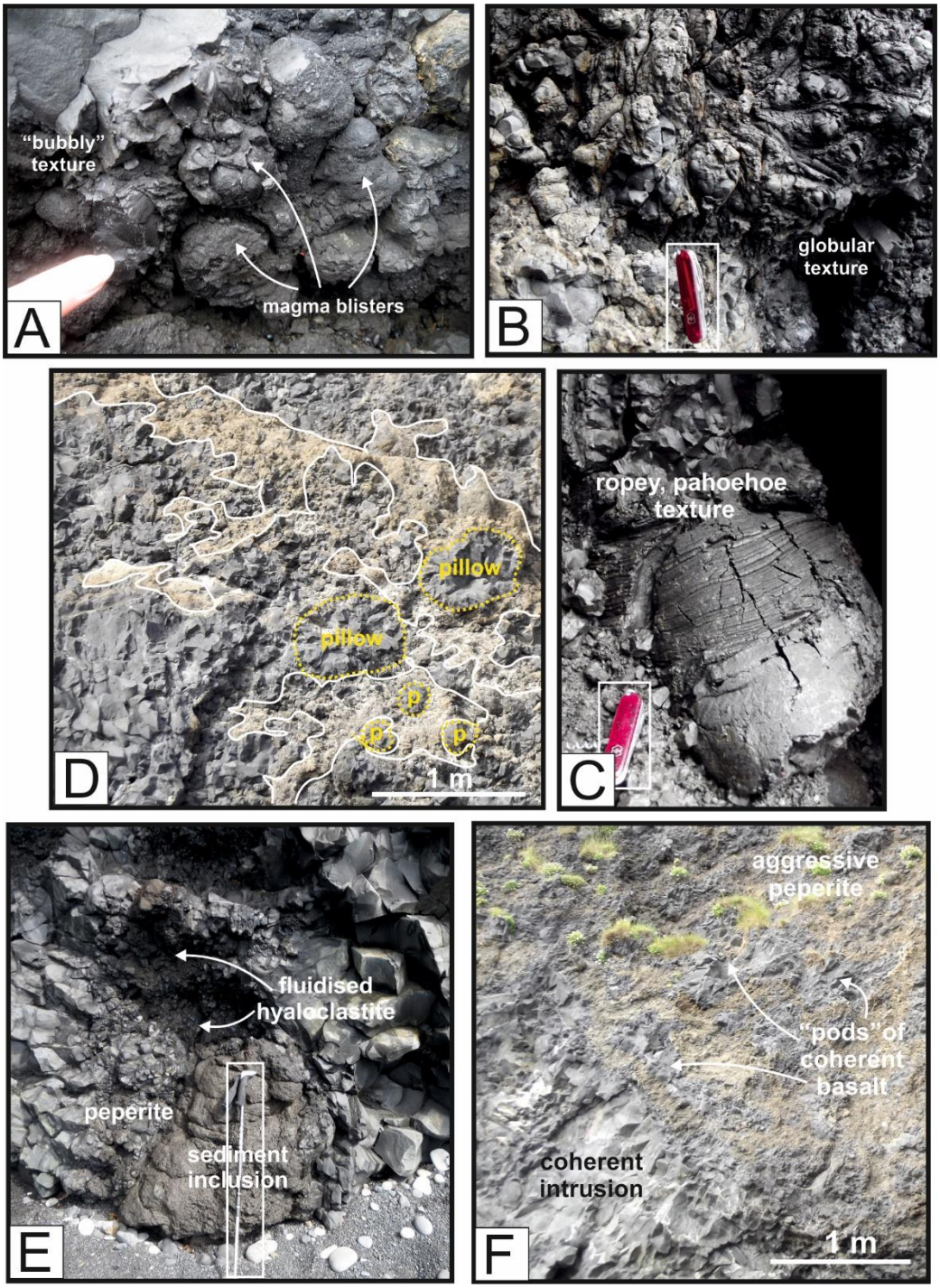

Figure 5.13: Features of the fragmental basalt breccia surrounding the intrusions. (A) Bubbly texture that is exhibited in the proximal sub-facies of the unit. Magma blisters are on a cm-scale. (B) Another example of the basalt breccia with a globular texture. Pen-knife is 10 cm long. (C) The rinds on some of the clasts exhibit a ropey pahoehoe texture. Pen-knife is 10 cm long. (D) Magma pseudo-pillows form at the tips of the intrusions and are highlighted in yellow dashed lines. Preserved proto-pillows are evident within some of the intrusions. (E) Host-rock inclusion within the basalt breccia. The hyaloclastite mingles with the breccia and suggests fluidisation of inclusion. Peperite formation at the margins of the inclusion. Walking stick is 1 m. (F) Pods of coherent basalt that can be interconnected to each other.

5.4.3.2. Peperite Formation

Peperite forms at the margins between the intrusive bodies and the host-rock. It could be suggested that the fragmental basalt breccia is effectively a 25 m wide dynamic peperitic margin (Rawcliffe 2016). However, this sub-section concentrates on the blocky peperite formed directly in contact

with host-rock (Figure 5.14A). The angular peperite clasts vary in size from sub-cm to decimetre-scale. The clasts <1 cm are likely to be formed by cooling contraction granulation and can commingle and homogenise with hyaloclastite host-rock. Many of the larger clasts (> 1cm) exhibit jig-saw fit and locally have vitrified margins. Fractures in the intrusion are filled with hyaloclastite host-rock that can extend into the intrusion for up to 1 m. Any stratification in the surrounding host-rock has been destroyed due to fluidisation of the host. Some of the dyke-lets that extend away from the top of the irregular sill, appear to fracture and fragment upon ascent, forming peperite dykes that continue to finger into the host (Figure 5.11B).

5.4.3.3. R-T structures

Aggressive mixing of two fluids, as a function of density, produces highly convolute and swirly morphologies. The presence of R-T structures suggest intensive mixing of fluids, in this case, molten or semi-molten magma and fluidised hyaloclastite host-rock. Several R-T structures are identified at the margin of the intrusive bodies and hyaloclastite host-rock (Figure 5.14B). The structures are on a decimetre scale, up to approximately 40 cm. The basalt has a quenched margin and the host-rock shows evidence for fluidisation (stratifications are destroyed adjacent to the structure).

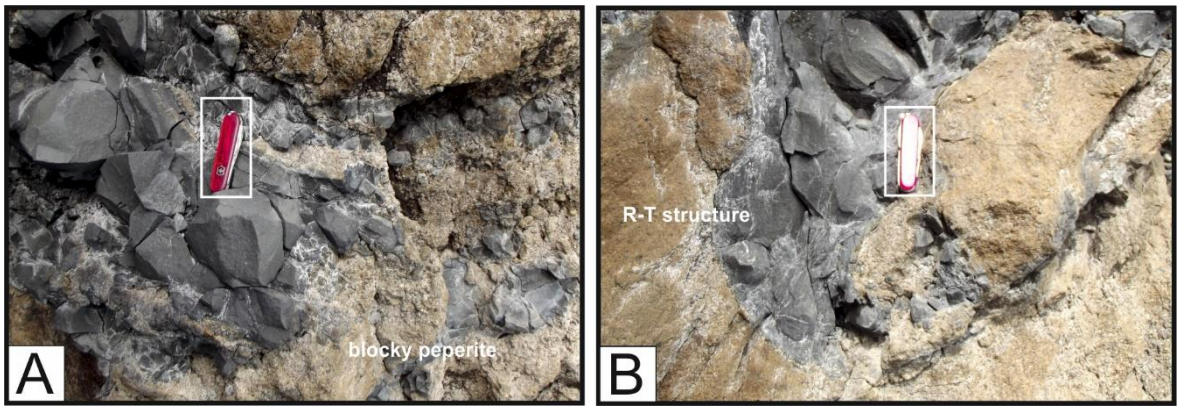

Figure 5.14: (A) Peperite forms at the boundary between intrusion and host-rock. The peperite is blocky and angular. Pen-knife is 10 cm. (B) R-T structures exhibit highly convolute and swirly morphologies. Pen-knife is 10 cm.

5.5. Interpretation

5.5.1. **Lithofacies of the Reynisdrangar tindar**

The characteristics of each of the lithofacies that construct the Reynisdrangar tindar, described above, provide an insight into the initial to late-stage sedimentation and development of the edifice. LFA A, LFA B and Lithofacies C represent three stages of the evolution of a tindar: (1) subaqueous and non-explosive interaction; (2) explosive interaction and (3) subaerial effusion (minimal explosivity). The interpretation of each of the lithofacies are described below. Palagonite alteration is common throughout LFA A and LFA B and is commonly associated with the hydrous alteration of basaltic glass (Jakobsson 1978).

5.5.1.1. LFA A: massive breccia and lapilli-tuffs with diffusely laminated sub-units

The clast-supported nature of the breccia sub-facies of LFA A containing pillows, fragmented pillows and abundant coarse blocky basalt clasts (Figure 5.5), is suggestive of mechanical disintegration and non-explosive fragmentation of an extrusive lava in a subaqueous environment. Pillows are formed by a low ratio of water to magma mixing and/or suppression of explosivity by suitable confining pressures (lithostatic or hydrostatic) (Kokelaar 1986; Griffiths and Fink 1992). Fragmentation occurs predominantly due to cooling contraction, where quenching of magma produces fractures, which fragment the magma in-situ (Smellie and Hole 1997). This is evident from tuff-filled fractures in intact pillows. The abundance of fragmented pillows could be a product of resedimentation after formation, where fragmentation of pillows occurs by slumping and mass flow of the volcano flanks or ridges (Jones 1970; Moore 1975; Cas et al. 2003; Graettinger et al. 2013). Clast-to-clast collision causes the extensive fragmentation of clasts.

LFA A is heavily intruded by irregular intrusions, which also spall pillows and produce hyaloclastite breccias and interconnected lava pods at the intrusion margins, due to explosive and non-explosive interaction with the water-saturated host (Figure 5.13). This interaction disrupts original bedding features in LFA A. Explosive disruption of existing pillows by the emplacement of intrusions could also result in fragmented pillows (Smellie and Hole 1997). The emplacement of these intrusions is discussed in Section 5.5.2.

The lapilli-tuff sub-facies of LFA A is matrix-supported with a fine grained lapilli-tuff matrix and is locally diffusely stratified (Figure 5.5C and D). Petrographical analysis of the matrix shows tachylite clasts have high vesicularities, and these vesicles are often elongated, indicative of explosive magmatic eruptions (Figure 5.4) (Houghton and Schmincke 1989; Houghton and Wilson 1989; Graettinger et al. 2013). It is likely the explosive fragmentation of these vesicular, cuspate clasts was initiated by rapid degassing of ascending magma due to a rapid decrease in pressure. Vesicles dictate where the clast fractures resulting in cuspate morphology (Figure 5.4) (Zimanowski et al. 1997; Mastin et al. 2009; Graettinger et al. 2013). It is suggested that the angular and sub-angular tachylite and basaltic clasts in the matrix are a product of non-explosive cooling-contraction granulation. It is proposed that the fragmentation of the matrix is a result of a combination of explosive magmatic fragmentation (via degassing) and simultaneous quenching during subaqueous eruptions (Wohletz 1983).

The lapilli-tuff subfacies of LFA A is locally diffusely planar stratified and the tephra tends to be coarse (>0.5 cm) (Figure 5.5). These characteristics likely indicate that the tephra was formed by subglacial eruptions and transported and deposited by a series of density-modified grain flows and/or localised turbidity currents and debris flows in relatively shallow water (Werner and Schmincke 1999; Schopka et al. 2006; Skilling 2009).

5.5.1.2. LFA B: stratified and diffusely stratified tuffs and lapilli-tuffs

The characteristics of LFA B are distinctly different from Facies A, indicating a change in eruption-type. The sedimentary structures found in LFA B (cross-bedding, channels etc.) clearly indicate lateral transport of tephra (Figure 5.6C). Without closer examination (no access), there are two possibilities for the deposition of LFA B: (1) a Surtseyan-type eruption into a shallow body of water creating typical phreatomagmatic activity including tephra jets and continuous uprush plumes, which collapse to form small PDCs (Kokelaar 1983) confined by the ice cover; and (2) subaqueous resedimentation and fining of tephra by meltwater drainage currents, creating thin, cross stratifications and channels. The addition of fine tephra from suspended ash in the water column would potentially add to the fine tephra exhibited in LFA B. Normally graded units also signify potential turbidity currents and debris flows from unstable volcano flanks (Smellie and Hole 1997).

5.5.1.3. Lithofacies C: massive and compound pahoehoe lavas

The broad, flat upper surface of lava likely formed as a subaerial lava cap, overlying the tephra-comprised ridge. Lava 1 in the lava succession displays splayed jointing patterns and typical columnar jointing, indicating water penetration during cooling (Figure 5.7). Lava 1 is a massive lava unit and is significantly thicker (~5 m) than the overlying flows (<1.5 m) (Fig.5.7B). The other lavas in the sequence do not develop coupled colonnade-entablature formations, or jointing, indicating that they are compound lava flows (Figure 5.7B and C). Subaerially erupted with low effusion rates, compound lava flows form from basalt with relatively low viscosity and on gentle slopes (Smellie and Hole 1997). The lack of hyaloclastite and/or pillow lavas indicates the lavas were not erupted into or did not flow into water (Skilling 1994). The Lithofacies C lavas likely represent the last phase of lava effusion in the development of the Reynisdrangar tindar. The lavas filled the topography created by minor erosion of the top of LFA B. The direction of onlap on to the palaeotopography, and the change in thickness from west to east indicates the lavas were erupted from a source along the western margin of the tindar (Figure 5.5C).

5.5.2. **Emplacement of intrusions**

5.5.2.1. Emplacement of intrusions

Nearly all the intrusions have intruded into LFA A. All of these intrusions have irregular morphologies (Figure 5.11) which suggests the host rock was unconsolidated at the time of intrusion and overlying lithostatic pressure was low, allowing for the ductile emplacement of magma (Stevenson et al. 2011). Fingering of the magma into the host-rock and metre-scale dyke-lets that disseminate away from the intrusion are the result of fluidisation and/or local host-rock deformation around the intrusions (Figure 5.11). The highly irregular nature of the intrusions is caused by instabilities in the vapour film surrounding the magma during emplacement. The vapour film fluctuates (but does not collapse) allowing highly convolute intrusion morphologies. Host-rock deformation is caused by the inflation and heating of the intrusions (Schofield et al. 2012), and local explosive interaction. Fluidisation is more likely to occur if the host is unconsolidated or partially consolidated due to the high efficiency of pore-fluid drainage, high pore fluid volume, and low mechanical strength in unconsolidated sediments (Kokelaar 1982; Busby-Spera and White 1987). When the host is fluidised and unstable, magma can flow in irregular pathways through the host-

rock and pond at any stratigraphical level (Kokelaar 1982). This is evident at Reynisdrangar from the large bulbous magmatic bodies that stem from anastomosing dyke-lets. Additionally, the presence of peperite and R-T structures provides widespread evidence for the syn-magmatic fluidisation of Facies A (Figure 5.14). R-T structures form as a response to density contrasts between two contrasting fluids, in this case molten or semi-molten magma and fluidised lapilli-tuff host-rock (Daly 1967; Allen 1982; Hall and Els 2002; McLean et al. 2016).

During the subaqueous fragmentation of LFA A, water would have become trapped within the deposit (Stevenson et al. 2011). Additionally, the meltwater from the thinning ice sheet would have percolated into the relatively porous media (unconsolidated with an open network of pores prior to palagonitisation), providing a water source for extensive non-explosive magma-water interaction and aiding host-rock fluidisation during intrusion emplacement. The characteristics of the intrusion margins (e.g. undulating, peperite, magma fingers and bulbous dykelets; Figure 5.11, 5.13 and 5.14) provide further evidence for a high water-magma ratio during magma emplacement and low magma-water mixing. The intrusions within Facies A also have erratic jointing patterns indicating water infiltrated the magma as it cooled (Figure 5.11). This further supports the evidence for syn-volcanic intrusion emplacement, where meltwater from the ice sheet (melting triggered by volcanism) continued to percolate through the host and into the magma.

Locally, intrusions have invaded into LFA B, where they display coherent, well-defined margins lacking well-developed peperite (Figure 5.10A), and exhibit regular columnar jointing. These characteristics suggest Facies B had lower water content at the time of intrusion, likely as a response to the fine grained nature and low porosity of LFA B. The intrusions emplaced into LFA B likely represent magmatic phases that fed subaerial extrusions of magma (Lithofacies C) during the late-stage development of the tindar. The large plug like body in the SW corner of the tindar probably represents the feeder to the subaerial vents on the contemporaneous surface.

The differing responses between LFA A and LFA B to intrusion emplacement suggests one or a combination of the following: (1) the intrusions able to propagate into LFA B had a higher magmatic pressure, and were able to bypass the water-saturated LFA A; (2) the intrusions within LFA B were

emplaced by brittle mechanisms (e.g. propagating fracture ahead of magma); and (3) LFA B host-rock was unable to fluidise partly due to the lower water content, preventing ductile emplacement.

5.5.2.2. Magma-water interaction and explosivity

Without having the access to sample LFA B and Lithofacies C and the upper portion of LFA A, quantitative analysis of the change in grain size and shape throughout the development of the Reynisdrangar eruption cannot be fully examined. Similarly, the aggressive mingling of the intrusive fragmental breccia and the host lapilli-tuffs and breccias disguises the amount of fragmentation (by magma-water interaction) during the emplacement of the intrusions. What can be deduced from field observations, however, is that the presence of pillows, proto-pillows and peperite at the margins of the intrusions, indicates non-explosive, passive interaction (Stevenson et al. 2011). Explosivity was likely suppressed by a combination of factors, primarily the lithostatic and hydrostatic pressure applied by the overburden (>1.3 MPa) and the high ratio of water to magma (water-saturated host) (Kokelaar 1986; Griffiths and Fink 1992; Smellie and Hole 1997). Peperite forms non-explosively at the margins of the intrusions and the intrusive pods by the process of cooling-contraction fragmentation. Evidence for this includes the size of the fragments within the brecciated margin proximal to the intrusions, which is comprised of cm-scale basalt clasts and fragments, and lacks the fine ash component (associated with phreatomagmatic fragmentation) (Figure 5.14A). Quench granulation only releases 10% of the thermal energy available (Schmid et al. 2010) and therefore characteristically creates larger particles (coarse ash and lapilli) than phreatomagmatic fragmentation (Graettinger et al. 2013).

The intrusions exhibit vesiculated zones, magma blisters and large gas cavities (Figure 5.12). Magma containing large, coalesced gas bubbles, like the intrusions at Reynisdrangar, will more readily tear apart, aiding the fragmentation of magma and aiding mingling with host-rock (Schipper and White 2016). Magmatic gas expansion, due to rapid pressure decrease in the shallow subsurface, likely produces the polylobate gas cavities exhibited within the intrusions at Reynisdrangar (Figure 5.12A) (Graettinger et al. 2013).

Due to the fine-grained nature of the particles within the elongate cavities (Figure 5.12D and E), it is likely that another mechanism was at play during magma intrusion. The fine particles are products

of more intensive fragmentation of the intrusion. This can either be achieved by: (1) energetic steam explosions; or (2) high energy thermohydraulic explosions (Zimanowski et al. 1997; Gudmundsson 2003; Graettinger et al. 2013). The rapid heat transfer from magma to water generates steam, increasing hydrostatic pressure (if water is confined) by up to 50 times (Delaney 1982). Such an increase in hydrostatic pressure can instantaneously overcome the lithostatic strength and fragment the magma (Wohletz 1983; Zimanowski 1998; Gudmundsson 2003). The expansion of steam within magma accelerates and transmits momentum to the magma-water-steam mix, resulting in the fine fragmentation of magma (Zimanowski 1998; Gudmundsson 2003). It is likely that the slurry of water, steam and fine ash to lapilli-sized fragments were energetically transmitted through the magma (in the direction of the lowest pressure), creating elongate cavities, where cavity walls were fragmented by the passage of the hot slurry (Figure 5.12D, E, F).

To conclude, magma fragmentation and brecciation during intrusion emplacement at Reynisdrangar was the product of mostly non-explosive interaction, with minor components of degassing and energetic steam explosions.

5.6. Discussion and conclusions

5.6.1. **Development of the Reynisdrangar tindar**

The cliff exposure at Reynisdrangar does not show any major unconformities between lithofacies; however, minor unconformities are present where erosional contacts are observed (e.g. between LFA B and Lithofacies C). These minor unconformities mark the erosional events that are integral in many sedimentary processes, for example, gravity-driven mass flows and turbidity currents, especially on active volcano flanks (Schopka et al. 2006). The lack of major unconformities suggests the formation of the volcano occurred in one magmatic event, likely with several magma pulses. The change in lithofacies is attributed to a change in the environmental conditions in which the magma was erupted into, indicating a monogenetic nature.

The Reynisdrangar edifice was formed by a rapidly changing palaeoenvironment at the time of eruption. The flat-lying subaerial lava (Lithofacies C) directly overlies subaqueously erupted hyaloclastite (LFA B), which suggests a relative lowering of the water level by up to 50 m (maximum thickness of LFA B). This change in water-level is unlikely to be reached by sea-level fluctuations

during the building of the volcano (Smellie and Skilling 1994). Therefore, a glacial palaeoenvironment at the time of eruption is inferred. The distribution and characteristics of each of the lithofacies shows a switching from subglacial processes to magmatic subaerial processes, typical in tindar formation (Figure 5.15) (Jones 1969; Jones and Nelson 1970; Skilling 1994; Smellie and Skilling 1994; Smellie and Hole 1997; Werner and Schminke 1999; Smellie 2000; Gudmundsson 2003; Schopka et al. 2006; Edwards et al. 2009; Skilling 2009; Stevenson et al. 2011).

5.6.1.1. Phase 1: glacially-confined pillow and hyaloclastite mound

Werner and Schminke (1999) describe the deposits of the initial stage of tindar or tuya development as a basal pillow complex (BPC). BPC deposits represent the effusive lava stage where magma is erupted in a deep lacustrine or subaqueous setting, or in this case magma is erupted beneath an ice sheet (Figure 5.15A). Usually, the confining pressure of the ice (and/or water) suppresses most of the explosive lava-water interaction, forming pillows intercalated with hyaloclastite. The pillow lavas form a steep-sided mound confined by the ice (Jones 1969). Heat is exchanged between the lava and ice and an ice chamber filled with meltwater is formed (Tuffen 2007). This heat exchange between lava and water allows for cooling-contraction brecciation and granulation producing hyaloclastite. As the ice progressively melts, minor explosive interaction between lava and water becomes viable due to decreasing confining pressures, producing hyaloclastite (Figure 5.15A). The pillow lava mound increasingly becomes more matrix-supported due to this production of hyaloclastite (Figure 5.15A) (Jones 1969; Smellie and Skilling 1994).

At Reynisdrangar, the pillow-only units are not exposed. This is possible for two reasons: (1) it is likely that the level of exposure along the Reynisdrangar cliff face obscures the more pillow-dominated lower portion of the edifice (buried by the sandur plains) (Figure 5.15D); and/or (2) the ice cover was too thin to completely suppress magmatic fragmentation so the pillow-dominated facies was not formed (Gudmundsson 2003). Tindars (e.g. Helgafell) can lack or have very small proportions of pillow-dominated deposits in Phase 1 if the ice cover is too thin to produce an adequate amount of hydrostatic pressure for pillow formation (Schopka et al. 2006). This leads to the facilitating of explosive subaqueous eruptions at the onset of subglacial explosive eruptions. Conversely, tindars or tuyas can often be built entirely of pillows if the ice thickness exceeds >500

m (Jones 1969) (e.g. Undirhlidar; Pollock et al. 2014). Ice thickness therefore, heavily dictates the resultant morphology and structure of the subglacial mound.

Using the transition marked between LFA B and Lithofacies C, the thickness of the ice sheet is estimated at 200-250 m thick (Paterson 1981; Smellie and Skilling 1994). An ice thickness of <500 m does not fully suppress explosive magma-water interaction (Jones 1969; Wilson and Head 2002), and therefore, the likely reason for the lack of a pillow-dominated facies at Reynsidrangar.

LFA A represents the equivalent of the initial pillow development stage (or BPC) well-documented in other subglacial edifices (Jones 1969; Smellie and Skilling 1994; Werner and Schminke 1999; Höskuldsson et al. 2006; Schopka et al. 2006; Tuffen 2007; Edwards et al. 2009; Skilling 2009; Graettinger et al. 2013), although it is comprised of mostly hyaloclastite with localised pillow zones. The pillows are mostly fragmented and/or incomplete; therefore the predominant process of deposition is likely to be eruption-fed mass flow events due to the collapse of the flanks of the edifice. It is suggested that Facies A was deposited near to the subglacial vent, where low effusion rates of pillows coincided with mild explosive eruptions and eruption-fed mass flows.

5.6.1.2. Phase 2: phreatomagmatic, shallow aqueous eruptions

As the mound increases in size both laterally and vertically the roof of the ice chamber collapses and melts, forming an intraglacial lake (Jones 1969). Magma continues to be effused into the shallow intraglacial lake causing explosive, Surtseyan processes to occur (Jones 1969). These explosive eruptions cause instantaneous fragmentation of magma and generate fine, vesiculated tephra during tephra jet propulsion or continuous uprush processes (Kokelaar 1983, 1986; Sohn and Chough 1992; Smellie and Skilling 1994) (Figure 5.15B). A high proportion of magmatic fragments and ash are lost to the atmosphere or are deposited outwith the intraglacial lake and so are not preserved (Werner and Schminke 1999). However, fragmented tephra falls back into the lake, or forms PDCs around the vent where they are deposited and reworked into stratified beds (Smellie and Hole 1997). Phase 2 corresponds to a period of rapid tuff cone growth, which can stimulate mass flow deposits and slumping recorded as discordances in the tuffs and lapilli-tuffs (Figure 5.15B) (Smellie and Hole 1997).

This transition to explosive eruptions is referred to as the passage zone (Jones 1969; Smellie and Hole 1997; Jakobsson and Gudmundsson 2008) and is evident from the distinct boundary between LFA B and Lithofacies C. LFA B at Reynisdrangar represents the eruption of fine, vitric and vesiculated tephra and the deposition of this material by direct fallout, small (ice-confined) PDCs, and reworking and resedimentation of existing deposits. Channel-like bodies and cross-stratification within LFA B indicate slump scars initiated by slope instability (Smellie and Skilling 1994).

5.6.1.3. Phase 3: magma intrusion and subaerial lava development

Considerable shoaling of the edifice results in the top of the mound becoming exposed subaerially and inhibiting Surtseyan explosivity, giving way to effusive subaerial lava formation (Figure 5.15C). The presence of free water during effusion of lava is indicated by locally erratic columnar jointing in the lower lava flow units in Lithofacies C. This free water is likely to be sourced from the confining ice sheet, and/or the remainder of the subglacial lake. As the lava sequence is thickest in the SW corner of the current Reynisdrangar tindar and the direction of onlap is from west to east, it is proposed that the venting zone that produced these lava flows was located in the SW corner. This corresponds with the large plug like body that likely fed this venting zone. There are over seven identified lava flows; however, it is unlikely these represent discrete lava eruptions but instead likely characterise several lava lobes of the one eruptive phase. The lava fills palaeotopography.

A striking difference of the Reynisdrangar tindar and other Icelandic, subglacial formations is the lack of a flow foot breccia (e.g. the Hlödufell, Laugarvatnsfjall and Middalsfjall tuyas; Jones 1969, Smellie and Hole 1997). Flow foot breccias form when subaerial lava flows in Phase 3 enter the intraglacial lake and form shallow-dipping hyaloclastite and pillow foresets at the margins of the tindar. The lack of flow foot breccias at Reynisdrangar suggests one of three possibilities: (1) the intraglacial lake had drained before the onset of subaerial volcanism; (2) flow foot breccias were formed at the very outer margins of the tindar but have been eroded away and/or not exposed; and (3) the ice sheet confined the distribution of the lavas.

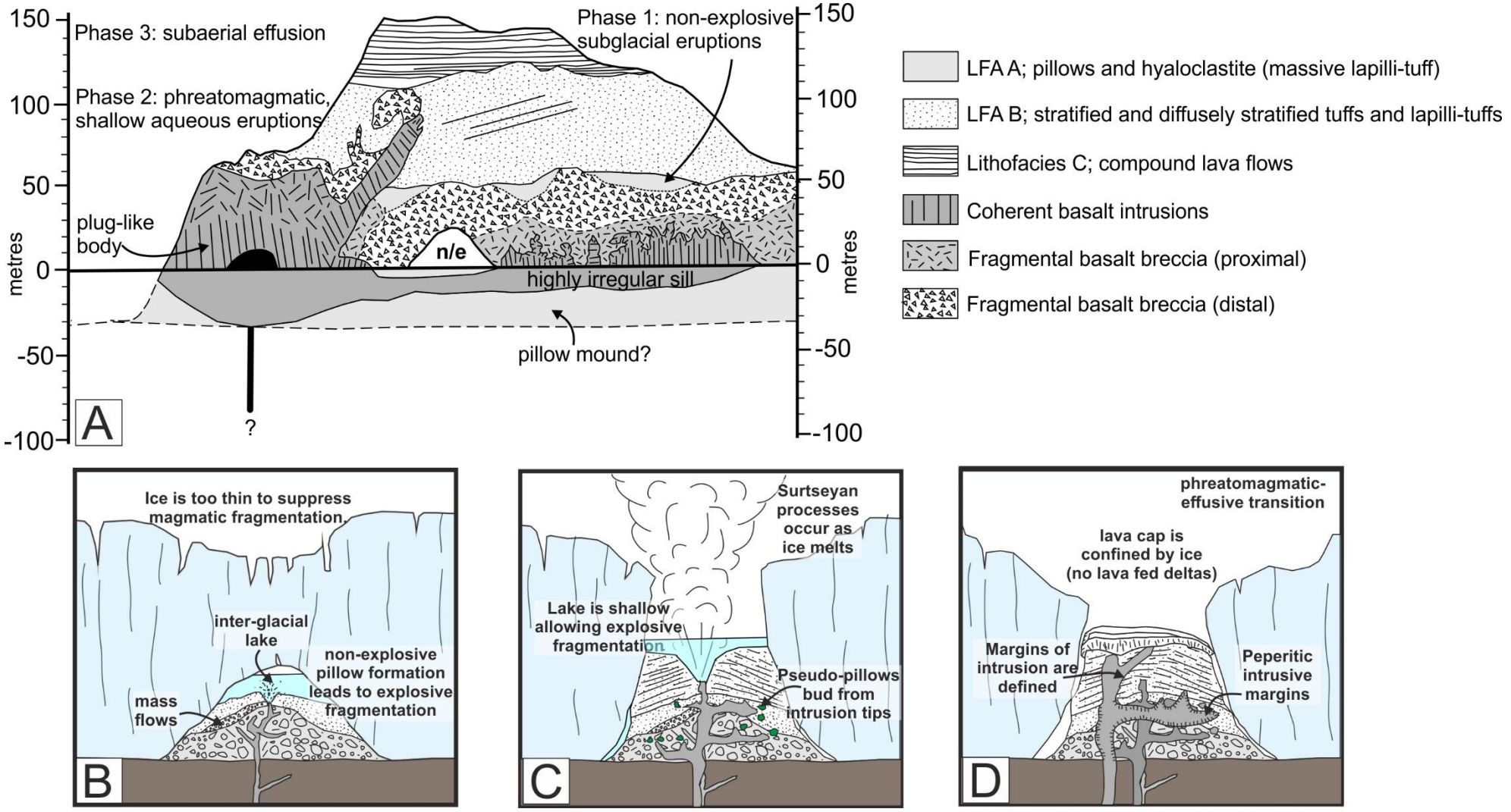
150
100
50
0
-50
-100
metres
Phase 3: subaerial effusion
Phase 2: phreatomagmatic, shallow aqueous eruptions
Phase 1: non-explosive subglacial eruptions
plug-like body
n/e
highly irregular sill
pillow mound?
?
A
LFA A; pillows and hyaloclastite (massive lapilli-tuff)
LFA B; stratified and diffusely stratified tuffs and lapilli-tuffs
Lithofacies C; compound lava flows
Coherent basalt intrusions
Fragmental basalt breccia (proximal)
Fragmental basalt breccia (distal)
Ice is too thin to suppress magmatic fragmentation
inter-glacial lake
non-explosive pillow formation leads to explosive fragmentation
mass flows
B
Surtseyan processes occur as ice melts
Lake is shallow allowing explosive fragmentation
Pseudo-pillows bud from intrusion tips
C
phreatomagmatic-effusive transition
lava cap is confined by ice (no lava fed deltas)
Margins of intrusion are defined
Peperitic intrusive margins
D

Figure 5.15: Development and evolution of the Reynisdrangar tindar. (A) Cross-section through the Reynisdrangar tindar. (B) Phase 1: the subaqueous effusive phase. Low effusion rates of magma in a subaqueous or subglacial setting produces pillows. Rapid heat transfer between magma and ice melts an ice cavity, which is filled by meltwater. As the mound grows, more ice melts, reducing the confining pressure and allowing for minor explosive interaction between magma and water. This produces hyaloclastite lapilli-tuffs and breccias with localised pillows (LFA A). (B) Phase 2: The ice continues to melt forming an intraglacial lake, confined by the remaining ice sheet. Surtseyan processes are initiated due to the relatively low hydrostatic pressure of the shallow lake. Tephra jets and continuous uprush forms highly fragmented ash and volcanic fragments, which are then deposited back into the lake and are subsequently reworked. Intrusions feeding these eruptions are highly irregular and pillows bud from intrusion tips. (C) The intraglacial lake drains away or the growth of the mound allows the top of the mound to emerge from the lake allowing for the formation of subaerial lavas. Peperitic margins form around the intrusions. (D) Deglaciation and erosion. Burial by the sandur plains obscures the lower (pillow-dominated) portion of the tindar.

5.6.2. **Monogenetic tindars can be fed by sills and inclined sheets**

The nature of the host-rock during the emplacement of intrusions at Reynisdrangar (water-saturation, consolidation and mechanically weak), promotes intrusion-induced fluidisation, resulting in the ductile emplacement of magma in the very shallow subsurface (<200 m beneath the palaeosurface) (Schofield et al. 2012). This is a common attribute for shallow magmatic bodies, where the low confining pressure of the overburden and the low mechanical strength of host-rocks in the shallow subsurface inhibits crack propagation and brittle emplacement (Lorenz and Haneke 2004; Martin and Németh 2007). Due to the failure of lithospheric strength, the magma can propagate further through the host-rock by displacing the fluidised sediment from around the leading front. Consequently, due to the monogenetic nature of subglacial edifices, throughout a subglacial eruption, magma is continually emplaced into water-saturated, unconsolidated hosts, promoting irregular intrusion morphologies (Jones 1969; Smellie and Hole 1997; Schopka et al. 2006; Jakobsson and Gudmundsson 2008; Graettinger et al. 2013).

Intrusions are common in exposed tindars (Smellie and Skilling 1994; Smellie and Hole 1997; Schopka et al. 2006; Stevenson et al 2006; McGarvie et al. 2007; Jakobsson and Gudmundsson 2008; Stevenson et al. 2011; Graettinger et al. 2013), and often show the characteristics displayed at Reynisdrangar (e.g. peperite, budding of pillows) (e.g. Werner and Schmincke 1999; Schopka et al. 2006; Jakobsson and Gudmundsson 2008); however, the scale of magma intruded into the Reynisdrangar is greater than other published studies (Jakobsson and Gudmundsson 2008). This could be a function of a lack of exposure at other tindars. However, Tuffen et al (2001, 2002) suggests that if the subglacial edifice fills the entire ice cavity, subsequent magma that intrudes into the edifice will quench because of the cool, water-saturated deposits and only a small proportion of ascending magma will reach the top of the edifice. This is the likely mechanism at Reynisdrangar, where late-stage intrusions pond in the shallow subsurface and only intermittently feed eruptions on the contemporaneous surface.

Tindars and tuyas are often built upon an unconformity, separating older, lithified rocks (greater mechanical strength) from the newly formed subglacial deposits (Smellie and Hole 1997; Wilson and Head 2002). The contrasting mechanical properties across the unconformity promote the

ponding of magma and the formation of sub-horizontal magmatic bodies (Burchardt 2008). The syn-volcanic conditions within a tindar, therefore promote the sub-horizontal propagation of magma. The outcrop at Reynisdrangar is a spectacular and important example of how sills and inclined sheets feed monogenetic subglacial volcanism, (Wilson and Head 2002).

5.6.3. **Magma-water interaction**

Magma-water interaction during subglacial intrusion emplacement is inevitable where melting ice provides a continuous supply of free water. The host-rock is therefore typically water-saturated and promotes non-explosive to explosive interaction depending on a number of factors, including: (1) water saturation of the host-rock (Smellie and Hole 1997; Tuffen 2007); (2) water content of the intruding magma (Wilson and Head 2002); (3) confining pressure (dependent on ice thickness and overlying host-rock thickness) (Jones 1969; Wilson and Head 2002); (4) volatile content of the magma (Zimanowski et al. 1997; Zimanowski 1998; Büttner et al. 1999; Zimanowski and Büttner 2003; Graettinger et al 2013); and (5) magma-water ratios (Kokelaar 1986; Wohletz 2002).

The intrusions at Reynsidrangar have undergone non-explosive interaction (proto-pillow, pillow and peperite formation) and energetic steam explosions (elongated, slurry-filled cavities, dynamic peperite domains). The intrusions were likely emplaced under a confining pressure that suppressed thermohydraulic explosions (Wohletz 1986). The presence of intrusive pillows indicates a high water to magma ratio which would also not be conducive for melt–water pre-mix generation and thermohydraulic MFCI explosions (Zimanowski et al. 1997; Wohletz 2002; Tuffen 2007).

The two mechanisms on display at the margins of the intrusions (non-explosive, cooling-contraction granulation; and steam explosions) are interrelated resulting in the overprinting and destruction of earlier textures in the host-rock (Graettinger et al. 2013).

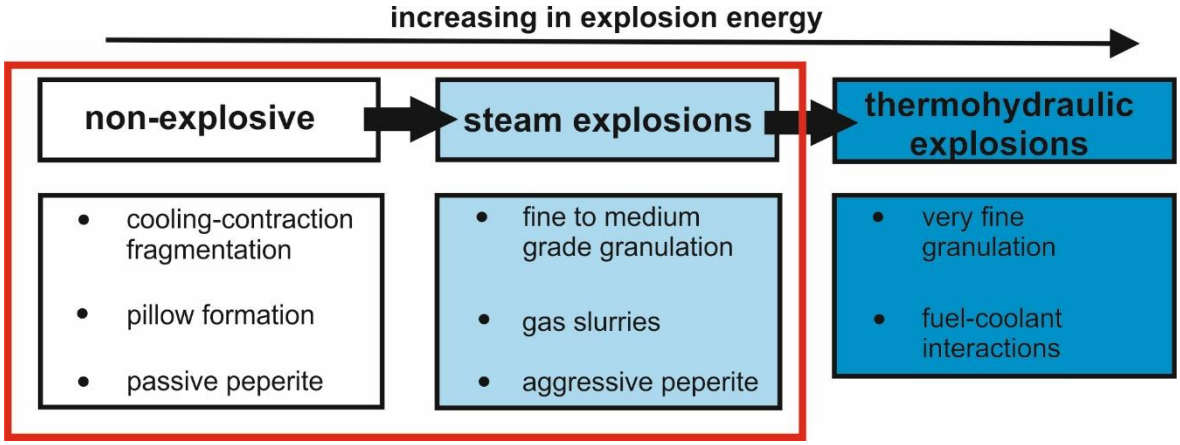

Figure 5.16: Magma-water explosivity index, indicating characteristic features of each type of magma-water interaction. Red box marks the magma-water interaction seen around the intrusions in Reynisdrangar.

Chapter 6 Subsurface groundwater setting; East Fife, Scotland

6.1. Introduction

In Fife, Scotland, there are over 100 volcanic vents. Most are inland, poorly exposed and have been determined by borehole data (Francis 1970; Leys 1982); however, along the east coast of Fife there are several diatremes that are well exposed. Five of these diatremes have been studied in detail in this chapter: (1) St Monans; (2) Ardross; (3) Elie; (4) Kincaird and (5) Ruddon's Point. The coastal exposure at these diatremes allows for the detailed examination of a horizontal cross-section through each diatreme, permitting the analysis and interpretation of the lithofacies and intrusion morphologies within the diatreme structure. The diatremes were first examined and described by Geikie (1902) and consequently by Cumming (1928, 1936), Francis (1960, 1970), Francis and Hopgood (1970) and Leys (1982). However, a re-interpretation of these diatremes is required to apply the recent diatreme research and terminology.

The volcanism in Fife is the result of crustal extension and rifting in the foreland of the Variscan Orogen during the Permian-Carboniferous (Lorenz and Nicholls 1984, Walker 1999, Gernon et al. 2013). The diatremes are exposed at different levels in the typical diatreme structure as determined by White and Ross (2011): upper bedded diatreme; lower non-bedded diatreme and root zone. The majority of the intrusions have been emplaced by ductile mechanisms, forming fluidal peperite at the margins and exhibiting highly irregular morphologies, locally, however, intrusions display evidence for brittle emplacement, likely during the latter stages of diatreme formation.

This case-study investigates the development of each diatreme through field and petrographical analysis and also examines how magma is emplaced into unconsolidated and water-saturated diatreme fill, late in the formation of the diatreme. Volcaniclastic investigations, including detailed logs of the diatreme deposits were undertaken to understand the development of each diatreme and a morphological analysis of the intrusions was undertaken to fully understand the controls of magma emplacement in subsequent eruptions of diatremes.

6.2. Geological Setting and History

The Midland Valley in Scotland extends from Ayrshire in the west, across the central belt to Angus, Perthshire, Fife and East Lothian in the east (Underhill et al. 2008). The Midland Valley is a Late Palaeozoic sedimentary basin, bounded by the Highland Boundary Fault to the north (Stonehaven to Arran) and the Southern Upland Fault to the south (Dunbar to Girvan) (Murchison and Raymond 1989; Waters et al. 2007) (Figure 6.1). The basin formed by transtensional rifting during the Namurian and Stephanian (Waters et al. 2007).

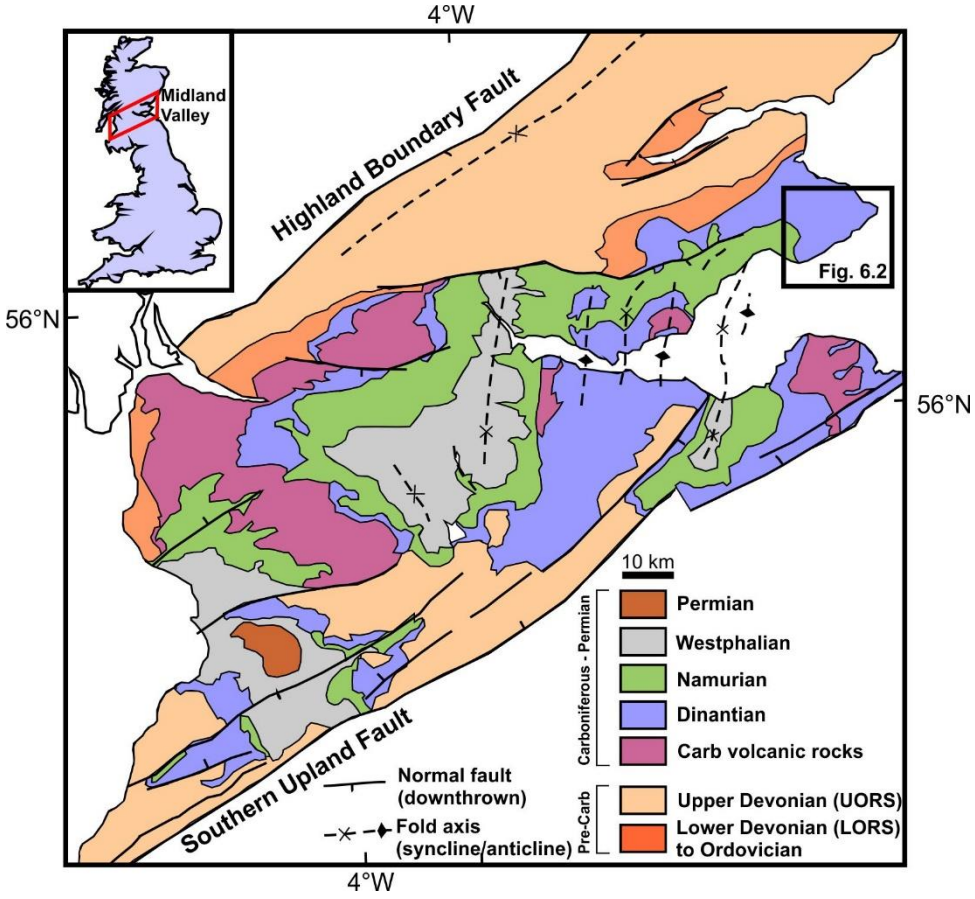

Figure 6.1: Simplified geological map of the Midland Valley (adapted from Underhill et al. 2008). The Highland Boundary Fault delineates the northern margin of the basin and the Southern Upland Fault defines the southern margin of the basin. Figure 6.2 is highlighted in the box showing the location of the study area in East Fife.

6.2.1. **Pre-Carboniferous**

The initial graben structure of the Midland Valley basin developed during the Devonian along significant lineaments associated with the formation of the Caledonian Orogeny (Cameron and Stephenson 1985; Murchison and Raymond 1989; Glennie and Underhill 1998; Underhill et al. 2008). The Caledonian Orogeny developed during the suturing and closure of the Iapetus Ocean in the Upper Silurian and Lower Devonian (Murchison and Raymond 1989; Underhill et al. 2008). Early

deposition within the basin occurred in the Devonian with the sedimentation of the Lower Old Red Sandstone, deposited during the initial subsidence of a fore-arc basin adjacent to the Caledonian mountains during the Lower Devonian (Figure 6.1) (Murchison and Raymond 1989). Conglomerates, coarse sandstones and gravels were deposited by outwash plains and alluvial fans (MacGregor 1968). Fish-beds are also present. Volcanic centres were also active during the Lower Old Red Sandstone and lavas, pyroclastic deposits and intrusions are present (MacGregor 1968). The Upper Old Red Sandstone is evident throughout the Midland Valley and was deposited in fluvial environments (Figure 6.1) (Chisholm and Dean 1974).

6.2.2. **Carboniferous-Permian**

The Midland Valley basin was the location for the accumulation of up to 3.5 km of sediment during the Carboniferous (Figure 6.1) (Fielding et al. 1988; Murchison and Raymond 1989). The Carboniferous stratigraphy of the Midland Valley of Scotland is divided into four major groups: (in order of youngest to oldest) (1) the Coal Measures Group (Upper, Middle and Lower); (2) Clackmannan Group (Passage Formation, Upper Limestone Formation, Limestone Coal Formation, Lower Limestone Formation); (3) Strathclyde Group (Pathhead Formation, Sandy Craig Formation, Pittenweem Formation, Anstruther Formation, Fife Ness Formation, West Lothian Oil-Shale Formation; Clyde Plateau Volcanic Formation) and (4) Inverclyde Group (Clyde Sandstone Formation; Ballagan Formation; Kinnesswood Formation) (MacGregor 1968; Browne et al. 1999; Waters et al. 2007). The Carboniferous sedimentary formations were deposited under cyclical swamp, deltaic and marine conditions (MacGregor 1968). Periodic increases in the relative sea level formed high-stand successions which buried coastal forests and deltas (MacGregor 1968; Waters et al. 2007). Thin limestone, marine shales and marine bands define these marine incursions. Prolonged accumulations of peat during this time has resulted in thick coal deposits (MacGregor 1968). The sediments are thought to be sourced from the Scottish Highlands to the north (Browne et al. 1999) with only minor accumulations derived from the Southern Highlands (Waters et al. 2007). The Carboniferous succession in Fife is described in Table 1 and is based on the lithostratigraphical nomenclature proposed by Browne et al. (1999).

Series	Stage	Groups	Formations	Lower Margins	General characteristics	Depositional environment
Westphalian	Bolsovian	Scottish Coal Measures	Upper Coal Measures	Skipsey's Marine Band	Repeated cycles of grey (upward-fining) sandstone, mudstone and coal/seatearth. Mudstones contain non-marine "musselbands". Marine bands are rare. Coal seams are economical in the Lower and Middle Formations	Swamps and wetland forests gave way to floodplain, fluvial and deltaic (prograding and distributary channelled) settings and shallow lakes.
	Duckmantian		Middle Coal Measures	Queenslie Marine Band		
	Langsettian		Lower Coal Measures	Lowstone Marine Band		
Namurian	Chokierian-Yeadonian	Clackmannan Group	Passage Formation	Castlecary Limestone	Cyclical beds of coarse-grained sandstones, conglomerates, mudstones, black shales and localised beds of limestone, coal and ironstone. Marine faunas are apparent at the base of the formation and gradually decrease.	Forested deltaic conditions with only minor marine incursions.
	Arnsbergian		Upper Limestone Formation	Index Limestone	Upward-coarsening repetitions of marine limestones, shales, siltstones and white sandstones, topped by coals and seatrocks. Localised ironstones	Cyclical sedimentation between forested deltaic conditions and prolonged shallow marine conditions. Clear-water limestone formation was inhibited so marine beds are rare (MacGregor 1968).
	Pendleian		Limestone Coal Formation	Top Hosie Limestone	Upward-coarsening mudstone, siltstone and white sandstone, topped by coal. Thin coal beds are evident. Clayband ironstone is well developed in the shales. Non-marine *Lingula* beds.	Forested deltaic conditions formed thick peat units (coal) with occasional marine incursions forming thin limestone bands.
Viséan	Brigantian		Lower Limestone Formation	Hurlet Limestone	Upward-coarsening repetitions of marine limestone, black mudstone, dark grey siltstone and white sandstone with minor beds of seatearth and coal. Clayband ironstones have developed in the shales.	Relative sea-level rise allowed the formation of clear water marine limestones in shelf seas. The limestones were flooded with silt and mud which gave way to prograding deltaic conditions and the formation of coastal forests. Another marine incursion buried forests and formed marine clays and later limestones formed.

Series	Stage	Groups	Formations		Lower Margins	General characteristics	Depositional environment
		Strathclyde Group	Pathhead Formation		West Braes Marine Band	Mudstone, siltstone and limestone/dolomite interbedded with cycles of white/pale sandstone. A few thin coal beds. Upward-coarsening deltaic cycles, topped by fluvial sequences.	Deltaic systems and swamp environments with minor marine incursions drowning forests and forming marine shales and limestones. Substantial lacustrine environments were evident due to the presence of algal-rich oil shales. *Clyde Plateau Volcanic Formation: Lavas, tuffs and volcaniclastic sedimentary sequences.
	Asbian		Sandy Craig Formation		St Andrews Castle Marine Band	Interbedded mudstone and siltstone. A few oil shale beds, coal and thin limestone and dolomite beds. Upward-coarsening deltaic cycles, topped by fluvial sequences.	
	Arundian-Holkerian		Pittenweem Formation	*Clyde Plateau Volcanic Formation	Cuniger Rock Marine Band	Interbedded mudstone and siltstone. Minor limestone, dolomite and marine mudstones beds. A few oil shale beds. Upward-coarsening deltaic cycles, topped by fluvial sequences.	
	Chadian		Anstruther Formation		Not known (transitional from sandstone-dominated to mudstone-dominated)	Thin cycles of mudstone, siltstone and sandstone with localised non-marine limestone. Oil shale beds present. Thin beds of coal are also present.	
	Chadian		Fife Ness Formation		Carbonate conglomerate in the "Fluke Dub" section	Upward-fining, white sandstone sequences interbedded with seatearths and argillaceous beds. No coal present.	
Tournaisian		Inverclyde Group	Clyde Sandstone Formation		Transitional from Ballagan Formation to white sandstone and pedogenic strata	Cyclical transitions between calcareous and dolomitic sandstones; and mudstones. Pedogenic carbonate beds and nodules, cementstones and evaporites (mainly gypsum) are evident.	Semi-arid climate. Sandstones and mudstones deposited in stable alluvial plains and marginal marine or lacustrine flats. Occasional dessication occurred producing evaporite beds. Alluvial fans deposited in the Ballagan Formation
	Courceyan		Ballagan Formation		Transitional from the Kinnesswood Formation to mudstone-cementstone		

Series	Stage	Groups	Formations	Lower Margins	General characteristics	Depositional environment
			Kinnesswood Formation	Transitional from Aeolian sandstone to carbonate bearing strata		

Table 6.1: Description and depositional environment of the Carboniferous stratigraphy in Fife (MacGregor 1968; Fielding et al 1988; Browne et al. 1999; Guirdham et al. 2003; Kassi et al. 2003; Waters et al. 2007). The distribution of these formations in East Fife is illustrated in the geological map in Figure 6.2.

During the Upper Carboniferous, Variscan lithospheric compression led to tectonic inversion and the reversal of shear sense on faults from sinistral to dextral (Stephenson et al. 2003). This reversal gave rise to compression and folding of the Carboniferous stratigraphy during Westphalian times, forming several folds of considerable amplitude (e.g. St Monans Syncline, Anstruther Anticline) (Figure 6.1) (MacGregor 1968; Read 1988; Stephenson et al. 2003; Underhill et al. 2008). Major faults are also recognised, the majority of which are thought to post-date volcanism in the Upper Carboniferous and Lower Permian (Figure 6.1) (Leys 1982; Underhill et al. 2008).

Volcanism occurred throughout the Carboniferous and into the Early Permian (Figure 6.1; Figure 6.2) (Stephenson et al. 2003; Monaghan and Browne 2010). During the Lower Carboniferous, significant lithospheric tensional stretching and back-arc extension formed major crustal fractures. Alkali olivine-basalt magmas were erupted from these fractures and formed large lava fields (Murchison and Raymond 1989; Stephenson et al. 2003). Dolerite sill complexes, plugs and eruptive centres were intruded during this time, including Arthur's Seat in Edinburgh, the Clyde Plateau Volcanic Formation and the Midland Valley Sill Complex (Figure 6.2), and are intruded into stratigraphy up to the Passage Formation (MacGregor 1968) (Table 1). During the Upper Carboniferous and Lower Permian, magma was erupted by major intracontinental rifting into lagoonal or shallow marine environments, which promoted phreatomagmatic and Surtseyan-type volcanic activity, producing monogenetic edifices, dyke swarms and widespread tuff horizons (Murchison and Raymond 1989; Stephens et al. 2003) (Figure 6.2). In Fife, lavas and tuffs are interbedded in the Sandy Craig and Pathhead Formations (Table 1) and are referred to as the Kinghorn Volcanic Formation (Browne et al. 1999; Guirdham et al. 2003; Rawcliffe 2016). Quartz dolerite sills and dykes were also intruded during the Upper Carboniferous, post folding (MacGregor 1968). In East Fife, alkaline basic magmas exploited crustal fractures forming the diatremes discussed in this chapter.

6.2.3. **Post-Permian**

There are no exposures of post-Carboniferous, pre-Pleistocene stratigraphy in the Fife area of the Midland Valley. It has been proposed that there may have been a thin Mesozoic sequence which has subsequently been eroded, however this is theoretical (MacGregor 1968).

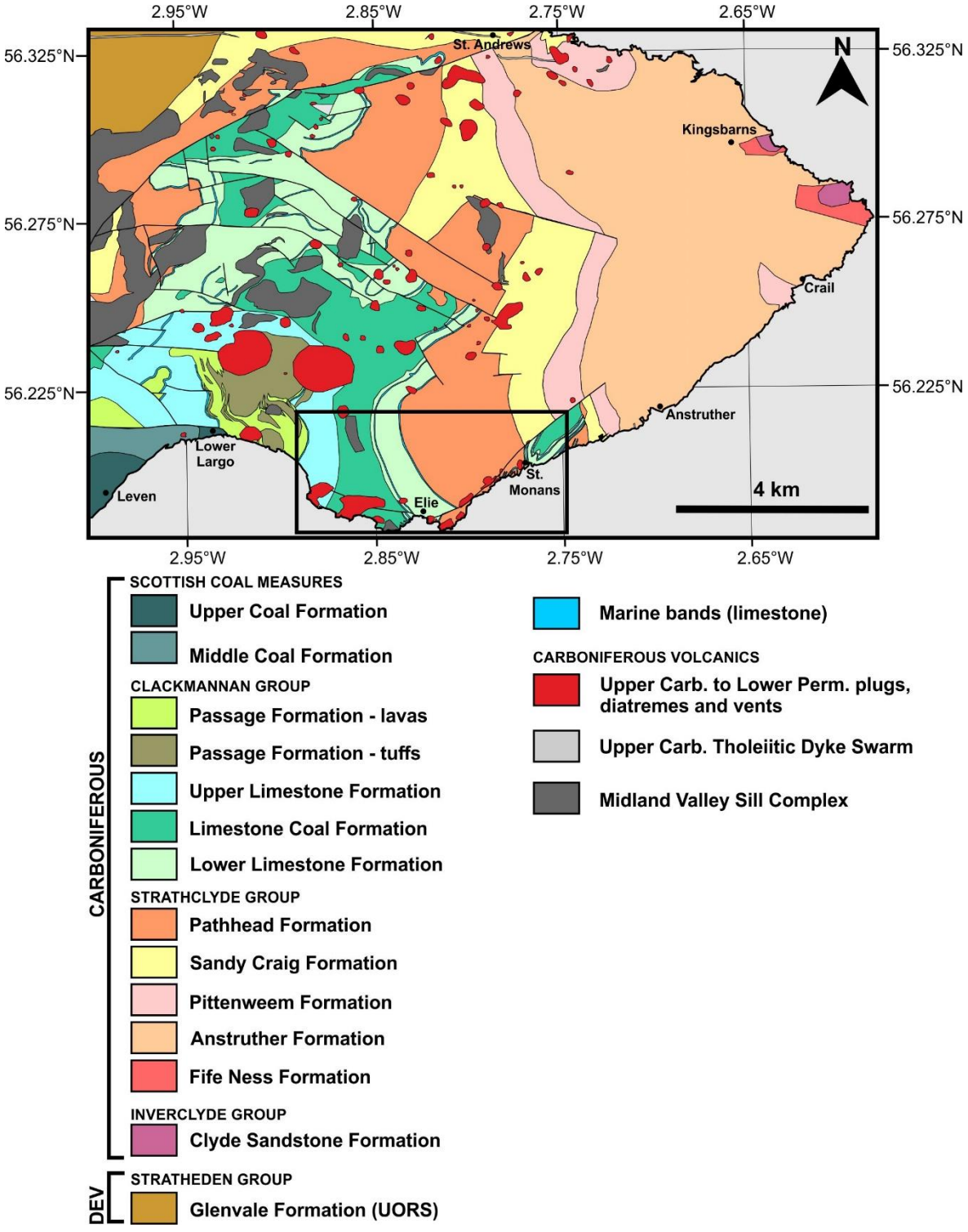

Figure 6.2: Simplified geology map of East Fife (location shown in Figure 6.1). Map shows the distribution of the stratigraphical formations described in Table 6.1. The distribution of intrusive volcanics (sills, diatremes) are also shown (red and grey shading). Location of study area is in the black box.

6.3. Location and Geomorphology

The five diatremes studied in this chapter are distributed along the Ardross Fault, which likely influenced the emplacement of magma and thus the distribution of the edifices (Francis and Hopgood 1970; Gernon et al. 2016). The diatremes are well exposed along the south and east coast of Fife (Figure 6.2). The location of the five diatremes are shown in Figure 6.3. The Ruddon's Point, Elie Ness, Ardross and St. Monans diatremes are exposed in the intertidal zone along the foreshore, providing a horizontal cross section through the diatreme fill deposits and host-rock margins. Conversely, the Kincaird diatreme consists of 20-40 m high cliffs which are accessible at low-tide via the Fife Chain Walk, and provide a vertical cross-section through the middle of the diatreme. At all the diatremes, the diatreme fill has a distinctive green colour due to significant alteration of the tuffs to clay and chloritisation of the pyroxenes within the basalt and tuff.

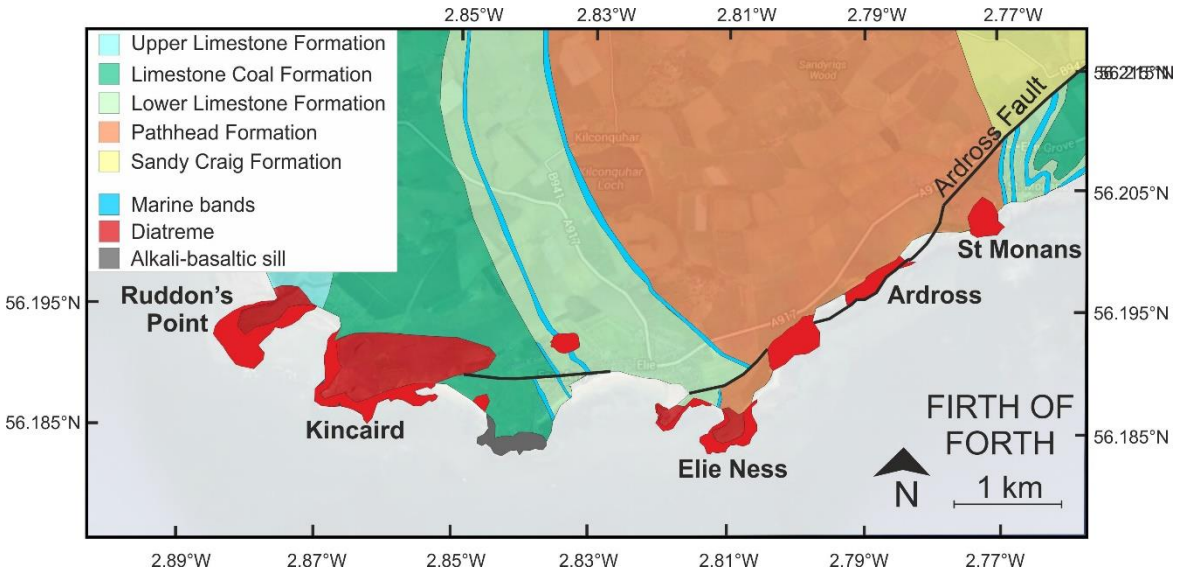

Figure 6.3: Location and geology map of the five diatremes selected for this study. The diatremes (Ruddon's Point, Kincaird, Elie, Ardross and St Monans) are all distributed along the Ardross Fault. Location of this study area is highlighted in Figure 6.2.

6.4. Lithofacies and Lithofacies Assocations: Observations and Interpretations

The diatreme fill in each of the diatremes is divided into the following lithofacies associations, based on their general structural and grain size characteristics: (A) stratified lapilli-tuffs and tuffs; (B) crudely bedded lapilli-tuffs and breccias; (C) massive breccia and lapilli-tuffs; (D) autolith-bearing breccia; (E) massive clast-supported basalt breccia and peperite; and (F) host-rock and volcanic breccia. coherent intrusions; and volcaniclastite injectite. A summary of the characteristics and mode of deposition/emplacement is shown in Table 6.2. The composition and distribution of each of these lithofacies associations at each of the diatremes is described and illustrated in Section 6.6. The disruption of the host-rock is described and interpreted in Chapter 7. An A3 fold out of maps of all the diatremes is provided in the Appendix (Appendix 10.3).

Lithofacies & Lithofacies Associations	Abbrev	Locality	Description	Interpretation	Diatreme zone
LFA A: Stratified lapilli-tuffs and tuffs	sLT/ sT	SM, E, K, R	Alternating tuff and lapilli-tuff layers, containing angular basalt clasts, angular to sub-rounded juvenile clasts (fluidal morphologies), host-rock inclusions, dispelled crystals (pyroxene and plagioclase) and pyroxenite clasts. Stratifications are mostly planar, although cross-stratification and channel-cut erosion is evident. Normal grading is apparent throughout. Bomb impact sags and scours are also seen.	Multiple small volume eruptions, produced numerous fully dilute, traction-dominated pyroclastic density currents (PDCs) at the surface of the diatreme. Additionally, ballistic transport mechanisms, base surge deposits and direct fallout from eruption columns are apparent.	Upper
LFA B: Crudely bedded lapilli-tuffs and breccia	dbLT/ dbBr	A, E, K, R	Diffusely bedded lapilli-tuffs and breccias which lack internal stratification. Bedding is 20 cm to 1.5 m thick. LFA B is often found within LFA A as thick basalt dominated breccias. Basalt clasts are angular and are up to 1.5 m wide.	Rapidly deposited by high energy, high particle concentration debris flows into the vent. The massive breccias are likely to indicate lahar deposits and the massive lapilli-tuffs were deposited by dense underflows in PDCs (Freundt and Schmincke 1985; Gernon et al. 2013).	Upper and middle
LFA C: Massive breccia and lapilli-tuff	mBr/mLT	SM, A, E, K, R	Breccias and/or lapilli-tuffs that have no internal structure and can have a discordant relationship with the surrounding bedded units. Found either in a discordant vertical column or at the margins of the diatreme. Regularly contain large and fluidal host-rock sediment inclusions and/or mingles with host-sediment. Also contain fluidal to angular juvenile clasts, sub-angular and sub-rounded basalt clasts and boulders. Matrix-supported or clast-supported	Discordant zones represent debris columns. Debris columns are the products of upward-projected debris jets consisting of a slurry of ash, volcaniclastic debris, steam and magmatic gases that are produced by subsurface phreatomagmatic explosions. Marginal massive zones are either produced by debris columns or subsidence zones. Subsidence zones are formed by subsidence of surface-derived material. The material slides down the walls of the diatreme	Debris columns; Upper and middle
Lithofacies D: Autolith bearing breccia	mLT(auto)	SM, A, K	Autolith-bearing, massive breccia. The angular autoliths are composed of massive and stratified tuffs and lapilli-tuffs (mT; mLT; dsT; dsLT; xsLT). Local sediment inclusions and basalt clasts. The autoliths range in size from sub-cm to metre-scale bodies (<2 m) and often display stratification and cross-stratification (mm- and cm-scale lamination). Commonly found at the margins of the diatremes.	Formed in subsidence zones around the margins of the diatreme. As the surface diameter of a diatreme gets wider through diatreme formation, it causes portions of the stratified tuff ring to collapse into the crater. These stratified megablocks become autoliths in marginal unbedded zones.	Upper and middle (margins)
LFA E:	mBrl	SM, A, E, K, R	Discordant zones of basalt-rich breccia and blocky peperite. Dyke-like intrusions brecciate into aligned and isolated pods of basalt or clastogenic bodies of basalt, which further feed peperitic zones. Tuffaceous matrix fills fractures within the	Peperitic domains are formed by non-explosive or mildly explosive interaction between newly invading hot magma and the unconsolidated and typically wet	Intrusion-related

Lithofacies & Lithofacies Associations	Abbrev	Locality	Description	Interpretation	Diatreme zone
Basalt breccia, peperite and pods of basalt			pods and peperite. The basalt breccia consists of angular basalt clasts (sub-cm to metre scale clasts) supported within a tuffaceous matrix. Rare pyroxenite crystal assemblages are evident within the matrix (Elie).	diatreme deposits. Pods of basalt are formed when mildly explosive interaction occurs.	Intra-diatreme fragmentation zones
Lithofacies F: Host-rock and volcanic breccia	mBr(sed)	SM, A	The breccia comprises matrix-supported metre-scale, coherent host-rock inclusions and basalt boulders within a tuffaceous matrix. The host-rock inclusions are up to 2 m across and retain depositional features including fossils (crinoids within limestones) and lamination.	Lithofacies F is partially formed by the widening of the diatreme causing metre-scale host-rock inclusions to become entrained within the diatreme.	Middle (margins)
Coherent Intrusions	-	SM, A, E, K, R	Basinite and foidite intrusions (<44% SiO_2). The intrusions are aphyric and locally porphyritic, and are fine to medium. Most intrusions are dykes which have brecciated upon emplacement into the soft diatreme deposits. Coherent inclined sheets (<30 m thick) are also present.	Coherent dykes represent the waning phase of volcanic activity but may also represent feeder dykes that fed high-level phreatomagmatic explosions. Dykes are emplaced by mostly non-brittle mechanisms. Clastogenic bodies are formed by the opening of brittle fractures due to cooling and quenching of a dyke. Mild to moderate steam explosions may occur to aid clast dispersal.	Upper and middle
Volcaniclastic injectite	mLT/ mBr	E, K	Injectites are commonly found around the margins of the diatremes or around debris columns and range from <5 cm to 90 cm. The margins of the injectites are typically well-defined and can exhibit both straight and undulating boundaries. The injectites are comprised of tuffs and lapilli-tuffs and contain juvenile clasts, basalt clasts, fluidised sediment inclusions (coal, sandstones, siltstones, mudstones and limestones) and tend to be thoroughly exploited by calcite hydrothermal veins.	Heat input by intrusion emplacement stimulates fluidisation and mobilisation of the diatreme fill (tuffs and lapilli-tuffs) which can be injected into the surrounding diatreme and/or host-rock.	Upper and middle (margins)

Table 6.2: Characteristics and interpretations of each of the main lithofacies and lithofacies associations (LFA) found within the diatreme. Abbreviated terms are suggested after White and Houghton (2006). Location of each of the lithofacies and LFA is stated (SM = St Monans; A = Ardross; E = Elie; K = Kincaird; R = Ruddon's Point).

6.4.1. **Lithofacies Association A (LFA A): Stratified lapilli-tuffs and tuffs (SM, E, K, R)**

6.4.1.1. Description

Lithofacies association A (LFA A) comprises alternating tuff and lapilli-tuff layers defined by grain size and composition (Figure 6.4A and B). The green lapilli-tuff layers are clast-supported and contain juvenile clasts (0.05 – 8 mm) (<70% clasts), locally displaying jigsaw fit textures, cm-scale, angular basalt clasts, rare pyroxenite clasts (<3 cm) and host-rock inclusions. The juvenile clasts display both angular morphologies (Figure 6.4C and D) and distinctive sub-rounded morphologies with fluidal margins (Figure 6.4E and F). The host-rock inclusions within LFA A have varying scales (sub-mm to decimetre) and varying composition (dependent on host-rock formation) (Figure 6.4B). The host-rock inclusions tend to have highly fluidal morphologies. The dark grey tuff stratifications are matrix-supported and contain a small proportion of angular juvenile clasts and basalt (<15%) (Figure 6.4A). The matrix is comprised of fine, palagonitised ash, tachylite fragments and contains comminuted black pyroxene and plagioclase feldspar crystals (sub-mm) (Figure 6.4D, F). Large decimetre-scale coherent, basalt clasts are present (<80 cm) and are angular to sub-rounded. Locally, the laminations surrounding these basalt clasts have been distorted and deformed by the deposition of the clast (Figure 6.4C).

The stratifications are both diffuse and convoluted (Figure 6.4G), and defined and planar (Figure 6.4A). The stratifications are 1 cm to 1.5 m thick and are mostly laterally continuous for up to 10 m however lenses are also evident that are laterally extensive for up to 1 m. At several localities, low angle cross-stratification and flat U-shaped channels are evident (Figure 6.4A, G and H) and pinching and swelling of beds is common. Normal grading within tuff laminations is also apparent, particularly at the Kincaird diatreme (Figure 6.4B). Some stratifications have eroded and undulating top margins (Figure 6.4H). Scouring of the underlying layers is also common throughout (Figure 6.4H). Where peperite is present within the unit, LFA A has fluidised forming diapirs and flame structures that disrupt the stratifications.

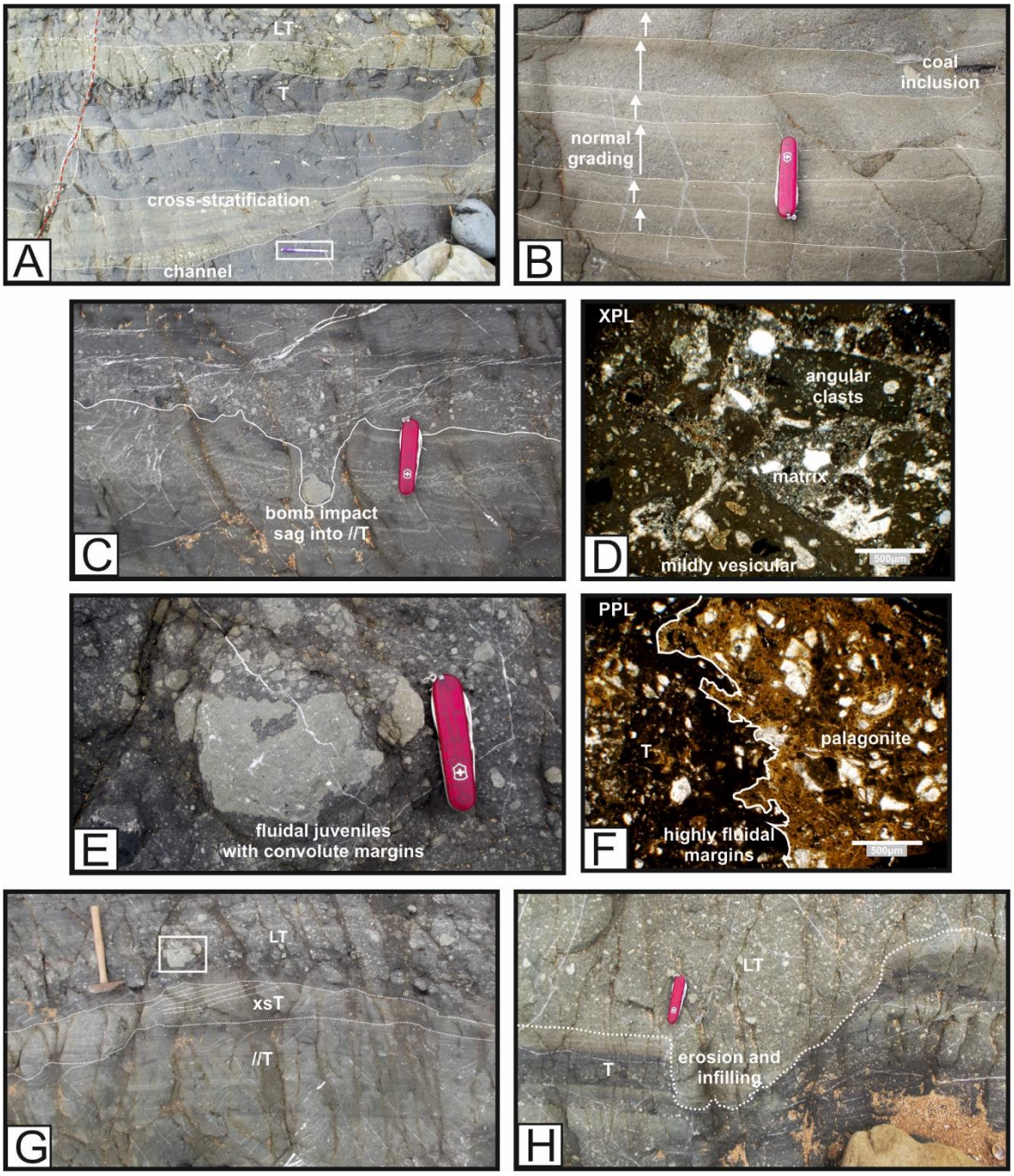

Figure 6.4: Images of LFA A from the Kincaird diatreme. Pen-knife is 10 cm long. (A) Alternating layers of green lapilli-tuff and dark grey fine tuff. The stratification is mostly planar but occasional channels are present filled with cross-stratified lapilli-tuffs. Pen is 15 cm long. (B) Normal grading is evident in tuffs. In this example there is a host-rock inclusion of coal within the tuffs. Laminations are 2-8 cm thick. (C) Impact sag within stratified tuffs. Bomb is 4 cm wide and has well-defined angular margins. The impact structure is infilled with subsequent lapilli-tuffs. (D) Photomicrograph of LFA A from the Ardross diatreme. Mildly vesicular, very fine basalt clasts are evident within an ashy matrix comprised of quartz grains (comminuted from host-rock inclusions), glass fragments and fine tuff fragments. The basalt clasts display very angular clast morphologies, occasionally cuspate where the margin intersects a vesicle. (E) Location of image is shown in (G). Large fluidal juvenile (~ 12 cm x 10 cm) with jigsaw fit textures and convolute margins. (F) Photomicrograph from LFA A from the Kincaird diatreme (Log 1). Tachylite (T) lapilli have very fluidal margins. (G) Planar-stratified and cross-stratified tuffs overlain by a diffusely-stratified lapilli-tuff unit. Box shows location of Figure 6.4D. Hammer is 40 cm long. (H) Scouring of underlying stratified beds and infilling with lapilli-tuff.

6.4.1.2. Interpretation

The characteristics of LFA A (multiple, thin layers; fine tuff to lapilli) are recognised as the products of multiple small volume eruptions, which are commonly associated with phreatomagmatic activity and diatreme formation (White and Ross 2011; van Otterloo and Cas 2016; Lorenz et al. 2017). These small phreatomagmatic eruptions can produce numerous pyroclastic density currents (PDCs) at the surface of the diatreme which deposit individual beds with varying thicknesses (a few millimetres to several decimetres) and variable characteristics (coarse lithic clasts, accidental lithics, bomb lapilli, lapilli ash and ash deposits) (Valentine et al. 2015; Cas et al. 2016; Lorenz et al. 2017). The planar stratification, low-angle cross stratification and flat U-shaped channels within LFA A indicate that the unit was deposited by fully dilute, traction-dominated PDCs (Branney and Kokelaar 2002; Graettinger et al. 2015; Valentine et al. 2015; van Otterloo and Cas 2016; Cas et al. 2016; Lorenz et al. 2017). Normal grading is common throughout Lithofacies A and demonstrates waning current competence during each individual eruption. Presence of scours at the base of layers, eroded top margins, lensing and pinching and swelling of beds indicates that the deposits were transported and deposited predominantly by base surge mechanisms (Sohn and Chough 1989; Lorenz and Zimanowski 2008; Graettinger et al. 2015; Valentine et al. 2015; Cas et al. 2016; Borrero et al. 2017; Saucedo et al. 2017).

In addition to deposition by PDCs and base surges, other transport and deposition mechanisms are involved. Fine, well sorted ash layers are attributed to ash fallout from small PDC plumes or eruption columns (van Otterloo and Cas 2016; Cas et al. 2016). Ballistic blocks of basalt have created impact sags in the lithofacies due to the soft nature of the deposits. The impact causes ductile deformation of the underlying deposits and indicates a ballistic transport mechanism (Sohn and Chough 1989; White and Ross 2011; Valentine et al. 2015; Cas et al. 2016; Lorenz et al. 2017; Saucedo et al. 2017). The presence of fluidal juvenile clasts suggests the juvenile clasts were still hot and malleable when they were erupted (Figure 6.4D). Fluidal juvenile clasts are produced directly from the magma source. Conversely, angular juvenile clasts suggest a relatively cool emplacement and are, therefore, likely to have undergone recycling within the diatreme.

The stratified nature of LFA A indicates the unit was formed at the surface. The beds are buried by subsequent erutpions. Subsidence occurs due to eruptions leaving voids within the root zone. Subsidence caused the centroclinal bedding patterns found at all the diatremes studied (see Appendix 10.3). The stratified nature of the LFA A beds are widely recognised as the upper zone within a diatreme (White and Ross 2011).

6.4.2. **Lithofacies Association B (LFA B): Crudely bedded lapilli-tuffs and breccias (A, E, K, R)**

6.4.2.1. Description

Lithofacies assocation B (LFA B) is composed of angular and fluidal juvenile clasts, angular and sub-angular basalt clasts (up to 1.5 m across), host-rock inclusions (usually fluidal and comprised of sandstones, limestones, shales and coals), dispersed crystals (pyroxene, plagioclase and rare garnets, biotites, amphiboles, quartz, zircons) and crystal assemblages (e.g. pyroxenite clasts). LFA B is mostly massive (Figure 6.5A) or in some cases the stratification is poorly defined (Figure 6.5B). LFA B can be found interbedded within LFA A. Beds are thick (>1 m). Basalt clasts are, on average, larger than the clasts found in LFA A and are more abundant (5 – 40%) (Figure 6.5A).

6.4.2.2. Interpretation

The thickness of the beds suggest LFA B was deposited rapidly by highly concentrated flows in a proximal location to the vent. The massive lapilli-tuffs within LFA B likely represent dense underflows in PDCs (Freundt and Schmincke 1985; Gernon et al. 2013). The diffuse stratification is a product of granular-flow dominated, fluid-based PDCs, which supports particle-particle interaction and percolation of fines and the large basalt clasts are the result of ballistic clasts that have rolled out of impact sags.

The breccia beds within LFA B likely represent lahar deposits, where wet tuff ring deposits collapse into the crater and are reworked and incorporated into the diatreme (Lorenz 1986, 2007; Boxer et al. 1989; Stachel 1990; Lorenz and Kurszlaukis 2007; Lorenz et al. 2017). Lahar deposits are commonly interbedded with thinly bedded PDC deposits in the upper diatreme zone (Lorenz et al. 2017). These lahar beds are typically 0.5 m to 10 m thick (Lorenz 1986, 2003; Boxer et al 1989; Stachel 1990). LFA B is commonly interbedded within Lithofacies A.

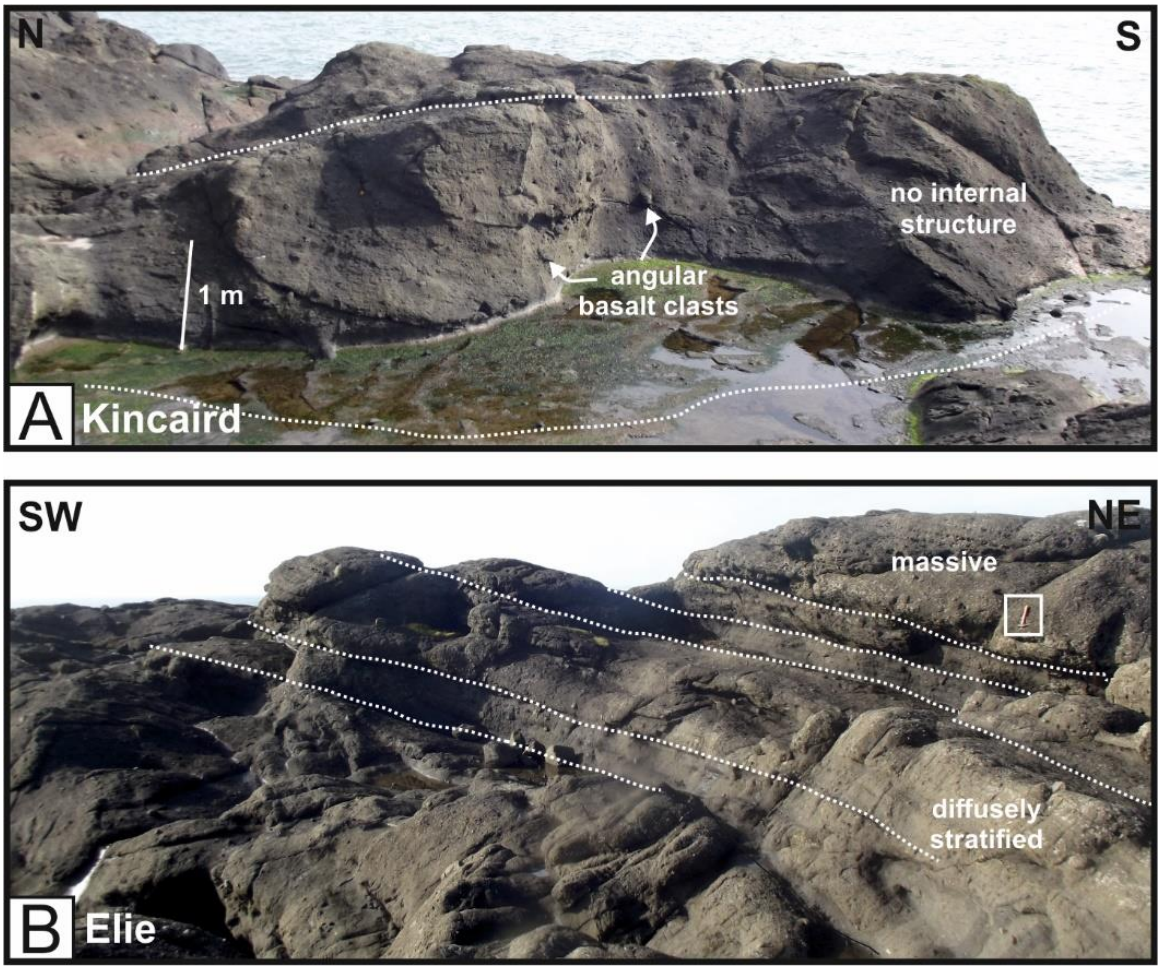

Figure 6.5: Images of LFA B. (A) Kincaird diatreme. Crudely bedded lapilli-tuffs and breccia. No internal structure within each bed and large angular basalt clasts (>10 cm). Beds are up to 2.5 m thick. (B) Elie diatreme. Crudely bedded lapilli-tuff. Locally, the beds are diffusely stratified. Hammer is 40 cm long (boxed).

6.4.3. **Lithofacies Association C (LFA C): Massive breccia and lapilli-tuffs (SM, A, E, K, R)**

6.4.3.1. Description

Lithofacies association C (LFA C) is characterised by a massive breccia or lapilli-tuff that commonly contains large host-rock sediment inclusions and/or mingles with host-sediment (mudstones, siltstones, sandstones, coals and limestones). LFA C is massive, with little to no internal structure and can be either matrix-supported or clast-supported. LFA C occurs either: (1) at the margins of the diatremes (<150 m wide margins) (Figure 6.6A); or (2) as discordant cylindrical bodies within the diatreme (Figure 6.6B). Zones of non-bedded pyroclastic material occur in all five diatremes studied, and proportionally occupy <5% to 50% of the exposures. The discordant bodies tend to have defined, steep contacts between bedded and non-bedded diatreme fill. In plan view the massive zones typically have oblate shapes and range from 10 to 50 m in diameter.

LFA C is comprised of very fine to coarse juvenile clasts and sub-angular and sub-rounded basalt clasts within an ash matrix. Additionally, pyroxenite crystal assemblages (2 – 3 cm) and disseminated individual pyroxene and plagioclase feldspar crystals (sub-mm) are evident within the matrix, and stratified tuff or lapilli-tuff autoliths (3 – 20 cm) are also present (Figure 6.6C). Proportions of these components differ across the diatreme localities.

The shape of the juvenile clasts vary at each location, displaying both highly fluidal and strung out morphologies (1 – 25 cm) (Figure 6.6D), and angular morphologies. The sub-angular and sub-rounded basaltic lithic clasts display both vesicular and non-vesicular textures (0% to ~35% vesicular). The maximum size of a coherent basalt clast is 1.5 m at Kincaird (Figure 6.6B). Boulders >1 m locally display columnar jointing. The composition and grain size of the sediment inclusions depends on the host-rock formation which the diatreme has intruded into. Commonly, however, fluidised red siltstone is evident at all diatremes, in particular Kincaird and St Monans (Figure 6.6E, G). These inclusions tend to form coherent, well-defined inclusions (Figure 6.6E, F) or are strung out and have highly fluidal morphologies that interdigitate with the surrounding diatreme fill (Figure 6.6G, H). They can be up to 4 m long. R-T structures are observed within the sediment inclusions (Figure 6.6E). Intensive mingling has produced a homogeneous mix of the host-sediment inclusions and ash, where quartz grains are comminuted from the host-rock inclusions in the tuff deposits (Figure 6.6G, H).

6.4.3.2. Interpretation

Zones of massive pyroclastic material (LFA C) are identified along the margins of the diatreme and within isolated, discordant cylindrical bodies. The discordant bodies likely represent debris columns that are commonly found in other diatreme volcanic systems (White 1991; Naidoo et al 2004; McClintock and White 2006; Ross and White 2006; Lefebvre et al. 2013). Debris columns are the products of upward-projected debris jets consisting of a slurry of ash, volcaniclastic debris (e.g. feeder dyke fragments and host-rock inclusions) steam and magmatic gases that are produced by subsurface phreatomagmatic explosions (Ross and White 2006; White and Ross 2011) (Figure 6.7).

These explosions can occur anywhere in the diatreme structure and are not just confined to the root zone, although they are commonly found in the lower, non-bedded zone of the diatreme

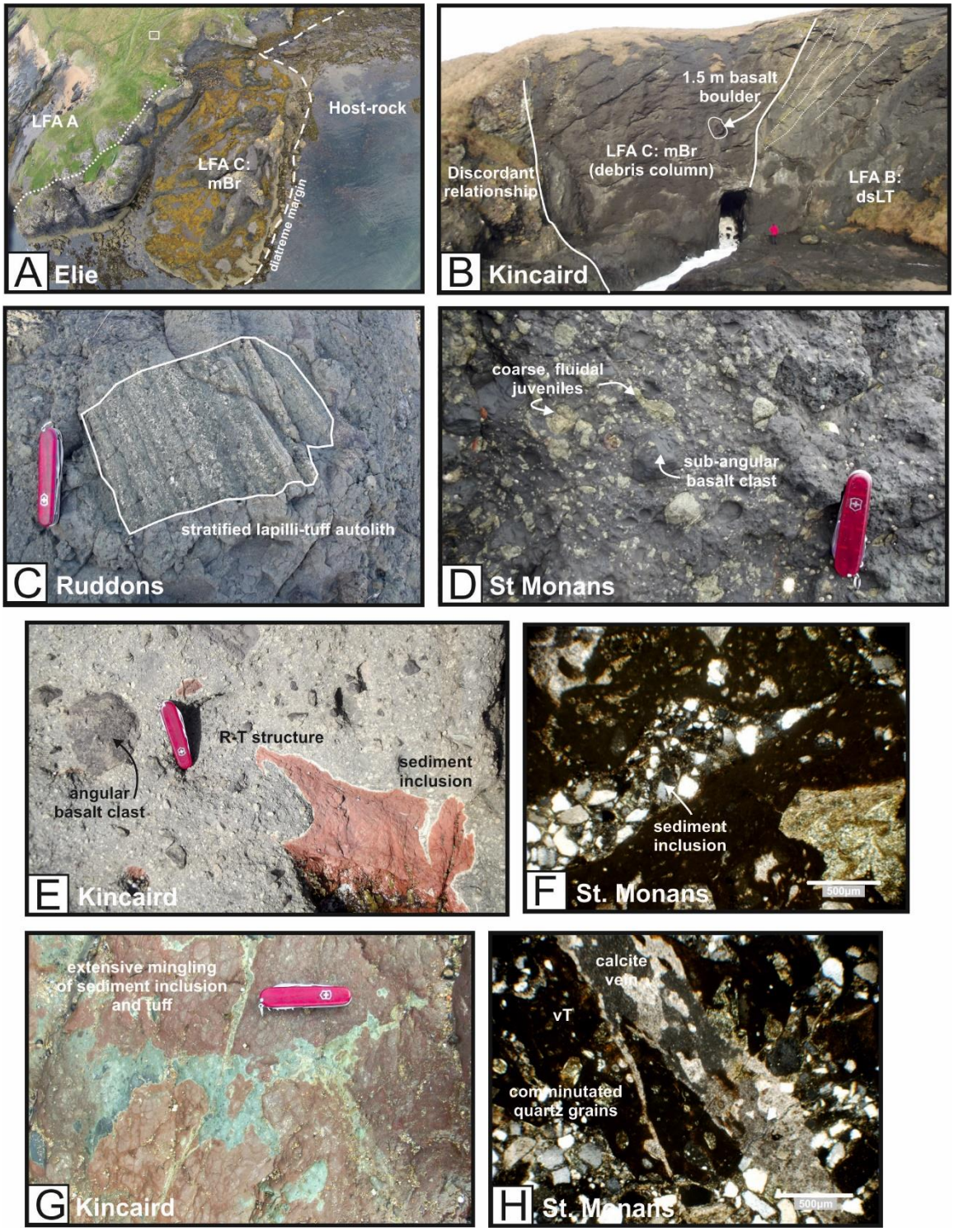

Figure 6.6: Images of LFA C. (A) Aerial photograph of the northeast margin of Elie diatreme. Person for scale (boxed). The massive breccia is located at the margins of diatremes. (B) LFA C is also located in discordant vertical bodies like the one seen in this image of Kincaird diatreme. Boulders within the column are up to 1.5 m in diameter. Person for scale. (C) Stratified lapilli-tuff autoliths are observed within LFA C (Ruddons diatreme). Pen-knife is 10 cm. (D) Juvenile clasts within LFA C display both fluidal morphologies and angular morphologies. This image is from the southwest margin of the St Monans diatreme and shows fluidal juvenile clasts. (E) Sediment inclusions from the host-rock stratigraphy are found throughout LFA C and display highly fluidal geometries. The sediment inclusion in this image is from Kincaird and displays R-T structures. (F) Photomicrograph (xpl) from LFA C within the St. Monans diatreme showing a coherent sediment inclusion within the tuff deposits. (G) Intensive mingling of sediment inclusions and tuff creates interdigitating stringers of tuff and sediment (Kincaird diatreme). (H) Intensive mingling of host-rock inclusions and tuff deposits results in comminution of quartz grains into the surrounding tuffs at a micro-scale. Photomicrograph(xpl) of LFA C at the margin of the St. Monans diatreme.

(Figure 6.7A; White and Ross 2011; Lefebvre et al 2013; Delpit et al. 2014). Debris jets can locally homogenise the diatreme. The presence of fluidal juvenile clasts in the debris columns in the East Fife diatremes suggests hot production and transportation of the juvenile clasts. The debris columns also contain autoliths of stratified tuff and angular juvenile clasts, which are likely to have been incorporated into the debris jet from the surrounding cooled diatreme deposits. The angular nature of these inclusions is due to brittle fragmentation and clast-clast collision of cool juvenile clasts within the debris jet. The phreatomagmatic explosions that form debris columns are typically less energetic (fragmentation is less efficient) or occur deeper in the diatreme and are unable to reach the surface. The phreatomagmatic explosions that can reach the surface and produce PDCs have more efficient fragmentation (more powerful) and/or occur at shallower depths within the diatreme.

The presence of fluidal host-rock sediment inclusions within the debris columns likely suggest the phreatomagmatic explosions occurred close to the diatreme margin where the debris jet could incorporate sediment inclusions from the surrounding host-rock (Figure 6.7B). The host-rock (siltstones, sandstones and mudstones) was easily fluidised within the debris jet, due to the soft nature of the host-rock and/or the hot temperature of the debris jet. Comminution of host-rock due to extensive fluidisation allows for clastic grains to become entrained within the diatreme tuff and allows for complete mixing of ash and clastic grains.

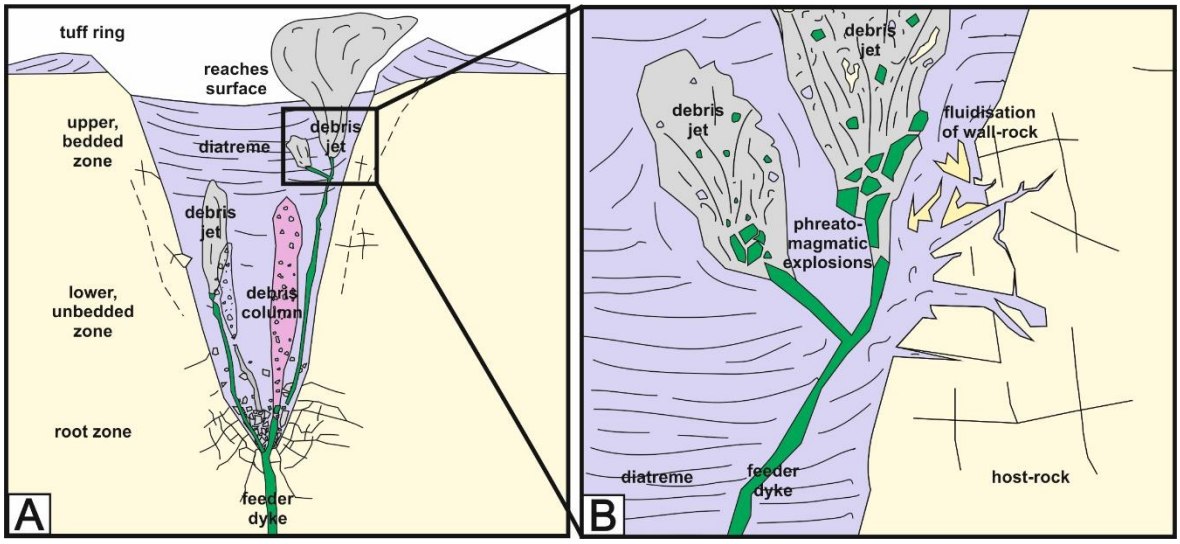

Figure 6.7: Schematic model of debris jets and debris columns. Not to scale. The host-rock is comprised of sandstone, siltstone, mudstone and limestone beds. (A) Debris columns are preserved remains of debris jets. Phreatomagmatic explosions that are more powerful or occur at a shallow level in the diatreme tend to reach the surface and produce PDCs. (B) If the phreatomagmatic explosion occurs near the margin of the diatreme, host-rock inclusions can be incorporated into the debris jet. The sediment inclusions within the debris column in the East Fife diatremes typically are highly fluidised as a result of the soft nature of the host-rock during entrainment and the heat of the debris jet.

The unbedded zones situated around the margins of the diatremes are likely to be marginal debris columns or subsidence zones. Subsidence zones are formed by subsidence of surface-derived material, (e.g. autoliths from the tuff ring or upper zone of the diatreme, host-rock inclusions from shallow stratigraphy) (Lorenz 1986; Gernon et al. 2008; 2013). This material slides down the walls of the diatreme. These collars of subsiding tuff ring deposits and floating reefs of host-rock are formed due to the the mass deficit in the root zone (Clement 1982; Boxer et al. 1989; Lorenz and Haneke 2004; White and Ross 2011; Delpit et al. 2014; Lorenz et al. 2017).

Fluidisation of the diatreme deposits is one particular mechanism that can transport large volumes of material downwards without internal disruption (Gernon et al. 2008). Gas exsolved from the magma streams upwards through the centre of the unconsolidated diatreme deposits and elutriates fines, suspending those fine particles in the upward moving stream. The gas flow creates a circular conveyor-belt system where upward directed flow is in the centre and downward directed flow occurs along the margins (Sparks et al. 2006; Gernon et al. 2008; Brown et al. 2009).

6.4.4. **Lithofacies D: Autolith-bearing breccia (SM, A, K)**

6.4.4.1. Description

Lithofacies D is a massive, homogeneous breccia comprised of various autoliths within a lapilli-containing tuffaceous matrix (Figure 6.8). The autoliths are composed of massive and stratified tuffs and lapilli-tuffs (mT; mLT; dsT; dsLT; xsLT). The autoliths have defined margins and are mostly angular or sub-angular (Figure 6.8A). Locally, there are sediment inclusions (e.g. coal, sandstone, mudstone, siltstone) and basalt clasts present within the breccia. The autoliths range in size from sub-cm to metre-scale (<2 m) and often display stratification and cross-stratification (mm- and cm-scale lamination) (Figure 6.8A and B). Lithofacies D is commonly found at the margins of the diatremes. At the Kincaird diatreme, bitumen residue (8 cm across) is evident within Lithofacies D (Figure 6.8D; See Kincaird map in Section 6.6.4).

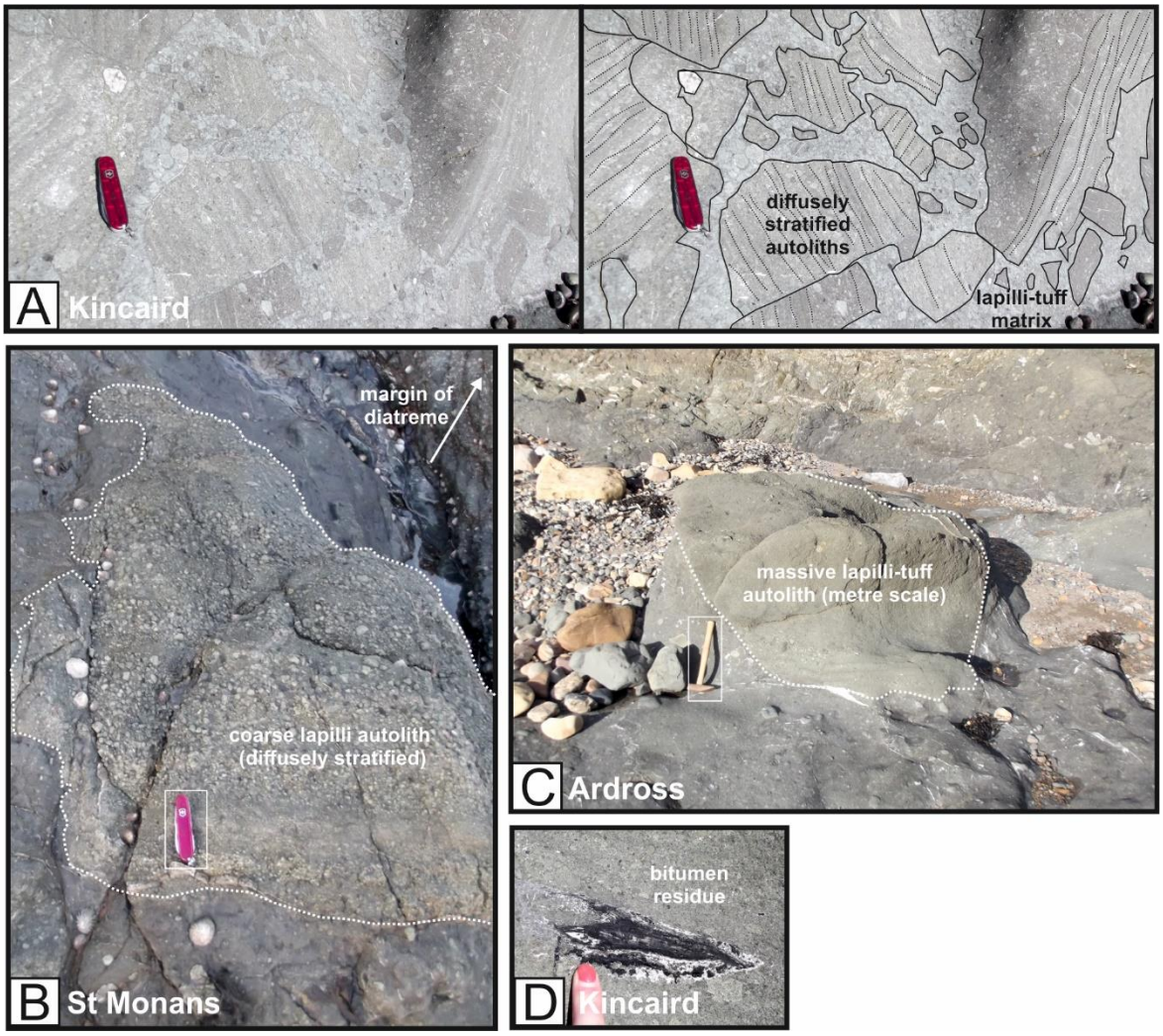

Figure 6.8: Images of Lithofacies D, collapsed bedding. (A) Photo and annotated photo of collapsed bedding at Kincaird diatreme. Autoliths are randomly orientated and are comprised of massive and stratified lapilli-tuff and tuffs. Autoliths are mostly angular and sub-angular. Pen-knife is 10 cm long. (B) Coarse lapilli autolith displaying diffuse stratification located within 2 m of the margin of the St Monans diatreme. Pen-knife is 10 cm. (C) Another metre-scale autolith displaying massive internal structure at St Monans. Hammer is 40 cm long. (D) Bitumen residue within Lithofacies D at the Kincaird diatreme.

6.4.4.2. Interpretation

Lithofacies D is formed in subsidence zones around the margins of the diatreme and is associated with Lithofacies C (massive breccias and lapilli-tuffs). Subsidence along the margins of surface-derived and upper diatreme-derived material occurs due to phreatomagmatic explosions at depth (Lorenz 1975, 1986) and/or fluidisation of the diatreme fill (Gernon et al. 2008; Brown et al. 2009). The latter process, as discussed above, occurs due to volatile release from the magma releasing an upward stream of gas. This upward movement in the centre of the diatreme is subsequently counterbalanced by a downward movement of particles along the margins due to brittle failure of upper diatreme deposits and host-rock (Gernon et al. 2008).

The surface diameter of a diatreme gets wider as the root zone gets deeper with progressive phreatomagmatic eruptions due to the drawdown of the hydrostatic pressure (Lorenz 2003; Lorenz and Kurszlaukis 2007) (Figure 6.9). This process causes portions of the stratified tuff ring or upper diatreme zone to collapse into the crater (Figure 6.9B). These collapsed blocks become autoliths in marginal unbedded zones. The zones tend to be steeply inclined breccias which likely formed through frictional drag along the pipe margins. The autoliths frequently retain internal stratification and tend to have angular or sub-angular shapes suggesting the tuff ring/upper zone was partially consolidated during widening of the diatreme.

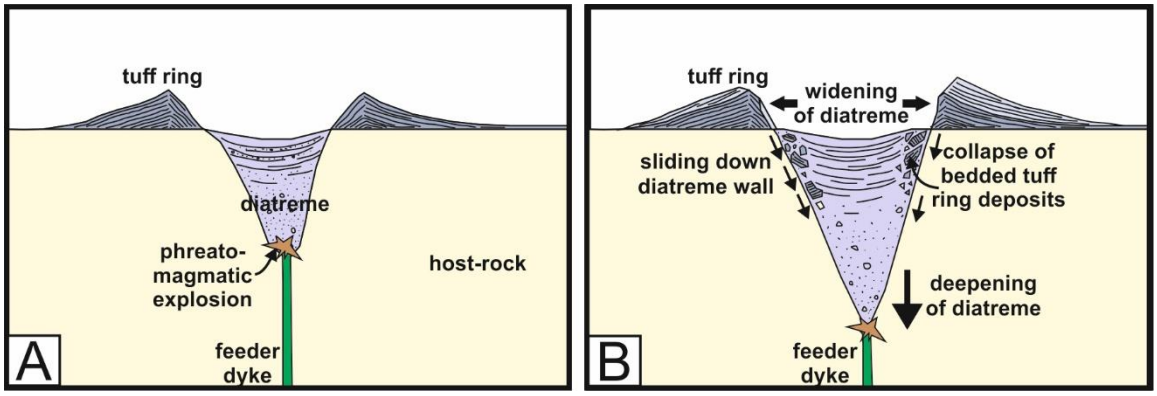

Figure 6.9: (A) Schematic diagram showing how marginal autolith-bearing breccias are formed. (B) The site of the subsurface phreatomagmatic explosion deepens, widening the diatreme at the surface and causing the collapse of the stratified tuff ring into the crater. Due to subsidence the autoliths (tuff ring and upper diatreme megablocks) slide down the wall of the diatreme. Not to scale.

6.4.5. **Lithofacies Association E (LFA E): Massive basalt breccia, peperitic domains and pods (SM, A, E, K, R)**

6.4.5.1. Description

In all five diatremes described in this chapter, there are discordant zones of basalt-rich monolithic breccia. In places, this unit can be described as peperite due to its direct relationship with surrounding intrusions and jig-saw fit textures (Figure 6.10A). Alternatively, in other places, the breccia is thoroughly dispersed, the clasts are randomly orientated and there are no nearby intrusions (Figure 6.10B). This is described as a basalt breccia.

Peperite tends to be blocky (although fluidal peperite is also present) and clast sizes decrease from the intrusion (Figure 6.10A). The dyke-like intrusions (discussed in Section 6.5) brecciate into aligned and isolated dyke segments, pods or clastogenic bodies of basalt, which further feed peperitic zones (Figure 6.10C, D). The result is large zones (>50 m wide) of jig-saw fit blocky peperite that

protrude from the flat-lying surface of the diatreme deposits. The tuffaceous matrix fills fractures within the pods and peperite (Figure 6.10A, D). The dyke segments have polyhedral fracturing.

The basalt breccia consists of matrix-supported angular basalt clasts that range in size from sub-cm to metre scale clasts (Figure 6.10E, F). The basalt breccia is comprised of >50 % basalt clasts which are supported within a tuffaceous matrix. Rare pyroxenite crystal assemblages are evident within the matrix (Elie).

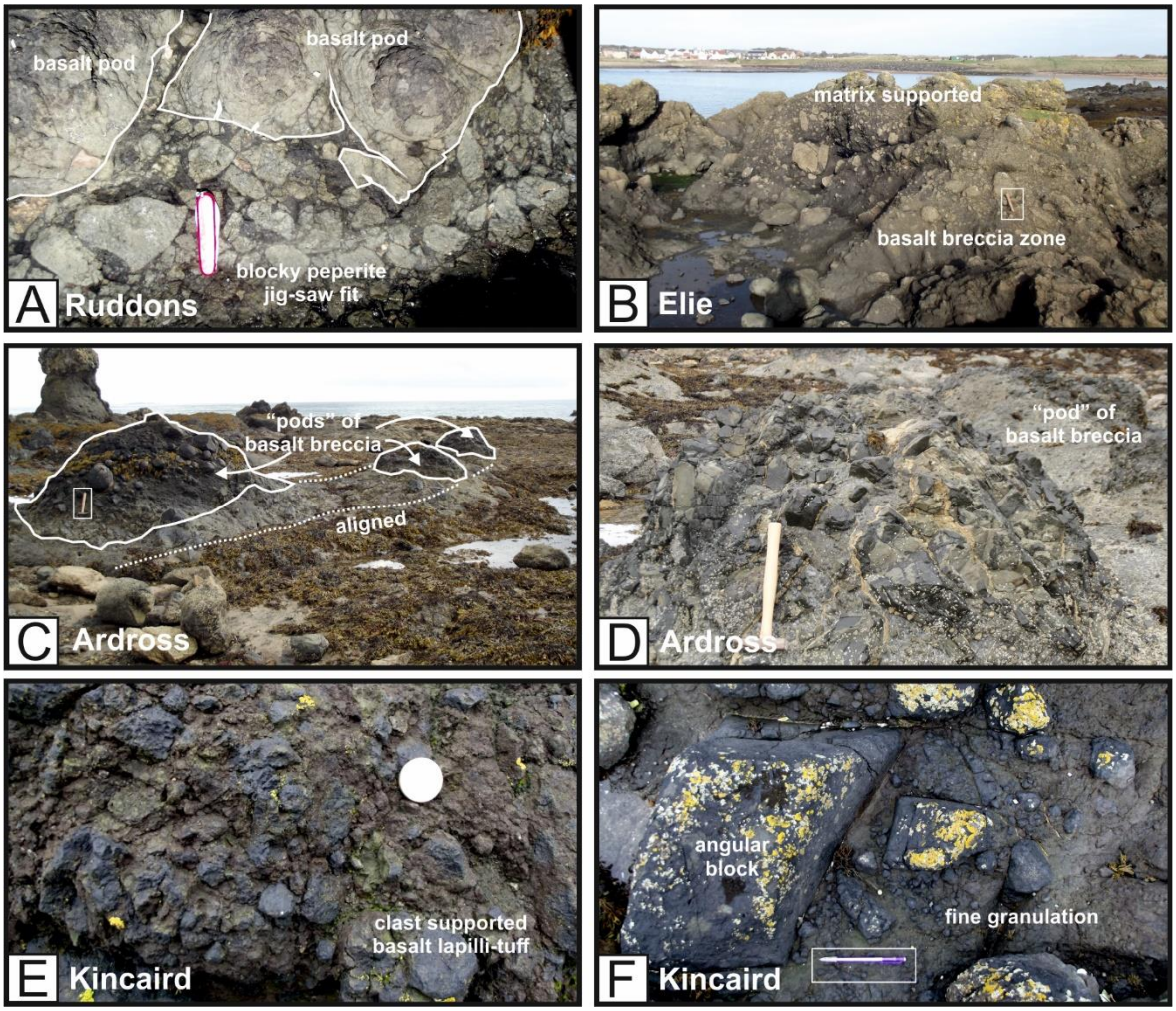

Figure 6.10: Images of LFA E, the massive basalt breccia. (A) Peperite forming around dyke-like intrusion segments. Peperite contains angular clasts, is clast-supported and has a tuffaceous matrix. The matrix has been injected into fractures and cracks in the intrusion. Jig-saw fit textures are apparent. Pen-knife is 10 cm long (Ruddons). (B) Matrix-supported basalt breccia zone. Large angular clasts of basalt (decimetre scale) in a tuffaceous and crystal-rich matrix (Elie). Hammer is 40 cm long (boxed). (C) Aligned basalt pods composed of clast-supported angular basalt cobbles and boulders. Pods are aligned with one another (Ardross). Hammer is 40 cm long (boxed). (D) Close-up image of a pod. (E) Fine granulation of clasts into cm-scale fragments. Clast-supported lapilli-tuff (Kincaird). Coin is 2 cm across. (F) Large angular clasts are surrounded by finely granulated clasts within a basalt breccia zone in the Kincaird diatreme. Pen is 15 cm long (boxed).

6.4.5.2. Interpretation

Extensive zones of peperite (LFA E) are attributed to the non-explosive or mildly explosive interaction between newly invading hot magma and the unconsolidated and typically wet diatreme deposits (White and Ross 2011). Brittle fractures open in the magma due to cooling and quenching, which reduces the lithostatic pressure, and allows for fluidisation of the adjacent tuffs and/or lapilli-tuffs. The fluidised tuffs are then injected into the fracture due to a differential pressure gradient (Kokelaar 2002). This process fragments the intrusions into blocky clasts (Figure 6.10A, E and F). The intrusions that create the peperite domains are likely to have a high magma flux, inhibiting powerful explosive interaction. Therefore, the peperite domains are not associated with the phreatomagmatic explosions that form debris jets in the centre of the diatremes (intra-diatreme fragmentation zones).

Intra-diatreme fragmentation zones are sites were dykes have risen into the diatreme and interacted explosively with wet diatreme deposits. The products of this interaction are fine, primary volcaniclastic deposits that are propagated upwards by debris jets (Zimanowski et al. 1997; Ross and White 2006; White and Ross 2011). In other words, intra-diatreme fragmentation zones are secondary root-zones at higher levels within the diatreme structure. In exposed diatremes, the sites of intra-diatreme explosions are difficult to locate because they produce very fine particles, cause widespread dispersal of their products and disrupt the surrounding diatreme deposits (White and Ross 2011).

6.4.6. **Lithofacies F: Host-rock and volcanic breccia (A, SM)**

6.4.6.1. Description

Lithofacies F is located at the margins of the Ardross and St. Monans diatremes and is only exposed at low tide. The breccia comprises matrix-supported metre-scale, coherent host-rock clasts and basalt boulders within a tuffaceous matrix. The host-rock inclusions are up to 2 m across and retain depositional features including fossils (crinoids within limestones) and lamination. Lithofacies F is thoroughly exploited by hydrothermal quartz and calcite veins (Figure 6.11A and B). At the St. Monans diatreme, the sediment inclusions have been highly fluidised and mingle with the tuffaceous

matrix (Figure 6.11A and B). Due to poor exposure, the boundary with the diatreme is difficult to determine but is likely to be gradational.

6.4.6.2. Interpretation

Similar to the formation of the collapsed bedding (Lithofacies D), Lithofacies F is partially formed by the widening of the diatreme causing metre-scale host-rock inclusions to become entrained within the diatreme. The heterogeneous nature and volume and host-rock clast size of Lithofacies F suggests that homogenisation and recycling is limited, likely due to a slowing or stopping o subsequent volcanic activity. The result is a poorly sorted and polymict breccia with large unfluidized sediment clasts.

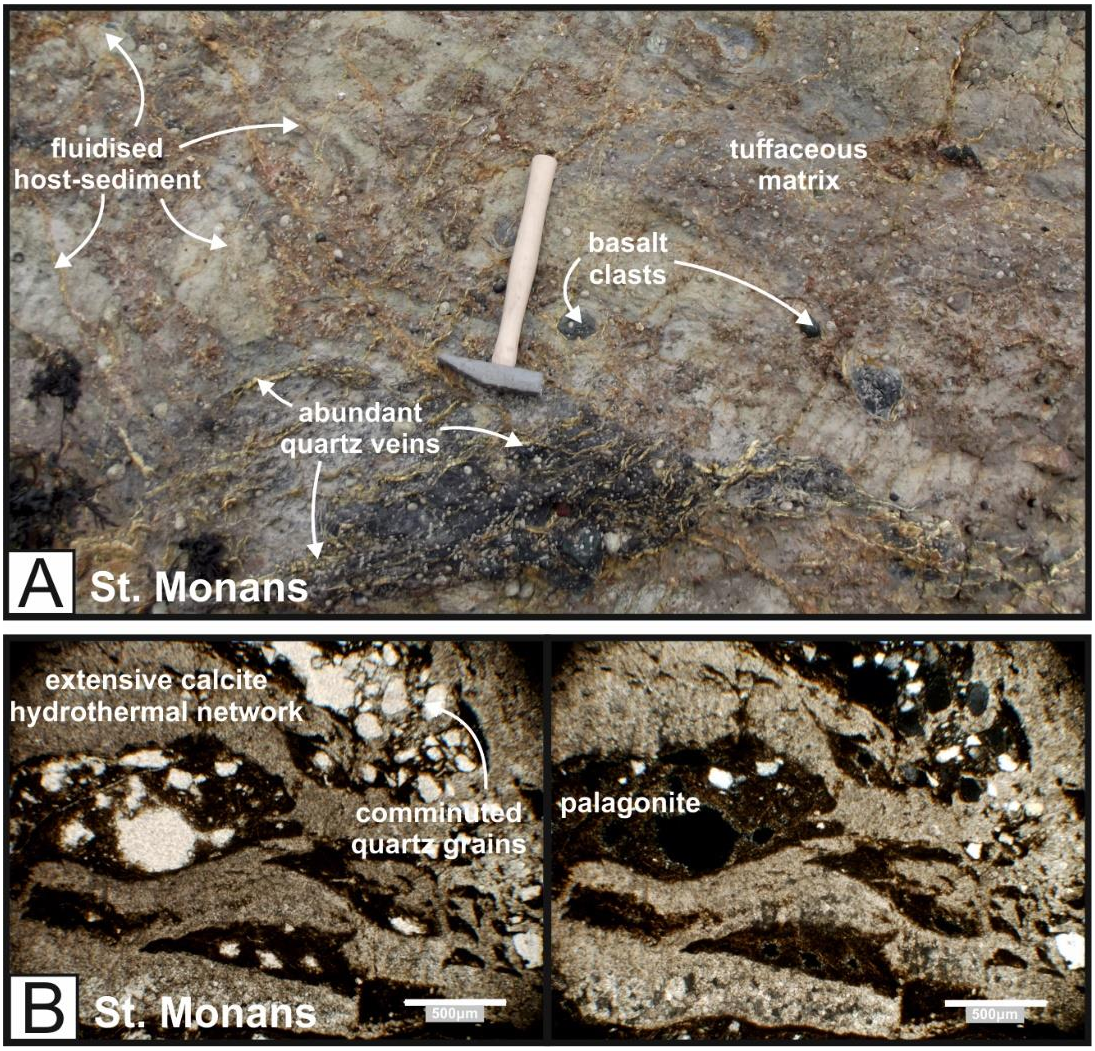

Figure 6.11: Lithofacies F from the SW margin of the St. Monans diatreme. (A) The host-rock and volcanic breccia contains >50% host-sediment inclusions that have been fluidised, abundant hydrothermal quartz veins and angular basalt clasts (<10 cm) in a tuffaceous matrix. Hammer is 40 cm long. (B) Photomicrographs (left image = ppl; right image = xpl) of Lithofacies F from the SW margin of the St. Monans diatreme. Calcite hydrothermal systems have extensively exploited the margin. Comminuted quartz grains are present within the palagonitised tuffs.

6.5. Intrusions and injectites

6.5.1. **Magmatic intrusions (SM, A, E, K, R)**

6.5.1.1. Observations

Coherent basalt intrusions are abundant around the margins of the diatreme. Compositionally, the intrusions are silica-poor (<44% SiO_2) and have mostly basanite signatures; however, XRF analysis of samples from Ardross and Elie are foidites (Figure 6.12; Appendix 10.4). The intrusions are both aphyric or porphyritic. Sub-mm to 12 mm vesicles in the centre of dykes are locally filled with calcite amygdales. Coarse pyroxene crystals (<2 mm) are apparent within the intrusions and rare pyroxenite crystal assemblages (<3 cm) are also present within several of the intrusions (e.g. Elie, Ardross). In a dyke at the southwest margin of the Ardross diatreme, lower crustal, ultrabasic xenoliths are present (Figure 6.13). These olivine-rich, spinel-bearing lherzolite xenoliths are up to 15 cm across, locally layered and have been thoroughly serpentinised (Figure 6.13A and B). Petrographical analysis of the xenoliths shows an arrangement of alteration products with chrysotile veins throughout (Figure 6.13C).

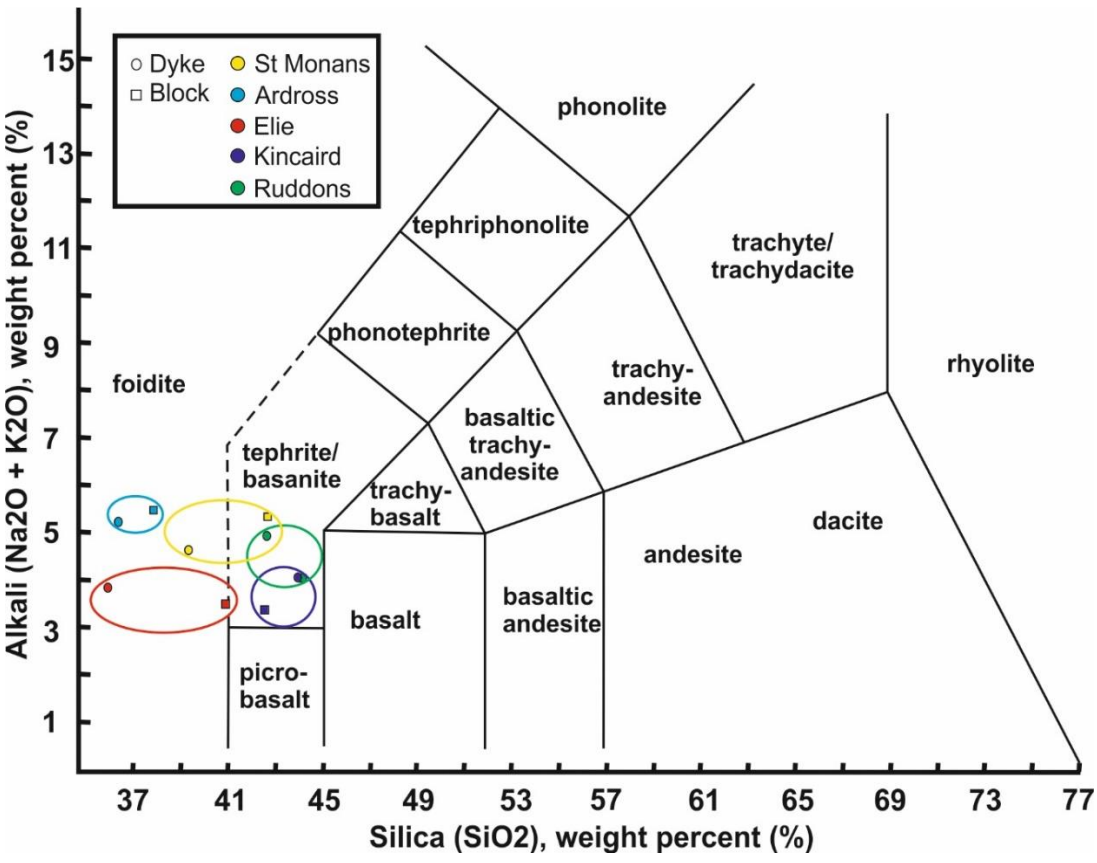

Figure 6.12: TAS diagram showing the distribution of samples taken from the diatremes in East Fife. Samples were taken from intrusions (small circles) and large basalt blocks (squares) in LFA C from the diatreme (boxes). Large circles indicate samples from the same diatreme.

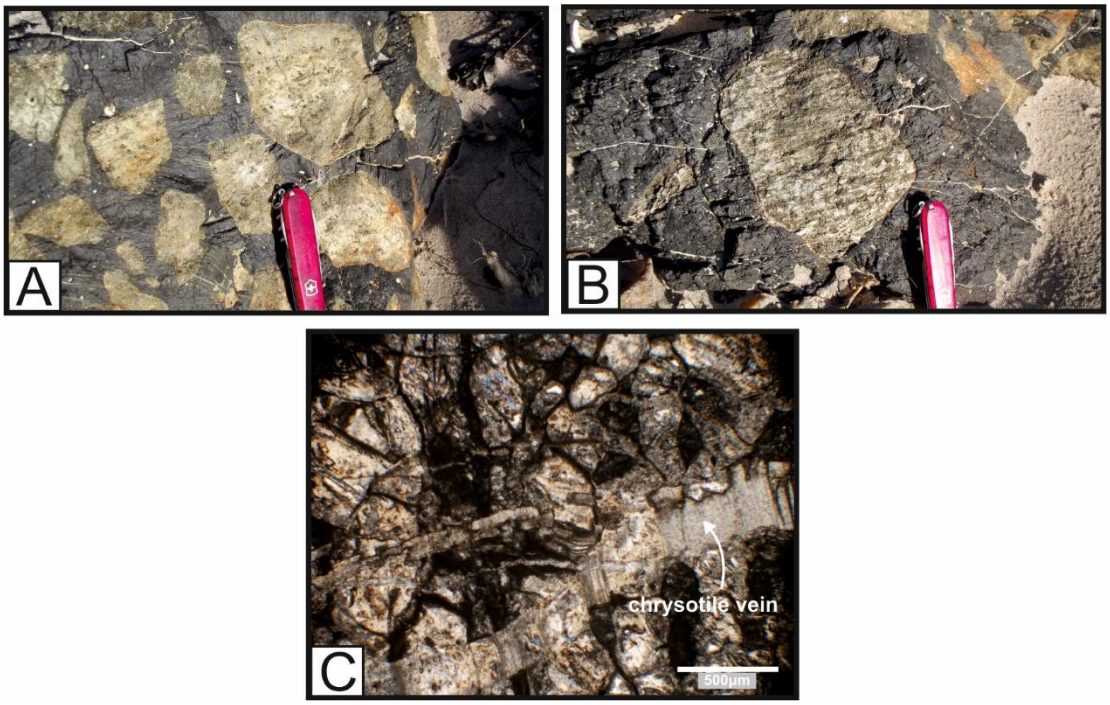

Figure 6.13: Xenoliths in a dyke in the Ardross diatreme. (A) Ultrabasic, olivine-rich, lower crustal xenoliths (B) Layered xenoliths of lherzolite are present Pen-knife is 10 cm. (C) Lower crustal xenolith in XPL showing serpentinised olivine crystals and chrysotile veins.

The magmatic intrusions are described in depth in Section 6.6 at each of the diatreme locations. However, the general characteristics of the magmatic intrusions are described here.

Dykes: Most intrusions within the diatremes are <3 m wide dyke-like bodies that exhibit irregular and wavy morphologies. Locally, the dykes bifurcate into two separate dykes and/or amalgamate into one, enclosing inclusions of diatreme tuffs and lapilli-tuffs within the dyke (Figure 6.14A). Finger-like protrusions intrude into the surrounding tuffs and lapilli-tuffs (Figure 6.14B), resulting in highly irregular and interdigitating margins (Figure 6.14C).

The dykes are commonly focussed around the debris columns and the margins of the diatremes. Where the dykes have come into contact with the host-rock stratigraphy, extensive fluidisation has occurred within the host-rock forming highly fluidal and convolute dyke margins and disrupting depositional features within the host-rock.

Many of the thicker dykes (1-3 m wide) have abrupt terminations whereas thinner dykes (<1 m) taper out within the diatreme. At abrupt dyke terminations (e.g. Ruddons, Ardross), the dykes disaggregate on a variety of scales into disconnected dyke segments, or pods, and blocky peperite (Figure 6.14D). Fluidal peperite is also evident where clasts have a ragged morphology.

Locally, seemingly intact dykes are, in reality, a clast-supported breccia of detached basalt clasts separated by fluidised diatreme tuffs. At the margins of these pseudo-dykes, fingers of basalt clasts intrude into surrounding diatreme deposits, where they become increasingly broken up into the surrounding tuffs and form peperite (LFA E) (Figure 6.14E and F). The thinner dykes (<1 m) usually remain intact and are not subjected to auto-brecciation.

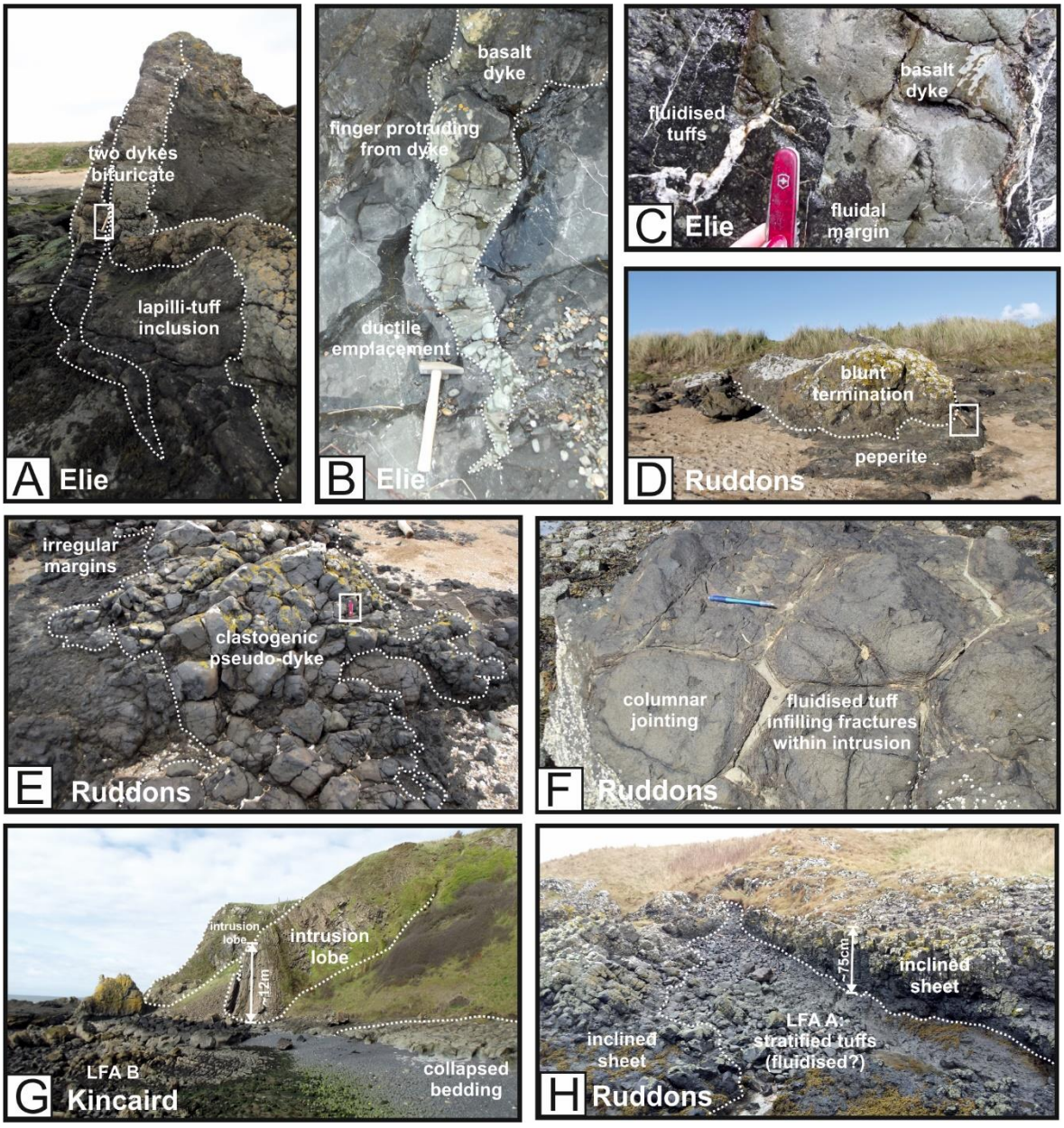

Figure 6.14: Common characteristics of the intrusions found in the East Fife diatremes. (A) Two bifurcating dykes enclosing a tuff inclusion. Hammer is 40 cm long (boxed). (B) Finger protruding from basalt dyke with convolute margins and a wavy morphology. Hammer is 40 cm long. (C) Margin between dyke and tuff at Elie. The tuffs were fluidised upon intrusion emplacement creating a highly interdigitating margin. Pen-knife is 10 cm long. (D) Thick dyke (~2 m wide) terminated abruptly and is surrounded by peperite on all sides. Hammer is 40 cm (boxed). (E) Clastogenic pseudo-dyke comprised of jig-saw fit angular dyke clasts and fluidised tuff which has been injected into fractures during cooling of dyke. Pen-knife is 10 cm (boxed). (F) Close-up of pseudo-dyke showing the columnar jointing which has been infilled by fluidised tuff. Pencil is 15 cm long. (G) Two intrusion lobes protrude from cliff face, both demonstrating columnar jointing at Kincaird diatreme. (H) Incrementally emplaced inclined sheets separated by thin beds of LFA A tuffs and lapilli-tuffs.

Inclined sheets: Within the diatremes at Kincaird and Ruddons, there are several larger intrusions that form inclined sheets (Figure 6.14G and H). These intrusions have extensive columnar jointing. In the centre of the Kincaird diatreme, two large, 40 m high sill lobes protrude from the cliff face (Figure 6.14G). The sill within the diatreme at Ruddon's Point displays a stepped character of incrementally emplaced sheets (Figure 6.14H).

6.5.1.2. Interpretations

Coherent intrusions indicate the last phase of volcanic activity as the intrusions have not been disrupted by subsequent activity e.g. passing debris columns or subsidence. The presence of coherent dykes suggests an increase in the magma-water ratio, preventing explosive magma-water interaction. It is likely that the water supply was restricted towards the end of diatreme formation. The decrease in water supply can be attributed to a drying out of the diatreme due to heat from the continuous magma input, or equally by increasing the magma input towards the end of diatreme formation. Thus, representing a switch from mainly phreatomagmatic to magmatic processes. However, a proportion of the coherent dykes likely represents feeder dykes that fed high-level (shallow) phreatomagmatic explosions and formed high level debris jets during diatreme formation. The inclined sheets and sills within the diatreme represent late-stage ponding of magma at a shallow level within the diatreme structure (Figure 6.14G and H).

Evidence for magma emplacement by non-brittle mechanisms are prominent in the dykes exposed in the East Fife diatremes, for example, wavy, irregular morphologies (Figure 6.14A); magma fingers (Figure 6.14B); fluidal margins (Figure 6.14C); and fluidal peperite. The diatreme fill was likely unconsolidated or partially consolidated during magma emplacement promoting ductile emplacement. Furthermore, during the Upper Carboniferous volcanism, host-rock sedimentation occurred in shallow marine, lagoonal and deltaic settings. The dykes, therefore, were expected to encounter water-saturated diatreme fill and/or host-rock during emplacement (Gernon et al. 2013), further promoting non-brittle emplacement mechanisms. Water-saturation of the host promotes ductile emplacement by increasing the host's susceptibility to fluidisation (Wohletz 2002). Fluidisation of the volcaniclastic deposits within the diatremes is evident in the form of peperite formation and injected material within the dykes (Figure 6.14E and F).

Clastogenic bodies, comprised of fluidised tuff injected between jigsaw-fit blocks of coherent basalt, are formed by the opening of brittle fractures due to cooling and quenching of a magmatic dyke (Figure 6.14F). The opening of the fracture reduces the lithostatic pressure, allowing for fluidisation of adjacent tuffs and the injection of fluidised tuffs into the fracture (Kokelaar 2002). This tends to be a non-explosive process, essentially large-scale cooling and quenching granulation, however White and Ross (2011) have noted that rapid crack-like injection of the diatreme fill is inferred to require high-rate injections and hence some form of explosive expansion. It is, therefore, suggested that during the emplacement of clastogenic dykes (Figure 6.14E), mild to moderate steam explosions occured to disperse clasts and brecciate the dyke.

6.5.2. **Volcaniclastite injectite (A, E, K)**

6.5.2.1. Description

At several of the diatremes, volcaniclastic injectites are present. The injectites are commonly, but not always, found around the margins of the diatremes or around debris columns and are injected into the diatreme (Figure 6.15A) and the surrounding host-rock (Figure 6.15B). The injectites found at the margins of the diatreme, tend to have a large component of sediment inclusions (Figure 6.15F). The width of the injectites range from <5 cm to 3.5 m (Figure 6.15A and C), however the extent of the injectites into the host-rock is difficult to determine due to level of exposure. The margins of the injectites are typically well-defined and can exhibit both straight (Figure 6.15A and F) and undulating boundaries (Figure 6.15B and C). The injectites are locally associated with magmatic dykes, for example at Elie where an injectite grades into a magmatic dyke.

These dyke-like, volcaniclastic bodies are comprised of tuffs and lapilli-tuffs and contain juvenile clasts, basalt clasts, fluidised sediment inclusions (coal, sandstones, siltstones, mudstones and limestones) and tend to be thoroughly exploited by calcite hydrothermal veins (Figure 6.15E, G). Hydrothermal calcite tends to fill pore spaces within the injectite and/or vesicles within basalt clasts (Figure 6.15G, H). Rounded and sub-rounded juvenile clasts are sub-mm to cm-scale and are matrix-supported within a green to black tuffaceous matrix (>65%) (Figure 6.15G). Locally, juvenile clasts are fluidal and have convolute and irregular margins. Sediment inclusions tend to be elongated and strung out and exhibit highly convoluted edges (Figure 6.15F). Comminution of sediment inclusions,

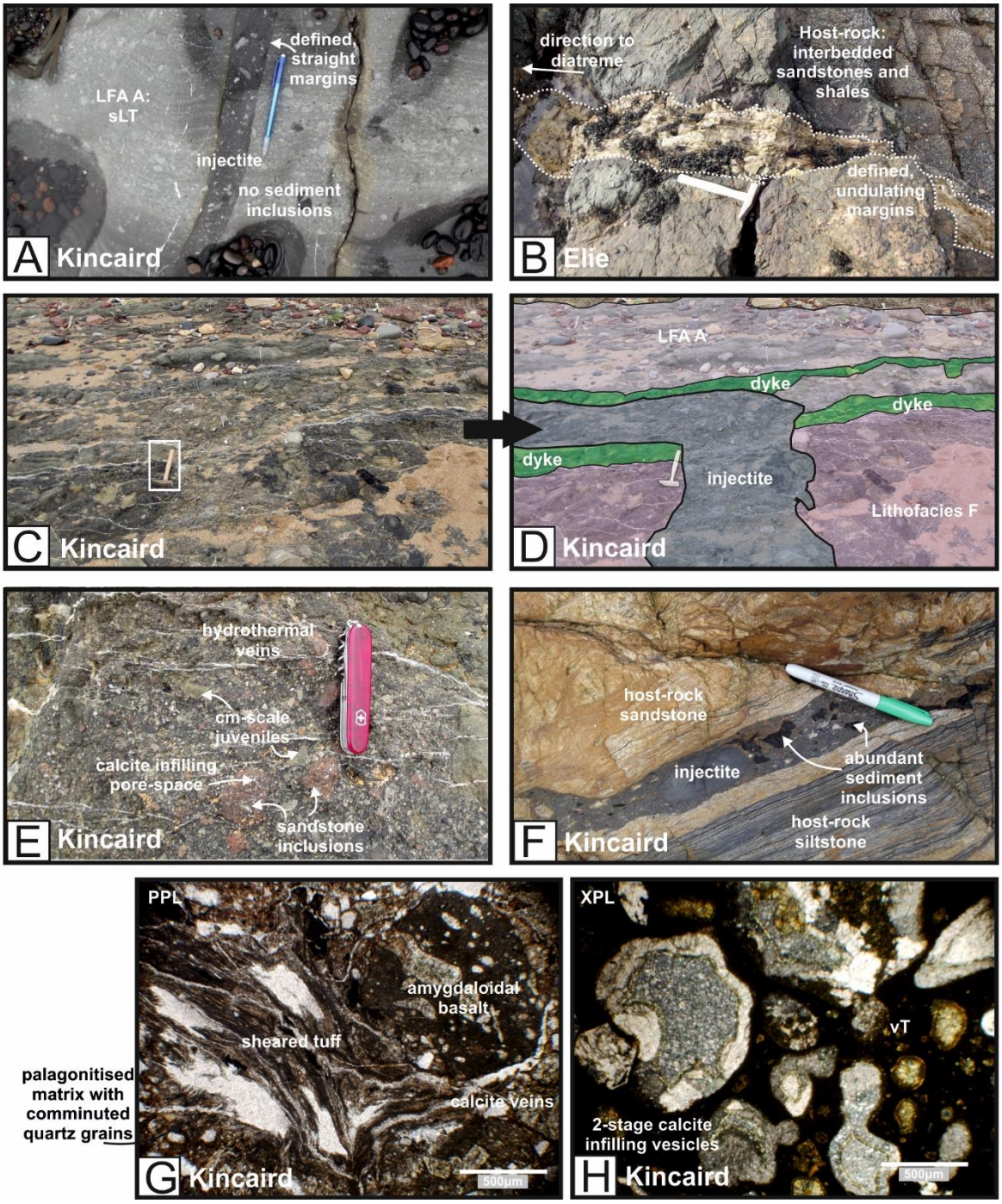

Figure 6.15: Characteristics of the volcaniclastic injectites found at Kincaird and Elie diatreme. (A) Volcaniclastic injectite through the stratified lapilli-tuffs. The injectite is a mLT, that contains no sediment inclusions and has defined, straight margins. Pencil is 15 cm long. (B) Tuff injectite injected into the surrounding host-rock at the margin of Elie diatreme. The injectite is thoroughly exploited by calcite veins. Hammer is 40 cm. (C) and (D) Photograph and annotated photograph of a volcaniclastic injectite at the margin of the Kincaird diatreme. The injectite cross-cuts dykes and is comprised of fluidal rags and juvenile clasts. Hammer is 40 cm. (E) Composition of an injectite at Kincaird, comprises cm-scale sub-angular juvenile clasts and sandstone inclusions. The pore-space within the inclusions is filled with hydrothermal calcite. Abundant calcite veins are present. Pen-knife is 10 cm. (F) Sediment inclusions within an injectite that has been emplaced into the surrounding host-rock at Kincaird diatreme. Pen is 15 cm long. (G) Photomicrograph of the volcaniclastic injectite at Kincaird (ppl) showing sheared tuff matrix and calcite infills. Hydrothermal (calcite) veins are abundant throughout. Sub-rounded, vesicular basalt lapilli are infilled by calcite. Comminuted quartz grains are present within the matrix. (H) Photomicrograph of the volcaniclastic injectite at Kincaird (xpl). Large (<3 mm) vesicular tachylite lapilli containing calcite amygdales. The amygdales show a two-stage infilling process with fibrous calcite coating the margins of the amygdale.

results in dispelled quartz grains becoming encorporated within the tuff injectite (Figure 6.15G). Locally, the injectites are faintly stratified or have been sheared and are defined by alternating layers of dark grey, fine tuff with sub-cm juvenile clasts, green lapilli-tuff with sediment inclusions and hydrothermal calcite (Figure 6.15G). The elongated clasts and direction of stratification show the direction of flow.

6.5.2.2. Interpretations

The majority of the volcaniclastic injectites have a massive internal structure where host-rock inclusions, juvenile clasts and basalt clasts are thoroughly mixed and homogenised (Figure 6.15A, C, E and F). This can be explained by fluidisation of a gas particle dispersion within a fracture (Gernon et al. 2009). Heat input by intrusion emplacement stimulates fluidisation and re-mobilisation of the diatreme fill (tuffs and lapilli-tuffs) which can be injected into the surrounding diatreme and/or host-rock.

Injectites are locally associated with magmatic dykes (e.g. Elie). In this situation, the gradational contact between the injectite and the magmatic dyke suggests the dyke encountered a water-saturated zone within the diatreme that triggered explosive fragmentation and produced a sub-horizontal debris jet (Gernon et al. 2013).

6.6. Structure of Diatremes

The main features of each of the five diatremes are described in this section using the lithofacies codes described in the Section 6.4.

6.6.1. **St. Monans**

6.6.1.1. Observations

The St. Monans diatreme is the most northerly diatreme along the Ardross Fault [N56203227 W002769795] and has been emplaced into the Pathhead Formation (Figure 6.16). The diatreme is an ovate shape: its longest axis measures ~220 m in a NNE-SSW orientation. Margins with the surrounding host-rock are exposed in the NE and SW of the diatreme, however poor exposure inland and offshore, restricts full geometric analysis of the diatreme (Figure 6.16). Exposure of the diatreme fill is limited in places due to tidal sand and vegetation, most notably in the centre of the diatreme structure.

Aerial photographs of the centre of the diatreme show a poorly developed bedded structure belonging to LFA A, where beds are inward-dipping and arranged in a centroclinal pattern. Laminations, where observed, are diffuse. Lack of exposure of the central deposits restricts compositional analysis, however generally Lithofacies A is comprised of >60% angular and sub-angular juvenile clasts, and varying proportions of host-rock sediment clasts (10-40%) and angular basalt clasts (<5-30%) (Figure 6.17). Host-rock inclusions tend to be fluidised red siltstone and are distributed along minor faults. Locally, highly fluidal silt-grade sediment inclusions have incorporated clasts of lapilli-tuff into the inclusion (Figure 6.18A).

Zones of massive breccias and lapilli-tuffs (LFA C) are distributed around the margins (Figure 6.16). On the SW margin, the marginal zone is ~45 m wide (Figure 6.18B). The undulating diatreme margin is clearly defined by a 20 cm-wide, fine, black mud with elongated, fluidal white sandstone clasts (Figure 6.18C). The elongated sandstone inclusions are horizontally elongated and are sub-parallel to the diatreme margin (Figure 6.18C). The first 10-15 m from the margin is attributed to Lithofacies F (host-rock and volcanic breccia in a tuffaceous matrix) due to its high proportion of sediment inclusions (>50%) (Figure 6.11). The sediment inclusions are primarily comprised of fluidised fine blonde sandstone, although coherent blonde sandstone rafts (<80 cm long) and >50 cm coherent

rafts of crinoid-rich limestone are present within Lithofacies F (Figure 6.18D). This marginal zone is thoroughly disrupted by hydrothermal quartz veins which tend to be spaced 5-15 cm apart (Figure 6.11; Figure 6.18B). Lithofacies F grades into an unstructured lapilli-tuff, which is comprised of <30% host-sediment inclusions (Figure 6.17). This massive zone is attributed to LFA C and extends inwardly from the margin into the diatreme for ~45 m (Figure 6.16 and Figure 6.18B). The unstructured marginal zone grades into the bedded deposits (LFA A) (Figure 6.16). The NE margin is more defined, exploited by a 2.5 m wide dyke. The marginal, massive zone on the northeast of the diatreme (LFA C) is ~5-10 m wide.

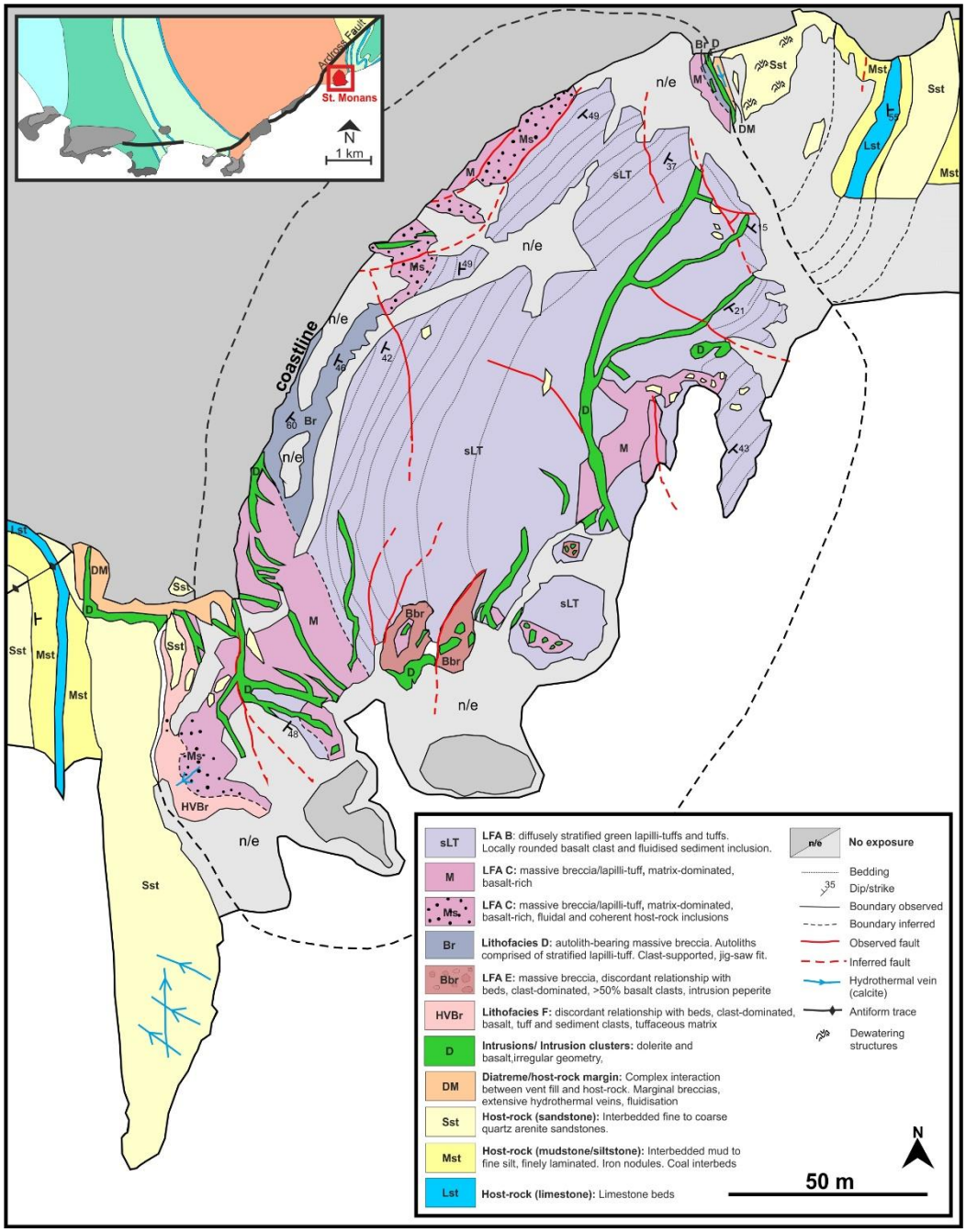

Figure 6.16: Geological map and key of the St. Monans diatreme. Inset: Location of St. Monans (red box).

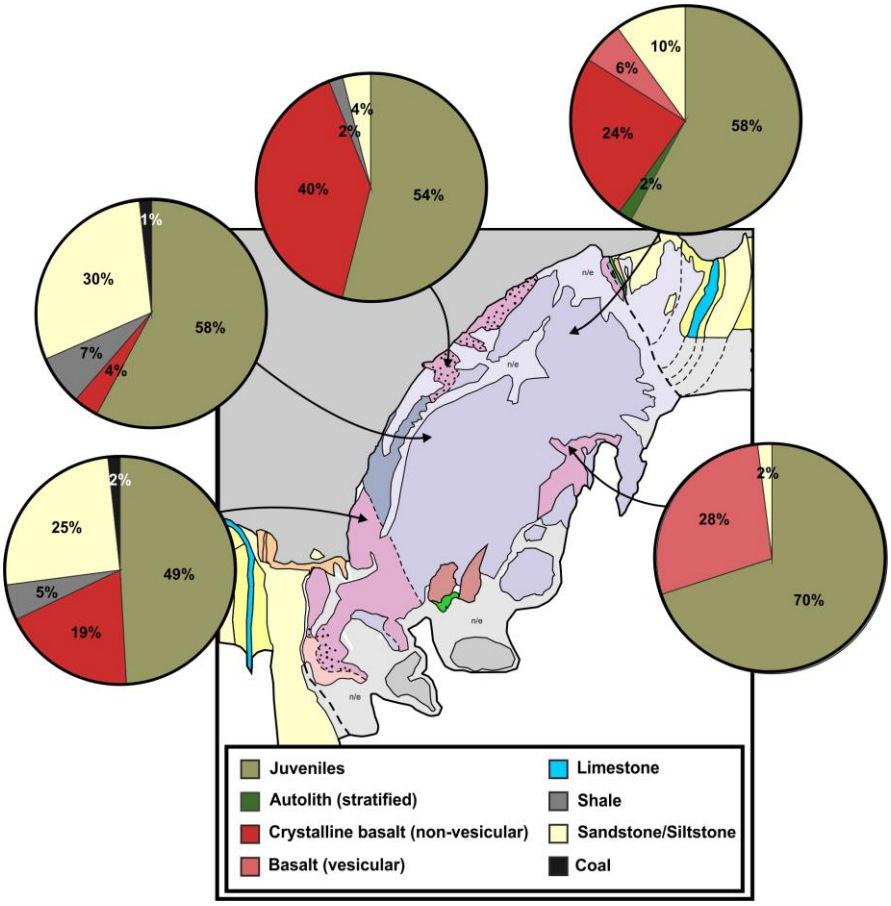

Figure 6.17: Summary geological map of the St. Monans diatreme showing the distribution of the main lithologies (see key in Figure 6.16), and pie charts illustrating the composition of the lithic clast population at corresponding localities on the map. N=100 for each clast count.

Cross-cutting, massive zones are also evident in the eastern section of the diatreme during low tide. These zones are likely to be near the SE margin of the diatreme, which is currently not exposed. The isolated massive zones are comprised of >65% juvenile clasts, >25% vesicular basalt clasts and lack significant amounts of host-rock (Figure 6.17). The boundaries of these zones are indefinite and grade into the surrounding bedded units. Locally, the cross-cutting zones are comprised of basalt-rich, clast-supported monolithic breccias (LFA E) that consist of angular basalt clasts (sub-cm to 50 cm). Intrusions are commonly associated with the zones of LFA E.

At the high-water line in the centre of the diatreme, the stratified beds gradually become more distorted (Figure 6.18E). Ductile deformation of the stratifications has formed minor collapse structures. The distorted beds grade into a zone of autolith-bearing breccia (Lithofacies D) comprised of sub-angular, stratified autoliths and fluidal (strung out) silt-grade sediment inclusions. Some of the sediment inclusions retain depositional lamination. Collapse breccias (Lithofacies D)

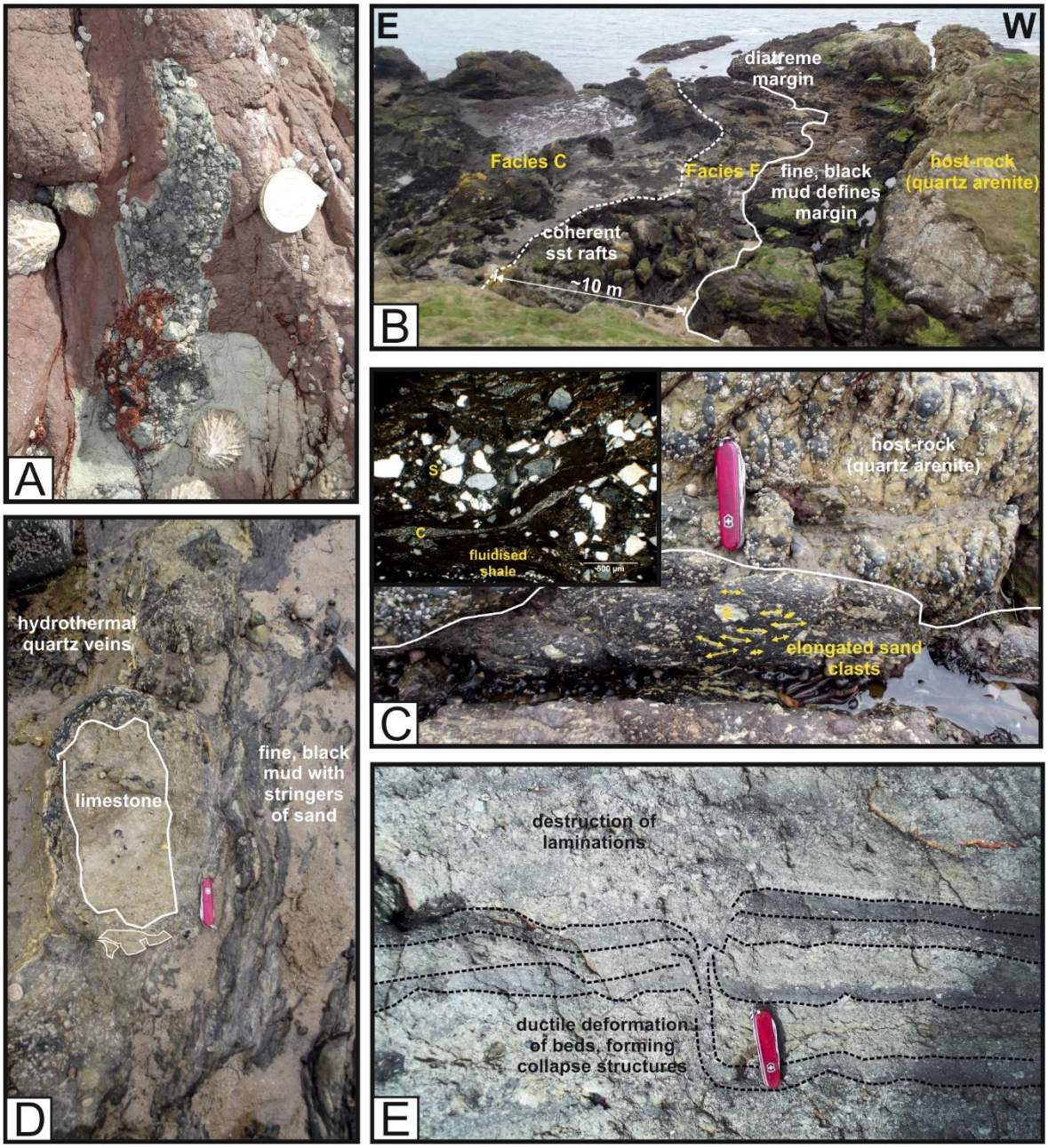

Figure 6.18: Photographs of features within the St. Monans diatreme. (A) Fluidised silt-grade host-rock incorporates lapilli-tuff from LFA A into the sediment inclusion. The host-rock inclusion has highly convolute margins. Pound coin is 22 mm across. (B) SW margin of the St. Monans diatreme. The marginal zone gradually becomes less host-rock-rich and more structured from the margin to the centre. The first 10-15 m from the margin is attributed to Lithofacies F, which grades into a massive lapilli-tuff (LFA C) and the stratified bedded centre (LFA A), approximately 45 m from the margin. Metre-scale coherent host-rock sandstone rafts are locally distributed in Lithofacies F. (C) The margin is defined by a black mud-grade sediment with elongated, fluidal clasts of sandstone. The clasts are sub-parallel to the diatreme margin. Inset: Photomicrograph (xpl) of the margin displaying fluidised and welded shale surrounding strung out sandstone fragments. (S = sandstone, C = calcite vein). (D) Limestone host-rock inclusions within Lithofacies F. Pen-knife is 10 cm long. (E) Ductile deformation of bedding within LFA A forming collapse structures. Lamination is deformed closer to Lithofacies D (See Figure 6.16).

are also observed along the NE margin of the St. Monans diatreme and contain metre-scale mega-blocks of coarse, stratified lapilli-tuff (Figure 6.8C).

Intrusions: Straight and irregular dykes are commonly associated with the marginal zones on either side of the diatreme (Figure 6.16). The thinner dykes (<50 cm) appear to taper out. The thicker

dykes (>50 cm) disintegrate into clastogenic bodies, where diatreme fill has been injected into the fractures between clasts. The margins of the dykes are typically well-defined, although locally, peperite has formed at the margins of the dykes, particularly where intrusions have come into contact with host-rock inclusions.

6.6.1.2. Interpretation

Diatremes can be divided into four main zones: tuff ring; upper, bedded zone; lower, unbedded zone; and root zone (Francis 1970; Lorenz 1986; White and Ross 2011). It is proposed that the St. Monans diatreme is exposed at the upper zone-lower zone transition (Figure 6.19), due to: (1) poorly developed, diffuse bedding; (2) large marginal zones, particularly in the SW of the diatreme; (3) an abundance of coherent dykes; and (4) large areas of collapsed bedding, with metre-scale intact blocks of well-developed bedded upper-diatreme deposits.

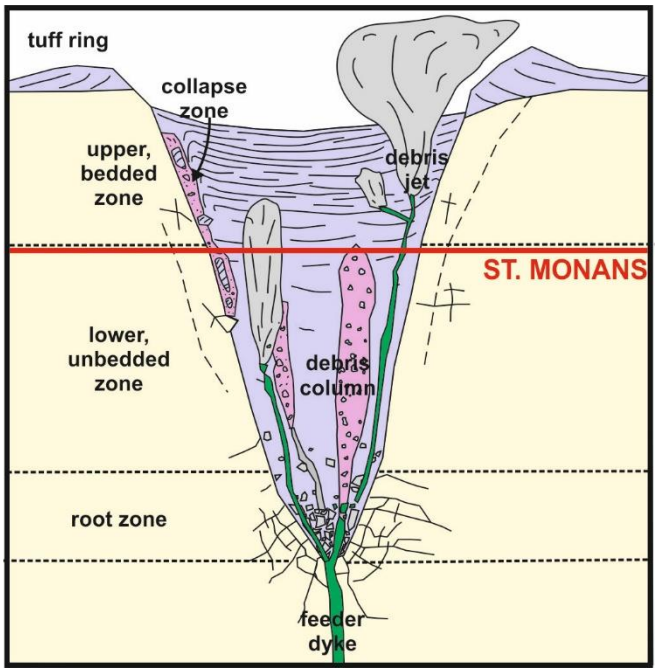

Figure 6.19: A typical diatreme structure showing the four main zones (tuff ring, upper bedded, lower unbedded and root zone). Debris columns and collapse zones are also evident within a typical diatreme. The proposed level of the exposed St. Monans diatreme within the typical diatreme structure is marked by the solid red line. Not to scale.

During phreatomagmatic activity, the interaction of magma with groundwater and/or slurry caused rapid quenching and brittle fragmentation of the magma, producing angular to fluidal juvenile clasts (White 1996; Zimanowski et al 1997). The juvenile clasts at St. Monans are non-vesicular or incipiently vesicular suggesting that the magma fragmented before volatile exsolution (Houghton and Wilson 1989; Mangan and Cashman 1996; Lefebvre et al. 2016). The juvenile-rich ejecta was

erupted at the surface, forming PDCs, base-surges and fall deposits, and producing beds of tuff and lapilli-tuff (White and Ross 2011). Subsidence in the centre of the diatreme caused the beds to become buried by subsequent eruption deposits and eroded by passing debris jets (Valentine and White 2012). Large volumes of host-rock were incorporated into the diatreme fill at St. Monans. The red siltstone was only partially consolidated at the time of eruption and readily fluidised, producing highly deformed sediment inclusions with convolute margins (Figure 6.18A).

The wide (~45 m) marginal zone in the SW of the diatreme and the presence of coherent wall rocks suggests that widening of the diatreme occurred mostly along the SW margin of the St. Monans diatreme. Dykes also preferentially exploited the SW margin. Large, coherent rafts of sandstone and limestone are found in the SW marginal zone of the St. Monans diatreme and were likely eroded from the walls of the diatreme, rotated and incorporated into the SW marginal fill (White and McClintock 2001; McClintock et al. 2008; Ross et al. 2008; White and Ross 2011) (Figure 6.18D). The sandstone and limestone rafts were sourced from more consolidated host-rock and were more resistant to fluidisation, incurring brittle failures.

Autolith-bearing breccia (Lithofacies D) around the margins of the St. Monans diatreme (Figure 6.18B) is a result of subsidence due to phreatomagmatic explosions at depth, creating voids beneath (Lorenz 1975, 1986) and/or fluidisation of the diatreme fill (Gernon et al. 2008). Intact, metre-scale blocks of stratified upper diatreme deposits along the NE margin (Figure 6.8C) indicates minimal disruption to subsiding material, suggesting negligible transport and/or downward movement (Gernon et al. 2008).

Intrusions: After phreatomagmatic activity ceased, a magmatic phase ensued, characterised by mildly irregular to straight dykes. It is possible that some of these dykes fed phreatomagmatic explosions further up in the diatreme, forming high level debris jets. Zones of monolithic basalt breccia in the south of the diatreme represent high level pipe-like intrusions, where intrusions have been emplaced into the diatreme (Figure 6.16). Non-explosive interaction is recognised by the presence of large angular clasts of basalt indicating inefficient fragmentation.

6.6.2. **Ardross**

6.6.2.1. Observations

The Ardross diatreme is often referred to as the Coalyard Hill diatreme (Francis 1970; Leys 1980), but for the purposes of this study, it is named the Ardross diatreme. The Ardross diatreme is located 800 m WSW of the St Monans diatreme [N56115801 W00247266] (Figure 6.20). It is also emplaced into the Pathhead Formation. The diatreme is an elliptical shape: its longest axis measures ~470 m in an ENE-WSW orientation. The Ardross Fault transects and displaces the eastern portion of the diatreme along a NE-SW orientation (Figure 6.20). Margins with the surrounding host-rock are poorly exposed but are evident locally in the SW of the diatreme. Exposure of the diatreme fill is limited in places due to tidal sand and vegetation, most notably at the margins of the diatreme structure (Figure 6.20).

The Ardross diatreme lacks well defined beds associated with LFA A. The diatreme consists of a central zone of crudely-bedded lapilli-tuffs (LFA B) and collapsed bedding (Lithofacies D), which is heavily intruded by dykes and pods of basalt-rich monolithic breccia (LFA E) (Figure 6.20). This central zone is surrounded by massive, unbedded zones with variable proportions of host-rock inclusions (LFA C and Lithofacies F) (Figure 6.20).

LFA B (crudely bedded lapilli-tuff) has metre-scale, steeply-dipping diffuse beds which have been displaced by minor faults. Generally, LFA B comprises varying proportions of juvenile clasts, autoliths (massive and stratified), basalt clasts, host-rock inclusions and pyroxenite glomerocrysts (Figure 6.21). Pyroxenite glomerocrysts are found as individual crystals and are also present within juvenile clasts, basalt clasts and autoliths. Host-rock inclusions are comprised of various lithologies including: crinoid-rich limestone; shale; coal; massive sandstone; laminated sandstone; and Dalradian schist (basement) (Figure 6.22). The centre of this LFA B unit (N5611847 W00247142) contains lower crust-derived minerals, for example, garnets (<5 mm); zircon (~8 mm); quartz (<40 mm); biotite (<20 mm); pyroxene (individual crystals and as pyroxenite; <25 mm); and amphibole (<3 mm) (Figure 6.21 and Figure 6.22). Juvenile clasts are typically sub-angular and have a modal grain size in the coarse ash to medium lapilli range.

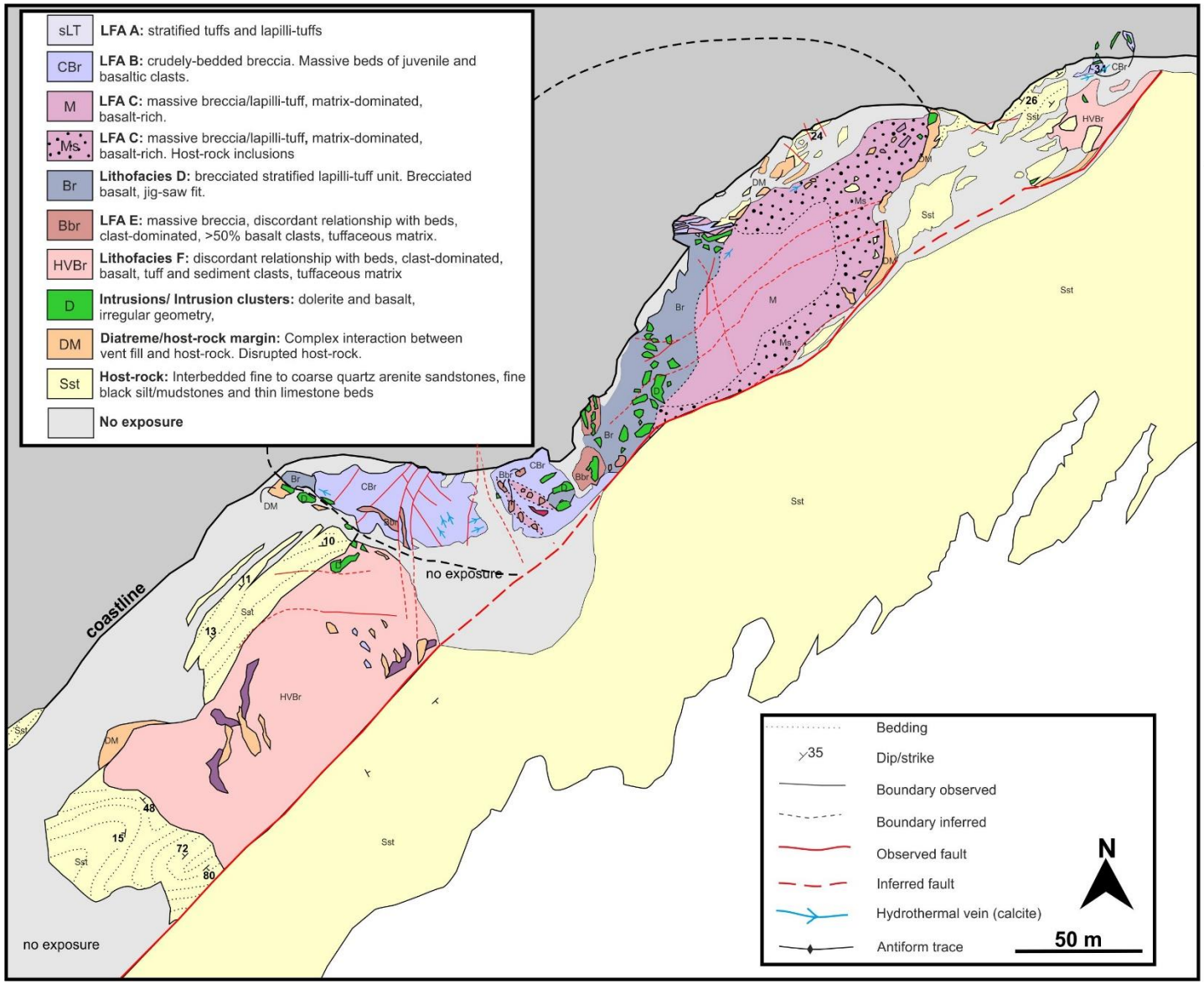

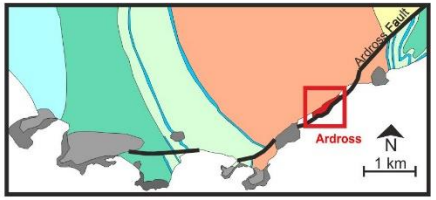

Figure 6.20: Geological map and key of the Ardross diatreme. Inset: Location of the Ardross diatreme with regards to the other East Fife diatremes. Dashed line represents proposed boundary of diatreme.

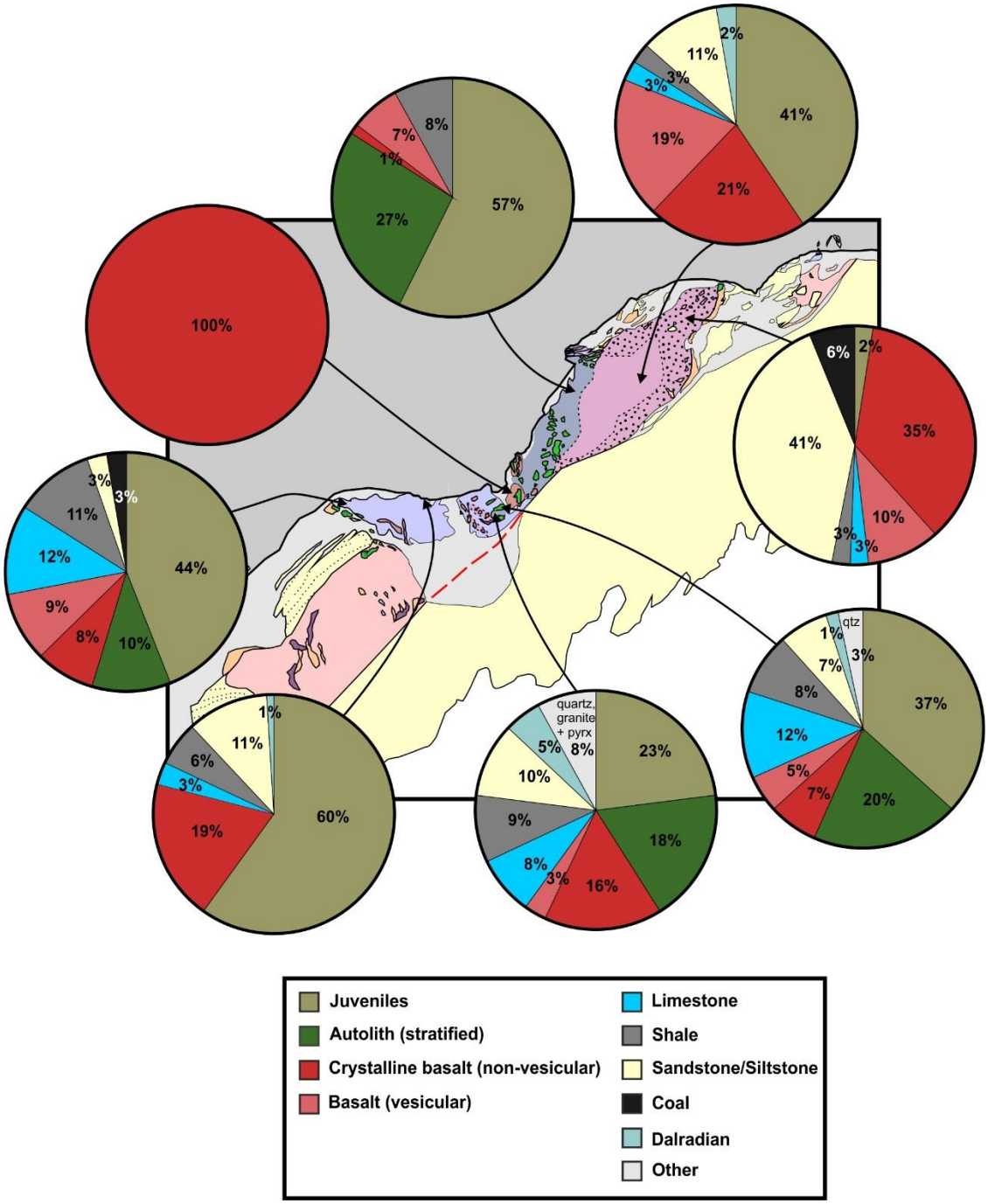

Figure 6.21: Summary geological map of the Ardross diatreme showing the distribution of the main lithologies (see key in Figure 6.20), and pie charts illustrating the composition of the lithic clast population at corresponding localities on the map. N = 100 for each clast count.

In the centre of the diatreme, LFA B grades into massive lapilli-tuffs bearing metre-scale rafts of stratified autoliths (>2 m; Lithofacies D). The boundary between the two lithofacies is obscured by a series of intrusions (Figure 6.20 and Figure 6.21).

The northwest and southeast flanks are obscured either by displacement along the Ardross Fault or by poor inland exposure. However, on the northeast flank of the Ardross diatreme, is a poorly exposed zone of massive lapilli-tuffs (LFA C) which gradually become less lapilli-rich and more host

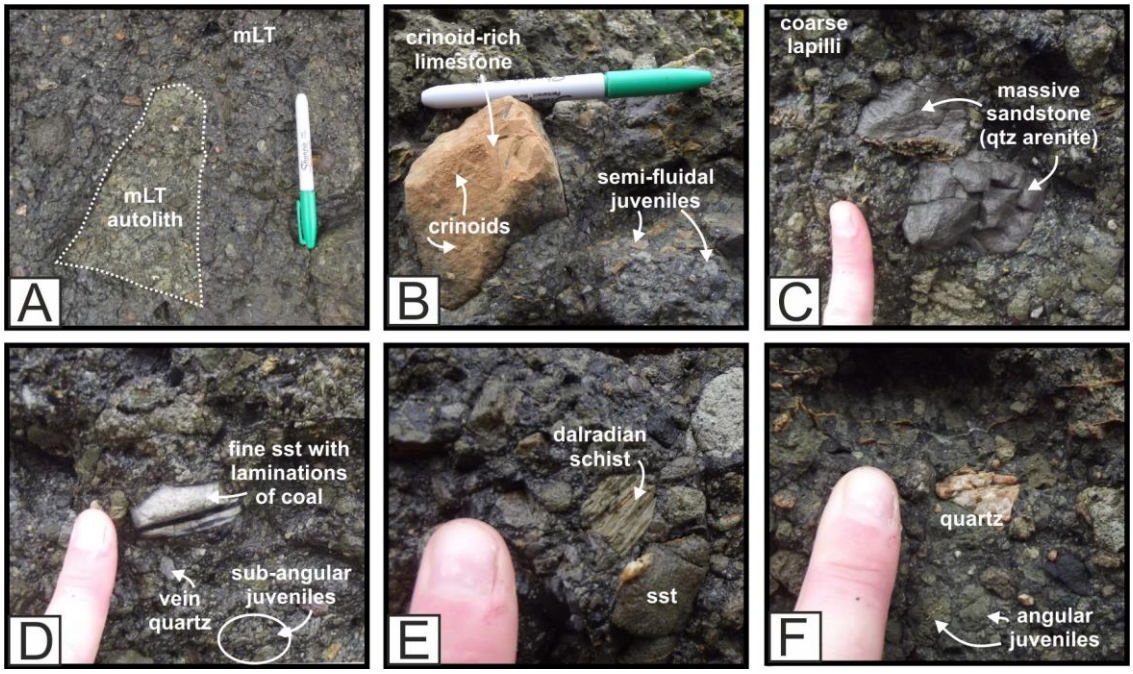

Figure 6.22: Various clast lithologies found within the Ardross diatreme. (A) massive lapilli-tuff autolith; (B) crinoid-rich limestone; (C) massive, medium-grained quartz arenite; (D) laminated fine-grained sandstone with coal stratifications; (E) Dalradian schist; (F) vein quartz, angular juvenile clasts. Pen is 15 cm.

sediment-rich, towards the edge of the diatreme structure (Figure 6.20 and Figure 6.21). The zone measures 125 m (NE-SW axis) by 60 m (NW-SE axis) and marks an unstructured, marginal zone. LFA C is comprised of mm-scale juvenile clasts, basalt clasts (<20 cm) and sediment inclusions within a fine tuff matrix. The proportion of sediment inclusions increases from ~20% of the clast population to ~50% towards the margins (Figure 6.21). Host-rock inclusions tend to comprise of coal, shale, red siltstone and medium to coarse sandstone clasts. The red siltstone and shale have highly fluidal morphologies, whereas the sandstone and coal inclusions tend to retain coherency and are preserved as angular and sub-angular blocks. Locally, the sandstone blocks are metre-scale (<2 m) and retain depositional bedding features. These large sandstone rafts are found within 50 m of the margin (Figure 6.20).

On the opposing southwestern flank of the Ardross diatreme, is a zone of volcanic and host-rock breccia (Lithofacies F) (Figure 6.23). The poorly exposed zone is 130 m by 60 m across and is comprised of >50% host-rock rafts within a tuffaceous matrix. Metre-scale blocks of basalt are also present. The host-rock rafts are <10 m across and retain the stratified host-rock stratigraphy.

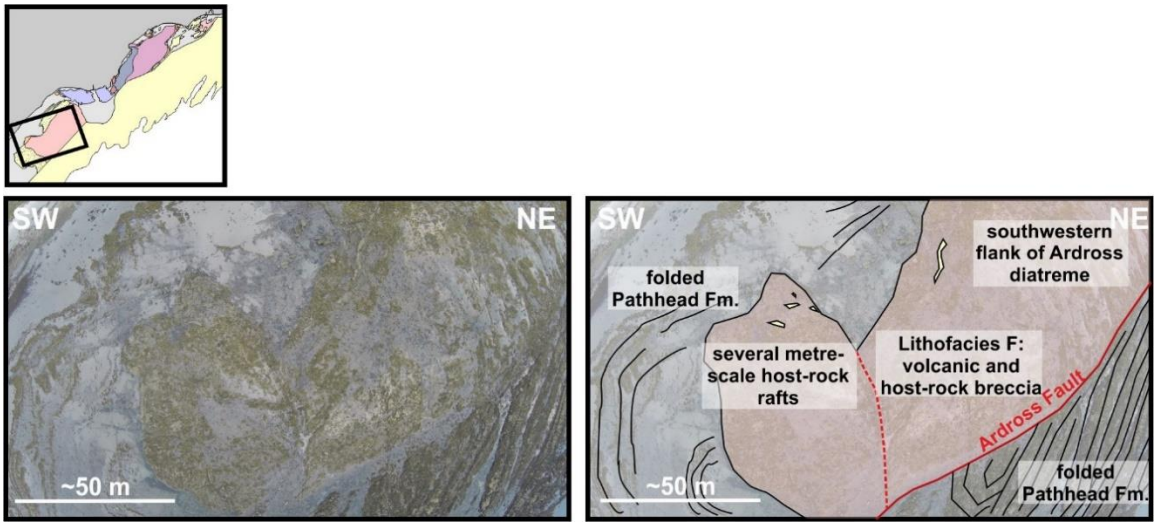

Figure 6.23: Aerial photograph and annotated photograph showing the southwest flank of the Ardross diatreme. Inset: Ardross map shows location of image. Several large host-rock rafts are evident (yellow). The rafts are up to 10 m long and are comprised of coherent segments of the Pathhead Formation.

Intrusions: Magmatic intrusions have exploited the middle of the diatreme, and can be characterised into two end members: (1) fully intact, relatively straight dykes; and (2) zones or pods of monolithic basalt breccia (LFA E) (Figure 6.24). However, varying degrees of intrusion fragmentation occurs and partially-intact dyke segments are common (Figure 6.24A). Intact dykes are up to 1.5 m wide and tend to be orientated along a NW-SE trend. Surrounding some of the dykes are cross-cutting lapilli-tuff injectites which dissect and displace the magmatic dykes by 15-20 cm. The injectites comprise a black tuffaceous matrix with angular and sub-angular, non-vesicular basalt clasts (sub-cm to 22 cm), sandstone and siltstone inclusions (<10%; sub-cm to 5 cm) and lapilli-tuff autoliths (<5%; <4 cm). Dyke segments (>55 cm wide) have become detached from the main dyke bodies and suspended within the lapilli-tuff.

Pods or zones of monolithic basalt breccia tend to be <1 – 20 m wide and are comprised of clast-supported, angular basalt clasts within a tuffaceous matrix (Figure 6.24B). Clasts are large (3 cm to 55 cm) and randomly orientated (no jigsaw fit). The tuffaceous matrix infills fractures within the clasts and contains ripped up partially consolidated lapilli-tuff clasts (mLT). Locally, the core of the pod is a coherent, unfractured dyke segment and clasts become increasingly more dispersed from the centre of the pod, forming peperitic margins. The pods are discretely aligned, delineating the trace of a dyke (Figure 6.10C; Figure 6.26B). The intrusions and clastogenic pods contain peridotite xenoliths (Figure 6.13). These olivine-rich xenoliths are up to 15 cm across, locally layered and have been serpentinised (Figure 6.13).

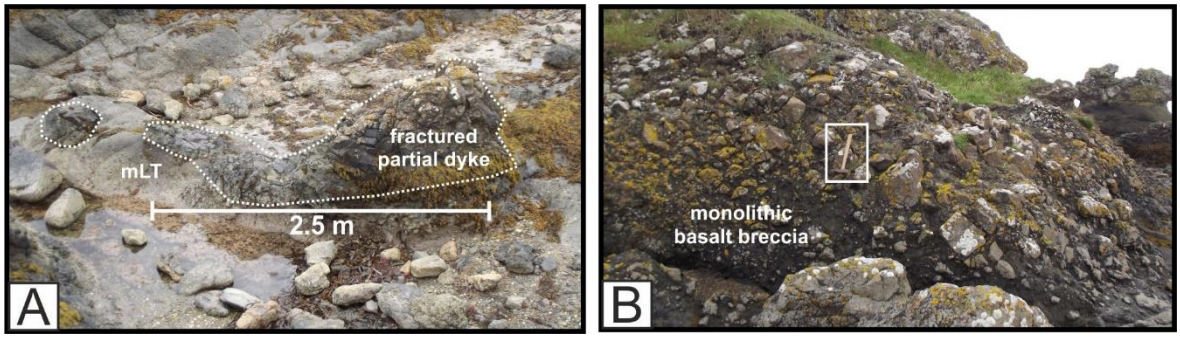

Figure 6.24: Various intrusion morphologies within the centre of the Ardross diatreme (Figure 6.20). (A) Partially fractured dyke segment. The dyke segment has irregular margins with the surrounding lapilli-tuff. (B) LFA E: Zone of coarse, matrix-supported basalt breccia. Hammer is 40 cm long.

6.6.2.2. Interpretation

It is proposed that the Ardross diatreme is exposed in the lower, unbedded zone (Figure 6.25), due to: (1) little to no bedded zones (crudely bedded); (2) large, heterogeneous marginal zones (3) an abundance of intrusions and clastogenic bodies; and (4) collapsed bedding, with metre-scale intact blocks of well-developed bedded upper-diatreme deposits.

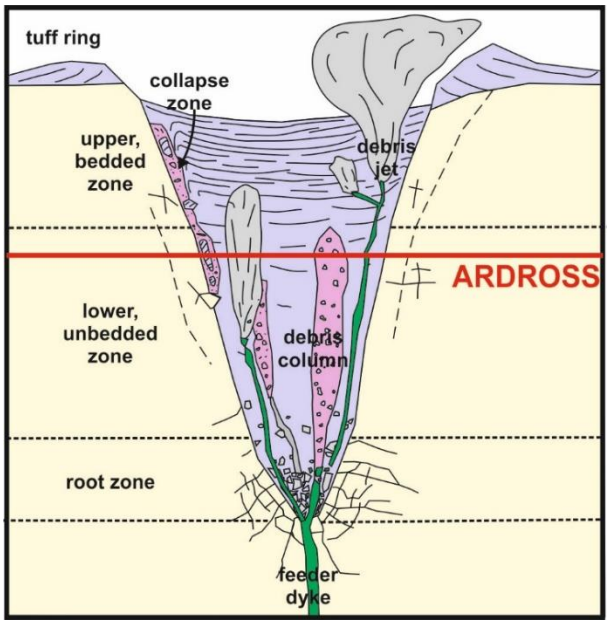

Figure 6.25: A typical diatreme structure showing the four main zones (tuff ring, upper bedded, lower unbedded and root zone). Debris columns and collapse zones are also evident within a typical diatreme. The proposed level of the exposed Ardross diatreme within the typical diatreme structure is marked by the solid red line. Not to scale.

The wide (>100 m) marginal zones on the southwest and northeast flanks of the diatreme consist of large, tabular semi-intact host-rock rafts (<10 m) (Figure 6.20 and Figure 6.23). The abundance of such rafts and a high proportion of host-rock (>50%) suggests this flank formed separately (and possibly simultaneously) to the main Ardross diatreme. It is suggested that discrete, high-level phreatomagmatic explosions occurred to the southwest and northeast of the main Ardross

diatreme, as a fissure-like system. The explosions brecciated host-rock and produced a small proportion of fine ash, which infilled the interstices between the clasts. The phreatomagmatic activity at these two flanks was relatively short-lived resulting in arrested diatreme development on either side of the main Ardross diatreme, and the fissure-controlled eruptions focussed to a single-centre volcano with time (Leys 1982). The result was a heterogeneous, host-rock-rich zone that encroached the main Ardross diatreme. The northwest flank has a higher percentage of tuffaceous and juvenile material (Figure 6.21), suggesting it was significantly longer lived than the southwest flank. Large, coherent rafts of sandstone are found in the NE flank of the Ardross diatreme and were likely eroded from the walls of the diatreme and incorporated into the NE marginal zone. The rafts are rotated suggesting some lateral transport during subsidence (White and Ross 2011).

Intrusions: The aligned pods of monolithic breccia in the centre of the Ardross diatreme are the remains of an intra-diatreme fragmentation zone (Figure 6.26; Ross and White 2006; Ross et al. 2008; White and Ross 2011; Valentine and White 2012). Magma was focussed into this central zone (Figure 6.20) during diatreme formation. The clastogenic zones and pods are created mostly by non-explosive interaction, producing large peperitic domains within the centre of the diatreme (Ross and White 2006). These peperitic domains are formed by rapidly quenching magma forming brittle fractures in the magma. This process causes fluidisation of the surrounding diatreme deposits/slurry, which infills the fractures (Kokelaar 2002). The pods of breccia are spatially aligned, but are not connected to each other which suggests finger-like emplacement of magma.

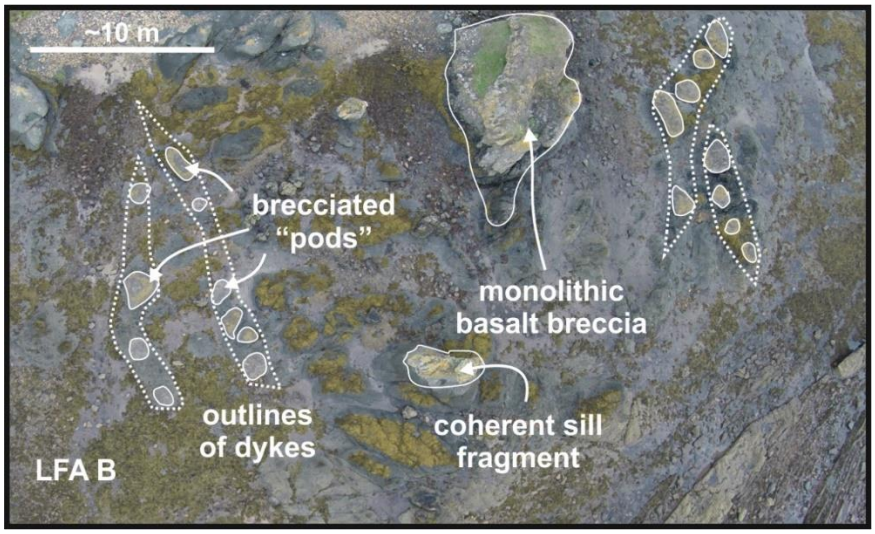

Figure 6.26: Aerial photograph of the proposed intra-diatreme fragmentation zone in the Ardross diatreme. Pods are highlighted by solid white lines and outlines of dykes are shown by dotted white lines.

6.6.3. **Elie Ness**

6.6.3.1. Observations

The Elie Ness diatreme is located 1410 m SW of the Ardross diatreme [N56111232 W00248287] and is emplaced into the Pathhead Formation and the Lower Limestone Formation (Figure 6.27). The Elie Ness diatreme has a slightly ovate shape: its longest axis measures ~504 m in an NE-SW orientation, its shortest axis measures ~348 m in a NW-SE orientation. Margins with the surrounding host-rock are only locally exposed along the NE margin of the diatreme. Exposure of the diatreme fill is good enabling a detailed study of the clast proportions at multiple locations within the diatreme structure and stratigraphical logging of the diatreme deposits (Figure 6.28 and Figure 6.29).

Aerial photographs of the Elie Ness diatreme clearly show well-developed centroclinal dipping bedding (Figure 6.30A). The beds dip at angles of between 9° and 54° and generally dip around a central point, as shown in Figure 6.27. However, in the west of the diatreme, the centroclinal pattern has been disrupted and has been gently folded to define a syncline orientated along an ENE–WSW trend (Figure 6.27). Along the NW margin of the diatreme, the well-developed bedding grades into crudely-bedded and massive lapilli-tuffs, locally hosting stratified autoliths (Lithofacies D). Discordant zones of monolithic basalt breccia (LFA E) and volcaniclastic injectites cut through the surrounding bedding. The Elie Ness diatreme is thoroughly disrupted by minor faults, hydrothermal veins (particularly around the margins) and magmatic intrusions (particularly in the NE of the diatreme) (Figure 6.27).

The well-developed bedded zone in the centre of the diatreme is comprised of stratified tuffs and lapilli-tuffs (LFA A) interbedded with diffusely bedded to massive, coarse lapilli-tuff or breccia layers (LFA B) (Figure 6.27 and Figure 6.30). The LFA A beds have distinctive planar, hummocky and low-angle cross stratification, defined by dark grey, fine tuff layers and coarse, juvenile-rich lapilli layers (Figure 6.29). The stratifications are sub-cm to 12 cm thick, although diffusely stratified medium to coarse lapilli layers tend to be up to a metre thick (Figure 6.29). Fine tuff layers tend to be laterally continuous and planar stratified. Generally, low-angle cross-bedded tuffs overlie fine to coarse, massive lapilli-tuffs. Scours and channels are present at the base of the massive lapilli-tuffs and are

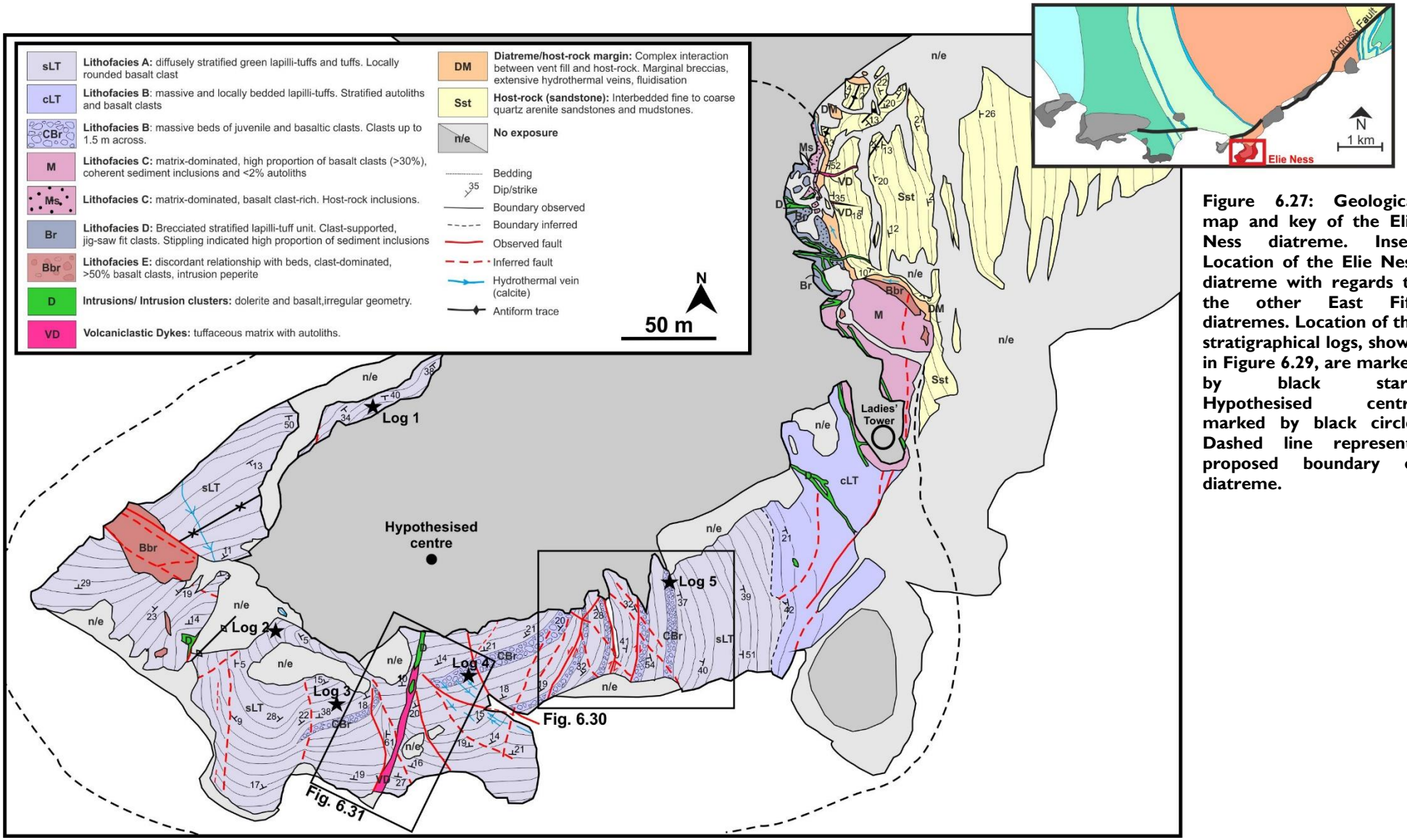

Figure 6.27: Geological map and key of the Elie Ness diatreme. Inset: Location of the Elie Ness diatreme with regards to the other East Fife diatremes. Location of the stratigraphical logs, shown in Figure 6.29, are marked by black stars. Hypothesised centre marked by black circle. Dashed line represents proposed boundary of diatreme.

laterally extensive on a metre-scale. LFA B is comprised of unstructured or incipiently stratified coarse lapilli-tuffs with sub-angular clasts of vesicular and non-vesicular dolerite and basalt, autoliths (mT/LT, //sT/LT) and varying proportions of host-rock (shale, fine sandstone, limestone) (Figure 6.28). Basalt/dolerite clasts range from sub-cm to 124 cm in size, contain coarse pyroxene phenocrysts (<3 mm) and are non-vesicular to mildly vesicular (0-10%) (Figure 6.28). The matrix contains pyroxenite glomerocrysts (<4 cm) and liberated pyroxene crystals (<1.6 cm). The LFA B interbeds are <1.5 m thick (Figure 6.5B).

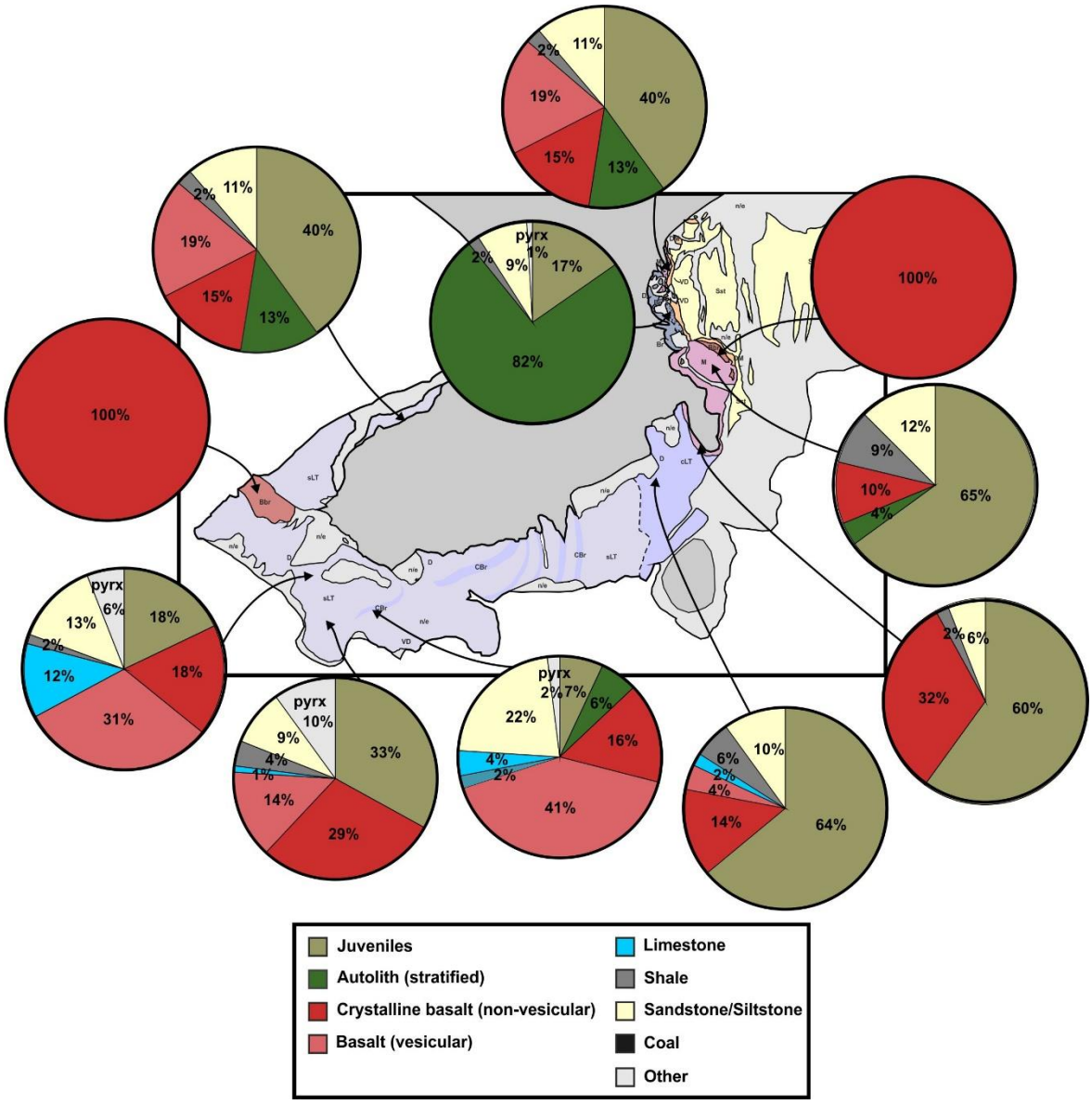

Figure 6.28: Summary geological map of the Elie Ness diatreme showing the distribution of the main lithologies (see key in Figure 6.27), and pie charts illustrating the composition of the lithic clast population at corresponding localities on the map. N = 100 for each clast count.

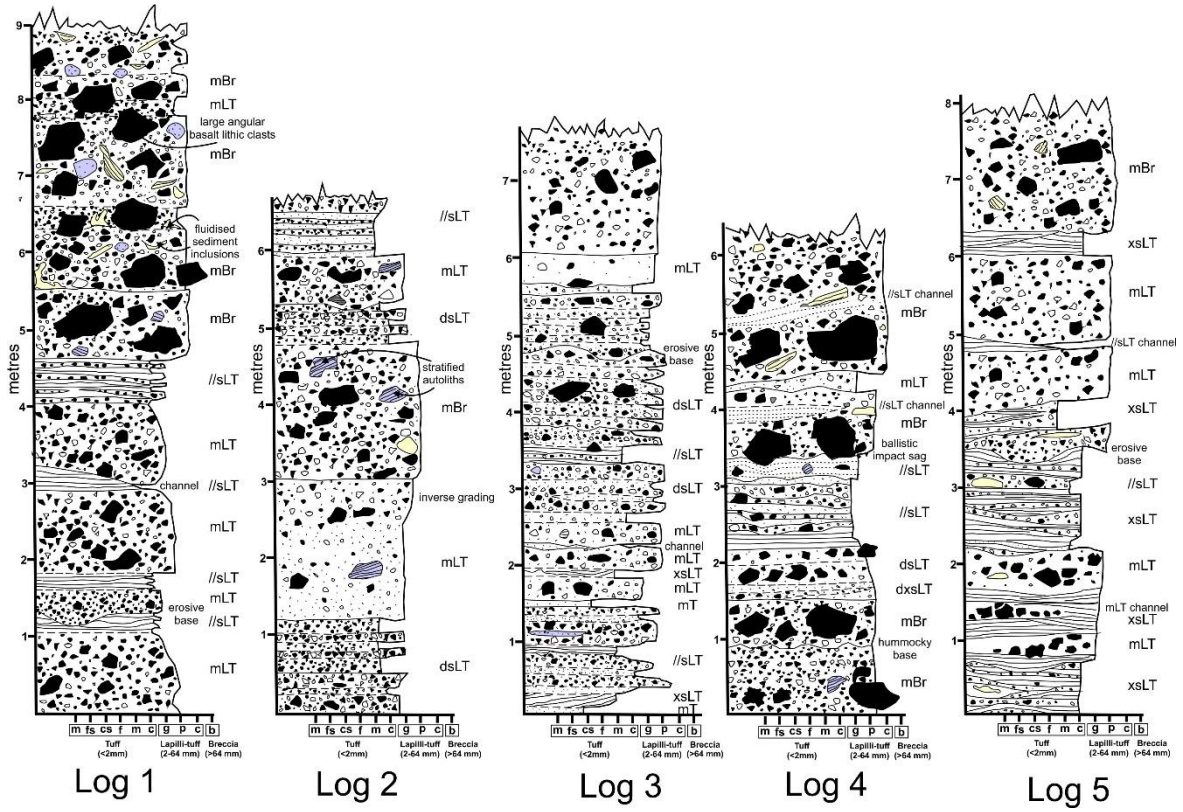

Figure 6.29: Representative stratigraphical logs through the bedded deposits in the Elie Ness diatreme. Interbedded coarse lapilli-tuffs and breccias (Log 1 and 4) and stratified tuffs and lapilli-tuffs, locally displaying hummocky cross-stratification and channels. Note that the tuff and fine lapilli-tuff layers are not laterally extensive. Host-rock inclusions and stratified and non-stratified autoliths are also evident within the successions. Locations of logs are shown in Figure 6.27.

LFA B beds are predominantly distributed around the centre of the diatreme. From the centre of the diatreme, the bed thickness decreases and become comprised entirely of LFA A (Figure 6.27 and Figure 6.30A). The thinly stratified beds grade into crudely bedded lapilli-tuffs, approximately 100 m southwest of the Ladies Tower (Figure 6.27). The crudely-bedded lapilli-tuffs consist of >60% juvenile clasts, ~15% non-vesicular basalt clasts and varying proportions of host-rock (sandstone, shale, limestone and coal) within a medium to coarse tuffaceous matrix (Figure 6.28). Juvenile clasts typically have fluidal morphologies and are up to ~15 cm across (Figure 6.30C). Locally, lapilli-rich layers define crude bedding, ~5–15 cm in thickness, although these layers do not tend to be laterally continuous. A significant component of the crudely-bedded lapilli-tuffs are coated lapilli or pelletal lapilli, which consist of small to medium size lapilli or pyroxene crystals that have subsequently been coated with quenched juvenile melt (Figure 6.30B). The pelletal lapilli have convolute margins (Figure 6.30B).

The crudely bedded lapilli-tuffs grade into unstructured, homogenised lapilli-tuffs, which are distributed along the NE margin of the diatreme (Figure 6.6A; Figure 6.27). The massive lapilli-tuffs

contain 60-70% fine to coarse juvenile lapilli, 10-30% non-vesicular basalt clasts and varying ratios of host-rock inclusions and stratified and non-stratified autoliths (Figure 6.28). The host-rock inclusions tend to be <10 cm. Towards the margin, the proportion of autoliths increases from <5% to >75%, representing a zone of collapsed bedding (Lithofacies D; Figure 6.27 and Figure 6.28). The autoliths are typically angular and stratified, defined by alternating fine ash layers and juvenile-rich layers, where juvenile clasts tend to be fine to coarse grade (Figure 6.30D). The autoliths increase in size towards the margin, from <1 cm to >2 m, and are distributed randomly, although locally jigsaw-fit textures are present. Furthermore, fine to coarse ash from the surrounding diatreme deposits appears to have been injected into the autoliths forming thin (<4 cm) volcaniclastic veins. Locally, small inclusions of host-rock, small cm-scale autoliths and juvenile clasts have been injected alongside the ash into the volcaniclastic vein.

Cross-cutting, monolithic breccias are evident in the western and northeastern corners of the diatreme (Figure 6.27). The boundaries of these zones are indefinite and grade into the surrounding

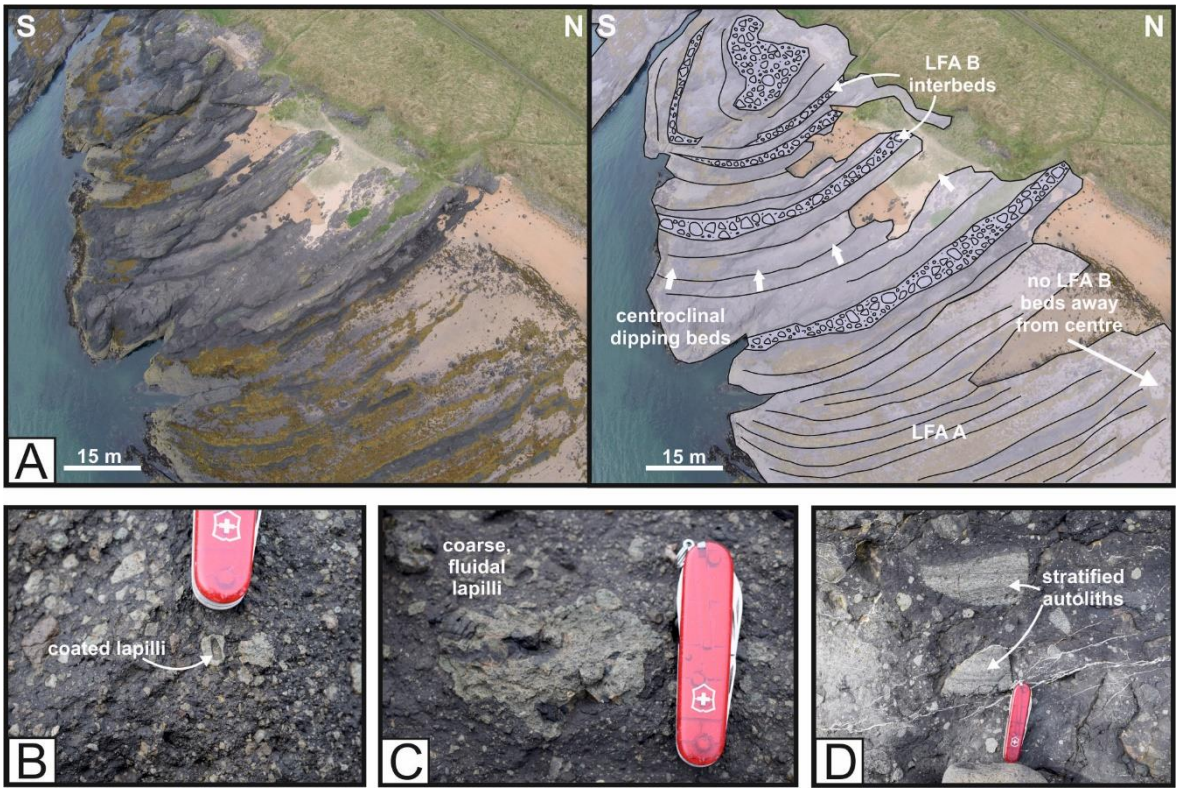

Figure 6.30: (A) Aerial photograph of the central zone of the Elie Ness diatreme clearly showing the beds dipping towards the centre of the diatreme. LFA B interbeds are evident within LFA A and progressively become less abundant away from the centre of the diatreme. Location of image shown in Figure 6.27. (B) Coated lapilli from the crudely bedded deposits. (C) Highly fluidal lapilli. (D) Stratified autoliths are abundant within the zone of collapsed bedding around the NE margin of the Elie diatreme. Pen-knife is 10 cm long.

bedded lapilli-tuffs and massive lapilli-tuffs respectively. The massive zones consist of matrix-supported angular blocks of non-vesicular to mildly vesicular, dense crystalline basalt (<5%ves), classified as LFA E (Figure 6.10B and Figure 6.28). Locally, jigsaw-fit textures are evident, suggesting in-situ fragmentation, and fragments of hexagonal columns have been identified (Figure 6.10B). The monolithic breccia in the NE corner of the diatreme is more thoroughly dispersed than the breccia in the western corner. The interstices between clasts consist of fine to medium grade tuff.

Intrusions: Magmatic intrusions within the Elie Ness diatreme are localised to the northeast corner and are emplaced into the massive, autolith-bearing lapilli-tuffs found within the marginal zone. The dyke-like intrusions have highly irregular, fluidal margins, curved morphologies, and occasionally bifurcate and amalgamate (Figure 6.31C). Locally, fluidal peperite forms along the margins of the intrusions and magma fingers extend into the surrounding diatreme deposits (Figure 6.14B, C and Figure 6.31C). The intrusions range from ~15 cm to >2 m wide and have intruded sub-perpendicular to the diatreme margin. The intrusions consist of porphyritic and occasionally amygdaloidal basalt and commonly contain pyroxenite glomerocrysts (2-3 cm). Pyroxene phenocrysts are up to 2 mm and amygdales consist of calcite (<12 mm) (Figure 6.31C). Some of the intrusions have vesicular cores (10-15%ves) with sub-mm vesicles.

A large volcaniclastic injectite has been emplaced into the Elie Ness diatreme (Figure 6.31A and B). The volcaniclastic injectite stems from a coherent basaltic dyke (1.5-2.5 m wide) which grades into a volcaniclastic breccia (5-10 m wide) (Figure 6.31A and B). The breccia consists of a tuffaceous matrix hosting a variety of vesicular basalt clasts, coarse lapilli and megablocks of coherent host-rock inclusions and crystalline basalt (likely sourced from the dyke). Metre-scale coherent basalt blocks are abundant within 10 m of the dyke termination. The coherent sandstone inclusions are 1-2 m wide and are only mildly deformed, retaining their internal laminations (Figure 6.31B). The volcaniclastic injectite is poorly sorted and matrix-supported. The boundaries with the diatreme deposits are straight and defined by hydrothermal quartz veins (Figure 6.31A and B). The dyke and initial 40 m of the injectite is aligned along an N-S orientation but rotates to a 207° heading (Figure 6.27).

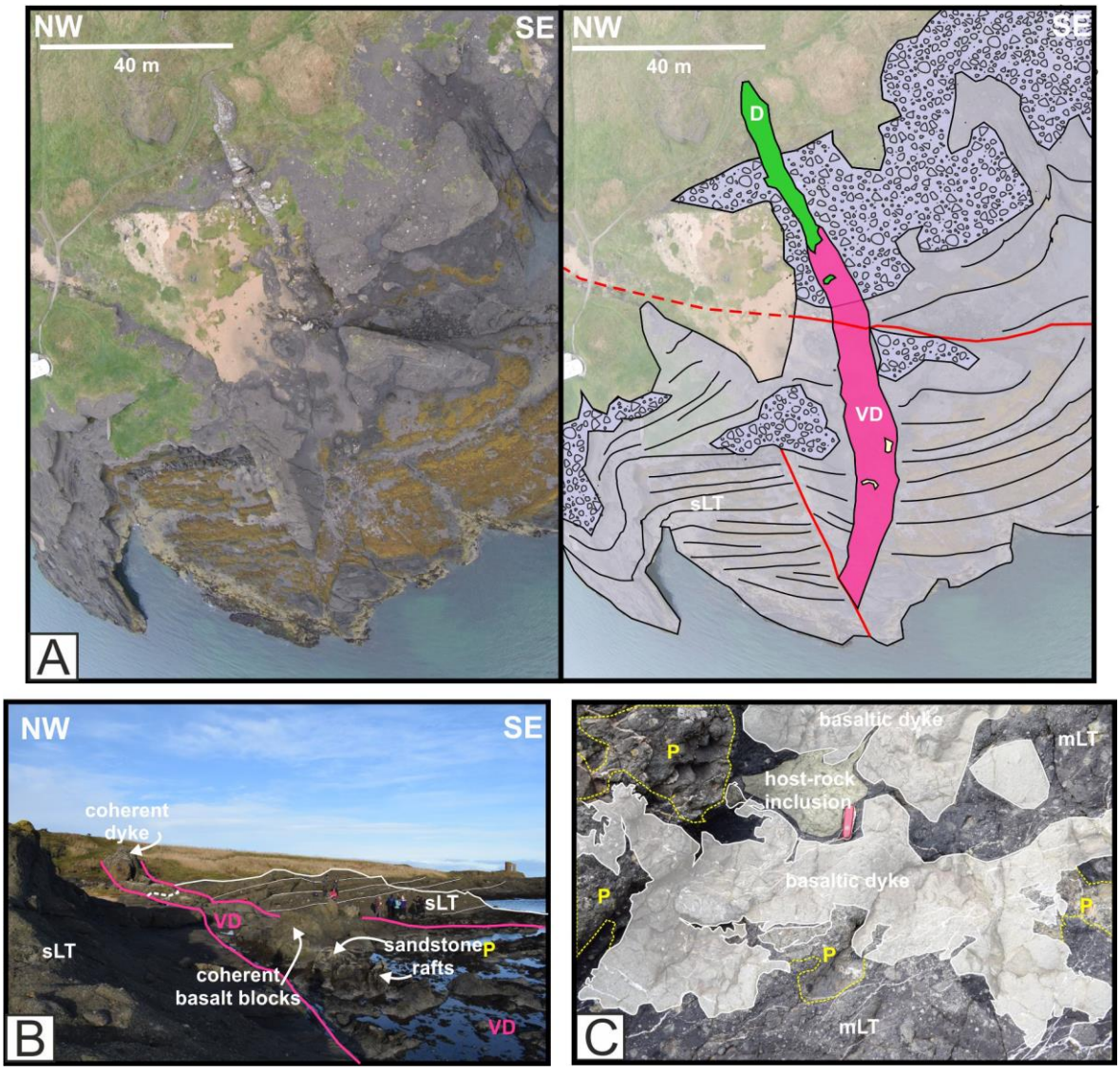

Figure 6.31: (A) Aerial photograph and annotated photograph of the volcaniclastic injectite situated in the centre of the Elie Ness diatreme. Location of image shown in Figure 6.27. A coherent basaltic dyke feeds the volcaniclastic injectite (VD). The injectite cross-cuts the surrounding layered diatreme deposits. (B) The injectite is comprised of large (metre-scale) basalt blocks and intact host-rock rafts within a tuffaceous matrix and has defined, relatively straight margins. Students for scale. (C) An example of a highly fluidal intrusion with extremely convolute margins. Image taken from the NE margin of the Elie Ness diatreme. The intrusion has intensively mingled with the diatreme deposits forming peperitic zones around the edges of the intrusion (labelled as "P"). The peperite has typically fluidal clasts, although locally some blocky clasts are evident. The dyke is comprised of amygdaloidal basalt (quartz amygdales) and quartz hydrothermal veins have extensively been injected into the marginal zone. A host-rock inclusion (laminated siltstone) has been partially fluidised and injected into a fracture within the intrusion.

6.6.3.2. Interpretations

It is proposed that the Elie Ness diatreme is exposed in the upper, bedded zone (Figure 6.32), due to: (1) the abundance of well-developed bedding; (2) lack of debris columns (bedding is not disrupted); and (3) metre-scale autoliths of well-developed bedded tuff ring deposits.

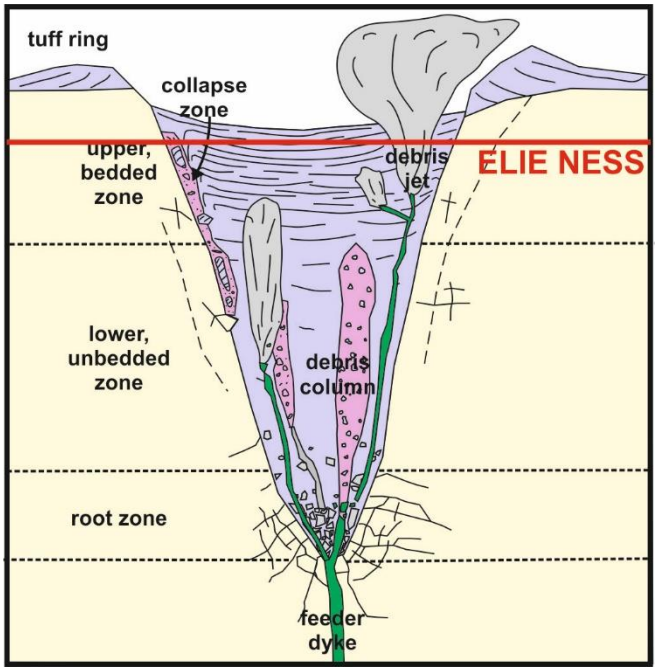

Figure 6.32: A typical diatreme structure showing the four main zones (tuff ring, upper bedded, lower unbedded and root zone). Debris columns and collapse zones are also evident within a typical diatreme. The proposed level of the exposed Elie Ness diatreme within the typical diatreme structure is marked by the solid red line. Not to scale.

The well-exposed deposits at Elie Ness, gives insight into the complex temporal and spatial development of the diatreme. The centroclinal dipping beds evident in the centre of the structure (LFA A and LFA B) are underlain by crudely-bedded massive lapilli-tuffs containing fluidal juvenile clasts and coated lapilli (Figure 6.27 and Figure 6.30). This suggests a switching from phreatomagmatic processes (initially forming the diatreme) to magmatic processes (forming the massive lapilli-tuffs with coated lapilli) back to phreatomagmatic and mass flow processes (forming the LFA A and LFA B beds in the centre of the diatreme).

The presence of coated lapilli indicates that during the formation of the Elie Ness diatreme, explosive phreatomagmatic activity was surpassed by explosions caused by the rapid expansion of volatiles, likely due to an increase in the magma-water ratio (Aranda-Gómez and Luhr 1996; Valentine 2012; Gernon et al. 2012, 2013). Volatiles within a new phase of magma rapidly exsolve upon emplacement into the diatreme, which drives high energy gas explosions. These explosions intensely fragment the melt into melt droplets which are sprayed upwards in explosive debris jets (Zhang 1999; Gernon et al. 2012). Discrete particles from earlier deposits are entrained within the debris jet due to the drag force exerted by the upward moving jet and are simultaneously fluidised and sprayed by the newly intruded, melt droplets (Gernon et al. 2009, 2012). The spray of melt

droplets forms a thin coating around earlier-formed particles which acts as a seed to this process. The coatings are not uniform in the deposits at Elie which suggests short-lived melt sprays.

The finely stratified nature of the tuffs and lapilli-tuffs (LFA A) that overlie the crudely bedded, coated-lapilli-bearing lapilli-tuffs in the centre of the diatreme, is typical for phreatomagmatic activity and marks a switch from magmatic processes, described above, to pulsed, small-volume phreatomagmatic eruptions (Lorenz 1986; White and Ross 2011). LFA A at Elie Ness demonstrates many characteristics of PDC and base surge deposits, including low-angle cross stratification, scours and flat U-shaped channels, erosive contacts, diffuse stratification and massive layers (Figure 6.29). Planar stratified, well-sorted ash layers are likely to be the product of direct fallout from discrete ash plumes (Figure 6.29) (Branney and Kokelaar 2002; van Otterloo and Cas 2016; Cas et al. 2016). Couplets of low-angle cross-stratified layers that are overlain by massive lapilli-tuff layers represents a change in current conditions, from a fully dilute, traction-dominated PDC to a more concentrated current, where mLT is deposited through a fluid-escape dominated flow boundary zone (Branney and Kokelaar 2002).

The LFA B interbeds in the centre of the diatreme, made up of coarse, angular blocks of basalt/dolerite (containing boulders >1 m), indicate that in the latter stages of diatreme formation, lahar and debris flow events were common and accompanied PDCs The lahar events likely resulted from the collapse of the tuff ring and pre-existing stratigraphy into the maar-crater and were activated by intense late-stage eruptions. The angular lithic blocks consist of medium to coarse dolerite and are typically non-vesicular, or mildly vesicular (<5%). Gernon et al. (2013) ascribe the blocks to fragments of lavas from a pre-eruptive stratigraphic horizon in the Midland Valley graben (basaltic-hawaiitic lava successions erupted between the Pathhead Formation and the Sandy Craig Formation; Table 6.1; Upton et al. 2004). However, due to the coarse crystal size and lack of vesicularity, it is suggested the blocks could also be derived from sill-like intrusions emplaced pre-diatreme.

Differential subsidence within the diatreme structure (greater subsidence in the centre) results in the centroclinal dipping beds, characteristic of the upper zone of diatremes. The gentle folding of the beds in the west of the Elie Ness diatreme has been attributed to post-emplacement folding

caused by movement along the Ardross Fault Zone (Francis and Hopgood 1970; Leys 1982; Gernon et al. 2013).

Widening of the diatreme occurred in the northwest portion of the Elie diatreme, where autolith-bearing, marginal breccias are present (Figure 6.27 and Figure 6.30). As the explosion locus deepened, the diatreme widened and surface-derived material, for example partially consolidated tuff ring deposits, collapsed into the crater (Lorenz 1986, 2003). Exposure of the diatreme margin is limited to the northeast side of the Elie Ness diatreme, which prevents full analysis of the processes associated with the deepening and widening of the diatreme, for example, asymmetric vs symmetric widening.

Intrusions: Intrusions within the northeast margin have highly fluidal morphologies (Figure 6.14C and Figure 6.31C). The irregularity of these bodies indicates the substrate (autolith-bearing massive lapilli-tuffs) was partially consolidated to unconsolidated at the time of emplacement allowing for extensive fluidisation and ductile emplacement. Fluidisation of the deposits surrounding the intrusions in the Elie Ness diatreme is evident in the form of fluidal peperite formation (Figure 6.31C), elutriation structures and thin volcaniclastic veins injected into autoliths. The formation of fluidal, locally dispersed peperite indicates a high (~40%) water content within the host (Busby-Spera and White 1987). Fluidal peperite is formed by molten fuel-coolant interactions (MFCIs) which are caused by instabilities in the vapour film surrounding the magma (Wohletz 1983, 1986; Busby-Spera and White 1987), and magma-sediment density contrasts (Donaire et al. 2002). To form fluidal peperite, without causing intensive thermohydraulic fracturing and phreatomagmatic explosions, the vapor film must be maintained continuously at the magma-sediment interface, insulating the magma (Busby-Spera and White 1987). Fragmentation is caused by surface tension and fluid-fluid shearing across the magma-sediment interface (Skilling 2002).

Zones of monolithic basalt breccia in the east and west of the diatreme (Figure 6.10B and Figure 6.27) represent high level debris columns formed when volatile-poor intrusions are emplaced at high levels within the diatreme and explosively interact with water-saturated diatreme deposits. The force of the explosion can brecciate pre-existing intrusions (emplaced prior to diatreme emplacement) and/or pre-existing volcanic stratigraphy (lavas). Angular blocks of the intrusions or

lavas are subsequently incorporated into the debris jet. The angular nature of the basalt blocks and the structureless, poorly sorted characteristics of the monolithic zones in the Elie Ness diatreme suggest they are high level debris columns.

The presence of the volcaniclastic injectite and its relationship with its feeder dyke (Figure 6.31), suggests that a late-stage, volatile-rich magma was emplaced into the diatreme where it encountered water-saturated diatreme deposits (Leys 1982; Gernon et al. 2013). The change in conditions triggered the fragmentation of the dyke and the formation of a volcaniclastic dyke which was forcefully injected into the surrounding lapilli-tuffs (Gernon et al. 2013). Host-rock rafts (laminated sandstone) are present within the volcaniclastic injectite (Figure 6.31A and B) which suggests that the locus of the explosive fragmentation occurred next to or near the host-rock margin. The explosion caused the surrounding host-rock to fragment, becoming incorporated in the volcaniclastic injectite. The host-rock rafts are suspended within a homogenised tuffaceous matrix which suggests that the tuffs were fluidised during emplacement.

6.6.4. **Kincaird**

6.6.4.1. Observations

The Kincaird diatreme is located 2650 m west of the Elie Ness diatreme [N56112023 00251676W] and is emplaced into the Limestone Coal Formation (Figure 6.33). The diatreme is an elliptical shape: its longest axis measures ~1150 m in an E-W orientation. Margins with the surrounding host-rock are locally exposed along the east and west margin of the diatreme. The host-rock adjacent to the margin is highly disrupted and deformed (See Chapter 7). The Kincaird diatreme consists of 20-40 m high cliffs which are accessible at low-tide via the Fife Chain Walk, and provide a vertical cross-section through the middle of the diatreme. Exposure of the diatreme fill is good enabling a detailed study of the clast proportions at multiple locations within the diatreme structure and stratigraphical logging of the diatreme deposits (Figure 6.34; Figure 6.35).

The Kincaird diatreme is comprised of both poorly-developed, diffuse beds and well-developed beds of LFA A and LFA B that dip into two separate centres (Figure 6.33). The beds, particularly in the centre of the diatreme, consistently dip at steep angles (>50°). Discordant, unstructured zones are emplaced into the stratigraphy and consist of massive lapilli-tuffs and breccias with varying proportions of fluidised sediment inclusions and non-vesicular and vesicular basalt lithic clasts (Figure 6.34). In the centre of the diatreme, there is a zone of well-exposed collapsed bedding and several thick sill-like intrusions (Figure 6.8A, Figure 6.14G and Figure 6.33). In the west of the Kincaird diatreme, the marginal zone consists of pods of peperite domains (Figure 6.33).

A large proportion of the Kincaird diatreme consists of stratified tuffs and lapilli-tuffs (LFA A; Figure 6.4A) interbedded with diffusely bedded to massive, coarse lapilli-tuff or breccia layers (LFA B; Figure 6.5A) (Figure 6.33 and Figure 6.35). LFA A is comprised of cross-stratified and planar stratified tuffs and lapilli-tuffs (Figure 6.4; Log 1 and Log 2, Figure 6.35). Beds are typically <120 cm and the stratifications are 1 to 8 cm thick. Normal grading is evident throughout LFA A (Figure 6.4B; Log 1, Figure 6.35). Erosive bases are locally present, and typically occur at the base of massive or diffusely-stratified lapilli-tuffs (Figure 6.4H). Similarly, scours and laterally-inconsistent channels (<3 m) are also present (Figure 6.4A). Impact sags are present where bombs/blocks of up to 10 to 15 cm in diameter descend below the eruptive surface by up to 15 cm (Figure 6.4C).

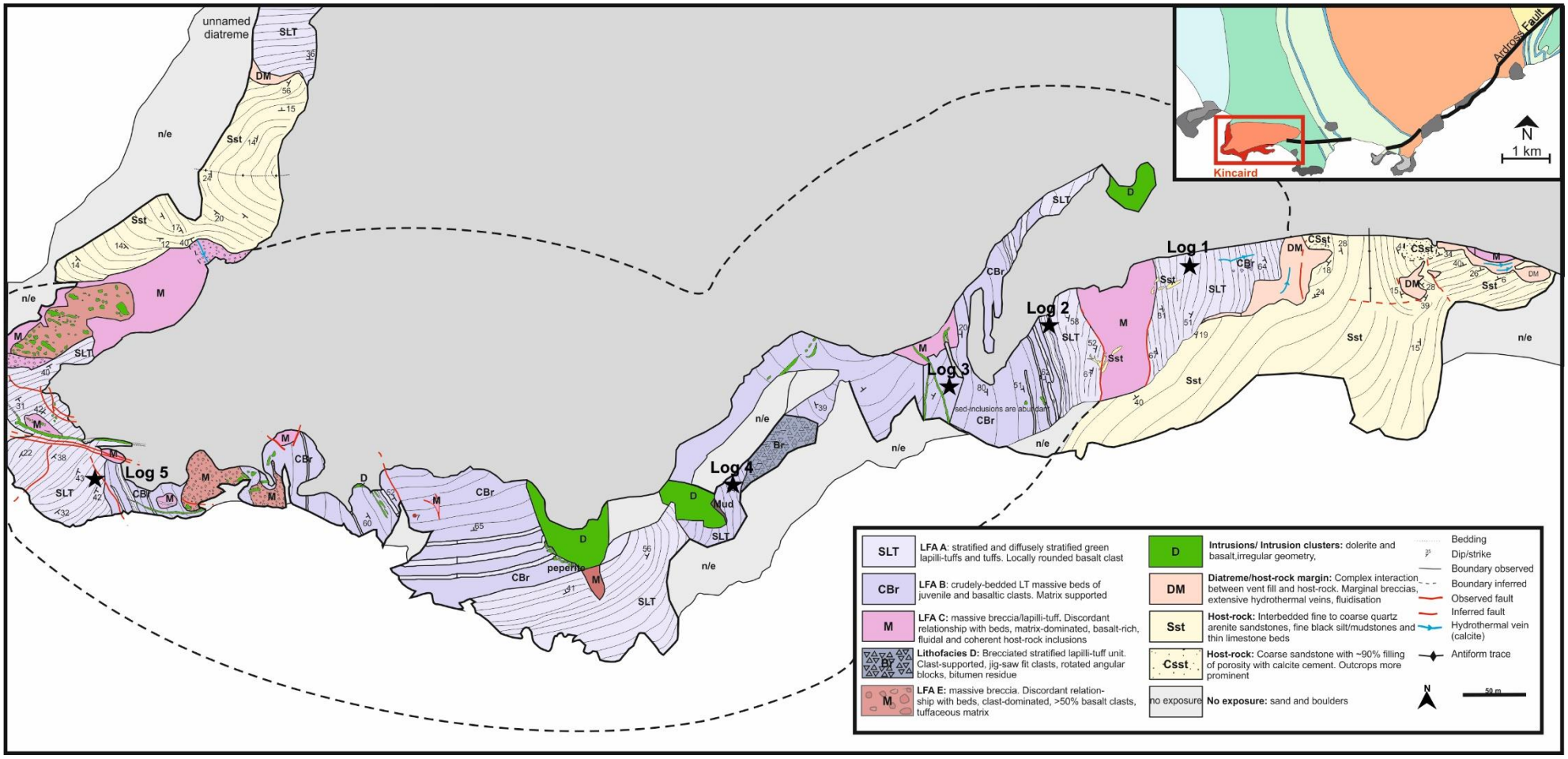

Figure 6.33: Geological map and key of the Kincaird diatreme. Inset: Location of the Kincaird diatreme with regards to the other East Fife diatremes. Locations of the stratigraphical logs, shown in Figure 6.35, are marked by black stars. Dashed line shows proposed diatreme boundary.

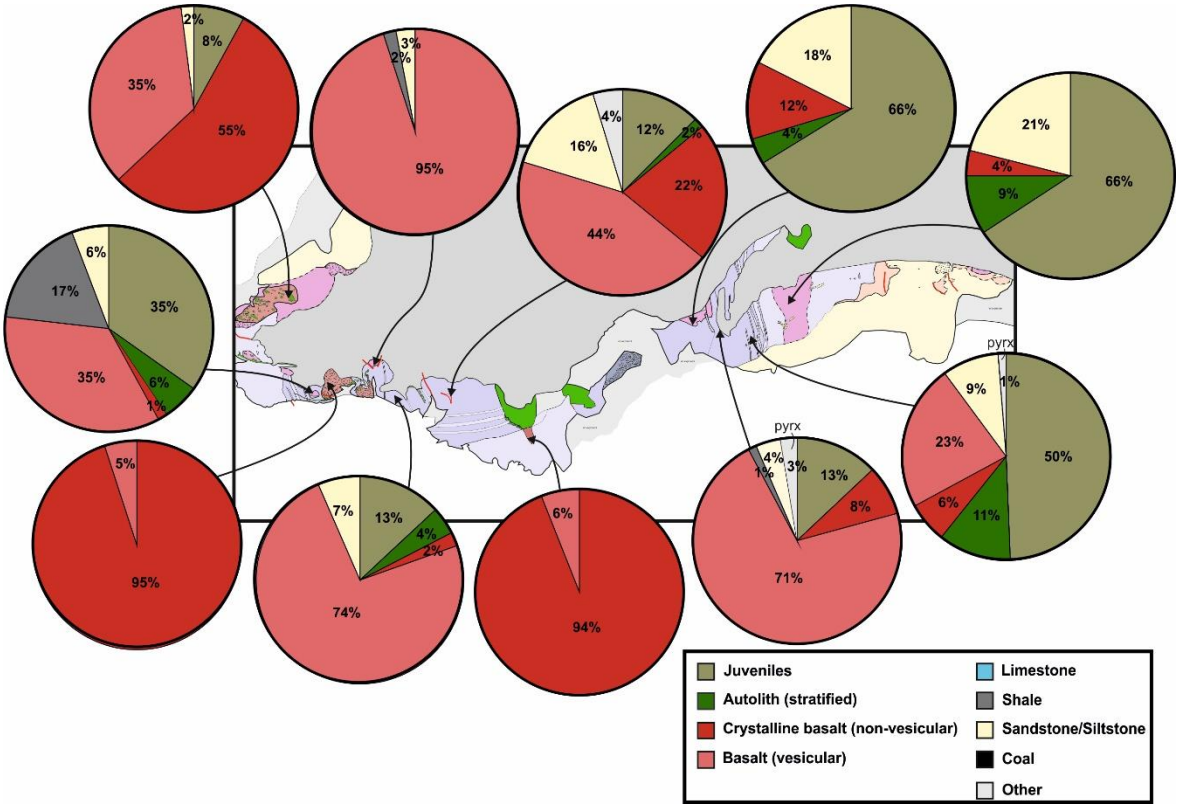

Figure 6.34: Summary geological map of the Kincaird diatreme showing the distribution of the main lithologies (see key in Figure 6.33), and pie charts illustrating the composition of the lithic clast population at corresponding localities on the map. N=100 for each clast count.

LFA A has a high proportion of juvenile clasts (>55% to 95%), with larger (>1 cm) juvenile clasts displaying fluidal morphologies (Figure 6.4E, F). Millimetre-scale juvenile clasts tend to be more angular. The stratified tuffs and lapilli-tuffs are typically matrix-supported. The beds progressively become coarser towards the centre of the diatreme: shifting from predominantly LFA A deposits (Log 1) to interbedded LFA A and LFA B deposits (Log 2, 4 and 5) and through to LFA B-dominated deposits in the centre of the diatreme (Log 3) (Figure 6.33 and Figure 6.35). The massive to diffusely-stratified breccia beds (LFA B) are mostly clast-supported and contain: sub-rounded, vesicular and amygdaloidal basalt clasts (<75 cm); sub-angular, non-vesicular and porphyritic basalt clasts (<45 cm); semi-convolute shale inclusions (<30 cm); sub-rounded juvenile clasts (sub-mm to 10 cm); and sub-rounded autoliths within a coarse tuff matrix (Figure 6.34). Calcite infills interstices within the matrix, and the beds contain calcite veins (sub-cm to 4 cm thick). Beds are ~1 m to 2.5 m thick.

Discordant, sub-vertical columns are identified cutting through the bedded deposits at several locations (Figure 6.36). The margins tend to be indistinct, however calcite hydrothermal veins or thin, irregular magmatic dykes typically delineate the boundary of the column. The columns consist

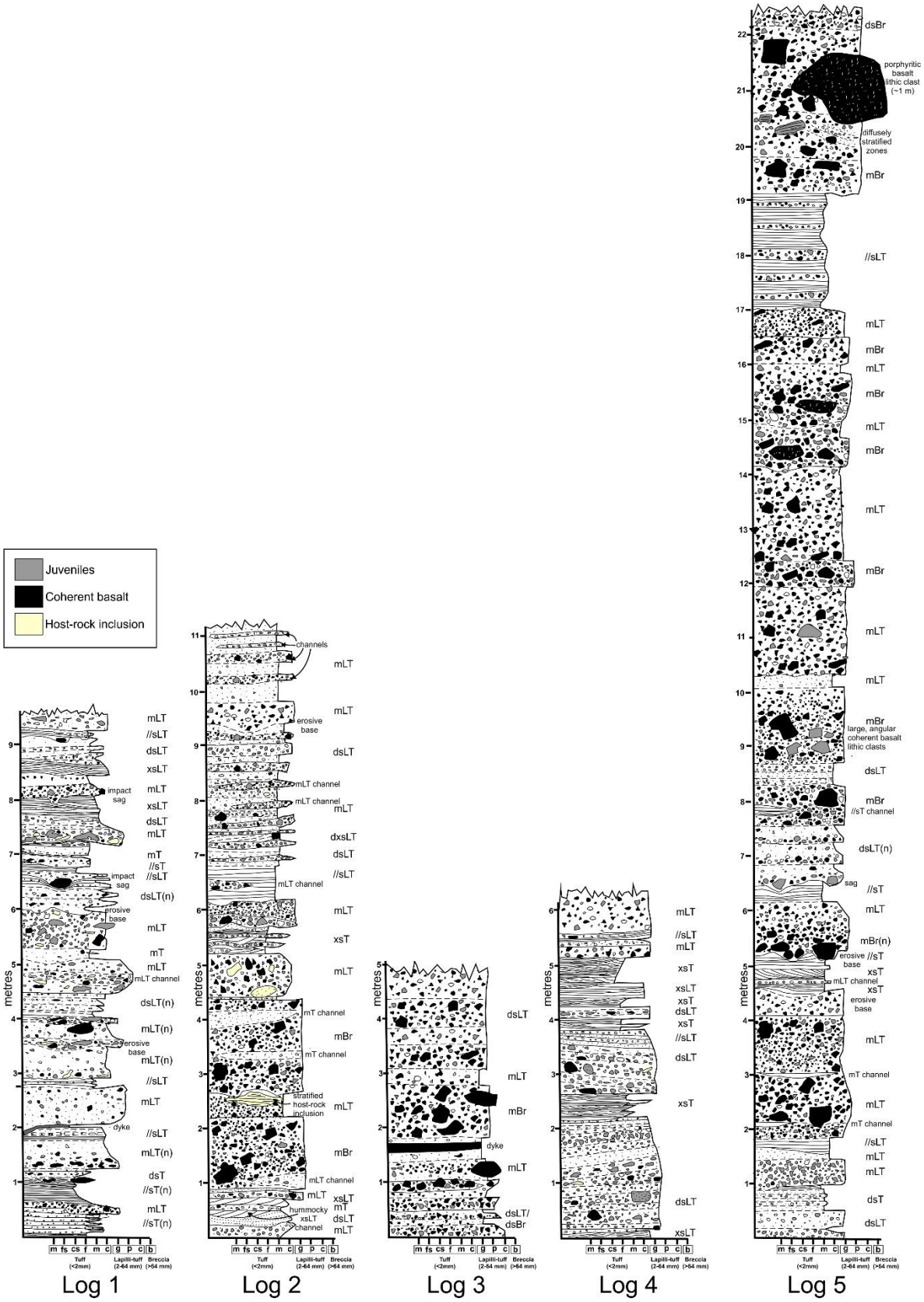

Figure 6.35: Representative stratigraphical logs through the bedded deposits in the Kincaird diatreme. Interbedded coarse lapilli-tuffs and breccias, and stratified tuffs and lapilli-tuffs, locally displaying hummocky cross-stratification and channels. Note that the tuff and fine lapilli-tuff layers are not laterally extensive. Host-rock inclusions and stratified and non-stratified autoliths are also evident within the successions. Locations of logs are shown in Figure 6.33.

of unstructured massive lapilli-tuff and breccia with highly variable constituents (LFA C and Lithofacies E) (Figure 6.34). Figure 6.36 shows the locations of the debris columns and Table 6.3 lists the characteristics of each debris column.

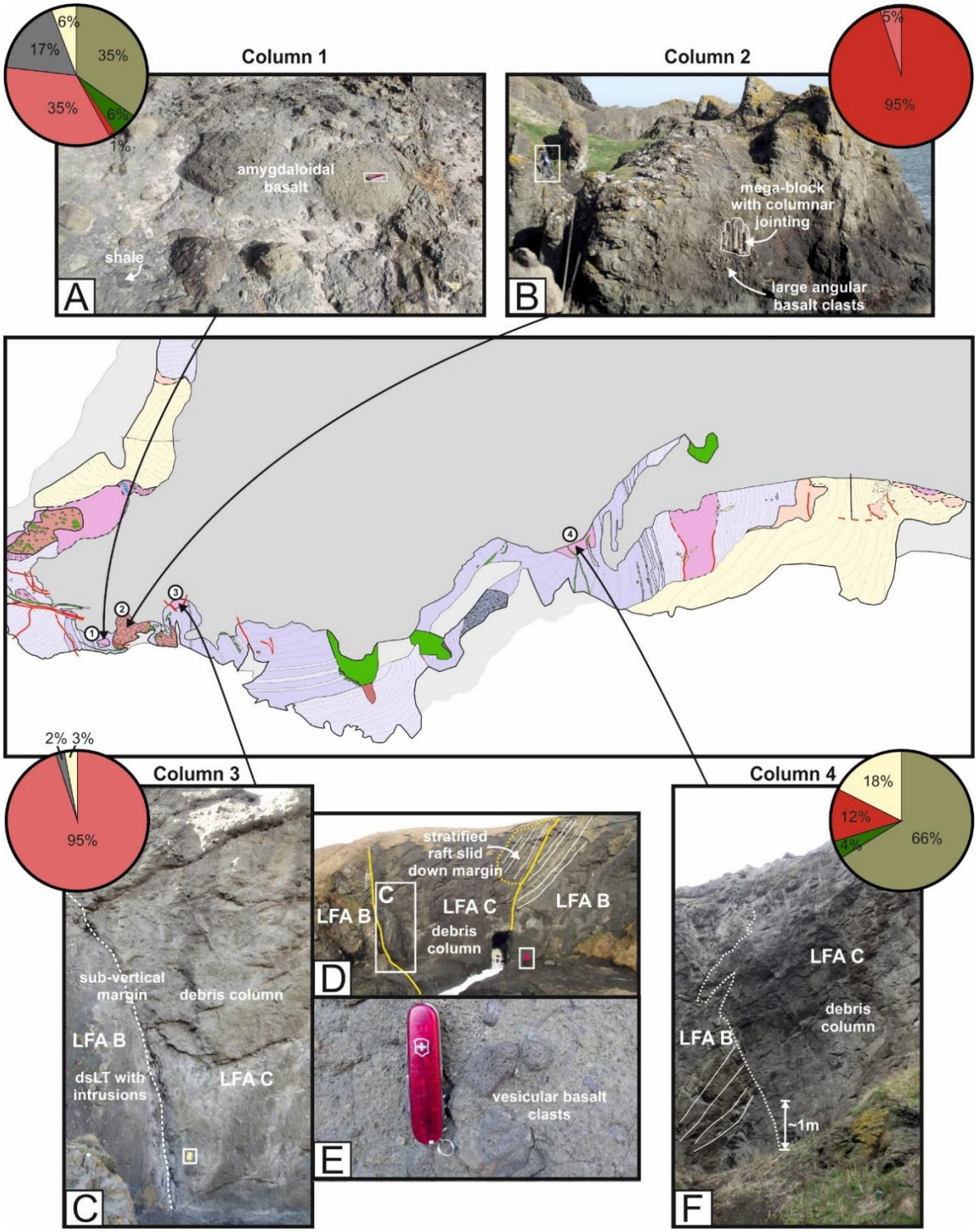

Figure 6.36: Debris columns located in the Kincaird diatreme, showing the clast proportions. Pen-knife is 10 cm. (A) Column 1 is comprised of a massive breccia with a high percentage of vesicular basalt clasts. (B) Column 2 is a monolithic basalt breccia that contains large blocks of non-vesicular basalt. Columnar jointing is observed within the blocks. Person for scale. (C) The margins of Column 3 are distinguishable and sub-vertical. Notebook is 20 cm long. (D) A large stratified raft from the surrounding diatreme fill has slid down the margin of the column. Person for scale. (E) Column 3 contains mostly vesicular basalt clasts. (F) Column 4 is hard to distinguish. For clast count key, refer to Figure 6.34.

Column	Max. diameter	Matrix/ clast supported	Clast types & proportions	Clast size	Comments
1	~10 m	Matrix-supported	Juvenile (35%); autoliths (6%); vesicular basalt (35%); non-vesicular basalt (1%); siltstone (17%); sandstone (6%)	1-77 cm	Figure 6.36A
2	~43 m	Clast-supported	Vesicular basalt (5%); non-vesicular basalt (95%)	3- >140 cm	Figure 6.36B; columnar jointing in large basalt boulders
3	26. 5 m	Matrix-supported	Vesicular basalt (95%); siltstone (2%); sandstone (3%)	Sub-cm to 130 cm	Figure 6.36C, D, E; column margins defined by calcite veins and dykes; large rafts of dsLT have slipped down the margins (<2 m)
4	Poorly exposed	Clast-supported	Juvenile (66%); autoliths (4%); non-vesicular basalt (12%); sandstone (18%)		Figure 6.36F; column margins defined by dykes; calcite infills the interstices

Table 6.3: Characteristics of each of the debris columns within the Kincaird diatreme. Location of each debris column is shown in Figure 6.36.

Within the centre of the diatreme is an area of collapsed bedding (Lithofacies D; Figure 6.33). The autoliths are typically angular and stratified, defined by alternating fine ash layers and juvenile-rich layers, where juvenile clasts tend to be fine to coarse grade (Figure 6.8A; Figure 6.37). Within the autoliths, minor faulting and slump planes are evident, displaying displacements of up to 5-7 cm (Figure 6.37A). Stratifications are mostly planar, however low-angle cross-bedding and erosive channels are also present (Figure 6.37B and C). The autoliths are suspended within a lapilli matrix and typically display jigsaw-fit textures, however, some autoliths have been rotated and are distributed randomly (Figure 6.8A). The collapsed bedding breccia grades into intact stratified lapilli-tuffs (Figure 6.37B and C). Fine to coarse ash from the surrounding diatreme deposits appears to have been injected into the autoliths forming thin (<4 cm) volcaniclastic veins (Figure 6.37D). Locally, small inclusions of host-rock, small cm-scale autoliths and juvenile clasts have been injected alongside the ash into the vein (Figure 6.37D).

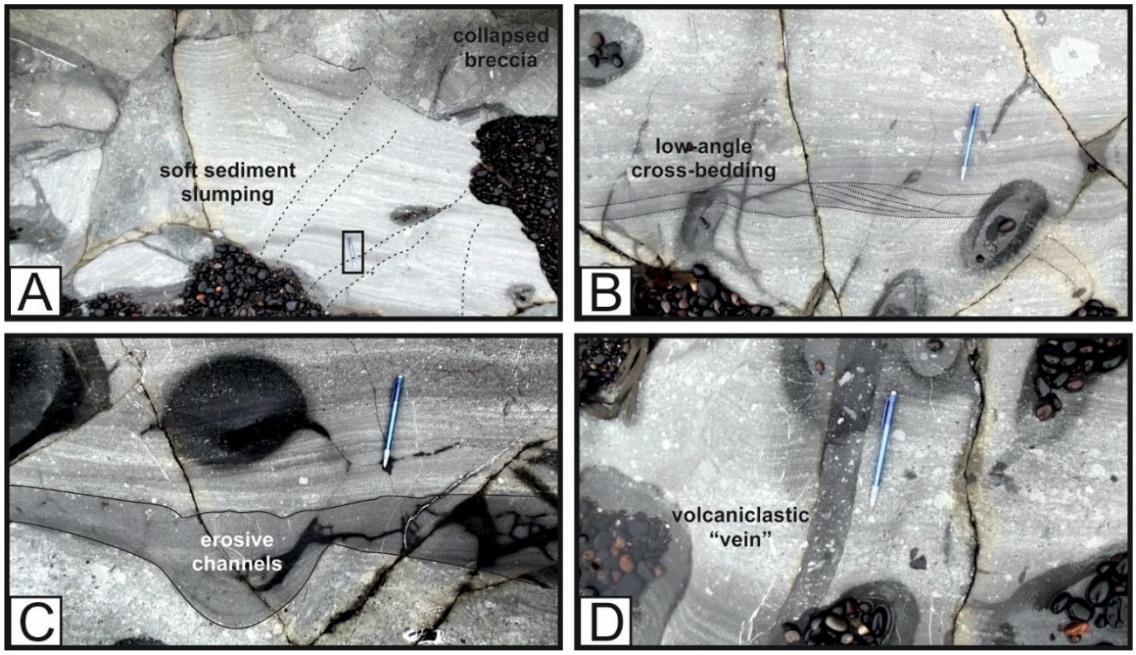

Figure 6.37: Collapsed bedding within the centre of the Kincaird diatreme (Lithofacies D). (A) Soft sediment slumping and minor faults are evident within large autoliths. Stratified autoliths are suspended within a matrix of lapilli-tuff. (B) The collapsed bedding grades into intact stratigraphy, displaying planar stratification and low-angle cross-bedding. (C) Erosive channels are present and extend downwards into the underlying substrate by up to 10 cm. (D) A volcaniclastic vein has been injected into the bedded diatreme deposits. Small fragments of the surrounding lapilli-tuffs have been incorporated into the volcaniclastic vein. Pencil is 15 cm long.

Intrusions: Intruded into the centre of the Kincaird diatreme are two large, 40 m high sill lobes which protrude from the cliff face (Figure 6.14G and Figure 6.33). These intrusions have extensive columnar jointing and have a NNW-SSE alignment (Figure 6.38A and B). Francis (1970) and Leys (1982) attribute the intrusions to an inverted cone shaped plug however the orientation of the columnar jointing indicates the sills were intruded along a sub-horizontal orientation and extended upwards into inclined limbs (Figure 6.14G and Figure 6.38A). At the base of the sill, the columnar jointing is highly organised, however the top 20 m of the sill displays chaotic jointing patterns (Figure 6.38A). The sill curves around an area of lapilli-tuff, where the margins of the sill are vitrified, indicating rapid cooling (Figure 6.38B).

Blocky peperite has formed locally along the base of the sills (Figure 6.38C). The peperite is closely-packed and displays jig-saw fit (Figure 6.38C). The clasts are up to 20 cm and are suspended within the surrounding lapilli-tuffs. A lobe of monolithic, clast-dominated breccia extends from the western sheet (Figure 6.38A). The lobe is 10 to 15 m across but tapers to a point, and is 7-8 m in height (Figure 6.38A). The lobe is comprised of clast-supported, angular basalt blocks which have been heavily fractured and locally display jig-saw fit textures (Figure 6.38D). Basalt blocks range in size

from 1-2 cm to >75 cm. The peperite lobe becomes increasingly more matrix-supported, the clast size generally decreases and jig-saw fit textures become less apparent, further from the intact sill.

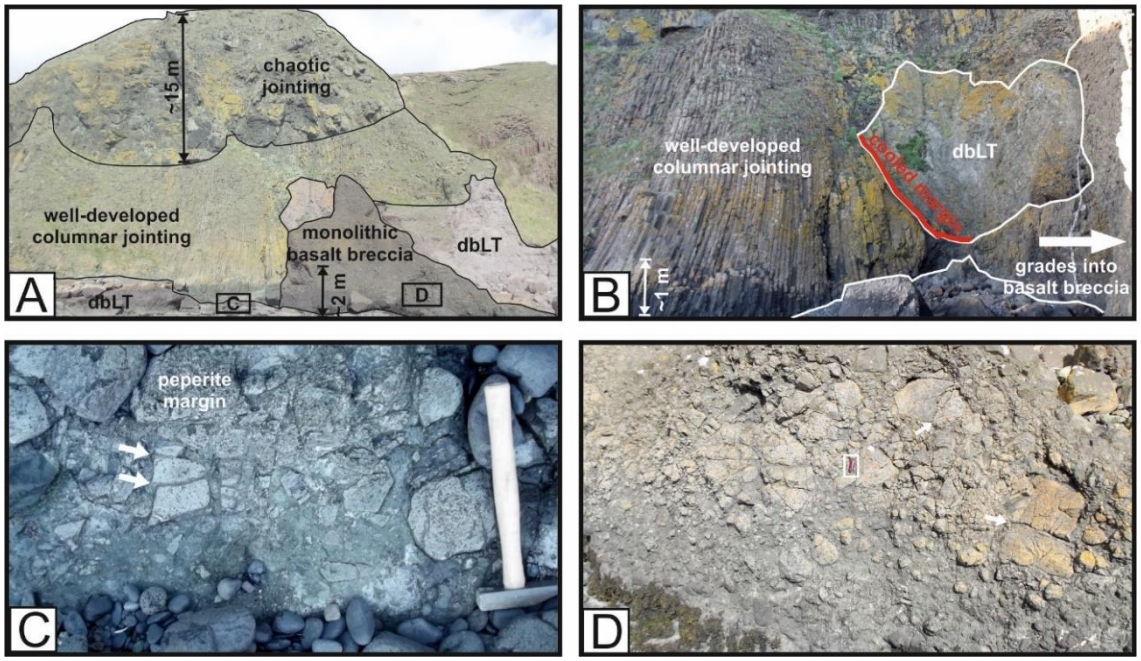

Figure 6.38: Photographs of the inclined sill within the centre of the Kincaird diatreme. (A) The sill can be divided into three zones: (1) peperite and a peperitic lobe that extends from the base of the sill; (2) well-developed columnar jointing; and (3) chaotic jointing. The locations of Figures 6.38C and D are shown. (B) The well-developed columnar jointing, becomes increasingly fractured and grades into the monolithic basalt breccia. Cooling margins (solid red line) are apparent locally when in contact with the surrounding diatreme deposits. The intrusion bifurcates around an area of lapilli-tuffs. (C) Peperitic margin at the base of the intact sill. Arrows show jig-saw fit textures. Hammer is 40 cm long. (D) Lobe of monolithic basalt breccia extends from the western sill and is comprised of angular, clast-supported basalt clasts. Arrows show jig-saw fit textures. Pen-knife is 10 cm long.

At the eastern margin of the Kincaird diatreme, an exposed volcaniclastic injectite cross-cuts LFA A and several coherent dykes (Figure 6.15C and Figure 6.39). The injectite is 80 cm across, has defined margins and changes direction abruptly (Figure 6.39). The injectite laterally grades from a massive lapilli-tuff consisting of rounded and sub-rounded lapilli (sub-mm to 15 cm) within a green, coarse tuffaceous matrix (Figure 6.39B) into a lapilli-tuff comprised of very fluidal lapilli (1 mm to 900 mm) within a black tuffaceous matrix (Figure 6.39C). The lapilli have a rag-like morphology with highly convoluted margins (Figure 6.39C). The injectite also contains clasts of coherent basalt (likely from the dykes the injectite cross-cuts, dyke i and iii) and various host-rock inclusions (coal, sandstone, siltstone and limestone). Surrounding the injectite, is a 5 cm border of coherent basalt (dyke ii; Figure 6.39A). The volcaniclastic injectite is cross-cut by subsequent magmatic dykes (Figure 6.39D). These dykes have defined, undulating margins, with local marginal, fluidal peperite (Figure

6.39E). The dykes finger into the injectite and surrounding substrate (Lithofacies F), incorporating large inclusions from the injectite into the dyke (0.5 m by 0.75 m) (Figure 6.39D).

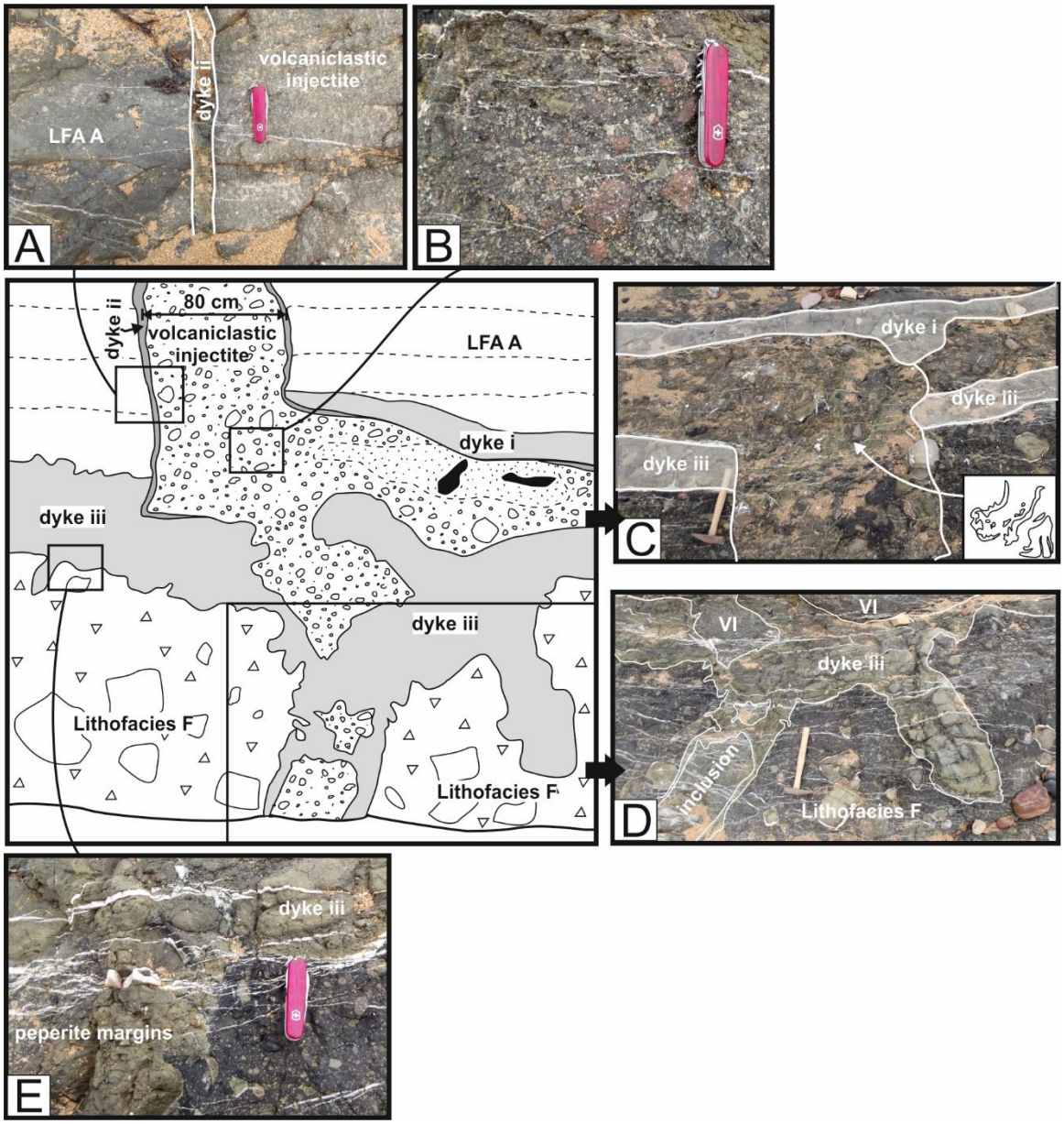

Figure 6.39: Schematic sketch of the volcaniclastic injectite in the eastern margin of the Kincaird diatreme. Grey shading indicates coherent magmatic dykes. Pen-knife is 10 cm long and hammer is 40 cm long. (A) Coherent magmatic dykes (dyke ii) are present along the margins of the volcaniclastic injectite (~5 cm thick). (B) Massive lapilli-tuff with rounded and sub-rounded lapilli hosting host-rock inclusions and clasts (red siltstone). Locally grading is present likely representing laminar flow during injection of the injectite (C) The volcaniclastic injectite laterally grades into a massive lapilli-tuff baring highly fluidal lapilli with rag-like morphologies (inset). Here, the injectite cross-cuts dyke iii. (D) Dyke iii fingers into the volcaniclastic injectite (VI), incorporating large inclusions of massive lapilli-tuff from the injectite into the dyke. Dyke iii has a very undulating margin. (E) Passive peperite forms at the margins of dyke iii.

6.6.4.2. Interpretations

It is proposed that the Kincaird diatreme is exposed in the lower portion of the upper, bedded zone (Figure 6.40), due to: (1) a combination of poorly developed, diffuse bedding and well-developed bedding; (2) steep bedding; (3) intrusion of a thick (<40 m) sill into the centre of the diatreme; (4) large areas of collapsed bedding, with metre-scale intact blocks of well-developed bedded upper-diatreme/tuff ring deposits; and (5) multiple debris columns that have been emplaced into the diatreme. The Kincaird diatreme is effectively two, coalesced diatremes that formed independently of each other and widened into a large, elongate diatreme with two centres. It, therefore, has a complex history with two diatreme development records. The proposed centres are shown in Figure 6.41.

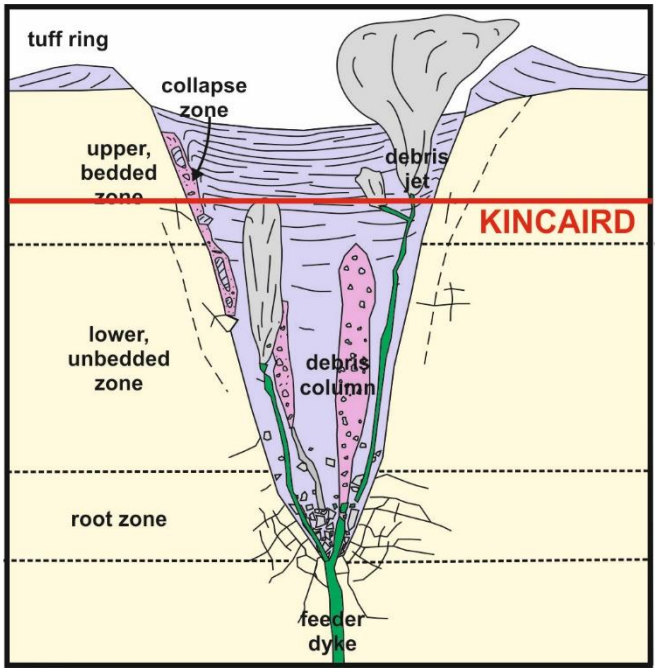

Figure 6.40: A typical diatreme structure showing the four main zones (tuff ring, upper bedded, lower unbedded and root zone). Debris columns and collapse zones are also evident within a typical diatreme. The proposed level of the exposed Kincaird diatreme within the typical diatreme structure is marked by the solid red line. Not to scale.

The diatreme deposits distributed around centre 1 (Figure 6.41) tend to have fairly well-developed bedding which grades from interbedded lapilli-tuffs and tuffs (LFA A) to diffusely bedded lapilli-tuffs and breccias (LFA B). The diatreme deposits around centre 2 (Figure 6.41) show a similar distribution of LFA A and LFA B, however towards the middle of this diatreme, the beds become very diffuse and often indiscernible.

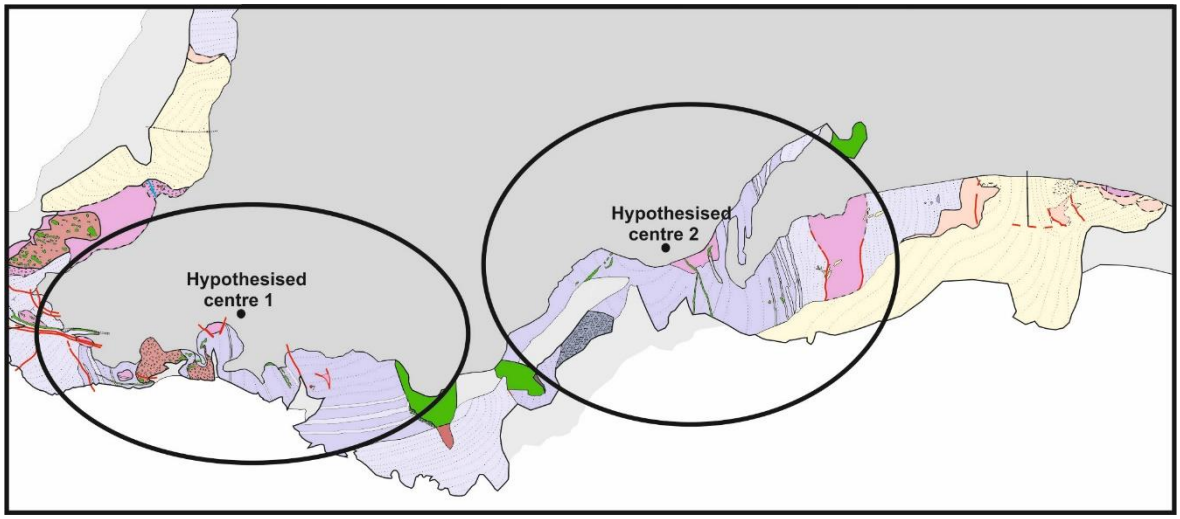

Figure 6.41: Approximate location for the two centres at Kincaird diatreme based on bedding orientations. Note the collapsed bedding is located near the margin of diatreme 2 and the large sill-like intrusions are emplaced between the two proposed centres.

Like many of the other diatremes in East Fife, the stratified nature of Lithofacies A at Kincaird is typical of pulsed, small volume phreatomagmatic eruptions (Lorenz 1986; White and Ross 2011) (Figure 6.4 and Figure 6.35). Waxing and waning of explosion energy and changes in the height of the explosion locus within the diatreme structure, produced PDCs of variable constituents and energy, and formed cyclical beds of tuffs and lapilli-tuffs. Impact sags are also common in LFA A at Kincaird caused by large juvenile clasts or ballistic blocks which have been ejected from the vent and impacted into the soft substrate. The juvenile bombs tend to have fluidal morphologies suggesting that they were still molten or semi-molten upon impact.

An increase in lahars and debris flows into the crater in the latter stages of diatreme formation is marked by an increase of LFA B beds within the centre of the diatreme. This is likely due to the widening of the maar crater, eroding the pre-existing stratigraphy. Basalt lithic clasts and blocks within LFA B are substantially more vesiculated than LFA A clasts (40-75%). This is attributed to the clasts being sourced from vesicular lava flows that were fragmented and incorporated into the diatreme during emplacement.

The columns of LFA C and LFA E described above, cross-cut the bedded deposits (Figure 6.36) and indicate sub-vertical, upwards movement of pyroclastic material. Similar cross-cutting columns are found in other diatremes (McClintock and White 2006; Ross and White 2006; Ross et al. 2008; White and Ross 2011). The cross-cutting relationships demonstrate that the diatreme deposits were unconsolidated during emplacement of the columns (White and Ross 2011). The lack of

(fluidal) juvenile clasts and the typically angular nature of the clasts within the Kincaird columns suggest that they were not a result of violent explosions but were formed due to the passing of debris jets, the product of violent phreatomagmatic explosions at depth (Ross and White 2006). The passage of upward-projected debris jets through an unconsolidated diatreme and the subsequent downward-moving material that flows around the debris jet results in internal mixing and homogenisation of products and the destruction of bedding (McClintock and White 2006; Ross et al. 2008; White and Ross 2011; Valentine and White 2012). The debris columns are commonly located near the proposed centres within the Kincaird diatreme (Figure 6.36 and Figure 6.41) suggesting late-stage magma was channelled into the centre of the diatremes. In the middle of diatreme centre 2, the bedding is very diffuse and locally appears completely unstructured which suggests that centre 2 was subjected to multiple debris jets that passed through the bedding and thoroughly churned the diatreme deposits. This possibly indicates a relatively long-lived diatreme (Valentine and White 2012).

Debris column 2 is comprised of 100% basalt blocks (95% non-vesicular and 5% vesicular) (Figure 6.34), which suggests one of two possibilities. Either the phreatomagmatic explosion occurred within lava units in the host-rock stratigraphy which was broken into fragments and erupted, or phreatomagmatic explosions in the root zone of the diatreme, began to brecciate an earlier-emplaced sill which was fragmented into large blocks and incorporated into a debris jet. The large boulders were transported upwards into the diatreme forming a debris column of mostly non-vesicular basalt clasts. It is possible that underlying the diatreme, there are lava flows that are not exposed at the surface, for example, the Kinghorn lavas which were erupted between the Pathhead Formation and the Sandy Craig Formation (Table 6.1). The boulders retain columnar joints. In either case, this process occurred towards the end of centre 1 formation, as Column 2 has not been mixed by subsequent debris jets, leaving a non-homogenised monolithic basalt breccia.

The expansion of either diatreme (centre 1 or 2) by the deepening and widening process proposed by Lorenz (1986, 2003) (Figure 6.9) caused the collapse of the upper diatreme deposits and/or surface-derived tuff ring deposits into the diatreme when they coalesced. The result is a zone of collapsed bedding, which is usually found at the margins of diatremes, in the centre of the Kincaird

diatreme (Figure 6.33). The autoliths within the collapsed bedding have well-developed cross-bedding and generally have a fine grain size (tuff or fine lapilli), indicating direct-fallout deposits (producing massive tuff beds) and fully-dilute, traction dominated PDC deposits (planar stratified and cross stratified tuffs) (Figure 6.37).

Intrusions: The timing of the amalgamation of the two diatremes is difficult to determine however the conjoining occurred prior to the emplacement of the late-stage magmatic sills and irregular dykes which are emplaced throughout the Kincaird diatreme (Figure 6.33 and Figure 6.38). The intrusions indicate a late-stage switching from primarily phreatomagmatic magma-water interaction with some explosivity caused by degassing, to a passive magmatic phase (Refer to Section 6.6.4). The large volume of magma emplaced suggests this switching was caused by a rapid increase in the magma-water ratio. The extensive zone of blocky peperite (lobe of peperite extends from the inclined sill into the surrounding diatreme; Figure 6.38A and D) indicates the diatreme deposits were unconsolidated and easily fluidised at the time of sill emplacement. The peperite has a jigsaw-fit texture and is closely-packed which is characteristic of in situ fragmentation (Brooks et al. 1982; Kokelaar 1982; Hanson and Wilson 1993; Doyle 2000; Skilling 2002). Therefore, it can be assumed that the peperite at the base of the sill in the Kincaird diatreme was generated by cooling-quenching fragmentation and autobrecciation (Skilling 2002).

The volcaniclastic injectite at the eastern margin of the diatreme was formed due to fluidisation and remobilisation of diatreme lapilli-tuffs, likely incorporating sediment inclusions from the nearby host-rock (Ross and White 2005a). The complex relationships between the volcaniclastic injectite and the surrounding magmatic dykes suggests a complicated history between dyke emplacement and the remobilisation of diatreme deposits (Figure 6.39). The dykes were emplaced by ductile mechanisms, evident by fluidal peperite, magma fingers and highly undulating dyke margins. Dyke-i is entirely cross-cut by the injectite indicating that it was emplaced prior to the remobilisation and injection of the diatreme deposits. Dyke-iii incorporates inclusions of massive lapilli-tuff from the volcaniclastic injectite (Figure 6.39D), suggesting dyke emplacement occurred after the injection of fluidised lapilli-tuff. However, elsewhere along the length of the volcaniclastic injectite, the injectite cross-cuts dyke-iii. Where this occurs, the injectite grades into a massive-lapilli tuff bearing highly

fluidal rag-like lapilli. This suggests that dyke-iii and the injectite were emplaced nearly simultaneously. It is likely that the emplacement of dykes caused the fluidisation and remobilisation of the diatreme deposits by vaporisation of porewater at the intrusion contacts (Ross and White 2005a). The rapid propagation of the injectite would have allowed it to advance through and cross-cut dyke-iii. Due to the highly fluidal, rag-like nature of the lapilli within the injectite, it is likely that the injectite ripped partially molten magma from the newly formed dyke-iii. These highly fluidal and malleable dyke fragments were then incorporated and mobilised within the injectite.

6.6.5. **Ruddon's Point**

6.6.5.1. Observations

The Ruddon's Point diatreme is located ~650 m WNW of the Kincaird diatreme [N 561140.88 W 0025221.19] and is emplaced into the Upper Limestone Formation (Figure 6.42). Poor exposure of the diatreme restricts a full morphometric analysis of its dimensions, however generally it is an elongate ellipsis (approximately 720 m by 390 m). Margins with the surrounding host-rock are only exposed along the northeast margin of the diatreme at low tide. Exposure of the diatreme fill is limited due to tidal sand and vegetation.

The Ruddon's Point diatreme consists of interbedded tuffs, lapilli-tuffs and local breccia beds, attributed to LFA A (Figure 6.42). In two separate areas (Shooter's Point and the east of the diatreme), large peperitic domains are observed which contain dyke segments of coherent basalt that appear to be aligned. Intact sills are also associated with these peperitic domains and display columnar jointing. Coherent intrusions (intact dykes and sills) are present throughout the Ruddon's Point diatreme. On the west side of the diatreme an elliptical zone cross-cuts the bedding and consists of LFA C (massive lapilli-tuff with a high host-sediment clast proportion). Faulting has disrupted the orientation of the centroclinal dipping beds.

LFA A consists of a high proportion of juvenile clasts (60-70%) and varying proportions of crystalline basalt (vesicular and non-vesicular); pyroxenite crystals and pyroxene megacrysts; and host-rock inclusions (Figure 6.43). Petrographic analysis of LFA A from Ruddon's Point diatreme shows that the non-vesicular juvenile clasts have typically angular or sub-angular clast morphologies and are up to 1-2 mm in size. Rare juvenile clasts are finely coated by an ashy rim. The well-developed bedding of LFA A comprises massive lapilli-tuffs (mLT) and planar stratified tuffs and fine lapilli-tuffs (//T; //LT) (Figure 6.44A and B). Occasionally low-angle cross-stratification is present. At the base of many of the massive lapilli-tuff layers, erosive margins are present and scours are evident (Figure 6.44A). Large (>10 cm) angular basalt clasts are present within the massive lapilli-tuff layers. The beds are typically laterally extensive, however, occasionally the stratified tuff layers are only laterally extensive for a few metres (~3-4 m) forming broad channels (Figure 6.44B). Locally, the bedding of LFA A has been disrupted and the deposits have a heterogeneous appearance (up to 10 m north

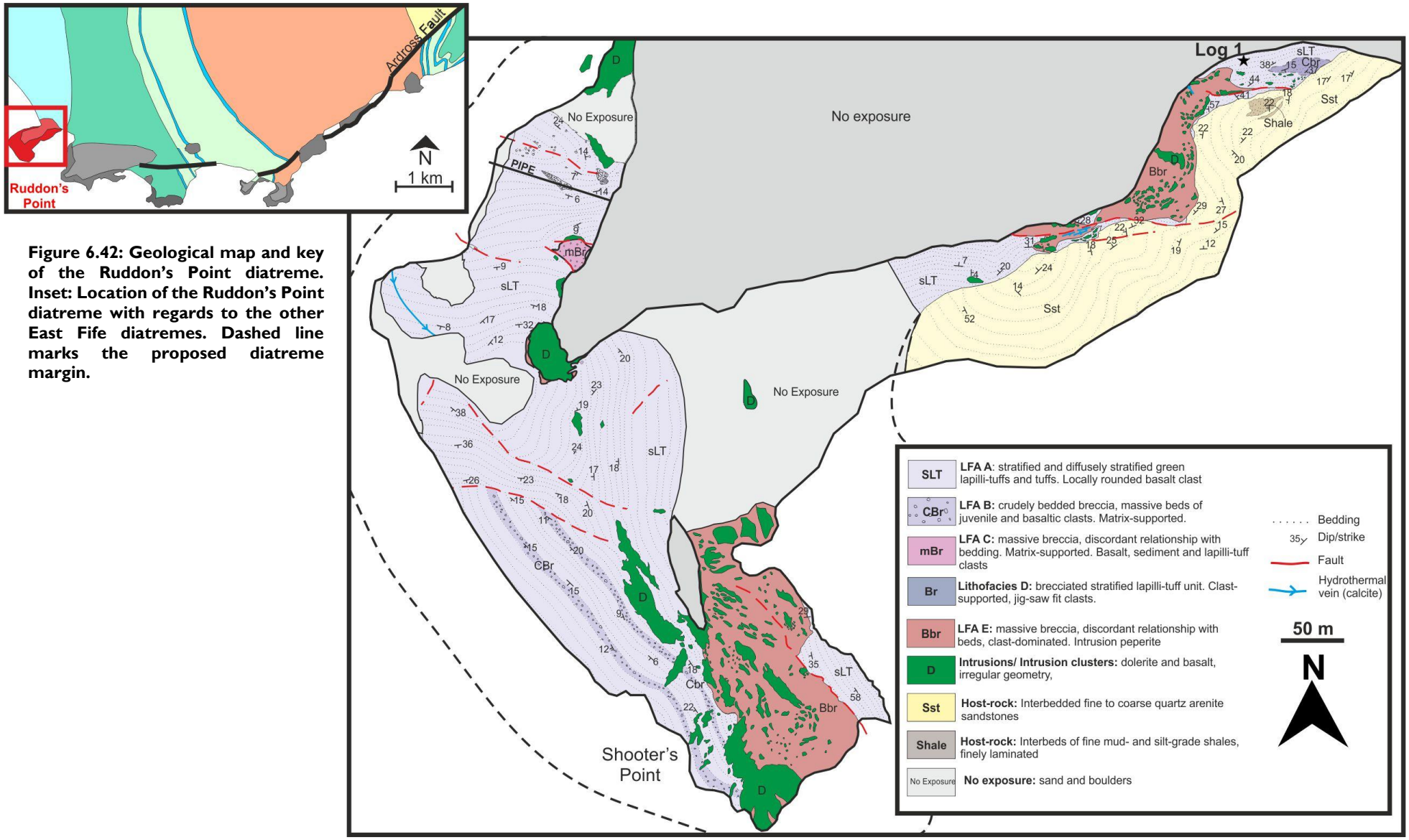

Figure 6.42: Geological map and key of the Ruddon's Point diatreme. Inset: Location of the Ruddon's Point diatreme with regards to the other East Fife diatremes. Dashed line marks the proposed diatreme margin.

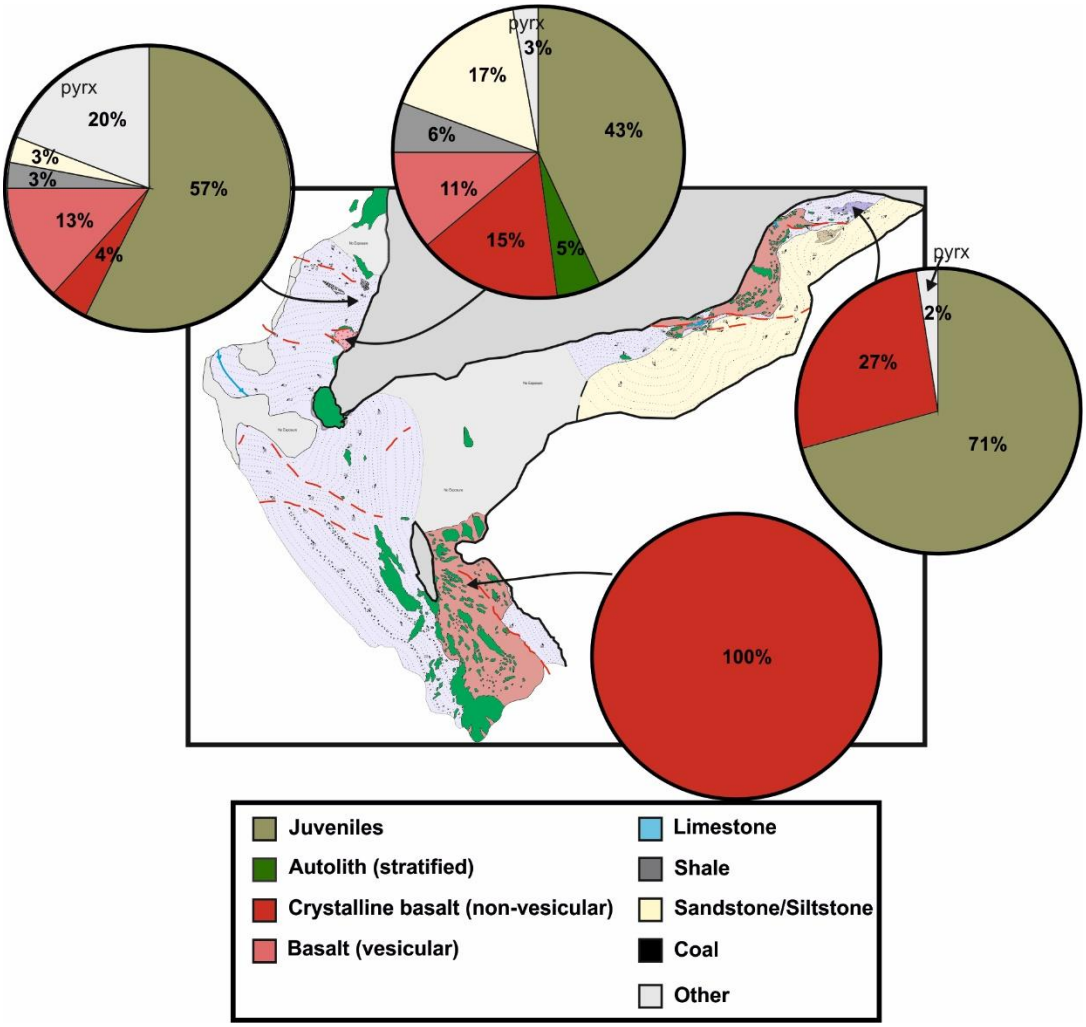

Figure 6.43: Summary geological map of the Ruddon's Point diatreme showing the distribution of the main lithologies (see key in Figure 6.33), and pie charts illustrating the composition of the lithic clast population at corresponding localities on the map. N = 100 for each clast count.

and 10 m south of the pipe on the west side of the diatreme, Figure 6.42). A fine to coarse, dark grey ash defines highly fluidal textures within the chaotic bedding (Figure 6.44C). The lapilli-tuff deposits have been distorted and coherent fragments of the lapilli-tuff have been incorporated into the fine ash, producing an extremely convolute margin between the lapilli-tuff and fine ash (Figure 6.44C).

On the W side of the diatreme, an elliptical body of unstructured breccia with a high proportion of host-rock inclusions (20-25%) cross-cuts the bedded deposits (Figure 6.42 and Figure 6.43). The host-rock inclusions are primarily coarse, red siltstone or fine, sandstone, and display fluidal morphologies. The host-rock inclusions are typically <5 cm but reach up to 22 cm. The massive breccia also contains non-vesicular and mildly vesicular angular basalt clasts, and stratified autoliths of interbedded coarse lapilli and fine lapilli layers. Calcite has infilled the interstices in the autoliths.

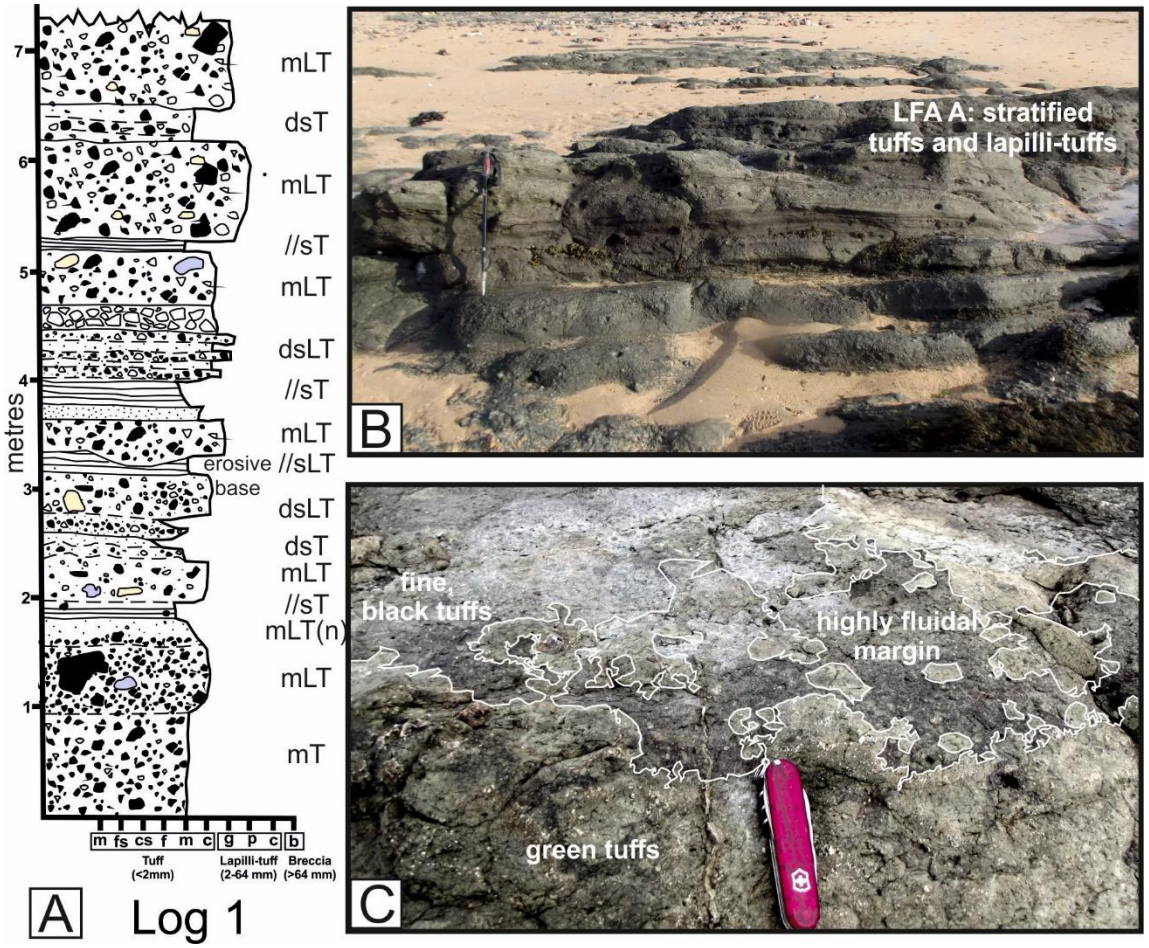

Figure 6.44: LFA A at Ruddon's Point diatreme. (A) Representative stratigraphical log through LFA A (See Figure 6.42 for location). Interbedded massive lapilli-tuffs and stratified tuffs. Erosive bases are evident at the base of the massive lapilli-tuff beds. (B) Photograph of log. Note the beds tend to be relatively laterally extensive, however locally the stratified beds are laterally extensive for several metres before they pinch out. Walking pole is 1 m long. (C) Evidence for fluidisation within LFA A showing the extremely heterogeneous nature of this lithofacies; note the fluidal ash (dark grey) that has been injected into the lapilli-tuffs. The margin is highly convolute. Pen-knife is 10 cm long.

Intrusions: In the east of the Ruddon's Point diatreme and at Shooter's Point (Figure 6.42), two large peperitic domains have intruded into the bedded deposits. At Shooter's Point, coherent dolerite and basalt sills, displaying columnar jointing, have intruded into the diatreme deposits. The intrusions have a NNW-SSE orientation and progressively thin from approximately 20 m wide to sub-metre towards the SSE. In the centre of the diatreme, the sill displays a stepped character of incrementally emplaced sheets (Figure 6.14H). Towards Shooter's Point, the sills bifurcate into several dyke-like branches which feed the peperitic domain (Figure 6.42). The dyke-like branches brecciate towards the SSE into aligned and isolated dyke segments of basalt (Figure 6.45A). The dyke segments are 0.5 to 1.7 m wide, heavily fractured and are typically disconnected (Figure 6.45A). Fractures within the joints have been infilled with fine tuff (Figure 6.45B). Locally, seemingly intact dykes or dyke segments are, in reality, a clast-supported breccia of detached basalt clasts separated

by fluidised diatreme tuffs (Figure 6.14E). At the margins of the dyke segments closely-packed, blocky peperite has formed which gradually becomes more dispersed away from coherent basalt (Figure 6.45C). The result is an area at Shooter's Point, approximately 110 m x 225 m wide, formed entirely of peperite and coherent basalt dyke segments.

The peperitic domain in the east of the diatreme shows similar features to Shooter's Point, where dykes and pseudo-dykes (clastogenic bodies of coherent basalt) feed peperitic zones (Figure 6.14D and E). The basalt fingers into the tuffs and lapilli-tuffs, forming peperite often displaying jig-saw fit

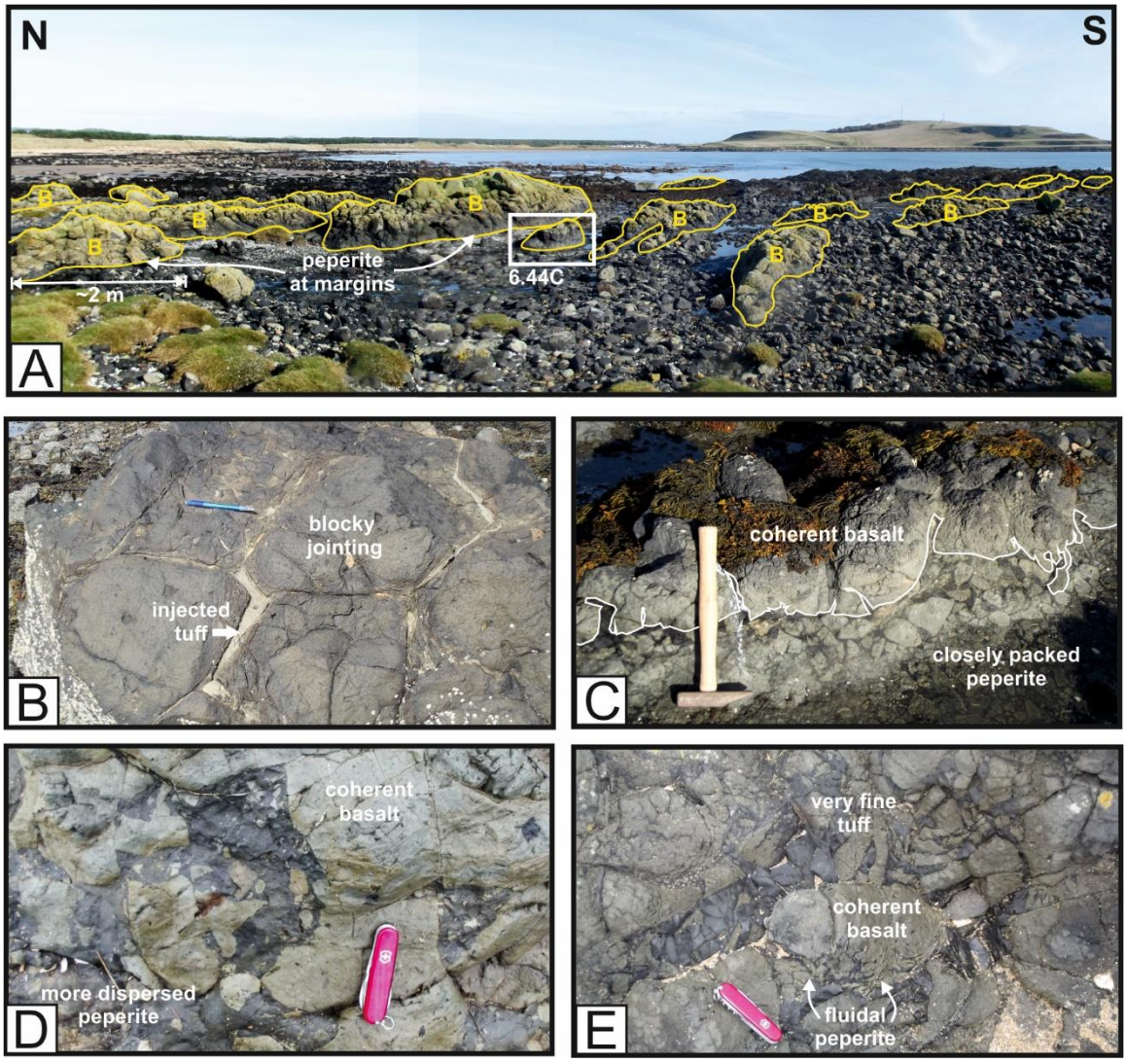

Figure 6.45: Annotated photographs of the intrusions and peperitic domains at the Ruddon's Point diatreme. (A) At the peperitic domain at Shooter's Point, coherent basalt dyke segments labelled "B" are aligned along a NNW-SSE orientation. (B) Close-up of pseudo-dyke showing the columnar jointing which has been infilled by fluidised tuff. Pencil is 15 cm long. (C) Closely-packed peperite is present at the base of the dyke segment and becomes progressively more dispersed away from the coherent basalt. Hammer is 40 cm long. (D) Coherent basalt intrusion fingers into the tuff deposits and produces angular peperite. Jigsaw-fit textures are evident. Pen-knife is 10 cm. (E) Fluidal peperite is formed where the intrusions invade into very fine grade tuffs. The fluidised fine tuffs mingle with the molten basalt forming an intimate boundary. Pen-knife is 10 cm long.

(Figure 6.45D). Where the intrusions have been emplaced into very fine tuffs, fluidal peperite has formed. The tuff invades into the basalt producing highly convolute boundaries and veins of tuff within the coherent basalt (Figure 6.45E).

6.6.5.2. Interpretations

It is proposed that the Ruddon's Point diatreme is exposed in the lower portion of the upper, bedded zone (Figure 6.46), due to: (1) a combination of poorly developed, diffuse bedding and a well-developed bedding; (2) angular juvenile clasts (reworked within the diatreme); (3) intrusion of a thick sills into the centre of the diatreme; and (4) a debris column that has been emplaced into the diatreme.

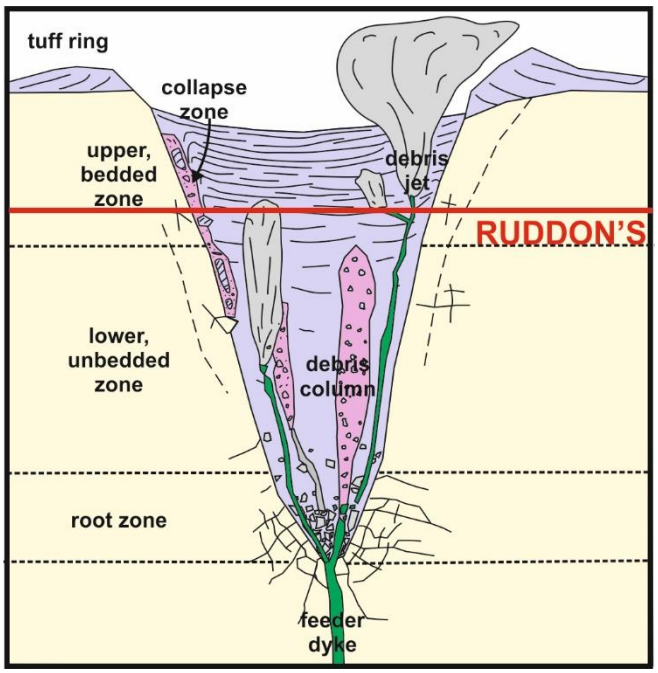

Figure 6.46: A typical diatreme structure showing the four main zones (tuff ring, upper bedded, lower unbedded and root zone). Debris columns and collapse zones are also evident within a typical diatreme. The proposed level of the exposed Ruddon's Point diatreme within the typical diatreme structure is marked by the solid red line. Not to scale.

The juvenile clasts at Ruddon's Point are non-vesicular suggesting that the magma fragmented before volatile exsolution. The majority of juvenile clasts within LFA A in the Ruddon's Point diatreme have angular or sub-angular clast morphologies suggesting reworking of primary juvenile clasts by entrainment within debris jets, particle-particle collision and eruption at the surface. Rare coated juvenile clasts indicate that some primary juvenile clasts were fluidised and sprayed by the newly intruded, melt droplets (Zank et al. 2001; Gernon et al. 2009, 2012). The spray of melt droplets forms a thin coating around earlier-formed particles which acts as a seed to this process.

The juvenile-rich ejecta was erupted at the surface, forming PDCs and producing beds of tuff and lapilli-tuffs (Figure 6.44A and B) (White and Ross 2011). Subsidence in the centre of the diatreme caused the beds to become buried by subsequent eruption deposits and being eroded by passing debris jets (Valentine and White 2012).

Locally within LFA A at Ruddon's Point, the bedding has been distorted and a fine, dark grey ash defines highly fluidal textures and mixing between the lapilli-tuff deposits and the ash (Figure 6.44C). This incomplete mixing of ash and lapilli-tuff indicates that LFA A underwent fluidisation during diatreme development (Wolfe 1980). Gernon et al. (2013) suggest that fluidisation of the diatreme fill is likely caused by the degassing of magma in the root zone of the diatreme, where ascending gas form upward-moving currents which elutriate particles within the diatreme (Gernon et al. 2008). The result is homogenisation of the diatreme fill. At Ruddon's Point the homogenisation process is incomplete and the lapilli-tuff beds and tuff beds are individually identifiable, although distorted.

The elliptical zone that cross-cuts the bedding and consists of LFA C (massive lapilli-tuff with a high host-sediment clast proportion) is a debris column and indicates sub-vertical, upwards movement of pyroclastic material (Figure 6.42). Like the debris columns at the Kincaird diatreme, the column is formed by the passing of debris jets, the product of violent phreatomagmatic explosions at depth (Ross and White 2006). Large volumes of host-rock were incorporated into the column at Ruddon's Point. In particular, large quantities of red siltstone were erupted with the juvenile volcanic ejecta. It is likely the red siltstone was only partially consolidated at the time of eruption due to its ability to readily fluidise, producing highly deformed sediment inclusions with convolute margins.

Intrusions: The peperitic domains and associated coherent basalt dyke segments within the Ruddon's Point diatreme are created mostly by non-explosive interaction between intruding late-stage dykes and sills and unconsolidated diatreme deposits (Skilling 2002; Ross and White 2006). These peperitic domains are formed by the passive quenching of magma forming brittle fractures in the magma (White et al. 2000). This process relieves pressure in the surrounding diatreme deposits and vaporises pore fluids, causing fluidisation of the tuffs and lapilli-tuffs and the injection of fluidised tuffs into the newly-formed fractures (Kokelaar 1982; Hanson and Wilson 1993; Doyle 2000; Skilling et al. 2002; Kokelaar 2002). The peperite within the peperitic domains at Ruddon's Point diatreme

is closely-packed and displays jigsaw-fit texture directly adjacent to the coherent intrusions, which is characteristic of in situ fragmentation (Brooks et al. 1982; Kokelaar 1982; Hanson and Wilson 1993; Doyle 2000; Skilling 2002). The peperite becomes more dispersed further from the intrusions, likely due to hydromagmatic explosions (energetic steam explosions) or dispersal by non-explosive processes (fluidised deposits transport peperite clasts away from the intrusion margin) (Busby-Spera and White 1987; Hanson and Hargrove 1999; Skilling 2002; McLean et al. 2016). It is likely that some degree of mildly explosive interaction between the magma and deposits must have occurred to facilitate the complete penetration of fluidised tuffs into the intrusions.

6.7. Discussion

6.7.1. **Plumbing system**

The ultrabasic character of the magma erupted in the East Fife diatremes and the presence of lower crustal, peridotite xenoliths, high-pressure xenocrysts (garnet, biotite, spinel, sub-calcic augites) and pyroxene glomerocrysts, as well as alkali feldspar megacrysts and basement fragments suggest the alkali basaltic magma must have risen rapidly to the surface (Chapman 1974; 1976; Spera 1984; Gernon et al. 2016) (Figure 6.12). Assessing the ascent rate of magma from lower crustal or mantle levels can be particularly difficult to ascertain (Spera 1984). However, attempts have been made to assess the magma ascent rate of the garnet-bearing inclusions within a dyke at the Ardross diatreme (Figure 6.13) and the garnet-bearing Elie Ness inclusions (Chapman 1976, Gernon et al. 2016). This data is evaluated by considering the pyroxene and garnet solidus of the inclusions. The results concluded that there was an extended pressure-temperature environment in which clinopyroxene could coexist with garnet in a basaltic liquid (Chapman 1976). In the ascending magma, a decrease in pressure below 20 kb or a change in temperature outwith of 1200 °C to 1400 °C, would result in garnet phenocrysts becoming unstable. In unstable conditions, the garnet inclusions would dissolve back into the liquid (Chapman 1976). The presence of these garnet inclusions within the diatreme deposits suggests xenolith residence times of approximately 4-8 hours and a minimum source depth of about 75 km at 1200 °C (Chapman 1976). This infers an ascent rate for these particular magmas near 2 to 5 m/s (Chapman 1976).

Typically, alkali basaltic magmas have ascent rates of between 10 cm/s to a few m/s (Spera 1984). Garnet-bearing alkali basaltic magmas, like the diatremes in Ardross and Elie Ness, tend to have, on average, faster ascent rates (1-10 m/s) (Spera 1984). It is, therefore, implied that the diatremes which do not contain or contain minimal proportions of garnet-bearing inclusions or deep-derived inclusions like pyroxenites (e.g. St Monans, Ruddon's Point, Kincaird), were likely sourced from slower ascending alkali basalt magmas, where pressure-temperature conditions inhibited the coexistence of lower-crustal derived phenocrysts. Further evidence for this is indicated by the magmas at the St. Monans, Ruddon's Point and Kincaird diatremes with a higher silica content (relatively more evolved) in comparison to the very low silica content at Ardross and Elie Ness.

The rapid ascent of alkali basaltic magmas from lower crustal or mantle depths are explained by exsolution of CO_2 during magma ascent (Bailey 1980; Spera 1984; Stoppa et al. 2003). Alkaline magma propagates upwards through magma-filled fractures (Bailey 1980; Stoppa et al. 2003). The rate of fracture-propagation is a function of exsolution of volatiles (Spera 1984).

The rapid ascent of magma in East Fife, is likely a function of the emplacement of the alkali-basalt magma along the Ardross Fault, a long-lived, deep-seated, north-easterly tectonic-volcanic structure which was recurrently active throughout the Upper Carboniferous and Early Permian (Francis and Hopgood 1970; Underhill et al. 2008). Dykes can propagate along pre-existing fractures or fault planes (e.g. Ardross Fault) if the fractures or planes are suitably orientated with appropriate principal stress orientations, providing an unrestricted pathway for magma propagation (Delaney et al. 1986; Valentine and Krogh 2006; Thomson 2007; Bédard et al. 2012; Gernon et al. 2016).

Broad variations in the composition of clinopyroxene within the diatremes indicates thorough mixing of magma batches within a lower crustal magma batch and can be explained by a network of semi-independent magma reservoirs in the deep crust (Gernon et al. 2016). Variations in the composition and presence of high pressure xenoliths and glomerocrysts across the five diatremes suggests that individual eruptions were fed from these semi-independent magma reservoirs deep within the lithosphere. The rapid ascent of each individual magma batch (aided by the Ardross Fault) prevented the magma accumulating peridotite from the conduit margins (Gernon et al. 2016).

The structure of the shallow plumbing system beneath the East Fife diatremes is, therefore, relatively simple, compared to the previous studies (Chapters 3, 4 and 5). The ultrabasic nature of the deposits and intrusions, clearly demonstrates that the plumbing system is dyke-dominated and there is no stoping of magma at upper crustal levels.

6.7.2. **Diatreme development**

The development of each diatreme is described in each of the sub-sections ("Interpretations"). The East Fife diatremes exhibit common features described in other field studies of diatremes, including debris columns and late stage magmatic phases (White 1991; Aranda-Gomez and Luhr 1996; McClintock and White 2006; Ross and White 2006; Valentine and Krogh 2006; White and Ross

2011; Ross and White 2012; Gernon et al. 2013; Delpit et al. 2014; Elliott et al. 2015; Lefebvre et al. 2016). A summary of the features at each diatreme is displayed in Table 6.4.

	St. Monans	Ardross	Elie Ness	Kincaird	Ruddon's Point
Well-developed bedding			X	X	X
Debris columns	X		X	X	X
Marginal zones	X	X	X	X	
Collapse zones	X	X	X	X	
Peperitic domains		X		X	X
Late-stage intrusions	X	X	X	X	X
Volcaniclastic injectites			X	X	
Gas fluidisation			X		X

Table 6.4: Summary table of the structural features at each diatreme.

As the processes involved in diatreme formation (e.g. magmatic, phreatomagmatic, fluidisation, PDC formation, mass flows, wall erosion etc.) evolve spatially and temporally during the creation of a diatreme, no two diatreme structures are identical. The cessation of diatreme formation can occur at any point during the eruption (depending on magma supply and magma-water ratios). If diatreme formation ceases near the beginning of the formation process, and debris jets do not erupt at the surface (or have minimal surface eruptions), then PDC formation and deposition is negligible. This will lead to a diatreme structure with no bedded diatreme deposits (White and Ross 2011). The diatremes in East Fife are exposed within the upper, bedded zone and lower, unbedded zone of the typical diatreme structure (Figure 6.47). However, while acknowledging a general structural level for each diatreme, it does not imply a specific stratigraphical level (White and Ross 2011). This is to say that the diatremes exposed in the unbedded zone (St. Monans and Ardross) may or may not have upper, bedded zones (Figure 6.47). It is important to consider the possibility of these diatremes having no upper, bedded zones.

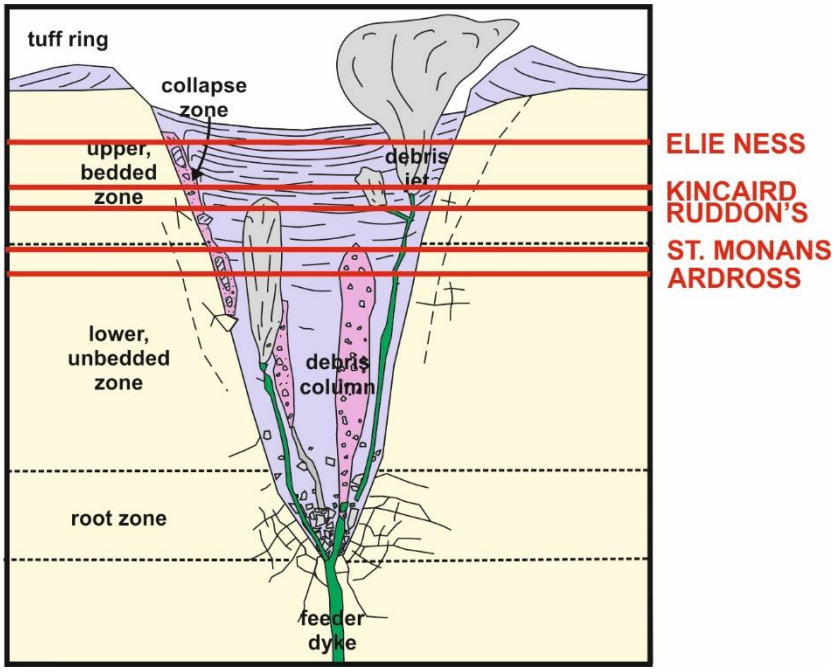

Figure 6.47: A typical diatreme structure showing the four main zones (tuff ring, upper bedded, lower unbedded and root zone). Debris columns and collapse zones are also evident within a typical diatreme. The proposed level (solid red line) of all the studied East Fife diatremes within the typical diatreme structure relative to each other is shown. Not to scale.

6.7.3. **Intrusions within diatremes**

The intrusions within the East Fife diatremes display a number of features which can be used to better understand the conditions of the substrate (diatreme deposits) as the intrusions were emplaced. These features have been described and interpreted within each diatreme's sub-heading and include: (1) straight dykes with minimal or no interaction with the substrate; (2) highly undulating margins; (3) passive blocky peperite; (4) dynamic blocky peperite (peperitic domains); (5) fluidal peperite; (6) clastogenic dyke-like bodies; (7) volcaniclastic injectites associated with dyke intrusion; and (8) sill intrusion and ponding of large volumes of magma in the very shallow subsurface. These intrusion features all provide evidence for shallow emplacement through ductile mechanisms. The loosely packed nature of the tuff and lapilli-tuff substrate within the diatreme and the high water content of the substrate during the emplacement of intrusions promoted fluidisation of the host and the formation of these non-brittle intrusion features.

6.7.4. **Magma-water interaction and volatile exsolution**

Within the East Fife diatremes, there is evidence for non-explosive interaction (peperite formation, coarse in-situ brecciation), energetic steam explosions (fine to medium granulation and dynamic peperite domains), and high energy phreatomagmatic fragmentation (very fine granulation) (Figure

6.48). As previously discussed in preceding chapters, the degree of explosivity is dependent on several factors: (1) confining pressure on the magma preceding and during water interaction; (2) rate of magma ascent and subsequently volume of exsolved volatiles; (3) amount of magma-water mixing (dependent on presence of vapour film); (4) magma viscosity; (5) mechanical strength of host-rock; and (6) water-magma ratios (Aranda-Gomez and Luhr 1996; Hooten and Ort 2002).

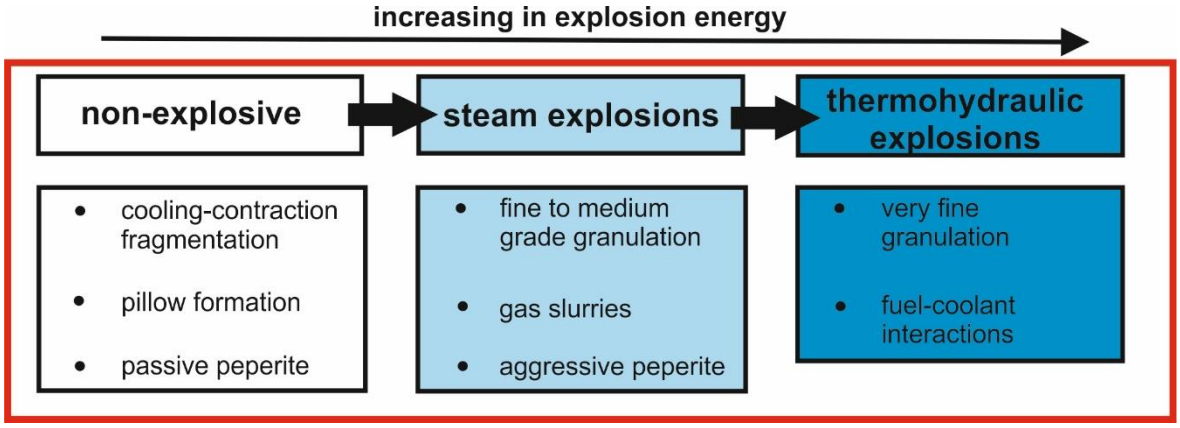

Figure 6.48: Magma-water explosivity index, indicating characteristic features of each type of magma-water interaction. Red box marks the magma-water interaction seen around the intrusions in the East Fife diatremes.

The process which creates high energy phreatomagmatic eruptions has been recreated in experiments using molten volcanic rocks (Zimanowski et al. 1991, 1997; Büttner and Zimanowski 2002). Passive magma-water interaction occurs when the vapour film, which develops between intruding magma and surrounding host-rock, remains stable. Alternatively, phreatomagmatic interaction occurs when the vapour film condensates and the magma is in direct contact with the porewater in the host-rock (Wohletz 1986; Zimanowski et al 1997; Büttner and Zimanowski 2002). Rapid heat transfer from magma to water results in rapid cooling of the magma and instantaneous expansion of water causing extensive and intensive fracturing of the magma (Wohletz 1986; Büttner and Zimanowski 2002). This process is enhanced by increasing the surface area of contact between the magma and water, where water filters into the fractures and causes further fracturing (Büttner and Zimanowski 2002). The product of this process is extremely fragmented magma (very fine ash; <130μm) and a high amount of kinetic energy (seismic waves) (Zimanowski et al. 1997; Büttner and Zimanowski 1999, 2002). It is these seismic waves that fragment and brecciate the surrounding host-rock. Phreatomagmatic explosions produce idiosyncratic products that are defined by their grain-size, clast morphologies, deposit thicknesses and bed-forms (Wohletz 1986). The generally

poor exposure at the East Fife diatremes and highly altered diatreme deposits restricts the analysis and calculation of the amount of phreatomagmatic fragmentation (Büttner and Zimanowski 2002). Juvenile clasts within diatremes can often have complex histories, where individual juvenile clasts and lithic clasts are often entrained in passing debris jets and reworked. Reworking can alter the primary clast morphology, due to particle-particle collision and fragmentation (White and McClintock 2001; McClintock and White 2006; Ross and White 2006; Ross and White 2012; Valentine and White 2012).

In typical dry, strombolian eruptions, degassing tends to occur in the initial stages of an eruption, leading to an increase in eruption intensity and the eruption of vesicular products. This increase in eruption intensity is followed by a waning phase as an eruption progresses. However, if magma interacts explosively with groundwater prior to degassing, the juvenile clasts remain poorly vesiculated during the initial stages of diatreme formation (Houghton and Wilson 1989; Mangan and Cashman 1996; Ross and White 2012; Lefebvre et al. 2016). This occurs if the magma ascends rapidly before it interacts explosively with water, or if the lithostatic pressure is sufficient enough to restrict volatile exsolution (Ross and White 2012). As the eruption progresses, excavation of the overlying host-rock above the eruption site decreases the lithostatic pressure, initiating vesiculation of the magma before it undergoes magma-water interaction. This produces vesiculated clasts in later stage deposits (Aranda-Gomez and Luhr 1996). The East Fife diatremes generally follow this trend from non-vesicular to vesicular clasts. Vesiculated basalt clasts are evident in several diatremes (St Monans, Elie Ness, Kincaird and Ruddon's Point). The vesicular clasts are located within either debris columns (SM, E, K, R), peperitic domains (R), or upper bedded deposits (E) which form in the latter stages of diatreme development.

Towards the end of diatreme formation, non-explosive magmatic processes tend to overcome phreatomagmatic processes due to an increase in the magma-water ratio. This is typically due to the water supply becoming limited, and not because there is an increase in magma flux. Coherent intrusions are common throughout the East Fife diatremes (SM, A, E, K, R) and represent this late-stage switching from phreatomagmatic to magmatic processes, where magma is passively emplaced into the diatreme and there is limited magma-water interaction. Peperite at the margins of intrusions

in all the East Fife diatremes (SM, A, E, K, R) represent in-situ brecciation caused by non-explosive cooling, quenching and brittle fracturing.

Explosivity is controlled by both phreatomagmatic and magmatic processes depending on the availability of water and the lithostatic pressure. This a complex, dynamic system, where fluctuating water availability can alter the intensity of the explosions from highly efficient wet phreatomagmatic eruptions to dry, strombolian eruptions (Saucedo et al. 2017). Wet, phreatomagmatic eruptions follow a similar trend to dry, strombolian eruptions where there is a waxing phase followed by a gradual waning phase. However, in phreatomagmatic eruptions this trend is overprinted by a highly fluctuating change in energy where phreatomagmatic eruptions can be weak and inefficient producing coarse phreatomagmtic deposits (dry phreatomagmatic) or intense and efficient producing very fine phreatomagmatic ash deposits (wet phreatomagmatic) depending on the availability of groundwater (Wohletz 1986; Cas et al. 2016). In diatreme and maar deposits, there are gradational changes from dry to wet to magmatic deposits, depending on the rate of groundwater recharge (Cas et al. 2016).

Chapter 7: Disruption of host-rock and hydrocarbon prospectivity; East Fife, Scotland

7.1. Introduction

This chapter examines the host-rock surrounding the diatremes in East Fife and the disruption associated with diatreme emplacement. The margin between the diatreme and host-rock is exposed locally at all the diatremes discussed in Chapter 6 (St. Monans, Ardross, Elie, Kincaird and Ruddon's Point). These exposures allow for detailed analysis of the physical disruption that occurs at the boundaries of diatremes in soft-rock substrates. The host-rock surrounding the St. Monans diatreme is fully exposed for >300 m from the northern diatreme boundary, and is suitable for quantitative analysis of the thermal disruption caused by diatreme emplacement.

White and Ross (2011) suggested that the physical and thermal effects associated with diatreme formation are remarkably few in number, however very few quantitative studies have been performed to assess this fully (Raymond and Murchison 1989). Well-studied diatreme fields, like Hopi Buttes, are exposed in a series of pinnacles, where the surrounding host-rock has been subsequently eroded. An accurate assessment of the amount of disruption, therefore, is difficult to establish. Furthermore, the thermal disruption caused by circulating hydrothermal fluids associated with diatreme formation is often overlooked. This disruption can be significant however to date there has been no significant quantitative investigation into the thermal effects of diatreme formation on host-rock.

Volcanic and magmatic systems can modify the characteristics of the host-rock, for example the organic matter maturation, porosity and permeability (Raymond and Murchison 1991; Barker et al. 1998; Ahmed 2002; Suchy et al. 2004; Cooper et al. 2007; Fjeldskaar et al. 2008; Santos et al. 2009; Muirhead, D.K. et al. 2012; Senger et al. 2014; Schofield et al. 2015). Although not prevalent in the hydrocarbon exploration of the Firth of Forth (Well 25/26-1, Conoco), the disruption to host-rock caused by phreatomagmatic volcanoes and other monogenetic volcanic activity nonetheless has an important bearing on the early maturation of source rocks and the reservoir potential in volcanic margin basins.

Using a combination of field and analytical techniques, the type and extent of physical deformation is observed and analysed, and the extent of thermal disruption is quantified. The St. Monans diatreme was used as the case-study because of its intact host-rock stratigraphy. Detailed stratigraphical logging of the host-rock away from the St. Monans diatreme was undertaken and samples collected at intervals from the diatreme margin. Vitrinite reflectance (VR) analysis and Raman spectroscopy were undertaken to assess the thermal impact of diatreme formation on shale host-rock. Fluid inclusion wafers were made from quartz arenite samples and the homogenisation temperatures of the fluid inclusions within quartz overgrowths were measured to assess the effect of hydrothermal fluids on sandstones.

7.2. Thermal and hydrocarbon history of East Fife

Although no stratigraphical successions post-Carboniferous and pre-Pleistocene are preserved in East Fife, the general vitrinite reflectivity values from the East Fife coastal exposures indicate a mild to moderate post-Carboniferous burial history (MacGregor 1968; Raymond and Murchison 1988; Marshall et al. 1994). The general value of vitrinite reflectance in shales located between St. Monans and the Ardross diatremes is Ro (average) ~0.55 % (Raymond and Murchison 1988). The relatively low values suggest a low to moderate cover of post-Carboniferous rocks, which has been calculated to a maximum thickness of 2-3 km by comparing the reflectivity values to the values of unconsolidated sediments (0.2-0.3%) (Marshall et al. 1994). Using the vitrinite reflectivity to temperature relationship of Barker and Pawlewicz (1986), the vitrinite reflectance value gives a geothermal gradient of 23 °C/km for the East Fife succession (Marshall et al. 1994). Comparing this gradient to calculated gradients in other parts of the Midland Valley, indicates that maximum burial was achieved in East Fife during the Carboniferous (Marshall et al. 1994).

Comparison of the vitrinite maturity values to the west of the Fife succession (Central Midland Valley), shows substantially higher vitrinite reflectivity in the west (Ro (average) >1.30%), suggesting a thicker post-Carboniferous cover and greater burial depths (Raymond and Murchison 1991). For example, the Coal Measures (Table 6.1; 6 km west of Ruddon's Point) has vitrinite reflectivity of 0.7-0.9%, reflecting bituminous grade (Raymond and Murchison 1991; Underhill et al. 2008). This has resulted in maturation levels in the central Midland Valley for the Upper Carboniferous successions (Strathclyde Group; Table 6.1) being greater than the oil window (Ro (average) 1.2%) and reaching gas-generating values (Raymond and Murchison 1988). Upper Carboniferous and Lower Permian magmatic intrusion events throughout the Midland Valley caused significant heating and thermal alteration to the surrounding stratigraphical successions (George 1993). In East Fife, the vitrinite values suggest the Upper Carboniferous successions (Strathclyde Group; Table 6.1) are only on the threshold of the oil window.

The Midland Valley has long been acknowledged as an area of hydrocarbon exploration potential, particularly in the early 20th century with the presence of natural seeps, oil-shale development and subsurface exploration (Underhill et al. 2008; Monaghan 2014). The East Midland Valley contains all

the elements for a working petroleum system, for example the Strathclyde Group oil-shales as a source rock, the interbedded sands and shales in the Strathclyde Group as reservoir-seal pairs, and structural trapping geometries (Table 6.1) (Underhill et al. 2008; Monaghan 2014). However, maturity and the timing of migration limit the extent of Midland Valley exploration (Underhill et al. 2008). In West Fife, initial maturation and petroleum charge occurred during the Carboniferous, prior to the emplacement of the Midland Valley Sill (Raymond and Murchison 1989; Underhill et al. 2008), petroleum charge arrested during uplift in the Permian to the Mesozoic, and resumed again during the Mesozoic, preceding Paleogene uplift (Underhill et al. 2008).

An exploration well (25/26-1) was drilled in the Firth of Forth, targeting a parasitic anticline on the eastern flank of the NNE-SSW trending Midlothian-Leven syncline, in 1990 by Conoco (Underhill et al. 2008). The well suggests that Dinantian source rocks in the limbs of the Midlothian-Leven syncline entered the oil window at the end of the Carboniferous and the axis of the Midlothian-Leven syncline entered the gas window during the Carboniferous and again in the late Mesozoic (Figure 7.1) (Ritchie et al. 2003; Underhill et al. 2008).

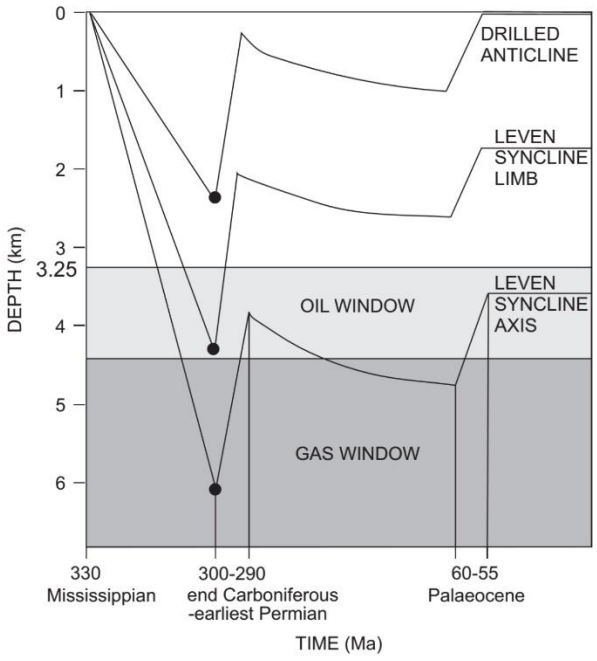

Figure 7.1: Schematic burial history plot for the West Lothian Oil-Shale Formation (Strathclyde Group; refer to Table 6.1) (from Underhill et al. (2008)). The three plots show the burial history of various positions within the Midlothian–Leven Syncline. For example, the top plot (drilled anticline) refers to well 25/26-1; the middle plot refers to the limb of the syncline; and the bottom plot refers to the axis of the syncline. The burial history shows that the limbs and axis reached maturity in the Late Carboniferous.

Alternatively, the exposed successions along the East Fife coast are all immature for hydrocarbon production; however, surrounding intrusions, liquid hydrocarbon generation was possible during the Carboniferous (Raymond and Murchison 1988; 1991). Although the diatremes in East Fife would have not have contributed significantly to the maturation of liquid hydrocarbons, the diatremes caused some disruption to potential reservoir-seal pairs, particularly in the Pathhead Formation.

7.3. Physical Disruption

The East Fife diatremes described in Chapter 6 intrude into the Pathhead Formation (Strathclyde Group), Limestone Coal Formation (Clackmannan Group) and the Upper Limestone Formation (Clackmannan Group). Stratigraphical logs of the host-rock adjacent to each diatreme are shown in Figure 7.2. The Pathhead Formation, intruded by the St. Monans, Ardross and Elie diatremes, consists of interbedded laminated shales (mud to fine sand grain size), blonde quartz arenite (fine to coarse sand grain size), coal (bituminous grade) and limestone beds. The shales contain ironstone nodules, and bivalves and brachiopods are present within the shales. The sandstone beds are massive, planar bedded and cross-bedded, often displaying symmetrical ripples on the upper bed margin. Ironstone nodules, rootlets, organic plant debris and *stigmaria* roots are present within the sandstones. Limestone beds form prominent markers within the sequence and contain crinoids, bivalves, brachiopods (locally intact *Productus* with spines) and sand-filled burrows (Figure 7.2).

The Limestone Coal Formation is intruded by the Kincaird diatreme. The exposure of host-rock directly adjacent to the Kincaird diatreme is characterised by interbedded organic-rich shales, carbonaceous siltstones; micaceous sandstones (fine to medium grain size) and bituminous coals (Figure 7.2). The shales contain rootlets, plant debris, bivalves and ironstone nodules. The shale successions often display reverse grading, suggesting an increase in sand input towards the top of the unit and a shallowing of deposition. The sandstones are characterised by symmetrical ripples and low angle cross stratification which tend to be defined by organic rich stratifications. Roots and bivalves are also present within the sandstones (Figure 7.2).

The Ruddon's Point diatreme has intruded into the Upper Limestone Formation, but the poor exposure of the host-rock prevents a representative log from being undertaken. However, the Upper Limestone Formation is similar to the Limestone Coal Formation and generally consists of interbedded fissile shales (mud to coarse silt grain size) and quartz-rich sandstones (fine to coarse grain size). The sandstones are massive or display hummocky cross-stratification. The general difference between the Upper Limestone Formation and the preceding Limestone Coal Formation is a marked increase in marine (limestone) beds (MacGregor 1968).

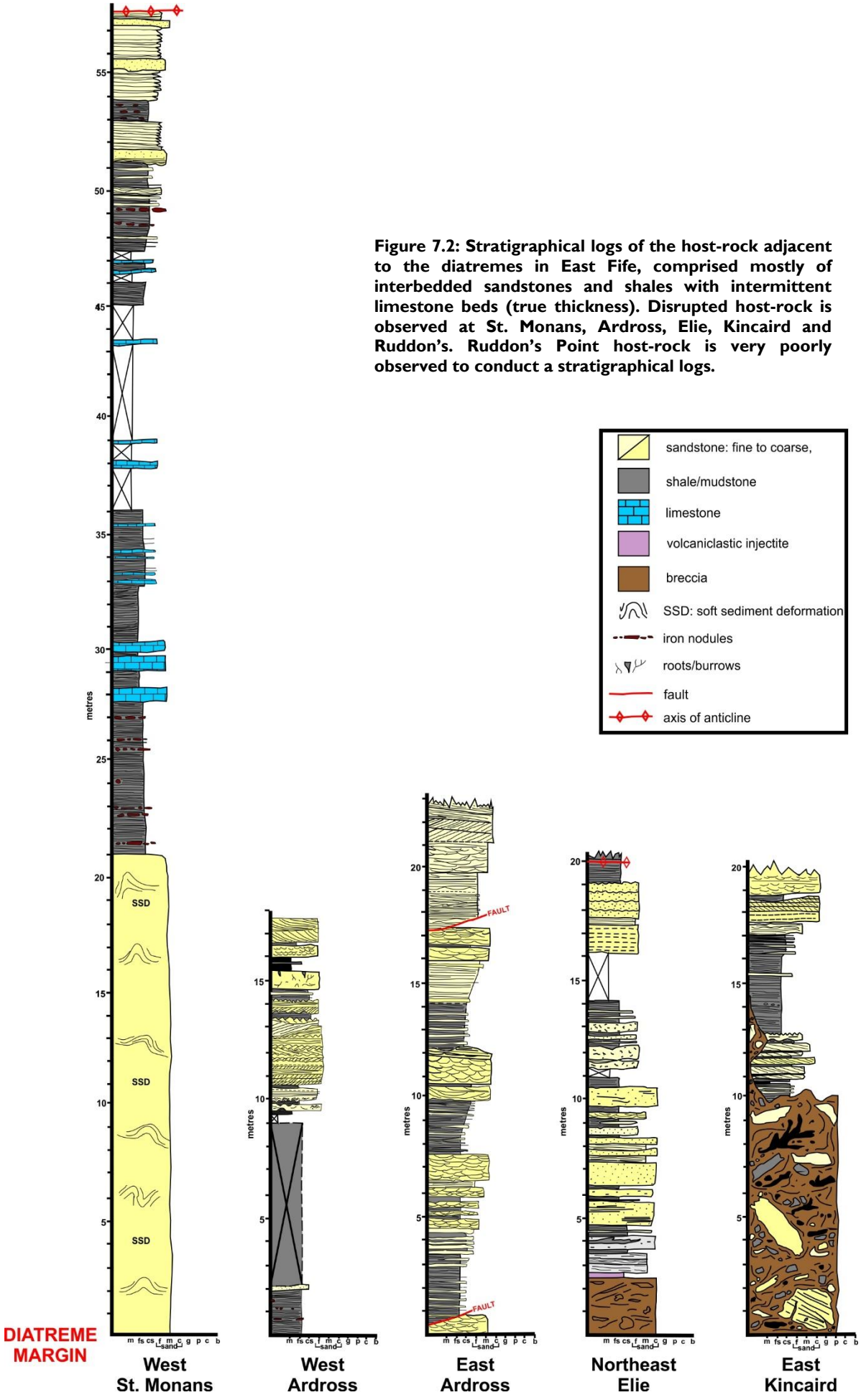

Figure 7.2: Stratigraphical logs of the host-rock adjacent to the diatremes in East Fife, comprised mostly of interbedded sandstones and shales with intermittent limestone beds (true thickness). Disrupted host-rock is observed at St. Monans, Ardross, Elie, Kincaird and Ruddon's. Ruddon's Point host-rock is very poorly observed to conduct a stratigraphical logs.

.

The margins of the diatremes take one of two forms: a defined, clear-cut margin with little disruption to the surrounding-host rock (Figure 7.3), or extensive zones of host-rock disruption. Zones of host-rock disruption extend up to 70 m from the diatreme margins. Various physical interactions occur within this zone including: (1) fluidisation of sands and silts (Figure 7.4); (2) mobilisation and commingling of sand and silt grains (Figure 7.4); (3) injection of mobilised sediments into surrounding strata (Figure 7.4); (4) brecciation of coal and consolidated sandstone (Figure 7.5); (5) ductile and brittle deformation of calcareous sands and marls (Figure 7.5); (6) extensive hydrothermal systems at the margins of the diatreme (up to 40 m into host) (Figure 7.6); (7) faulting (Figure 7.7); and (8) intrusion of dykes (Figure 7.7).

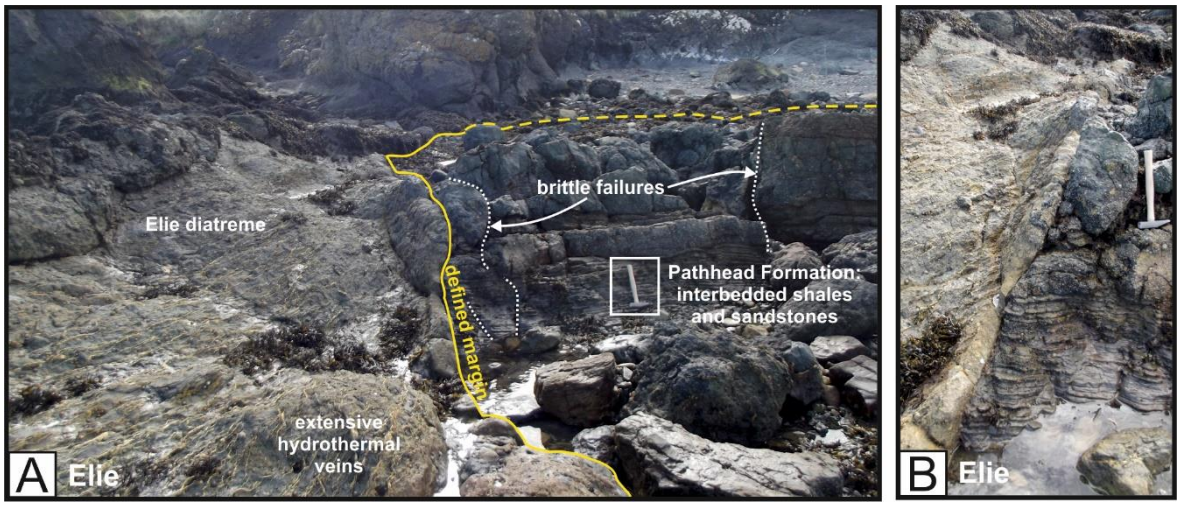

Figure 7.3: Defined margin with minimal host-rock disruption at the NW margin of the Elie Ness diatreme. (A) Solid yellow line marks definitive boundary between the Pathhead Formation and the Elie Ness diatreme. Within the diatreme, extensive hydrothermal veins are present. Only minimal host-rock disruption (brittle failures and minor displacement along failures) occurs in the adjacent Pathhead Formation. (B) Close-up photograph showing steeply-dipping margin. Hammer is 40 cm long.

7.3.1. Fluidisation and brecciation

The host-rock surrounding the diatremes has been extensively fluidised resulting in reconstitution of sediments and the complete loss of the original stratigraphy (Figure 7.4). Fluidisation of host-rock occurs up to 70 m from the margin of the diatremes (Kincaird, Elie). The sandstone and shales are inconsistently affected by fluidisation, where either the sandstones are fluidised, the shales are fluidised or both. Commingling of sediment grains is evident in the Kincaird host-rock, where fluidised silt has invaded the surrounding fine to medium grained sandstones. Fragments of the sandstone are supported in the structureless silty matrix (Figure 7.4A). The fragments

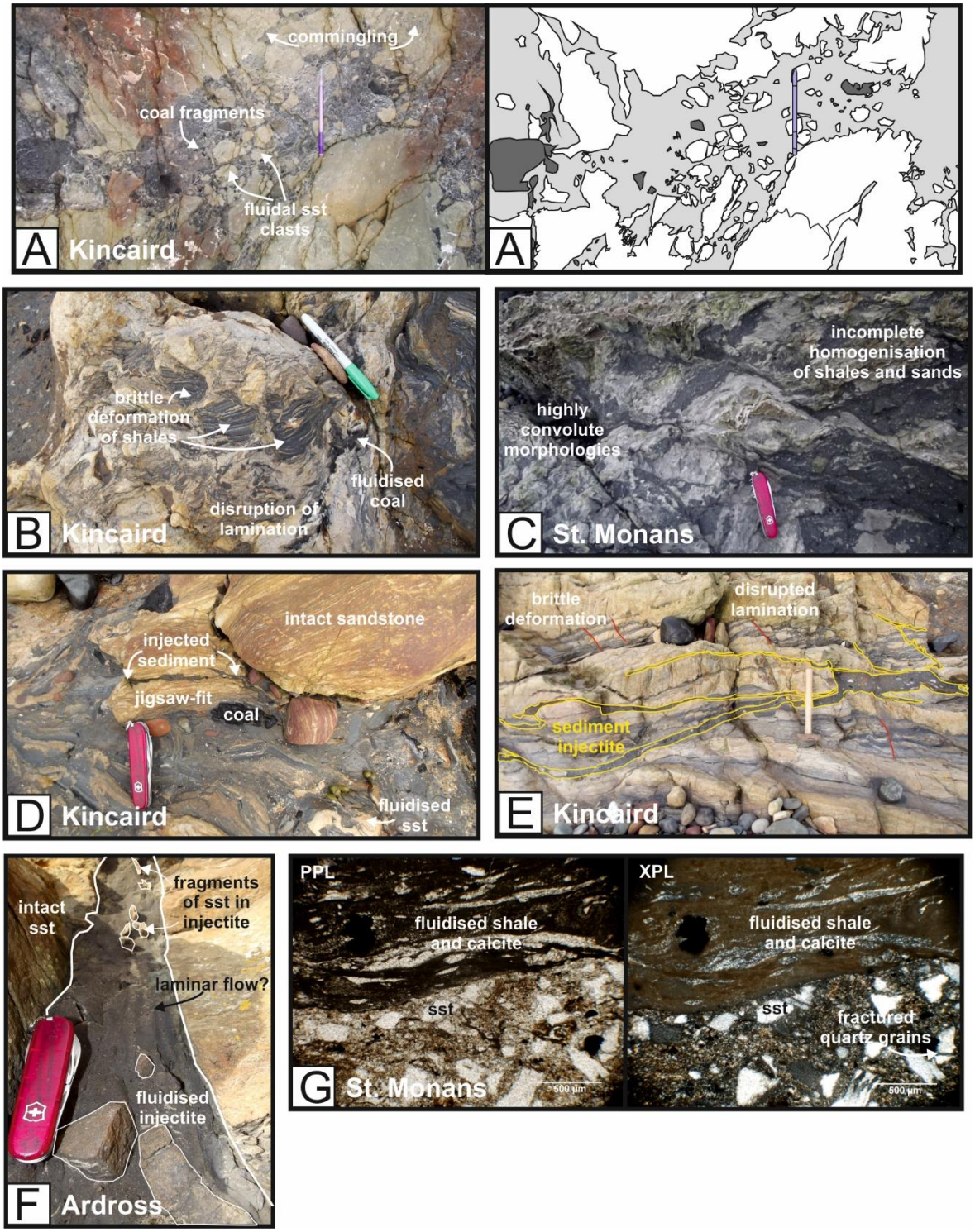

Figure 7.4: Photographs of various fluidisation textures. (A) Photograph and annotated photograph of intensely fluidised silts and muds from the shale interbeds which have intruded into the surrounding sandstone at Kincaird. Fluidal sandstone clasts and angular coal clasts are suspended in the fluidised sediment matrix. Commingling of grains occurs locally within sandstone clasts (top right of the image). Pencil is 15 cm long. (B) Fluidised sandstone disrupts the surrounding shale layers. More consolidated shale layers retain internal lamination and undergo brittle fracturing, while softer shales are prone to fluidisation and ductile deformation. Coal interbeds are also deformed. Pen is 15 cm. (C) Fluidisation of interbedded sands and shales at St. Monans. The incomplete mixing creates highly convolute morphologies. (D) Sandstone remains coherent (has not undergone fluidisation). Shale has undergone fluidisation and mobilisation and has been injected into existing fractures in the sandstone, breaking fragments off and causing in-situ brecciation. (E) Sediment injectite cross-cuts bedded host-rock stratigraphy. Hammer is 40 cm long. (F) Sediment injectite (comprised of silt from shale interbed) is sub-vertically injected into the overlying sandstone layer at Ardross. The injectite breaks off and entrains fragments of sandstone. Pen-knife is 10 cm long. (G) Photomicrograph (ppl and xpl) of the fluidised shale from the St. Monans host-rock. Quartz grains appear to be fractures in the sandstone.

typically have semi-fluidal margins which suggest that the sands were also fluidised to some degree. Quartz grains within the sandstone, appear to be fractured which indicates that mobilisation creates shearing and fracturing within individual quartz grains (Figure 7.4G). Similarly, fluidised sands have invaded shale interbeds (Figure 7.4B). Intact, angular shale fragments are suspended within the sandy matrix. The shale fragments still retain their internal laminations, although the laminations are often displaced by minor brittle failures, likely associated with the brecciation and rotation of the clast (Figure 7.4B). Fluidisation of both sands and shales result in complex mixing and produces highly intricate, convolute morphologies, locally displaying R-T structures (Figure 7.4C).

The fluidised sediments have been remobilised and have formed sediment dykes or injectites in the surrounding stratigraphy (Figure 7.4D, E and F). Minor injectites can cause in-situ brecciation of coherent host-rock (mostly medium to coarse sandstones), forming jigsaw-fit textures (Figure 7.4C). At Kincaird several sediment injectites, consisting of sub-angular sandstone, coal and shale clasts entrained within a silt matrix, have intruded into the interbedded hosts and have compartmentalised the strata (Figure 7.4E). The injectites have distinct, straight margins and cross-cut the bedding at shallow angles. Similarly, sub-vertical host-rock injectites are apparent in the host-rock surrounding several of the diatremes (Figure 7.4F). These sub-vertical injectites are present where shales underlying coarse sandstone units have fluidised and injected upwards into the overlying sandstone layer. Often the passing sediment injectite entrains angular sandstone fragments. One injectite in particular (Ardross) displays a laminated appearance, suggesting the injectite was formed by laminar flow processes (minimal turbulent flow) (Figure 7.4F).

At all the diatremes, homogenisation of the sediments has produced an angular host-rock breccia which consists of a dark-grey/red, silt grade matrix with randomly orientated limestone, laminated and massive shale, red siltstone, blonde sandstone and coal clasts (Figure 7.5A, B and C; Table 7.1). The clasts are poorly sorted and range in size from sub-cm to ~50 cm, displaying a variety of clast morphologies (Figure 7.5A, B and C). Large sandstone rafts are also evident within the host-rock breccia, measuring up to 4 m (Figure 7.5D). The rafts retain the internal depositional lamination (Figure 7.5D) and have defined, straight margins. The dip orientation and steepness of beds suggests the raft has been displaced from its in-situ position and rotated.

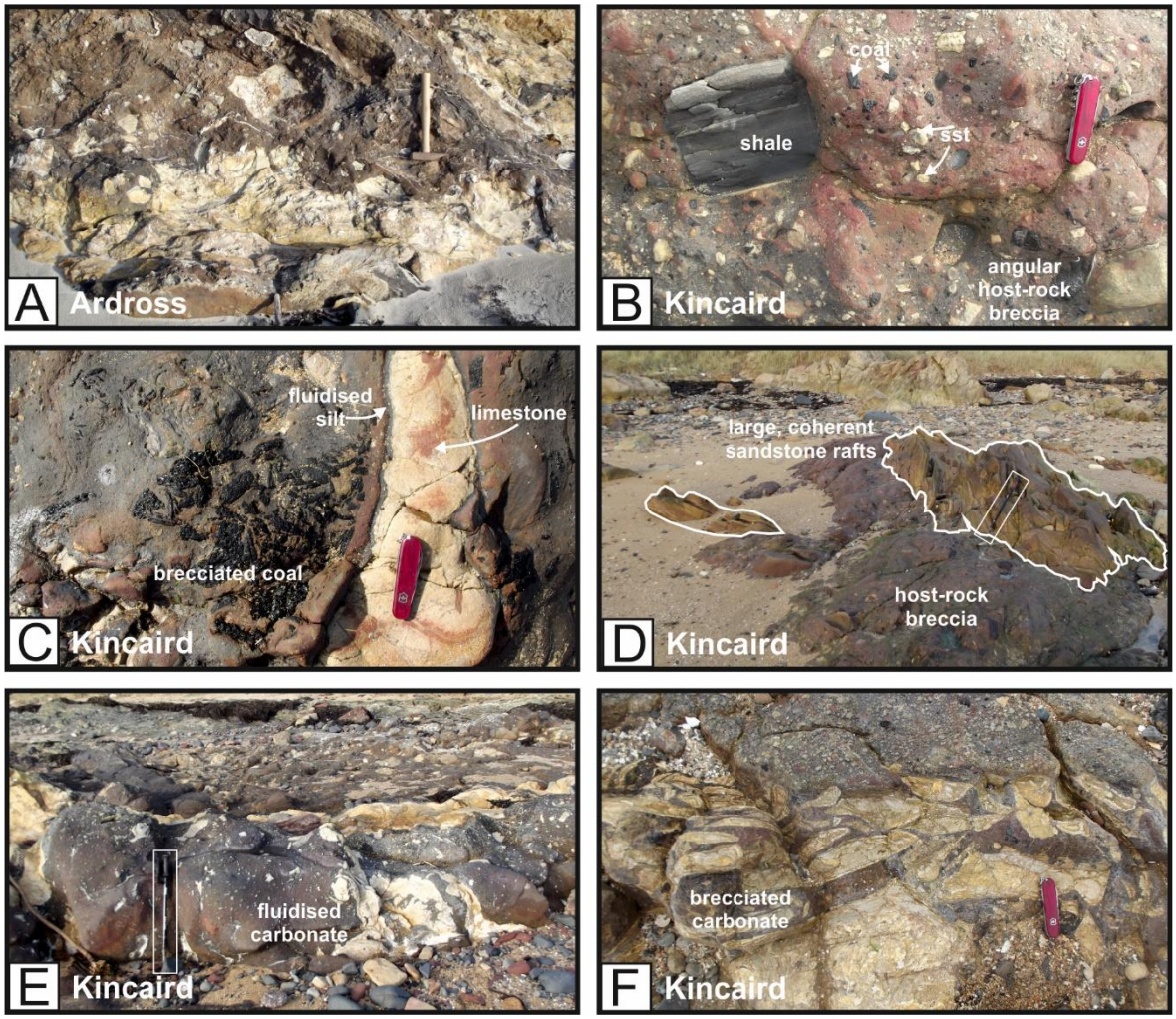

Figure 7.5: Photographs of brecciated host-rock. (A) Brecciated host-rock at the SW margin of the Ardross diatreme. Clasts of carbonate host-rock (white rock) become suspended within the sediment matrix. Hammer is 40 cm long. (B) Host-rock breccia commonly seen at the margins of the Kincaird diatreme. Shale clasts often retain lamination. Host-rock breccia also contains bituminous coal and sandstone clasts within a silt-grade sediment matrix. (C) Brecciated bituminous coal. (D) Large host-rock (sandstone) rafts suspended within the host-rock breccia. Rafts are rotated from original in-situ position and often contain laminations. Walking pole is 1 m long. (E) Carbonate layers are thoroughly distorted by fluidised host-rock breccia. The carbonate layers display highly convolute morphologies. Walking pole is 1 m long. (F) Carbonate has undergone brittle brecciation. Pen-knife is 10 cm long.

The morphology of the clasts reflects deformation under brittle and ductile conditions, for example, siltstone and fine sandstone clasts display a wispy geometry indicating ductile deformation. Carbonate clasts display two different clast morphologies: fluidal (Figure 7.5E) and sub-angular (Figure 7.5F). The tabular clasts have rounded corners and exhibit jigsaw-fit textures (Figure 7.5F). These characteristics are typical of autobrecciation (Chough et al. 2001). Autobrecciation of carbonates tends to be the result of compaction during burial and the expulsion of pore water (Chough et al. 2001). However, within the host-rock breccia surrounding diatremes, autobrecciation is likely to be the result of brittle fracturing along primary cracks. The cracks widen due to the infiltration of fluidised silt. Rounding of the angular clasts may be caused by grain attrition

by sustained fluidisation of the sediment matrix and enhanced by surface tension (Stanistreet and Hughes 1984; Chough et al. 2001).

Lithology of clast	Clast population (%)	Minimal clast size	Maximum clast size	Clast morphology
Med-coarse sandstone	**11.6%**	**sub-cm**	**4 m**	**fluidal; occasionally retaining laminations**
Silt to fine sandstone	**18.5%**	**sub-cm**	**50 cm**	**Wisps and shards; small clasts (<4 cm) are fluidal. large (>4 cm) are sub-rounded to angular**
Shale	**21.2%**	**0.3 cm**	**22 cm**	**laminated and massive; angular, defined clasts**
Bituminous coal	**24.2%**	**sub-mm**	**16 cm**	**angular, occasionally convolute; laths**
Carbonate	**24.6%**	**1 cm**	**31 cm**	**fluidal, convolute margins; locally sub-angular**

Table 7.1: Host-rock breccia clast lithologies at Kincaird, clast population (n=475), and max. and min. clast sizes.

7.3.2. Hydrothermal Systems

At all the East Fife diatremes, hydrothermal veins are present to varying degrees (Figure 7.6). The hydrothermal systems appear to extend up to 30-40 m from the diatreme margin (Figure 7.6B). The veins are comprised of either quartz or calcite (depending on location) and locally, calcite infills pore spaces (Kincaird) (Figure 7.6E, F and G). The veins range in thickness from very fine (sub-mm) to thick (5 cm) and cover <1% to >80% of the host-rock (Figure 7.6A and D). The spacing between the veins ranges from >1 m to <1 cm, and locally they form intensive hydrothermal networks (Figure 7.6D). The veins cut across and also engulf host-rock clasts within the disrupted zone (Figure 7.6C, G). The spatial association of veins and diatremes indicates that the hydrothermal systems were contemporaneous with diatreme formation, and that the diatremes were the likely cause of such systems. Furthermore, the veins are absent across one of the sediment injectites at Kincaird, showing that the hydrothermal systems preceded some episodes of clastic intrusion. The hydrothermal veins may be indicative of CO_2-rich, steam-heated waters that formed as a result of heating by the diatreme, particularly where magmatic dykes are present within the diatreme. Twinned calcite (in xpl) is present within large vesicles in juvenile clasts the volcaniclastic injectite at Elie which provides evidence for low temperature thermal deformation (Figure 7.6E).

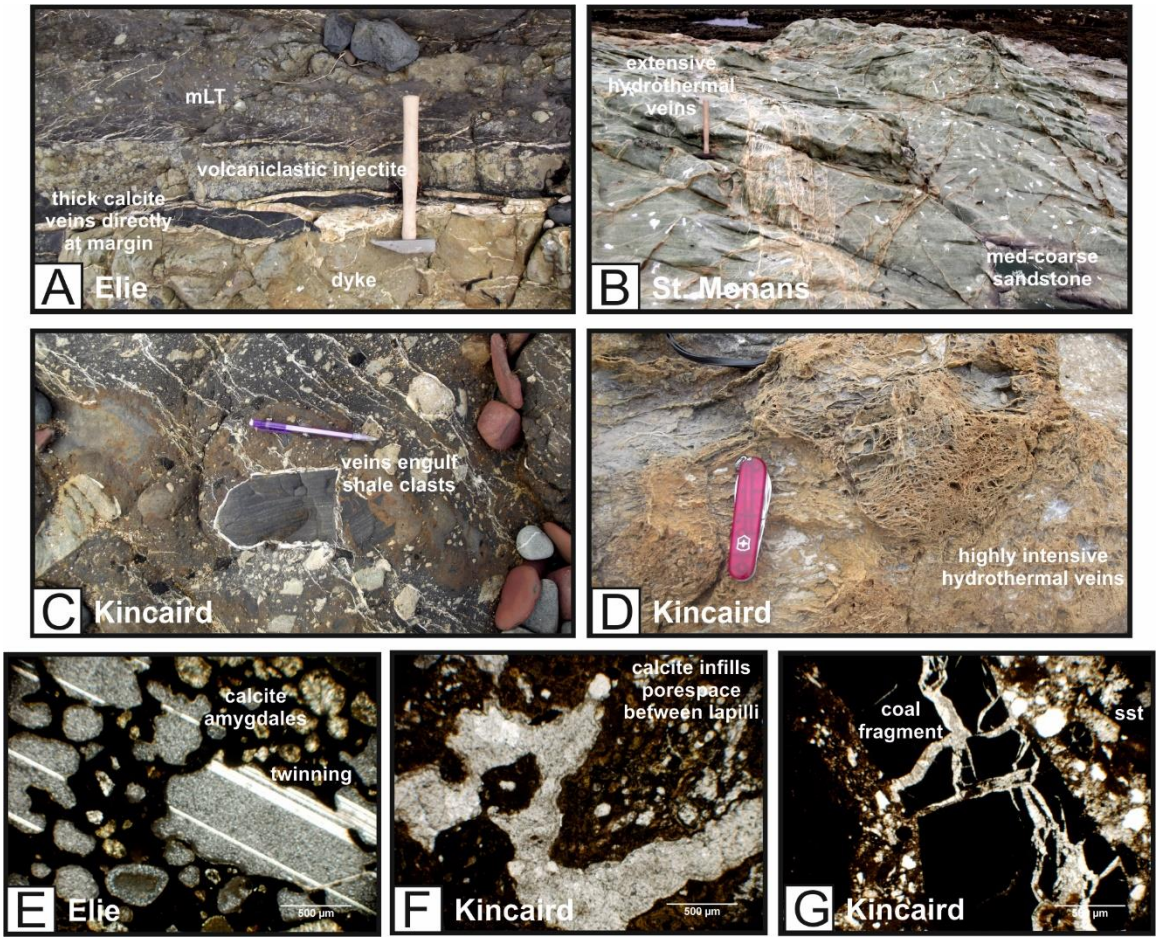

Figure 7.6: Photographs of the extensive hydrothermal systems that have intruded the host-rock surrounding the diatremes. (A) Thick calcite veins delineate the margin of the diatreme at Elie (NE margin). (B) Extensive hydrothermal veins in medium to coarse sandstone 20-25 m from the St. Monans diatreme margin (S margin). Hammer is 40 cm long. (C) Hydrothermal veins engulf shale clasts within the host-rock breccia, approximately 10 m from the Kincaird diatreme margin (E margin). Pencil is 15 cm long. (D) Highly intensive hydrothermal vein network within a sandstone approximately 7-8 m from diatreme margin (E margin at Kincaird). Pen-knife is 10 cm. (E) Photomicrograph from a volcaniclastic injectite at Elie showing calcite amygdales within a juvenile. The calcite shows multiple twinning in xpl indicating low temperature thermal deformation e.g. heating. (F) Photomicrograph (xpl) of the volcaniclastic injectite at Kincaird showing calcite infilling the pore space between clasts/juvenile clasts. (G) Photomicrograph of veins within highly disrupted, fluidised and brecciated host-rock. Calcite veins brecciate a coal fragment within a fluidised sandstone.

7.3.3. Faults and dykes

Brittle failures are present in the host-rock surrounding the East Fife diatremes and typically increase in number towards the diatreme margin (Figure 7.7). Fault gouges and fault breccias are present within some of the host-rock faults in Elie, which are orientated parallel or sub-parallel to the diatreme margin (Figure 7.7A). The clasts within the fault breccias tend to be fragments of coherent sandstone host-rock which are suspended within a fluidised silt (shale) matrix (Figure 7.7A). Brittle failures in the host-rock tend to affect the sandstone beds which are more coherent than the shale interbeds (Figure 7.7B). The shale and mudstone interbeds typically respond to failure in a ductile manner (Figure 7.7B).

Highly irregular dykes have intruded into the host-rock surrounding the Ardross diatreme. The dykes tend to intrude into the shale horizons and have highly convolute margins (Figure 7.7C). Locally the dykes intrude along fault planes (Figure 7.7D). Fluidal peperite forms at the margins of the dykes (Figure 7.7D)

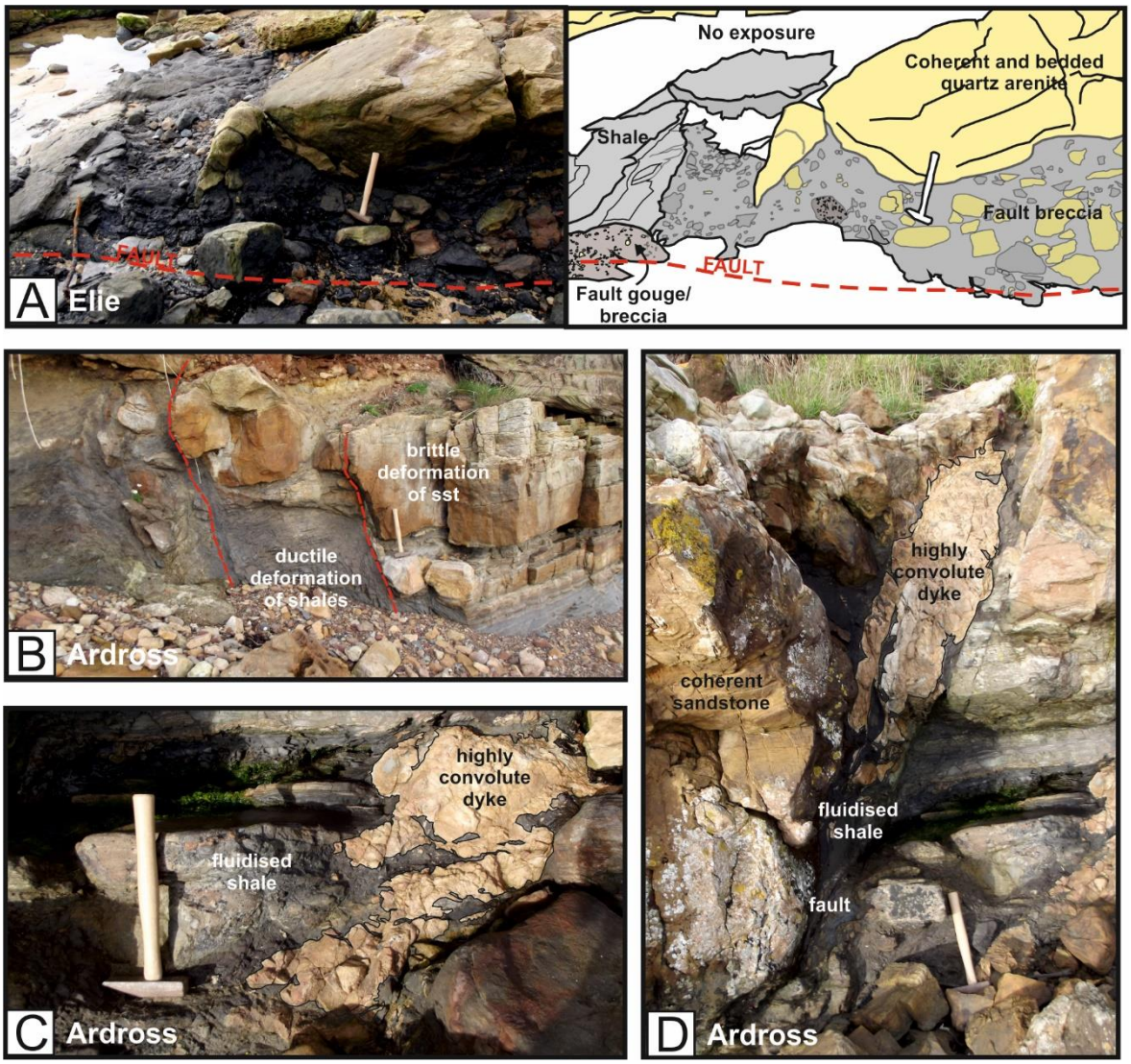

Figure 7.7: Photographs of faulting and dyke intrusion within the host-rock surrounding the diatremes in East Fife. (A) Photograph and annotated photograph of a fault ~40 m from the Elie diatreme margin (NE margin). The fault is orientated parallel to the diatreme margin. Host-rock disruption is observed between the fault and the margin. Fault gouge and fault breccia are present within the fault. Breccia clasts are up to 20 cm wide and are randomly orientated in a fluidised shale matrix. (B) Brittle failures in the host-rock surrounding the Ardross diatreme (NE margin). Displacement is 60 – 85 cm. Shale has undergone ductile deformation, whereas the sandstone has experienced brittle deformation. (C) Irregular dyke emplacement into fluidised shale (~20 m from diatreme margin). Dyke has a highly convolute morphology. (D) Dyke within fault at margin of Ardross diatreme. Hammer is 40 cm long.

7.4. Thermal Disruption

7.4.1. Vitrinite Reflectance

Vitrinite reflectance is an indicator of thermal maturity and has become a widely used tool in examining the thermal history of a basin, particularly in the oil and gas industry (Stach et al. 1982; Tissot et al. 1987; Sweeney and Burnham 1990). Vitrinite reflectance is primarily set during heating, either by maximum burial, geothermal systems or igneous intrusions (Bostick and Pawlewicz 1984; Raymond and Murchison 1988; Barker et al. 1998). The lateral extent of the heating effects of magmatic intrusions on the organic composition of sedimentary host-rocks varies considerably from zero to seven times the intrusion thickness (Bishop and Abbott 1995). The thickness of the aureole is often considered to be the result of differences in host-rock porewater volumes (Raymond and Murchison 1988). On average, however, the lateral extent of the thermal effect from an intrusion is 70% of the intrusion thickness (Bishop and Abbott 1995).

Vitrinite is an organic maceral derived from structured plant tissue (cell wall material or woody tissue) which has amalgamated during diagenesis causing its original structure to be deformed (Marshall et al. 1994). Vitrinite can have many different compositions, for example telinite, vitrodetrinite, collodetrinite, gelinite and corpogelinite (Potter et al 1998). Vitrinite reflectance (%R) is a measurement of the percentage of light reflected off the vitrinite maceral and is affected by burial and heating.

Shale, marl and coal samples from the Pathhead Formation were collected at intermittent intervals from the St. Monans diatreme margin (Figure 7.8). Analysis of the type of macerals, vitrinite reflectance, matrix staining and spore fluorescence were conducted on each collected sample to identify the change in thermal maturity of the organic matter from the diatreme (Figure 7.9B, C and D). The results are shown in Table 7.2. The reflecting particles are comprised of primary vitrinite, recycled vitrinite, inertinite, coal fragments and minor constituents of semi-fusinite, alginite and sporinite. The majority of the alginite is *Botryococcus braunii* type which is indicative of fresh water algae, and reflects deposition within fresh-water lacustrine environments.

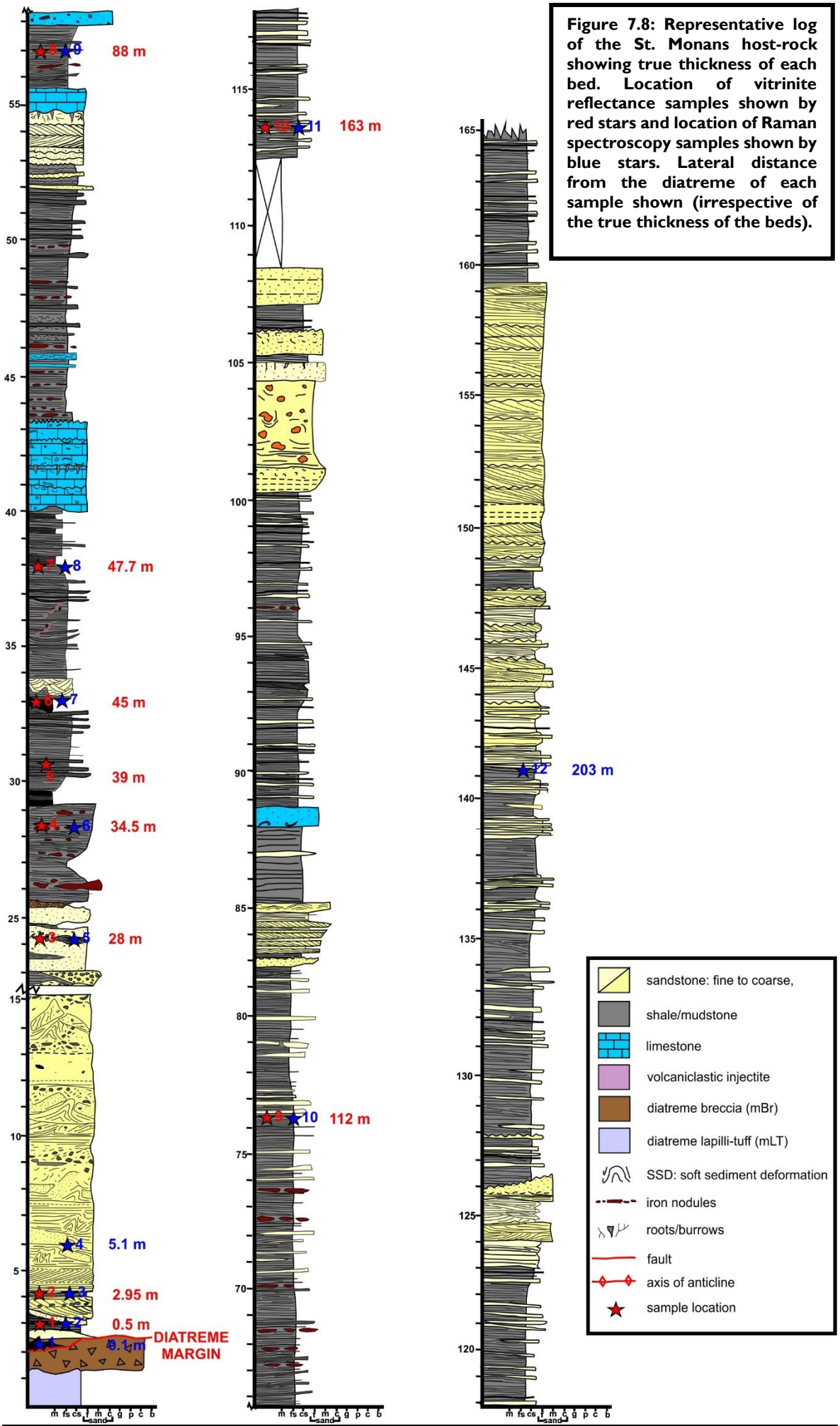

Figure 7.8: Representative log of the St. Monans host-rock showing true thickness of each bed. Location of vitrinite reflectance samples shown by red stars and location of Raman spectroscopy samples shown by blue stars. Lateral distance from the diatreme of each sample shown (irrespective of the true thickness of the beds).

Sample number	Lithology	Distance from diatreme (m)	Vitrinite reflectivity (%Ro)	Standard deviation	Reflecting particles	Mineral matrix staining	Spore fluorescence	Thermal maturity
Sh01	micrinitic calcareous marl	0.5	1.69	0.06	solid bitumen; inertinite; stringers of vitrinite	medium to dark brown bitumen	orange to mid orange with moderate intensity	wet gas/ condensate zone
Sh02	mudstone	2.9	0.72	0.03	inertinite; primary vitrinite	light brown bitumen; localised haematite	light orange to mid orange with moderate intensity	early peak oil
Sh03	marl	28.0	0.79*	0.07	very low OC; recycled coal-like fragments	no bitumen; localised haematite spots	none	early peak oil
Sh04	marl	34.5	0.46*	0.01	very low OC; infrequent primary vitrinite; recycled coal fragments	no bitumen; localised haematite spots	mid orange to dark orange spore	recycled fragments at late oil window
Sh05	mudstone	39.0	0.52	0.04	inertinite and recycled vitrinite	light brown bitumen; localised haematite spots	yellow-orange to light orange	early oil window
Sh06	coal	44.0	0.55	0.08	telocollinite vitrinite' inertinite; semi-fusinite; alganite†; sporinite	none	yellow-orange to light orange with moderate intensity	early oil window
Sh07	calcareous shale	48.0	0.52	0.06	coal fragments; primary vitrinite	light to, moderate red-brown bitumen	dull light orange	early oil window
Sh08	shale	88.0	0.73	0.07	primary vitrinite; recycled vitrinite; inertinite	moderate reddish brown stain	mid orange with low intensity	early peak oil
Sh09	shale (pyrite)	112.0	0.74	0.07	primary vitrinite; recycled vitrinite; inertinite	moderate to strong red-brown bitumen	light orange to mid orange with low intensity	early peak oil

Sample number	Lithology	Distance from diatreme (m)	Vitrinite reflectivity (%Ro)	Standard deviation	Reflecting particles	Mineral matrix staining	Spore fluorescence	Thermal maturity
Sh10	shale	163.0	0.67	0.08	coal-like stringers; primary vitrinite; recycled vitrinite; inertinite; semi-fusinite, alginite† and sporinite	moderate reddish brown	mid orange with moderate intensity	early oil window to early peak oil

Table 7.2: Table showing the lithology of each of the samples taken for VR analysis, the distance at which the samples were taken in relation to the diatreme margin, the vitrinite reflectivity (%Ro), the standard deviation of all the readings of VR, the type of maceral which VR analysis was conducted on, the mineral matrix staining, the colour and intensity of spore fluorescence, and the thermal maturity in relation to the oil window. (* = very low organic content so thermal maturation is based on poorly constrained data. Fragments with high reflectivity in these samples are possible contaminants. † = alganite is *Botryococcus braunii* type which is indicative of fresh water algae).

The bitumen staining of the matrix tends to be colourless to light brown with local haematite spots, except in the samples closest to the diatreme (Sh01) and in several samples between 88 m and 163 m, where the matrix is stained a moderate red-brown colour (Table 7.2).

The vitrinite reflectance values indicate a similar trend, where the background Ro values (0.55%) are maintained in samples (Sh04 to Sh07) (Figure 7.9A). This represents the baseline on which the effects of contact metamorphism from the intrusion of the diatreme have been superimposed. The background Ro values of these samples (0.46% to 0.55%) indicate the thermal maturity of the organic material is in the early oil window (Figure 7.9A). There are two spikes in the Ro data: (1) in the first three samples from the diatreme margin (0.5 m, 2.9 m, and 28 m); and (2) in the

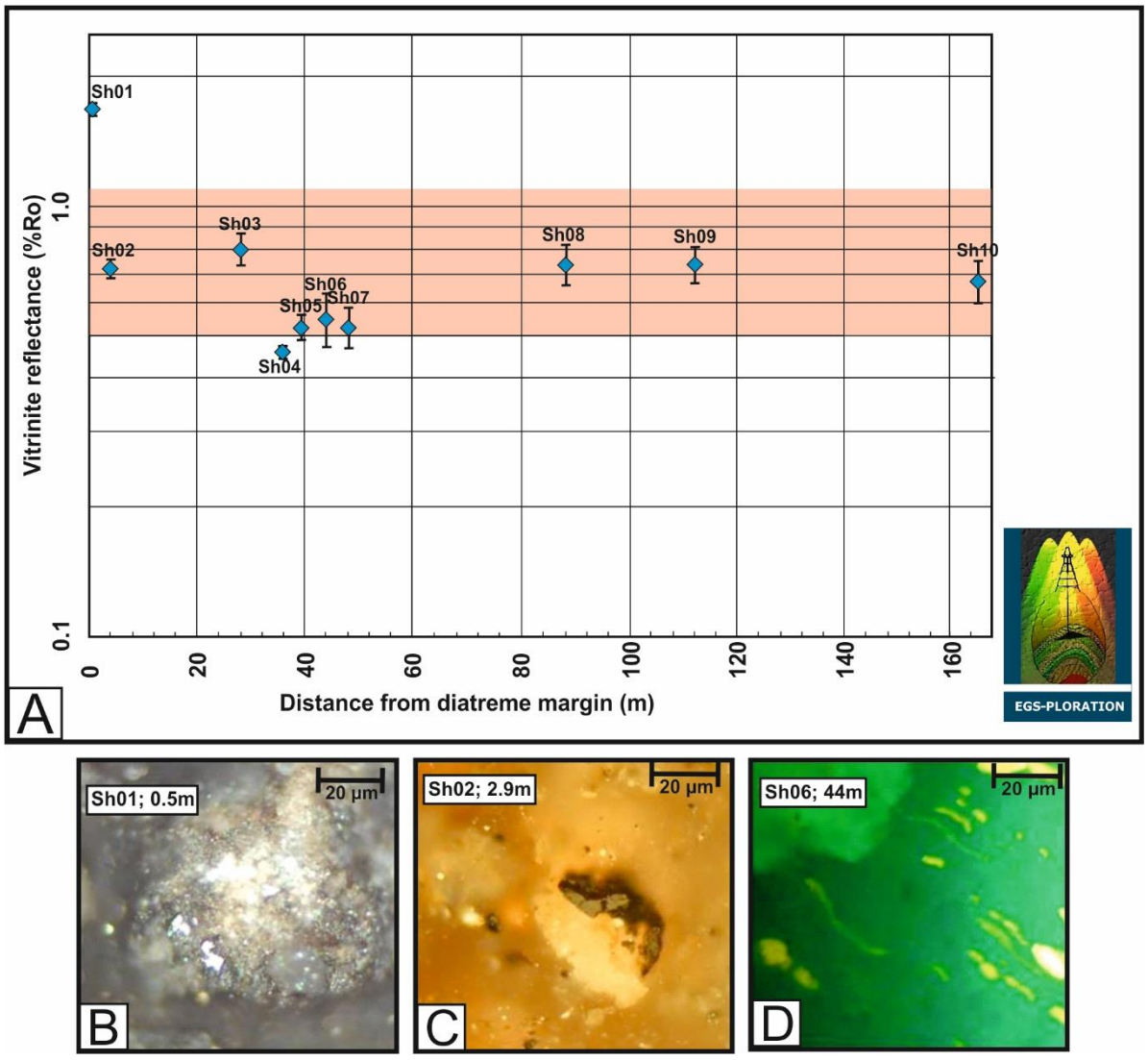

Figure 7.9: Plot of the vitrinite reflectance values of each sample against the distance (in metres) from the diatreme margin. The shaded box shows the average VR values for the oil window. (B) and (C) Photomicrographs in incident white light of the macerals in the marl in sample Sh01 (B) and mudstone in sample Sh02 (C). (D) Photomicrograph in incident blue light highlighting the sporinite (yellow-orange to light orange with moderate intensity) in sample Sh06.

samples between 88 m and 163 m (Figure 7.9A).

Directly adjacent to the diatreme margin (Sh01), Ro values are 1.69%, pushing the marl out of the oil window and into the wet gas/condensate zone (Figure 7.9A). Samples Sh02, Sh03, Sh08 and Sh09 had Ro values of c. 0.72% to 0.79%, equivalent to early peak oil temperatures, which are higher than the base level 0.55% Ro.

7.4.2. Raman Spectroscopy

Raman spectroscopy is widely used to evaluate the thermal history of carbonaceous material in shales and other organic carbon-rich rocks (Tuinstra and Koenig 1970; Landis 1971; Nemanich and Solin 1979; Ferrari and Robertson 2001; Beyssac et al. 2002; Muirhead, D.K. et al. 2012 and 2016). When carbonaceous material is thermally altered, its chemical structure is reordered from a disordered arrangement to a highly ordered arrangement, known as graphite. Graphite consists of aromatic compounds that are stacked in layers in an organised fashion (Ferrari and Robertson 2001; Muirhead, D.K. et al. 2016). Quantification of this structural reordering, and hence the amount of thermal alteration, is based on several parameters of two broad first order Raman bands (spectral peaks): (1) the G peak (graphite peak, also known as the O peak) at c. 1585 cm^{-1}, and (2) the D peak (disordered peak) at c. 1350 cm^{-1}. The G peak is composed of several amalgamated spectral peaks at 1615 cm^{-1}, 1598 cm^{-1}, and 1545 cm^{-1}. Peak deconvolution is implemented on the G peak as it is not possible to separate these bands in disorganised carbon (Beyssac et al. 2002).

The amount of thermal alteration is evaluated by looking at several parameters associated with the Raman peaks, including the position and width (FWHM) of the G peak (Wopenka and Pasteris 1993); D/G peak ratios (Yui et al. 1996); and crystalline size (*La*) (Wopenka and Pasteris 1993). Thermally altered carbon is characterised by an increase in the proportion of organised carbon (G peak), and is indicated by a narrowing of the G peak and an increase in the G peak position towards 1615cm^{-1} (Wopenka and Pasteris 1993). In thermally unaltered carbon, the disorganised structure results in a broad G peak positioned around 1585cm^{-1}. The spectral peaks are generated by Stokes Raman scattering which is induced by a laser (see "Methods").

Shale samples were collected from the host-rock at St. Monans at the locations shown in Figure 7.8 and Raman spectroscopy undertaken. Ten readings were obtained from each sample (where possible). The stacked first order representative Raman spectra for all the samples in this study are presented in Figure 7.10 and the results are summarised in Table 7.3. The peak position of the G peak and the peak full-width at half-maximum (FWHM-G) were measured (Table 7.3). The results from samples Sh08-Sh012 were inconclusive, likely due to the lack of measurable organic carbon. The results show that the average FWHM-G generally increases in samples further from the

diatreme, except for Sh04 (Figure 7.10: Stacked first order representative Raman spectra for samples SH01 to Sh07. Spectra are offset by 8%. Note the increase in G peak width with increasing distance from the diatreme and a shift of the G peak position from c. 1600 cm^{-1} to 1582 cm^{-1}.; Table 7.3). Similarly the average G-peak position shifts from *c.* 1600 cm^{-1} at the diatreme margin to *c.* 1582 cm^{-1} at 44 m from the diatreme (Figure 7.10; Table 7.3). The values of G peak wavelengths (peak position) and FWHM-G are consistent with a higher degree of structural order in the organic carbon and are attributed to initial metamorphism of the host rock.

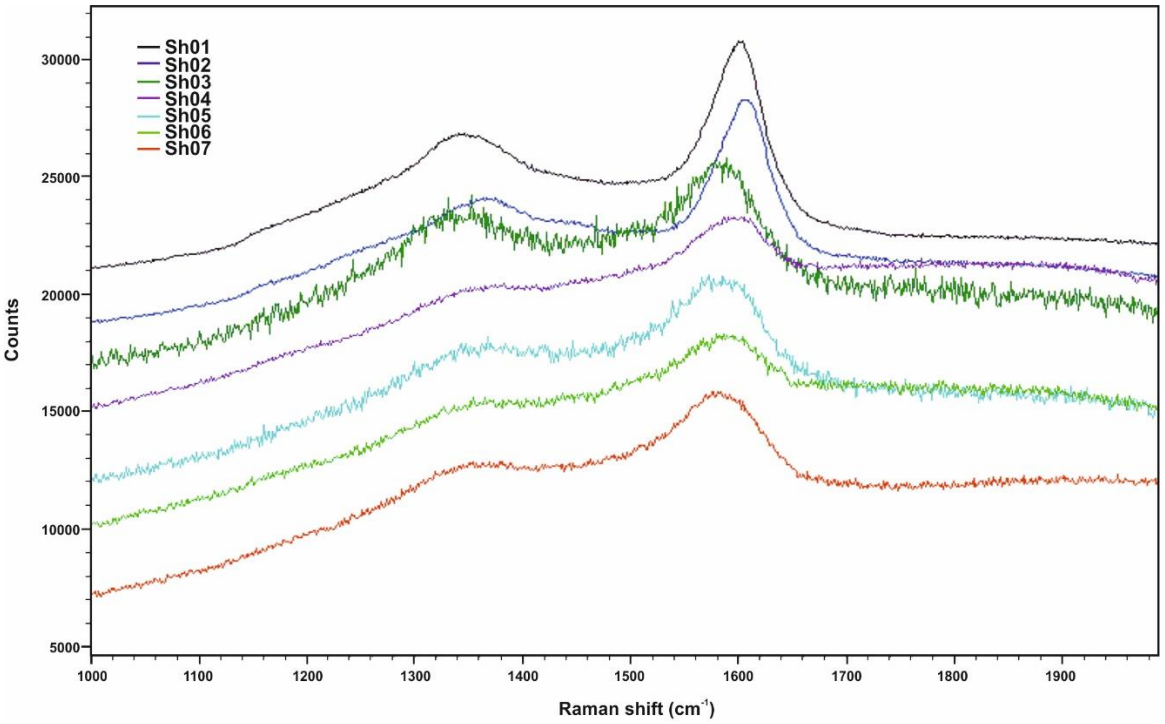

Figure 7.10: Stacked first order representative Raman spectra for samples SH01 to Sh07. Spectra are offset by 8%. Note the increase in G peak width with increasing distance from the diatreme and a shift of the G peak position from c. 1600 cm^{-1} to 1582 cm^{-1}.

By plotting the width of the G-peaks (FWHM-G) against the G-peak position, the trend is clear (Figure 7.11). All the samples plot well away from the field of graphite of Wopenka and Pasteris (1993), which represents completely organised carbon (Figure 7.11). The data can be attributed to one of two clusters: (1) the samples taken from 0 to 5 m from the diatreme margin (Sh01, Sh02 and Sh04) are within or adjacent to the kerogen field, and (2) the samples taken further from the margin (>28 m) appear to have some scatter and plot below the kerogen field (Figure 7.11). The extent of the thermal effect is between 5.1 m and 28 m from the diatreme. Unfortunately due to the interbedded nature of the host-rock, the extent of the thermal alteration cannot be more accurately measured due to the lack of shale interbeds between 5 and 28 m.

Sample No.	Distance from diatreme (m)	Average FWHM-G (cm^{-1})	Average G peak position (cm^{-1})	Average I_D/I_G	Average A_D/A_G	*La* (Å)	$A_D(A_D+A_G)$ *100
Sh01	0.1	63.84	1594.49	0.207	0.207	214.75	17.11
Sh02	0.5	59.38	1600.94	0.152	0.146	292.26	12.64
Sh03	2.95	75.71	1584.11	0.377	0.435	117.93	29.86
Sh04	5.1	69.10	1592.59	0.340	0.400	133.64	28.10
Sh05	28	85.79	1584.84	0.251	0.264	180.25	20.69
Sh06	34.5	80.99	1584.00	0.306	0.298	147.81	22.82
Sh07	44	85.46	1582.28	0.238	0.254	189.80	20.09
Sh08	47.7	inconclusive data					
Sh09	88	no data					
Sh10	112	inconclusive data					
Sh11	163	no data					
Sh12	203	no data					

Table 7.3: Raman spectroscopy results from shale samples (Sh01 to Sh07). The sample locations are shown in Figure 7.8. The results are plotted in Figure 7.11, Figure 7.12 and Figure 7.13. FWHM-G is the full-width at half-maximum of the G band and La is the crystallite size.

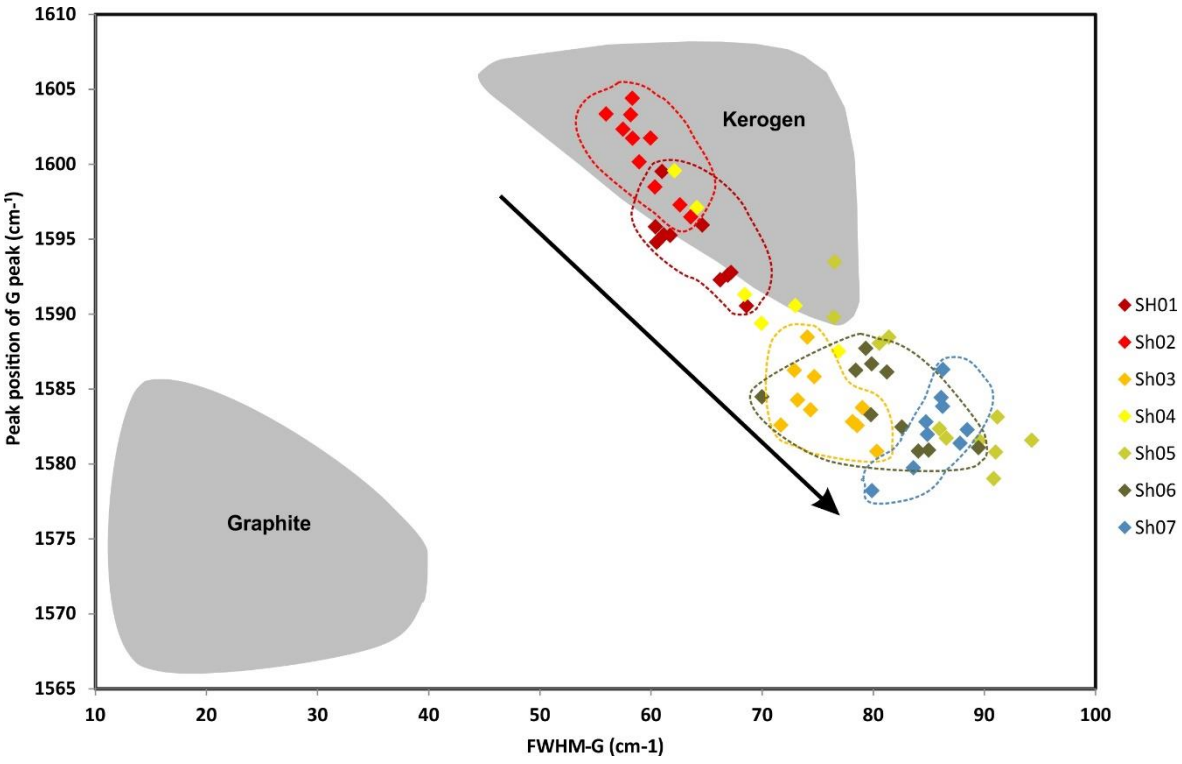

Figure 7.11: Plot of FWHM-G against the peak position of G (cm^{-1}). Samples close to the margin (Sh01 and Sh02) plot within the kerogen field. Graphite and kerogen fields from Wopenka and Pasteris (1993).

The peak ratio between D- and G- peaks also offers a way of identifying thermal maturity. Two ratios are determined to evaluate this: (1) I_D/I_G (difference in the height of the D and G peaks); and (2) A_D/A_G (difference in the area of the D and G peaks). The D/G peak ratios (I_D/I_G and A_D/A_G ratios) decrease with an increase in thermal maturation (Yui et al. 1996; Bonal et al. 2006; Quirico

et al. 2009; Marshall et al. 2012; Muirhead, D.K. et al. 2016). The I_D/I_G ratios for the St. Monans samples range from 0.152 to 0.377, and the A_D/A_G ratios range from 0.146 to 0.4 (Table 7.3). Plotting these two ratios produces a continuum from thermally mature organic material adjacent to the diatreme (low D/G ratios) to less mature organic material (higher D/G ratios) (Figure 7.12) (Pasteris & Wopenka 1991; Jehlicka & Bény 1992). Samples Sh03 (2.95 m) and Sh04 (5.1 m) show distinctive scatter and appear to be anomalies to this trend (Figure 7.12). The high I_D/I_G ratio of samples Sh03 and Sh04 is a characteristic feature of early thermal alteration which is evident particularly in relatively homogenous samples (Rouzaud et al. 1983; Muirhead, D.K. et al. 2012, 2016).

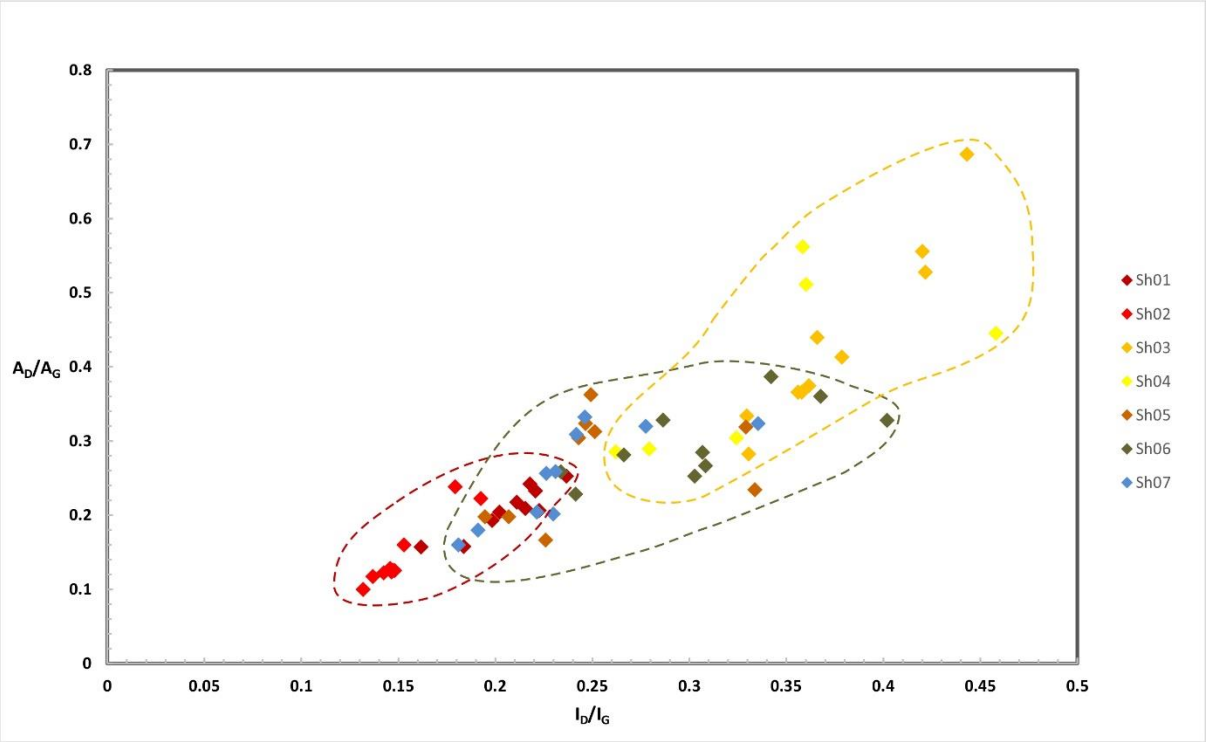

Figure 7.12: Plot of D/G ratios with I_D/I_G against A_D/A_G. There is a general trend where samples close to the margin have low D/G ratios (highlighted by dashed, red line) and samples further from the diatreme have relatively high D/G ratios (highlighted by dashed green line). Note how samples Sh03 and Sh04 are widely scattered with relatively high I_D/I_G and A_D/A_G ratios, indicating early thermal alteration (highlighted by dashed yellow line).

Figure 7.13 shows the close association between the Raman spectral features and the grade of metamorphism of the carbon material within the samples (Sh01-Sh07). This correlation, between the metamorphic grade and the Raman parameters, was achieved by Wopenka and Pasteris (1993) using a suite of similar rock types (mostly pelites and some coals) with identifiable metamorphic grades and measurable organic material. The four spectral zones identified are classified according to their metamorphic mineral assemblages: (1) chlorite; (2) biotite and garnet; (3) staurolite, kyanite

and andalusite; and (4) sillimanite (Wopenka and Pasteris 1993) (Figure 7.13). The spectral zones are generally associated with the D/G ratios, where a decrease in the D/G ratios tends to be associated with an increase in metamorphic grade, and vice versa.

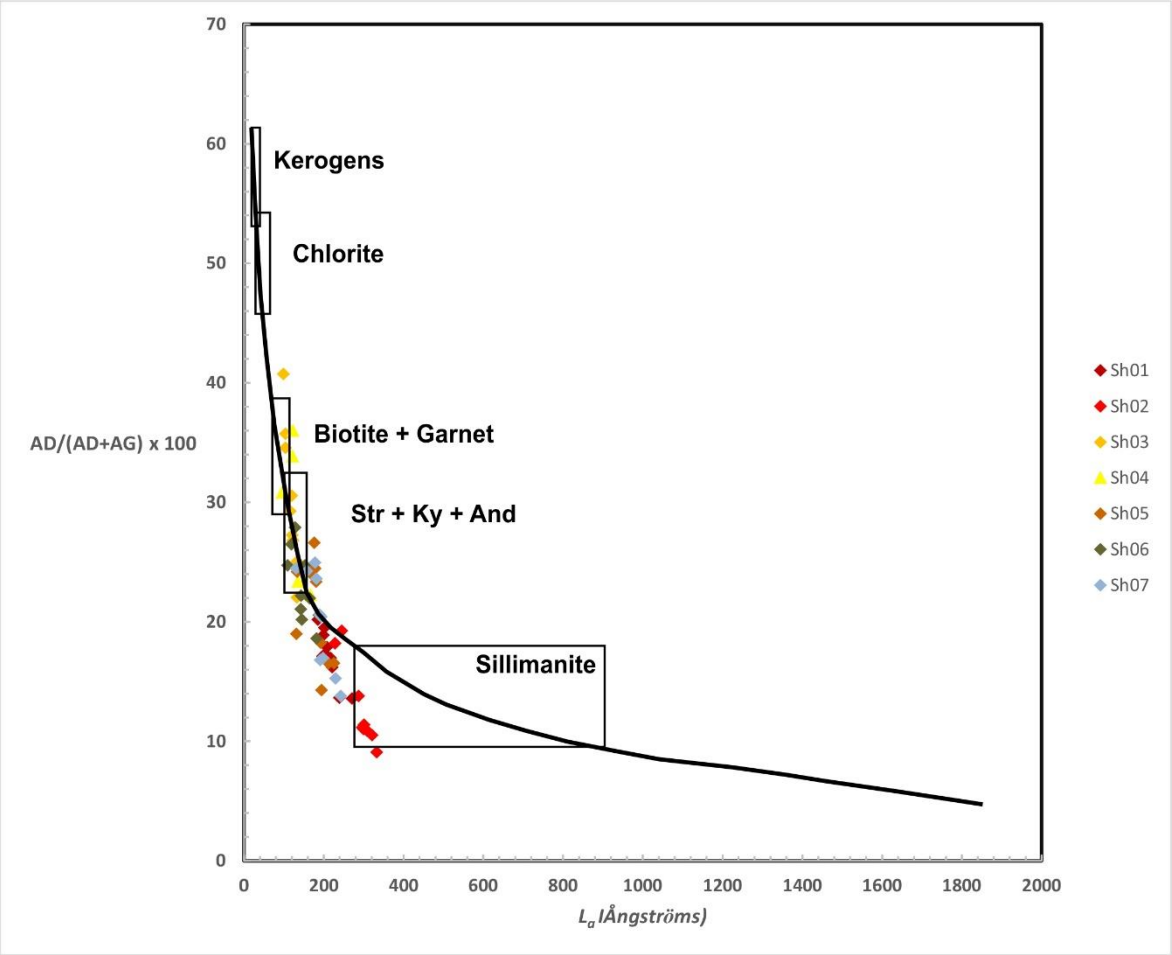

Figure 7.13 Correlation curve between specific area of D peak ($A_D/(A_D+A_G)$] x 100) and crystallite size (*La*). The correlation curve is derived from Tuinstra and Koenig (1970) and Beny-Basseaz and Rouzaud (1985). Boxes indicate the four spectral zones based on the metamorphic grade defined by Wopenka and Pasteris (1993). The results from the samples at St. Monans are plotted the marginal samples (Sh01 and Sh02) plot within the sillimanite zone, Sh03 and Sh04 plot in the biotite and garnet zone, and the remaining samples (Sh05, Sh06, Sh07) plot in the staurolite, kyanite and andesite zone or between the staurlote, kyanite and andesite zone and the sillimanite zone.

The samples from the host-rock at St. Monans have been plotted on Figure 7.13 and follow the correlation curve derived by Tuinstra and Koenig (1970) and Beny-Basseaz and Rouzaud (1985). The results show that samples Sh01 (0.1 m) and Sh02 (0.5 m) plot in the sillimanite zone or between the staurolite, kyanite and andesite zone and sillimanite zone, whereas the rest of the samples plot in the staurolite, kyanite and sillimanite zone (Figure 7.13). Samples Sh03 (2.95 m) and Sh04 (5.1 m) are an exception and commonly plot in the biotite and garnet zone (Figure 7.13). The results for

samples Sh03 and Sh04 correlate with the results for the D/G ratios, where higher I_D/I_G ratios typically demonstrate lower metamorphic grades.

The results of the Raman data clearly show a trend from organised carbon to disorganised carbon with increasing distance from the diatreme margin, and indicates that thermal alteration, caused by the emplacement of the diatreme, triggered the chemical structure of the carbon to change. Using the spectra parameters (FWHM-G and the G peak position), the distance at which the change in the structure of carbon occurs is between 5.1 m and 28 m from the diatreme margin (Figure 7.11). All samples had a composition associated with kerogen, rather than graphite, which is characteristic of a low level of metamorphism (Muirhead, D.K. et al. 2016).

7.4.3. Fluid-inclusion analysis

Fluid inclusion microthermometric analysis is used for estimating the timing, pore fluid origin and temperature of several diagenetic minerals in reservoir rocks (Walderhaug 1990; Tobin and Claxton 2000). Fluid inclusions record the minimum temperature of precipitating fluids during quartz cementation (amongst other uses) and can constrain the possible sources of quartz cement. Fluid inclusions are typically concentrated at the boundaries between quartz grains and quartz overgrowths (Roedder 1979; Pagel et al. 1986; Konnerup-Madsen and Dypvik 1988; Walderhaug 1990, 1994). By measuring the homogenisation temperature of fluid inclusions (T_h), the temperature at which the fluid inclusion formed can be recorded. The homogenisation temperature (T_h) records the trapping temperature at the time the inclusion closed and trapped the precipitating fluid (Barker et al. 1998). It is classified as the mean of the maximum temperature where a gas bubble is present and the minimum temperature where a gas bubble is not present (Walderhaug 1994). T_h can be a useful approximation of the maximum temperature reached in a sedimentary system (Barker and Goldstein 1990). The method (see Methods, Section 1.3.7) can be used for a maximum homogenisation temperature of 330 °C, covering the temperature and thermal maturity range related to burial diagenesis and very low grade metamorphism. During laboratory experiments, fluid inclusions are restored during cooling of the microscope stage. This rapid re-equilibration of the fluid inclusion indicates that in nature, the process would capture the temperature instantaneously and, therefore, may give a good record of short-lived thermal events demonstrating T_{peak} conditions (Barker and Goldstein 1990).

Sandstone samples were collected from the host-rock at St. Monans at the locations shown on the representative stratigraphical log in Figure 7.14. Fluid inclusion wafers were produced from the samples and examined on a temperature controlled microscope stage (see Methods, Section 1.3.7). The samples were slightly altered from weathering, however the individual quartz grains were distinguishable and locally quartz overgrowths were present. Fluid inclusions within the overgrowths were identified (Figure 7.15) and the maximum temperature at which the gas bubbles were present was recorded for each sample (Table 7.4; Appendix). One to twenty readings were obtained from each sample (where possible), except SM01, SM03, SM06 and SM11, which were too fragile to make measurable FI wafers or were too altered.

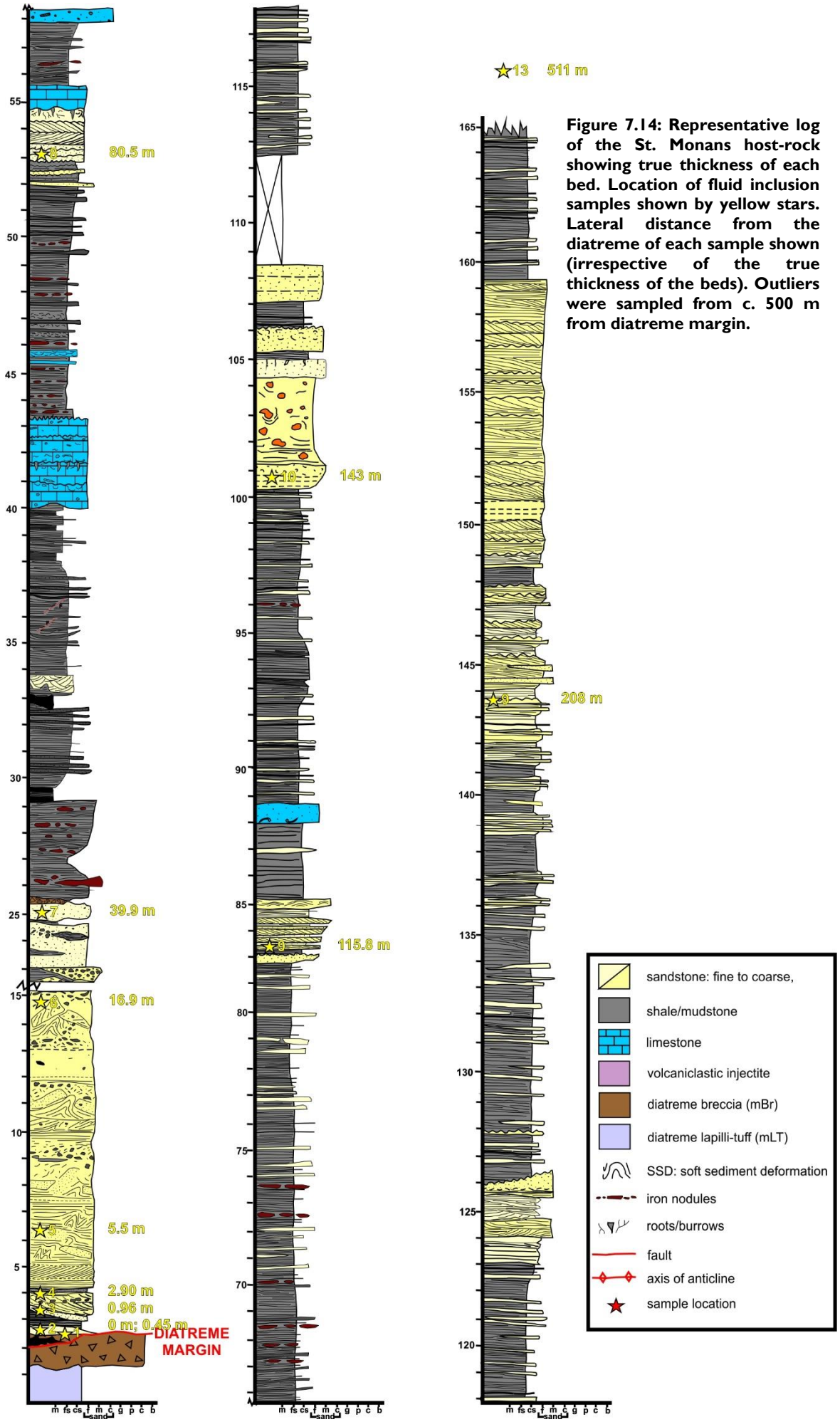

Figure 7.14: Representative log of the St. Monans host-rock showing true thickness of each bed. Location of fluid inclusion samples shown by yellow stars. Lateral distance from the diatreme of each sample shown (irrespective of the true thickness of the beds). Outliers were sampled from c. 500 m from diatreme margin.

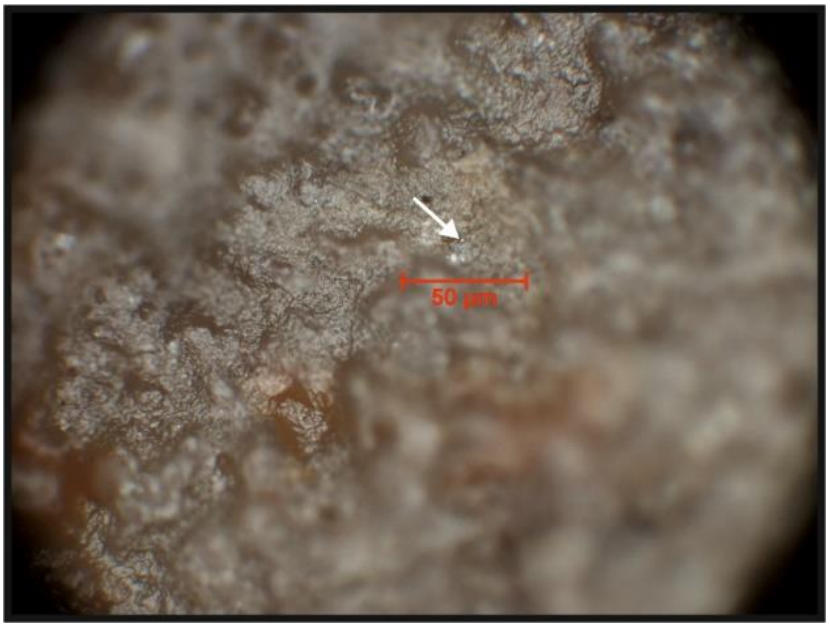

Figure 7.15: Image of fluid inclusion under transmitted light. Arrow shows location of fluid inclusion.

Sample No.	Distance from diatreme margin (m)	No. of readings	Mean homogenisation temp (°C)
SM01	0	no sample	n/a
SM02	0.45	6	>330
SM03	0.96	no sample	n/a
SM04	2.9	10	211.5
SM05	5.5	11	133.5
SM06	16.5	no sample	n/a
SM07	39.9	20	64.0
SM08	80.5	20	66.4
SM09	115.8	1*	66.0*
SM10	143.1	8	70.5
SM11	208	too altered	n/a
SM12	511	10	65.3

Table 7.4: Homogenisation temperatures of the fluid inclusion within each sample (SM01-SM12). Three samples (SM01, SM03 and SM06) were too brittle to form measurable FI wafers. Sample SM11 was too altered to measure any fluid inclusions. SM02, SM04 and SM05 all indicate significant heating close to the diatreme margin. Background homogenisation temperatures appear to be between 64 °C and 70.5 °C. Fluid inclusion resulst are given in Appendix 10.7.

The homogenisation temperatures can be classed into two orders: (1) background temperatures, c. 64-70.5 °C, and (2) elevated temperatures, ranging from 133.5 °C to >330 °C. The first sample with background temperatures is sample SM07, which was sampled at 39.9 m from the diatreme margin (lateral distance). Elevated temperatures are evident in samples SM02 (0.45 m), SM04 (2.9 m) and SM05 (5.5 m). The homogenisation temperatures are plotted against the distance from the diatreme margin in Figure 7.16 and clearly show that precipitating fluids in the first 5 m from the

diatreme were hot (>133.5 °C). The extent of these fluids cannot be fully quantified due to the lack of a viable SM06 sample (16.5 m) (Table 7.4).

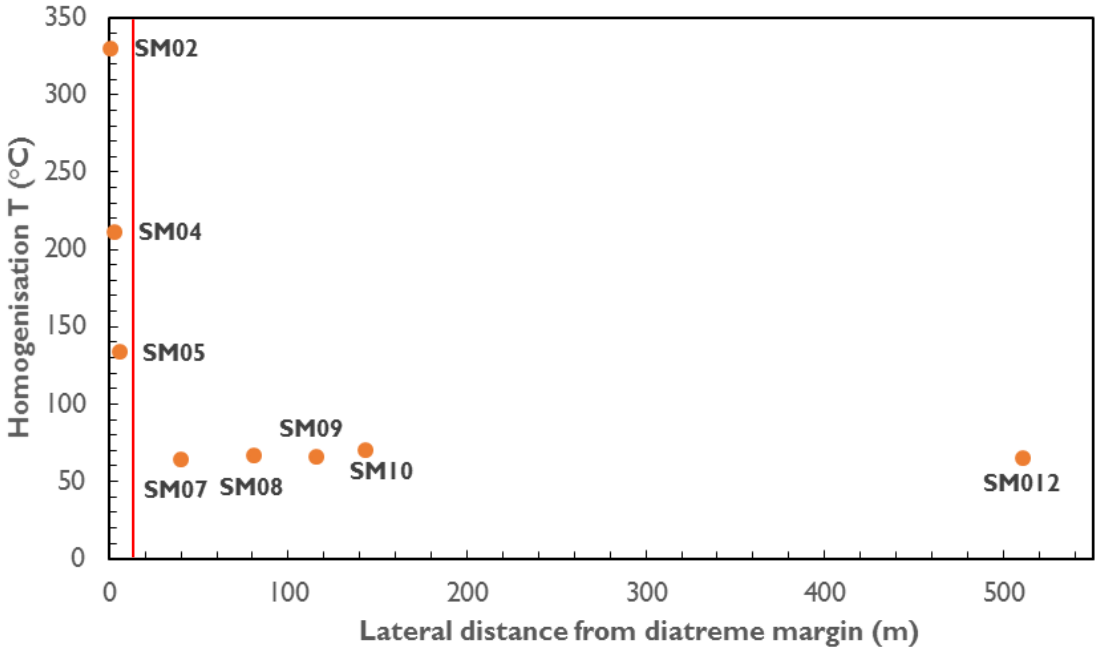

Figure 7.16: Fluid inclusion data showing the homogenisation temperature of each sample (in °C). Samples SM01, SM03, SM06 and SM011 were unsuitable or inconclusive for fluid inclusion analysis. The results show a rapid increase in homogenisation temperatures between SM07 and SM05. Red line shows extent of thermal disruption.

7.5. Discussion

7.5.1. Lateral extent of thermal alteration

The results from the vitrinite reflectance analysis, fluid inclusion data and Raman spectroscopy are all in accordance with one another. The VR data and fluid inclusion analysis for the samples unaffected by the diatreme, or the background readings, indicate that before the emplacement of the diatreme, temperatures reached a maximum of c. 64-71 °C due to diagenetic processes. Fluid inclusions show that T_{peak} systematically increases towards the diatreme margin at least to 330 °C. The zone of elevated T_h, R% and ordered carbon is at least 5.1 m from the contact, however this zone could extend up to 28 m (Figure 7.9A, Figure 7.11 and Figure 7.16). For greater resolution of the extent of this zone, samples between 5.1m and 28 m would be needed; however, it was not possible in this study as there were no shale interbeds for VR and Raman analysis, and a fluid inclusion wafer could not be made from sample SM06 (16.5 m).

It is assumed that diatremes are cool fragmental bodies (White and Ross 2011). For example, Van Otterloo and Cas (2016) calculate the emplacement temperatures of PDC deposits as 180-270 °C at the Blue Lake East and the Valley Lake maar craters in the Mt Gambier Volcanic Complex, a monogenetic volcanic field in southern Australia. Similarly, thermoremnant magnetization studies of kimberlite pipes in Botswana and South Africa have shown that erupted PDC deposits have emplacement temperatures of 200-440 °C and debris flow deposits of <180 °C (Fontana et al. 2011). However, thermoremnant magnetization studies of the pipe-filling pyroclastic deposits in kimberlite pipes show temperatures of >570 °C (Fontana et a. 2011).

Numerous magmatic intrusions exploit diatremes (particularly at the margins) and significant hydrothermal systems are evident at their margins and in the surrounding host-rock (Figure 7.6). These features are often overlooked when assessing the thermal impact of diatreme formation on the host-rock. The lateral extent of thermal alteration is, however, remarkably low considering the size of the St. Monans diatreme (*c.* 220 m) and it accounts for only c. 2.23% of the diameter of the diatreme.

The form of temperature profiles extending away from an intrusion (or in this case a diatreme) can be compared to various heat-flow models to deduce whether the intrusion cooled by conduction,

incipient convection or a convection cell (Barker et al. 1998). If a hot body (e.g. a magmatic intrusion) cools by conduction, heat is absorbed by vaporising the porewater in the surrounding substrate (Barker et al. 1998). The result is that temperatures in the contact aureole rapidly decrease from the temperature at the contact. Using the dyke width rule formulated by Middleton (1991), the temperature should increase from background levels to the maximum temperature at the contact over a distance that equals the dyke thickness (Barker et al. 1998). However, if heat transfer is by convection, heated porewater is discharged away from the contact which consequently draws in cooler waters and decreases the heating effect of the intrusion (Delaney 1987). The result of incipient convection cooling is that background levels are reached at much less than one dyke width (Barker et al. 1998). If a closed system convection cell is formed (hydrothermal fluids are recirculated), then the heating profile away from the intrusion can be extended and/or become cyclical (Delaney 1987).

The temperature profiles generated by the St. Monans datasets suggest that the diatreme was emplaced at relatively cool temperatures (c. 330 °C) and cooled by incipient convection cooling (Figure 7.9 and Figure 7.16). The presence of hydrothermal veins at the margin of the St. Monans diatreme and into the surrounding host-rock provides evidence for this mode of cooling (Figure 7.6). Evaluation of other diatreme host-rock temperature profiles would allow for the relationship between diatreme diameter and size of the contact aureole to be elucidated further. In particular, the host-rock surrounding the Kincaird diatreme is extensively disrupted (Figure 7.4, Figure 7.5 and Figure 7.6) and hydrothermal veins extend up to 40 m from the diatreme contact, suggesting that thermal alteration would be more prolific here.

7.5.2. Comparing geothermometers

Vitrinite reflectance data (R%) is closely associated with the homogenisation temperature of fluid inclusions, T_h (Barker and Goldstein 1990; Barker and Pawlewicz 1994; Barker et al. 1998). Numerous efforts have been made to correlate VR data and the homogenisation temperatures of fluid inclusions, most notably by Barker and Goldstein (1990). However, this is a complex process and is influenced by a variety of factors, including different thermal regimes (geothermal versus diagenesis), fluid inclusions with different origins (primary versus secondary), and scatter of data

(data not consistent enough) (Tobin and Claxton 2000). Barker and Goldstein (1990) evaluated T_h (as a measure of T_{peak}) in fluid inclusions within calcite from a range of thermal settings and compared the data to the mean vitrinite reflectance data. Reduced major-axis regression was used to produce a line equation for T_h versus R%. The equation which it generates is:

$$\ln(R\%) = 0.00811(T_h) - 1.26 \qquad \text{(Equation 1)}$$

where R% is the vitrinite reflectance and T_h is the mean homogenisation temperature (°C) (Barker and Goldstein 1990). Equation (1) is used to evaluate the equivalent R% values using the T_h data from the fluid inclusion analysis from the sandstone samples at St. Monans. The modelled R% values are plotted alongside the measured R% in Figure 7.17. The results from the modelled data are closely aligned with the measured data, except for a discrepancy next to the diatreme, where the predicted R% value is higher than the measured R% (Figure 7.17).

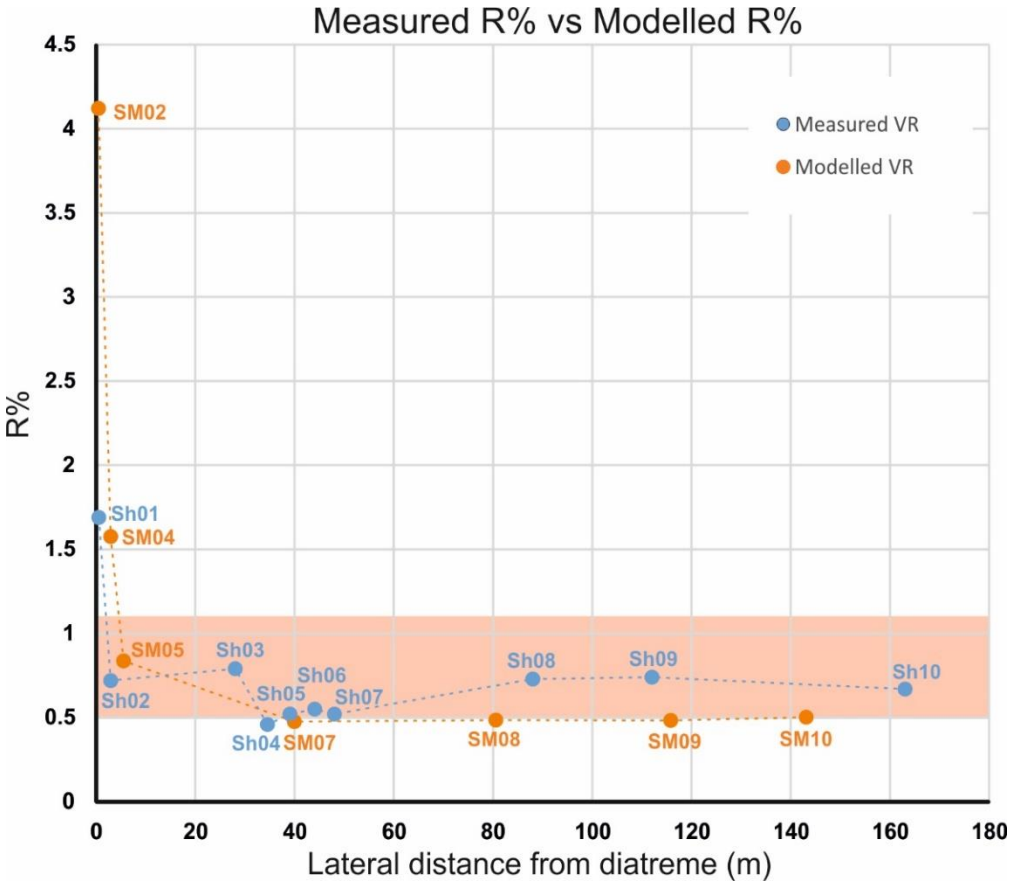

Figure 7.17: The plot shows the measured VR (R%) from the shale samples and the modelled R% calculated using Equation 1 from the T_h temperatures analysed from the sandstone samples. The orange box represents the oil window. The geothermometers are well correlated except nearest the diatreme margin, where the predicted R% vastly overestimates the measured VR.

The anomalous value of the modelled R% closest to the diatreme (SM02 has a predicted R% of 4.12% compared to the measured value, 1.69%) is likely due to contact metamorphism next to the diatreme. Contact metamorphism can alter pre-existing inclusions which can then record anomalous T_{peak} (Barker et al. 1998). Furthermore, contact metamorphism adjacent to intrusions, or in this case diatremes, induces thermal shock which can cause fractures to form, parallel or sub-parallel to the intrusion or diatreme (Somerton 1992; Barker et al. 1998). These fractures are rapidly sealed by high- and low- temperature hydrothermal fluids (Brenan 1991), forming new high temperature fluid inclusions. Additionally, the measured homogenisation temperatures of the sample directly adjacent to the margin is within the range where measuring the homogenisation temperature becomes inaccurate (Barker et al. 1998).

Similarly, Equation (1) is used to predict the T_h values from the shale samples at St. Monans, using the R% values from the vitrinite reflectance analysis. The modelled T_h values are plotted alongside the measured T_h in Figure 7.18. The results from the modelled data are relatively closely aligned

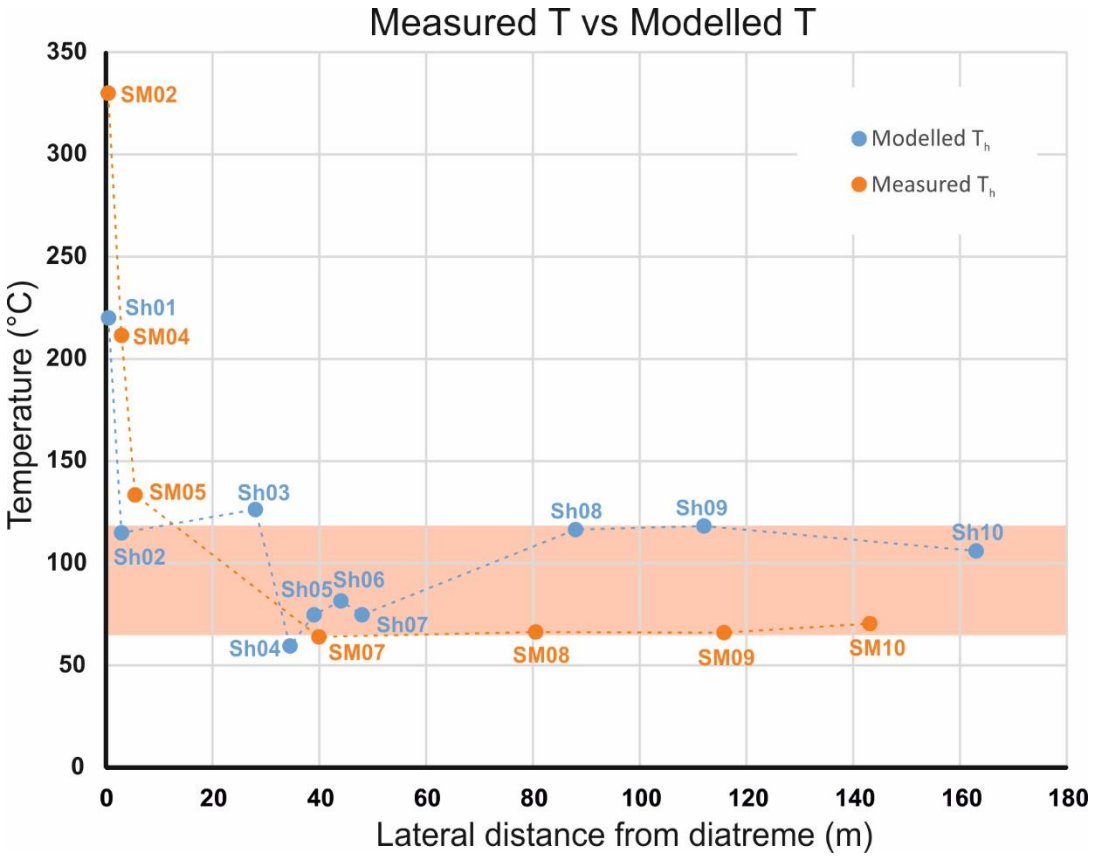

Figure 7.18: The plot shows the measured mean T_h from the sandstone samples and the modelled T_h calculated using Equation 1 from the R% analysed from the shale samples. The orange box represents the oil window. The geothermometers are relatively well correlated except nearest the diatreme margin, where the measured T_h is much higher than the predicted T. The modelled Th tends to show higher background temperatures (100-110 °C) than the measured T_h (60-70 °C).

with the measured data, however there are several discrepancies in the predicted T_h values where the R% value predicts higher than measured T_h (Figure 7.18). The reasons for the disparity adjacent to the diatreme margin are outlined above. The modelled T_h tends to show higher background temperatures (100-110 °C) than the measured T_h (60-70 °C). This discontinuity in results is likely attributed to the difficulty in attaining vitrinite for measurement because of a low organic content and more variable reflectance domains, particularly in sample Sh03 which has very low TOC (total organic content) (Figure 7.18).

7.5.3. Physical effect of diatreme formation on host-rock

This study has provided evidence for thermal alteration by incipient convection where alteration of the host-rock is hydrous, and explains the lack of metamorphism associated with diatreme formation because of cool emplacement temperatures (White and Ross 2011). Nonetheless, the heating effect of the St. Monans diatreme does provide a natural accelerator for premature maturation of organic rich host-rock close to the diatreme (>5 m) from the early oil window to peak oil window and into the condensate gas window. Arguably, however, the physical disruption of the host-rock (fluidisation, brecciation, hydrothermal systems and faulting) is more pertinent to the disruption of host-rock than the restricted heating effects at the margin. Physical disruption is evident up to 70 m from the diatreme margin at all the diatremes in East Fife and is locally prolific. Fluidisation and brecciation of the host-rock destroys porosity and permeability of potential reservoir rocks and damages potential seal horizons (Ahmed 2002).

Fluidisation of the surrounding host-rock occurs when fluid flowing through cohesionless granular sediment imparts drag that counteracts the downward-acting force produced by the weight of the grain (Allen 1982; Owen 1987, 2003; Maltman and Bolton 2003). If the fluid velocity exceeds the particle settling velocity, particles or clasts become entrained within the fluid (Lowe 1975, Allen 1982; Owen 1987). For soft-sediment deformation to occur, two conditions must be met (Allen 1986; Rodríguez-López et al. 2007; Owen and Moretti 2011; Owen et al. 2011): (1) a triggering mechanism must induce deformation; and (2) the sediment or rock must be susceptible to deformation (Chen and Lee 2013). It is proposed that overpressure generated from the boiling of pore fluids near the diatreme-sediment interface is the driving mechanism for fluidisation. This will

result in a short-lived, fluid-driven system able to brecciate consolidated or partially consolidated sediments in the disrupted zone and fluidise sand and silts. The resultant deformation will be pervasive and ductile since fluidisation involves changing the character of the sediment body from a solid to a fluid-like material (Owen and Moretti 2011).

The sediment or rock conditions (e.g. porosity, permeability, and cohesion) determine the rheological behaviour and degree of deformation (Chen and Lee 2013). The relatively shallow burial of the Strathclyde Group in East Fife prior to diatreme emplacement promotes extensive fluidisation (Chen and Lee 2013) (Figure 7.4). Cohesionless materials, such as dry or fully saturated sand with high porosities are susceptible to fluidisation (Owen 1987; Maltman and Bolton 2003). Sediment injectites or clastic dykes form when fluid pressure gradients are very high (Svensen et al. 2010) (Figure 7.4F). At the boundary between non-fluidised and fluidised sediment, in this case sandstone and shale respectively, water-cavities may develop (Allen 1982; Nichols et al. 1994; Owen 1996, 2003). If the pore pressure within the cavity increases, the pore fluid and sediment can be ejected upwards from the cavity forming a sub-vertical injectite (Owen 2003) (Figure 7.4F). These injectites may provide pathways for subsequent fluid flow.

When phreatomagmatic explosions occur during diatreme formation, the shock waves that dissipate into the surrounding host-rock decrease in strength, and therefore the rocks become increasingly less fractured with distance from the diatreme (Lorenz et al. 2002). This is evident surrounding the diatremes in East Fife, where the majority of faults and failures occur close to the diatreme margin (Figure 7.7). The impact zone of these shock wave causes a halo of host-rock around most of the diatreme to have a lower density than the surrounding host-rock (Brunner et al 1999). These rocks have a lower density because of relaxation of rocks towards the open crater (Lorenz and Kurszlaukis 2007). In this halo, existing fractures and joints in the host-rock widen, and new fractures are created increasing the host-rock mass permeability, which has implications for hydrocarbon migration (Evans et al. 2005; Lorenz and Kurszlaukis 2007). Additionally, mobilised ash and lapilli from the diatremes and fluidised sediments from the host-rock can be driven into these fractures by explosive activity, sealing the newly created permeability. These lapilli- and ash-filled fractures have been observed in the East Fife diatremes (e.g. Elie Ness) (Figure 6.16B).

The extensive hydrothermal systems surrounding a number of the East Fife diatremes, infill pore space and decrease the porosity of the sandstones (Figure 7.6). As the burial history of the Strathclyde Group in East Fife suggests, a maximum burial of 2 km (Figure 7.1), would prevent closure of primary porosity. However, due to diatreme emplacement which induced hydrothermal systems this primary porosity was sealed (Figure 7.6D).

7.5.4. Diatreme fields

As diatremes tend to form in clusters or alignments in monogenetic fields, it is important to assess the effect, at a basin-scale, of multiple diatremes and their thermal aureoles. There are over 100 Permian diatremes dispersed in Fife (Lorenz and Nicholls 1984, Walker 1999, Gernon et al. 2013). Further studies of the host-rock surrounding other exposed diatremes, for example Kincaird, Ardross and Elie Ness (Ruddon's Point host-rock is poorly exposed), is beyond the scope of this study but would allow the relationship between the extent of the physical and thermal effect of diatreme emplacement, and the size and level of the diatremes to be elucidated. By considering the scale of the thermal imprint of several diatremes, and the distribution of the diatremes in East Fife, an estimation of the total volume of compromised host-rock in Fife due to diatreme emplacement can be predicted.

Chapter 8 Discussion and conclusions

This thesis presents three field studies and one seismic study to provide an insight into the shallow plumbing systems beneath monogenetic volcanic fields. The morphology of the shallow plumbing network beneath monogenetic fields is assessed and the effect of host-rock structure and lithology on the plumbing system determined. A comprehensive list compiling the range of intrusion features produced by ductile magma emplacement in the shallow subsurface is produced. The eruption histories of each of the field studies has been established to ascertain the environmental conditions (e.g water saturation, substrate consolidation) of the host-rock during magma emplacement and to assess the factors that affect magma intrusion during the formation of monogenetic edifices. Furthermore, the impacts of monogenetic plumbing systems on sedimentary basins has been addressed and quantified.

In the introduction to this thesis a number of research questions regarding shallow monogenetic plumbing systems were posed. These questions are addressed and the outcomes of the research are discussed below.

8.1. Effect of host-rock structure on magma migration

To better understand how magma migrates in the shallow sub-surface and feeds monogenetic volcanic edifices through detailed analysis of 3D seismic data. In particular, analysing the varying effects of host-rock lithology and structure on magma emplacement and gaining a better understanding of how these factors affect the distribution of monogenetic volcanic edifices.

The seismic data presented in Chapter 3 provides an insight into how monogenetic volcanic fields are fed, and how the distribution of edifices can be primarily influenced by the structure of the substrate. The plumbing system beneath the monogenetic Ben Nevis Volcanic Field is characterised by a series of overlapping saucer-shaped sills, half-saucer shaped sills and inclined sheets, which are connected by seismically unresolvable feeder dykes, over a vertical thickness of ~3 km. The abundance of saucer-shaped and half-saucer shaped intrusions in the plumbing systems is the result of strong host-rock control and exploitation of compliant horizons in the stratigraphy (e.g. shales). The sills are comprised of coalesced magma fingers and lobes which extend upwards and outwards

from a central dish. The depth of emplacement (<2 km) of the sills and presence of magma fingers and lobes suggests ductile emplacement mechanisms are active in the intrusion of the monogenetic plumbing system.

It is commonly thought that pre-existing crustal faults and fractures can help to migrate magma to the surface (Galland et al. 2003; Valentine and Krogh 2006; Valentine and Perry 2006; Kavanagh et al. 2006; Le Corvec et al. 2013), but the stratigraphical crustal structure is often overlooked when assessing the distribution of edifices within a monogenetic volcanic field. The anticlinal Ben Nevis Structure beneath the Ben Nevis Volcanic Field significantly influenced the structure of the plumbing system and the subsequent distribution of volcanic edifices on the surface. Magma beneath the BNVF exploited a distinctive rheological boundary between the anticline and onlapping strata, and fed two alignments of edifices along the axis of the Ben Nevis Structure.

Similarly, vertically-stacked edifices suggest that magma pathways in the subsurface are exploited multiple times during the lifetime of a volcanic field, producing spatially clustered edifices. After feeding an earlier (buried) cone, a sill in BNVF provided a strong mechanical discontinuity between the sill and the surrounding host-rock. A new magma pulse, feeding the monogenetic edifices on the top volcanic surface, exploited this contact, stacking the intrusions. The observation of buried edifices beneath the monogenetic field gives a unique perspective of how a monogenetic volcanic field evolves through time.

This study has shown that it is important to consider the lithology contrasts and structure (e.g. folds, onlap structures, pre-existing intrusions) of the underlying stratigraphy beneath monogenetic volcanic fields, as well as the pre-existing faults, when assessing the distribution of monogenetic edifices. This data can give an understanding of the characteristics and distribution of plumbing systems in active volcanic fields, or where ancient volcanic fields are poorly exposed in the field.

8.2. Structure of shallow plumbing systems

To recognise the connectivity of shallow monogenetic plumbing systems using both seismic data and field data.

This study has shown that monogenetic plumbing systems can be relatively simple (e.g. East Fife) or highly complex (e.g. Ben Nevis Volcanic Field), depending on: (1) the magma ascent rate, and (2) the host-rock stratigraphy and structure. The East Fife study shows that rapid magma ascent and a significant magma pathway (the Ardross Fault) prevented the formation of a shallow crustal plumbing system. Therefore, the diatremes were all formed by individual magma batches. That being said, sub-horizontal intrusions are present in the very shallow subsurface (<1 km) and in monogenetic edifices where the host-rock is unconsolidated or partially consolidated (e.g. Dyrhólaey stepped sills, Reynisdrangar irregular sill, and inclined sheets in Kincaird diatreme in East Fife).

Contrastingly, the Ben Nevis seismic data shows that magma entering sedimentary basins can form highly connected sill complexes due to the nature of the host-rock (e.g. multiple host-rock interfaces and compliant horizons). Branches of a sill complex can feed different volcanic eruptions but are still genetically related (Figure 8.1). Sill-dominated plumbing systems, like the plumbing system beneath the BNVF, are likely to be present beneath other monogenetic volcanic fields, particularly in extensional settings (e.g. Al Haruj, Libya; Camargo, Mexico; Chaine des Puys, France; Chichinautzin, Mexico; Eifel, Germany; Jaraguay, Mexico; Potrillo, USA; Auckland, New Zealand; San Borja, Mexico; San Francisco, USA; Snake River, USA; Springerville, USA; Todra, Niger; Yucca Mountain, USA) (Le Corvec et al. 2013 and the references therein). Therefore, it is important to consider lateral migration of magma and the connectivity of volcanic edifices when assessing a magmatic source.

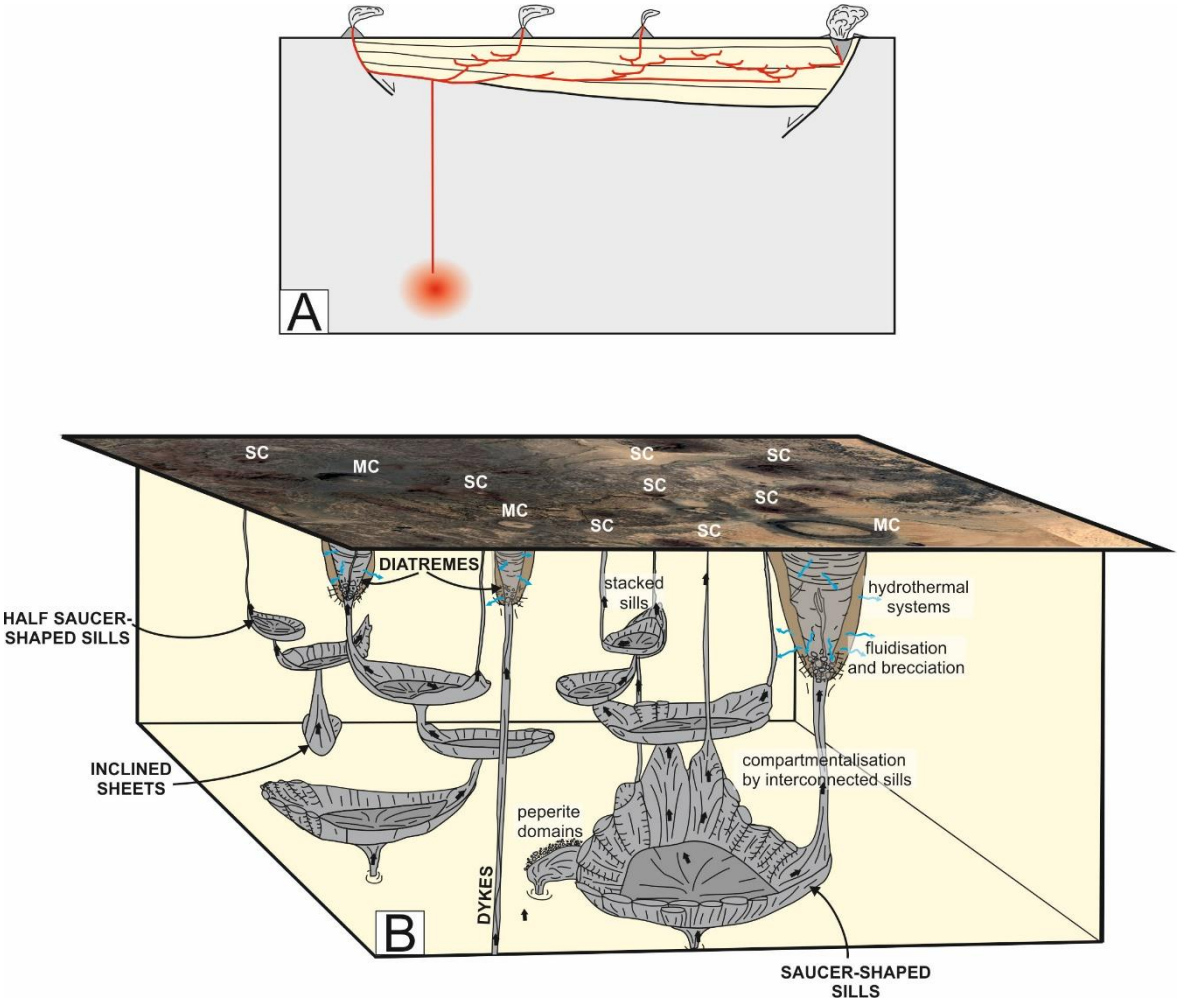

Figure 8.1: Schematic representation of a monogenetic plumbing system. (A) Extrusion sites can be laterally offset from the magma source. As magma enters a sedimentary basin, a laterally extensive sill complex can form. Branches of the sill complex feed different volcanic eruptions. Adapted from Magee et al. 2016. (B) Schematic representation of a monogenetic plumbing system, showing a complex interconnected network of saucer-shaped intrusions, half-saucer shaped intrusions, inclined sheets and diatremes. Pinacate Volcanic Field is used as an analogue because of its well-preserved and distinct edifices (Pinacate Volcanic Field is in a compressional tectonic environment). Saucer-shaped intrusions are formed of individual magma lobes which coalesce, often trapping host-rock screens. The interconnected nature of the plumbing system can compartmentalise a basin, restricting fluid and/or hydrocarbon flow and preserving primary porosity in compartmentalised zones. Peperite can form at the margins of intrusions also affecting reservoir potential. Sills can often be stacked, where magma exploits the rheological difference between an earlier intrusion and the surrounding host-rock. This often results in spatially adjacent edifices. Collars of host-rock disruption and deformation form around diatremes, brecciating and fluidising host-rock. Hydrothermal systems also filter into the host-rock surrounding diatremes affecting porosity and permeability. SC= scoria cone; MC= maar crater.

8.3. Non-brittle intrusion features

To document and characterise the geometries, scales and morphologies of shallow-level intrusions that have been emplaced by ductile mechanisms. Assess how magma-water interaction plays a role in the shallow subsurface and document how this affects intrusion morphology and fragmentation.

Chapters 3-6 address in detail the interaction between shallow plumbing systems and water-saturated host-rock. A number of features have been recognised previously (e.g. peperite, highly irregular dykes etc.), however this study compiles a comprehensive assessment of the

characteristics of very shallow plumbing systems (<200 m) within a variety of water-saturated settings. (Table 8.1, Figure 8.2).

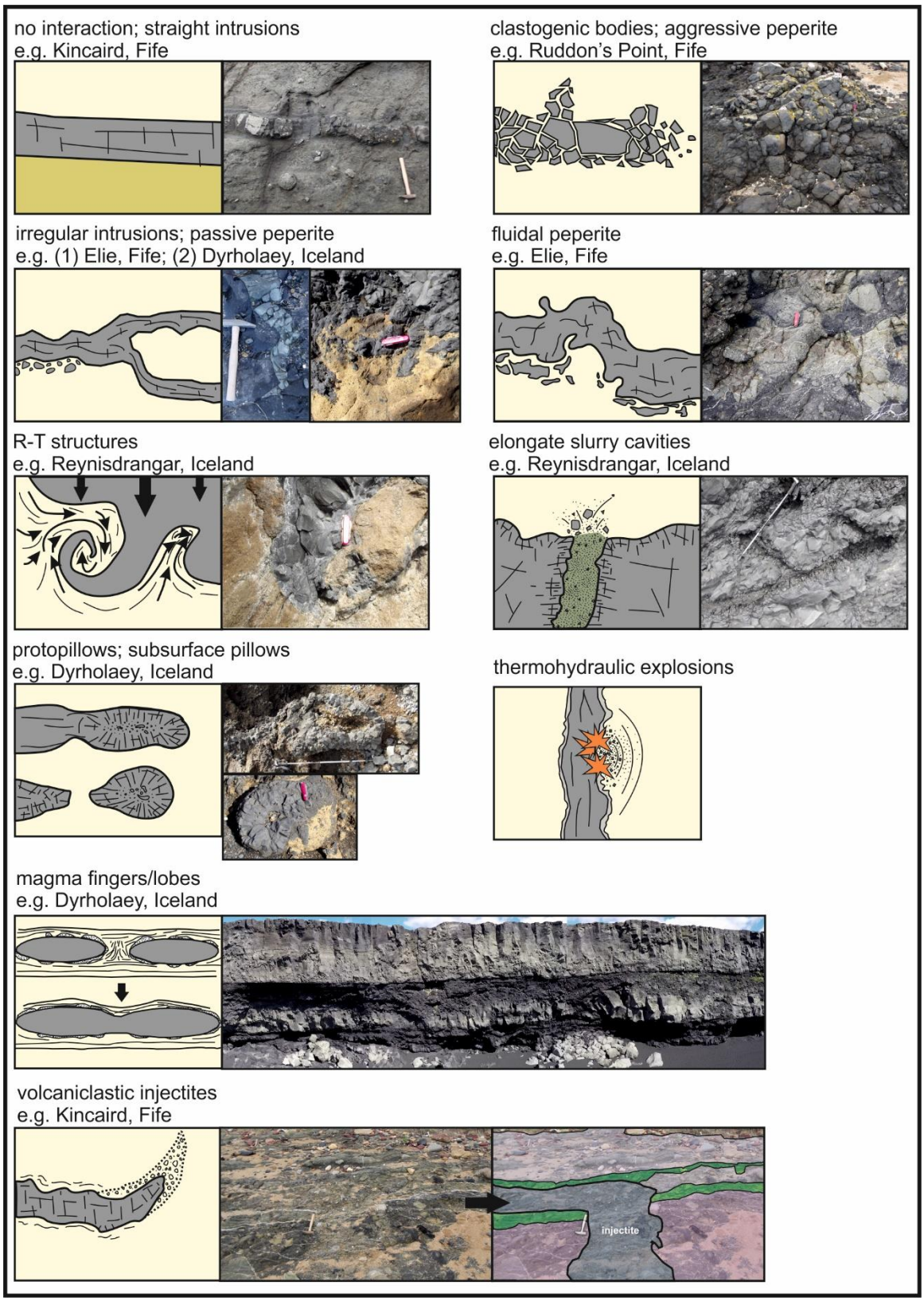

Figure 8.2: The main ductile intrusion features documented in this research and examples of each feature from the three field case-studies.

Intrusion features	Dyrhólaey	Reynis-drangar	East Fife	Mechanism	Explosivity	Magma-water ratio	Confining pressure*	Fuel-coolant mixing
stepped sills	X			exploits preferential horizons; fluidisation	non-explosive	porewater allows for more efficient fluidisation	dependent on lithology of compliant horizon	Low
inclined sheets	X	X	X	exploits preferential horizons/faults; fluidisation	non-explosive	porewater allows for more efficient fluidisation	dependent on lithology of complaint horizon	Low
plug-like intrusion		X	X	ponding	non-explosive	Very high	Low	Low
highly irregular dykes	X	X	X	oscillation in vapour film (MFCI)	non-explosive	Med to high	Low to med	Low
highly irregular sills		X		oscillation in vapour film (MFCI)	non-explosive	Med to high	Low to med	Low
localised inflation zones	X			inflation and host-rock fluidisation	non-explosive	n/a	Low to med	n/a
magma fingers and host-rock bridges	X			overlap and inflation	non-explosive	porewater allows for more efficient fluidisation		Low
blocky peperite (passive/dynamic)	X	X	X	cooling contraction fragmentation	non-explosive to mildly explosive	Med to high	Low to med	Low
fluidal peperite			X	oscillation in vapour film (MFCI)	non-explosive to mildly explosive	Low	Low to med	Low to med

Intrusion features	Dyrhólaey	Reynis-drangar	East Fife	Mechanism	Explosivity	Magma-water ratio	Confining pressure*	Fuel-coolant mixing
clastogenic pseudo-dykes			X	cooling contraction fragmentation & steam explosions	non-explosive to mildly explosive	Med	Low to med	Low to med
proto-pillows	X	X		host-rock fluidisation & intact vapour film (MFCI)	non-explosive	Low to med	Med to high	Low
spalled subsurface pillows	X	X		host-rock fluidisation & intact vapour film (MFCI)	non-explosive	Low to med	Med to high	Low
gas cavities/magma blisters	X	X		Exsolving volatiles	mildly explosive to explosive	n/a	Low	n/a
elongate slurry cavities		X		Steam explosion & slurry mobilisation	mildly explosive to explosive	Med	Low	Med to high
R-T structures		X	X	density contrasts & host-rock fluidisation	non-explosive	porewater allows for more efficient fluidisation	Low	Low
aligned intrusive pods			X	thermohydraulic explosion (MFCI) and brecciation of surrounding intrusion	highly explosive	0.35	Low	Very high

Table 8.1: A summary of the main features of shallow intrusion emplacement observed at each field locality (Chapters 4-6). Ductile emplacement of magma leads to a variety of intrusion morphologies. *Confining pressure is relative to the maximum depth of fluidisation (e.g. the ductile regime) and is equivalent to between 1.6 and 2.2 km of depth (Kokelaar 1982; Schofield et al. 2012). Magma-water ratios range from: very high = 100 (dry) to very low = 0.01 (pillow forming) (Wohletz and McQueen 1984). Fuel-coolant mixing (or magma-host mixing) is dependent on the presence and nature of an insulating vapour film.

The range of features displayed within the four case-studies essentially demonstrates that a variety of processes affect the emplacement of magma in the ductile zone (Table 8.1). These processes include: (1) exploiting preferential horizons by host-rock fluidisation; (2) exploiting boundaries in the host-rock by rotation of principal stresses (e.g. stacked intrusions in BNVF); (3) host-rock fluidisation in unconsolidated or partially consolidated hosts; (4) magmatic inflation and overburden uplift; (5) explosive magmatic degassing; (6) cooling–contraction fragmentation; (7) explosions caused by rapid vapourisation of porewater; (8) a variety of molten fuel-coolant interactions (non-explosive to highly explosive) depending on the condition of the vapour film surrounding the intruding magma; and (9) density contrasts.

8.4. Monogenetic edifices and environmental conditions during magma emplacement

Comprehensively map, log and record the monogenetic edifices which the intrusions are emplaced into (three field case-studies), to better understand the eruption histories of the edifice prior to and during magma emplacement. This will also help to understand the characteristics of the host-rock during magma emplacement and allow an assessment of environmental conditions (e.g. confining pressure, magma-water ratios and magma-host mixing) suitable for certain intrusion features.

The edifices in Chapters 4, 5 and 6 display varying fragmentation processes, deposition mechanisms and have complex eruption histories. The following paragraphs provide a short summary of each edifice.

8.4.1. **Eruption histories**

The edifice at Dyrhólaey (Chapter 4) is a tuff cone comprised of interbedded pyroclastic deposits onlapped by a series of compound lavas. Due to shallowing water depths, submarine processes (e.g. extrusion of pillow lavas and graded hyaloclastite units, and fire-fountaining) gave way for Surtseyan volcanic processes producing tephra jets and continuous uprush plumes, which subsequently collapsed forming PDCs and dense fallout clouds. Locally the deposits have been reworked. The remnants of the funnel-shaped vent beneath the tuff cone edifice is observed and provides some insight into the composition, features and processes occurring in the slurry beneath Surtseyan vents, including fingering of the slurry into the surrounding host-rock, slumping and sliding of host-rock

rafts into the vent, shearing at the margins of the vent and fragmented pillows. The Surtseyan processes switched to magmatic processes whereby thin pahoehoe lava flows and Hawaiian and Strombolian fire fountaining deposits onlapped the tuff cone. A series of intrusions were then emplaced into the tuff cone and lava flows, which likely fed further subaerial eruptions.

The tindar at Reynisdrangar is comprised of three distinctive units each representing a discrete eruption phase: subglacial non-explosive (pillows and hyaloclastite), subglacial explosive (hyaloclastite) and subaerial effusive (compound lavas). As the ice progressively melts, non-explosive magma-ice interaction gives way for Surtseyan processes (e.g. tephra jets and continuous uprush) producing hyaloclastite deposited by direct fallout mechanisms, small (ice-confined) PDCs, and reworking and resedimentation of existing deposits. Considerable shoaling of the edifice results in the top of the mound becoming exposed subaerially and inhibiting Surtseyan explosivity, giving way to effusive subaerial lava formation. Highly irregular sill-like bodies and inclined sheets have intruded into the edifice during edifice formation and thoroughly disrupted the subglacial deposits. The intrusions disseminate large bulbous magmatic bodies that stem from anastomosing dyke-lets and form interconnected pods and subsurface pillows that bud from the intrusion tips.

The diatremes in east Fife are comprised of pyroclastic deposits erupted from subsurface phreatomagmatic explosions and deposited by PDCs, base surges and debris flows. The centroclinal dipping beds are caused by subsidence in the centre of the diatremes (due to mass deficit in the root zone). Lahar deposits become more prevalent in the centre of some of the diatremes (e.g. Elie, Kincaird) due to the instability of the tuff ring. Collapse zones, at the margins of the diatremes, are formed due to the widening of the diatreme and the failure of upper diatreme and tuff ring deposits. Debris columns are also observed cross-cutting the bedded diatreme deposits formed by passing debris jets. Extensive peperite domains, anastamosing intrusions and inclined sheets indicate non-explosive late-stage magma emplacement. Volcaniclastic injectites are observed, formed by fluidisation and re-mobilisation of the diatreme fill. Gas fluidisation of the diatreme deposits is prevalent at several diatremes (Elie, Ruddon's Point).

8.4.2. **Host-rock properties during intrusion emplacement**

The occurrence of ductile intrusion features in Table 8.1 depends on several contributing factors. One of the most significant of these factors is the ability of the host-rock to readily fluidise, which is dependent on the mechanical strength of the host, the porosity and permeability of the host, the host rheology and the confining pressure (hydrostatic and lithostatic) (Maltman and Bolton 2003). In the three field areas described (Dyrhólaey, Reynisdrangar and East Fife), the host (during magma emplacement) is tephra deposited from preceding eruptions or eruption phases which had not yet been consolidated, buried and lithified, thus promoting high porosities, a low mechanical strength and low confining pressures. These conditions enabled the host to be readily fluidised. The submarine, subglacial and groundwater settings would have supported a high degree of water saturation within the host, further aiding fluidisation. Grain size of the host appears to be the biggest influence pertaining to sediment properties, whereby finer host-sediments have minimal or passive magma interaction due to lower porosities and more cohesion between grains.

8.4.3. **Magma properties during intrusion emplacement**

The differences in ductile intrusion features can be constrained by magmatic factors, for example, magma viscosity, volatile content of the magma, magma-water ratios, magma injection velocity, rate of heat transfer, amount of magma-host mixing and the confining pressure (Kokelaar 1982; Busby-Spera and White 1987; Hanson and Wilson 1993; Doyle 2000; Squire and McPhie 2002; Skilling et al. 2002). This research focusses on the magma-water ratio, the amount of magma and host mixing (and therefore the rate of heat transfer) and the confining pressure as the most significant influences on magma emplacement and fragmentation. As this research focusses on the ductile regime, the relative confining pressure is low, the equivalent of less than c. 1.6 to 2.2 km depth (Kokelaar 1982; Schofield et al. 2012). Therefore, the amount of confining pressure is relative to this maximum in Table 8.1.

Typically, non-explosive magma-water interaction is a consequence of a medium to high magma-water ratio and a low amount of mixing between host and magma, due to an intact vapour film (Table 8.1). Conversely, explosive interaction has a high degree of magma-host mixing and an optimum magma-water ratio (close to 0.35) (Table 8.1). This relationship is illustrated in Figure 8.3.

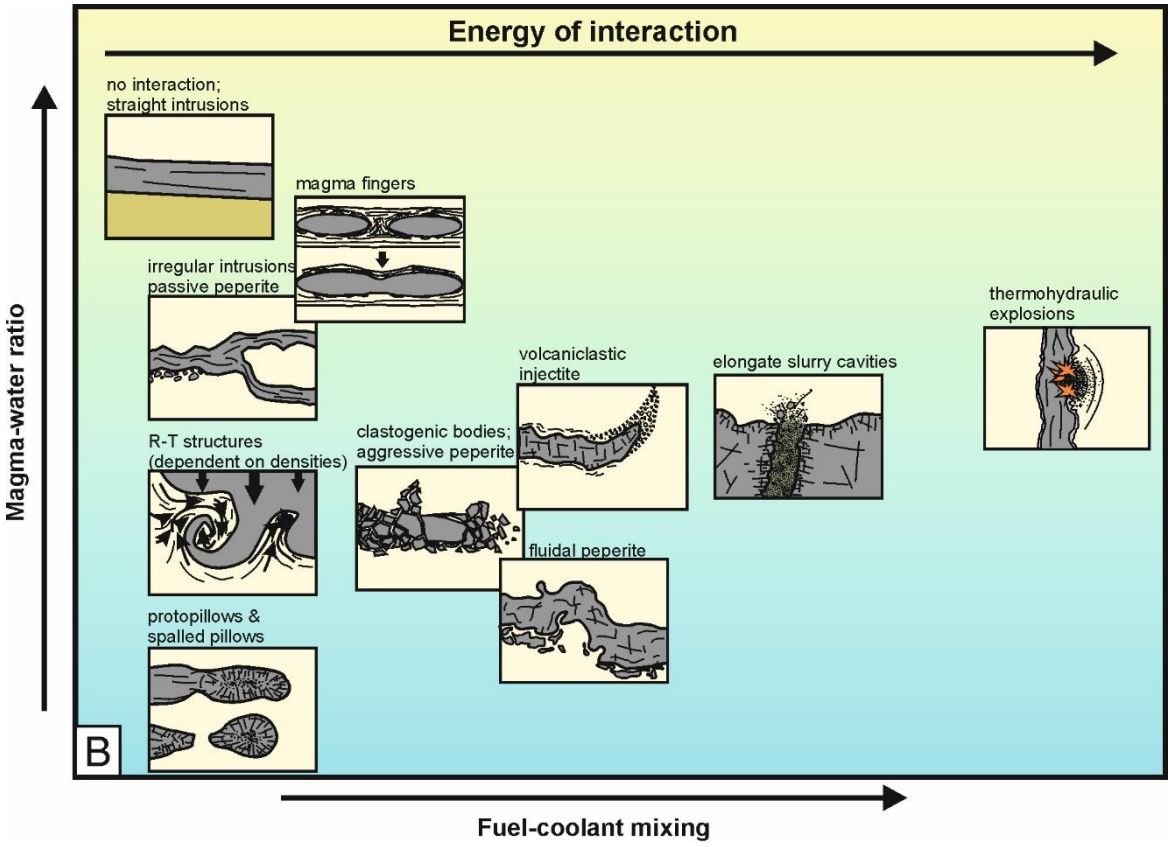

Figure 8.3: Intrusion features are influenced by the magma-water ratio and the amount of fuel-coolant mixing, which in turn significantly influences the explosive energy of the magma-water interaction.

8.5. Sub-seismic characteristics

Use the field studies to determine the sub-seismic characteristics of shallow plumbing systems in order to aid recognition of the impact of monogenetic volcanism in hydrocarbon-bearing volcanic basins.

Understanding the shallow sub-surface intrusive system and the structure of monogenetic edifices has implications for the hydrocarbon industry, where volcanological expertise is needed in exploration studies to understand the positive and negative impacts of plumbing systems and monogenetic edifices on hydrocarbon prospectivity and fluid migration pathways after burial (Schutter 2003). The resolution of seismic data (even at 10 Hz) vastly restricts detailed analysis of the structure and morphology of monogenetic edifices and their associated plumbing systems. Using field examples is, therefore, the only way to obtain the sub-seismic detail needed to aid recognition of the impact of monogenetic volcanism in hydrocarbon-bearing volcanic basins (Figure 8.4 and Figure 8.5).

The field examples discussed in this research demonstrate that intrusions are prolific throughout wet monogenetic edifices and can be extremely variable in thickness, morphology and jointing

patterns. Infiltration of water into magma causes erratic columnar jointing patterns to form (e.g. Dyrhólaey, Reynisdrangar) which can make these intrusions permeable to fluid migration and can also increase reservoir potential (Hutchinson 1994). Furthermore, magmatic volatisation in the shallow subsurface creates large gas cavities and vesicular intrusions (e.g. Dyrhólaey and Reynisdrangar) which increases porosity and permeability and allows for potential fluid and hydrocarbon migration. These gas cavities would also alter the seismic response of the intrusions. In the very shallow subsurface (<200 m), sub-horizontal intrusions are evident in all environmental settings, even where the magmatic plumbing systems are simple. In seismic data, the impedance difference between these sub-horizontal intrusions and the volcanic deposits may limit the imaging of these intrusions.

The emplacement of magma in the shallow subsurface (<1 km) produces a variety of magma-water interaction products which may affect the reservoir or seal potential of the host substrate. A range of peperite textures are formed in the shallow subsurface in Dyrhólaey, Reynsidrangar and East Fife which range from passive to dynamic (Rawcliffe 2016). Peperite facies, present around shallow sub-volcanic intrusions and within maar craters, can provide an adequate hydrocarbon reservoir rock if there is a high ratio (>60%) of reservoir-quality host-rock to magmatic juvenile clasts (Barrabé 1932; Ridd 1983; Schutter 2003). For example, in the Limogne Graben in France, an area renowned for maar-diatreme volcanoes, oil shows are present within peperite (Barrabé 1932). Thick peperite domains surrounding intrusions (e.g. Dyrhólaey and Reynisdrangar) have a low ratio of host-rock to magmatic juvenile clasts and would therefore be considered a seal, due to compartmentalisation of the host, providing challenges for connectivity and any accumulations within a potential reservoir.

Here, an interpretation of a postulated tuff cone and maar-diatreme structure from the Ben Nevis Monogenetic Volcanic Field are presented (Figure 8.4 and Figure 8.5). Using an example of each type of edifice from the Ben Nevis Monogenetic Volcanic Field, the seismic data can be populated with images from the field: the Dyrhólaey tuff cone in Iceland (Figure 8.4) and the East Fife diatremes in Scotland (Figure 8.5) respectively. Comparison between a seismic example of a tindar and the Reynisdrangar tindar is not possible due to a lack of seismic data. Figure 8.4 and Figure 8.5 show that the complexity of wet monogenetic edifices is reduced to very simple seismic representations.

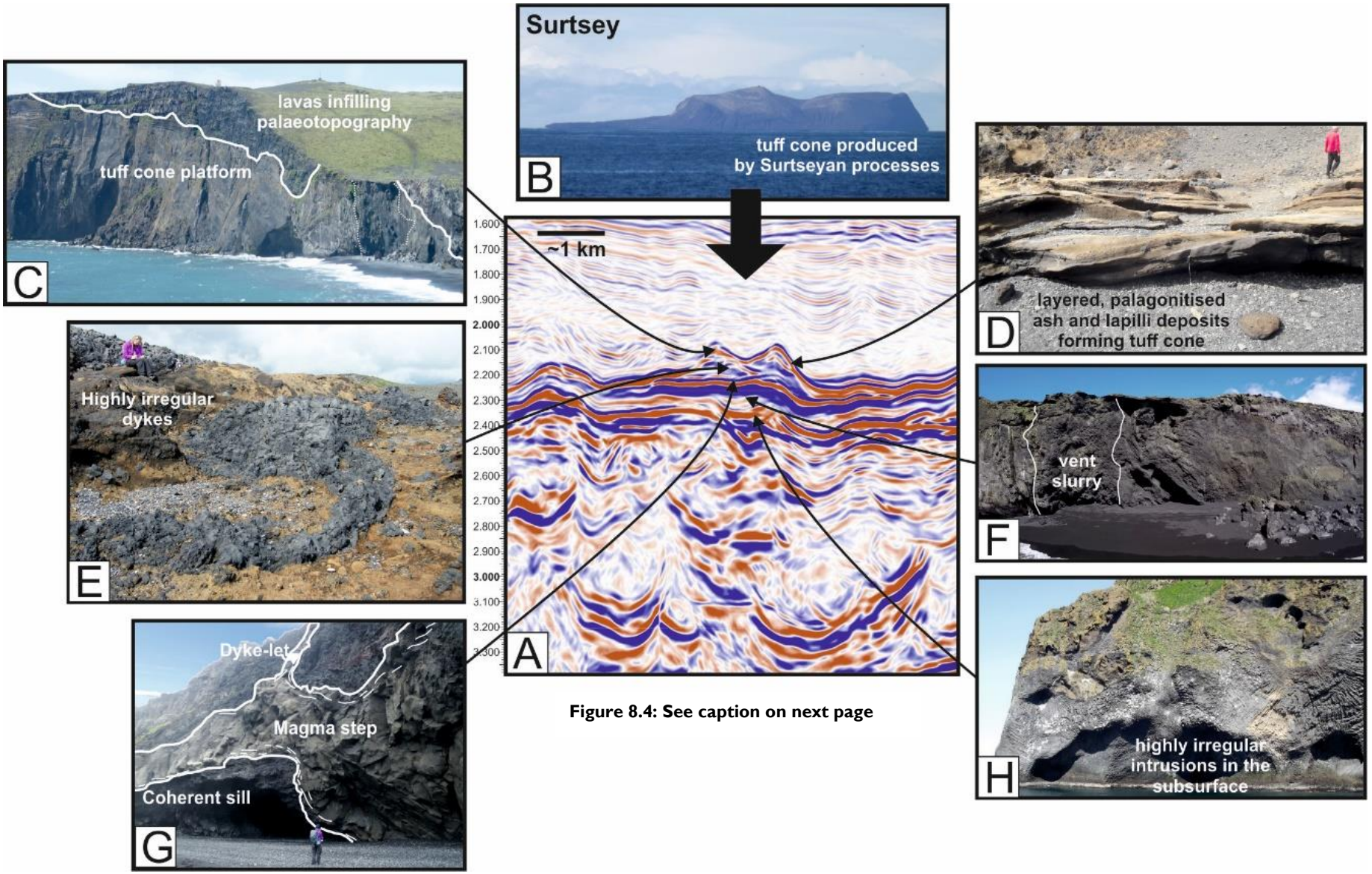

Figure 8.4: See caption on next page

(previous page)

Figure 8.4: (A) Populated seismic line of an emergent tuff cone from the Ben Nevis Monogenetic Volcanic Field, Faroe-Shetland Basin, NW Scotland using field examples from Dyrhólaey, S. Iceland (and the Vestmannaeyjar Islands where stated). (B) Photograph of a present-day emerging edifice, Surtsey, in the Vestmannaeyjar Islands. Surtsey formed through an evolving monogenetic eruption from submarine (pillows), through Surtseyan eruption (tuff cone), to magmatic (compound lava flows). (C) Thin pahoehoe lava flows can cap tuff cones. (D) Tuff cone deposits comprising interbedded palagonitised lapilli-tuffs, tuffs and breccias. (E) Highly irregular intrusions disrupt the tuff cone stratigraphy. Due to volatile degassing in the shallow subsurface, vesicular basalt intrusions can provide fluid and hydrocarbon pathways. (F) A highly chaotic breccia forms the remains of the vent slurry which feeds Surtseyan processes. (G) Coherent sills are emplaced into the edifice. Magma lobes and host-rock bridges are formed due to ductile emplacement. (H) Large irregular intrusions can be emplaced into the edifice which have complex fracturing patterns and contain host-rock rafts and inclusions. Photograph from Heimaey in the Vestmannaeyjar Islands.

(next page)

Figure 8.5: (A) Populated seismic line of a maar-diatreme from the Ben Nevis Monogenetic Volcanic Field, Faroe-Shetland Basin, NW Scotland using field examples from the East Fife diatremes in E. Scotland (and an aerial photograph from the Pinacate Volcanic Field in Mexico where stated). (B) Comparison of maar crater in the Ben Nevis Monogenetic Volcanic Field and an example of a present-day maar crater in the Pinacate Volcanic Field. The two craters are on similar scales and have low relief tuff rings which surround an open crater. (C) Debris columns comprised of brecciated feeder intrusions, juvenile clasts and sediment inclusions cut through surrounding stratified deposits (photograph: Kincaird diatreme). (D) Upper diatreme deposits are comprised of centroclinal dipping beds of tuff, lapilli-tuffs and breccias (photograph: Elie Ness diatreme). (E) In soft-rock settings, diatreme formation can cause extensive disruption of the surrounding host-rock. Hydrothermal systems and fluidisation can alter the porosity and permeability of host-rock. Heating causes some marginal thermal effects (photograph: Kincaird diatreme). (F) Large sheet intrusions can be present within diatremes. These intrusions can display a variety of jointing patterns (Photograph: inclined sheet within the Kincaird diatreme). (G) Large peperitic domains occur where late-stage intrusions have mingled with wet, unconsolidated diatreme deposits. Tuffs can be injected into the intrusions due to fluidisation of the diatreme deposits (photograph: peperitic domain in the Ruddon's Point diatreme). (H) Lower diatreme deposits consist of sediment inclusions and feeder dyke fragments suspended within a tuff matrix (photograph: Dovecot diatreme, not mentioned in chapters). (I) Peperite forms at the margin of intrusions and can produce either passive peperite facies or dynamic peperite (photgraph: peperite domains within Ruddon's Point diatreme).

Figure 8.5: See caption on previous page

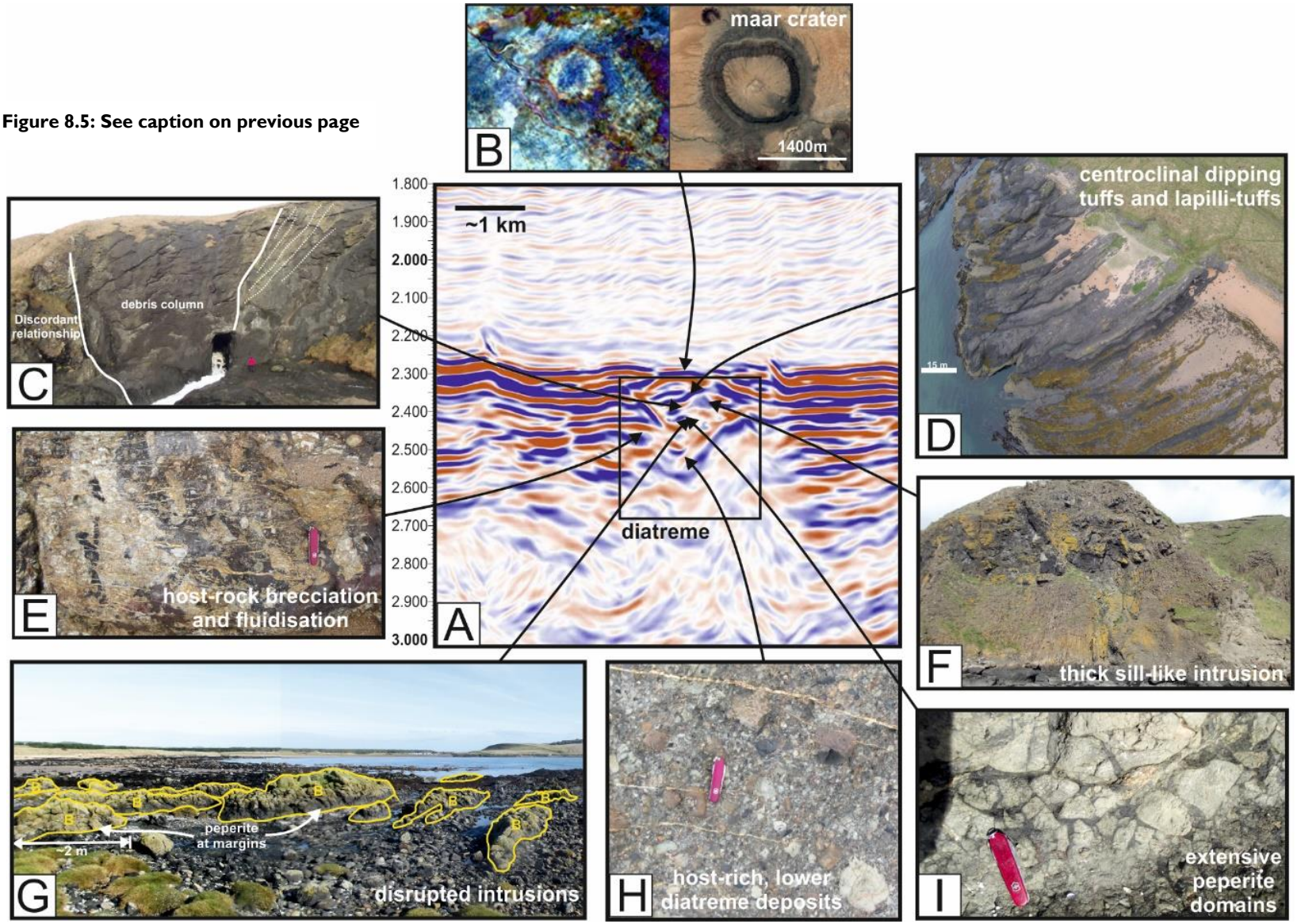

A useful tool for identifying edifices in seismic data is spectral decomposition. Spectral extraction of the top volcanic horizon of the Ben Nevis dataset allowed for enhanced imaging of the monogenetic edifices. The monogenetic edifices in the Ben Nevis Volcanic Field are directly comparable to modern day analogues (e.g. the Pinacate Volcanic Field, Mexico), which has led to a clearer interpretation of the BNVF edifice morphology and formation mechanisms (Figure 8.6).

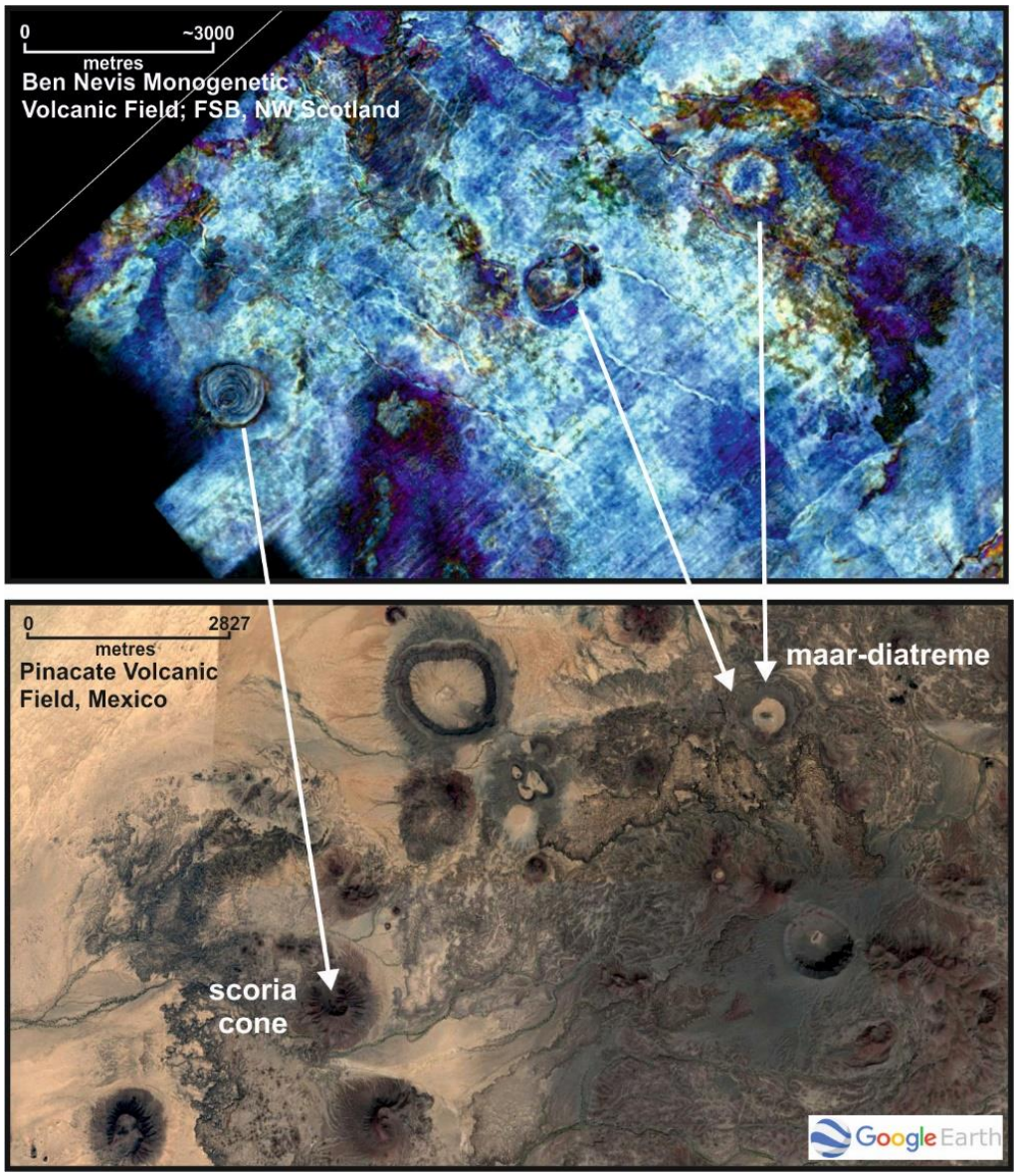

Figure 8.6: Comparison between the seismic data from the Ben Nevis Monogenetic Volcanic Field in the Faroe-Shetland Basin, NW Scotland (Chapter 3) and a modern-day analogue, the Pinacate Volcanic Field in Mexico. The Pinacate Volcanic Field is made up of 400 scoria cones and 8 maar-diatremes.

8.6. Effects of diatreme formation on sedimentary basins

To better understand the effects of monogenetic plumbing systems on sedimentary basins, particularly the effects of diatreme formation.

Emplacement of intrusions at shallow depths can: (1) provide an accelerator for premature maturation or over-maturation of shallow source-rocks hydrocarbons; (2) disrupt the potential of reservoir rocks; (3) provide, alter or change migration pathways; and (4) provide seals and/or destroy potential seals (Schutter 2003; Archer et al. 2005). From the East Fife field study (Chapter 6 and 7), this research has shown that diatreme formation causes intensive physical damage and thermal disruption to the host-rock. Diatreme formation causes host-rock fluidisation; mobilisation and commingling of sand and silt grains; injection of mobilised sediments into surrounding strata; brecciation of host-rock; extensive hydrothermal systems at the margins of the diatreme; faulting of host-rock; and intrusion of dykes. This disruption can be significant if it causes fluidisation and brecciation of potential reservoir rocks.

Typically, thermal aureoles around magmatic intrusions extend from a half to five times its thickness (Schutter 2003). The thermal aureole of the St. Monans diatreme, however, is significantly smaller in proportion to the diatreme diameter (2.23%). Within this aureole, potential source rocks have over-matured beyond the oil window. This volume of compromised host-rock can be inconsequential when assessing the prospectivity of a hydrocarbon system.

That being said, the most pertinent disruption of host-rock is the extensive hydrothermal systems that form around diatremes. The Kincaird diatreme in East Fife, in particular, shows extensive hydrothermal networks which extend up to 30-40 m from the diatreme margin. The hydrothermal alteration occurs by incipient convection where alteration of the host-rock is hydrous. These hydrothermal networks have altered the porosity and permeability of the substrate which can subsequently alter fluid migration pathways.

8.7. Further work

Future work arising from the findings of this research could include the following:

- Further work is required to use this study, and others like it, to aid the forecasting of magma migration beneath active fields, and produce accurate hazard assessments of the next eruption site. To evaluate the probability of the formation of a new volcano at a given location, several determining factors must be assessed: (1) the size and location of potential magma source zones; (2) shallow structures (including lithology contrasts and stratigraphical structure of the upper crust); and (3) surface topography. Detailed geological mapping of the subsurface, combined with measuring ground deformation (e.g. forced folds) and tracking seismic activity would enable better understanding of magma migration beneath such fields.

- Using the interpreted edifice types in the Ben Nevis dataset to more accurately identify the form and characteristics of monogenetic edifices in other seismic datasets (e.g. accurately identifying maar-diatreme volcanoes, as opposed to hydrothermal or clastic vents). In seismic data, maar-diatremes present as well-defined V-shaped seismic responses, typically delineated by bright, high amplitude reflectors. These V-shaped vent structures tend to underlie a crater excavated within the palaeosurface and a low-angle tuff ring usually comprising bright, ordered reflectors. Suitable diatreme depths range up to 2 km beneath the palaeo-surface. In comparison, hydrothermal vent complexes can be several kilometres deep and are characterised by eye-, crater- or dome-shaped features underlain by a chimney of disrupted seismic horizons surrounded by inward dipping reflections. There is often doming or disruption of the overburden which is not featured above maar-diatreme structures. It is thought the maar-diatremes described in Chapter 3 will aid the interpretation of edifices in seismic data.

- Using the geothermometers discussed in this research on other diatremes (and their surrounding host-rock) to gather more data on the thermal effect of diatreme formation on host-rock, and test the conclusions made here. Furthermore, the prevalence of hydrothermal systems around diatremes poses questions about the effects of diatreme

formation on the porosity and permeability of the host-rock. Quantitative measurements on the porosity and permeability of the host-rock surrounding diatremes could be conducted and would more accurately measure the effect of diatreme formation on reservoir potential and fluid migration pathways in the surrounding host.

- In-depth quantitative techniques could be employed to more accurately assess the particle sizes, vesicle size range and vesicularity of deposits within the edifices described in this research (e.g. East Fife, Dyrhólaey, Reynisdrangar). This would provide more detail of the temporal and spatial evolution of the edifices. Such work was beyond the scope of the research presented here, which focussed on the emplacement of the intrusions within these edifices.

9. References

Ahmed, W. (2002). Effects of heat-flow and hydrothermal fluids from volcanic intrusions on authigenic mineralization in sandstone formations. Bulletin of the Chemical Society of Ethiopia, 16(1), 37-52.

Airoldi, G., Muirhead, J.D., White, J.D., and Rowland, J., (2011). Emplacement of magma at shallow depth: Insights from field relationships at Allan Hills, south Victoria Land: East Antarctica: Antarctic Science-Institutional Subscription, 23(3), 281,

Airoldi, G. M., Muirhead, J. D., Long, S. M., Zanella, E., & White, J. D. (2016). Flow dynamics in mid-Jurassic dikes and sills of the Ferrar large igneous province and implications for long-distance magma transport. Tectonophysics, 683, 182-199.

Albert, H., Costa, F., & Martí, J. (2016). Years to weeks of seismic unrest and magmatic intrusions precede monogenetic eruptions. Geology, 44(3), 211-214.

Allen, C. C. (1980). Icelandic subglacial volcanism: thermal and physical studies. The Journal of Geology, 88(1), 108-117.

Allen, J.R.L., (1982). Sedimentary structures, their character and physical basis (Vol. 1). Elsevier, Amsterdam

Allen, J. R. L., (1984). Parallel lamination developed from upper-stage plane beds: a model based on the larger coherent structures of the turbulent boundary layer. Sedimentary Geology, 39(3-4), 227-242.

Allen, J. R. L. (1986). Earthquake magnitude-frequency, epicentral distance, and soft-sediment deformation in sedimentary basins. Sedimentary Geology, 46(1-2), 67-75.

Allen, R.M., Nolet, G., Morgan, W.J., Vogfjörd, K., Bergsson, B.H., et al. (1999). The thin hot plume beneath Iceland. Geophysics Journal International, 137, 51–63.

Anderson, E. M. (1951). The dynamics of faulting and dyke formation with applications to Britain. Hafner Publishing Company, New York.

Anketell, J.M., Cegla, J., Dzulynski, S., (1970). On the deformational structures in systems with reversed density gradients. Annales de la Société Géologique de Pologne, 40: 3-29.

Annen, C., Blundy, J. D., Leuthold, J., & Sparks, R. S. J. (2015). Construction and evolution of igneous bodies: Towards an integrated perspective of crustal magmatism. Lithos, 230, 206-221.

Aranda-Gómez, J., & Luhr, J. F. (1996). Origin of the Joya Honda maar, San Luis Potosi, Mexico. Journal of Volcanology and Geothermal Research, 74(1-2), 1-18.

Archer, S. G., Bergman, S. C., Iliffe, J., Murphy, C. M., & Thornton, M. (2005). Palaeogene igneous rocks reveal new insights into the geodynamic evolution and petroleum potential of the Rockall Trough, NE Atlantic Margin. Basin Research, 17(1), 171-201.

Baer, G. (1991). Mechanisms of dike propagation in layered rocks and in massive, porous sedimentary rocks. Journal of Geophysical Research: Solid Earth, 96(7), 11911-11929.

Bailey, D. K. (1980). Volatile flux, geotherms, and the generation of the kimberlite-carbonatite-alkaline magma spectrum. Mineralogical Magazine, 43(695), 9.

Ballard, R. D., Holcomb, R. T., & Andel, T. H. (1979). The Galapagos Rift at 86 W: 3. Sheet flows, collapse pits, and lava lakes of the rift valley. Journal of Geophysical Research: Solid Earth, 84(B10), 5407-5422.

Barker, C. E. (1983) The influence of time on metamorphism of sedimentary organic matter in selected geothermal systems, western North America. Geology,11, 384–38.

Barker, C. E., & Pawlewicz, M. J. (1986). The correlation of vitrinite reflectance with maximum temperature in humic organic matter. Paleogeothermics, Springer Berlin Heidelberg, 79-93.

Barker, C. E., Goldstein, R. H. (1990) Fluid inclusion technique for determining maximum temperature in calcite and its comparison to the vitrinite-reflectance geothermometer. Geology, 18, 1003–1006.

Barker, C. E., & Pawlewicz, M. J. (1994). Calculation of vitrinite reflectance from thermal histories and peak temperatures. In: P. K. Mukhopadhyay & W. G. Dow (eds) Vitrinite Reflectance as a Maturity Parameter (pp. 216–229) NewYork, American Chemical Society

Barker, C. E., Bone, Y., & Lewan, M. D. (1998). Fluid inclusion and vitrinite-reflectance geothermometry compared to heat-flow models of maximum paleotemperature next to dikes, western onshore Gippsland Basin, Australia. International Journal of Coal Geology, 37(1), 73-111.

Barnett, W.P., (2006). A model for stress controlled pipe growth. Journal of Volcanology and Geothermal Research, Special Issue. Selected papers from the 2nd International Maar Conference. 159, 108–125.

Barnett, Z. A., & Gudmundsson, A. (2014). Numerical modelling of dykes deflected into sills to form a magma chamber. Journal of Volcanology and Geothermal Research, 281, 1-11.

Barrabi, L. (1932). Oil in Limagne area, France. American Association of Petroleum Geologists, Bulletin, 16, 825-832.

Bédard, J. H., Naslund, H. R., Nabelek, P., Winpenny, A., Hryciuk, M., Macdonald, W., ... & Dewing, K. (2012). Fault-mediated melt ascent in a Neoproterozoic continental flood basalt province, the Franklin sills, Victoria Island, Canada. Geological Society of America Bulletin, 124(5-6), 723-736.

Befus, K. S., Hanson, R. E., Lehman, T. M., & Griffin, W. R. (2008). Cretaceous basaltic phreatomagmatic volcanism in west Texas: maar complex at Pena Mountain, Big Bend National park. Journal of Volcanology and Geothermal Research, 173(3), 245-264.

Bell, B., & Butcher, H. (2002). On the emplacement of sill complexes: evidence from the Faroe-Shetland Basin. Geological Society London Special Publications, 197(1), 307-329.

Beny-Bassez, C., & Rouzaud, J. N. (1985). Characterization of carbonaceous materials by correlated electron and optical microscopy and Raman microspectroscopy. Scanning electron microscopy, 1, 119-132.

Beyssac, O., Goffe, B., Chopin, C. & Rouzaud, J.N. (2002). Raman spectra of carbonaceous material in metasediments: a new geothermometer. Journal of Metamorphic Geology. 20, 859–871.

Bishop, A. N., & Abbott, G. D. (1995). Vitrinite reflectance and molecular geochemistry of Jurassic sediments: the influence of heating by Tertiary dykes (northwest Scotland). Organic Geochemistry, 22(1), 165-177.

Bjarnason, I.T., Wolfe, C.J., Solomon, S.C., Gudmundsson, G., (1996). Initial results from the ICEMELT experiment: body-wave delay times and shear-wave splitting across Iceland. Geophysical Research Letters, 23, 459–462.

Björnsson, H. (2003). Subglacial lakes and jökulhlaups in Iceland. Global and Planetary Change, 35(3), 255-271.

Bonal, L., Quirico, E., Bourot-Denise, M. & Montagnac, G. (2006). Determination of the petrologic type of CV3 chondrites by Raman spectroscopy of included organic matter. Geochimica et Cosmochimica Acta, 70, 1849–1863.

Bonini, M., & Mazzarini, F. (2010). Mud volcanoes as potential indicators of regional stress and pressurized layer depth. Tectonophysics, 494(1), 32-47.

Borrero, C., Murcia, H., Agustin-Flores, J., Arboleda, M. T., & Giraldo, A. M. (2017). Pyroclastic deposits of San Diego maar, central Colombia: an example of a silicic magma-related monogenetic eruption in a hard substrate. In: Németh, K., Carrasco-Núñez, G., Aranda-Gómez, J. and Smith I.E.M. (eds), Monogenetic Volcanism, Geological Society, London, Special Publications, 446(1), 361-374.

Bostick, N. H., & Pawlewicz, M. J. (1984). Paleotemperatures based on vitrinite reflectance of shales and limestone in igneous dike aureoles in the Upper Cretaceous Pierre shale, Walsenburg, Colorado. Rocky Mountain Association of Geologists, 387.

Boxer, G., Lorenz, V. & Smith, C.B. (1989). The geology and volcanology of the Argyle AK1 lamproite pipe, Western Australia. In: Ross, J., Jaques, A.L., Ferguson, J., Green, D.H., O'Reilly, S.Y., Danchin, R.V. & Janse, A.J.A. (eds) Kimberlites and Related Rocks. Volume 1: Their Composition, Occurrence, Origin, and Emplacement. Proceedings of the 4th International Kimberlite Conference 1986, Perth, Australia. Geological Society of Australia, Special Publications, 14, 140– 152.

Branney, M. J., & Kokelaar, B. P. (2002). Pyroclastic density currents and the sedimentation of ignimbrites. Bath, UK, Geological Society of London, 51-84.

Brenan, J. M., & Watson, E. B. (1991). Partitioning of trace elements between olivine and aqueous fluids at highP-T conditions: implications for the effect of fluid composition on trace-element transport. Earth and Planetary Science Letters, 107(3-4), 672-688.

Brenna, M., Cronin, S., Németh, K., Smith, I., and Sohn, Y., (2011). The influence of magma plumbing complexity on monogenetic eruptions, Jeju Island, Korea. Terra Nova, 23(2), 70-75.

Brenna, M., Cronin, S., Smith, I., Sohn, Y., and Maas, R., (2012). Spatio-temporal evolution of a dispersed magmatic system and its implications for volcano growth, Jeju Island Volcanic Field, Korea. Lithos, 148, 337-352.

Brooks, E. R., Wood, M. M., & Garbutt, P. L. (1982). Origin and metamorphism of peperite and associated rocks in the Devonian Elwell Formation, northern Sierra Nevada, California. Geological Society of America Bulletin, 93(12), 1208-1231.

Brown, R., Kavanagh, J., Sparks, R., Tait, M., and Field, M., (2007). Mechanically disrupted and chemically weakened zones in segmented dike systems cause vent localization: Evidence from kimberlite volcanic systems. Geology, 35 (9), 815.

Brown, R. J., Tait, M., Field, M., & Sparks, R. S. J. (2009). Geology of a complex kimberlite pipe (K2 pipe, Venetia Mine, South Africa): insights into conduit processes during explosive ultrabasic eruptions. Bulletin of Volcanology, 71(1), 95-112.

Brown, R. J., & Valentine, G. A. (2013). Physical characteristics of kimberlite and basaltic intraplate volcanism and implications of a biased kimberlite record. Geological Society of America Bulletin, 125(7-8), 1224-1238.

Browne, M., Dean, M., Hall, I. H., McAdam, A. D., Monro, S. K., & Chisholm, J. I. (1999). A lithostratigraphical framework for the Carboniferous rocks of the Midland Valley of Scotland. Version 2. British Geological Survey Research Report, RR/99/07. British Geological Survey, Keyworth.

Brunner, I., Friedel, S., Jacobs, F., Danckwardt, E., (1999). Investigation of a tertiary maar structure using three-dimensional resistivity imaging. Geophysical Journal International, 136(3), 771–780

Buchanan, D. J. (1974). A model for fuel-coolant interactions. Journal of Physics D: Applied Physics, 7(10), 1441.

Buck, W. R., P. Einarsson, and B. Brandsdóttir (2006), Tectonic stress and magma chamber size as controls on dike propagation: Constraints from the 1975–1984 Krafla rifting episode. Journal of Geophysical Research, 111, B12404.

Burchardt, S. (2008). New insights into the mechanics of sill emplacement provided by field observations of the Njardvik Sill, Northeast Iceland. Journal of Volcanology and Geothermal Research, 173(3), 280-288.

Busby-Spera, C.J., White, J.D., (1987). Variation in peperite textures associated with differing host-sediment properties. Bulletin of Volcanology, 49: 765-776.

Büttner, R., Dellino, P., & Zimanowski, B. (1999). Identifying magma–water interaction from the surface features of ash particles. Nature, 401(6754), 688-690.

Büttner, R., Dellino, P., La Volpe, L., Lorenz, V., & Zimanowski, B. (2002). Thermohydraulic explosions in phreatomagmatic eruptions as evidenced by the comparison between pyroclasts and products from Molten Fuel Coolant Interaction experiments. Journal of Geophysical Research: Solid Earth, 107(B11).

Cameron, I. B., & Stephenson, D. (1985). British regional geology: the Midland Valley of Scotland (No. 5). Hmso Books, London.

Cartwright, J., & Hansen, D. M. (2006). Magma transport through the crust via interconnected sill complexes. Geology, 34(11), 929-932.

Cas, R. A. F., Landis, C. A., & Fordyce, R. E. (1989). A monogenetic, Surtla-type, Surtseyan volcano from the Eocene-Oligocene Waiareka-Deborah volcanics, Otago, New Zealand: a model. Bulletin of Volcanology, 51(4), 281-298.

Cas, R. A. F., Yamagishi, H., Moore, L., & Scutter, C. (2003). Miocene submarine fire fountain deposits, Ryugazaki Headland, Oshoro Peninsula, Hokkaido, Japan: implications for submarine fountain dynamics and fragmentation processes. In Explosive Subaqueous Volcanism (eds J. D.L. White, J. L. Smellie and D. A. Clague), American Geophysical Union, Washington, D. C., 299-316.

Cas, R. A., & Giordano, G. (2014). Submarine volcanism: a review of the constraints, processes and products, and relevance to the Cabo de Gata volcanic succession. Italian Journal of Geosciences, 133(3), 362-377.

Cas, R. A. F., van Otterloo, J., Blaikie, T. N., van den Hove, J. (2016) The dynamics of a very large intra-plate continental basaltic volcanic province, the Newer Volcanics Province, SE Australia, and implications for other provinces. In: Németh, K., Carrasco-Núñez, G., Aranda-Gómez, J. and Smith I.E.M. (eds), Monogenetic Volcanism, Geological Society, London, Special Publications, 446, 123-172.

Chapman, N. A. (1974). Ultrabasic inclusions from the Coalyard Hill vent, Fife. Scottish Journal of Geology, 10(3), 223-227.

Chapman, N. A. (1976). Inclusions and megacrysts from undersaturated tuffs and basanites, East Fife, Scotland. Journal of Petrology, 17(4), 472-498.

Chen, J., & Lee, H. S. (2013). Soft-sediment deformation structures in Cambrian siliciclastic and carbonate storm deposits (Shandong Province, China): Differential liquefaction and fluidization triggered by storm-wave loading. Sedimentary Geology, 288, 81-94.

Chisholm, J. I., & Dean, J. M. (1974). The Upper Old Red Sandstone of Fife and Kinross: a fluviatile sequence with evidence of marine incursion. Scottish Journal of Geology, 10(1), 1-30.

Chough, S. K., Kwon, Y. K., Choi, D. K., & Lee, D. J. (2001). Autoconglomeration of limestone. Geosciences Journal, 5(2), 159-164.

Clement, C. R. (1982). A comparative geological study of some major kimberlite pipes in the Northern Cape and Orange Free State. PhD Thesis. University of Cape Town.

Cole, P., Guest, J., Duncan, A., and Pacheco, J., (2001), Capelinhos 1957-1958, Faial, Azores: deposits formed by an emergent surtseyan eruption. Bulletin of Volcanology, 63(2-3), 204-220.

Cooper, J. R., Crelling, J. C., Rimmer, S. M., & Whittington, A. G. (2007). Coal metamorphism by igneous intrusion in the Raton Basin, CO and NM: implications for generation of volatiles. International Journal of Coal Geology, 71(1), 15-27.

Connor, C. B., & Conway, F. M. (2000). Basaltic volcanic fields. Encyclopedia of volcanoes, 331-343.

Connor, C. B., Stamatakos, J. A., Ferrill, D. A., Hill, B. E., Ofoegbu, G. I., Conway, F. M., Sagar, B., & Trapp, J. (2000). Geologic factors controlling patterns of small-volume basaltic volcanism: Application to a volcanic hazards assessment at Yucca Mountain, Nevada. Journal of Geophysical Research: Solid Earth, 105(B1), 417-432.

Corcoran, P. L., & Moore, L. N. (2008). Subaqueous eruption and shallow-water reworking of a small-volume Surtseyan edifice at Kakanui, New Zealand. Canadian Journal of Earth Sciences, 45(12), 1469-1485.

Cortés, J. A., Smith, E. I., Valentine, G. A., Johnsen, R., Rasoazanamparany, C., Widom, E., ... & Ruth, D. (2015). Intrinsic conditions of magma genesis at the Lunar Crater Volcanic Field (Nevada), and implications for internal plumbing and magma ascent. American Mineralogist, 100(2-3), 396-413.

Cumming, G. A., (1928). The lower limestones and associated volcanic rocks of a section of the Fifeshire coast. Transactions of the Edinburgh Geological Society, 12, 124–140.

Cumming, G. A., (1936). The structure and volcanic geology of the Elie-St Monance district, Fife. Transactions of the Edinburgh Geological Society, 13, 340–365.

Daly, B. J., (1967). Numerical Study of Two Fluid Rayleigh Taylor Instability. Physics of Fluids (1958-1988) 10: 297-307.

Daniels, K. A., Kavanagh, J. L., Menand, T., and Sparks, R.S.J., (2012). The shapes of dikes: Evidence for the influence of cooling and inelastic deformation. Geological Society of America Bulletin, 124(7-8), 1102-1112.

De Rosa, R., (1999). Compositional models in the ash fraction of some modern pyroclastic deposits: their determination and significance. Bulletin of Volcanology, 61, 162–173.

Delaney, P. T., & Pollard, D. D. (1981). Deformation of host rocks and flow of magma during growth of minette dikes and breccia-bearing intrusions near Ship Rock, New Mexico USGPO 1202. Department of the Interior, Geological Survey, Washington.

Delaney, P. T. (1982). Rapid intrusion of magma into wet rock: groundwater flow due to pore pressure increases. Journal of Geophysical Research: Solid Earth, 87(B9), 7739-7756.

Delaney, P. T., Pollard, D. D., Ziony, J. I., & McKee, E. H. (1986). Field relations between dikes and joints: emplacement processes and paleostress analysis. Journal of Geophysical Research: Solid Earth, 91(B5), 4920-4938.

Delaney, P. T. (1987). Heat transfer during emplacement and cooling of mafic dykes. In H. C. Halls and W. F. Fahrig (eds), Mafic Dyke Swarms, 31-46.

Dellino, P., Isaia, R., & Veneruso, M. (2004). Turbulent boundary layer shear flows as an approximation of base surges at Campi Flegrei (Southern Italy). Journal of Volcanology and Geothermal Research, 133(1), 211-228.

Delpit, S., Ross, P. S., & Hearn, B. C. (2014). Deep-bedded ultramafic diatremes in the Missouri River Breaks volcanic field, Montana, USA: 1 km of syn-eruptive subsidence. Bulletin of Volcanology, 76(7), 832.

Donaire, T., Sáez, R., & Pascual, E. (2002). Rhyolitic globular peperites from the Aznalcóllar mining district (Iberian Pyrite Belt, Spain): physical and chemical controls. Journal of Volcanology and Geothermal Research, 114(1), 119-128.

Doré, A. G., & Lundin, E. R. (1996). Cenozoic compressional structures on the NE Atlantic margin; nature, origin and potential significance for hydrocarbon exploration. Petroleum Geoscience, 2(4), 299-311.

Doré, A. G., Lundin, E. R., Birkeland, O., Eliassen, P. E., & Jensen, L. N. (1997). The NE Atlantic margin; implications of late Mesozoic and Cenozoic events for hydrocarbon prospectivity. Petroleum Geoscience, 3(2), 117-131.

Downey, W. S., & Lentz, D. R. (2006). Igneous rock associations 6. modelling of deep submarine pyroclastic volcanism: a review and new results. Geoscience Canada, 33(1), 5-24.

Doyle, M. G. (2000). Clast shape and textural associations in peperite as a guide to hydromagmatic interactions: Upper Permian basaltic and basaltic andesite examples from Kiama, Australia. Australian Journal of Earth Sciences, 47(1), 167-177.

Duffield, W. A., Bacon, C. R., & Delaney, P. T. (1986). Deformation of poorly consolidated sediment during shallow emplacement of a basalt sill, Coso Range, California. Bulletin of Volcanology, 48(2-3), 97-107.

Ebdon, C. C., Granger, P. J., Johnson, H. D., & Evans, A. M. (1995). Early Tertiary evolution and sequence stratigraphy of the Faeroe-Shetland Basin: implications for hydrocarbon prospectivity. Geological Society, London, Special Publications, 90(1), 51-69.

Edwards, B. R., Skilling, I. P., Cameron, B., Haynes, C., Lloyd, A., & Hungerford, J. H. (2009). Evolution of an englacial volcanic ridge: Pillow Ridge tindar, Mount Edziza volcanic complex, NCVP, British Columbia, Canada. Journal of Volcanology and Geothermal Research, 185(4), 251-275.

Eide, C. H., Schofield, N., Jerram, D. A., & Howell, J. A. (2016). Basin-scale architecture of deeply emplaced sill complexes: Jameson Land, East Greenland. Journal of the Geological Society, 18.

Einarsson, T., & Albertsson, K. J. (1988). The glacial history of Iceland during the past three million years. Philosophical Transactions of the Royal Society of London B: Biological Sciences, 318(1191), 637-644.

Einarsson, P. (2008). Plate boundaries, rifts and transforms in Iceland. Jökull, 58(12), 35-58.

Einsele, G., Gieskes, J. M., Curray, J., Moore, D. M., Aguayo, E., Aubry, M. P., Fornari, D., Guerrero, J., Kastner, M., Kelts, K. and Lyle, M., (1980). Intrusion of basaltic sills into highly porous sediments, and resulting hydrothermal activity. Nature, 283(5746), 441-445.

Elliott, H. A. L., Gernon, T. M., Roberts, S., & Hewson, C. (2015). Basaltic maar-diatreme volcanism in the Lower Carboniferous of the Limerick Basin (SW Ireland). Bulletin of Volcanology, 77(5), 37.

Ellis, D., & Stoker, M. S. (2014). The Faroe–Shetland Basin: A regional perspective from the Paleocene to the present day and its relationship to the opening of the North Atlantic Ocean. Geological Society, London, Special Publications, 397(1), 11-31.

Evans, K. F., Genter, A., & Sausse, J. (2005). Permeability creation and damage due to massive fluid injections into granite at 3.5 km at Soultz: 1. Borehole observations. Journal of Geophysical Research: Solid Earth, 110(B4).

Ferrari, A.C. & Robertson, J. (2001). Resonant Raman spectroscopy of disordered, amorphous and diamond-like carbon. Physical Review B, 64, 075414.

Fielding, C. R., Al-Rubaii, M., & Walton, E. K. (1988). Deltaic sedimentation in an unstable tectonic environment–the Lower Limestone Group (Lower Carboniferous) of East Fife, Scotland. Geological Magazine, 125(03), 241-255.

Fisher, R. V., & Schmincke, H. U. (1984). Pyroclastic rocks. Springer, Berlin, 265-296.

Fitch, F.J., Heard, G.L. & Miller, J.A. (1988) Basaltic magmatism of late Cretaceous and Palaeogene age recorded in wells NNE of the Shetlands. Geological Society of London. Special Publication, 39, 253–262.

Fitch, E. P., Fagents, S. A., Thordarson, T., & Hamilton, C. W. (2017). Fragmentation mechanisms associated with explosive lava–water interactions in a lacustrine environment. Bulletin of Volcanology, 79(1), 12.

Fjeldskaar, W., Helset, H. M., Johansen, H., Grunnaleite, I., & Horstad, I. (2008). Thermal modelling of magmatic intrusions in the Gjallar Ridge, Norwegian Sea: implications for vitrinite reflectance and hydrocarbon maturation. Basin Research, 20(1), 143-159.

Flóvenz, Ó. G., & Saemundsson, K. (1993). Heat flow and geothermal processes in Iceland. Tectonophysics, 225(1-2), 123-138.

Francis, E. H., (1959). A Volcanic Vent in the Bogside Mines, Fife1. Geology Magazine, 96(6), 457.

Francis, E. H., (1960). Intrusive tuffs related to the Firth of Forth volcanoes. Transactions of the Edinburgh Geological Society, 18(1), 32-50.

Francis E. H. (1970). Bedding in Scottish (Fifeshire) tuff-pipes and its relevance to maars and calderas. Bulletin of Volcanology, 34, 697–712

Francis E. H., Hopgood A. M., (1970) Volcanism and the Ardross Fault, Fife, Scotland. Scottish Journal of Geology, 6, 162–185.

Freundt, A., & Schmincke, H. U. (1985). Lithic-enriched segregation bodies in pyroclastic flow deposits of Laacher See Volcano (East Eifel, Germany). Journal of Volcanology and Geothermal Research, 25(3), 193-224.

Funiciello R, Locardi E, Lombardi G, Parotto M (1976). The sedimentary ejecta from phreatomagmatic activity and their use for location of potential geothermal areas. In: International Congress on Thermal Waters, Geothermal Energy and Volcanology of the Mediterranean Area, Athens, National Technical University, Department of Mineralogy, Petrology and Geology, 227-240.

Gaffney, E. S., Damjanac, B., & Valentine, G. A. (2007). Localization of volcanic activity: 2. Effects of pre-existing structure. Earth and Planetary Science Letters, 263(3), 323-338.

Galland, O., De Bremond d'Ars, J., Cobbold, P. R., & Hallot, E. (2003). Physical models of magmatic intrusion during thrusting. Terra Nova, 15(6), 405-409.

Galland, O., Cobbold, P. R., Hallot, E., de Bremond d'Ars, J., Delavaud, G. (2006). Use of vegetable oil and silica powder for scale modelling of magmatic intrusion in a deforming brittle crust. Earth and Planetary Science Letters, 243, 786-804

Galland, O., Planke, S., Neumann, E. R., & Malthe-Sørenssen, A. (2009). Experimental modelling of shallow magma emplacement: application to saucer-shaped intrusions. Earth and Planetary Science Letters, 277(3), 373-383.

Galland, O., Gisler, G. R., & Haug, Ø. T. (2014). Morphology and dynamics of explosive vents through cohesive rock formations. Journal of Geophysical Research: Solid Earth, 119(6), 4708-4728.

Geikie, A. (1902). The geology of east Fife. Memoirs of the Geological Survey, Scotland.

Geirsdóttir, Á. (2004). Extent and chronology of glaciations in Iceland; a brief overview of the glacial history. Developments in Quaternary Sciences, 2, 175-182.

George, S. C. (1993). Black sandstones in the Midland Valley of Scotland: thermally metamorphosed hydrocarbon reservoirs?. Transactions of the Royal Society of Edinburgh: Earth Sciences, 84(01), 61-72.

Gernon, T. M., Gilbertson, M. A., Sparks, R. S. J., & Field, M. (2008). Gas-fluidisation in an experimental tapered bed: insights into processes in diverging volcanic conduits. Journal of Volcanology and Geothermal Research, 174(1), 49-56.

Gernon, T. M., Gilbertson, M. A., Sparks, R. S. J., & Field, M. (2009). The role of gas-fluidisation in the formation of massive volcaniclastic kimberlite. Lithos, 112, 439-451.

Gernon, T. M., Brown, R. J., Tait, M. A., & Hincks, T. K. (2012). The origin of pelletal lapilli in explosive kimberlite eruptions. Nature communications, 3, 832.

Gernon, T. M., Upton, B. G. J., & Hincks, T. K. (2013). Eruptive history of an alkali basaltic diatreme from Elie Ness, Fife, Scotland. Bulletin of volcanology, 75(5), 704.

Gevers, T. W. (1928). The volcanic vents of the Western Stormberg. Transactions of the Geological Society of South Africa, 31, 43-62.

Glennie, K. W., & Underhill, J. R. (1998). Origin, development and evolution of structural styles. In: K. W. Glennie (eds), Petroleum Geology of the North Sea: Basic Concepts and Recent Advances, Fourth Edition, Blackwell Science Ltd, Oxford, UK, 42-84.

Goulty, N. R. (2005). Emplacement mechanism of the Great Whin and Midland Valley dolerite sills. Journal of the Geological Society, London. 62, 1047-1056.

Goulty, N. R., & Schofield, N. (2008). Implications of simple flexure theory for the formation of saucer-shaped sills. Journal of Structural Geology, 30(7), 812-817.

Grady, D.E., Kipp, M.E., (1987). Dynamic rock fragmentation. In: Atkinson, B.K. (Ed.), Fracture Mechanics. Academic Press, London, 429-475.

Graettinger, A. H., Skilling, I., McGarvie, D., Höskuldsson, Á., (2013). Subaqueous basaltic magmatic explosions trigger phreatomagmatism: A case study from Askja, Iceland. Journal of Volcanology and Geothermal Research, 264, 17-35.

Graettinger, A. H., Valentine, G. H., Sonder, I. (2015) Circum-crater variability of deposits from discrete, laterally and vertically migrating volcanic explosions: Experimental evidence and field implications, Journal of Volcanology and Geothermal Research, 308, 61-69.

Griffiths, R. W., & Fink, J. H. (1992). Solidification and morphology of submarine lavas: A dependence on extrusion rate. Journal of Geophysical Research. 97(B13), 19729–19737.

Grove, C. (2013) Submarine hydrothermal vent complexes in the Paleocene of the Faroe-Shetland Basin: insights from three dimensional seismic and petrographical data. Geology, 41, 71–74.

Gudmundsson, A. (1986). Mechanical aspects of postglacial volcanism and tectonics of the Reykjanes Peninsula, Southwest Iceland. Journal of Geophysical Research: Solid Earth, 91(B12), 12711-12721.

Gudmundsson, G. H. (1997). Basal-flow characteristics of a non-linear flow sliding frictionless over strongly undulating bedrock. Journal of Glaciology, 43(143), 80-89.

Gudmundsson, A., (2002) Emplacement and arrest of sheets and dykes in central volcanoes. Journal of Volcanology and Geothermal Research, 116, 279–298.

Gudmundsson, M. T. (2003) Melting of Ice by Magma-Ice-Water Interactions During Subglacial Eruptions as an Indicator of Heat Transfer in Subaqueous Eruptions. In: Explosive Subaqueous Volcanism (eds White, J.D.L., Smellie J.L. and Clague, D.A.), American Geophysical Union, Washington, D. C. 61-72.

Gudmundsson, M. T., Sigmundsson, F., Björnsson, H., & Högnadóttir, T. (2004). The 1996 eruption at Gjálp, Vatnajökull ice cap, Iceland: efficiency of heat transfer, ice deformation and subglacial water pressure. Bulletin of Volcanology, 66(1), 46-65.

Gudmundsson, A., & Brenner, S. L. (2004). How mechanical layering affects local stresses, unrests, and eruptions of volcanoes. Geophysical Research Letters, 31(16), L16606.

Gudmundsson, A., (2006), How local stresses control magma-chamber ruptures, dyke injections, and eruptions in composite volcanoes: Earth-Science Reviews, 79, 1–31.

Gudmundsson, A. (2011). Deflection of dykes into sills at discontinuities and magma-chamber formation. Tectonophysics, 500(1), 50-64.

Guirdham, C., Andrews, J. E., Browne, M. A. E., & Dean, M. T. (2003). Stratigraphic and palaeoenvironmental significance of microbial carbonates in the Asbian Sandy Craig Formation of Fife. Scottish Journal of Geology, 39(2), 151-168.

Gurioli, L., Colo, L., Bollasina, A. J., Harris, A. J., Whittington, A., & Ripepe, M. (2014). Dynamics of Strombolian explosions: Inferences from field and laboratory studies of erupted bombs from Stromboli volcano. Journal of Geophysical Research: Solid Earth, 119(1), 319-345.

Hall, R.C.B., Els, B.G., (2002). The origin and significance of load-induced deformation structures in soft-sediment and lava at the base of the Archaean Ventersdorp Supergroup, South Africa. Journal of African Earth Sciences, 35, 135-145.

Hansen, D. M. (2006). The morphology of intrusion-related vent structures and their implications for constraining the timing of intrusive events along the NE Atlantic margin. Journal of the Geological Society, 163(5), 789-800.

Hansen, D. M., & Cartwright, J. (2006). The three-dimensional geometry and growth of forced folds above saucer-shaped igneous sills. Journal of Structural Geology, 28(8), 1520-1535.

Hanson, R.E., Wilson, T.J. (1993) Large-scale rhyolite peperites (Jurassic, southern Chile). Journal of Volcanology and Geothermal Research, 54, 247-264.

Hardarson, B.S., Fitton, J.G., Ellam, R.M., Pringle, M.S., (1997). Rift relocation—a geochemical and geochronological investigation of a palaeo-rift in Northwest Iceland. Earth and Planetary Science Letters, 153, 181–196.

Heiken, G. (1978). Characteristics of tephra from cinder cone, Lassen volcanic national park, California. Bulletin of Volcanology, 41(2), 119-130.

Heiken, G., Wohletz, K., and Eichelberger, J., (1988). Fracture fillings and intrusive pyroclasts, Inyo Domes, California. Journal of Geophysical Research, 93(B5), 4335.

Henry, R. E., & Miyazaki, K. (1978). Effects of system pressure on the bubble growth from highly superheated water droplets. In: S. G. Bankoff (ed), Topics in two-phase heat transfer and flow, American Society of Mechanical Engineers, New York, 1-10.

Hernando, I. R., Franzese, J. R., Llambías, E. J., & Petrinovic, I. A. (2014). Vent distribution in the Quaternary Payún Matrú Volcanic Field, western Argentina: Its relation to tectonics and crustal structures. Tectonophysics, 622, 122-134.

Herzer, R. H. (1995). Seismic stratigraphy of a buried volcanic arc, Northland, New Zealand and implications for Neogene subduction. Marine and petroleum geology, 12(5), 511-531.

Hickson, C. J. (2000). Physical controls and resulting morphological forms of Quaternary ice-contact volcanoes in western Canada. Geomorphology, 32(3), 239-261.

Hindmarsh, R. C., & Rijsdijk, K. F. (2000). Use of a viscous model of till rheology to describe gravitational loading instabilities in glacial sediments. Geological Society, London, SpecialPublications, 176(1), 191-201.

Hitchen, K., & Ritchie, J. D. (1987). Geological review of the West Shetland area. In: Graham and Trotman, Petroleum Geology of North West Europe, London, 737-749.

Holford, S., Schofield, N., MacDonald, J., Duddy, I., & Green, P. (2012). Seismic analysis of igneous systems in sedimentary basins and their impacts on hydrocarbon prospectivity: Examples from the southern Australian margin. Australian Petroleum Production & Exploration Association, 52, 229-252.

Holford, S. P., Tassone, D. R., Stoker, M. S., & Hillis, R. R. (2016). Contemporary stress orientations in the Faroe–Shetland region. Journal of the Geological Society, 173(1), 142-152.

Hooten, J. A., & Ort, M. H. (2002). Peperite as a record of early-stage phreatomagmatic fragmentation processes: an example from the Hopi Buttes volcanic field, Navajo Nation, Arizona, USA. Journal of Volcanology and Geothermal Research, 114(1), 95-106.

Höskuldsson, A., Sparks, R. S., & Carroll, M. R. (2006). Constraints on the dynamics of subglacial basalt eruptions from geological and geochemical observations at Kverkfjöll, NE-Iceland. Bulletin of Volcanology, 68(7-8), 689.

Houghton, B. F., & Schmincke, H. U. (1989). Rothenberg scoria cone, East Eifel: a complex Strombolian and phreatomagmatic volcano. Bulletin of Volcanology, 52(1), 28-48.

Houghton, B., and Wilson, C., (1989). A vesicularity index for pyroclastic deposits. Bulletin of Volcanology, 51(6), 451-462.

Houghton, B.F. and Nairn, I.A., (1991). The 1976–1982 Strombolian and phreatomagmatic eruptions of White Island, New Zealand: eruptive and depositional mechanisms at a 'wet' volcano. Bulletin of Volcanology, 54(1), 25-49.

Houghton, B., and Smith, R., (1993). Recycling of magmatic clasts during explosive eruptions: estimating the true juvenile content of phreatomagmatic volcanic deposits. Bulletin of Volcanology, 55(6), 414-420.

Houghton, B. F., Wilson, C. J. N., & Smith, I. E. M. (1999). Shallow-seated controls on styles of explosive basaltic volcanism: a case study from New Zealand. Journal of Volcanology and Geothermal Research, 91(1), 97-120.

Hutchinson, P. J. (1994). Upper Cretaceous (Austin Group) volcanic deposits as a hydrocarbon trap. Gulf Coast Association of Geological Societies, Transactions, 44, 293-303.

Hutton, D. H. W. (2009). Insights into magmatism in volcanic margins: bridge structures and a new mechanism of basic sill emplacement–Theron Mountains, Antarctica. Petroleum Geoscience, 15(3), 269-278.

IGC Excursion Guide 5 (2008). Geology of Iceland. Eds. Norðdahl, H. et al. Compiled for the pre- and post- excursions of the 33 IGC.

Jackson, M. D., & Pollard, D. D. (1988). The laccolith-stock controversy: New results from the southern Henry Mountains, Utah. Geological Society of America Bulletin, 100(1), 117-139.

Jackson, M. D., & Pollard, D. D. (1990). Flexure and faulting of sedimentary host rocks during growth of igneous domes, Henry Mountains, Utah. Journal of Structural Geology, 12(2), 185-206.

Jackson, C. A. L. (2012). Seismic reflection imaging and controls on the preservation of ancient sill-fed magmatic vents. Journal of the Geological Society, 169(5), 503-506.

Jackson, C. A., Schofield, N., & Golenkov, B. (2013). Geometry and controls on the development of igneous sill–related forced folds: A 2-D seismic reflection case study from offshore southern Australia. Geological Society of America Bulletin, 125(11-12), 1874-1890.

Jakobsson, S. P., & Gudmundsson, M. T. (2008). Subglacial and intraglacial volcanic formations in Iceland. Jökull, 58, 179-196.

Jakobsson, S. P., & Johnson, G. L. (2012). Intraglacial volcanism in the Western Volcanic Zone, Iceland. Bulletin of volcanology, 74(5), 1141-1160.

Jamtveit, B., Svensen, H., Podladchikov, Y. Y., & Planke, S. (2004). Hydrothermal vent complexes associated with sill intrusions in sedimentary basins. Geological Society of London, Special Publications, 234, 233-241.

Jaupart, C., and Allègre, C.J., (1991). Gas content, eruption rate and instabilities of eruption regime in silicic volcanoes. Earth and Planetary Science Letters, 102, 413–429.

Jehlicka, J. & Bény, C. (1992). Application of Raman microspectrometry in the study of structural changes in Precambrian kerogens during regional metamorphism. Organic Geochemistry, 18, 211–213.

Jerram, D., and Stollhofen, H., (2002) Lava-sediment interaction in desert settings; are all peperite-like textures the result of magma water interaction? Journal of Volcanology and Geothermal Research, 114(1-2), 231-249.

Jóhannesson, H., (1980). Jardlagaskipan og þróun rekbelta á Vesturlandi (Stratigraphy and evolution of rift zones in West Iceland). Náttúrufrædingurinn, 50, 13–31.

Jóhannesson, H., (2014). Geological Map of Iceland. Bedrock Geology. 1:600 000. Reykjavik, The Icelandic Institute of Natural History.

Johnson, E. R., Wallace, P. J., Cashman, K. V., Granados, H. D., & Kent, A. J. (2008). Magmatic volatile contents and degassing-induced crystallization at Volcán Jorullo, Mexico: implications for melt evolution and the plumbing systems of monogenetic volcanoes. Earth and Planetary Science Letters, 269(3), 478-487.

Jolly, R. J. H., & Sanderson, D. J. (1997). A Mohr circle construction for the opening of a pre-existing fracture. Journal of Structural Geology, 19(6), 887-892.

Jones, J. G. (1969). Intraglacial volcanoes of the Laugarvatn region, south-west Iceland—I. Quarterly Journal of the Geological Society, 124(1-4), 197-211.

Jones, J. G. (1970). Intraglacial volcanoes of the Laugarvatn region, southwest Iceland, II. The Journal of Geology, 78(2), 127-140.

Jones, J. G., & Nelson, P. H. H. (1970). The flow of basalt lava from air into water–its structural expression and stratigraphic significance. Geological Magazine, 107(01), 13-19.

Jones, A.P. and Omoto, K., (2000). Towards establishing criteria for identifying trigger mechanisms for soft sediment deformation: A case study of Late Pleistocene lacustrine sands and clays, Onikobe and Nakayamadaira Basins, northeastern Japan. Sedimentology, 47, 1211-1226.

Kano, K., (1990). An ash-flow tuff emplaced in shallow water, Early Miocene Koura formation, southwest Japan. Journal of Volcanology and Geothermal Research, 40(1), 1-9.

Kassi, A. M., Weir, J. A., McManus, J., & Browne, M. A. E. (2003). Lithofacies and sedimentary cycles within the Late Dinantian (late Brigantian) of Fife and East Lothian: is a sequence stratigraphical approach valid? Transactions of the Royal Society of Edinburgh: Earth Sciences, 94(02), 95-113.

Kavanagh, J. L., Menand, T., & Sparks, R. S. J. (2006). An experimental investigation of sill formation and propagation in layered elastic media. Earth and Planetary Science Letters, 245(3), 799-813.

Kavanagh, J. L., & Sparks, R. S. J. (2011). Insights of dyke emplacement mechanics from detailed 3D dyke thickness datasets. Journal of the Geological Society, 168(4), 965-978.

Kavanagh, J. L., Boutelier, D., & Cruden, A. R. (2015). The mechanics of sill inception, propagation and growth: Experimental evidence for rapid reduction in magmatic overpressure. Earth and Planetary Science Letters, 421, 117-128.

Keating, G. N., Valentine, G. A., Krier, D. J., & Perry, F. V. (2008). Shallow plumbing systems for small-volume basaltic volcanoes. Bulletin of Volcanology, 70(5), 563-582.

Kennedy, G. C., & Holser, W. T. (1966). Section 16: Pressure-volume-temperature and phase relations of water and carbon dioxide. Geological Society of America Memoirs, 97, 371-384.

Kereszturi, G., & Németh, K. (2012). Monogenetic basaltic volcanoes: genetic classification, growth, geomorphology and degradation. INTECH Open Access Publisher.

Kiyosugi, K., Connor, C. B., Wetmore, P. H., Ferwerda, B. P., Germa, A. M., Connor, L. J., & Hintz, A. R. (2012). Relationship between dike and volcanic conduit distribution in a highly eroded monogenetic volcanic field: San Rafael, Utah, USA. Geology, 40(8), 695-698.

Kokelaar, B. P. (1982). Fluidisation of wet sediments during the emplacement and cooling of various igneous bodies. Journal of the Geological Society 139, 21-33.

Kokelaar, B. P. (1983). The mechanism of Surtseyan volcanism. Journal of the Geological Society, 140(6), 939-944.

Kokelaar, B., and Durant, G., (1983). The submarine eruption and erosion of Surtla (Surtsey), Iceland. Journal of Volcanology and Geothermal Research, 19(3-4), 239-246.

Kokelaar, B. P. (1986). Magma-water interactions in subaqueous and emergent basaltic. Bulletin of Volcanology, 48(5), 275-289.

Kokelaar, B. P. (2002). Setting, chronology and consequences of the eruption of Soufrière Hills Volcano, Montserrat (1995-1999). Geological Society of London, Memoirs, 21(1), 1-43.

Konnerup-Madsen, J., & Dypvik, H. (1988). Fluid inclusions and quartz cementation in Jurassic sandstones from Haltenbanken, offshore mid-Norway. Bulletin de Minéralogie, 111, 401-411.

Knight, D. S. & White, W. B. (1989) Characterization of diamond films by Raman spectroscopy. Journal of Materials Research, 4, 385–393.

Knott, S. D., Burchell, M. T., Jolley, E. J., and Fraser, A. J. (1993). Mesozoic and Cenozoic plate reconstruction of the North Atlantic and hydrocarbon plays of the Atlantic margins. In: Parker, J. R. (ed), Petroleum geology of northwest Europe, proceedings of the 4th conference London, The Geological Society, London, 953-974.

Krigström, A. (1962). Geomorphological studies of sandur plains and their braided rivers in Iceland. Geografiska Annaler, 44(3/4), 328-346.

Kristjánsson, L., (1982). Geomagnetic polarity mapping in Icelandic lavas. Comparison with ocean-floor magnetic lineations. Earth Evolutionary Science, 2, 126–129.

Kristjansson, L., Hardarson, B. S., & Audunsson, H. (2003). A detailed palaeomagnetic study of the oldest (≈ 15 Myr) lava sequences in Northwest Iceland. Geophysical Journal International, 155(3), 991-1005.

Kurszlaukis, S. (1994). Geology and geochemistry of the carbonatitic Gross Brukkaros Volcanic field and the ultrabasic Blue Hills Intrusive Complex, southern Namibia (PhD dissertation), National Autonomous University of Mexico.

Kurszlaukis, S., and Lorenz, V., (1997). Volcanological features of a low-viscosity melt: the carbonatitic Gross Brukkaros Volcanic Field, Namibia. Bulletin of Volcanology, 58(6), 421-431.

Kwon, C. W., & Sohn, Y. K. (2008). Tephra-filled volcanic neck (diatreme) of a mafic tuff ring at Maegok, Miocene Eoil Basin, SE Korea. Geosciences Journal, 12(4), 317-329.

Lamers, E., & Carmichael, S. M. M. (1999). The Paleocene deepwater sandstone play West of Shetland. In Petroleum Geology Conference series 5, Geological Society of London, London, 645-659.

Landis, C.A. (1971) Graphitisation of dispersed carbonaceous material in metamorphic rocks. Contributions to Mineralogy and Petrology, 30, 34–45.

Larsen, G. (2002). A brief overview of eruptions from ice-covered and ice-capped volcanic systems in Iceland during the past 11 centuries: frequency, periodicity and implications. Geological Society of London, Special Publications, 202(1), 81-90.

Le Corvec, N., Spörli, K. B., Rowland, J., & Lindsay, J. (2013). Spatial distribution and alignments of volcanic centers: clues to the formation of monogenetic volcanic fields. Earth-Science Reviews, 124, 96-114.

Leat, P., and Thompson, R., (1988), Miocene hydrovolcanism in NW Colorado, USA, fuelled by explosive mixing of basic magma and wet unconsolidated sediment. Bulletin of Volcanology, 50(4), 229-243.

Lefebvre, N. S., White, J. D. L., & Kjarsgaard, B. A. (2012). Spatter-dike reveals subterranean magma diversions: Consequences for small multivent basaltic eruptions. Geology, 40(5), 423-426.

Lefebvre, N. S., White, J. D. L., & Kjarsgaard, B. A. (2013). Unbedded diatreme deposits reveal maar-diatreme-forming eruptive processes: Standing Rocks West, Hopi Buttes, Navajo Nation, USA. Bulletin of Volcanology, 75(8), 739.

Lefebvre, N. S., White, J. D., & Kjarsgaard, B. A. (2016). Arrested diatreme development: Standing Rocks East, Hopi Buttes, Navajo Nation, USA. Journal of Volcanology and Geothermal Research, 310, 186-208.

Leys, C.A., (1982). Volcanic and sedimentary processes in phreatomagmatic volcanoes. PhD thesis, University of Leeds.

Liss, D., Owens, W.H., and Hutton, D.H.W., 2004, New palaeomagnetic results from the Whin Sill complex: Evidence for a multiple intrusion event and revised virtual geomagnetic poles for the late Carboniferous for the British Isles. Journal of the Geological Society, 161, 927–938.

Liu, E. J., Cashman, K. V., Rust, A. C., & Gislason, S. R. (2015). The role of bubbles in generating fine ash during hydromagmatic eruptions. Geology, 43(3), 239-242

Long, P. E., & Wood, B. J. (1986). Structures, textures, and cooling histories of Columbia River basalt flows. Geological Society of America Bulletin, 97(9), 1144-1155.

Lorenz, V. (1975). Formation of phreatomagmatic maar-diatreme volcanoes and its relevance to kimberlite diatremes. Physics and Chemistry of the Earth, 9, 17-27.

Lorenz, V. (1984). Explosive volcanism of the West Eifel volcanic field/Germany. Developments in Petrology, 11, 299-307.

Lorenz, V., & Nicholls, I. A. (1984). Plate and intraplate processes of Hercynian Europe during the Late Paleozoic. Tectonophysics, 107(1-2), 25-56.

Lorenz, V., (1986). On the growth of maars and diatremes and its relevance to the formation of tuff rings. Bulletin of Volcanology, 48, 265–274.

Lorenz, V., Zimanowski, B. and Büttner, R., (2002). On the formation of deep-seated subterranean peperite-like magma-sediment mixtures. Journal of Volcanology and Geothermal Research, 114, 107-118.

Lorenz, V., (2003). Maar-diatreme volcanoes, their formation, and their setting in hardrock and soft-rock environments. Geolines, 15, 72–83.

Lorenz, V., and Haneke, J., (2004) Relationship between diatremes, dykes, sills, laccoliths, intrusive-extrusive domes, lava flows, and tephra deposits with unconsolidated water-saturated sediments in the late Variscan intermontane Saar-Nahe Basin, SW Germany. Geological Society of London, Special Publications. 234, 75-124.

Lorenz, V. and Kurszlaukis, S. (2007). Root zone processes in the phreatomagmatic pipe emplacement model and consequences for the evolution of maar-diatreme volcanoes. Journal of Volcanology and Geothermal Research, 159(1-3), 4-32.

Lorenz, V., and Zimanowski, B. (2008). Volcanology of the West Eifel Maars and its relevance to the understanding of kimberlite pipes. In: 9th International Kimberlite Conference field trip 7-10.

Lorenz, V., Suhr, P. and Suhr, S. (2017) Phreatomagmatic maar-diatreme volcanoes and their incremental growth: a model. In: Németh, K., Carrasco-Núñez, G., Aranda-Gómez, J. and Smith I.E.M. (eds), Monogenetic Volcanism, Geological Society, London, Special Publications, 446, 29-59.

Lowe, D. R. (1975). Water escape structures in coarse-grained sediments. Sedimentology, 22(2), 157-204.

MacGregor, M. & A.G. (1968). British Regional Geology. The Midland Valley of Scotland. Second Edition, Revised (6th imp.), HMSO Books, Edinburgh.

Magee, C., Stevenson, C.T.E., O'Driscoll, B., and Petronis, M.S., (2012). Local and regional controls on the lateral emplacement of the Ben Hiant Dolerite intrusion, Ardnamurchan (NW Scotland). Journal of Structural Geology, 39, 66–82.

Magee, C., Jackson, C. A. L., & Schofield, N. (2013). The influence of normal fault geometry on igneous sill emplacement and morphology. Geology, 41(4), 407-410.

Magee, C., Jackson, C. L., & Schofield, N. (2014). Diachronous sub volcanic intrusion along deep water margins: insights from the Irish Rockall Basin. Basin Research, 26(1), 85-105.

Magee, C., Duffy, O. B., Purnell, K., Bell, R. E., Jackson, C. A. L., & Reeve, M. T. (2015). Fault-controlled fluid flow inferred from hydrothermal vents imaged in 3D seismic reflection data, offshore NW Australia. Basin Research, 28, 1-20.

Magee, C., Muirhead, J. D., *et al.* (2016). Lateral magma flow in mafic sill complexes. Geosphere, GES01256-1.

Magill, C. R., McAneney, K. J., & Smith, I. E. (2005). Probabilistic assessment of vent locations for the next Auckland volcanic field event. Mathematical Geology, 37(3), 227-242.

Maicher, D., (2003). A cluster of surtseyan volcanoes at Lookout Bluff, North Otago, New Zealand: Aspects of edifice spacing and time. In: J. D.L. White, J. L. Smellie and D. A. Clague (eds), Explosive Subaqueous Volcanism, American Geophysical Union, Washington, D. C, 167-178.

Maizels, J. K. (1993). Quantitative regime modelling of fluvial depositional sequences: application to Holocene stratigraphy of humid-glacial braid-plains (Icelandic sandurs). Geological Society of London, Special Publications, 73(1), 53-78.

Malthe-Sørenssen, A., Planke, S., Svensen, H., and Jamtveit, B., (2004). Formation of saucer- shaped sills. In: Breitkreuz, C., and Petford, N., (eds), Physical geology of high-level magmatic systems: Geological Society of London Special Publication 234, 215–227.

Maltman, A.J., and Bolton, A., (2003). How sediments become mobilized. Geological Society of London, Special Publications, 216, 9-20.

Mangan, M. T., & Cashman, K. V. (1996). The structure of basaltic scoria and reticulite and inferences for vesiculation, foam formation, and fragmentation in lava fountains. Journal of Volcanology and Geothermal Research, 73(1), 1-18.

Manton, B. (2015) The mechanics of sill propagation and associated venting, investigated using 3D seismic data from offshore Norway. PhD Thesis, Cardiff University.

Marshall, J. E.A., Haughton, P.D.W., & Hillier, S. J. (1994) Vitrinite reflectivity and the structure and burial history of the Old Red Sandstone of the Midland Valley of Scotland. Journal of the Geological Society of London, 151(12) 423-438.

Marshall, A.O., Emry, J.R. & Marshall, C.P. (2012). Multiple generations of carbon in the Apex chert and implications for preservation of microfossils. Astrobiology, 12, 160–166.

Martin, U., and Németh, K., (2007) Blocky versus fluidal peperite textures developed in volcanic conduits, vents and crater lakes of phreatomagmatic volcanoes in Mio/Pliocene volcanic fields of Western Hungary. Journal of Volcanology and Geothermal Research, 159, 164-178.

Mastin, L. G., Guffanti, M., Servranckx, R., Webley, P., Barsotti, S., Dean, K., & Schneider, D. (2009). A multidisciplinary effort to assign realistic source parameters to models of volcanic ash-cloud transport and dispersion during eruptions. Journal of Volcanology and Geothermal Research, 186(1), 10-21.

Mathieu, L., De Vries, B. V. W., Holohan, E. P., & Troll, V. R. (2008). Dykes, cups, saucers and sills: Analogue experiments on magma intrusion into brittle rocks. Earth and Planetary Science Letters, 271(1), 1-13.

Mathieu, L., Burchardt, S., Troll, V.R., Krumbholz, M., and Delcamp, A., (2015). Geological constraints on the dynamic emplacement of cone-sheets: The Ardnamurchan cone-sheet swarm, NW Scotland. Journal of Structural Geology, 80, 133–141.

Matthews, W. H. (1947). 'Tuyas'. Flat-topped volcanoes in northern British Columbia. American Journal of Science, 245, 560-570.

Mattsson, H., & Höskuldsson, Á. (2003). Geology of the Heimaey volcanic centre, south Iceland: early evolution of a central volcano in a propagating rift? Journal of Volcanology and Geothermal Research, 127(1), 55-71.

Mattsson, H., (2010). Textural variation in juvenile pyroclasts from an emergent, Surtseyan-type, volcanic eruption: The Capelas tuff cone, Sao Miguel (Azores). Journal of Volcanology and Geothermal Research, 189(1-2), 81-91.

Mazzarini, F., Le Corvec, N., Isola, I., & Favalli, M. (2016). Volcanic field elongation, vent distribution, and tectonic evolution of a continental rift: The Main Ethiopian Rift example. Geosphere, 12(3), 706-720.

McArdle, N. J., & Ackers, M. A. (2012). Understanding seismic thin-bed responses using frequency decomposition and RGB blending. First Break, 30(12), 57-65.

McBirney, A. R. (1963). Factors governing the nature of submarine volcanism. Bulletin of Volcanology, 26(1), 455-469.

McBirney, A., and Murase, T., (1970) Factors governing the formation of pyroclastic rocks. Bulletin Volcanologique, 34(2), 372-384.

McBirney, A. R., Taylor, H. P., & Armstrong, R. L. (1987). Paricutin re-examined: a classic example of crustal assimilation in calc-alkaline magma. Contributions to Mineralogy and Petrology, 95(1), 4-20.

McClintock, M., & White, J. D. (2006). Large phreatomagmatic vent complex at Coombs Hills, Antarctica: wet, explosive initiation of flood basalt volcanism in the Ferrar-Karoo LIP. Bulletin of Volcanology, 68(3), 215-239.

McClintock, M., White, J.D.L., Houghton, B.F., Skilling, I.P., (2008). Physical volcanology of a large crater-complex formed during the initial stages of Karoo flood basalt volcanism, Sterkspruit, Eastern Cape, South Africa. Journal of Volcanology and Geothermal Research, 172, 93–111.

McGarvie, D. W., Stevenson, J. A., Burgess, R., Tuffen, H., & Tindle, A. G. (2007). Volcano–ice interactions at Prestahnúkur, Iceland: rhyolite eruption during the last interglacial–glacial transition. Annals of Glaciology, 45(1), 38-47.

McGetchin, T. R., Settle, M., & Chouet, B. A. (1974). Cinder cone growth modeled after northeast crater, Mount Etna, Sicily. Journal of Geophysical Research, 79(23), 3257-3272.

McLean, C. E., Brown, D. J., & Rawcliffe, H. J. (2016). Extensive soft-sediment deformation and peperite formation at the base of a rhyolite lava: Owyhee Mounta-ins, SW Idaho, USA. Bulletin of Volcanology, 78(6), 1-17.

McLean, C. E., Schofield, N., Brown, D. J., Jolley, D. W., Reid, A. (2017) 3D seismic imaging of the shallow plumbing system beneath the Ben Nevis Monogenetic Volcanic Field: Faroe-Shetland Basin. Journal of the Geological Society of London.

Menand, T. (2008). The mechanics and dynamics of sills in layered elastic rocks and their implications for the growth of laccoliths and other igneous complexes. Earth and Planetary Science Letters, 267(1), 93-99.

Menand, T. (2011). Physical controls and depth of emplacement of igneous bodies: A review. Tectonophysics, 500(1), 11-19.

Middleton, M.F., (1991). Thermal effects of intrusions on coal: Permian coals of eastern Australia. Australian Bureau Mineral Resources Bulletin, 231, 395–400.

Millett, J. M., Hole, M. J., Jolley, D. W., Schofield, N., & Campbell, E. (2016). Frontier exploration and the North Atlantic Igneous Province: new insights from a 2.6 km offshore volcanic sequence in the NE Faroe–Shetland Basin. Journal of the Geological Society, 173(2), 320-336.

Mills, P. C. (1983) Genesis and diagnostic value of soft-sediment deformation structures—a review. Sedimentary Geology, 35, 83-104.

Monaghan, A. A., & Browne, M. A. E. (2010). Nine 40Ar/39Ar dates from Carboniferous igneous rocks of the Midland Valley of Scotland. British Geological Survey, Keyworth, 1-41.

Monaghan, A.A. (2014). The Carboniferous shales of the Midland Valley of Scotland: geology and resource estimation. British Geological Survey for Department of Energy and Climate Change, London, UK.

Moore, J. G., & Schilling, J. G. (1973). Vesicles, water, and sulfur in Reykjanes Ridge basalts. Contributions to Mineralogy and Petrology, 41(2), 105-118.

Moore, J. G. (1975). Mechanism of formation of pillow lava: pillow lava, produced as fluid lava cools underwater, is the most abundant volcanic rock on earth, but only recently have divers observed it forming. American Scientist, 63(3), 269-277.

Moore, J. G., & Calk, L. C. (1991). Degassing and differentiation in subglacial volcanoes, Iceland. Journal of Volcanology and Geothermal Research, 46(1-2), 157-180.

Moy, D. J., & Imber, J. (2009). A critical analysis of the structure and tectonic significance of rift-oblique lineaments ('transfer zones') in the Mesozoic–Cenozoic succession of the Faroe–Shetland Basin, NE Atlantic margin. Journal of the Geological Society, 166(5), 831-844.

Muirhead, D. K., Parnell, J., Taylor, C., & Bowden, S. A. (2012). A kinetic model for the thermal evolution of sedimentary and meteoritic organic carbon using Raman spectroscopy. Journal of Analytical and Applied Pyrolysis, 96, 153-161.

Muirhead, J. D., Airoldi, G., Rowland, J. V., & White, J. D. (2012). Interconnected sills and inclined sheet intrusions control shallow magma transport in the Ferrar large igneous province, Antarctica. Geological Society of America Bulletin, 124(1-2), 162-180.

Muirhead, J. D., Kattenhorn, S. A., & Le Corvec, N. (2015). Varying styles of magmatic strain accommodation across the East African Rift. Geochemistry, Geophysics, Geosystems, 16(8), 2775-2795.

Muirhead, J. D., Van Eaton, A. R., Re, G., White, J. D., & Ort, M. H. (2016a). Monogenetic volcanoes fed by interconnected dikes and sills in the Hopi Buttes volcanic field, Navajo Nation, USA. Bulletin of Volcanology, 78(2), 1-16.

Muirhead, J. D., Kattenhorn, S. A., Lee, H., Mana, S., Turrin, B. D., Fischer, T. P., Kianji, G., Dindi, E., and Stamps D. S (2016b). Evolution of upper crustal faulting assisted by magmatic volatile release during early-stage continental rift development in the East African Rift. Geosphere, GES01375-1.

Muirhead, D.K., Parnell, J. Spinks, S. Bowden, S.A. (2016). Characterization of organic matter in the Torridonian using Raman spectroscopy. In: Brasier, A. T., McIlroy, D. & McLoughlin, N.

(eds) Earth System Evolution and Early Life: a Celebration of the Work of Martin Brasier. Geological Society, London, Special Publications, 448.

Murchison, D. G., & Raymond, A. C. (1989). Igneous activity and organic maturation in the Midland Valley of Scotland. International Journal of Coal Geology, 14(1-2), 47-82.

Murphy, B., Corcoran, P., and Moore, L., (2008). Subaqueous eruption and shallow-water reworking of a small-volume Surtseyan edifice at Kakanui, New Zealand. Canadian Journal of Earth Sciences, 45(12), 1469-1485.

Naidoo, P., Stiefenhofer, J., Field, M., & Dobbe, R. (2004). Recent advances in the geology of Koffiefontein Mine, Free State Province, South Africa. Lithos, 76(1), 161-182.

Naylor, P. H., Bell, B. R., Jolley, D. W., Durnall, P., & Fredsted, R. (1999). Palaeogene magmatism in the Faeroe–Shetland Basin: influences on uplift history and sedimentation. In: Petroleum Geology Conference series 5, Geological Society of London, 545-558.

Nemanich, R. J. & Solin, S. A. (1979) First and second order Raman scattering from finite-size crystals of graphite. Physical Review B, 20, 392–401.

Németh, K., White, J. D., Reay, A., & Martin, U. (2003). Compositional variation during monogenetic volcano growth and its implications for magma supply to continental volcanic fields. Journal of the Geological Society, 160(4), 523-530.

Németh, K., & Martin, U. (2007). Shallow sill and dyke complex in western Hungary as a possible feeding system of phreatomagmatic volcanoes in "soft-rock" environment. Journal of Volcanology and Geothermal Research, 159(1), 138-152.

Németh, K. (2010). Monogenetic volcanic fields: origin, sedimentary record, and relationship with polygenetic volcanism. Geological Society of America Special Papers, 470, 43-66.

Neidell, N. S. (1979). Stratigraphic modeling and interpretation: Geophysical principles and techniques (No. 13). American Association of Petroleum Geologists.

Nichols, R. J., Sparks, R. S. J., & Wilson, C. J. N. (1994). Experimental studies of the fluidization of layered sediments and the formation of fluid escape structures. Sedimentology, 41(2), 233-253.

Nicholson, R., & Pollard, D. D. (1985). Dilation and linkage of echelon cracks. Journal of Structural Geology, 7(5), 583-590.

Norrish, K., & Hutton, J. T. (1969). An accurate X-ray spectrographic method for the analysis of a wide range of geological samples. Geochimica et cosmochimica acta, 33(4), 431-453.

Oskarsson, N., Sigvaldason, G. E., & Steinthorsson, S. (1982). A dynamic model of rift zone petrogenesis and the regional petrology of Iceland. Journal of Petrology, 23(1), 28-74.

Óskarsson, N., Steinþórsson, S., Sigvaldason, G.E., (1985). Iceland Geochemical anomaly: origin, volcanotectonics, chemical fractionation and isotope evolution of the crust. Journal of Geophysics Research, 90 (B12), 10011–10025.

Owen, G. (1987). Deformation processes in unconsolidated sands. Geological Society of London, Special Publications, 29(1), 11-24.

Owen G (1996) Experimental soft sediment deformation: structures formed by the liquefaction of unconsolidated sands and some ancient examples. Sedimentology, 43, 279-293.

Owen G (2003) Load structures: gravity-driven sediment mobilisation in the shallow subsurface: Geological Society, London, Special Publications 216: 21-34. In: Subsurface Sediment Mobilisation, R. Van Rensbergen, R. R. Hillis, A. J. Maltman, C. K. Morley, G. Owen, M. Moretti, P. Alfaro (eds) (2011) Recognising triggers for soft-sediment deformation: current understanding and future directions: Sedimentary Geology 235: 133-140.

Owen, G., & Moretti, M. (2011). Identifying triggers for liquefaction-induced soft-sediment deformation in sands. Sedimentary Geology, 235(3), 141-147.

Owen, G., Moretti, M., & Alfaro, P. (2011). Recognising triggers for soft-sediment deformation: current understanding and future directions. Sedimentary Geology, 235(3), 133-140.

Pagel, M., Walgenwitz, F., & Dubessy, J. (1986). Fluid inclusions in oil and gas-bearing sedimentary formations. Collection colloques et séminaires-Institut français du pétrole, (44), 565-583.

Passey, S. R., & Jolley, D. W. (2008). A revised lithostratigraphic nomenclature for the Palaeogene Faroe Islands Basalt group, NE Atlantic Ocean. Earth and Environmental Science Transactions of the Royal Society of Edinburgh, 99(3-4), 127-158.

Passey, S., Hitchen, K., (2011) Cenozoic (igneous). In: Ritchie, J. D., Ziska, H., Johnson, H., & Evans, D. (eds). Geology of the Faroe-Shetland Basin and adjacent areas. British Geological Survey, Nottingham, UK.

Pasteris, J.D. & Wopenka, B. (1991). Raman spectra of graphite as indicators of degree of metamorphism. Canadian Mineralogist, 29, 143–153.

Paterson, W. S. B., (1981). The physics of glaciers. Pergamon Press, Oxford.

Paulsen, T. S., & Wilson, T. J. (2010). New criteria for systematic mapping and reliability assessment of monogenetic volcanic vent alignments and elongate volcanic vents for crustal stress analyses. Tectonophysics, 482(1), 16-28.

Planke, S., Alvestad, E., & Eldholm, O. (1999). Seismic characteristics of basaltic extrusive and intrusive rocks. The Leading Edge, 18(3), 342-348.

Planke, S., Rasmussen, T., Rey, S. S., & Myklebust, R. (2005). Seismic characteristics and distribution of volcanic intrusions and hydrothermal vent complexes in the Vøring and Møre basins. In: Petroleum Geology Conference series (Vol. 6) Geological Society of London, 833-844.

Pollard, D. D. (1973). Derivation and evaluation of a mechanical model for sheet intrusions. Tectonophysics, 19(3), 233-269.

Pollard, D. D., & Johnson, A. M. (1973). Mechanics of growth of some laccolithic intrusions in the Henry Mountains, Utah, II: bending and failure of overburden layers and sill formation. Tectonophysics, 18(3-4), 311-354.

Pollard, D. D., Muller, O. H., & Dockstader, D. R. (1975). The form and growth of fingered sheet intrusions. Geological Society of America Bulletin, 86(3), 351-363.

Pollock, M., Edwards, B., Hauksdóttir, S., Alcorn, R., & Bowman, L. (2014). Geochemical and lithostratigraphic constraints on the formation of pillow-dominated tindars from Undirhlíðar quarry, Reykjanes Peninsula, southwest Iceland. Lithos, 200, 317-333.

Polteau, S., Mazzini, A., Galland, O., Planke, S., & Malthe-Sørenssen, A. (2008). Saucer-shaped intrusions: occurrences, emplacement and implications. Earth and Planetary Science Letters, 266(1), 195-204.

Potter, J., Stasiuk, L. D., & Cameron, A. R. (Eds.). (1998). Petrographic Atlas of Canadian Coal Macerals and Dispersed Organic Matter. The Survey. Calgary.

Price, S., Brodie, J., Whitham, A., & Kent, R. A. Y. (1997). Mid-Tertiary rifting and magmatism in the Traill Ø region, East Greenland. Journal of the Geological Society, 154(3), 419-434.

Quirico, E., Montagnac, G., Rouzaud, J. N., Bonal, L., Bourot-Denise, M., Duber, S., & Reynard, B. (2009). Precursor and metamorphic condition effects on Raman spectra of poorly ordered carbonaceous matter in chondrites and coals. Earth and Planetary Science Letters, 287(1), 185-193.

Rawcliffe, H. J. (2016). Lava-water-sediment interaction: processes, products and petroleum systems (Doctoral dissertation, University of Glasgow).

Raymond, A. C., & Murchison, D. G. (1988). Development of organic maturation in the thermal aureoles of sills and its relation to sediment compaction. Fuel, 67(12), 1599-1608.

Raymond, A. C., & Murchison, D. G. (1989). Organic maturation and its timing in a Carboniferous sequence in the central Midland Valley of Scotland: comparisons with northern England. Fuel, 68(3), 328-334.

Raymond, A. C., & Murchison, D. G. (1991). Influence of exinitic macerals on the reflectance of vitrinite in Carboniferous sediments of the Midland Valley of Scotland. Fuel, 70(2), 155-161.

Re, G., White, J. D. L., & Ort, M. H. (2015). Dikes, sills, and stress-regime evolution during emplacement of the Jagged Rocks Complex, Hopi Buttes Volcanic Field, Navajo Nation, USA. Journal of Volcanology and Geothermal Research, 295, 65-79.

Re, G., White, J. D., Muirhead, J. D., & Ort, M. H. (2016). Subterranean fragmentation of magma during conduit initiation and evolution in the shallow plumbing system of the small-volume Jagged Rocks volcanoes (Hopi Buttes Volcanic Field, Arizona, USA). Bulletin of Volcanology, 78(8), 55.

Reynolds, P., Schofield, N., Brown, R. J., & Holford, S. (2016). The architecture of submarine monogenetic volcanoes–insights from 3D seismic data. Basin Research.

Richardson, J. A., Connor, C. B., Wetmore, P. H., Connor, L. J., & Gallant, E. A. (2015). Role of sills in the development of volcanic fields: Insights from lidar mapping surveys of the San Rafael Swell, Utah. Geology, 43(11), 1023-1026.

Rickwood, P., (1990). The anatomy of a dyke and the determination of propagation and magma flow directions. In: Parker, A.J., et al., (eds), Mafic dykes and emplacement mechanisms, Balkema, Rotterdam, 81–100.

Ridd, M. F. (1983). Aspects of the Tertiary geology of the Faeroe-Shetland Channel. In: Bott, M. H. P., Saxov, S., Talwani, M. & Thiede, J. (eds) Structure and development of the Greenland-Scotland Ridge. Plenum Press, New York, 91-108.

Ritchie, J. D., Gatliff, R. W., & Richards, P. C. (1999). Early Tertiary magmatism in the offshore NW UK margin and surrounds. In Geological Society, London, Petroleum Geology Conference series (Vol. 5), Geological Society of London, 573-584.

Ritchie, J. D., Johnson, H., & Kimbell, G. S. (2003). The nature and age of Cenozoic contractional deformation within the NE Faroe–Shetland Basin. Marine and Petroleum Geology, 20(5), 399-409.

Ritchie, J. D., Ziska, H., Johnson, H., & Evans, D. (eds) (2011). Geology of the Faroe-Shetland Basin and adjacent areas. British Geological Survey, Nottingham, UK.

Rodríguez-López, J. P., Meléndez, N., Soria, A. R., Liesa, C. L., & Van Loon, A. T. (2007). Lateral variability of ancient seismites related to differences in sedimentary facies (the synrift

Escucha Formation, mid-Cretaceous, eastern Spain). Sedimentary Geology, 201(3), 461-484.

Roedder, E. (1979). Fluid inclusion evidence on the environments of sedimentary diagenesis, a review. The Society of Economic Paleontologists and Mineralogists Special Publication, 26, 89-107.

Rohrman, M. (2007). Prospectivity of volcanic basins: Trap delineation and acreage de-risking. American Association of Petroleum Geologists Bulletin, 91(6), 915-939.

Rouzaud, J., Deldicque, D., Charon, E. & Pageot, J. (2015). Carbons at the heart of questions on energy and environment: a nanostructural approach. Comptes Rendus Geoscience, 347, 124–133.

Ross, P.-S., (2005). Volcanology of the Mawson Formation at Coombs and Allan Hills, South Victoria Land, Antarctica. PhD Thesis, University of Otago, Dunedin, 400 pp.

Ross, P. S., Peate, I. U., McClintock, M. K., Xu, Y. G., Skilling, I. P., White, J. D., & Houghton, B. F. (2005). Mafic volcaniclastic deposits in flood basalt provinces: a review. Journal of Volcanology and Geothermal Research, 145(3), 281-314.

Ross, P. S., & White, J. D. (July 2005). Unusually large clastic dykes formed by elutriation of a poorly sorted, coarser-grained source. Journal of the Geological Society, 162(4), 579-582.

Ross, P. S., & White, J. D. (November 2005). Mafic, large-volume, pyroclastic density current deposits from phreatomagmatic eruptions in the Ferrar large igneous province, Antarctica. The Journal of Geology, 113(6), 627-649.

Ross, P. S., & White, J. D. (2006). Debris jets in continental phreatomagmatic volcanoes: a field study of their subterranean deposits in the Coombs Hills vent complex, Antarctica. Journal of Volcanology and Geothermal Research, 149(1), 62-84.

Ross, P. S., White, J. D., Zimanowski, B., & Büttner, R. (2008). Multiphase flow above explosion sites in debris-filled volcanic vents: Insights from analogue experiments. Journal of Volcanology and Geothermal Research, 178(1), 104-112.

Ross, P. S., Delpit, S., Haller, M. J., Németh, K., & Corbella, H. (2011). Influence of the substrate on maar–diatreme volcanoes—an example of a mixed setting from the Pali Aike volcanic field, Argentina. Journal of Volcanology and Geothermal Research, 201(1), 253-271.

Ross, P. S., & White, J. D. (2012). Quantification of vesicle characteristics in some diatreme-filling deposits, and the explosivity levels of magma–water interactions within diatremes. Journal of Volcanology and Geothermal Research, 245, 55-67.

Rubin, A.M., (1995) Propagation of magma filled cracks. Annual Review of Earth and Planetary Sciences, 23, 287–336.

Rumph, B., Reaves, C.M., Orange, V.G. & Robinson, D.L. (1993) Structuring and Transfer Zones in the Faroe Shetland Basin in a Regional Tectonic Context. In: Petroleum Geology of Northwest Europe, Proceedings of the 4th Conference, The Geological Society of London, London, 999–1009.

Sæmundsson, K., (1979) Outline of the geology of Iceland. Jökull, 29, 7–28.

Santos, R. V., Dantas, E. L., de Oliveira, C. G., de Alvarenga, C. J. S., dos Anjos, C. W. D., Guimarães, E. M., & Oliveira, F. B. (2009). Geochemical and thermal effects of a basic sill on black shales and limestones of the Permian Irati Formation. Journal of South American Earth Sciences, 28(1), 14-24.

Saucedo, R., Macías, J. L., Ocampo-Díaz, Y. Z. E., Gómez-Villa, W., Rivera-Olguín, E., Castro-Govea, R., ... & Carrasco-Núñez, G. (2017). Mixed magmatic–phreatomagmatic explosions during the formation of the Joya Honda maar, San Luis Potosí, Mexico. In: Németh, K., Carrasco-Núñez, G., Aranda-Gómez, J. and Smith I.E.M. (eds), Monogenetic Volcanism, Geological Society, London, Special Publications, 446(1), 255-279.

Schipper, C.I., White, J.D.L., Houghton, B.F., Shimizu, N., Stewart, R.B., (2010). Explosive submarine eruptions driven by volatile-coupled degassing at Lo'ihi Seamount, Hawai'i. Earth and Planetary Science Letters, 295, 497–510.

Schipper, C. I., & White, J. D. (2016). Magma-slurry interaction in Surtseyan eruptions. Geology, 44(3), 195-198.

Schmid, A., Sonder, I., Seegelken, R., Zimanowski, B., Büttner, R., Gudmundsson, M. T., & Oddsson, B. (2010). Experiments on the heat discharge at the dynamic magma-water-interface. Geophysical Research Letters, 37(20), L20311.

Schofield, N., Stevenson, C., & Reston, T. (2010). Magma fingers and host rock fluidization in the emplacement of sills. Geology, 38(1), 63-66.

Schofield, N. J., Brown, D. J., Magee, C., & Stevenson, C. T. (2012). Sill morphology and comparison of brittle and non-brittle emplacement mechanisms. Journal of the Geological Society, 169(2), 127-141.

Schofield, N., & Jolley, D. W. (2013). Development of intra-basaltic lava-field drainage systems within the Faroe–Shetland Basin. Petroleum Geoscience, 19(3), 273-288.

Schofield, N., Alsop, I., Warren, J., Underhill, J. R., Lehné, R., Beer, W., & Lukas, V. (2014). Mobilizing salt: Magma-salt interactions. Geology, 42(7), 599-602.

Schofield, N., Holford, S., *et al. (*2015). Regional magma plumbing and emplacement mechanisms of the Faroe‐Shetland Sill Complex: implications for magma transport and petroleum systems within sedimentary basins. Basin Research, 29, 41-63.

Schopka, H. H., Gudmundsson, M. T., & Tuffen, H. (2006). The formation of Helgafell, southwest Iceland, a monogenetic subglacial hyaloclastite ridge: sedimentology, hydrology and volcano–ice interaction. Journal of Volcanology and Geothermal Research, 152(3), 359-377.

Schutter, S. R., (2003). Hydrocarbon occurrence and exploration in and around igneous rocks. In: Petford, N. and McCaffrey, K.J.W. (eds) Hydrocarbons in Crystalline Rocks. Geological Society of London, Special Publications, London, 214, 7-33.

Self, S. (1976). The recent volcanology of Terceira, Azores. Journal of the Geological Society, 132(6), 645-666.

Senger, K., Planke, S., Polteau, S., Ogata, K., & Svensen, H. (2014). Sill emplacement and contact metamorphism in a siliciclastic reservoir on Svalbard, Arctic Norway. Norwegian Journal of Geology, 94, 155-169.

Sheridan, M., and Wohletz, K., (1983). Hydrovolcanism: Basic considerations and review. Journal of Volcanology and Geothermal Research, 17 (1-4), 1-29.

Sigmundsson, F. (1991). Post-glacial rebound and asthenosphere viscosity in Iceland. Geophysical Research Letters, 18(6), 1131-1134.

Simpson, K., & McPhie, J. (2001). Fluidal-clast breccia generated by submarine fire fountaining, Trooper Creek Formation, Queensland, Australia. Journal of Volcanology and Geothermal Research, 109(4), 339-355.

Skilling, I. P. (1994). Evolution of an englacial volcano: Brown Bluff, Antarctica. Bulletin of Volcanology, 56(6), 573-591.

Skilling, I. P., White, J. D. L., & McPhie, J. (2002). Peperite: a review of magma–sediment mingling. Journal of Volcanology and Geothermal Research, 114(1), 1-17.

Skilling, I. P. (2009). Subglacial to emergent basaltic volcanism at Hlöðufell, south-west Iceland: a history of ice-confinement. Journal of Volcanology and Geothermal Research, 185(4), 276-289.

Smallwood, J. R., Staples, R. K., Richardson, K. R., & White, R. S. (1999). Crust generated above the Iceland mantle plume: from continental rift to oceanic spreading center. Journal of Geophysical Research: Solid Earth, 104, 22885-22902.

Smallwood, J. R., & Maresh, J. (2002). The properties, morphology and distribution of igneous sills: modelling, borehole data and 3D seismic from the Faroe-Shetland area. Geological Society of London, Special Publications, 197(1), 271-306.

Smallwood J. R., White R. S. (2002). Ridge-plume interaction in the North Atlantic and its influence on continental breakup and seafloor spreading. In: Jolley D. W., Bell B. R. (eds) The North

Atlantic Igneous Province: Stratigraphy, Tectonic, Volcanic and Magmatic Processes. Geological Society, London, Special Publications, 197, 15–37.

Smellie, J. L., & Skilling, I. P. (1994). Products of subglacial volcanic eruptions under different ice thicknesses: two examples from Antarctica. Sedimentary Geology, 91(1-4), 115-129.

Smellie, J. L., & Hole, M. J. (1997). Products and processes in Pliocene–Recent, subaqueous to emergent volcanism in the Antarctic Peninsula: examples of englacial Surtseyan volcano construction. Bulletin of Volcanology, 58(8), 628-646.

Smellie, J. L. (2000) Subglacial eruptions. In: Sigurdsson, H.; Houghton, B.; Rymer, H.; Stix, J.; McNutt, S., (eds.)), Encyclopedia of Volcanoes. Elsevier, Amsterdam, 403-418.

Smith, I. E. M., Blake, S., Wilson, C. J. N., & Houghton, B. F. (2008). Deep-seated fractionation during the rise of a small-volume basalt magma batch: Crater Hill, Auckland, New Zealand. Contributions to Mineralogy and Petrology, 155(4), 511-527.

Smythe, D. K. (1983). Faeroe-Shetland escarpment and continental margin north of the Faeroes. In: Bott, M.H.P., Saxov, S., Talwani, M., Thiede, J (eds) Structure and Development of the Greenland-Scotland Ridge, Springer US, New York, 109-119.

Sohn, Y.K., Chough, S.K., (1989). Depositional processes of the Suwolbong tuff ring, Cheju Island (Korea). Sedimentology, 36, 837–855.

Sohn, Y.K., Chough, S.K., (1992). The Ilchulbong tuff cone, Cheju Island, South Korea: depositional processes and evolution of an emergent, Surtseyan-type tuff cone. Sedimentology, 39, 523–544.

Sohn, Y., And Chough, S., (1993), The Udo tuff cone, Cheju Island, South Korea: transformation of pyroclastic fall into debris fall and grain flow on a steep volcanic cone slope. Sedimentology, 40(4), 769-786.

Sohn, Y., and Park, K., (2005). Composite tuff ring/cone complexes in Jeju Island, Korea: possible consequences of substrate collapse and vent migration. Journal of Volcanology and Geothermal Research, 141(1-2), 157-175.

Sohn, Y., Cronin, S., Brenna, M., Smith, I., Németh, K., White, J., Murtagh, R., Jeon, Y., and Kwon, C., (2011). Ilchulbong tuff cone, Jeju Island, Korea, revisited: A compound monogenetic volcano involving multiple magma pulses, shifting vents, and discrete eruptive phases. Geological Society of America Bulletin, 124(3-4), 259-274.

Solgevik, H., Mattsson, H., and Hermelin, O., (2007). Growth of an emergent tuff cone: Fragmentation and depositional processes recorded in the Capelas tuff cone, Sao Miguel, Azores. Journal of Volcanology and Geothermal Research, 159(1-3), 246-266.

Somerton, W. H. (1992). Thermal properties and temperature-related behavior of rock/fluid systems (Vol. 37). Elsevier, Amsterdam.

Sorrentino, L., Cas, R., and Stilwell, J., (2011). Evolution and facies architecture of Paleogene Surtseyan volcanoes on Chatham Islands, New Zealand, Southwest Pacific Ocean. Journal of Volcanology and Geothermal Research, 202(1-2), 1-21.

Sparks, R. S. J. (1978). The dynamics of bubble formation and growth in magmas: a review and analysis. Journal of Volcanology and Geothermal Research, 3(1-2), 1-37.

Sparks, R.S.J., Baker, L., Brown, R.J., Field, M., Schumacher, J., Stripp, G., Walters, A. (2006). Dynamical constraints on kimberlite volcanism, Journal of Volcanology and Geothermal Research, 155 (1), 18-48.

Spera, F. J. (1984). Carbon dioxide in petrogenesis III: role of volatiles in the ascent of alkaline magma with special reference to xenolith-bearing mafic lavas. Contributions to Mineralogy and Petrology, 88(3), 217-232.

Spry, A. (1962). The origin of columnar jointing, particularly in basalt flows. Journal of the Geological Society of Australia, 8(2), 191-216.

Squire, R.J., and McPhie, J., (2002), Characteristics and origin of peperite involving coarse-grained host sediment. Journal of Volcanology and Geothermal Research, 114, 45-61.

Stach, E. (1982). Stach's textbook of coal petrology. Lubrecht & Cramer Ltd, New York.

Stachel, T. 1990. The Ellendale Volcanic Field (Western Australia) – volcanology, petrography, and geochemistry of 4 pipes. PhD thesis, University of Wurzburg.

Stanistreet, I. G., & Hughes, M. J. (1984). Pseudoconglomerate and a re-examination of some paleoenvironmental controversies. Geology, 12(12), 717-719.

Stephenson, D., Loughlin, S.C., Millward, D., Waters, C.N. & Williamson, I.T., (2003), Carboniferous and Permian Igneous Rocks of Great Britain North of the Variscan Front, Geological Conservation Review Series, No. 27, Joint Nature Conservation Committee, Peterborough, 1-374 pages.

Stevenson, J. A., McGarvie, D. W., Smellie, J. L., & Gilbert, J. S. (2006). Subglacial and ice-contact volcanism at the Öræfajökull stratovolcano, Iceland. Bulletin of volcanology, 68(7-8), 737-752.

Stevenson, J. A., Gilbert, J. S., McGarvie, D. W., & Smellie, J. L. (2011). Explosive rhyolite tuya formation: classic examples from Kerlingarfjöll, Iceland. Quaternary Science Reviews, 30(1), 192-209.

Stevenson, J. A. (2014). A tuya is a flat-topped constructional table mountain formed during a subglacial volcanic eruption. (Definition).

Stoppa, F., Cundari, A., Rosatelli, G., & Woolley, A. R. (2003). Leucite melilitolites in Italy: genetic aspects and relationships with associated alkaline rocks and carbonatites. Periodico di mineralogia, 72(1), 223-251.

Stovall, W. K., Houghton, B. F., Hammer, J. E., Fagents, S. A., & Swanson, D. A. (2012). Vesiculation of high fountaining Hawaiian eruptions: episodes 15 and 16 of 1959 Kīlauea Iki. Bulletin of volcanology, 74(2), 441-455.

Suchý, V., Šafanda, J., Sýkorová, I., Stejskal, M., Machovič, V., & Melka, K. (2004). Contact metamorphism of Silurian black shales by a basalt sill: geological evidence and thermal modeling in the Barrandian Basin. Bulletin of Geosciences, 79(3), 133-145.

Svensen, H., Jamtveit, B., Planke, S., & Chevallier, L. (2006). Structure and evolution of hydrothermal vent complexes in the Karoo Basin, South Africa. Journal of the Geological Society, 163(4), 671-682.

Sweeney, J. J., & Burnham, A. K. (1990). Evaluation of a simple model of vitrinite reflectance based on chemical kinetics (1). American Association of Petroleum Geologists Bulletin, 74(10), 1559-1570.

Svensen, H., Aarnes, I., Podladchikov, Y. Y., Jettestuen, E., Harstad, C. H., & Planke, S. (2010). Sandstone dikes in dolerite sills: Evidence for high-pressure gradients and sediment mobilization during solidification of magmatic sheet intrusions in sedimentary basins. Geosphere, 6(3), 211-224.

Svensen, H., Corfu, F., Polteau, S., Hammer, Ø., & Planke, S. (2012). Rapid magma emplacement in the Karoo large igneous province. Earth and Planetary Science Letters, 325, 1-9.

Taddeucci, J., Sottili, G., Palladino, D. M., Ventura, G., & Scarlato, P. (2010). A note on maar eruption energetics: current models and their application. Bulletin of Volcanology, 72(1), 75-83.

Thomson, K., & Hutton, D. (2004). Geometry and growth of sill complexes: insights using 3D seismic from the North Rockall Trough. Bulletin of Volcanology, 66(4), 364-375.

Thomson, K. (2007). Determining magma flow in sills, dykes and laccoliths and their implications for sill emplacement mechanisms. Bulletin of Volcanology, 70(2), 183-201.

Thomson, K., & Schofield, N. (2008). Lithological and structural controls on the emplacement and morphology of sills in sedimentary basins. Geological Society, London, Special Publications, 302(1), 31-44.

Thorarinsson, S., Einarsson, T., Sigvaldason, G., & Elisson, G. (1964). The submarine eruption off the Vestmann Islands 1963–64. Bulletin Volcanologique, 27(1), 435-445.

Thordarson, T., & Self, S. (1993). The Laki (Skaftár Fires) and Grímsvötn eruptions in 1783–1785. Bulletin of Volcanology, 55(4), 233-263.

Thordarson, T., & Larsen, G. (2007). Volcanism in Iceland in historical time: Volcano types, eruption styles and eruptive history. Journal of Geodynamics, 43(1), 118-152.

Thordarson, T., & Höskuldsson, Á. (2008). Postglacial volcanism in Iceland. Jökull, 58, 197-228.

Thordarson, T., & Höskuldsson, A., (2014). Iceland: Second Edition. Edinburgh, Dunedin Academic Press.

Tibaldi, A. (2015). Structure of volcano plumbing systems: A review of multi-parametric effects. Journal of Volcanology and Geothermal Research, 298, 85-135.

Tissot, B. P., Pelet, R., & Ungerer, P. H. (1987). Thermal history of sedimentary basins, maturation indices, and kinetics of oil and gas generation. American Association of Petroleum Geologists Bulletin, 71(12), 1445-1466.

Tobin, R. C., & Claxton, B. L. (2000). Multidisciplinary thermal maturity studies using vitrinite reflectance and fluid inclusion microthermometry: a new calibration of old techniques. American Association of Petroleum Geologists Bulletin, 84(10), 1647-1665.

Tuffen, H., Gilbert, J., & McGarvie, D. (2001). Products of an effusive subglacial rhyolite eruption: Bláhnúkur, Torfajökull, Iceland. Bulletin of Volcanology, 63(2), 179-190.

Tuffen, H., McGarvie, D. W., Gilbert, J. S., & Pinkerton, H. (2002). Physical volcanology of a subglacial-to-emergent rhyolitic tuya at Rauðufossafjöll, Torfajökull, Iceland. Geological Society, London, Special Publications, 202(1), 213-236.

Tuffen, H. (2007). Models of ice melting and edifice growth at the onset of subglacial basaltic eruptions. Journal of Geophysical Research: Solid Earth, 112(B3), B03203.

Tuffen, H., Owen, J., & Denton, J. (2010). Magma degassing during subglacial eruptions and its use to reconstruct palaeo-ice thicknesses. Earth-Science Reviews, 99(1), 1-18.

Tuinstra, F. & Koenig, J.L. (1970). Raman spectrum of graphite. Journal of Chemical Physics, 53, 1126–1130.

Underhill, J. R., Monaghan, A. A., & Browne, M. A. (2008). Controls on structural styles, basin development and petroleum prospectivity in the Midland Valley of Scotland. Marine and Petroleum Geology, 25(10), 1000-1022.

Upton, B. G. J., Stephenson, D., Smedley, P. M., Wallis, S. M., & Fitton, J. G. (2004). Carboniferous and Permian magmatism in Scotland. In: Wilson, M., Neumann, E, R., Davies, G. R., Timmerman, M. J., Heeremans, M., Larsen, B. T. Permo-Carboniferous Magmatism and Rifting in Europe. Geological Society, London, Special Publications, 223(1), 195-218.

Urai, J. L., Schléder, Z., Spiers, C. J., & Kukla, P. A. (2008). Flow and transport properties of salt rocks. In: R. Littke, U. Bayer, D.Gajewski, S. Nelskamp (eds), Dynamics of complex intracontinental basins: the Central European Basin system, Springer, Berlin, 277-290.

Valentine, G. A., Krier, D., Perry, F. V., & Heiken, G. (2005). Scoria cone construction mechanisms, Lathrop Wells volcano, southern Nevada, USA. Geology, 33(8), 629-632.

Valentine, G. A., & Krogh, K. E. (2006). Emplacement of shallow dikes and sills beneath a small basaltic volcanic center–The role of pre-existing structure (Paiute Ridge, southern Nevada, USA). Earth and Planetary Science Letters, 246(3), 217-230.

Valentine, G. A., & Perry, F. V. (2007). Tectonically controlled, time-predictable basaltic volcanism from a lithospheric mantle source (central Basin and Range Province, USA). Earth and Planetary Science Letters, 261(1), 201-216.

Valentine, G. A. (2012). Shallow plumbing systems for small-volume basaltic volcanoes, 2: evidence from crustal xenoliths at scoria cones and maars. Journal of Volcanology and Geothermal Research, 223, 47-63.

Valentine, G., and White, J., (2012). Revised conceptual model for maar-diatremes: Subsurface processes, energetics, and eruptive products. Geology, 40(12), 1111-1114.

Valentine, G. A., & Cortés, J. A. (2013). Time and space variations in magmatic and phreatomagmatic eruptive processes at Easy Chair (Lunar Crater Volcanic Field, Nevada, USA). Bulletin of Volcanology, 75(9), 752.

Valentine, G. A., & de Vries, B. V. W. (2014). Unconventional maar diatreme and associated intrusions in the soft sediment-hosted Mardoux structure (Gergovie, France). Bulletin of Volcanology, 76(3), 807.

Valentine, G. A., Sottili, G., Palladino, D. M., & Taddeucci, J. (2015). Tephra ring interpretation in light of evolving maar–diatreme concepts: Stracciacappa maar (central Italy). Journal of Volcanology and Geothermal Research, 308, 19-29.

van Otterloo, J., & Cas, R. A. (2016). Low-temperature emplacement of phreatomagmatic pyroclastic flow deposits at the monogenetic Mt Gambier Volcanic Complex, South Australia, and their relevance for understanding some deposits in diatremes. Journal of the Geological Society of London, 173(4), 701-710.

Vink, G.E., (1984). A hotspot model for Iceland and the Voring Plateau. Journal of Geophysics Research, 89, 9949–9959

Waagstein, R. (1988). Structure, composition and age of the Faeroe basalt plateau. Geological Society, London, Special Publications, 39(1), 225-238.

Walderhaug, O. (1990). A fluid inclusion study of quartz-cemented sandstones from offshore mid-Norway-possible evidence for continued quartz cementation during oil emplacement. Journal of Sedimentary Research, 60(2), 203-210.

Walderhaug, O. (1994). Precipitation rates for quartz cement in sandstones determined by fluid-inclusion microthermometry and temperature-history modeling. Journal of Sedimentary Research, 64(2), 324-333.

Walker, G. P. (1964). Geological investigations in eastern Iceland. Bulletin of Volcanology, 27(1), 351-363.

Walker, G. P. (1999). Volcanic rift zones and their intrusion swarms. Journal of Volcanology and Geothermal Research, 94(1), 21-34.

Waters, C., Browne, M., Dean, M., & Powell, J. (2007). Lithostratigraphical framework for Carboniferous successions of Great Britain (onshore). British Geological Survey, London.

Watton, T. J., Jerram, D. A., Thordarson, T., & Davies, R. J. (2013). Three-dimensional lithofacies variations in hyaloclastite deposits. Journal of Volcanology and Geothermal Research, 250, 19-33.

Werner, R., & Schmincke, H. U. (1999). Englacial vs lacustrine origin of volcanic table mountains: evidence from Iceland. Bulletin of Volcanology, 60(5), 335-354.

White, R. S. (1989) Initiation of the Iceland Plume and Opening of the North Atlantic, Chapter 10, In: A. J. Tankard, H. R. Balkwill (eds), Extensional Tectonics and Stratigraphy of the North Atlantic Margins, AAPG Memoir, 149-154.

White, J. D. (1991). Maar-diatreme phreatomagmatism at Hopi Buttes, Navajo Nation (Arizona), USA. Bulletin of Volcanology, 53(4), 239-258.

White, R.S., Brown, J.W., and Smallwood J.R., (1995). The temperature of the Iceland plume and origin of outward-propagating V-shaped ridges. Journal of the Geological Society of London, 152, 1039–1045.

White, J. D. (1996). Impure coolants and interaction dynamics of phreatomagmatic eruptions. Journal of Volcanology and Geothermal Research, 74(3-4), 155-170.

White, J.D.L., McPhie, J., Skilling, I. (2000) Peperite: a useful genetic term. Bulletin of Volcanology. 62, 65–66.

White, J. D. L., & Houghton, B. (2000). Surtseyan and related phreatomagmatic eruptions. Encyclopedia of volcanoes. Academic, San Diego, 495-513.

White, J. D. L., & McClintock, M. K. (2001). Immense vent complex marks flood-basalt eruption in a wet, failed rift: Coombs Hills, Antarctica. Geology, 29(10), 935-938.

White JDL, Houghton BF (2006) Primary volcaniclastic rocks: Geology, 34: 677-680.White, J. D., & Ross, P. S. (2011). Maar-diatreme volcanoes: a review. Journal of Volcanology and Geothermal Research, 201(1), 1-29.

White, J. D., & Ross, P. S. (2011). Maar-diatreme volcanoes: a review. Journal of Volcanology and Geothermal Research, 201(1), 1-29.

White, J. D., & Valentine, G. A. (2016) Magmatic versus phreatomagmatic fragmentation: Absence of evidence is not evidence of absence. Geosphere, 12(5), 1478-1488.

Whitham, A. G., & Sparks, R. S. J. (1986). Pumice. Bulletin of Volcanology, 48(4), 209-223.

Wilson, L., & Head, J. W. (2002). Heat transfer and melting in subglacial basaltic volcanic eruptions: implications for volcanic deposit morphology and meltwater volumes. Geological Society, London, Special Publications, 202(1), 5-26.

Wohletz, K. H. (1983). Mechanisms of hydrovolcanic pyroclast formation: grain-size, scanning electron microscopy, and experimental studies. Journal of Volcanology and Geothermal Research, 17(1), 31-63.

Wohletz, K. H., & Sheridan, M. F. (1983). Hydrovolcanic explosions; II, Evolution of basaltic tuff rings and tuff cones. American Journal of Science, 283(5), 385-413.

Wohletz, K.H., McQueen, R.G., (1984). Experimental studies of hydromagmatic volcanism. In: Explosive Volcanism: Inception, Evolution and Hazards. Studies in Geophysics, National Academy Press, Washington, DC, 158-169.

Wohletz, K., (1986). Explosive magma-water interactions: Thermodynamics, explosion mechanisms, and field studies. Bulletin of Volcanology, 48(5), 245-264.

Wohletz, K. (2002). Water/magma interaction: some theory and experiments on peperite formation. Journal of Volcanology and Geothermal Research, 114(1), 19-35.

Wolfe, J. A. (1980). Fluidization versus phreatomagmatic explosions in breccia pipes. Economic Geology, 75(7), 1105-1109.

Wolfe, C.J., Bjarnason, I.T., Van Decar, J.C, Solomon, S.C., (1997). Seismic structure of the Iceland mantle plume. Nature, 385, 245–247

Wood, C. A. (1980). Morphometric evolution of cinder cones. Journal of Volcanology and Geothermal Research, 7(3), 387-413.

Wopenka, B., & Pasteris, J. D. (1993). Structural characterization of kerogens to granulite-facies graphite: applicability of Raman microprobe spectroscopy. The American Mineralogist, 78(5-6), 533-557.

Wright, K. A., Davies, R. J., Jerram, D. A., Morris, J., & Fletcher, R. (2012). Application of seismic and sequence stratigraphic concepts to a lava-fed delta system in the Faroe‐Shetland Basin, UK and Faroes. Basin Research, 24(1), 91-106.

Wright, K. A. (2013) Seismic Stratigraphy and Geomorphology of Palaeocene Volcanic Rocks, Faroe-Shetland Basin. Doctoral thesis, Durham University.

Yui, T. F., Huang, E., & Xu, J. (1996). Raman spectrum of carbonaceous material: a possible metamorphic grade indicator for low-grade metamorphic rocks. Journal of Metamorphic Geology, 14(2), 115-124.

Zank, J., Kind, M. & Schlünder, E. U. (2001). Particle growth and droplet deposition in fluidised bed granulation. Powder Technology, 120, 76–81.

Zanon, V., Pacheco, J., & Pimentel, A. (2009). Growth and evolution of an emergent tuff cone: Considerations from structural geology, geomorphology and facies analysis of São Roque volcano, São Miguel (Azores). Journal of Volcanology and Geothermal Research, 180(2), 277-291.

Zhang, Y. (1999). A criterion for the fragmentation of bubbly magma based on brittle failure theory. Nature, 402(6762), 648-650.

Zhou, Z., & Fyfe, W. S. (1989). Palagonitization of basaltic glass from DSDP Site 335, Leg 37: Textures, chemical composition, and mechanism of formation. American Mineralogist, 74(9), 1045-1053.

Zimanowski, B., Fröhlich, G., & Lorenz, V. (1991). Quantitative experiments on phreatomagmatic explosions. Journal of Volcanology and Geothermal Research, 48(3), 341-358.

Zimanowski, B., Fröhlich, G., & Lorenz, V. (1995). Experiments on steam explosion by interaction of water with silicate melts. Nuclear Engineering and Design, 155(1), 335-343.

Zimanowski, B., Büttner, R., Lorenz, V., & Häfele, H. G. (1997). Fragmentation of basaltic melt in the course of explosive volcanism. Journal of Geophysical Research: Solid Earth, 102(B1), 803-814.

Zimanowski, B. (1998). Phreatomagmatic explosions. From magma to tephra. Elsevier, Amsterdam, 4, 25-53.

Zimanowski, B., & Büttner, R. (2002). Dynamic mingling of magma and liquefied sediments. Journal of Volcanology and Geothermal Research, 114(1), 37-44.

Zimanowski, B., & Büttner, R. (2003). Phreatomagmatic explosions in subaqueous volcanism. In: Explosive subaqueous volcanism, J. D. L. White, J. L. Smellie, D. A. Clague (eds), American Geophysical Union, Washington, D. C., 51-60.

Zimanowski, B., Wohletz, K., Dellino, P., & Büttner, R. (2003). The volcanic ash problem. Journal of Volcanology and Geothermal Research, 122(1), 1-5.

10. Appendix

10.1. Owyhee Paper

Published in the Bulletin of Volcanology.

Bull Volcanol (2016) 78:42
DOI 10.1007/s00445-016-1035-2

RESEARCH ARTICLE

Extensive soft-sediment deformation and peperite formation at the base of a rhyolite lava: Owyhee Mountains, SW Idaho, USA

Charlotte E. McLean[1] · David J. Brown[1] · Heather J. Rawcliffe[1]

Received: 26 October 2015 / Accepted: 21 April 2016

Abstract In the Northern Owyhee Mountains (SW Idaho), a >200-m-thick flow of the Miocene Jump Creek Rhyolite was erupted on to a sequence of tuffs, lapilli tuffs, breccias and lacustrine siltstones of the Sucker Creek Formation. The rhyolite lava flowed over steep palaeotopography, resulting in the forceful emplacement of lava into poorly consolidated sediments. The lava invaded this sequence, liquefying and mobilising the sediment, propagating sediment subvertically in large metre-scale fluidal diapirs and sediment injectites. The heat and the overlying pressure of the thick Jump Creek Rhyolite extensively liquefied and mobilised the sediment resulting in the homogenization of the Sucker Creek Formation units, and the formation of metre-scale loading structures (simple and pendulous load casts, detached pseudonodules). Density contrasts between the semi-molten rhyolite and liquefied sediment produced highly fluidal Rayleigh-Taylor structures. Local fluidisation formed peperite at the margins of the lava and elutriation structures in the disrupted sediment. The result is a 30–40-m zone beneath the rhyolite lava of extremely deformed stratigraphy. Brittle failure and folding is recorded in more consolidated sediments, indicating a differential response to loading due to the consolidation state of the sediments. The lava-sediment interaction is interpreted as being a function of (1) the poorly consolidated nature of the sediments, (2) the thickness and heat retention of the rhyolite lava, (3) the density contrast between the lava and the sediment and (4) the forceful emplacement of the lava. This study demonstrates how large lava bodies have the potential to extensively disrupt sediments and form significant lateral and vertical discontinuities that complicate volcanic facies architecture.

Keywords Peperite · Rhyolite · Soft-sediment deformation · Fluidisation

Editorial responsibility: P-S Ross

✉ Charlotte E. McLean
c.mclean.1@research.gla.ac.uk

[1] School of Geographical and Earth Sciences, University of Glasgow, Gregory Building, Lilybank Gardens, Glasgow G12 8QQ, UK

Published online: 13 May 2016

Introduction

Rhyolite magmas typically extrude comparatively small-volume lava domes of high viscosity, yet some rhyolitic volcanic fields produce voluminous lava flows, often hundreds of metres thick (Bonnichsen 1982; Henry et al. 1990; Bonnichsen and Kauffman 1987; Branney et al. 2008). Large volume silicic volcanism producing extensive, high temperature silicic lava flows and lava-like ignimbrites is characterised as "SR-type", or "Snake River-type" volcanism by Branney et al. (2008) and is typical of the bimodal Columbia River-Yellowstone Volcanic Province in the NW of the USA. Thick rhyolite lava flows (>50 m) can impose huge amounts of downward force and heat on to the underlying substrate. When this substrate is soft, unconsolidated sediment, the effects of loading and heat can significantly modify the local stratigraphic architecture, either by local compaction and induration (Christiansen and Lipman 1966; Henry et al. 1990) or sediment fluidisation and peperite formation (Kokelaar 1982). Exposure of the contact between rhyolite lava flows and underlying sediment is rare, notably because rhyolite lava domes tend to form as opposed to lava flows (Branney et al. 2008) and can be poorly exposed either due to insufficient erosion or talus cover (Dadd 1992; Manley 1996). A road-cut exposure on Route 95 (N 43° 24′ 26.1″, W 116° 51′ 54.4″) through the Jump Creek Rhyolite (JCR), a

SR-type rhyolite lava flow, in the Owyhee Mountains, SW Idaho, provides a valuable opportunity to study the contact between a voluminous rhyolite lava flow and the underlying sediments, allowing for the construction of a detailed 2-D cross-section through the lava pile and the volcaniclastic sediment substrate, the Sucker Creek Formation (SCF) (Bonnichsen et al. 2004; Bonnichsen and Godchaux 2006).

The majority of research recording disruption along a rhyolite-sediment contact documents the remobilisation of sediments and peperite formation surrounding rhyolitic *intrusive* bodies (e.g. Hanson and Schweickert 1982; Kokelaar 1982; Hanson and Wilson 1993; Hanson and Hargrove 1999; Dadd and Van Wagoner 2002; Donaire et al. 2002; Skilling et al. 2002; Németh et al. 2008). In contrast, there have been very few studies on peperite formation and sediment fluidisation at the base of a rhyolite *lava flow* (Henry et al. 1990; Tuffen et al. 2001; Branney et al. 2008), where the sediment substrate is often less confined and where surface topography and environmental setting (e.g. water-logged sediments) are important factors (Skilling et al. 2002). Determining the processes that occur at the base of rhyolite lavas is important for a number of reasons, including the interpretation of volcanic successions in difficult ancient terranes where textures can often be obscured, and understanding the flow mechanics of large volume lava flows over soft substrates.

This paper presents a field-based textural analysis of the complex and extensive deformation along a rhyolite lava-sediment contact and identifies and discusses the formation of metre-scale structures formed in fluid-saturated sediments beneath thick lava flows (>50 m), including: (1) brittle failures and folding, (2) soft-sediment deformation structures (diapirs and elutriation), (3) reverse-density structures (load casts, pseudonodules) and (4) peperite. The origin of widespread deformation beneath the JCR is addressed by considering the consolidation and water saturation of the sediments, the volume of loading, the rate of cooling of the lava flow, the density contrast between the rhyolite and sediments and the palaeotopography at time of lava emplacement. We propose that due to the thickness and heat retention of rhyolite flows, the likelihood of prolonged fluidisation and liquefaction increases, allowing deformation structures to be up to ten times larger than the submetre-scale deformation commonly identified in basalt systems (Needham 1978; Hall and Els 2002; Waichel et al. 2007).

Nomenclature and terminology

Soft-sediment deformation structures occur in completely or partially unconsolidated, fluid-saturated sediments and form when sediments are remobilised by any of several driving mechanisms: liquefaction, fluidisation, reverse-density gradients and shear stress (Mills 1983; Jones and Omoto 2000). The remobilisation of sediment is initiated by several different "triggers", including: (1) rapid sediment loading, (2) seismic activity, (3) slope failure, (4) heat and (5) oscillation of water waves and groundwater currents (Owen et al. 2011). The loading of a lava on to unconsolidated sediments is also considered a trigger for soft-sediment deformation (e.g. Owen 1996; Jones and Omoto 2000; Hall and Els 2002). The remobilisation of sediments is primarily driven by liquefaction and/or fluidisation and is dependent on pore fluid pressure (Maltman and Bolton 2003; Owen et al. 2011). The increase in pore fluid pressure can occur by both internal and external means, either by the application of a load with which pore fluid drainage is unable to keep pace and remain at constant hydrostatic pressure or by pore fluid vaporisation and expansion (Mills 1983).

Both liquefaction and fluidisation can be defined as the rapid breakdown of the grain supported structure of unconsolidated or partially consolidated sediments (Mills 1983). Here, we define liquefaction as having occurred when sediment is supported solely by pore fluid and there is little or no cohesion between grains and thus, no strength (Allen 1982; Owen 1996, 2003; Owen et al. 2011). The sediment unit can then deform as a fluid (Maltman and Bolton 2003). Deformation by liquefaction occurs homogeneously throughout the sediment unit or units. Fluidisation is defined as the transmitting of fluids through sediment causing the particles to become supported and entrained within the fluid (Allen 1982; Owen 1996; Skilling et al. 2002; Owen et al. 2011). The shear stress of the upward directed fluid matches the weight of the grains (Owen et al. 2011). Fluidisation typically occurs locally within a unit, with fluid movement controlled by vertical conduits (e.g. fluid escape structures and clastic dykes) (Owen et al. 2011). When mobilised, the sediment will become entrained in this upward moving current, forming sediment diapirs and elutriation structures.

Geological overview

Geological history and setting

The JCR, the focus of this study, sits at the intersection of the Oregon-Idaho Graben (OIG) and the Western Snake River Plain (WSRP) (Fig. 1a, b). The OIG is a Miocene-age, N-S-trending, extensional graben situated in southwestern Idaho and southeastern Oregon at the most northerly extent of the Basin and Range Province (Pierce and Morgan 1992; Manley 1995; Cummings et al. 2000; Wood and Clemens 2002) (Fig. 1a). The WSRP, an extensional graben associated with the bimodal Colombia River-Yellowstone Volcanic Province, partially cuts the north of the OIG (Wood and Clemens 2002) (Fig. 1a). Lake Bruneau, a lake equivalent to the size of the present day Great Lakes of North America, filled the OIG

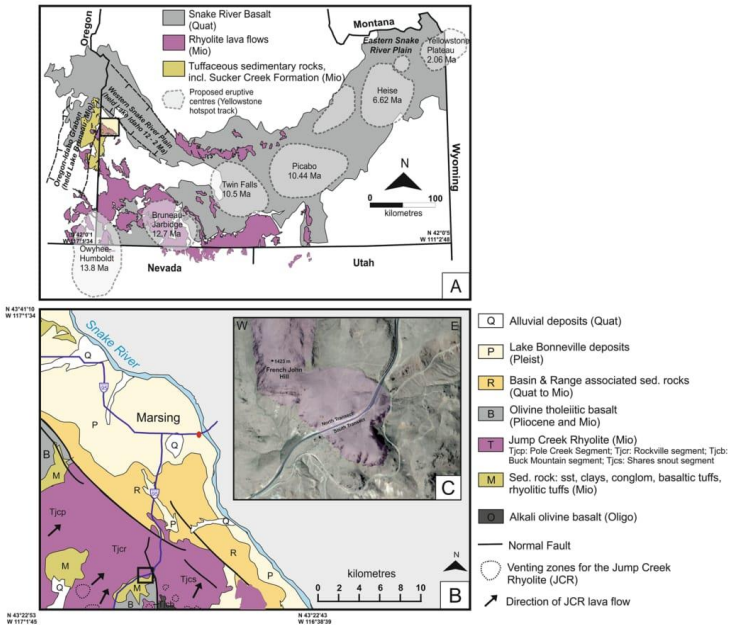

Fig. 1 Location map of the study area. **a** Map primarily of S. Idaho and SE. Oregon, showing the distribution of Miocene rhyolite lava flows and the Sucker Creek Formation. Note arcuate geometry of the Snake River Plain shown in *grey*. Proposed eruptive centres of the Yellowstone hotspot track highlighted and dates of initial volcanism specified. Figure adapted from Walker and MacLeod (1991), Pierce and Morgan (1992), Cummings et al. (2000) and Lewis et al. (2012). Owyhee Mountains highlighted by *box*. **b** Geological map of field area, south of the Snake River (Bonnichsen and Godchaux 2006). "Owyhee Front" rhyolite venting zones highlighted by *dotted areas*, and direction of lava flows indicated (Bonnichsen et al. 2004). The Jump Creek Rhyolite JCR is differentiated into segments. Study locality boxed. **c** Aerial photograph of French John Hill and the road-cut locality, showing the position of the north and south transects illustrated in Fig. 2. The JCR lava lobe is highlighted in *purple*

during the Mid-Late Miocene (Warner 1977). Thick accumulations of sediment (estimates between 500 and 2000 m) were deposited into Lake Bruneau, are now recognised as the Mascall Formation, the Sucker Creek Formation, the Drip Spring Formation, and the Trout Creek Formation (Warner 1977; Altaner and Grim 1990; Cummings et al. 2000), and are exposed today mainly in SW Oregon (Kimmel 1982) (Fig. 1a).

The cessation of OIG development at around 11 Ma was marked by a switching of regional tectonic stresses and the formation of the northwest-orientated WSRP (Cummings et al. 2000). The WSRP is situated 100 km north of the Yellowstone hotspot trail (Pierce and Morgan 1992; Shervais and Hanan 2008) (Fig. 1a). The thermal anomaly of the Yellowstone hotspot softened the lithosphere, triggering failure along planes with weak lithostatic strength and initiated rifting (Pierce and Morgan 1992; Wood and Clemens 2002; Bonnichsen et al. 2004, 2008). Rifting of the WSRP began at ~12 Ma, correlating with the passage of the hotspot to the south and ceased at ~7 Ma (Pierce and Morgan 1992; Wood and Clemens 2002; Bonnichsen et al. 2004). The low topography of the WSRP was filled with Lake Idaho from its formation at 12 to 2 Ma (Wood and Clemens 2002; Branney et al. 2008) (although it is unclear if the lake was consistently present during this time) (Bonnichsen et al. 2004). It is estimated that Lake Idaho covered an area of 20,000 km^2 at its maximum (Branney et al. 2008).

Associated with the initial rifting of the WSRP, between 11.7 and 11.0 Ma, localised rhyolite lavas, the "Owyhee Front volcanism" (the Jump Creek Rhyolite lava, the Reynolds Creek Rhyolite lava, the Cerro el Otoño Dome Field and the Wilson Creek Ignimbrite) were extruded from venting zones at the margins of the WSRP (Pierce and Morgan 1992; Perkins and Nash 2002; Bonnichsen et al. 2004, 2008; Bonnichsen

and Godchaux 2006; Fig. 1b). Large lava sheets were formed rather than rhyolite domes due to high temperatures and high effusion rates (Bonnichsen and Kauffman 1987).

The Jump Creek Rhyolite lava (11.1 ± 0.2 Ma)

The Jump Creek Rhyolite is the most extensive of the Owyhee Front rhyolite lavas, covering an area of up to 100 km^2 and is locally up to 300 m thick (Kittleman et al. 1965; Cummings et al. 2000; Bonnichsen et al. 2004). Isotopic dating (K/Ar) indicates an age of 11.1 ± 0.2 Ma (Rockville Segment, see below) (Armstrong et al. 1980), which suggests an association with the beginning of the WSRP rifting event (Bonnichsen and Godchaux 2006). Age and chemical similarities with the lavas extruded from the Bruneau-Jarbidge hotspot centre, a Late Miocene Yellowstone hotspot centre (Fig. 1a), suggests the JCR, and the other Owyhee Front rhyolites, were associated with the same magmatic and tectonic events that erupted the rhyolite magmas at the Bruneau-Jarbidge centre (Bonnichsen et al. 2004).

Bonnichsen et al. (2004) provide a detailed account of the characteristics, petrographic ages and geochemistry of the JCR, which is summarised here. The JCR can be separated into four distinctive units: the Shares Snout Segment, the Rockville Segment, the Pole Creek Top Segment and the Buck Mountain Segment, which are separated by screens of older rock formations (Bonnichsen et al. 2004). These lavas typically flowed from vents in the southwest to the northeast towards the southern margins of the WSRP (Fig. 1a). It is suggested that some of the lavas flowed over steep escarpments and/or into Lake Idaho, where magma-water interactions brecciated the lava flows (Bonnichsen et al. 2004). This study concentrates on a portion of the Rockville Segment. The Rockville Segment has a typical thickness of 50 to 200 m, and its volume has been estimated at 5–15 km^3 (Bonnichsen et al. 2004).

The Sucker Creek Formation (Mid-Late Miocene)

The Sucker Creek Formation (SCF) is a lacustrine and fluvial succession (flood plain) consisting of lignite-rich shales (hydrocarbon-bearing), clay-rich siltstones, sandstones and volcaniclastic sediments and tuffs, which were initially deposited in the lacustrine and fluvial systems associated with Lake Bruneau and later Lake Idaho in the Mid-Late Miocene (Altaner and Grim 1990; Warner 1977). The formation also contains some welded and non-welded ignimbrites and minor rhyolite flows (Walker and MacLeod 1991). Sediments were deposited by southeast to northwest flowing fluvial systems, originating from the uplifted volcanic terranes on the eastern margin of the OIG in SW Idaho (Cummings et al. 2000). The SCF has been dated using $^{40}Ar/^{39}Ar$ to 14.93 ± 0.08 Ma, from a silicic tuff from SE Oregon (Perkins et al. 1998). Widespread sedimentation of the SCF continued into the Late Miocene and is associated with the last stage of evolution of the OIG, dated to 12.6–10.5 Ma (Cummings et al. 2000). The development of Lake Idaho around this time (12 Ma), suggests the SCF was likely to have been deposited into the drainage system of Lake Idaho in the latter stages of SCF deposition. Late Miocene silicic eruptions from the Owyhee Front volcanism, Bruneau-Jarbidge hotspot centre and the caldera forming rhyolite eruptions on the flanks of the OIG, deposited ash and volcanic detritus into these systems and were later reworked (Cummings et al. 2000).

Field observations

In the Northern Owyhee Mountains (SW Idaho) (Fig. 1b), the Rockville Segment of the JCR was partially erupted on to an unconsolidated/poorly consolidated sequence of the SCF (Bonnichsen et al. 2004) (Fig. 1b). The key exposure in this study is located on opposing sides of an ~500 m long road cut (North and South transects, Fig. 2) along Route 95, located at the base of French John Hill (N 43° 24′ 26.1″, W 116° 51′ 54.4″) (Fig. 1c). This exposure provides a vertical section, ~30 to 40 m high, through the rhyolite lava and underlying volcaniclastic succession, allowing for detailed examination of the interaction that occurred at this contact.

Lithofacies of the Sucker Creek Formation

The sediment substrate exposed in the road cut consists of various tuffs and reworked tuffs representing a succession of ash fall deposits deposited in both terrestrial and lacustrine environments. Ash was deposited into shallow bodies of water associated with fluvial systems and small, localised lakes connected to Lake Idaho (Branney et al. 2008) (Table 1). Subaerial exposure between the deposition events allows for the oxidation of the top of the unit and the possible development of a thin palaeosol, reflecting the ephemeral nature of the lacustrine system (Table 1; Fig. 3). The presence of a coarse, fluvial conglomerate unit (Fig. 2f), further supports the interpretation of a continually fluctuating system of small, ephemeral lakes, large fluvial streams and terrestrial environment. There is evidence for steep, pronounced topography, such as fault escarpments, due to the presence of a coarse mass flow deposit (volcaniclastic breccia).

Extensive liquefaction and fluidisation of the sediment substrate, due to the emplacement of the lava, has resulted in a chaotic mix of these volcaniclastic sediments, classified as a "megabreccia" by Bonnichsen et al. (2004). The volcaniclastic and sedimentary succession is divided into non-disrupted units (NU; that can be logged) and disrupted units (DU). From field relationships, the majority of the deformation occurs in the chaotic units above the NU logged in

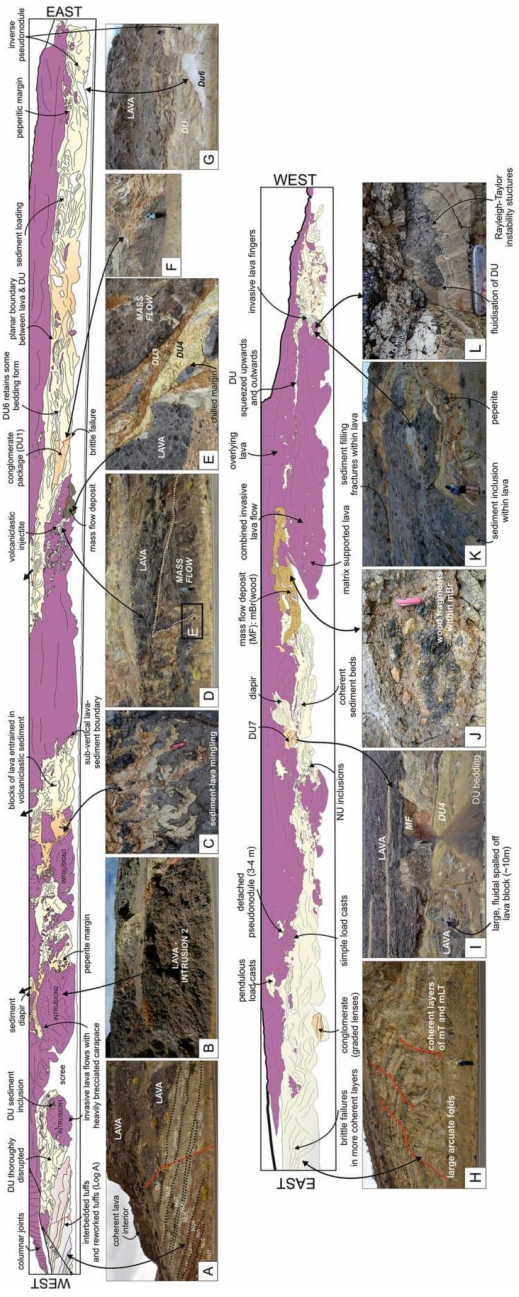

Fig. 2 *North*: line tracing of North Transect with associated field images. See Tables 1 and 2 for lithofacies codes. *Purple shading* represents the JCR. Peperite is recognised at the base of the JCR and around the "intrusions". Diapirs are observed and recorded in the disrupted sediment (DU). **a** Stratified tuffs and lapilli tuffs (see Fig. 3 for detail) displaced by normal faulting. In the *top left of the photograph*, the non-brecciated interior of the lava is observed ~200 m behind the road cut. **b** Invasive lava flow lobe burrowed into soft tuff units. **c** DU interdigitates with lava. **d** Fluidised sediment injectite exploit the boundary between lava and the unfluidised, coherent massive volcaniclastic breccia (mass flow deposit). *Inset*: **e** close-up image of interaction production in (**d**). Orange mT (DU3) and yellow mLT (DU4) thoroughly disrupted and fluidised during emplacement. Spalled lava blocks with cooled and quenched margins within partially homogenised sediment. **f** Intact bedding in the conglomerate unit (DU1). Minor faulting displaces conglomerate. **g** DU6 has a wave-like geometry whilst *orange*, *yellow*, *red* and *grey* DU subunits are intermixed with each other. *South*: line tracing of South Transect with associated field images. Density contrast structures and loading structures are recognised throughout (e.g. pendulous load casts, detached pseudonodules and diapirs). **h** Minimal fluidisation and liquefaction at the eastern edge of the road-cut, although brittle failures and folding are evident in more coherent sediment packages. **i** Autobrecciated lava flow burrowing into DU and spalling off fragments of rhyolite, which are quenching into sediment. Mass flow deposit (*MF*) remains coherent and is relatively undistorted. **j** Wood fragments within the mass flow deposit. **k** Lava fingers projecting into sediment. Fractures injected by sediment within lava body. Sediment inclusions (mT, mLT) apparent within lava. **l** Fine-grained autobrecciated lava fingers with sediment "replacing" matrix. Loading structures are apparent at a micro-scale

Table 1 Description and mechanisms of emplacement of the non-disrupted units (NU)

Subunit	Thickness (m)	Description	Mechanism
NU1	1.4	Light-grey, planar-stratified, pumice-rich lapilli tuff (//sLTp). Variable and diffuse normal and reverse grading is evident and the unit is composed of alternating fine to coarse tuff and lapilli tuff (between 4 and 14 mm) (Fig. 3d, e). Towards the top 20 cm of the unit, fine, black, vitreous grains of obsidian and perlitic rhyolite become evident within the fine ash matrix.	Terrestrial ash fall deposit. Atypical SR-type parallel-stratified rhyolitic ash fall deposit (Branney et al. 2008).
NU2	0.6	Grey, massive, pumice-rich tuff (mTp) where the top 40 cm has been reddened and oxidised.	Ash fall possibly deposited into a shallow body of water associated with the fluvial systems and small lakes connected to Lake Idaho (Cummings et al. 2000). Subaerial exposure between the deposition of NU2 and NU3 allows for oxidation of the top of the unit and the possible development of a thin palaeosol, reflecting the ephemeral nature of the lacustrine system.
NU3	0.98	Grey diffuse-stratified eutaxitic lapilli tuff (dsLTe). Contains 10 % quartz crystals, <5 % vitrified lithics and ~50 % of pumice fiamme in an ash matrix.	Terrestrial deposition from a high temperature column (possibly collapsed to form a pyroclastic density current?). Pumice lapilli welded and/or sheared.
NU4	0.92	Grey, crystal-rich (plagioclase feldspar) massive tuff (mTcr) where the top 20 cm has been reddened and oxidised.	Ash fall possibly deposited into a shallow body of water associated with the fluvial systems and small lakes connected to Lake Idaho (Cummings et al. 2000). Subaerial exposure between the deposition of NU4 and NU5 allows for oxidation of the top of the unit and the possible development of a thin palaeosol, reflecting the ephemeral nature of the lacustrine system.
NU5	4	Greenish-grey, massive siltstone (reworked mT) with no crystals or lithics.	Ash fall deposit reworked by gentle aqueous currents in a lacustrine-type environment (Lake Idaho?).
NU6	1.4	White, massive tuff (mT). Clearly visible without a hand lens are large bubble cuspate shards (up to 15 mm) within a frothy ash matrix.	Terrestrial ash fall deposit. Typical SR-type parallel-stratified rhyolitic ash fall deposit (Branney et al. 2008).
NU7 and NU8	3 and 2	Compositionally similar massive, coarse siltstones (reworked mLT), however, the units are defined by reddened, oxidised tops. Minor mingling of NU8 and autobrecciated rhyolite lava is present within the top 40 cm of NU8.	Ash fall deposit reworked by gentle aqueous currents in a lacustrine-type environment (Lake Idaho?).

m massive, *//s* parallel-stratified, *ds* diffusely stratified, *T* tuff, *LT* lapilli tuff, *p* pumice rich, *cr* crystal rich, *e* eutaxitic

Fig. 3. The non-disrupted and disrupted units are mostly described using primary volcaniclastic terminology (after White and Houghton 2006). In cases where there is definitive evidence of reworking or fluvial/lacustrine deposition, we have used secondary volcaniclastic terminology.

Non-disrupted units: intact volcaniclastic succession (NU1–8)

At the western edge of the North Transect, the original stratigraphy of the NU has only been mildly disrupted by the overlying lava (Figs. 2a and 3; Table 1). The succession mostly represents typical Snake River-type volcanism defined by Branney et al. (2008), including abundant bi- and tri- cuspate, bubble wall shards, very few lithics and stratified beds, which are commonly less than 5 m thick (Branney et al. 2008; Ellis et al. 2013).

An ash fallout deposition is inferred for NU4–8 due to lateral consistency and lack of grading and/or stratification (Branney et al. 2008). NU5, NU7 and NU8 were likely deposited into a quiescent water body as these units are significantly thicker (2–4 m thick) than the other NU and lack

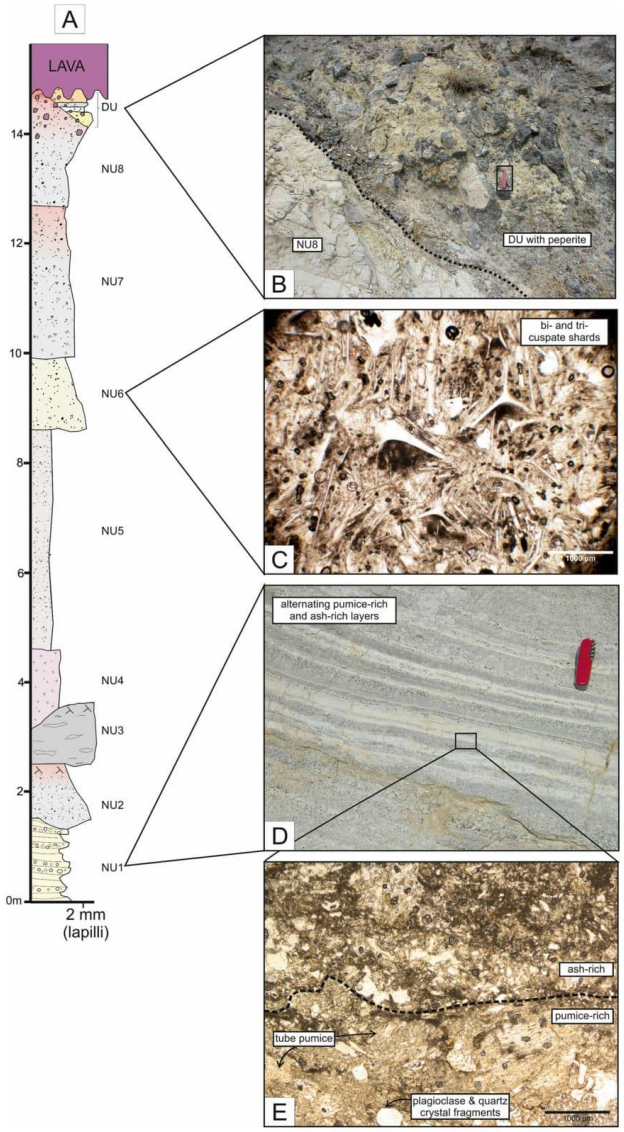

Fig. 3 **a** Graphic log through layered non-disrupted units (NU). Location of A noted in Fig. 2a. A sequence of tuffs, lapilli tuffs and reworked siltstones (see Table 1 for details). An ephemeral lacustrine environment is suggested by the oxidised tops on some of the subunits and the massive structure of some of the units. **b** Disrupted units (*DU*) interact with overlying lava forming blocky peperite. **c** Photomicrograph (ppl) of well-preserved bi- and tri- cuspate silicic shards in NU6, typical of Snake River volcanism (Branney et al. 2008). **d** Field photograph of stratified NU1. **e** Photomicrograph (ppl) of NU1. Alternating tube-pumice-rich and ash-rich layers in non-welded tuff

stratification. The cuspate shards in NU6 are on a centimetre scale indicating the vesicles or bubbles that formed during fragmentation were on a macroscopic scale (Branney et al. 2008). NU4–8 are compositionally and texturally similar (NU6 contains shards), indicating NU4–8 were erupted from the same or similar sources. Palaeosols between some of the units (Table 1) imply periods of volcanic quiescence between eruption and deposition of units. The indication of highly explosive eruptions and a similarity to other SR-type tuffs in basins south of the Snake River Plain (e.g.

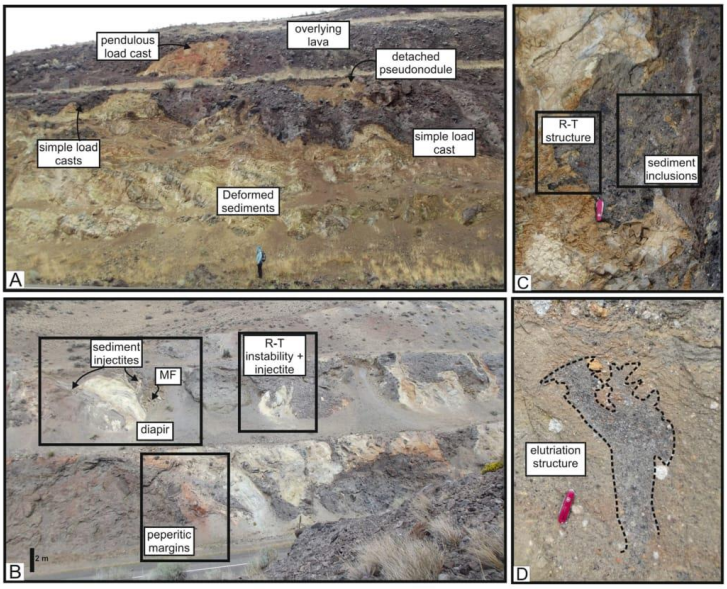

Fig. 4 Soft-sediment deformation features: **a** density contrast and loading structures forming at the interface between the JCR and underlying Sucker Creek Formation (*SCF*). Simple and pendulous load casts and detached pseudonodules are evident (see Table 3 for formation mechanism). *MF* mass flow deposit. **b** Remobilised sediment forms large fluidal diapirs. Disrupted sediment is injected into the rhyolite lava surrounding the diapirs. Peperitic margins in Fig 6a. **c** The lava-sediment boundary has a sinuous appearance and the two materials appear to have mingled as two contrasting fluids, providing evidence for Rayleigh-Taylor instabilities. Intensive mixing allowed sediment inclusions to become incorporated within the lava. Penknife is 10 cm long. **d** Dendritic elutriation structure that contains a higher relative proportion of juvenile rhyolite clasts and is coarser grained than the surrounding sediment, demonstrating vertical movement of fluids. Penknife is 10 cm long

Trapper Creek, Goose Creek, Big Cottonwood Canyon) (Perkins and Nash 2002; Branney et al. 2008; Ellis et al. 2013), including few lithics, thin layers (<5 m), evidence of reworking and shard-rich units, would suggest the source was related to volcanism associated with the Bruneau-Jarbidge centre, ~150 km to the southeast (Fig. 1a). Ash from the explosive stage of the Bruneau-Jarbidge eruptions was widely dispersed, correlating with thick metre scale ash deposits thousands of kilometres from the Snake River Plain (Perkins and Nash 2002).

Preservation of pumice-rich and eutaxitic units in NU1–3 is atypical for SR-type volcanism and implies the ash in these

Table 2 Composition and structure of the disrupted unit (*DU*) subunits

Subunit	Nomenclature	Colour	Composition				Structure
			Pumice (%)	Crystals (%)	Lithics (%)	Matrix (%)	
DU2	dsTcr	White	0	10	5	85	Diffusely laminated (<1 cm)
DU3	mTp	Orange	<5	5	5	85–90	Massive, random fibrous pumice
DU4	mLTl	Yellow	0	<5	30	70	Massive
DU5	mT	Grey	10	10	0	80	Massive
DU6	mTp	White	10	<5	0	85 (v. fine ash)	Massive
DU7	mTcr	Red/purple altering to green	?	10	0	90	Massive

Mechanism of emplacement and chronological order cannot be accurately determined due to the thorough disruption of the subunits

m massive, *ds* diffusely stratified, *T* tuff, *LT* lapilli tuff, *p* pumice rich, *l* lithic rich, *cr* crystal rich

units was derived from a different and potentially more proximal source than the later NU4-8. Between 12.6 and 10.5 Ma, widespread sedimentation in the OIG, including the deposition of the Sucker Creek Formation, coincided with eruption of caldera forming rhyolitic ignimbrites and extrusion of rhyolite flows that erupted from vents at the margins of the OIG (Cummings et al. 2000) (Fig. 1a). It is inferred that NU1–3 were sourced from volcanism related to the OIG, implying that the Sucker Creek Formation succession beneath the JCR had multiple ash sources.

The loading of the lava on to the partially consolidated volcaniclastic sediments (NU1–7) has caused the bedding of the sequence to sag beneath the overlying lava, creating large arcuate open folds in the intact stratigraphy (Fig. 2h). Where the intact stratigraphy is preserved, a series of normal and reverse faults are present (Fig. 2a, h). The displacement along these faults ranges from 10 cm to 3–4 m.

Disrupted units: deformation zone (DU1-7)

Extensive churning and mixing of the subsequent units above NU8 has resulted in a complete loss of the original stratigraphy and therefore, a chronology and accurate interpretation of the deposition of these units cannot be determined (Fig. 4). The disrupted units are classified as one unit, DU, due to their overprinted textural parameters. Where possible, the DU is divided into subunits, DU1 to DU7, characterised in the field by colour, grain size and structure (Table 2; Figs. 3b and 4). The thickness of the DU is ~20–40 m (Fig. 2, North).

Subunit DU1 consists of a bedded conglomerate unit, comprising subrounded pebble-dominated packages interbedded with gravel dominated packages. The bedding in the conglomerate subunit remains intact despite DU1 being surrounded by highly deformed sediments of later DU (Fig. 2f). Interbeds are between 2 and 24 cm thick and are laterally discontinuous. Clasts within the pebble dominated packages are up to 14 cm across and comprise basalt, quartzite and rhyolite. Low gradient crossbeds consist of thin lenticular volcaniclastic sediment lenses of coarse sand grade. Crossbedding of pebble and gravel grades suggest a fluvial system with cyclical changes in energy. Sharp contacts with the surrounding DU indicate loading induced brittle deformation, suggesting partial consolidation pre-lava emplacement (Fig. 2f); however, locally, rounded basalt clasts (<1 to 9 cm) from subunit DU1 have been separated from the subunit and incorporated into the surrounding mixture of DU.

Mass flow deposit

Incorporated locally within the DU, but overlying all the DU units, is a massive, matrix-supported volcaniclastic breccia

Table 3 Summary of deformation structures and the mobilisation mechanisms required to form such structures

		Structure	Figure	Definition	Trigger	Soft-sediment remobilisation mechanism
Soft-sediment deformation	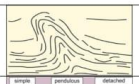	Diapir	4b and 6a	Deformation of a planar boundary caused by loading. Upward directed protrusion or antiform, which can potentially disrupt overlying stratigraphy. Flame-like structure (Mills 1983).	Loading and forceful emplacement	Liquefaction
	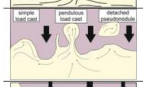	Loading structures (load casts; detached pseudonodule)	4a	Density contrasts deform the interface between 2 layers. A spectrum of deformation structures form. Simple load casts: upper layer is continuous, wavy interface. Pendulous load casts: perpetuation of deformation process, attached to the upper layer by a narrow neck. Detached pseudonodule: developed from pendulous load casts if the rising of the lower layer is more vigorous than the sinking of load casts (Owen 2003).	Loading and density contrast	Liquefaction
	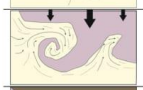	R-T instabilities	4c	Similar to the 2-layer system defined above, where both layers are liquefied (Hindmarsh and Rijsdijk 2000). The instability is controlled by the less dense layer (Mills 1983). "Swirly", highly convolute morphologies.	Density contrast	Liquefaction
		Sediment injectite	2d, e	Mobilised sediment that is able to penetrate into weaknesses in overlying strata (e.g. fractures, faults, boundaries).	Loading and forceful emplacement	Liquefaction
	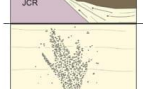	Elutriation structure	4d	Vertically directed expulsion of fluid (Mills 1983).	Loading and heat	Fluidization
Lava interaction		Fracture injectite	4b and 6f, g	Opening of a brittle fracture due to cooling and quenching in a cooling body, which reduces the lithostatic pressure, allowing for fluidisation of adjacent sediments and the injection of fluidised sediments into the fracture (Kokelaar 2002).	Cooling	Fluidization
		Peperite	6a–d	Rock formed essentially in situ by disintegration of magma intruding and mingling with unconsolidated or poorly consolidated, typically wet sediments (White et al. 2000). Can form at margins of intrusions and base of lavas (and ignimbrites, Branney et al. 2008). Rhyolite magmas produce blocky peperite textures, due to the high viscosity of the magmas (Busby-Spera and White 1987; Dadd and Wagoner 2002).	Heat	Fluidization

(Fig. 2d, I) with large wood fragments (~15 cm) (Fig. 2j). The breccia consists of granule to cobble size (2 mm to ~40 cm) clasts that are subangular and subrounded and are mostly composed of rhyolite, basalt and tuff, in a fine-sand-grade matrix. Volcaniclastic sediment inclusions (from the older DU) are mingled within the breccia, and some of the inclusions retain internal, mildly deformed laminations (mm-scale).

Soft-sediment deformation structures (DU2–7)

A range of deformation structures are present in the sediment and are defined, and their formation mechanisms are summarised in Table 3. Further details of these structures are described below.

Diapiric ascent of sediment into the overlying lava is evident on both sides of the road-cut exposure, where giant simple and pendulous load casts (1–4 m in length) are present at the rhyolite-sediment interface (eastern margin of South Transect) (Fig. 4a). Locally, where the necks of the pendulous load casts have closed, detached pseudonodules of sediment have developed in the overlying lava (Woidt 1978; Owen 2003). The pseudonodules are metre-scale isolated zones of sediment incorporated into the rhyolite (Fig 4a). The sediment also forms large diapirs that extend vertically and penetrate the base of the overlying lava for up to ~15–20 m (Fig. 4b). The boundary between the lava and the sediment diapirs is highly fluidal and the two materials appear to be mixing like two contrasting fluids (Fig. 4c). Locally, laminations and primary bedding are still preserved in the diapirs.

Sediment (DU2–4) has been forcefully injected into the boundary between the lava and the mass flow deposit on the north side of the road cut (Fig. 2d, e). The subvertical "injectite" extends for ~10 m, and grades from distinguishable subunits at the base to a dendritic form with thin sediment veins splaying into the adjacent lava unit at the top of the structure (Fig. 2d). The sediment subunits intimately interact with a range of boundary morphologies: planar and fluidal at the base of the injectite and increasingly more convoluted until separate subunits are indiscernible at the top of the injectite. Isolated rhyolite clasts are present in the injectites, spalled from the adjacent lava (Fig. 2e). Larger rhyolite clasts (greater than 10 cm) have glassy rims, indicating hot emplacement into sediment (Fig. 2e).

Elutriation structures are present in the DU and demonstrate vertical movement of fluids (Fig. 4d) (Busby-Spera and White 1987). These fluid escape structures lack fines and are composed mainly of granule to cobble sized rhyolite fragments. The elutriation structures are on a decimetre scale and have a dendritic, lobate appearance.

Locally, the subunits of the deformed zone are discernible from one another. In particular, a very fine, white massive tuff (DU6) retains its coherency and has not been fluidised extensively like the other DU subunits. Locally, fragments of DU6 beds are isolated in homogenised DU. At the eastern margin of the North Transect, DU6 displays distinctive wave-like geometries. The other subunits of the DU surround the "waves", and isolated pseudonodules of detached DU6 are spalled off at the "wave crest" (Fig. 2g).

Jump Creek Rhyolite lava

The JCR lava extends northwards behind the road cut where it forms the French John Hill (Fig. 1c). Three prominent cliffs of this hill are seen ~100 m to 300 m behind the road cut. The

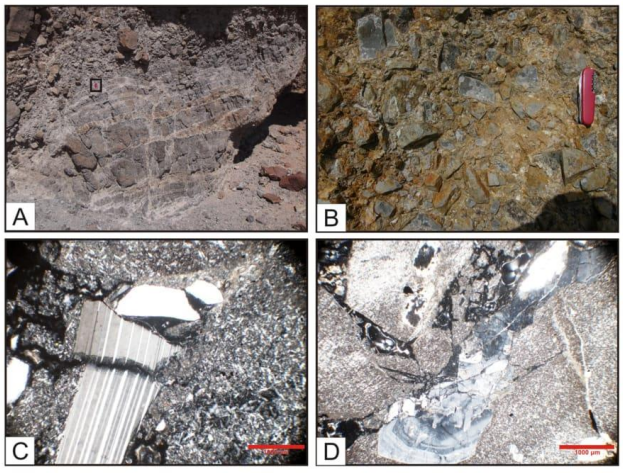

Fig. 5 Features of rhyolite lava. **a** Flow banding in autobrecciated block (~1.5 m long). Penknife (in *box*) is 10 cm long. **b** Matrix-supported flow-banded rhyolite autobreccia from the invasive conduit. **c** Photomicrograph (xpl) of sample taken from rhyolite in intrusion. Fractured plagioclase feldspar phenocrysts, demonstrating jigsaw fit, within fine, quartz-feldspar groundmass. **d** Photomicrograph (xpl) of sample taken from intrusion. Fractured plagioclase phenocryst (*highlighted*) was crushed between two rhyolite lava autobrecciated clasts

highest cliff (N 43° 40′ 80.3″, W 116° 87′ 37.8″) comprises a massive porphyritic, microcrystalline rhyolite with thick columnar joints. On lower sections of this cliff, the rhyolite is more intensely fractured, marking the gradational boundary from coherent lava interior to the autobrecciated lava in cliffs further down slope, typical of SR-type rhyolite lava flows (Branney et al. 2008). Flow banding and plagioclase feldspar phenocrysts (<12 mm) are evident in the middle and bottom cliffs (N 43° 40′ 62.9″, W 116° 87′ 40.1″). Flow banding within blocks is up to 60 cm wide and defined by glassy aphanitic bands (Fig. 5a). Bonnichsen et al. (2004) observed a high abundance of subvertical fractures here, which is unusual for the JCR, and suggests an unusual structural emplacement.

The rhyolite at road-cut height (N 43° 40′ 50.9″, W 116° 87′ 08.5″) is a matrix-dominated and matrix-supported flow-banded rhyolite basal autobreccia that contains angular glassy blocks (maximum 1.5 m) within a coarse granulated matrix (Fig. 5b). The cross-section in Fig. 2 (North) shows the steeply inclined boundary between the lava and sediment reflecting steep palaeotopography at the time of lava emplacement. Petrographic analysis of the autobrecciated rhyolite from the road cut shows angularly fragmented groundmass

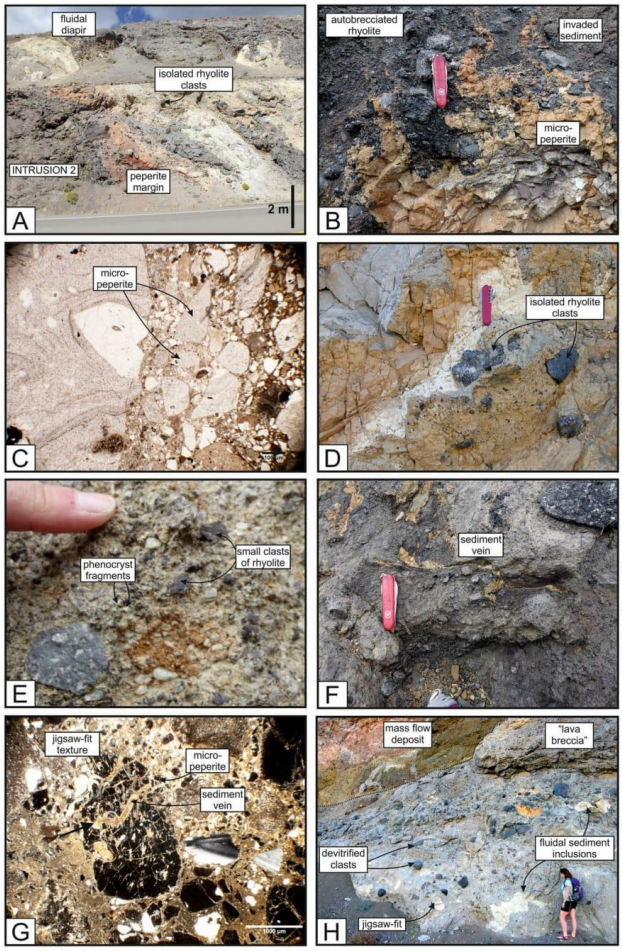

Fig. 6 Lava-sediment interaction. **a** Blocky peperite margin surrounding intrusion. Peperite margin up to 10 m into sediment. Fluidal diapir (Fig. 4b) visible in the *top left of the image*. **b** Micro-scale peperite at lava-sediment interface. Fragmented rhyolite clasts (<3 cm) within sediment. **c** Photomicrograph of micro-scale peperite (ppl). Perlitic rhyolite clast (12 mm) with angular, fractured edge on the *left of the image*. Fractured microclasts of perlitic rhyolite in a brown, indistinguishable groundmass on the *right side of the image*. **d** Isolated blocky rhyolite clasts in sediment. Clasts spalled ~8 m from margin of lava. **e** Sediment 1.6 m from edge of lava. Sediment matrix comprises DU sediments, phenocryst fragments (plagioclase feldspar), small rhyolite clasts (<25 mm) and subrounded quartz crystals. **f** Thin sediment vein near margin of lava intrusion (~2 m) formed by injection of sediment into lava. **g** Photomicrograph (xpl) of the diffuse DU-lava boundary showing sediment filling fractures (*highlighted by arrow*) within a small rhyolite lava clast, reflecting small-scale cooling contraction granulation and forming a sediment vein. Crystal fragments (plagioclase and quartz) in the sedimentary matrix. **h** On the south side of the road cut, the invasive conduits become one (Fig. 2, South). Intense mixing of rhyolite autobreccia matrix with sediment results in a matrix-supported breccia with a high percentage of fluidal sediment inclusions and blocky rhyolite clasts

material with fragmented plagioclase and zoned alkali feldspar phenocrysts. Shearing between fractures has resulted in phenocrysts being sheared and crushed between autobrecciated clasts (Fig. 5c, d).

Rhyolite-sediment interaction

On the north side of the road cut, three shallow invasive lobes, fed by the extrusive lava flow, have forcefully invaded/burrowed into the soft volcaniclastic substrate (DU; labelled on Fig. 2). These "intrusions" are annular shaped conduits (10–12 m in height) and are composed of clast-supported rhyolite autobreccia with angular, flow-banded blocks up to 3 m. Associated with the invasive conduits, juvenile rhyolite lava clasts have thermally spalled off, rotated and commingled into the DU sediment mix, forming blocky peperite at a meso and micro-scale (Fig. 6a–c). Equant to subequant blocks are present up to 10 m away from the edge of the "intrusion" margin and are thoroughly mixed with the volcaniclastic sediment (Fig. 6d). Petrographically, the peperite margin consists of a very fine undifferentiated matrix containing cuspate shards, tube-pumice fragments, angular vesiculated pumice fragments, altered plagioclase phenocrysts, microlites, perlitic rhyolite microclasts, mineral fragments (plagioclase, alkali feldspar and quartz) and microcrystalline quartz filling veins and fractures (Fig. 6e, g). Perlitic textures are evident in thin section. Some rhyolite clasts and fragments exhibit "jigsaw" fit, where fine sediment veins separate individual clasts (Fig. 6f). In the larger clasts of rhyolite (>1 mm), the sediment has been injected into fractures and microfractures (Fig. 6g). The sediment extends into fractures between <1 mm (microscale) and 1.75 m. In the outer carapace of the shallow "intrusions" (2–3 m from the margin), lenticular sediment inclusions have been incorporated into the rhyolite lava (<1 m in length) (Fig. 2c, k and l). These sediment stringers make up <1 % of the clasts in the autobreccia.

On the south side of the road cut, the invasive lobes merge into one large "intrusion", ~15 m in height and 125 m in length (Fig. 2, South). On the south side, the clast-supported autobreccia grades into a matrix-supported "lava breccia" and is paler, indicative of more intensive mingling with surrounding sediment (Fig. 6h). The rhyolite groundmass has commingled with the granular volcaniclastic sediments creating a homogenous matrix. Sediment inclusions are not restricted to the margins of the intrusion (like on the north side) but are distributed throughout. Here, the sediment inclusions have fluidal margins and contribute ~25 % of the total clast population, with the remaining ~75 % glassy rhyolite clasts (Fig. 6f). The rhyolite "lava breccia" invasively fingers into the disrupted sediment (up to 3 m in length) (Fig. 2k).

Consolidation state of the SCF and triggers for subsurface mobilisation

This case study presents evidence for three types of lava-sediment interaction (Fig. 7), which occur simultaneously and cause complex disruption of the volcaniclastic facies

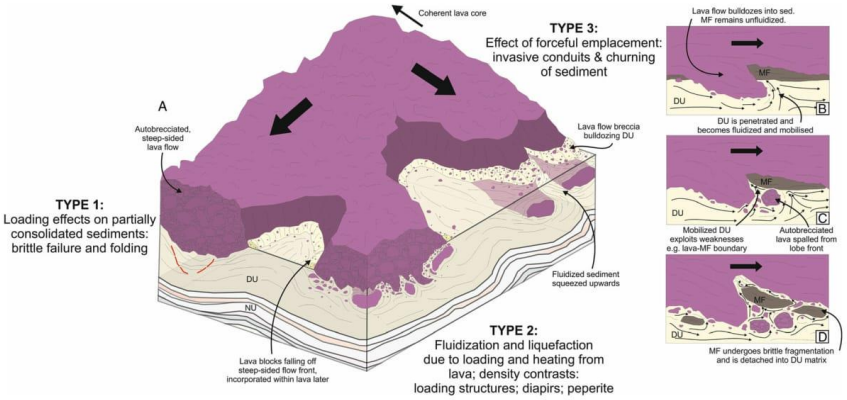

Fig. 7 **a** Schematic emplacement model, highlighting the three types of lava-sediment interaction. Type 1: loading of lava causes folding at the boundaries of the lava flow and brittle failure along discrete shear surfaces. This type affected the more consolidated sediments that retained some degree of mechanical strength. Folding of more cohesive sediments. Type 2: loading structures and peperite. Disrupted lava-sediment interface. Type 3: the effects of forceful emplacement in unconsolidated sediments were diapiric ascent of sediment, invasive lava intrusions, and extensive churning and homogenization of sediment. Inset: types 2 and 3—**b** lava burrowed into and broke through localised MF (mass flow deposit) and intruded DU; **c** DU sediments were mobilised and injected into weaknesses and fractures within lava, aiding autobrecciation and exploiting the boundary between lava and MF. **d** Lava was spalled from the lava "intrusion" front and rotated and sheared into the DU sediment. Peperitic margins formed, which were further displaced by hypermobile sediment

architecture: (1) brittle deformation structures and folds in the partially consolidated sediments (NU, DU1) (Fig. 2f, h), (2) loading structures (Fig. 4a) and peperite formation (Fig. 6a–c) and (3) extensive mobilisation and upward ascent of sediment into the overlying lava due to forceful emplacement, exploiting boundaries, churning and homogenising sediment (Figs. 2d, e, 4b and 6e). Here, we consider the physical properties of the SCF at the time of JCR emplacement to understand the scale of sediment mobilisation and the triggers of extensive subsurface remobilisation.

Consolidation state of sediments and timing of lava emplacement

The presence of a fluvial conglomerate unit (DU1) and thick lacustrine deposits (DU7 and DU8) has established that the SCF was deposited in a fluctuating fluvial and lacustrine-type environment. At the time of lava emplacement, it is suggested that the sediments remained considerably water saturated, allowing the sediments to be fluidised effectively and contributing to the effects of dewatering (elutriation structures, Fig. 4d) and peperite formation (Fig. 6a–d; Table 3). A differential response to liquefaction and fluidisation occurs between the two facies, the NU and the DU. The DU displays complex ductile soft-sediment deformation (Fig. 4a–c; Table 3), implying that the DU was completely unconsolidated at the time of the Owyhee Front Rhyolites (the JCR) volcanism and was rapidly loaded by the JCR. Brittle failures are present in the NU and the conglomerate package (DU1) (Fig. 2a, h), which are estimated to have been buried by up to 20 m. Brittle deformation can occur in cohesionless sediments along discrete shear surfaces, during rapid loading events where pore pressure is sufficiently high (Maltman 1984, 1987; Owen 1987, 2003). However, the conglomerate subunit (DU1) is considered a cohesive unit, implying partial consolidation of the NU before lava emplacement. Folding of the NU also suggests that sediments in the non-disrupted beds retain some coherency.

Triggers

Due to the scale of the soft-sediment deformation features, it is important to consider the triggers and mechanisms of how the sediments beneath the JCR were mobilised (Table 3).

Loading and heat

Subsurface mobilisation of sediments can occur if sediments become liquefied or fluidised (Maltman and Bolton 2003). The height of vertical sediment displacement at the road cut (fluidal diapirs up to 15 m) (Fig. 4a) suggests extensive liquefaction (Table 3). There are two proposed mechanisms for extensive liquefaction in the SCF. Firstly, the liquefaction is triggered by penecontemporaneous loading of the lava, instantaneously overburdening the sediments and increasing hydrostatic pore pressure above critical state (Anketell et al. 1970; Jones and Omoto 2000). Secondly, unlike other examples of loading triggers, such as cyclical (e.g. waves) (Pestana et al. 2000; Alfaro et al. 2002), mass flows (Postma 1984; Owen 1996) and glacial (Le Heron et al. 2005), lava-induced loading is also associated with a temperature increase in the underlying sediments. Numerical models suggest that rhyolite lava flows hundreds of metres thick, like the JCR, can retain heat for decades by forming a top carapace, locking in heat, and increasing their ability to produce internal latent heat (Manley 1992). Correspondingly, models testing the cooling rates of Snake River Plain rhyolite ignimbrites using groundmass crystallisation, have indicated that the base of the 60 m Grey's Landing Ignimbrite (Central Snake River Plain) remained above 400 °C for on the order of 10 years (Ellis et al. 2015). If rhyolites can stay molten or semi-molten at the base for decades, porewater in the underlying substrate can cross the phase boundary, from liquid to vapour for extended periods of time (Kokelaar 1982). In the SCF, this phase change increased the hydrostatic pore pressure of the vapour-supported grains allowing for extensive and prolonged liquefaction.

Both loading induced and heat-induced mobilisation mechanisms are proposed to occur simultaneously, where loading of the JCR on to the SCF instigated a pressure gradient that was sufficient to allow for voluminous vertical sediment migration. Such vigorous and continuous liquefaction would support diapirism on the scales we see beneath the JCR (Fig. 4a, b). The diapiric ascent of sediment formed metre-scale pendulous load casts (Fig. 4a), detached sediment pseudonodules (Fig. 4a) and large, 15–20 m diapirs (Fig. 4b). Liquefied sediments were also forced upwards, penetrating and exploiting boundaries, forming sediment injectites (Fig. 2d, e). The dendritic nature of the injectites reflects the waning energy of the upward projecting sediment.

Fluidisation requires a continuous source of fluid and a sustained heat source to inhibit condensation of the vapour produced in sediments due to heating (Kokelaar 1982; Owen et al. 2011). The basal section of the thick JCR provided a sustained heat source for continuous vaporisation of pore fluids (Kokelaar 1982). Localised heating and/or fracture induced pressure release, vaporised small volumes of fluid, transmitted upwards forming vertical, fine-depleted elutriation structures (Fig. 4d; Table 3) and peperite (Fig. 6a–d; Table 3) (Kokelaar 1982; Busby-Spera and White 1987; Skilling et al. 2002).

Density contrasts

Reverse-density structures formed at the interface between the semi-molten rhyolite lava (2.49 g/cm^3) and the partially unconsolidated, liquefied volcaniclastic sediment (1.36 to

1.65 g/cm^3). The interface became unstable, representing a Rayleigh-Taylor (R-T) instability (Daly 1967; Allen 1982; Hall and Els 2002) and simple, planar boundaries between the two materials deformed into various types of load structures (e.g. Anketell et al. 1970; Allen 1982; Mills 1983; Owen 2003). Negative buoyancy controls the downward movement of rhyolite lava into the sediment and positive buoyancy controls the upward movement of the sediment. When the sediments in the DU are liquified (by mechanisms outlined above), the two fluids can interact. The turbulent mixing and "swirling" of the two fluids produces highly convolute and fluidal morphologies (Fig. 4c). If the rhyolite cools or the sediment solidifies, the R-T structures can no longer form and only true load structures (load casts, pseudonodules etc.) develop (Owen 2003).

The structure of DU6 remains fairly intact, with distinctive wave-like geometries (Fig. 2g), unlike the malleable DU sediments. The very fine-grained nature of DU6 suggests it is less thixotropic than the rest of the DU. The tightly spaced grains limit the volume of porewater, decreasing the probability for liquefaction. Consequently, DU6 retains significant residual shear strength in response to loading and liquefaction and so can only deform in a plastic manner (Owen 2003). As the fluidised sediments flowed over the internally coherent DU6, shear instabilities were generated across the

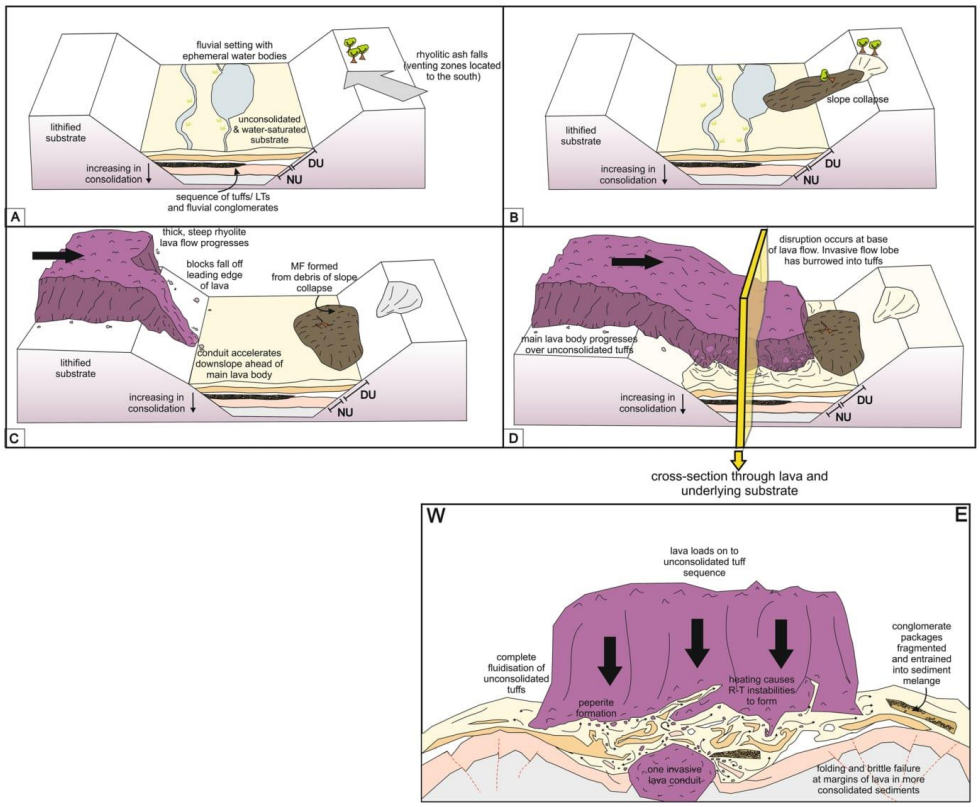

Fig. 8 Temporal model showing emplacement of the Jump Creek Rhyolite on to the Sucker Creek Formation and how topography controlled the scale of disruption. **a** The Sucker Creek Formation was deposited predominantly as a series of rhyolitic ash falls and conglomerate units reworked by lacustrine or fluvial processes. **b** Mass flow/debris flow deposit at the side of a valley incorporating plant debris. **c** Lava flowed over steep topography and accelerated. **d** Lava intruded into soft sediment to form extrusively fed intrusions. The main body of the JCR flowed over the top of the Sucker Creek Formation; Inset: Cross-section through lava shows soft-sediment deformation occurring at the base of the rhyolite lava flow. An individual "intrusion" is shown here

interface between the two subunits and wave-like geometries were formed. These geometries may also be exaggerated by a relatively significant density contrast between DU6 and the other DU sediments. The result of shearing and this density contrast is the deformation of the DU6 interface, forming the wave-like structures (Fig. 2g) (Owen 2003).

Forceful emplacement of JCR

Extrusively fed rhyolite intrusions have bulldozed into the partially consolidated SCF, subsequently inflated and squeezed liquified tuffs into lobate, vertical diapirs (Fig. 4b), which propagated into the base of the main body of the lava flow. Invasive lava flows have been documented in komatiitic lavas and are explained by a large density contrast between the lava and partially unconsolidated sediment (1.6–1.8 g/cm^3) (Beresford and Cas 2001). In the case of the JCR, the three exposed intrusions, and extensive sediment disruption, are localised beneath the main lava body. Due to the large volumes of sediment displaced and the steep angle of intrusion (Fig. 2, North; "Soft-sediment deformation structures (DU2–7)"), it is suggested that a further "trigger" was required for the lava to abruptly intrude into the sediment. The formation of the intrusions is attributed here to an abrupt change in the underlying substrate to the less dense, soft volcaniclastic sediments of the SCF. This relatively abrupt transition can be explained by the presence of a steep valley side or fault escarpment (Bonnichsen et al. 2004) (Fig. 8). Rifting of the WSRP would have formed fault escarpments creating the steep topography suggested here ("The Jump Creek Rhyolite lava (11.1 ± 0.2 Ma)"). Bonnichsen et al. (2004) attribute prevalent subvertical fractures observed in the road cut (uncommon for the JCR) to an unusual structural emplacement, such as it having "cascaded" into a palaeocanyon. The localised occurrence of the volcaniclastic breccia with wood fragments (mass flow deposit) (Fig. 2j) also suggests debris (angular boulders, pebbles and plant material) was washed/collapsed down a steep slope into a valley (Fig. 8). A change in topography would promote relatively forceful emplacement of a comparatively coherent lava lobe front into the sediment. The lava extended into three distinct channels forming the three extrusively fed intrusions (Fig. 2, North). An increase in lava flow velocity would have been able to force sediment upwards and churn the sediment in the extensive manner that is observed at the road cut (Figs. 4 and 8e). Density contrasts between the rhyolite and SCF would have also aided the downward intrusion of the rhyolite lava.

Peperite formation and dispersal

As the JCR cooled on contact with the SCF, it quenched at the margins of the rhyolite lava and opened angular fractures, relieving pressure in the surrounding host sediment and vaporising pore fluids (Kokelaar 1982; Hanson and Wilson 1993; Doyle 2000; Skilling et al. 2002). Sediment was injected into the newly opened fractures in the rhyolite (Fig. 6e), allowing for entrainment of isolated sediment inclusions into the lava conduits and in situ fragmentation of rhyolite (Fig. 6e) (Skilling et al. 2002). The result is peperite with a jigsaw fit texture and fine sediment veins separating individual clasts (Fig. 6f, g). Petrographic analysis of samples taken from the peperitic margins of the conduits shows that in situ fragmentation is scale invariant, occurring on both micro- and meso-scales (Fig. 6a, b). Small-scale contraction granulation has shattered blocks of rhyolite into subcentimetre juvenile rhyolite fragments (with perlitic textures), which have been incorporated into the sediment matrix (Fig. 6c, e) and remobilised away from the margin.

Dispersal of the peperitic margin

In the JCR, widely dispersed juvenile clasts are observed (Fig. 6a, d) (Hanson and Wilson 1993). Dispersal occurs as liquefied and hypermobile sediments (see "Triggers") entrain juvenile clasts and phenocrysts and displace this pre-existing peperite away from the lava margin into the partially homogenised sediments by non-explosive mechanisms (Hanson and Wilson 1993; Skilling et al. 2002). Similar features are documented surrounding rhyolite sills, demonstrating a spectrum of dispersal patterns and scales, from micro jigsaw fit fractures in rhyolite to widely dispersed juvenile clasts (e.g. Hanson and Wilson 1993; Hanson and Hargrove 1999; Németh et al. 2008). The inflation of the "intrusions" would have caused further disruption, squeezing the sediment upwards and entraining and displacing the pre-existing peperite away from the site of formation.

Conclusions

A road cut exposure in the Owyhee Mountains, allows analysis of processes that took place when a Late Miocene (11.1 ± 0.1 Ma) rhyolite lava flow of the Jump Creek Formation (the Rockville Segment) rapidly loaded on to a water-saturated and unconsolidated succession of the Sucker Creek Formation. Evidence for reworking and the presence of a fluvial conglomerate unit indicate the Sucker Creek Formation was deposited in a series of lakes and rivers associated with Lake Idaho. A mass flow deposit, the steep lava-sediment boundary, bulldozing of extrusively fed intrusions and highly mobilised sediments indicate that the rhyolite flowed over steep topography and was forcefully emplaced into the saturated, unconsolidated sediment. The extrusive lava-fed intrusions propagated into the sediment.

Emplacement of the JCR on to the Sucker Creek Formation induced extensive fluidisation, liquefaction and subsurface remobilisation in the shallow volcaniclastic sediments (DU; 0–20 m) and generated a range of large soft-sediment deformation structures (diapirs, simple load casts, pendulous load casts and detached pseudonodules, elutriation structures) and Rayleigh-Taylor instability structures. Peperite was also formed at the base of the JCR and around the extrusively fed intrusions. In the more consolidated and coherent sediments (NU; 20–30 m), the loading induced brittle faults and large folds formed. The interaction between the JCR and underlying substrate demonstrates how large lava bodies can extensively disrupt sediments and form significant lateral and vertical discontinuities that complicate volcanic facies architecture.

Acknowledgements This manuscript was written whilst CM held a University of Glasgow PhD College Scholarship. We appreciate the constructive reviews of Karoly Nemeth, Ben Ellis and John Wolff as well as the associate editor, Pierre-Simon Ross.

References

Alfaro P, Delgado J, Estévez A, Molina J, Moretti M, Soria J (2002) Liquefaction and fluidisation structures in Messinian storm deposits (Bajo Segura Basin, Betic Cordillera, southern Spain). Int J Earth Sci 91:505–513

Allen JRL (1982) Liquidization, liquidized sediment, and the sedimentation of dense particle dispersions. In: Sedimentary structures: their character and physical basis. Developments in sedimentology. 30B Amsterdam, Elsevier. ISBN: 978-0-444-41945-3

Altaner SP, Grim RE (1990) Mineralogy, chemistry, and diagenesis of tuffs in the Sucker Creek Formation (Miocene), Eastern Oregon. Clay Clay Miner 38:561–572

Anketell JM, Cegla J, Dzulynski S (1970) On the deformational structures in systems with reversed density gradients. Ann Soc Géol Pol 40:3–29

Armstrong RL, Harakal JE, Neill WM (1980) K-Ar dating of Snake River Plain (Idaho) volcanic rocks—new results. Isochron 27:5–10

Beresford SW, Cas RA (2001) Komatiitic invasive lava flows, Kambalda, Western Australia. Can Mineral 39:525–535

Bonnichsen B (1982) Rhyolite lava flows in the Bruneau-Jarbidge eruptive center, southwestern Idaho: cenozoic geology of Idaho. Idaho Bur Mines Geol Bull 26:283–320

Bonnichsen B, Kauffman DF (1987) Physical features of rhyolite lava flows in the Snake River Plain volcanic province, southwestern Idaho. Geol Soc Am Spec Pap 212:119–145

Bonnichsen B, McCurry M., Godchaux MM (2004) Miocene Snake River Plain Rhyolites of the Owyhee Front, Owyhee County, Idaho. In: Haller KM and Wood SH (eds) Geological field trips in Southern Idaho, Eastern Oregon, and Northern Nevada: Geological Society of America. Rocky Mountain Section. Meeting and Geological Society of America. pp 156–175

Bonnichsen B, Godchaux MM (compilers) (2006) Geologic map of the Murphy 30′ × 60′ Quadrangle, Ada, Canyon, Elmore, and Owyhee Counties, Idaho: Idaho Geological Society, scale 1:100000

Bonnichsen B, Leeman WP, Honjo N, McIntosh WC, Godchaux MM (2008) Miocene silicic volcanism in southwestern Idaho: geochronology, geochemistry, and evolution of the central Snake River Plain. Bull Volcanol 70:315–342

Branney MJ, Bonnichsen B, Andrews GDM, Ellis B, Barry TL, McCurry M (2008) 'Snake River (SR)-type' volcanism at the Yellowstone hotspot track: distinctive products from unusual, high-temperature silicic super-eruptions. Bull Volcanol 70:293–314

Busby-Spera CJ, White JD (1987) Variation in peperite textures associated with differing host-sediment properties. Bull Volcanol 49:765–776

Christiansen RL, Lipman PW (1966) Emplacement and thermal history of a rhyolite lava flow near Fortymile Canyon, southern Nevada. Geol Soc Am Bull 77:671–684

Cummings ML, Evans JG, Ferns ML, Lees KR (2000) Stratigraphic and structural evolution of the middle Miocene synvolcanic Oregon-Idaho graben. Geol Soc Am Bul 112:668–682

Dadd KA (1992) Structures within large volume rhyolite lava flows of the Devonian Comerong Volcanics, southeastern Australia, and the Pleistocene Ngongotaha lava dome, New Zealand. J Volcanol Geotherm Res 54:33–51

Dadd KA, Van Wagoner NA (2002) Magma composition and viscosity as controls on peperite texture: an example from Passamaquoddy Bay, southeastern Canada. J Volcanol Geotherm Res 114:63–80

Daly BJ (1967) Numerical study of two fluid Rayleigh Taylor instability. Phys Fluids 10:297–307

Donaire T, Sáez R, Pascual E (2002) Rhyolitic globular peperites from the Aznalcóllar mining district (Iberian Pyrite Belt, Spain): physical and chemical controls. J Volcanol Geotherm Res 114:119–128

Doyle MG (2000) Clast shape and textural associations in peperite as a guide to hydromagmatic interactions: Upper Permian basaltic and basaltic andesite examples from Kiama, Australia. Aust J Earth Sci 47:167–177

Ellis BS, Wolff JA, Boroughs S, Mark DF, Starkel WA, Bonnichsen B (2013) Rhyolitic volcanism of the central Snake River Plain: a review. Bull Volcanol 75:1–19

Ellis BS, Cordonnier B, Rowe MC, Szymanowski D, Bachmann O, Andrews GDM (2015) Groundmass crystallisation and cooling rates of lava-like ignimbrites: the Grey's Landing ignimbrite, southern Idaho, USA. Bull Volcanol 77:1–15

Hall RCB, Els BG (2002) The origin and significance of load-induced deformation structures in soft-sediment and lava at the base of the Archaean Ventersdorp Supergroup, South Africa. J Afr Earth Sci 35:135–145

Hanson RE, Hargrove US (1999) Processes of magma/wet sediment interaction in a large-scale Jurassic andesitic peperite complex, northern Sierra Nevada, California. Bull Volcanol 60:610–626

Hanson RE, Schweickert RA (1982) Chilling and brecciation of a Devonian rhyolite sill intruded into wet sediments, northern Sierra Nevada, California. J Geol 90:717–724

Hanson RE, Wilson TJ (1993) Large-scale rhyolite peperites (Jurassic, southern Chile). J Volcanol Geotherm Res 54:247–264

Henry CD, Price JG, Rubin JN, Laubach SE (1990) Case study of an extensive silicic lava: the Bracks Rhyolite, Trans-Pecos Texas. J Volcanol Geotherm Res 43:113–132

Jones AP, Omoto K (2000) Towards establishing criteria for identifying trigger mechanisms for soft sediment deformation: a case study of Late Pleistocene lacustrine sands and clays, Onikobe and Nakayamadaira Basins, northeastern Japan. Sedimentology 47:1211–1226

Kimmel PG (1982) Stratigraphy, age, and tectonic setting of the Miocene-Pliocene lacustrine sediments of the western Snake River Plain,

Oregon and Idaho. Cenozoic geology of Idaho. Idaho Bur Mines Geol Bull 26:559–578
LR, Green AR, Hagood AR, Johnson AM, McMurray JM, Russell RG, Weeden DA (1965) Cenozoic stratigraphy of the Owyhee region, southeastern Oregon: Eugene, University of Oregon Museum of Natural History Bulletin 1, 45
Kokelaar BP (1982) Fluidisation of wet sediments during the emplacement and cooling of various igneous bodies. J Geol Soc 139:21–33
Le Heron DP, Sutcliffe OE, Whittington RJ, Craig J (2005) The origins of glacially related soft-sediment deformation structures in Upper Ordovician glaciogenic rocks: implication for ice-sheet dynamics. Palaeogeogr Palaeoclimatol Palaeoecol 218:75–103
Lewis RS, Link PK, Stanford LR, Long SP (compilers) (2012) Geologic map of Idaho. Idaho Geological Survey. 1:750,000. ISBN: 978-1-55765-118-1
Maltman A (1984) On the term "soft-sediment deformation". J Struct Geol 6:589–592
Maltman AJ (1987) Shear zones in argillaceous sediments—an experimental study. Geol Soc Lond Spec Publ 29:77–87
Maltman AJ, Bolton A (2003) How sediments become mobilised. Geol Soc Lond Spec Publ 216:9–20
Manley CR (1992) Extended cooling and viscous flow of large, hot rhyolite lavas: implications of numerical modeling results. J Volcanol Geotherm Res 53:27–46
Manley CR (1995) How voluminous rhyolite lavas mimic rheomorphic ignimbrites: eruptive style, emplacement conditions, and formation of tuff-like textures. Geology 23:349–352
Manley CR (1996) Physical volcanology of a voluminous rhyolite lava flow: the Badlands lava, Owyhee Plateau, southwestern Idaho. J Volcanol Geotherm Res 71:129–153
Mills PC (1983) Genesis and diagnostic value of soft-sediment deformation structures—a review. Sediment Geol 35:83–104
Needham RS (1978) Giant scale hydroplastic deformation structures formed by the loading of basalt onto water saturated sand, Middle Proterozoic, Northern Territory: Australia. Sedimentology 25:285–295
Németh K, Pécskay Z, Martin U, Gméling K, Molnár F, Cronin SJ (2008) Hyaloclastites, peperites and soft-sediment deformation textures of a shallow subaqueous Miocene rhyolitic dome-cryptodome complex, Pálháza, Hungary. Geol Soc Lond Spec Publ 302:63–86
Owen G (1987) Deformation processes in unconsolidated sands: Geological Society, London, Special Publications 29: 11–24. In: Jones ME, Preston RMF (eds) Deformation of sediments and sedimentary rocks. doi: 10.1144/GSL.SP.1987.029.01.02
Owen G (1996) Experimental soft sediment deformation: structures formed by the liquefaction of unconsolidated sands and some ancient examples. Sedimentology 43:279–293
Owen G (2003) Load structures: gravity-driven sediment mobilisation in the shallow subsurface: Geological Society, London, Special Publications 216: 21–34. In: Van Rensbergen R, Hillis RR, Maltman AJ, Morley CK Owen G, Moretti M, Alfaro P (eds) (2011) Subsurface sediment mobilisation. Recognising triggers for soft-sediment deformation: current understanding and future directions. Sedimentary Geology 235: 133–140.
Owen G, Moretti M, Alfaro P (2011) Recognising triggers for soft-sediment deformation: current understanding and future directions. Sedimentary Geology 235:133–140.
Perkins ME, Nash BP (2002) Explosive silicic volcanism of the Yellowstone hotspot: The ash fall tuff record. Geol Soc Am Bull 114:367–381
Perkins ME, Brown FH, Nash WP, Williams SK, McIntosh W (1998) Sequence, age, and source of silicic fallout tuffs in middle to late Miocene basins of the northern Basin and Range province. Geol Soc Am Bull 110:344–360
Pestana JM, Biscontin G, Nadim E, Andersen K (2000) Modeling cyclic behavior of lightly overconsolidated clays in simple shear. Soil Dyn Earthq Eng 19:501–519
Pierce KL, Morgan LA (1992) The track of the Yellowstone hot spot: volcanism, faulting, and uplift. Geol Soc Am Mem 179:1–54
Postma G (1984) Slumps and their deposits in fan delta front and slope. Geology 12:27–30
Shervais JW, Hanan BB (2008) Lithospheric topography, tilted plumes, and the track of the Snake River–Yellowstone hot spot. Tectonics 27:TC5004
Skilling IP, White JDL, McPhie J (2002) Peperite: a review of magma–sediment mingling. J Volcanol Geotherm Res 114: 1–17
Tuffen H, Gilbert J, McGarvie D (2001) Products of an effusive subglacial rhyolite eruption: Bláhnúkur, Torfajökull, Iceland. Bull Volcanol 63:179–190
Waichel BL, de Lima EF, Sommer CA, Lubachesky R (2007) Peperite formed by lava flows over sediments: an example from the central Paraná Continental Flood Basalts, Brazil. J Volcanol Geotherm Res 159:343–354
Walker GW, MacLeod NS (compliers) (1991) Geologic map of Oregon. U.S. Geological Survey. Scale 1:500,000
Warner MM (1977) The Cenozoic of the Snake River Plain of Idaho. Rocky Mountain thrust belt geology and resources. In: 29th Annual Field Conference Guidebook: 313–326
White JDL, Houghton BF (2006) Primary volcaniclastic rocks. Geology 34:677–680
Woidt WD (1978) Finite element calculations applied to salt dome analysis. Tectonophysics 50:369–386
Wood SH, Clemens DM (2002) Geologic and tectonic history of the western Snake River Plain, Idaho and Oregon, Tectonic and Magmatic Evolution of the Snake River Plain Volcanic Province. Idaho Geol Surv Bull 30:69–103

10.3. East Fife Maps

Attached fold out.

Sample name	SiO2 (%)	Al2O3 (%)	Fe2O3 (%)	MgO (%)	CaO (%)	Na2O (%)	K2O (%)	TiO2 (%)	MnO (%)	P2O5 (%)	Balance (%)	(%)
Ruddon dyke 01	42.58	14.62	12.92	9.90	5.62	3.40	1.536	2.881	0.256	0.611	5.56	99.89
Ruddon block 002	44.09	13.54	12.01	7.65	11.64	2.96	1.097	2.684	0.223	0.634	3.25	99.78
Ardross block 003	37.81	15.21	12.21	5.21	8.98	2.68	2.746	3.457	0.207	0.774	10.14	99.42
Ardross dyke 004	36.25	15.60	11.76	4.77	10.38	0.53	4.788	2.982	0.195	0.911	11.63	99.80
St. Monans dyke 005	39.23	13.25	13.83	13.06	4.88	2.97	1.672	2.905	0.212	0.928	6.78	99.71
St. Monans block 006	42.72	14.07	12.07	10.18	6.34	3.75	1.575	2.981	0.291	0.687	4.98	99.64
Elie dyke 007	35.95	14.40	15.26	9.48	7.39	1.59	2.290	2.802	0.186	0.565	9.55	99.46
Elie block 008	41.01	12.03	15.26	8.69	11.60	2.20	1.215	3.274	0.562	0.699	3.23	99.77
Kincaird dyke 009	43.99	13.74	11.90	8.79	9.93	3.32	0.774	2.759	0.447	0.591	3.70	99.94
Kincaird block 010	42.61	14.62	12.93	9.27	8.89	2.80	0.464	3.043	0.479	0.621	4.21	99.93

Table 10.1: XRF data for the Fife diatremes

10.5. Vitrinite Reflectance Data

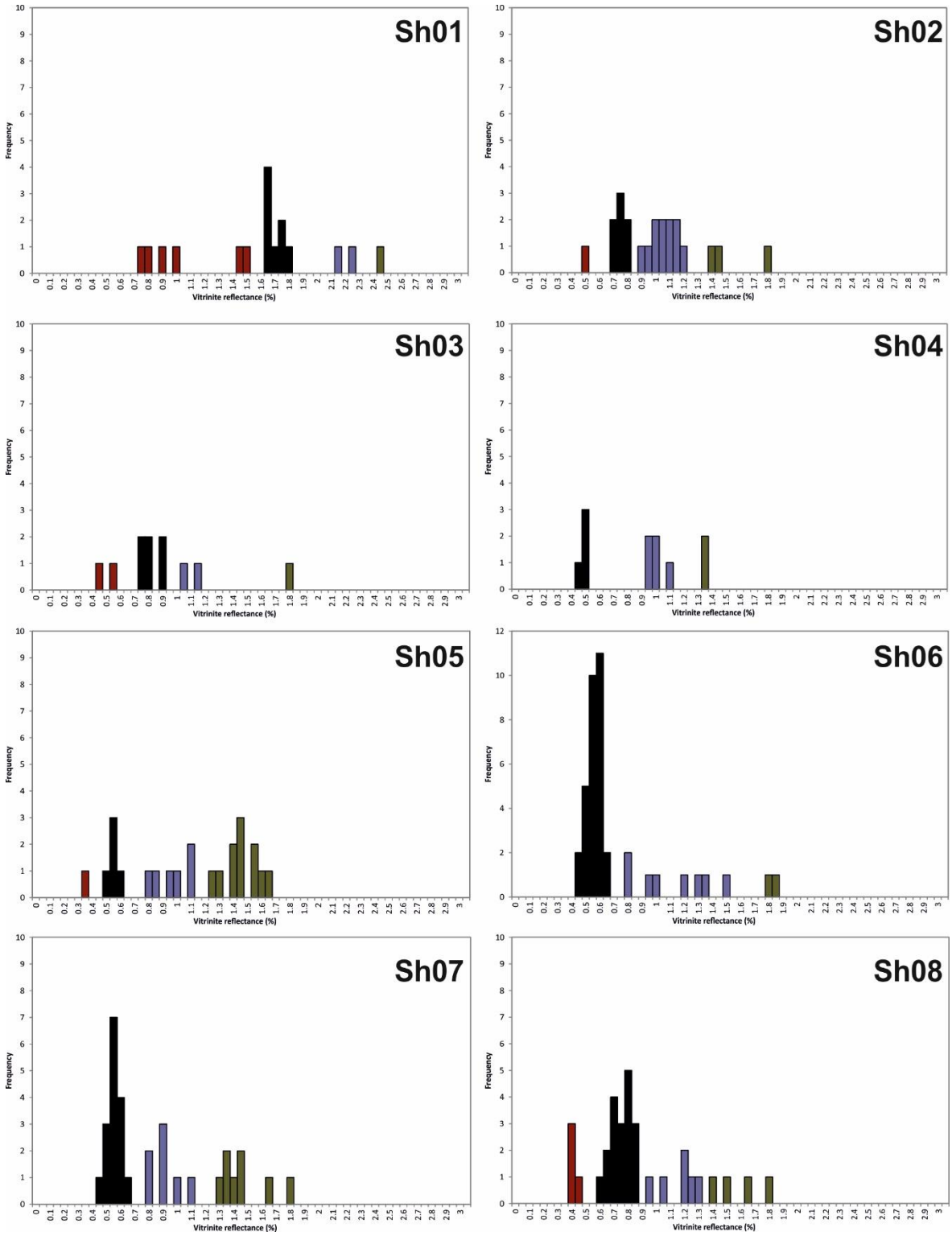

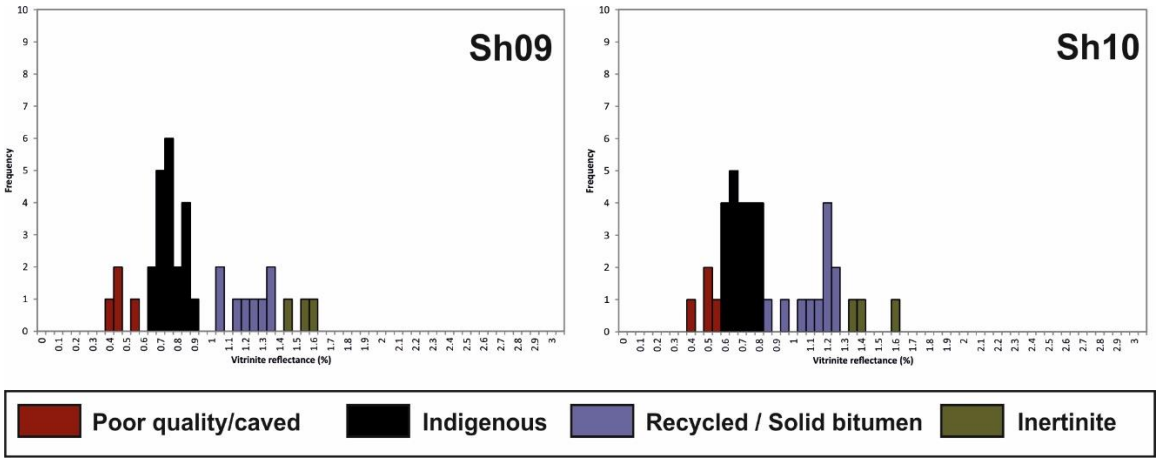

Figure 11.1: Histograms of vitrinite data of each shale sample from the St. Monans host-rock.

10.6. Raman Spectra

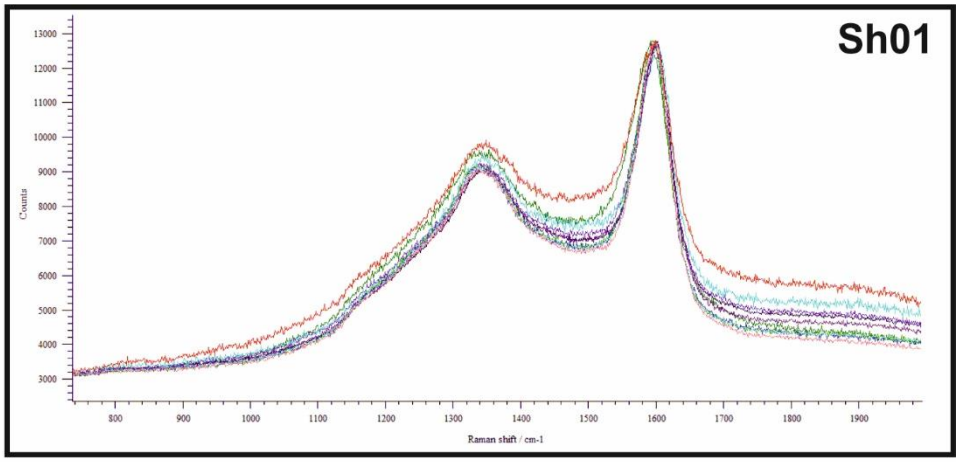

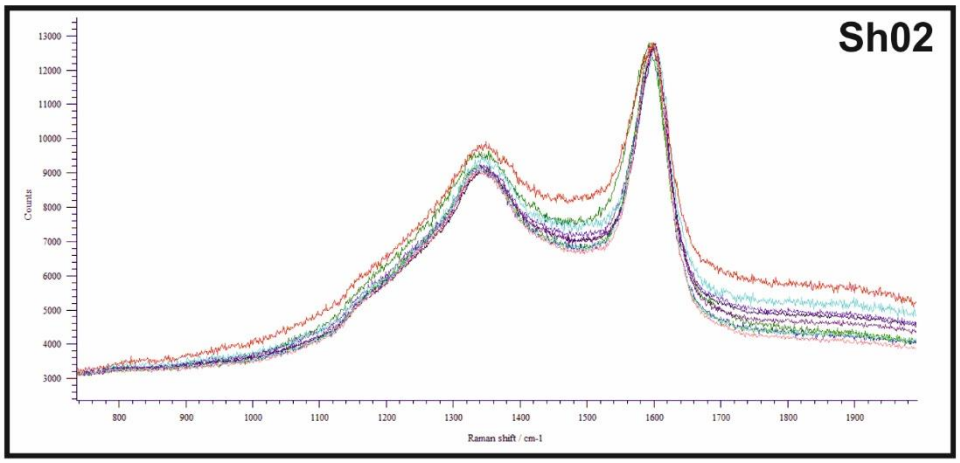

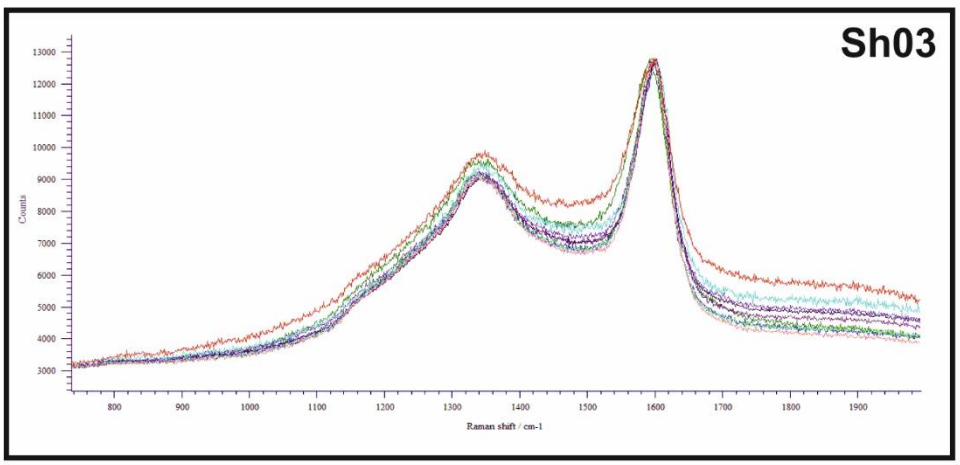

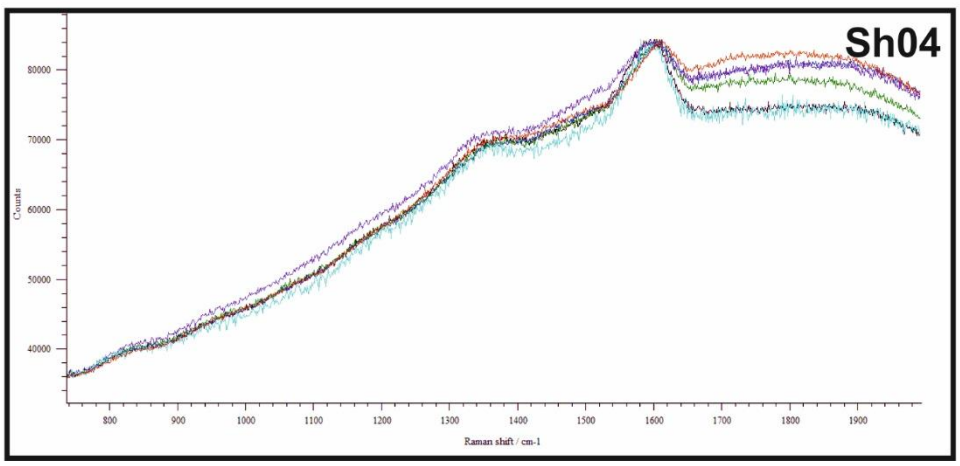

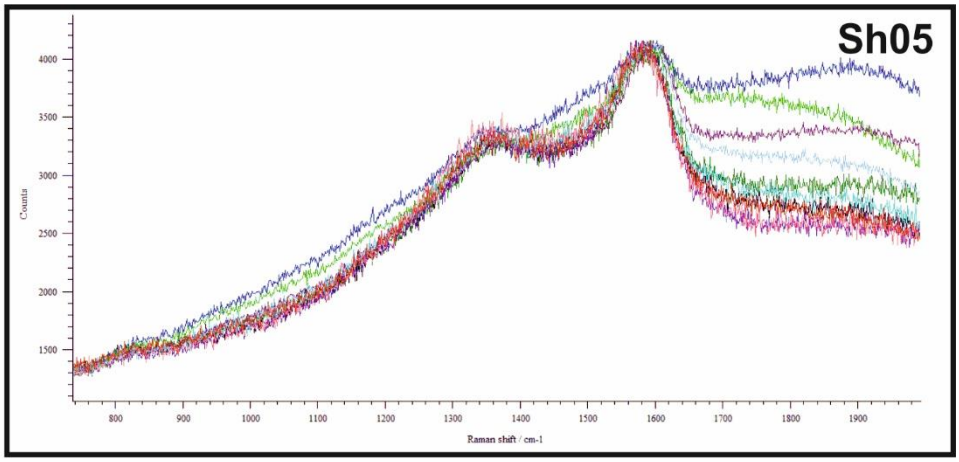
Sh05
Counts
Raman shift / cm-1

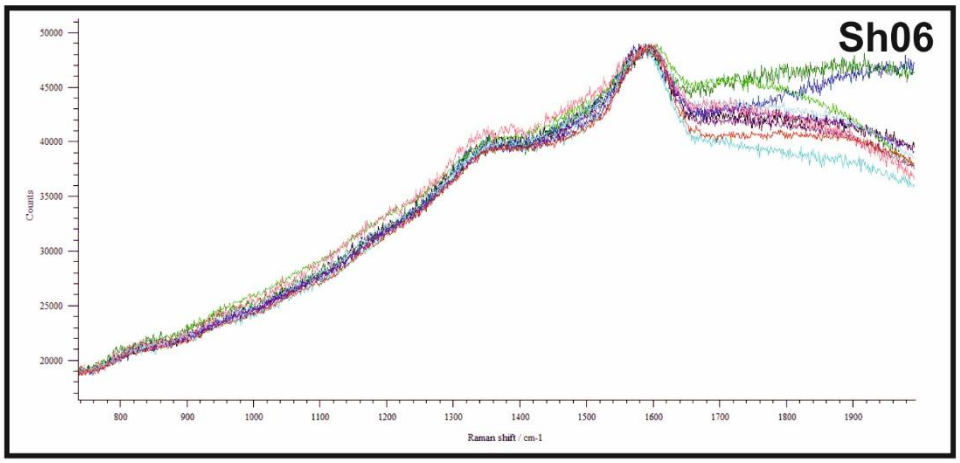
Sh06
Counts
Raman shift / cm-1

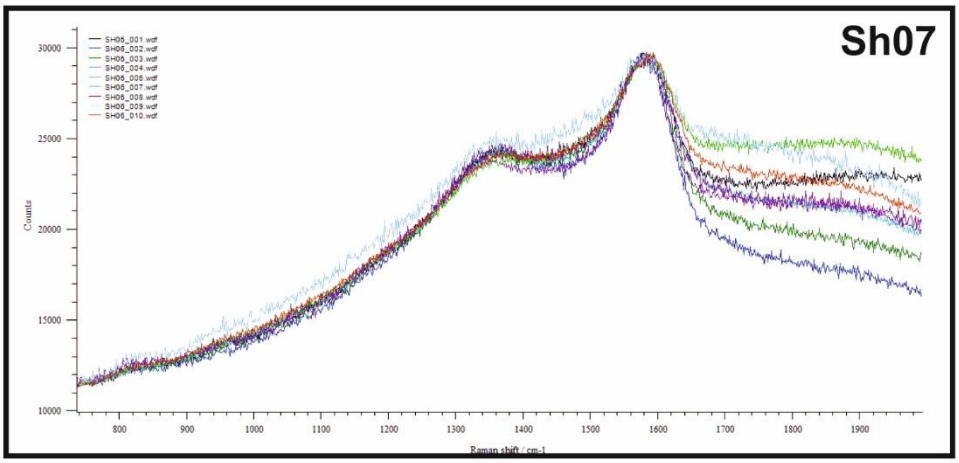
Sh07
SH06_001.wdf
SH06_002.wdf
SH06_003.wdf
SH06_004.wdf
SH06_005.wdf
SH06_007.wdf
SH06_008.wdf
SH06_009.wdf
SH06_010.wdf
Counts
Raman shift / cm-1

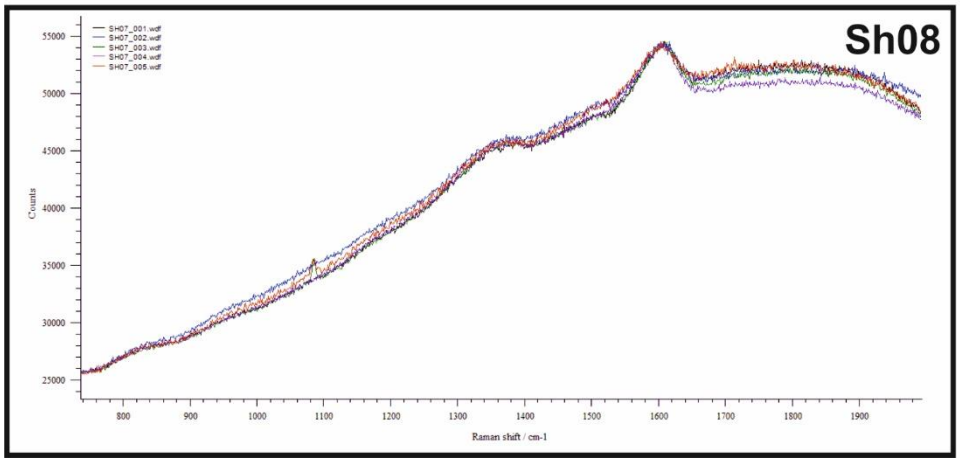
Sh08
SH07_001.wdf
SH07_002.wdf
SH07_003.wdf
SH07_004.wdf
SH07_005.wdf
Counts
Raman shift / cm-1

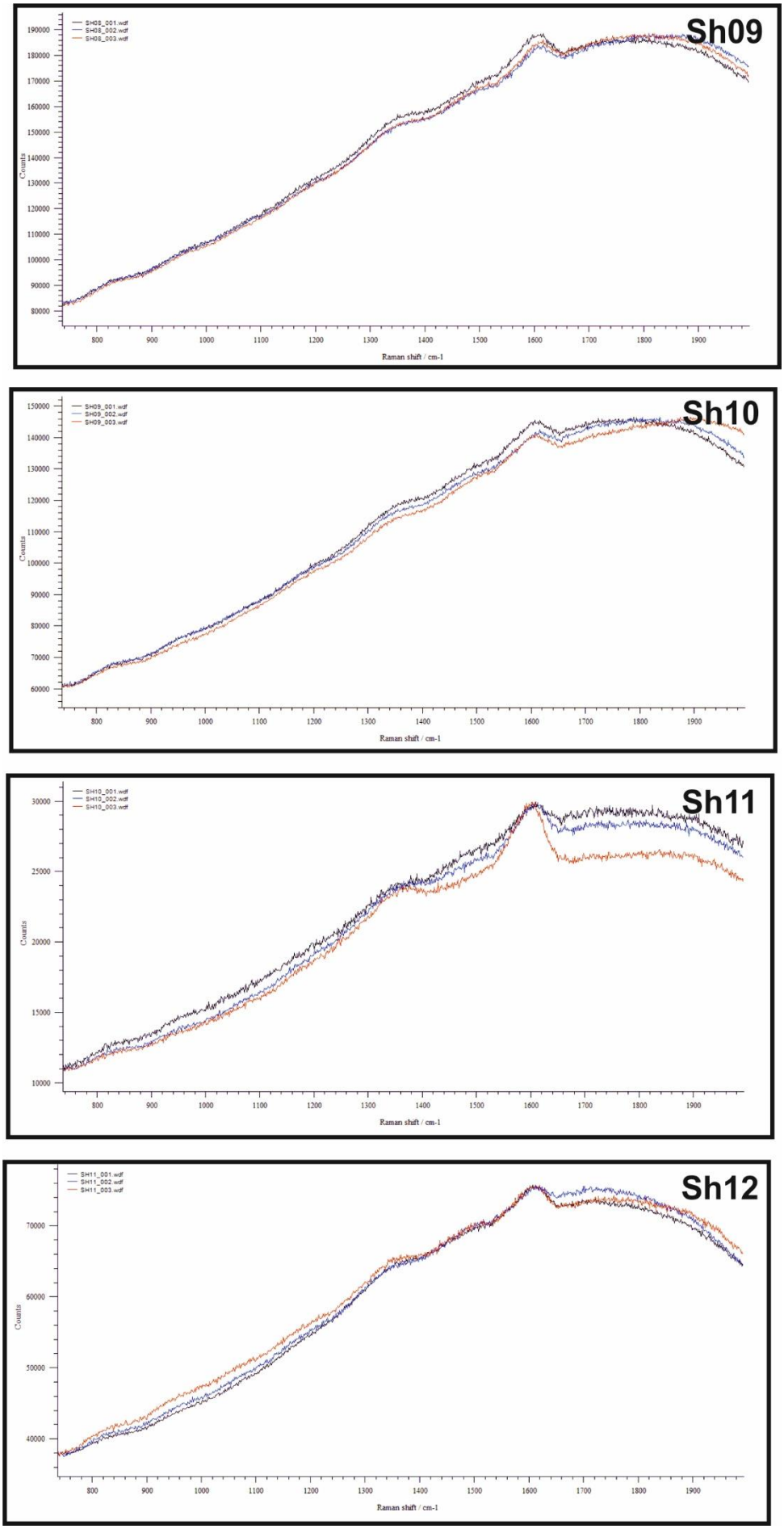

Figure 11.2: Raman peak spectra for each shale sample from the St. Monans host-rock.

Sample No.	SM001	SM002	SM003	SM004	SM005	SM006	SM007	SM008	SM009	SM010	SM011	SM012
Distance from diatreme margin (m)	0	0.45	0.96	2.9	5.5	16.5	39.9	80.5	115.8	143.1	208	511
Homogenisation T (°C)	no sample	>330	no sample	233	125	no sample	63	66	not many	66	too altered	64
		>330		241	133		65	64	inclusions	83		69
		>330		231	136		62	65	66	77		69
		>330		123	125		57	65		62		78
		>330		278	161		62	68		74		60
		>330		134	132		68	66		68		57
				125	116		64	68		73		74
				231	139		69	64		61		62
				238	138		68	67				55
				281	125		65	68				65
					139		65	65				
							64	63				
							66	67				
							63	68				
							65	64				
							64	66				
							63	70				
							63	69				
							61	66				
							63	69				
Mean		330		211.5	133.5455		64	66.4	66	70.5		65.3
Median		>330		232	133		64	66	66	70.5		64.5
Standard Dev				60.89016	12.18378		3.591657	1.595131		7.615773		7.303728

Table 10.2: Fluid inclusion data for all sandstone samples from the St. Monans host-rock.